U.PORTO
FACULDADE DE CIÊNCIAS
UNIVERSIDADE DO PORTO

PhD

On the relation between magnetic activity and stellar oscillations

Ângela Raquel Gonçalves dos Santos

Tese de Doutoramento apresentada à
Faculdade de Ciências da Universidade do Porto,
Instituto de Astrofísica e Ciências do Espaço,
Astronomia

2017

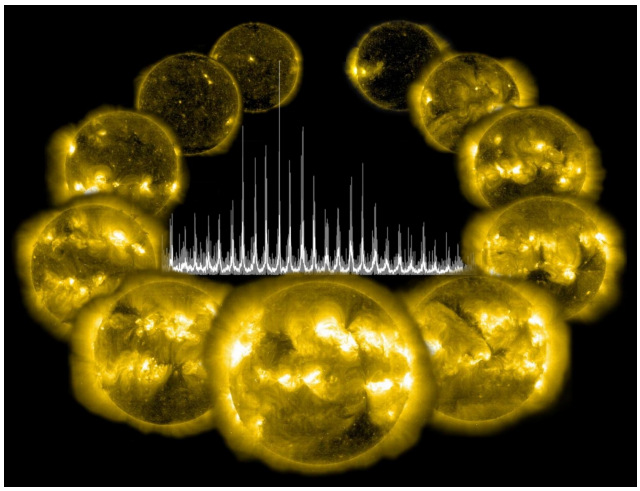

On the relation between magnetic activity and stellar oscillations

Ângela Raquel Gonçalves dos Santos
Plano Doutoral em Astronomia
Departamento de Física e Astronomia
2007

Orientador
Margarida Salvador Cunha
Instituto de Astrofísica e Ciências do Espaço

Coorientador
William James Chaplin
School of Physics and Astronomy, University of Birmingham

PhD

Title page:
Extreme ultraviolet images of the Sun over the solar cycle 23 – Image credits: SOHO (ESA & NASA) – and solar power spectrum obtained from VIRGO/SPM data.

Abstract

In the Sun, as the magnetic cycle progresses and the activity level increases, the frequencies of the solar acoustic modes are observed to increase. Although the activity-related frequency variations have been known since the mid 1980s, the different contributions and their relative importance to the observed variations are not completely understood. These activity-related variations are expected to be common among solar-type pulsators. In fact, evidences for such signature of the magnetic activity were reported for nine solar-type stars so far.

With the above in mind, my Thesis project includes theoretical and observational work, aimed at a better understanding of the relation between the stellar magnetic activity and the stellar oscillations.

We derive an empirical model to estimate the spot-induced frequency shifts, which takes into account the sunspot properties, such as area and latitude. The comparison between the model predictions obtained from the daily sunspot records and the observed frequency shifts suggests that the contribution from the stochastic spot-induced component to the total frequency shifts is about 30%. The remaining 70% are related with a global long-term component, interpreted as a result of the changes in the solar overall magnetic field.

We also propose a new observable to investigate the short- and mid-term variations of the frequency shifts, which is insensitive to the long-term variations contained in the data. On the shortest time scales the variations in the frequency shifts are strongly correlated with the variations in the total area covered by sunspots. However, a significant loss of correlation is still found, which cannot be fully explained by the ignoring of the far-side of the Sun when accounting for the total sunspot area. We also verify that the epochs when the frequency shifts and the sunspot areas do not vary in a similar way tend to coincide with the epochs of the maximum of the quasi-biennial variations found in the seismic data.

Also, we develop a parameterized model to simulate the properties of the spot distribution (e.g. number of spots, spot areas and lifetimes, and spot latitudes) over an activity cycle. The tool was applied to the solar cycle and has been useful to study the frequency shifts. The spot cycle model has, however, other possible applications, such as in the context of the study of the spot modulation in the stellar light curves and/or in the context of searching for exoplanets.

We also study the impact of the starspots on the stellar light curves and resulting periodograms. The (quasi-)periodic spot modulations enclose important information about the stellar surface (differential) rotation and stellar magnetic properties. Recently, Reinhold & Arlt proposed a method based on the periodogram analysis of the light curve to identify the sign of the differential rotation, i.e. whether the equator rotates faster than the poles or the opposite. We find that, under some conditions, the periodogram anlaysis can actually provide an estimate of the spot latitudes and/or the stellar inclination angle. Moreover, we find that the impact of the spot on the ratio between the heights of the second and first harmonics of the main peaks in the periodogram can be described by a single parameter, the relative visibility time of the spot. Finally, we also identify possible sources of false positives/negatives for the sign of the differential rotation.

The observational component of the Thesis is focused on the detection and characterization of magnetic cycles through asteroseismology. We make use of the unprecedented high quality long-term photometric time-series obtained by *Kepler* to search for activity-related temporal variations in the frequencies of the acoustic modes. To do so, we develop a Bayesian peak-bagging tool to perform a global fit of the acoustic modes. After validating the tool with solar data, we have analysed a large sample of *Kepler* solar-type stars. We find that some of those targets show evidence for periodic changes in the acoustic frequencies.

Key words: Sun: activity – Sunspots – Sun: oscillations – asteroseismology – stars: solar-type – stars: activity – stars: rotation – starspots – stars: oscillations – method: data analysis

Resumo

No Sol, à medida que o ciclo de actividade magnética avança e o nível de actividade aumenta, as frequências dos modos acústicos também aumentam. Embora as variações nas frequências acústicas, como resultado da actividade solar, sejam conhecidas desde meados dos anos 1980, as diferentes contribuições e a sua importância relativa não são completamente compreendidas. Espera-se que este tipo de variações sejam comuns em estrelas semelhantes ao Sol. De facto, até à data, foram reportadas evidências de tal assinatura da actividade magnética em nove estrelas do tipo solar.

Tendo isto em mente, o meu projecto de Tese é composto por trabalho teórico e observacional, ambos dedicados a uma melhor compreensão da relação entre as propriedades magnéticas e as oscilações das estrelas.

Nós deduzimos um modelo empírico para estimar os desvios nas frequências acústicas induzidas por manchas solares. O modelo inclui diferentes propriedades das manchas, tais como a sua área e latitude. A comparação entre as previsões teóricas, obtidas através dos registos diários das manchas solares, e os desvios nas frequências observados sugere que a contribuição da componente associada ao efeito das manchas e que varia em escalas de tempo curtas constitui cerca de 30% dos desvios totais. Os restantes 70% resultam de uma componente que varia em escalas de tempo longas e que resulta do efeito do campo magnético solar global.

Também propomos uma nova observável para estudar as variações nas frequências acústicas em escalas de tempo curtas e intermédias. Esta observável não é afectada pelas variações em escalas de tempo longas contidas nos dados. Encontramos que, na escala de tempo mais curta, as variações nas frequências estão fortemente correlacionadas com as variações na área coberta por manchas solares. Contudo, existe ainda uma perda de correlação significativa que não pode ser explicada apenas pelo facto de ignorarmos o lado invisível do Sol aquando do cálculo da área coberta por manchas. Também verificamos que as épocas em que a área coberta por manchas e os desvios nas frequências se comportam de maneira diferente tendem a coincidir com momentos de máximo da variação quase bianual que foi detectada nas frequências dos modos acústicos do Sol em trabalhos anteriores.

Desenvolvemos também um modelo paramétrico para simular as propriedades da distribuição de manchas (e.g. número de manchas, área e tempos de vida das manchas, e as suas latitudes) ao longo de um ciclo de actividade magnética. A ferramenta foi aplicada ao ciclo solar e tem vindo a ser útil para o estudo dos desvios nas frequências acústicas que resultam da actividade magnética. O modelo do ciclo de manchas tem, contudo, outras possíveis aplicações, tais como no contexto do estudo da modelação das curvas de luz de estrelas causada por manchas que atravessam o seus discos visíveis e/ou no contexto da procura de planetas extra-solares.

Para além disso, nós também investigamos o impacto das manchas nas curvas de luz das estrelas e no periodograma resultante. As modelações (quase) periódicas contêm informação importante a cerca da rotação (diferencial) da superfície estelar e das propriedades magnéticas da estrela. Recentemente, Reinhold & Arlt proposeram um método, baseado na análise de periodogramas de curvas de luz, para

identificar o sinal de rotação diferencial, i.e. se o equador roda mais rápido do que os pólos ou o oposto. Encontramos que, sob algumas condições, o periodograma pode na verdade fornecer uma estimativa da latitude das manchas e/ou do ângulo de inclinação da estrela. Também encontramos que o impacto das manchas no rácio das alturas do segundo e primeiro harmónicos do período de rotação pode ser descrito por um parâmetro apenas, o tempo de visibilidade relativo das manchas. Finalmente, também identificamos possíveis causas para falsos positivos/negativos do sinal de rotação diferencial.

A componente observacional da Tese foca-se na detecção e caracterização de ciclos magnéticos das estrelas através da astrossismologia. Nós fazemos uso das, sem precedente, séries temporais fotométricas de elevada qualidade e de longa duração obtidas pelo satélite *Kepler* para procurar variações temporais nas frequências dos modos acústicos causadas pela actividade magnética das estrelas. Para tal, desenvolvemos uma ferramenta Bayesiana capaz de fazer um ajuste global dos modos acústicos. Depois de validar a ferramenta com dados solares, nós analisamos uma larga amostra de estrelas do tipo solar observadas pelo satélite *Kepler*, encontrando evidências para variações periódicas nas frequências acústicas de algumas estrelas.

Palavras-chave: Sol: actividade – manchas solares/estelares – Sol: oscilações – astrossismologia – estrelas: tipo solar – estrelas: actividade – estrelas: rotação – estrelas: oscilações – método: análise de dados

Acknowledgments

First of all, I would like to thank my supervisors, Margarida Cunha and William Chaplin, for their guidance, advice, and support throughout these years. I am also extremely grateful to Tiago Campante and Pedro Avelino, both were a determinant help and support for the work developed in this Thesis.

I am also grateful to my colleagues and collaborators, Rafael García, Savita Mathur, Mikkel Lund, and René Kiefer. I thank also the Professors and my colleagues at Instituto de Astrofísica e Ciências do Espaço, in particular my office mates, for the useful discussions.

I am very grateful to Instituto de Astrofísica e Ciências do Espaço for hosting and supporting me during this journey. I have to thank University of Birmingham and my colleagues from there for hospitality and support. I also acknowledge University of Birmingham's BlueBEAR HPC service for providing the computational facilities for the demanding peak-bagging analysis. Also, I am very grateful for the support from the High Altitude Observatory and the colleagues there.

I acknowledge the support from Fundação para a Ciência e a Tecnologia (FCT) through the Fellowship SFRH/BD/88032/2012.

I also thank all team mates and coaches I had since I started my PhD, namely in the Faculty of Sciencies' team, in Alfa Académico Clube, and in Atlético Clube Alfenense.

Last but not the least, I thank for all the love, friendship, support, and motivation from my friends and family (including those with fluffy paws).

Obrigada!

Contents

List of Figures

List of Tables

List of Publications

Refereed papers

- "Starspot signature on the light curve: Learning about the latitudinal distribution of spots"
  A. R. G. Santos, M. S. Cunha, P. P. Avelino, R. A. García, & S. Mathur, 2017
  Astronomy & Astrophysics, 599, A1
  DOI: 10.1051/004-6361/201629923

- "A thorough analysis of the short- and mid-term activity-related variations in the solar acoustic frequencies"
  A. R. G. Santos, M. S. Cunha, P. P. Avelino, W. J. Chaplin, & T. L. Campante, 2017
  Monthly Notices of the Royal Astronomical Society, 464, 4408
  DOI: 10.1093/mnras/stw2716

- "On the contribution of sunspots to the observed frequency shifts of solar acoustic modes"
  A. R. G. Santos, M. S. Cunha, P. P. Avelino, W. J. Chaplin, & T. L. Campante, 2016
  Monthly Notices of the Royal Astronomical Society, 461, 224
  DOI: 10.1093/mnras/stw1348

- "Spin-Orbit Alignment of Exoplanet Systems: Ensemble Analysis Using Asteroseismology"
  T. L. Campante, M. N. Lund, J. S. Kuszlewicz, G. R. Davies, W. J. Chaplin, et al., 2016
  The Astrophysical Journal, 819, 85
  DOI: 10.3847/0004-637X/819/1/85

- "Spot cycle reconstruction: an empirical tool: Application to the sunspot cycle"
  A. R. G. Santos, M. S. Cunha, P. P. Avelino, & T. L. Campante, 2015
  Astronomy & Astrophysics, 580, A62
  DOI: 10.1051/0004-6361/201425299

Conference proceedings

- "On the relation between activity-related frequency shifts and the sunspot distribution over the solar cycle 23"

  A. R. G. Santos, M. S. Cunha, P. P. Avelino, W. J. Chaplin, & T. L. Campante, 2017

  EPJ Web of Conferences, in press [arXiv:1611.07475]

  https://arxiv.org/abs/1611.07475

- "Learning about the latitudinal distribution of starspots through the periodogram analysis of photometric data"

  A. R. G. Santos, M. S. Cunha, P. P. Avelino, R. A. García, & S. Mathur, 2017

  EPJ Web of Conferences, in press [arXiv:1611.07464]

  https://arxiv.org/abs/1611.07464

- "Empirical solar/stellar cycle simulations"

  A. R. G. Santos, M. S. Cunha, P. P. Avelino, 2015

  EPJ Web of Conferences, Volume 101, id.06055

  DOI: 10.1051/epjconf/201510106055

- "Empirical solar/stellar cycle simulations"

  A. R. G. Santos, M. S. Cunha, P. P. Avelino, 2014

  Proces. of ENAA XXIV, page 38

  feupload.fe.up/get/7Csonj1nXzHKoN1

1. Introduction: Solar-type pulsators

Periodic variations in the luminosity of stars have been known for centuries, since Jan Fokkens Holwarda found, in 1638, that the magnitude of the star Mira varies with a periodicity of 11 months (e.g. Hoffleit 1997). However, only in the twentieth century, it was understood that these variations are intrinsic to the stars and are due to stellar oscillations (Shapley 1914). About at the same time, Henrietta Leavitt noticed that Cepheids with longer periods are more luminous than those with shorter periods (Leavitt 1908; Leavitt & Pickering 1912). Her discovery, known as the Period-Luminosity relation, allows for the determination of the distance to those stars.

Acoustic oscillations were first discovered in the Sun by Leighton et al. (1962) and later interpreted by Ulrich (1970) and Leibacher & Stein (1971). Currently, acoustic solar-type oscillations are known for a large number of stars other than the Sun. The study of the solar/ stellar oscillations - Helioseismology/Asteroseismology - provides a unique way to "look" inside the stars and probe directly their internal structure and dynamics, such as internal rotation, composition, and age.

Acoustic oscillations (or p-modes, since pressure is the restoring force) travel through the stellar interior with the sound speed, being stochastically excited by near-surface turbulent convection. Therefore, stars that are cool enough to harbor convective outer layers, such as low-mass main-sequence stars, are expected to exhibit solar-type oscillations.

For a spherical, non-rotating star, the stellar oscillations can be expressed, in spherical polar coordinates, in terms of the spherical harmonics as (e.g. Christensen-Dalsgaard 2003)

$$\xi_r(r,\theta,\phi;t) = \sqrt{4\pi}\tilde{\xi}_r(r)\,Y_l^m(\theta,\phi)\exp(-i2\pi\nu t), \tag{1.1}$$

where ξ_r is the radial component of the displacement, $\tilde{\xi}_r$ is an amplitude function of r, ν is the linear oscillation frequency, and Y_l^m are the spherical harmonics (some examples are illustrated in Fig. 1.1 - Fig. from Christensen-Dalsgaard 2003).

Each oscillation mode is characterized by three wave numbers n, l, and m. The radial order n is related to the number of nodes in the radial direction, the angular degree l gives the number of nodes on surface, and the azimuthal order m measures the number of nodes along the equator and takes values between $-l \leq m \leq l$.

The study of the solar oscillations can be split into two categories: local and global helioseismology. Local helioseismology studies the local properties of the wave propagation, while the global helioseismology (on which this Thesis is mainly focused) studies the global oscillation modes of the Sun. In turn, global helioseismology makes use of two types of observations: Sun-as-a-star (unresolved) and resolved observations[1]. Sun-as-a-star observations, that detect the integrated sunlight, are only sensitive to the lowest angular degree modes (mostly $l \leq 3$) averaging the oscillation modes over the solar disc. Furthermore, the frequencies of the $2l+1$ azimuthal components of a given (n,l)

[1] A comparison between the oscillation frequencies of low-degree modes obtained from Sun-as-a-star and resolved observations is made in Chaplin et al. (2004a).

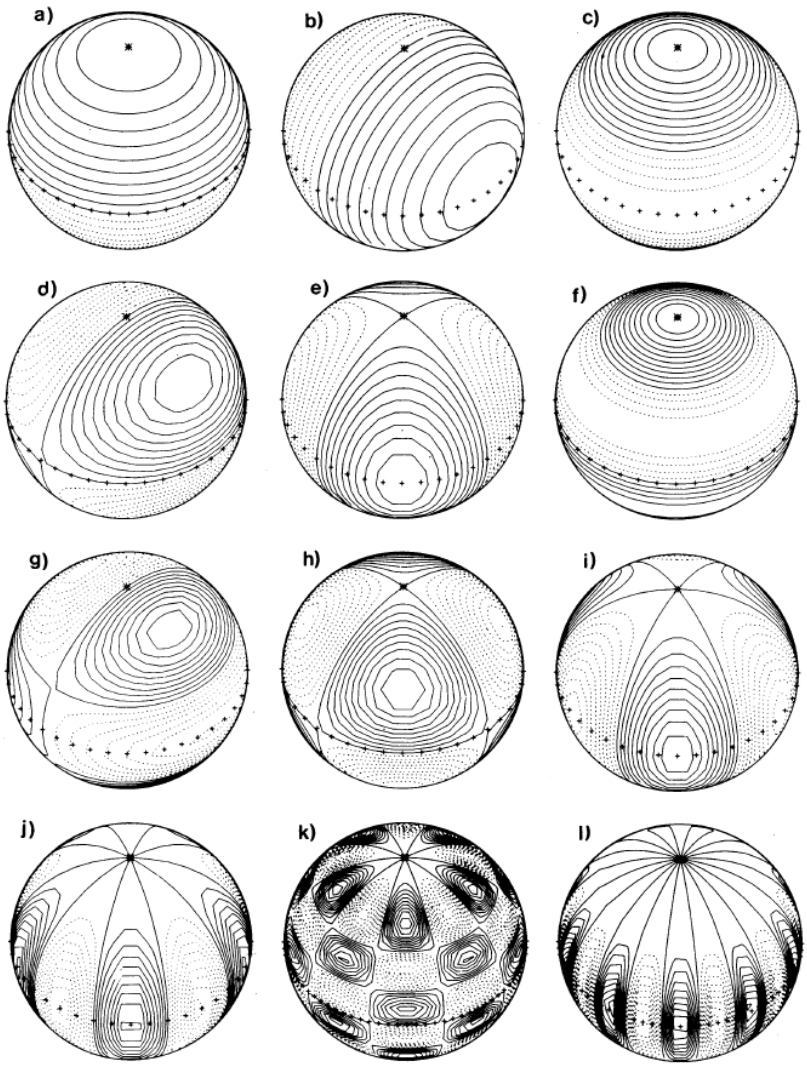

Fig. 1.1 – Contour plots of the real part of the spherical harmonics for: a) $l = 1$, $m = 0$; b) $l = 1$, $m = 1$; c) $l = 2$, $m = 0$; d) $l = 2$, $m = 1$, e) $l = 2$, $m = 2$; f) $l = 3$, $m = 0$; g) $l = 3$, $m = 1$; h) $l = 3$, $m = 2$, i) $l = 3$, $m = 3$; j) $l = 5$, $m = 5$; k) $l = 10$, $m = 5$; l) $l = 10$, $m = 10$. The solid and dashed lines indicate the positive and negative contours, respectively. The stellar equator is marked by then plus signs. Figure from Christensen-Dalsgaard (2003).

multiplet will hardly be distinguishable (see Sect. 1.2.1). Sun-as-a-star observations are obtained, for example, with BiSON (ground-based Birmingham Solar-Oscillations Network; Aindow et al. 1988; Elsworth et al. 1995; Chaplin et al. 1996), GOLF (Global Oscillations at Low Frequencies; Gabriel et al. 1995) on board SOHO (SOlar and Heliospheric Observatory), and VIRGO/SPM (Variability of solar IRradiance and Gravity Oscillations, where SPM stands for sunphotometers; Fröhlich et al. 1995, 1997; Jiménez et al. 2002) also on board SOHO. Resolved observations as those obtained with the ground-based Global Oscillations Network Group (GONG; Harvey et al. 1996), where the solar visible disc is imaged over many pixels, allow to detect high-degree modes and their $2l + 1$ azimuthal components.

1.1 Properties of the acoustic modes

Neglecting the perturbation to the gravitational potential (Cowling approximation) and assuming that locally the derivatives of gravity and radius can be neglected, linear adiabatic oscillations can be described by the wave equation (e.g. Deubner & Gough 1984; Gough 1993)

$$\frac{d^2\Xi}{dr^2} + K\Xi = 0, \tag{1.2}$$

where $\Xi = c^2\rho^{1/2}\nabla\cdot\vec{\xi}$, $c = \sqrt{\gamma p/\rho}$ is the adiabatic sound speed, γ is the adiabatic exponent, p and ρ are the gas pressure and density, and

$$K(r) = \frac{\omega^2}{c^2}\left[1 - \frac{\omega_c^2}{\omega^2} - \frac{S_l^2}{\omega^2}\left(1 - \frac{\mathcal{N}^2}{\omega^2}\right)\right] \equiv \frac{\omega^2}{c^2}\left(1 - \frac{\omega_{l,+}^2}{\omega^2}\right)\left(1 - \frac{\omega_{l,-}^2}{\omega^2}\right), \tag{1.3}$$

where ω is the mode angular frequency ($\omega = 2\pi\nu$), S_l is the acoustic (or Lamb) frequency, $\mathcal{N}$ is the bouyancy (or Brunt-Väisälä) frequency, ω_c is the cut-off frequency, and $\omega_{l,\pm}^2$ are the critical frequencies given by $\omega_{l,\pm}^2 = 1/2\left(S_l^2 + \omega_c^2\right) \pm \left[1/4\left(S_l^2 + \omega_c^2\right) - \mathcal{N}^2 S_l^2\right]^{1/2}$. The behaviour of the oscillation mode is, thus, determined by the characteristic frequencies defined as

$$S_l^2 = \frac{l(l+1)c^2}{r^2}, \tag{1.4}$$

$$\mathcal{N}^2 = g\left(\frac{1}{\gamma}\frac{d\ln p}{dr} - \frac{d\ln\rho}{dr}\right), \tag{1.5}$$

$$\omega_c^2 = \frac{c^2}{4H^2}\left(1 - 2\frac{dH}{dr}\right), \tag{1.6}$$

where $H = -(d\ln\rho/dr)^{-1}$ is the density scale height. For a fully ionized ideal gas (good approximation for most of the stars), the sound speed can be expressed as

$$c^2 \simeq \frac{5}{3}\frac{k_B T}{\mu m_u}, \tag{1.7}$$

where k_B is the Boltzmann's constant, T is the temperature, μ is the mean molecular weight, and m_u is the atomic mass unit.

Figure 1.2 shows the propagation diagram for a model of the Sun (Fig. taken from Christensen-Dalsgaard 2003). The oscillation mode propagates where $K(r) > 0$ (where $\omega > \omega_{l,+}$ or $\omega < \omega_{l,-}$) and is evanescent, varying exponentially, where $K(r) < 0$ (where $\omega_{l,-} < \omega < \omega_{l,+}$). The observed frequencies of the acoustic modes in a main-sequence, solar-like pulsator are typically much larger than the Brunt-Väisälä frequency, i.e. $\omega \gg \mathcal{N}$. Moreover, near the surface, $S_l \ll \omega$ and the behaviour of the acoustic mode is determined by the cut-off frequency ω_c, which is very small in the remainder of the star. Therefore, in the interior of the Sun $\omega_{l,+} \simeq S_l$ and $\omega_{l,-} \simeq \mathcal{N}$, while near the surface $\omega_{l,+} \simeq \omega_c$ and $\omega_{l,-}$ is small. Thus, for acoustic modes, except near the surface where ω_c becomes dominant over S_l, we may rewrite equation (1.3) as

$$K(r) \simeq \frac{1}{c^2}\left(\omega^2 - S_l^2\right), \tag{1.8}$$

where $K = \kappa^2$, and κ being the radial component of the acoustic wave number. The horizontal component of the wave number corresponds to $\kappa_h = S_l/c$, i.e.

$$\kappa_h^2 = \frac{l(l+1)}{r^2}. \tag{1.9}$$

The upper turning point of the acoustic modes is determined by the cut-off frequency and corresponds to the radius where $\omega = \omega_c$, while the lower turning point is located at r_t where $\omega = S_l$, i.e. where

$$\frac{c(r_t)^2}{r_t^2} = \frac{\omega^2}{l(l+1)}. \tag{1.10}$$

The acoustic modes are thus trapped between the lower turning point r_t, which is very small for low-degree modes, and essentially the stellar surface.

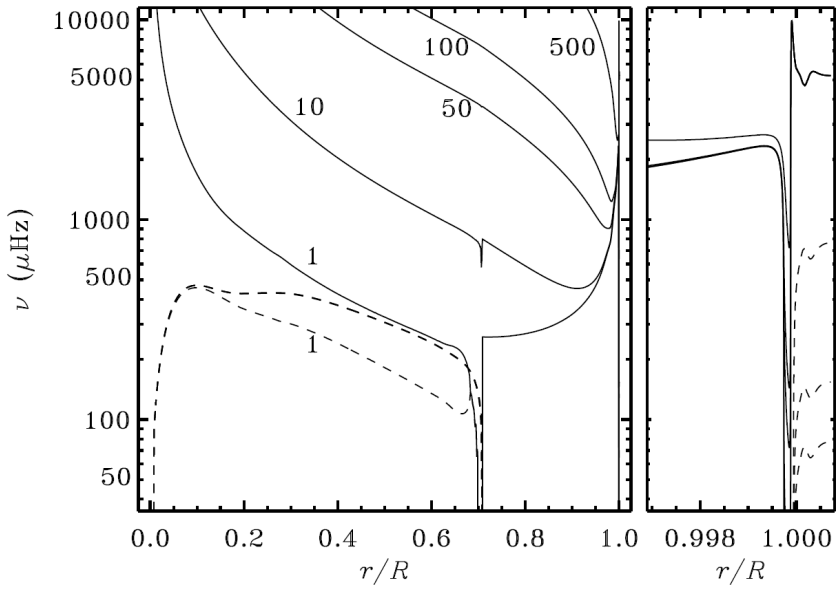

Fig. 1.2 – Propagation diagram for a model of the Sun and modes of degree $l = 1, 50, 100, 500$. The solid and dashed lines correspond to the critical frequencies $\omega_{l,+}/(2\pi)$ and $\omega_{l,-}/(2\pi)$, respectively. An acoustic mode of degree l and frequency ν propagates where $\nu > \omega_{l,+}/(2\pi)$. Figure from Christensen-Dalsgaard (2003).

The acoustic frequencies of low-degree modes ($\nu_{nl} = \omega_{nl}/(2\pi)$) satisfy, to first order, the following asymptotic relation (e.g. Vandakurov 1967; Tassoul 1980)

$$\nu_{nl} \sim \Delta\nu \left(n + \frac{l}{2} + \epsilon \right), \tag{1.11}$$

where ν_{nl} is the frequency of a given (n, l) mode , ϵ depend on the frequency and is determined by the conditions near the stellar surface, and $\Delta\nu$ is the inverse sound travel time over the stellar diameter

$$\Delta\nu = \left(2 \int_0^{R_\star} \frac{dr}{c} \right)^{-1}, \tag{1.12}$$

where $R_\star$ is the stellar radius.

Equation (1.11) predicts that modes of same angular degree l are uniformly spaced in frequency and the difference between modes of same l and consecutive n, i.e.

$$\Delta\nu_{nl} = \nu_{n+1\,l} - \nu_{nl} \sim \Delta\nu, \tag{1.13}$$

is known as the large frequency separation. Also, from equation (1.11), the frequencies of modes with degree of same parity are degenerated, i.e. $\nu_{nl} \simeq \nu_{n-1\,l+2}$. Finally, even and odd modes are uniformly spaced by $\Delta\nu/2$.

The second order departure from equation (1.11) leads to the existence of a small frequency separation between the almost degenerate modes,

$$d\nu_{nl} = \nu_{nl} - \nu_{n-1\,l+2} \simeq -(4l+6)\frac{\Delta\nu}{4\pi^2\nu_{nl}}\int_0^{R_\star}\frac{dc}{dr}\frac{dr}{r}. \tag{1.14}$$

Figure 1.3 shows the power density spectrum of the Sun, where the regular pattern of the solar-type oscillations is clearly seen.

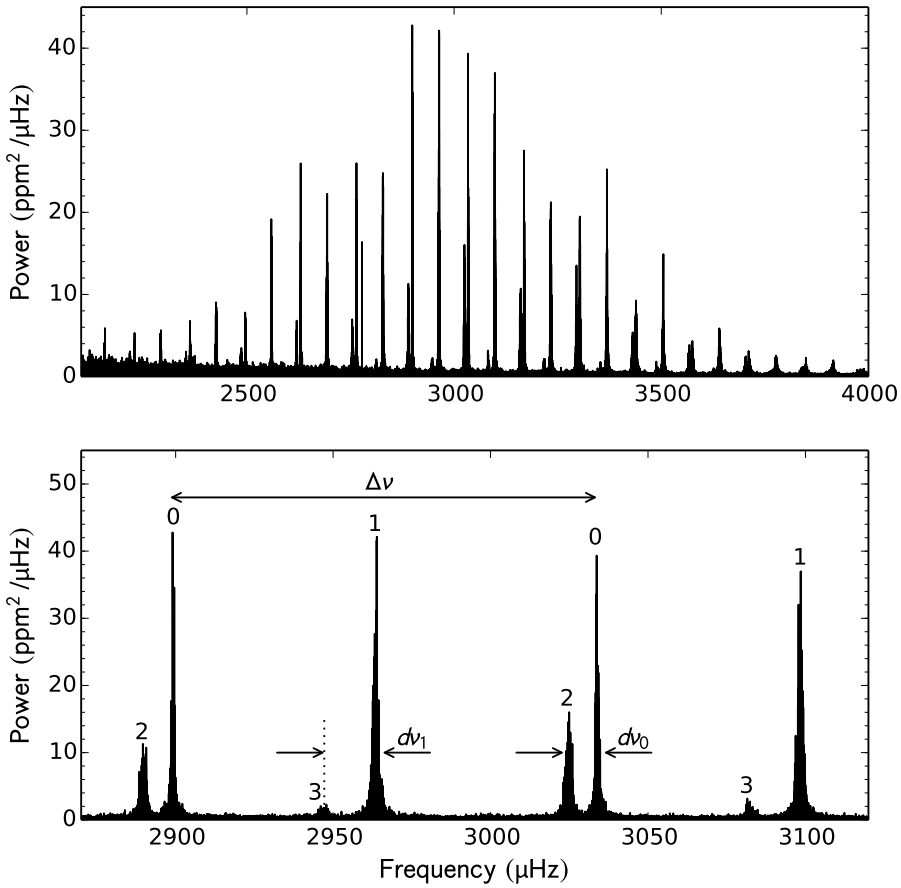

Fig. 1.3 – Top: Power density spectrum of the Sun corresponding to the frequency range of the acoustic oscillations. Bottom: Close-up of the central part of the frequency range of the top panel. Each oscillation mode is marked by its angular degree (i.e $l = 0$, 1, 2, or 3), and the large and small frequency separations ($\Delta\nu$, $d\nu_0$, and $d\nu_1$) are indicated by the arrows. The power spectrum was obtained from VIRGO/SPM data.

The regular spacing of the solar-type oscillations is the basis of the échelle diagram (first proposed by Grec et al. 1983), which is commonly used as a diagnostic tool. Here the mode frequencies are expressed as

$$\nu_{nl} = \nu_0 + k\Delta\nu + \tilde{\nu}_{nl}, \tag{1.15}$$

where ν_0 is a reference frequency, k is an integer, and $\tilde{\nu}_{nl}$ is the reduced frequency taking values between 0 and $\Delta\nu$. The échelle diagram corresponds to plotting $\nu_0 + k\Delta\nu$ as a function of the reduced frequency. If the mode frequencies obey the asymptotic relation given in equation (1.11), modes of same angular degree will form vertical ridges in the échelle diagram. However, this relation does not hold exactly, as the large frequency separation depends on the angular degree and frequency. An example of the échelle diagram is shown in Fig. 1.4 (Fig. from Davies et al. 2016) for the solar-type star KIC 11295426.

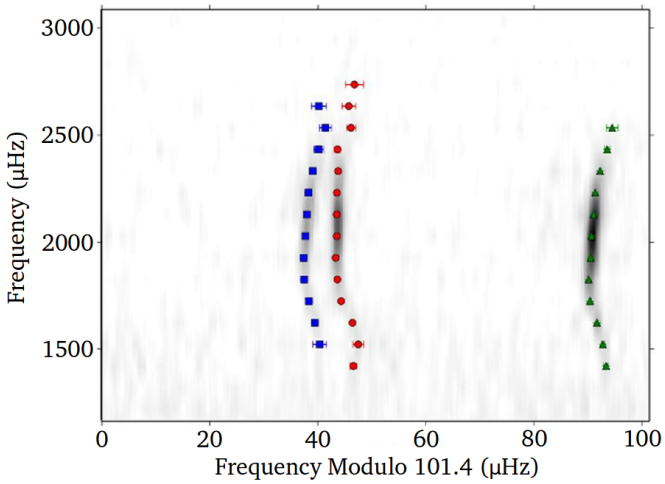

Fig. 1.4 – Échelle diagram for the solar-type pulsator KIC 11295426. The power spectrum is given in grey scale from white (low power) to black (high power). The radial ($l = 0$), dipole ($l = 1$), and quadrupole ($l = 2$) modes are marked by the red circles, green triangles, and blue squares, respectively. Figure from Davies et al. (2016).

The large frequency separation is related with the dynamical timescale of the star, $t_{\rm dyn}$, as

$$\Delta\nu \propto t_{\rm dyn}^{-1} \propto \left(\frac{R_\star^3}{GM_\star}\right)^{-1/2} \propto \langle\rho\rangle^{1/2}, \tag{1.16}$$

where $M_\star$ is the stellar mass and G is the gravitational constant. Therefore, $\Delta\nu$ provides a measure of the mean stellar density.

The small frequency separation is mostly sensitive to the sound-speed structure in the stellar core. As the star evolves and hydrogen is burned into helium in the stellar core, the mean molecular weight increases and the sound speed decreases (equation 1.7), leading to an inversion of the sound speed in the stellar core. In turn, the small separation (equation 1.15) decreases as the star evolves, thus, providing a measure of the evolutionary state of the star.

Figure 1.5 shows the C-D diagram (e.g. Christensen-Dalsgaard 1988), which shows the stellar evolution in terms of the global seismic parameters, $\Delta\nu$ and $d\nu_{nl}$.

Finally, while the small frequency separation is still sensitive to the properties of the near-surface, Roxburgh & Vorontsov (2003) showed that the ratios between the small and large frequency separation, such as

$$r_{02} = \frac{\nu_{n0} - \nu_{n-12}}{\nu_{n1} - \nu_{n-11}}, \tag{1.17}$$

are mostly independent on the surface layers, thus providing a reliable measure of the properties of stellar cores.

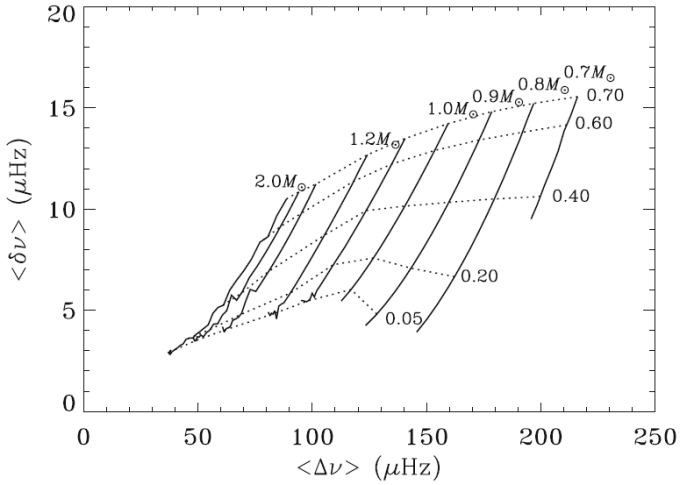

Fig. 1.5 – C-D diagram (e.g. Christensen-Dalsgaard 1988), showing the stellar evolution in terms of the large and small frequency separations. The solid lines show the evolutionary tracks for stellar masses between 0.7 and 2.0 $M_\odot$, while the dotted lines show curves of constant hydrogen abundance ($X_c =$ 0.05, 0.20, 0.40, 0.60, and 0.70). Figure from Cunha et al. (2007).

1.2 Power spectrum of a solar-type pulsator

The acoustic modes are stochastically excited and intrinsically damped. Therefore, they can be described by a damped harmonic oscillator driven by a random forcing function (e.g. Duvall & Harvey 1986; Anderson et al. 1990), whose equation is given by

$$\frac{d^2y}{dt^2} + 2\eta\frac{dy}{dt} + \omega_0^2 y(t) = x(t), \tag{1.18}$$

where $y(t)$ is the displacement, $x(t)$ is the forcing function, ω_0 is the undamped oscillator angular frequency, and η is the constant describing the damping.

If $Y(\omega)$ and $X(\omega)$ are the Fourier transforms of the functions $y(t)$ and $x(t)$ given by

$$\begin{aligned} Y(\omega) &= \int y(t) e^{i\omega t} dt, \\ X(\omega) &= \int x(t) e^{i\omega t} dt, \end{aligned} \tag{1.19}$$

the Fourier transform of equation (1.18) becomes

$$\left(\omega_0^2 - \omega^2 + 2i\eta\omega\right) Y(\omega) = X(\omega). \tag{1.20}$$

An estimate of the power spectrum of a finite realization (with length $T_{\rm obs}$) of the $y(t)$ process, is given by

$$P(\omega) = |Y(\omega)|^2 = \frac{|X(\omega)|^2}{(\omega_0^2 - \omega^2)^2 + 4\eta^2\omega^2}, \tag{1.21}$$

The power spectrum of a random function is uncorrelated at angular frequency separations of $2\pi/T_{\rm obs}$, and at a fixed frequency, the power spectra of different realizations of $y(t)$ are distributed according to a χ^2 distribution with two degrees of freedom (e.g. Gabriel 1994).

In general, the damping rate η is much smaller than the oscillation frequency, which implies that $\omega \approx \omega_0$. Thus, the limit power spectrum obtained from an infinite number of realizations is given by a Lorentzian profile of the form

$$\langle P(\omega)\rangle \simeq \frac{1}{4\omega_0^2} \frac{\langle X(\omega)\rangle}{(\omega_0 - \omega)^2 + \eta^2}. \tag{1.22}$$

Therefore, the power density spectrum of an acoustic mode (as those seen in Figs. 1.3 and 1.6) can be described by a Lorentzian function.

1.2.1 Effect of stellar rotation

For a spherically symmetric star the mode properties are independent on the azimuthal orders. However, stellar rotation breaks the symmetry and leads to the splitting of the azimuthal components. For a slow rotator, assuming a rigid-body rotation, and neglecting the splitting due to magnetic fields, the frequency of a given (n, l, m) mode is (Ledoux 1951)

$$\omega_{nlm} = \omega_{nl0} + m\langle\Omega\rangle_{nl}(1 - C_{nl}), \tag{1.23}$$

where $\langle\Omega\rangle_{nl}$ is an average of the stellar angular velocity over the interior and depends on the properties of the eigenfunctions in the non-rotating model, and C_{nl} is the Ledoux constant which represents the effect of the Coriolis force. For high-order acoustic modes $C_{nl} < 10^{-2} \ll 1$ (e.g. Gizon & Solanki 2003) and the rotation splitting is well approximated by $\langle\Omega\rangle_{nl}$.

The relative visibility of the different azimuthal components allows for the estimation of the stellar inclination angle (i.e. the angle between the stellar rotation axis and the line of sight). Assuming the energy equipartition between the azimuthal components, the relative visibility, $\mathcal{E}_{lm}$, within the (n, l) multiplet is given by (Gizon & Solanki 2003)

$$\mathcal{E}_{lm} = \frac{(l - |m|)!}{(l + |m|)!} \left[P_l^{|m|}(\cos i)^2\right], \tag{1.24}$$

where $P_l^{|m|}$ are the Legendre functions.

Figure 1.6 shows a close-up of the solar spectrum (from 180-day VIRGO/SPM data). The black line shows the fitted model. The profile of the radial mode (right-hand side) corresponds to a single Lorentzian function, while the profile of the quadrupole mode (left-hand side) combines the different azimuthal components, each described by a Lorentzian profile. Note that for $i \sim 90°$, only the modes with even $|l-m|$ are visible, i.e. for $l=2$, only the $m=\pm 2$ and $m=0$ components are visible.

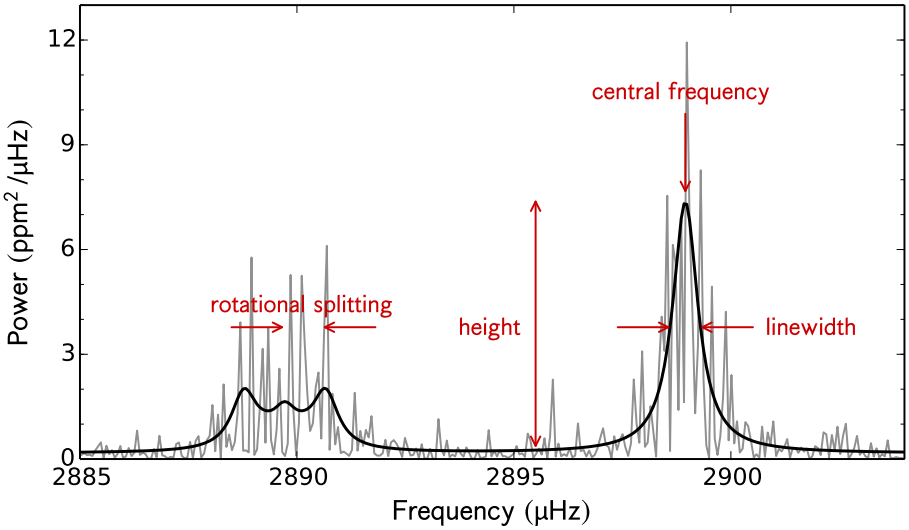

Fig. 1.6 – Power density spectrum from an 180-d VIRGO/SPM time-series (grey). The black solid line shows the fitted model (see Chapter 5). In the left-hand side, the rotational splitting of the azimuthal components of the $l=2$ mode is visible. In the right-hand side, the $l=0$ mode is described by a single Lorentzian profile.

1.3 Activity-related variations in the properties of the solar acoustic modes

The properties of the acoustic modes are sensitive to the physical conditions of the solar interior, including magnetic fields. Therefore, as a result of the solar magnetic cycle, the properties of the acoustic oscillations are observed to vary in a periodic way: as the activity level increases, the mode frequencies and linewidths increase, while the amplitudes decrease (e.g. Woodard & Noyes 1985; Elsworth et al. 1990; Libbrecht & Woodard 1990; Chaplin et al. 1998, 2000; Jiménez et al. 2002; Salabert & Jiménez-Reyes 2006; Metcalfe et al. 2007; Salabert et al. 2015; Howe et al. 2015).

The amplitude of the acoustic modes decreases with increasing magnetic activity. However, the physical mechanism responsible for this decrease is still matter of discussion. On one hand the mode excitation by turbulent convection is less efficient within magnetic regions (e.g. Goldreich & Keeley 1977; Goldreich & Kumar 1988). On the other hand, it has been suggested that the magnetic structures in the solar photosphere are strong absorbers of the acoustic waves (e.g. Braun et al. 1987; Haber et al. 1999; Jain & Haber 2002; Khomenko & Collados 2015; Zhao & Chou 2016; Rabello-Soares et al. 2016), either through scattering of incoming waves or through mode conversion.

The mode linewidths Γ are observed to increase towards the solar maximum, due to an increase on the damping rates ($\eta = \pi\Gamma$; equation 1.22) and, consequently, a decrease in the mode lifetimes

($\tau = 1/\eta$). The activity-related variations in the damping rates are possibly related to changes in the convective motions (Houdek et al. 2001). Figure 1.7 shows the variations of the mode amplitudes and linewidths over the solar cycle 23 (with maximum activity around 2001) obtained from VIRGO/SPM data (Fig. from Salabert et al. 2011a).

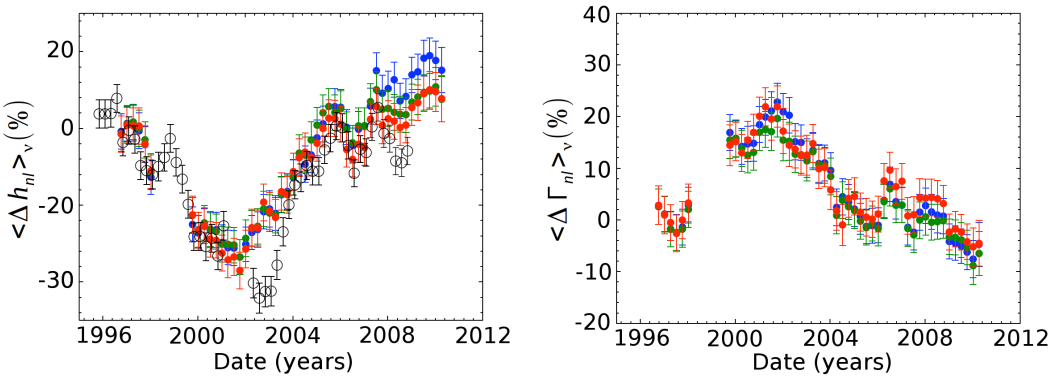

Fig. 1.7 – Activity-related variations in the mode amplitudes (left) and linewidths (right) over the solar cycle 23 obtained from VIRGO/SPM (blue, green, and red symbols corresponding to the blue, green, and red channels) and GONG (open circles) data. Figure from Salabert et al. (2011a).

The acoustic frequencies vary in phase with the activity level, increasing with increasing activity. The frequency variations are also, dependent on the mode degree and frequency (e.g. Libbrecht & Woodard 1990; Elsworth et al. 1994; Chaplin et al. 1998, 2001, 2004b, 2007b; Salabert et al. 2015; Howe et al. 2015). Figure 1.8 shows the activity-related frequency shifts as a function of time, where the dependence on the mode degree and frequency is also clear.

The dependence of the frequency shifts on the mode degree is mainly related to the mode inertia, E_{nl}, defined as (Christensen-Dalsgaard & Berthomieu 1991)

$$E_{nl} = \frac{4\pi}{M_\odot} \int_0^R |\xi|^2 \rho r^2 dr = \frac{M_{nl}}{M_\odot}, \tag{1.25}$$

where R and $M_\odot$ are the solar radius and mass, ξ is the normalized displacement, and M_{nl} is the modal mass (i.e. the "mass" associated with a given mode). At a fixed frequency, M_{nl} and, thus, E_{nl} decrease with increasing degree (e.g. Howe et al. 1999; Chaplin et al. 2001). Therefore, the high-degree modes are more sensitive to the changes associated with the solar magnetic cycle than the low-degree modes. Multiplying the frequency shifts (left panel of Fig. 1.9) by the inertia ratio removes the dependence on the angular degree of the frequency shifts (right panel of Fig. 1.9). Here, the inertia ratio is defined as (Christensen-Dalsgaard & Berthomieu 1991)

$$Q_{nl} = \frac{E_{nl}}{E_0(\nu_{nl})}, \tag{1.26}$$

where $E_0(\nu_{nl})$ corresponds to the inertia of a radial mode ($l = 0$) with frequency ν_{nl}. However, for modes of low-degree (e.g. $l \leq 3$) the variation in the mode inertia is not significant. Therefore, the most important contribution to the l dependence of the frequency shifts for low-degree modes is not the mode inertia, but the latitudinal distribution of the surface magnetic field.

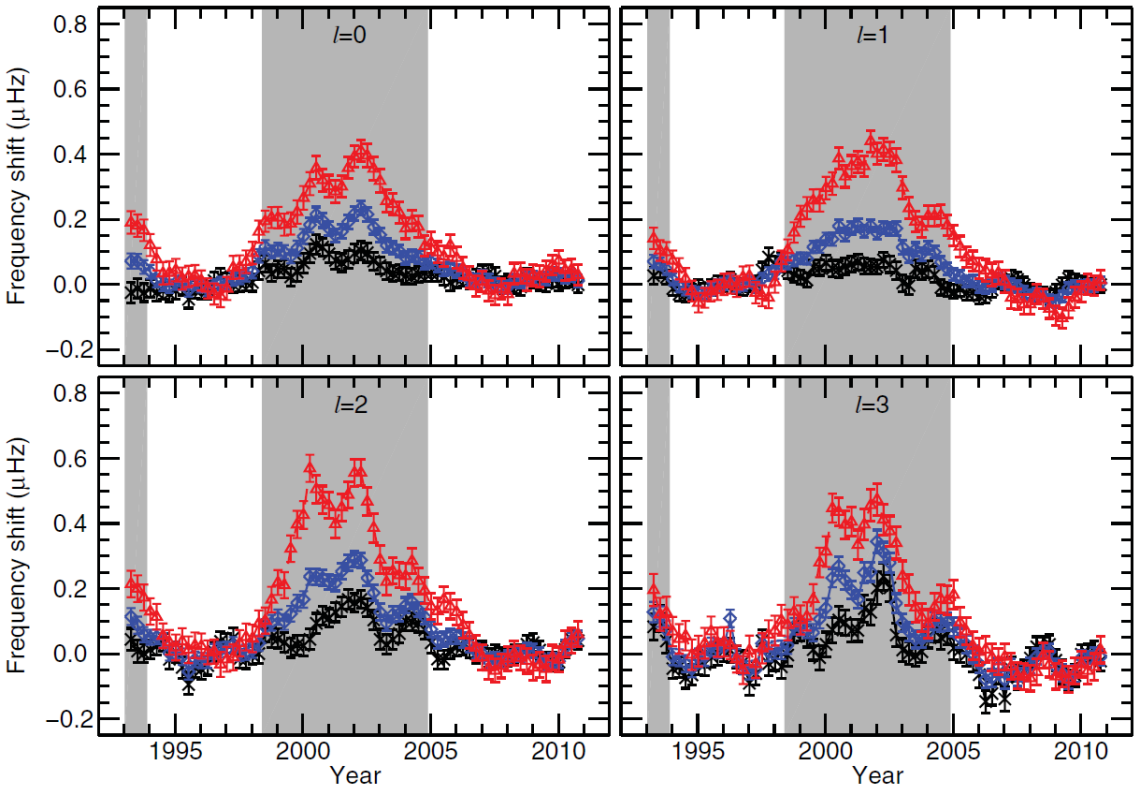

Fig. 1.8 – Frequency shifts obtained from BiSON data for the individual angular degrees ($l = 0$, $l = 1$, $l = 2$, and $l = 3$) and for the total frequency range ($1860 - 3720\,\mu$Hz; blue), low-frequency range ($1860 - 2770\,\mu$Hz; black), and high-frequency range ($2800 - 3720\,\mu$Hz; red). The shaded regions mark the times of high activity level. Figure from Broomhall et al. (2012).

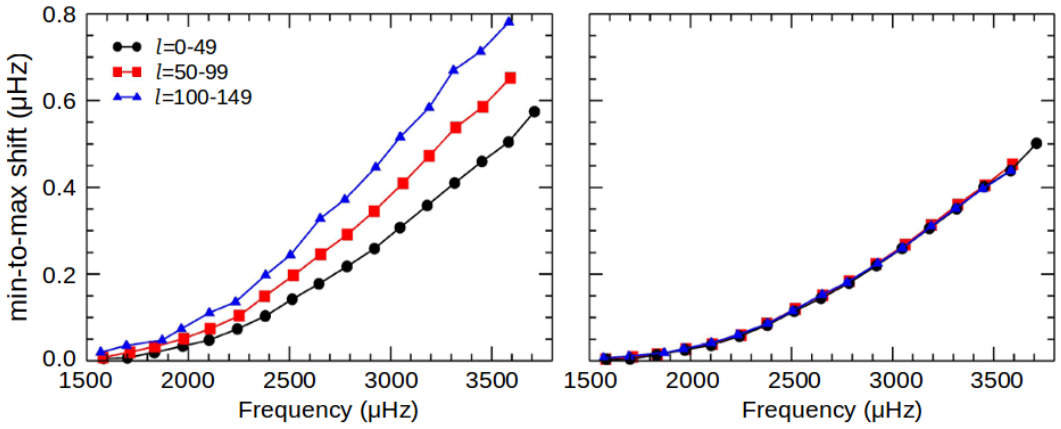

Fig. 1.9 – Frequency shifts, obtained from GONG data, between the solar maximum and the solar minimum as a function of frequency before (left) and after (right) being scaled by the inertia ratio, Q_{nl}. Figure from Broomhall et al. (2014).

The frequency dependence of the frequency shifts (Figs. 1.8 and 1.9) allows us to determine the region where the activity-related changes, that affect the oscillation frequencies, are taking place. The higher-frequency modes have their maximum energy density in upper layers than the lower-frequency

modes and thus, the former are more sensitive to the outermost layers than the latter (e.g. Libbrecht & Woodard 1990; Jiménez et al. 2002; Basu et al. 2012). The frequency dependence of the activity-related frequency shifts suggest, therefore, that those are caused by near-surface changes in the solar magnetism. Furthermore, the oscillation frequencies of modes below $\sim 1800\,\mu$Hz are almost unaffected by the solar cycle, indicating that the origin of the perturbation is located above the upper turning points of these modes (see Fig. 1.2; e.g. Basu et al. 2012), i.e. above $0.996\,R_\odot$.

The activity-related variations in the acoustic frequencies can result from different contributions, whose impact is still not well understood. Magnetic cycles lead to periodic changes in the global magnetic field, as well as in the total area covered by active regions, where sunspots emerge. The impact of the global magnetic field and its associated structural and thermal variations on the oscillations was addressed by, for example, Dziembowski & Goode (2005). The authors argued that the indirect (thermal and structural) effects dominate over the direct effect (Lorentz force), as the magnetic fields in the near-surface layers are generally weak. However, localized regions of strong magnetic field exist, that can also contribute with direct and indirect effects.

From the analysis of observational data, it has been argued that the frequency shifts result from variations of both the weak and strong components of the solar magnetic field (Tripathy et al. 2007; Jain et al. 2009; Broomhall & Nakariakov 2015). This is corroborated by their strong correlation with the 10.7-cm flux (Chaplin et al. 2007b; Tripathy et al. 2007; Jain et al. 2009; Broomhall et al. 2012; Simoniello et al. 2012), which is mostly sensitive to the weak component, but also affected by the strong component of the magnetic field (e.g. Covington 1969; Tapping 1987; Tapping & Detracey 1990), and their strong correlation with the sunspot areas (Jain et al. 2012; Broomhall & Nakariakov 2015). Furthermore, as discussed above, the activity-related frequency shifts are sensitive to the latitudinal distribution of active regions (e.g. Libbrecht & Woodard 1990; Hindman et al. 2000; Howe et al. 2002; Chaplin et al. 2004b; Broomhall et al. 2012; Howe et al. 2015). Figure 1.10 shows the latitudinal distribution of the frequency shifts (Fig. from Broomhall et al. 2014), which resembles the latitudinal distribution of sunspots (see Fig. 2.2).

The relation between the observed frequency shifts and the different activity indicators is almost linear (Fig. 1.11 - from Salabert et al. 2015). However, the frequency shifts follow slightly different paths in the rising and declining phases of the solar cycle (e.g. Jiménez-Reyes et al. 1998; Tripathy et al. 2000; Chaplin et al. 2007b; Jain et al. 2009, 2012; Basu et al. 2012; Salabert et al. 2015; Broomhall et al. 2014; Broomhall & Nakariakov 2015). This behaviour is known as magnetic hysteresis and results from the different latitudinal distribution of active regions (strong component of the magnetic field) over the rising and declining phases, as the active regions migrate towards the equator over the solar magnetic cycle (see Sect. 2.1.2).

Despite the frequency shifts being well correlated with other activity indicators, different studies have shown a decrease in the correlation around the maximum of the solar cycle (e.g. Jain et al. 2009; Simoniello et al. 2012; Broomhall & Nakariakov 2015). Also, the frequency shifts show a temporal offset, being ahead, in relation to those activity indicators (e.g. Jain et al. 2009; Salabert et al. 2009, 2015).

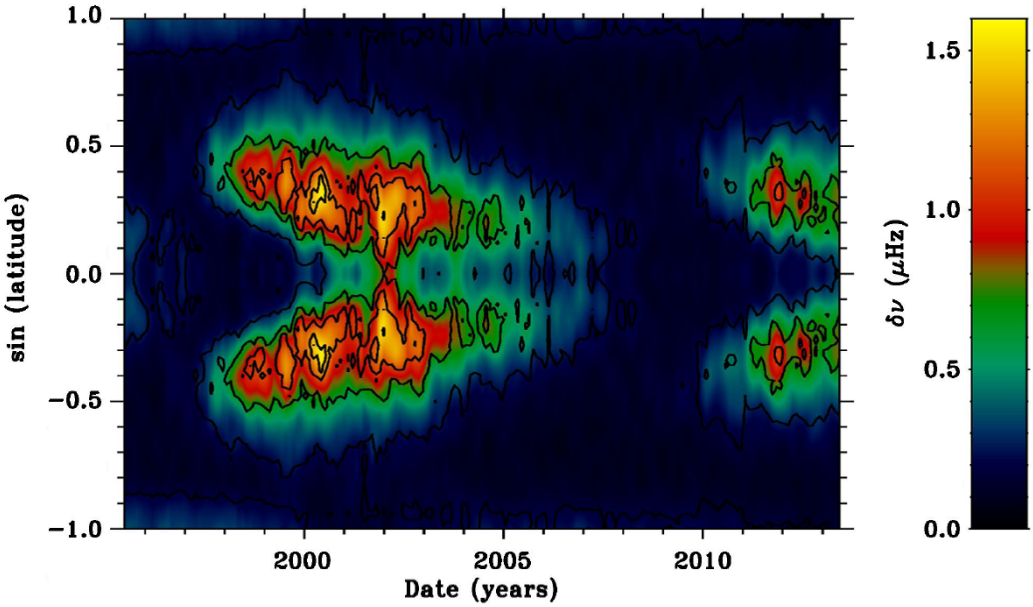

Fig. 1.10 – Latitudinal distribution of the frequency shifts obtained from GONG data using modes with $40 \leq l \leq 80$ and $9 \leq n \leq 11$. Figure taken from Broomhall et al. (2014), being an updated version of the figure in Howe et al. (2002).

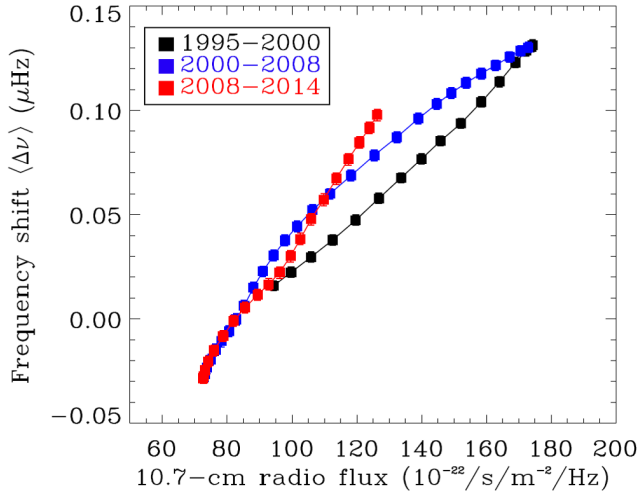

Fig. 1.11 – Smooth frequency shifts obtained from GOLF data as a function of the 10.7-cm flux. The different colours indicate the rising (black) and declining (blue) phases of the solar cycle 23, and the rising phase of the cycle 24 (red). Figure from Salabert et al. (2015).

In addition to the long-term variation (on the timescale of the solar cycle), the solar acoustic frequencies also show a quasi-biennial variation (Fletcher et al. 2010; Broomhall et al. 2012; Simoniello et al. 2012, 2013; Broomhall & Nakariakov 2015), which is strongly correlated with the mid-term periodicities found in other activity proxies (Broomhall et al. 2012; Broomhall & Nakariakov 2015). Figure 1.12 (taken from Fletcher et al. 2010) displays the residuals left after removing the 11-yr signal for different frequency ranges. The signature of the quasi-biennial variation is seen over all

phases of solar activity. However, its amplitude is highest around the solar maximum, suggesting that it is modulated by the 11-yr cycle. These mid-term frequency shifts show a weaker dependence on the frequency than the longer term (11-yr) frequency shifts (Fletcher et al. 2010; Broomhall et al. 2012; Simoniello et al. 2013), which has been interpreted as an indication that they originate from changes in layers that are located deeper than those, near-surface layers, inducing the 11-yr signal.

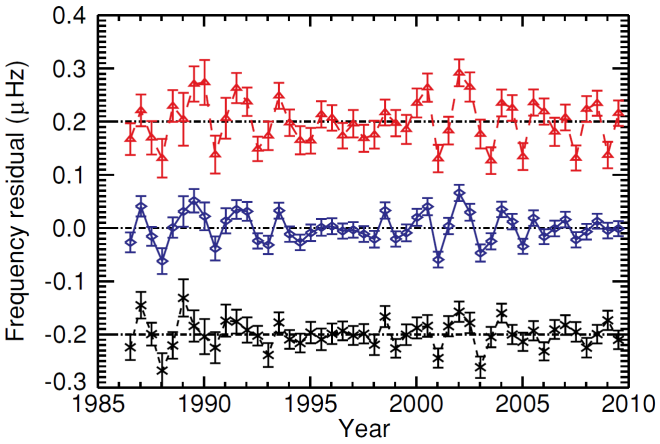

Fig. 1.12 – Frequency residuals, obtained from BiSON data for the solar cycles 22 and 23, left after removing the long-term, 11-yr, variation. Different colours indicate the frequency range used to estimate the frequency shifts: total frequency range ($1860-3720\,\mu$Hz; blue), low-frequency range ($1860-2770\,\mu$Hz; black; displaced by $-0.2\,\mu$Hz), and high-frequency range ($2800-3720\,\mu$Hz; red; displaced by $+0.2\,\mu$Hz). Figure from Fletcher et al. (2010).

1.3.1 Variational principle: from phase shifts to frequency shifts

Later, in Chapter 3, we will address the contribution of the strong component of the solar magnetic field (associated with sunspots/active regions) to the observed variations in the frequencies of the acoustic modes. To do so, we will use a variational principle applied in the context of magnetic perturbations to the frequencies by Cunha & Gough (2000), which relates the phase shift in the eigenfunctions with the shifts in the eigenfrequencies.

Active regions, localized regions of strong magnetic field, can affect the wave propagation and, consequently, the oscillation properties through direct (via Lorentz force) and indirect (associated with thermal and structural changes) effects.

The greatest thermal and structural changes within an active region are expected to take place in the uppermost layers. Furthermore, the direct effect of the magnetic field on the oscillations is important also only in the near-surface layers, where the magnetic pressure is comparable or larger than the gas pressure. Therefore, the main contribution from active regions to the observed frequency shifts results from the uppermost layers. Deeper in the stellar interior, the gas pressure dominates and the effect of the magnetic field is negligible.

With the above in mind, the star can be divided into two regions (Campbell & Papaloizou 1986; Cunha & Gough 2000): surface boundary layer and interior, i.e. above and below the region of influence of the active region (at depth R^*). In this approach, while the surface boundary layer

is under the influence of a strong magnetic field (non-spherically symmetric case), the interior is essentially non-magnetic and, thus, unperturbed (spherically symmetric case). Therefore, the initial problem is reduced to a perturbation problem, where only the boundary condition at the top (i.e. at R^*) is perturbed.

In the stellar interior, for acoustic modes (with typical frequencies $\omega \gg N$; see Sect. 1.1), the wave equation for the scalar function Ψ, under the Cowling approximation, is given, in spherical polar coordinates (r,θ,ϕ), by (e.g. Gough 1993)

$$\nabla^2\Psi + \frac{\omega^2 - \omega_c^2}{c^2}\Psi = 0, \tag{1.27}$$

where $\Psi = r\rho^{-1/2}\omega^{-1}\delta p$ and δp is the Lagrangian pressure perturbation. Near the surface, but still in the region where the magnetic and acoustic modes are decoupled (where the gas pressure dominates), in the JWKB approximation, Ψ behaves locally as (e.g. Gough 1993)

$$\Psi(r,\theta,\phi) \sim Br^{-1}\kappa^{-1/2}\sin\left(\int_r^{R^*}\kappa dr + \delta(R^*,\theta)\right)Y_l^m, \tag{1.28}$$

where B is a constant, κ is the radial component of the acoustic wave number (see equation 1.8), and δ is the phase. Differentiating equation (1.28), the boundary condition at $r = R^*$ that must be satisfied by equation (1.27) is

$$\frac{\partial\Psi}{\partial r} + \alpha\Psi = 0, \tag{1.29}$$

where $\alpha = \kappa\cot\delta$.

Multiplying equation 1.27 by the complex conjugate $\Psi^\dagger$ of Ψ, and integrating over the volume V^* within the the surface S^* at $r = R^*$, Cunha & Gough (2000) found

$$\omega^2\int_{V^*} c^{-2}\Psi^\dagger\Psi dV = \int_{S^*}\alpha\Psi^\dagger\Psi dS + \int_{V^*}\frac{\omega_c^2}{c^2}\Psi^\dagger\Psi dV + \int_{V^*}\nabla\Psi^\dagger\cdot\nabla\Psi dV. \tag{1.30}$$

To first order, the magnetic perturbation to the function Ψ is zero and, thus, the perturbation to the eigenfrequency is given by

$$\frac{\Delta\omega}{\omega_0} = \frac{1}{2\omega_0^2}\frac{\int_{S^*}\Delta\alpha\Psi_0^\dagger\Psi_0 dS}{\int_{V^*}c^{-2}\Psi_0^\dagger\Psi_0 dV}, \tag{1.31}$$

where 0 denotes the unperturbed values, $\alpha = \alpha_0 + \Delta\alpha$, and $\omega = \omega_0 + \Delta\omega$. Writing the perturbed phase as $\delta = \delta_0 + \Delta\delta$, and combining equations (1.28-1.31), the relation between the frequency and phase shifts becomes (Cunha & Gough 2000)

$$\frac{\Delta\omega}{\omega} \simeq -\frac{\overline{\Delta\delta}}{\omega^2\int_{r_1}^{R^*}c^{-2}\kappa^{-1}dr} \tag{1.32}$$

where $\overline{\Delta\delta}$ is the integral phase difference given by

$$\overline{\Delta\delta} = \frac{\int_0^{2\pi}\int_0^{\pi}\Delta\delta(Y_l^m)^2\sin\theta d\theta d\phi}{\int_0^{2\pi}\int_0^{\pi}(Y_l^m)^2\sin\theta d\theta d\phi}. \tag{1.33}$$

$\Delta\delta$ corresponds to the phase shift induced (through direct and indirect effects of the magnetic field) in the surface boundary layer. Thus, knowing the phase shifts, the activity-related variation in the mode frequency can be estimated.

1.4 Asteroseismology of stellar magnetic cycles

The activity-related variations in the properties of the acoustic modes (Sect. 1.3) are expected to be common among solar-type stars.

The small amplitudes of the solar-type oscillations hamper the observation of Sun-like pulsators. Furthermore, the amplitudes of the acoustic modes are suppressed by magnetic activity, which provides an additional barrier in detecting solar-type oscillations and, consequently, activity-related variations in their properties. Nevertheless, the improvement of the observational techniques and development of highly precise photometric instruments aimed at the search for exoplanets, such as the CoRoT (Convection, Rotation, and planetary Transits; Baglin et al. 2006) and *Kepler* (Borucki et al. 2010) satellites, opened a new door also for Asteroseismology.

In 2010, García et al. reported the first detection of activity-related variations in the oscillation properties of a star other than the Sun, the CoRoT solar-type star HD 49933. The authors found the mode frequencies (middle panel of Fig. 1.13) and amplitudes (top panel of Fig. 1.13) varying in anti-phase, which resembles what is found in the solar observations. The frequency and amplitude variations were found to be related with a variation in the photometric indicator (bottom panel of Fig. 1.13). Similarly to the solar case, a temporal offset is found between the seismic (amplitude and frequency shifts) and photometric activity indicators. Later, Salabert et al. (2011b) found evidence for a frequency dependence of the observed frequency shifts of HD 49933, which once more agrees with the solar observations.

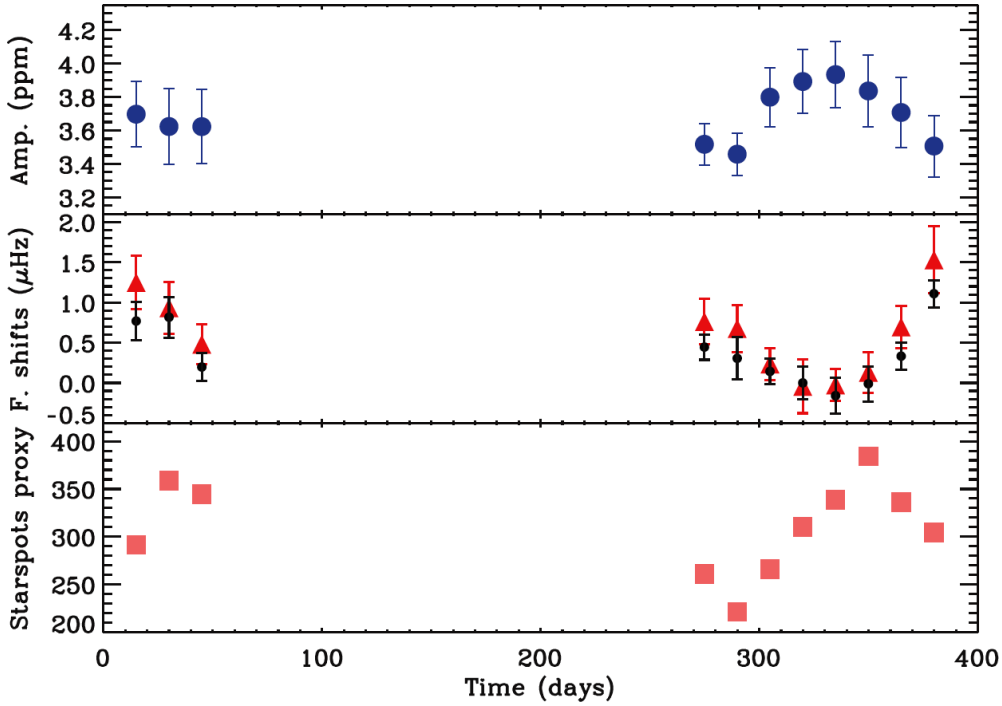

Fig. 1.13 – Temporal variation in the seismic and photometric indicators: mode amplitudes (top), frequency shifts (middle) obtained from cross-correlation (red) and from a local fit to the p-modes (black), and starspot proxy derived from the light curve (bottom). Figure from García et al. (2010b).

Early last year, Salabert et al. (2016) successfully detected activity-related frequency shifts in an active (Mathur et al. 2014; García et al. 2014a) young solar-analog observed by *Kepler*, KIC 10644253. The observed frequency variations agree with the inferred photometric activity. In addition, similarly to the observations of the Sun and HD 49933, the frequency shifts are found to increase as a function of the mode frequency. Furthermore, the results from high-resolution spectroscopic observations obtained with the HERMES spectrograph confirmed that the solar-analog KIC 10644253 is an active star (about 18% chromospherically more active than the Sun; Salabert et al. 2016).

Later in 2016, Régulo et al. confirmed the activity-related frequency shifts in the CoRoT star HD 49933 and detected evidence for frequency shifts in the active (Mathur et al. 2014; García et al. 2014a) solar-type star KIC 3733735. More recently, Kiefer et al. (2017) analyzed *Kepler* data for 24 solar-type stars. The authors found significant variations in the acoustic frequencies of 23 stars. From those, six stars show anti-correlated temporal variations in the oscillation frequencies and heights (similar to the Sun and HD 49933), which suggest that these six stars show activity-related frequency shifts. In particular and similarly to the Sun (and to the solar-type stars HD 49933 and KIC 10644253), the authors found that the frequency shifts increase with the mode frequency of KIC 8006161.

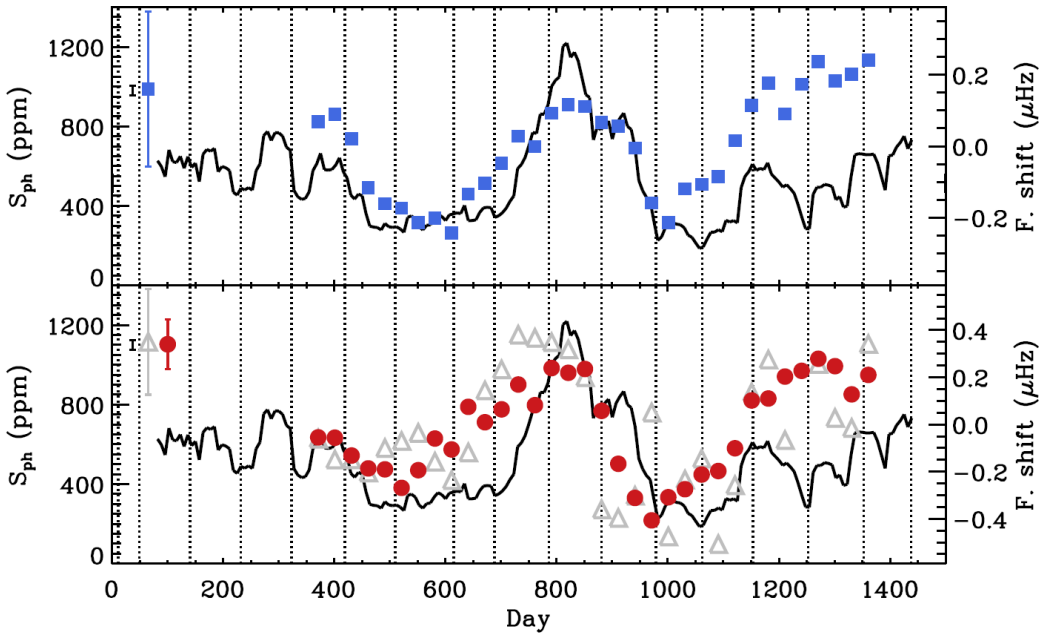

Fig. 1.14 – Temporal variation in the photometric activity indicator (S_{ph}; black solid lines) and in the acoustic frequencies (different symbols) for KIC 10644253. The different symbols correspond to the frequency shifts obtained from a cross-correlation method (blue squares) and from the local fit of the $l = 0$ (grey triangles) and $l = 1$ (red circles) modes. The respective mean uncertainties are shown in the top left-hand side of each panel. The dotted lines mark the *Kepler* quarters. Figure from Salabert et al. (2016).

1.5 Purpose of this Thesis

The activity-related variations in the frequencies of the solar acoustic modes have been known for three decades, since Woodard & Noyes (1985) found evidences for a decrease, from 1980 (near solar maximum) to 1984 (near solar minimum), of $\sim 0.42\,\mu$Hz in the solar acoustic frequencies. Those activity-related frequency shifts may include contributions from the changes in the global solar magnetic field, as well as, from localized regions of strong magnetic field, that can be associated with different phenomena, such as sunspots and plages. However, the relative importance of the different contributions to the observed frequency shifts and the precise origin of those are not completely understood.

With the above in mind, my Thesis project includes a theoretical and an observational components, aimed at a better understanding of the relation between magnetic and seismic properties of stars. The first component concerns the theoretical study of the magnetically-induced frequency shifts (Chapters 3 and 4), where, in particular, we have been trying to determine the contribution from the sunspots (strong component of the solar magnetic field) to the observed frequency shifts.

The observational component is focused on the detection of stellar magnetic cycles in *Kepler* targets through asteroseismology (Chapter 5). At the time we started this project, the only star (other than the Sun) that was known to exhibit activity-related temporal variations in the seismic properties was the CoRoT solar-type star HD 49933 (García et al. 2010b). Interestingly, the frequency shifts found for HD 49933 are significantly larger than those observed for the Sun and suggest a magnetic cycle significantly shorter than the 11-yr solar cycle. Furthermore, one may expect relatively short cycles for fast rotators (e.g. Baliunas et al. 1996; Böhm-Vitense 2007; Oláh et al. 2009). Therefore, the findings of García et al. (2010b) opened the interesting possibility of extending the characterization of magnetic cycles to other solar-type stars through asteroseismology, in particular using the *Kepler* satellite, whose time-series have, at maximum, a length of $\sim 4\,$yr.

We also have developed a toy model for sun/starspot cycles, which simulates the main properties of the spot distribution over a magnetic cycle (Chapter 2). This model has been useful in the study of the frequency shifts (Chapters 3 and 4), having many more possible applications.

Finally, we also study the impact of starspots on the observed stellar flux (Chapter 6). The resulting spot modulation in the stellar light curves allow us to learn about the stellar surface (differential) rotation, which is a key ingredient to the stellar magnetism, and also about stellar magnetism itself.

2. Spot cycle simulations: empirical tool

The increasing interest in understanding stellar magnetic activity cycles is a strong motivation for the development of parameterized starspot models which can be constrained observationally. Starspot simulations can be used to study how the activity-induced variability in the light curve and in the oscillation properties depends on the characteristics of the activity cycle. These simulations are important in other astrophysical contexts, such as in the quest for exoplanets, where they can be used to design new strategies to reduce the signatures induced by stellar activity on the radial velocity and transit observations (e.g. Pont et al. 2008; Czesla et al. 2009; Figueira et al. 2010; Dumusque et al. 2011; Oshagh et al. 2013, 2014).

With the above in mind, we developed a stochastic model capable of simulating spot cycles (Santos et al. 2015). The empirical model takes into account a number of input parameters related to the spot properties. The model was first applied and calibrated to the solar case, being relatively complex in order to successfully reproduce the quantity and quality of the solar data. However, it can easily be applied to stars other than the Sun with different cycles, by adapting the input parameters accordingly.

2.1 Properties of the sunspot cycle and input parameters of the model

In order to reproduce the sunspot cycle, a number of observational constraints must be considered. Those properties are, then, used as inputs in the model and are mainly related to: the number of sunspot groups and its dependence on the phase of the cycle; the sunspots' areas and their relation with the sunspots' lifetimes; the sunspot formation zone; and the differential rotation of the solar surface.

The choice of the final input parameters is based on the results from the Kolmogorv-Smirnov test (Sect. 2.2.1; Kolmogorov 1933; Smirnov 1939), which allowed a gradual improvement of the spot cycle model.

In the following sections, the key observational properties of the sunspot cycle and their implementation in the model are summarized. The properties of the sunspot emergence are cycle-dependent (e.g. Solanki et al. 2008; Jiang et al. 2011). To callibrate the model we have used the observational data of solar cycle 23.

2.1.1 Number of sunspot groups

As sunspots are regions of strong magnetic fields, the number of sunspots on the solar surface is a proxy for the magnetic activity level. In fact, the number of sunspots and sunspot groups is observed to vary as the solar cycle progress: increasing from minimum to maximum and, then, decreasing towards the next minimum. However, this behaviour is not symmetric in time, with the rising phase being faster than the declining phase of the solar cycle.

Different functions have been proposed to describe the asymmetric shape of the cycle (e.g. Setwart & Panofsky 1938; Elling & Schwentek 1992; Hathaway et al. 1994; Sabarinath & Anilkumar 2008; Volobuev 2009; Du 2011). Figure 2.1 shows the comparison between the number of sunspot groups observed over the solar cycle 23 (computed from the daily records of the National Geophysical Data Center, part of the National Oceanic and Atmospheric Administration - NGDC/NOAA[1]) and three different functional forms (Hathaway, Wilson, & Reichmann 1994; Sabarinath & Anilkumar 2008; Du 2011). Hathaway et al. (1994) found that the observed number of sunspots is nicely fitted by the following function of time (with 4 parameters; red line in Fig. 2.1),

$$N_{\rm H}(t) = \frac{a_1(t-t_0)^3}{\exp[(t-t_0)^2/b_1^2] - c_1}\,, \tag{2.1}$$

where t_0 is the starting time expressed in years, a_1 is the amplitude, b_1 is related to the length of the cycle, and c_1 is related to the asymmetry of the cycle. Instead, Sabarinath & Anilkumar (2008) used a modified binary mixture of Laplace density functions (with six parameters; green line in Fig. 2.1) which takes into account the double peak at the solar maximum

$$N_{\rm S\&A}(t) = \frac{a_2}{2b_2}\exp\left(-\frac{|t-t_{\rm m_2}|}{b_2}\right) + \frac{a_3}{2b_3}\exp\left(-\frac{|t-t_{\rm m_3}|}{b_3}\right) \tag{2.2}$$

where t_{m_2} and t_{m_3} are the times of each peak expressed in months, b_2 and b_3 control the width and amplitude of the cycle, and a_2 and a_3 are related to the amplitude of the cycle. Du (2011) used the following modified Gaussian function (with four parameters; blue line in Fig. 2.1) to describe the asymmetric shape of the cycle

$$N_{\rm Du}(t) = a_4\exp\left(-\frac{(t-t_{\rm m_4})^2}{2b_4^2[1+c_4(t-t_{\rm m_4})]^2}\right), \tag{2.3}$$

where a_4 is related to the amplitude of the cycle, $t_{\rm m4}$ is the time of the maximum expressed in years, b_4 is related with the length of the cycle, and c_4 is the parameter for the asymmetry.

The curves shown in Fig. 2.1 represent the best fits to the number of observed sunspot groups obtained with equations (2.1)-(2.3). The corresponding parameters are summarized in Table 2.1. Figure 2.1 also shows that the fits obtained with the functions proposed by Hathaway et al. (1994) and Du (2011) are very similar. Although, the function proposed by Sabarinath & Anilkumar (2008) seems to be a better representation of the solar maximum, it clearly overestimates the number of observed sunspot groups in the beginning of the rising phase and then underestimates it.

Model implementation

Our model generates sunspot groups, by considering them as independent events. At each time step (fixed on one day to be comparable to the daily records of the sunspot data), N groups are formed. The number of generated groups is randomly determined using a Poisson distribution with a time-

[1] http://www.ngdc.noaa.gov

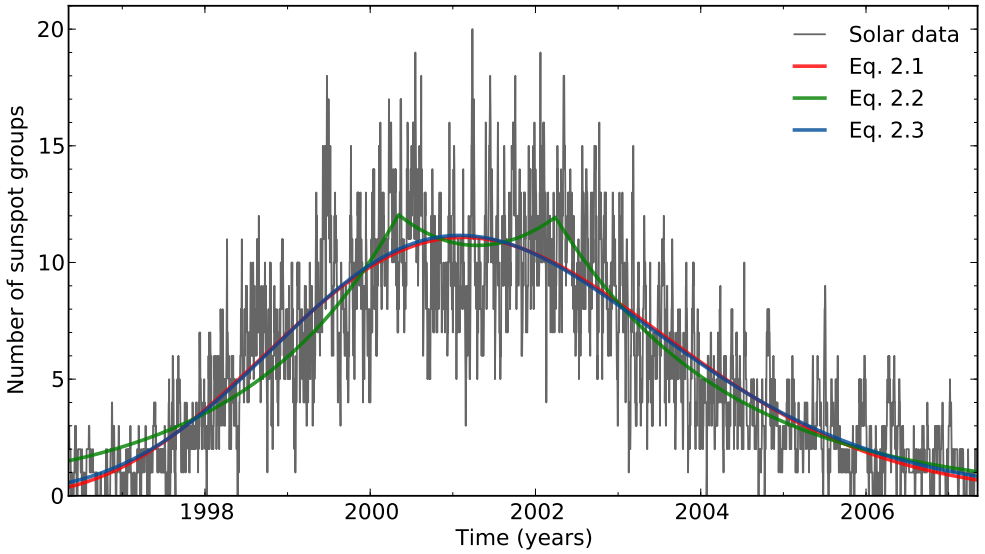

Fig. 2.1 – Number of sunspot groups observed over the solar cycle 23 (grey) and the corresponding best fits obtained with the functions defined by Hathaway et al. (1994, red), Sabarinath & Anilkumar (2008, green), and Du (2011, blue) – equations 2.1 - 2.3. Observational data from NGDC/NOAA.

Hathaway et al. (1994) (equation 2.1)		Sabarinath & Anilkumar (2008) (equation 2.2)		Du (2011) (equation 2.3)	
a_1	0.26	a_2	355.58	a_4	11.16
t_0	1995.10	b_2	21.53	t_{m_4}	2001.08
b_1	4.77	t_{m_2}	47.88	b_4	2.29
c_1	-0.29	a_3	473.99	c_4	0.03
		b_3	26.12		
		t_{m_3}	70.659		

Table 2.1 – Approximate values of the parameters that best fit the observed number of sunspot groups over solar cycle 23.

dependent mean value, N_m. N_m is taken to be one sixth ($F_N = 1/6$) of the mean number of sunspot groups observed throughout the solar cycle, N_S.

We have chosen the function defined by Hathaway et al. (1994, equation 2.1) to describe the mean number of observed sunspot groups, i.e. $N_S = N_H$. With this choice, we find that the synthetic data is always in reasonable agreement with the observational solar data (see Sect. 2.2.1).

We also investigated whether or not the functions defined by equations (2.2) and (2.3) are a better representation of the solar data. As one could expect from Fig. 2.1, the implementation of equation (2.3) yields comparable results to those obtained with equation (2.1). However, the results obtained using equation (2.2) are considerable worse than those obtained with the previous functions (see Sect. 2.2.1).

2.1.2 Sunspot formation zone

As was first reported by Carrington (1863), the sunspot formation latitude also varies periodically in time. The first spots of a new cycle appear at latitudes of about ±40°. The subsequent spots form at progressively lower latitudes, being rarely observed within ±5°. At the solar minimum, while the last spots of the cycle emerge at low latitudes, the spots of the new cycle start to form at high latitudes. This behaviour is known as the Spörer law and it may be seen in the butterfly diagram (or Maunder diagram; Maunder 1904), as shown in Fig. 2.2 for cycles 22 and 23 (data from NGDC/NOAA).

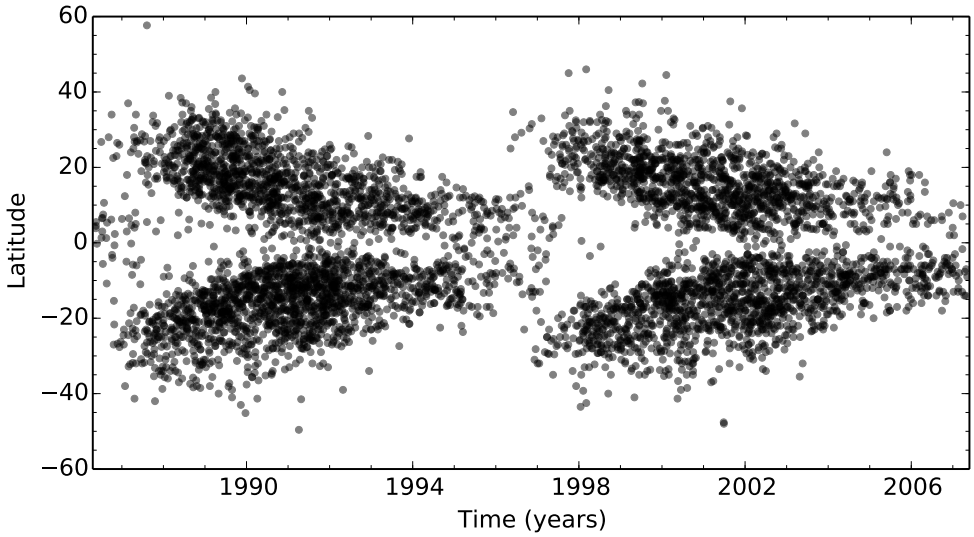

Fig. 2.2 – Butterfly diagram, also known as Maunder diagram, showing the latitudinal distribution of sunspots over time. Observational data from NGDC/NOAA.

Despite the presence of short plateaus at intermediate latitudes ($\sim 10°$ - around the solar maximum; Chang 2012), Hathaway (2011) found that the drift of the sunspot zones follows an exponential function, where the average latitude is given by

$$L_{\mathrm{H}}(t) = L_0 \exp\left(-\frac{t - t_0}{7.5}\right), \tag{2.4}$$

where L_0 is the mean latitude at the time t_0, and t is expressed in years. Instead, by considering the intermediate phases of the cycle where there is no overlap between consecutive cycles, Jiang et al. (2011) verified that the mean spot latitude can also be described by a second-order polynomial of the form

$$L_{\mathrm{J}}(t) = a_{\mathrm{L}} + b_{\mathrm{L}} \frac{t - t_{\mathrm{min}}}{P_{\mathrm{c}}} + c_{\mathrm{L}} \left(\frac{t - t_{\mathrm{min}}}{P_{\mathrm{c}}}\right)^2, \tag{2.5}$$

where a_{L}, b_{L}, and c_{L} are the coefficients of the polynomial, t_{min} is the time at the solar minimum, and P_{c} is the period of the cycle.

In this work, for simplification, we consider that the Northern and Southern hemispeheres are symmetric. However, we note that the solar cycle is characterized by a Northern-Southern asymmetry

(e.g. Newton & Milsom 1955; Waldmeier 1971; Temmer et al. 2002; Li et al. 2003; Temmer et al. 2006; Solanki et al. 2008; Li et al. 2009; Norton & Gallagher 2010), both in

- phase: systematic temporal lag between the activity level in the two hemispheres;
- and strength: the solar activity is not equally distributed between the two hemespheres (see also Sect. 2.2.1).

Figure 2.3 compares the observed latitudinal distribution of the spot groups over the solar cycle 23 and the mean latitudes as defined by equations (2.4) and (2.5). The parameter t_0 of equation (2.4) is, in this case, fixed at the value found in Sect. 2.1.1. The remaining parameters were determined by fitting the data for the northern hemisphere and then assumed to be valid for the southern hemisphere. From the inspection of Fig. 2.3, one can conclude that the two functional forms are similar, differing mostly at the end of the solar cycle.

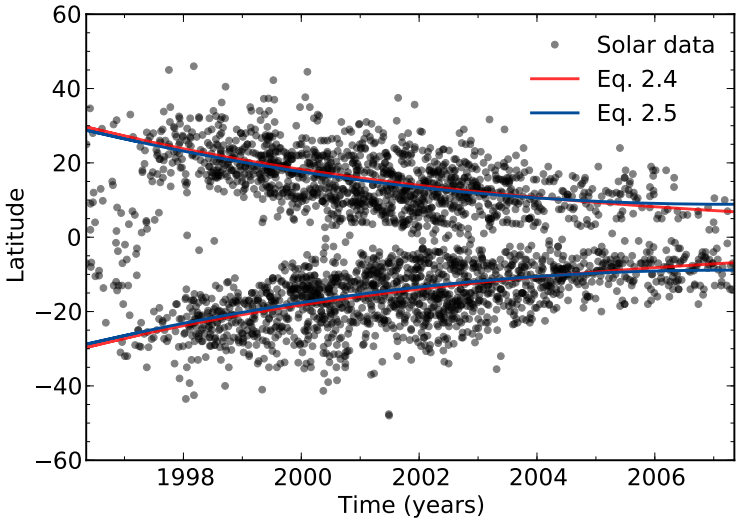

Fig. 2.3 – Comparison between the group latitudes over the solar cycle 23 and the two function forms that were explored: an exponential (red; equation 2.4; Hathaway 2011) and a polynomial (blue; equation 2.5; Jiang et al. 2011) fits. Observational data from NGDC/NOAA.

The width of the sunspot formation zone, σ_L, also varies over the solar cycle (e.g. Gleissberg 1958; Miletskii & Ivanov 2009; Jiang et al. 2011). According to Jiang et al. (2011), this width can be described in relation to the average sunspot group latitude by a second-order polynomial of the form

$$\frac{\sigma_L(t)}{L_S(t)} = a_\sigma + b_\sigma \frac{t - t_{min}}{P_c} + c_\sigma \left(\frac{t - t_{min}}{P_c} \right)^2 , \tag{2.6}$$

where a_σ, b_σ, and c_σ are the coefficients of the polynomial. Figure 2.4 shows the ratio between the dispersion of the observed spot latitudinal distribution and its average value as a function of time (black dots). The red line corresponds to the best fit to the data obtained with equation (2.6), by assuming $L_S = L_H$ (equation 2.4). According to other works by Miletskii & Ivanov (2009), Ivanov et al. (2011), and Ivanov & Miletskii (2011), the width of the spot formation zone can be instead described as linear function of the activity level. The blue line in Fig. 2.4 represents the width of the

spot formation zone that was assumed in previous versions of the model (see the following section for details), which was based on the linear relations found by these authors. Table 2.2 summarizes the parameters found while fitting the equations (2.4)-(2.6) to the sunspot data.

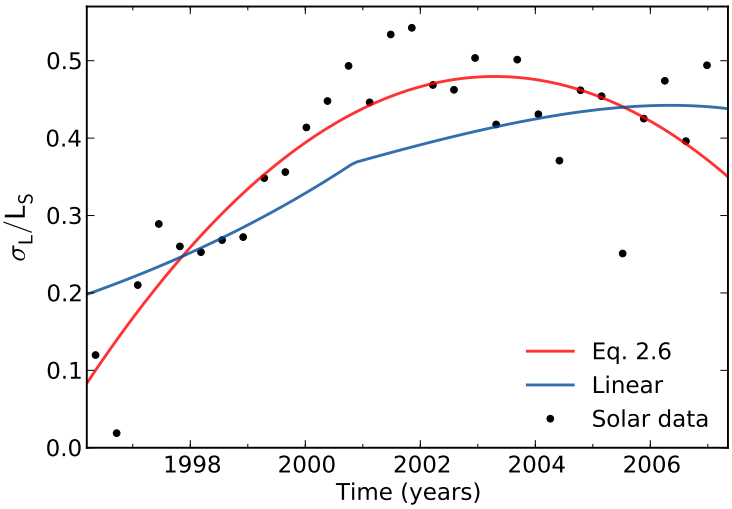

Fig. 2.4 – Ratio between the standard deviation of the latitudinal distribution of the observed groups and the its average value (black dots). The red line corresponds to the best fit obtained with the equation (2.6; Jiang et al. 2011). For the blue line, the width of the spot formation zone (σ_L) is first assumed to be constant from minimum to maximum and, then, a decreasing linear function from maximum to minimum. Observational data from NGDC/NOAA.

Hathaway (2011) (equation 2.4)		Jiang et al. (2011) (equation 2.5)		Jiang et al. (2011) (equation 2.6)	
L_0	34.97	a_L	28.77	a_σ	0.10
t_0	1995.10	b_L	-40.48	b_σ	1.20
		c_L	20.58	c_σ	-0.95

Table 2.2 – Approximate values of the parameters that best fit the observed mean latitude and width of the sunspot formation zone for solar cycle 23.

Model implementation

In our spot cycle model, the absolute latitude of each sunspot group, L, is determined randomly through a Gaussian distribution, which is characterized by a mean latitude, L_S, and dispersion, σ_L, both dependent on time as mentioned before. Although, Chang (2012) found that the spatial distribution of the sunspot groups at each time t is bimodal and that it can be described by a double Gaussian, Ivanov et al. (2011) have shown that one single Gaussian describes the data reasonably well. Therefore, we opted for a single-Gaussian distribution. We use Hathaway's exponential function (equation 2.4 - red line in Fig. 2.3) to determine the reference mean latitude ($L_S = L_H$). For σ_L, we assume a second-order polynomial, as suggested by Jiang et al. (2011, equation 2.6 - red line in Fig. 2.4). The

spots' hemisphere is then chosen randomly with equal probability of a spot emerging on the northern or southern hemisphere.

Other functions were considered to describe the latitudinal distribution of the sunspot groups (both for L_S and σ_L). As it will be shown in Sect. 2.2.1, considering a polynomial function for L_S (equation 2.5; Jiang et al. 2011, blue line in Fig. 2.3) leads to a lower level of agreement between the synthetic and the observational data. For the width of the sunspot formation zone, in a previous version of the model we stared by considering a linear dependence on the level of activity, as suggested by Ivanov et al. (2011). We found a better agreement between our simulations and the solar data when assuming a constant dispersion (σ_L) from minimum to maximum and a linearly decreasing dispersion towards the next minimum (blue line in Fig. 2.4). However, this assumption also leads to a lower level of agreement between the synthetic and observational data (see Sect. 2.2.1) when compared with the current version of the model where the width of the sunspot formation zone is determined by a polynomial function (equation 2.6).

We recall again that the current version of the model does not account for the Northern-Southern hemispheric asymmetry. However, we also note that the input parameters of the model can be easily adapted to reproduce the asymmetric hemispheres.

2.1.3 Sunspot group areas and lifetimes

Having defined the procedure to generate the number of sunspot groups and their position in latitude at each time step of the simulations, one needs to associate an area to each group.

Bogdan et al. (1988) were the first to notice that the accumulated umbral areas distribution (derived from daily records by counting each spot as many times as the number of days it remains visible) can be described by a log-normal distribution. Since the ratio between the umbral area and the total area of the spot does not depend significantly on the spot size (e.g. Brandt et al. 1990; Solanki 2003; Vaquero et al. 2005; Kiess et al. 2014), the accumulated spot areas also follow a log-normal distribution definied as

$$f(A) = \frac{H_A}{A\sigma_A\sqrt{2\pi}} \exp\left[-\frac{(\ln(A)-\mu_A)^2}{2\sigma_A^2}\right], \tag{2.7}$$

where A is the spot group area, H_A is related with the height of the distribution, and μ_A and σ_A are the mean and standard deviation of $\ln(A)$. This finding was confirmed by later studies (e.g. Baumann & Solanki 2005; Hathaway & Choudhary 2008; Kiess et al. 2014). Moreover, Baumann & Solanki (2005) have shown that the log-normal distribution also nicely fits the observed distributions for the instantaneous area and for the maximum area of sunspots. Figure 2.5 shows the maximum (derived by considering each group only once and its maximum area) and accumulated area distribution for the sunspot groups of solar cycle 23 and the corresponding log-normal fits. The parameters of the log-normal distributions are presented in Table 2.3. Although Jiang et al. (2011) reported that the area distribution for groups smaller than 60 MSH is better described by a power law, we do not find evidences for that on the data sets we use.

During its life, a given sunspot group grows until it reaches a maximum area and then decays.

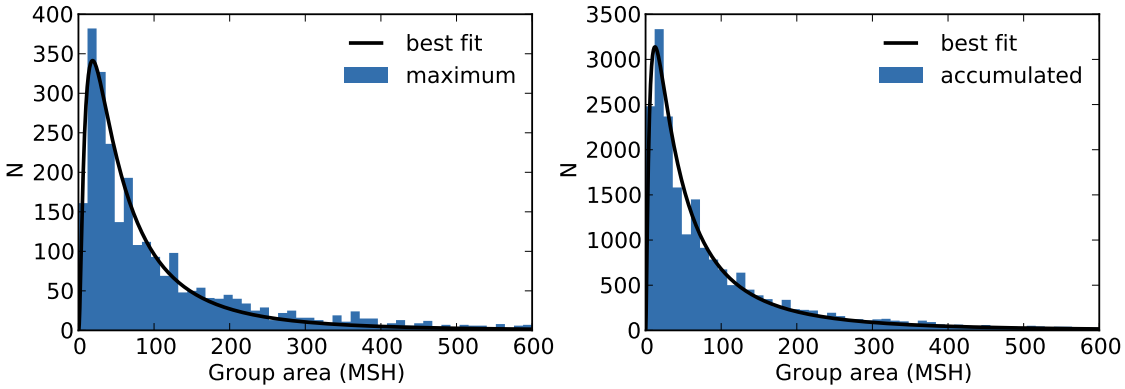

Fig. 2.5 – Maximum (left) and accumulated (right) area distributions for the sunspot groups observed over the solar cycle 23 (data from NGDC/NOAA). The black solid lines represent the best log-normal fits. MSH means millionth of the solar hemisphere.

Maximum area distribution	
H_{A_m}	0.29×10^5
σ_{A_m}	1.05
μ_{A_m}	4.04

Accumulated area distribution	
$H_{A_{acc}}$	2.37×10^5
$\sigma_{A_{acc}}$	1.19
$\mu_{A_{acc}}$	3.94

Table 2.3 – Approximate parameters of the log-normal distributions that describe the observed maximum (denoted by 'm') and accumulated (denoted by 'acc') area distributions of the sunspot groups observed over solar cycle 23.

The growth (Ψ) and decay (Γ) rates, i.e. the time derivative of the group's area during each of these phases, are found to be dependent on the group areas, the activity cycle, the phase of the cycle, and the latitude (e.g. Moreno-Insertis & Vázquez 1988; Howard 1992; Petrovay & van Driel-Gesztelyi 1997; Hathaway & Choudhary 2008; Javaraiah 2012). Small groups grow faster than they decay, while the growth rates of large groups are smaller than their decay rates (Howard 1992). Hathaway & Choudhary (2008) found a linear relation between the decay rates and the group area, but the erosion model proposed earlier by Petrovay & van Driel-Gesztelyi (1997) indicates a non-linear relation of the type $\Gamma \propto A^{0.5}$, where A is the group area at a given time. More recently, Javaraiah (2012) suggested that the relation between the decay rates and areas could be better described by a power law of the form

$$\Gamma = \exp(\gamma_1) A^{\gamma_2}. \tag{2.8}$$

The constant γ_2 was found to vary from ~ 0.45 to ~ 0.70, when considering individual cycles and different phases of each cycle (with A expressed in MSH). When assuming the sunspot data from 1874-2011, Javaraiah (2012) found that $\gamma_1 \sim 0.26$ and $\gamma_2 \sim 0.613$. On the other hand, the same study did not produce conclusive results regarding the relation between the group's growth rate and its area.

The areas of sunspots and sunspot groups are also related to their lifetimes, which can range from hours to months, depending on their size. This dependency is described by the Gnevyshev-Waldmeier

(GW) rule (Gnevyshev 1938; Waldmeier 1955), according to which the group maximum area (A_m) and lifetime (T) are proportional,

$$A_m = D_{GW}\, T\,, \tag{2.9}$$

where D_{GW} is a constant of proportionality (around 10 MSH day^{-1}). The determination of a precise value for D_{GW} is hampered by the difficulty in measuring the spots' lifetimes due to the nightfall, the solar rotation (lack of observations of the far-side of the Sun), and limb darkening (e.g. Henwood et al. 2009; Blanter et al. 2006; Solanki 2003). In spite of these difficulties, some studies have been carried out, indicating that D_{GW} might be larger than first estimated. Petrovay & van Driel-Gesztelyi (1997) found that D_{GW} is 10.89 ± 0.18 MSH day^{-1} for individual sunspots. More recently, Henwood et al. (2009) studied long-lived sunspot groups (lasting longer than ~ 20 days) and estimated that $D_{GW} = 11.73 \pm 0.26$ MSH day^{-1}.

Model implementation

In order to reasonably reproduce the group evolution, we then consider in the empirical model four main ingredients: maximum area, lifetime, and area growth and decay. For each generated group we obtain the maximum area through the log-normal distribution that fits the observational data (left panel of Fig. 2.5).

With the sunspot maximum area in hand, one can in principle determine the group's lifetime through the GW rule, for which we have assumed $D_{GW} = 10$ MSH day^{-1}. However, while considering the GW rule for all ranges of group areas, we found that the accumulated area distribution recovered from the synthetic data does not agree with the observed area distribution (right panel of Fig. 2.5) for the smallest groups (see Sect. 2.2.1). The GW rule is based on the observation of long-lived spot groups (e.g. groups that live longer than ~ 20 days Henwood et al. 2009). Hence, it is possible that this rule may not be adequate for the smallest groups. In fact, by tracking the small groups in the solar data for cycle 23 and comparing the time they remain visible with the lifetime predicted by the GW rule, it is possible to verify that the GW rule generally underestimates the lifetimes of the small groups. With this in mind, we have checked whether increasing the lifetimes for the small groups would improve the agreement between the observed and synthetic accumulated area distributions and found that substituting the GW linear relation by an exponential relation at the lower areas end, our model produces an accumulated area distribution that is in better agreement with the observed one (as it will be shown in Sect. 2.2). The modification of the GW rule for groups with areas smaller than $A_m = 85$ MSH used in our model is

$$T = \tau_1 \exp(\tau_2 A_m), \tag{2.10}$$

where $\tau_1 = 5.00$ and $\tau_2 \simeq 6.26 \times 10^{-3}$.

Figure 2.6 compares the time that spots are visible and their lifetime as predicted from the GW rule and from the modified GW rule. Since there is no observations of the far-side of the Sun, depending on the position in longitude, the measured visibility time of the sunspots can be a lower limit of the actual lifetime. Thus, the area-lifetime we assume (the modified GW rule) slightly overestimates the

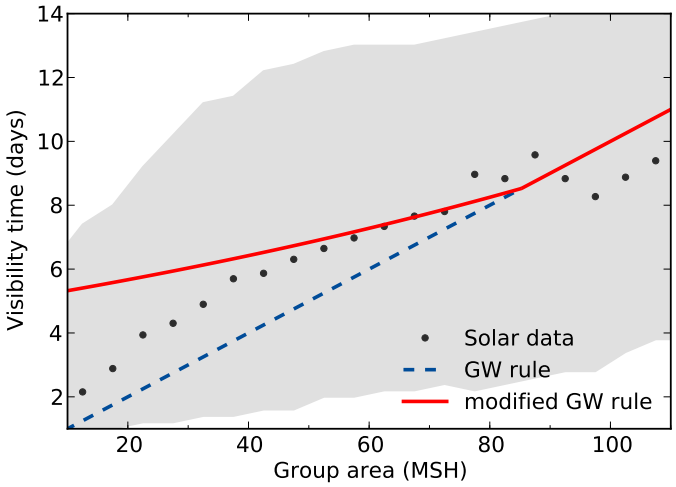

Fig. 2.6 – Sunspot group area-lifetime relation. Black dots mark the average visibility time of the sunspot groups observed over the solar cycle 23 (data from NGDC/NOAA). The grey region marks the interval of measured visibility times for a given area range. The upper and lower limits were smoothed for a better visual representation. The red solid line corresponds to the modified GW rule that is implemented in the model for the sunspot cycle, while the dashed blue line shows the lifetime predicted for small groups by the GW rule.

average visibility time of the spots (grey dots), being still shorter than the maximum visibility time for spots within a given area range (marked by the upper limit of the light grey region).

Taking the group's maximum area and lifetime, we determine the group's area at a posterior time (while $A > 0$) by applying a decay rate of the form $\Gamma = \exp(\gamma_1) A^{\gamma_2}$. We then assume that the period during which the group grows corresponds to the difference between its lifetime and the decay time. In the absence of a well-established relation between the group's growth rate and its area, we opted for a power law to describe that relation, i.e.

$$\Psi = \exp(\psi_1) A^{\psi_2}. \tag{2.11}$$

We started by considering the values found by Javaraiah (2012) for γ_1 and γ_2, making $\gamma_1 = \psi_1 = 0.26$ and $\gamma_2 = \psi_2 = 0.613$. These parameters were progressively changed until a reasonable agreement between the observations and the synthetic data was reached. The current version of the model considers $\Psi = \exp(0.17)\, A^{0.46}$ and $\Gamma = \exp(0.17)\, A^{0.47}$, which is consistent with the fact that large groups have higher decay rates than growth rates. For small groups the growth and decay rates given by the expressions above are essentially the same. However, since the growth time is taken as the difference between the lifetime and the decay time, in practice the smallest groups do not show a growth phase in the daily records, which might be interpreted as a fast growth, when they reach the maximum area in a time shorter than the interval between consecutive records (one day). We also tested the linear relation found by Hathaway & Choudhary (2008), but we found that decay rates are too high when compared with the lifetime of the group. Assuming the linear relation for the growth and decay rates, the time interval from the first appearance (with $A \sim 0$) to the last appearance (with $A \sim 0$) is much shorter than the lifetime from the modified GW rule.

2.1.4 Sunspot visibility

The daily sunspot records are limited to the observations of the near-side of the Sun. As the Sun rotates, spots that emerged on the near-side/far-side may become invisible/visible.

Also, sunspots are slightly depressed in relation to the solar surface. This effect is known as Wilson depression, which may range from 400 to 1000 Km (e.g. Gokhale & Zwaan 1972; Giovanelli 1982; Balthasar & Woehl 1983). Therefore, sunspots follow the rotation of the subphotospheric layers, i.e. slightly faster than the solar surface (e.g. Zappalà & Zuccarello 1991; Zuccarello 1993; Abuzeid & Marik 1997; Schou et al. 1998; Kitchatinov 2011). Since the spots' depths decrease as they evolve, the rotation rate also depends on the spot age, with the younger spots moving faster than the older spots.

Model implementation

To reproduce the daily sunspot records of the Sun, we take into account the solar rotation and the fact that spots are observed only when they are on the Sun's visible side.

The group's longitude is determined randomly from a uniform distribution between 0 and 2π. If this quantity is smaller than π, we consider that the sunspot group is on the visible side, otherwise we consider that it cannot be observed.

For simplification and taking into account that the rotation velocity of the subphotospheric layers is not very different from that of the solar surface, we assume the following parameterization for the rotation rate of the sunspot groups, ω, as a function of their latitude, L (Snodgrass 1983a; Snodgrass & Ulrich 1990b)

$$\omega(L) = a_\omega + b_\omega \sin^2 L + c_\omega \sin^4 L, \tag{2.12}$$

where $a_\omega = 14.71$, $b_\omega = -2.33$, and $c_\omega = -1.78$. Spot groups that emerge on the visible side of the Sun can move towards the invisible side and then eventually become visible again depending on their lifetimes and on the solar angular velocity at the latitude they emerge. Moreover, groups that emerge on the invisible side of the Sun can become visible. Both these facts are taken into account in our model. Moreover, only groups with an area greater than $A_{\rm min} \sim$10 MSH are considered visible (in analogy to the sunspot data).

In summary, the main input parameters of the current version of the spot cycle model, as calibrated to the solar cycle, are:

1. time-dependent mean number of generated sunspot groups;
2. time-dependent sunspot formation zone, characterized by a mean latitude and width;
3. maximum group area distribution;
4. area-lifetime relation;
5. spot area evolution (growth and decay);
6. solar surface differential rotation.

We note that the properties described above vary from solar cycle to solar cycle and some are found to be correlated (e.g. Solanki et al. 2002, 2008; Hathaway 2010; Jiang et al. 2011). By adapting the input parameters to the properties of the cycle of interest our model can be used to describe different cycles (as it will be shown in Sect. 2.2.2).

Finally, we note again that the model for the spot cycle can be easily adapted to reproduce spot cycles of stars other than the Sun with different properties. Again, this can be achieved by changing accordingly the input parameters mentioned above.

Figures 2.7 and 2.8 provide a schematic summary of the procedure underlaying the spot cycle simulations. In particular, the second diagram (shown in Fig. 2.8) illustrates the treatment of the evolution of a sunspot group. The yellow rectangle includes the functional forms used to describe the main properties of the spot cycle. The coloured rectangles and coloured circles are related to:

- blue → general properties of the spot cycle simulations: length of the cycle (P_c), time at the minimum (t_{min}), initial time (t_i), time step of the simulation ($dt = 1$ d);
- red → the average number generated groups (equation 2.1);
- green → the sunspot group areas and lifetime (equations 2.7-2.11);
- purple → the latitudinal distribution and rotation rate (equations 2.4, 2.6, and 2.12);
- magenta → the outputs of the model which are consistent with the sunspot daily records: time of the observation, group area, lifetime, latitude, initial longitude, rotation rate, and identification number (ID).

2.2 Synthetic sunspot cycles

The synthetic data produced with the spot cycle model provide information about each generated group. In analogy to what is done in the NGDC/NOAA databases, the code yields the sunspot group records, which include date, latitude, group area, lifetime, position in longitude, rotation rate of the solar surface at the group's latitude, and an identification number. These records are then used to compare our results with observed data.

2.2.1 Results for the solar cycle 23

In this section, we present the reconstruction of the solar cycle 23 obtained with the empirical tool described above.

As mentioned in Sect. 2.1.1, we simulate sunspot groups by considering them as independent events. This could not be assumed for individual spots, since those within the same sunspot group are not independent. This is shown in Fig. 2.9, which compares the number of observed and synthetic sunspot groups and sunspots. In the left panel, obtained while simulating sunspot groups, the similarity in the shape and spread of the two curves is quite evident. Instead, the synthetic data shown in the right panel is obtained while simulating individual sunspots. The dispersion around the mean sunspot number at a given time is larger in the real sunspot data than in the synthetic data, illustrating the dependence of the emergence/decay of sunspots within the same group.

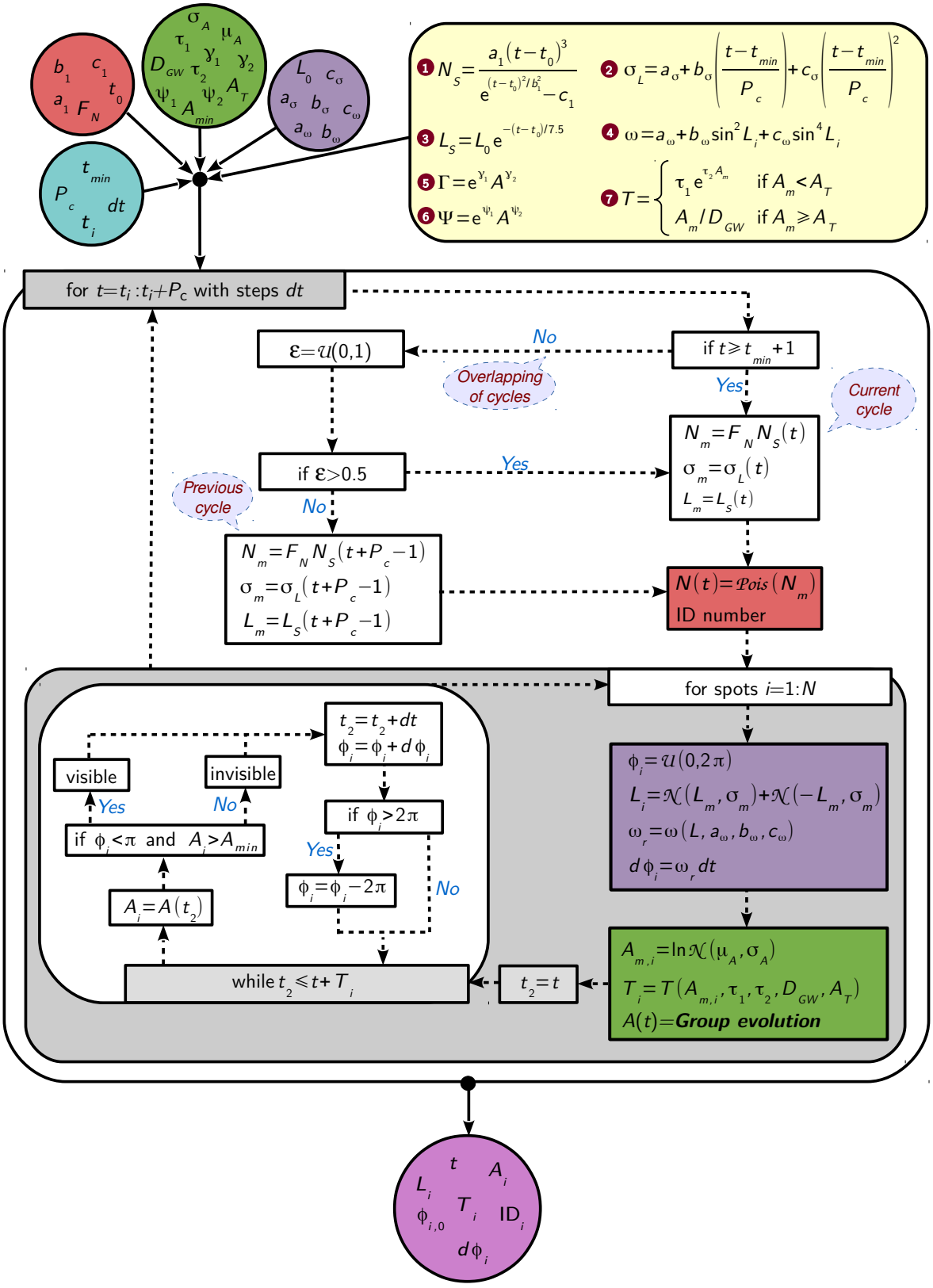

Fig. 2.7 – Diagram summarizing the spot cycle model applied to the solar cycle.

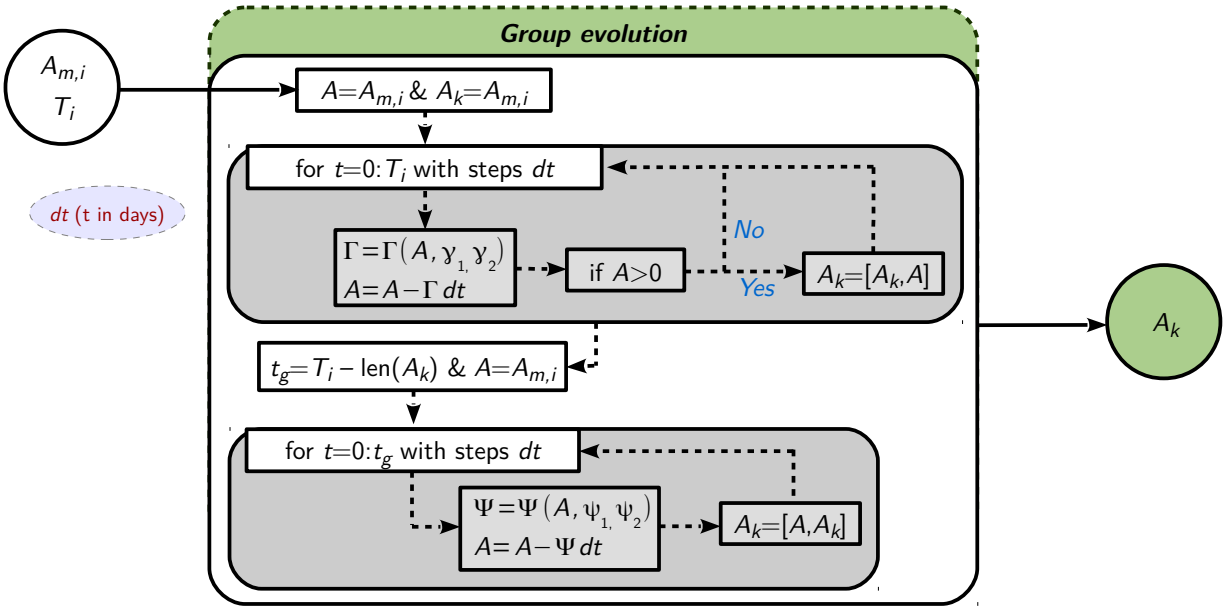

Fig. 2.8 – Diagram summarizing the group evolution (growth and decay) incorporated in the model and represented in the green box of Fig. 2.7.

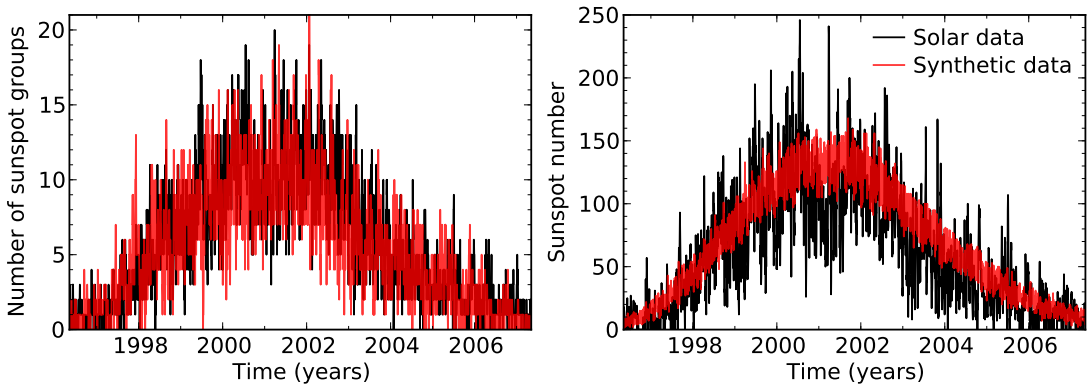

Fig. 2.9 – Comparison between the number of observed and synthetic sunspot groups and sunspots. Left: Synthetic data obtained while simulating sunspot groups. The level of agreement shows that our approach reproduces reasonably well the real sunspot data (from NGDC/NOAA). Right: Synthetic data obtained while simulating individual sunspots, illustrating why sunspots cannot be treated as independent. Sunspot Number from WDC-SILSO, Royal Observatory of Belgium, Brussels.

Figure 2.10 compares the latitudinal distribution and the total sunspot area, showing a reasonable agreement between synthetic and real sunspot data. The total sunspot area corresponds to the area covered by all visible sunspot groups on a given day.

As for the NGDC/NOAA daily records, the accumulated area distribution can be also computed for the synthetic data. The left panel of Fig. 2.11 shows the accumulated distribution (red) for the same synthetic cycle as shown above, obtained by assuming the modified GW rule as the area-lifetime

relation. The black line corresponds to the log-normal distribution that describes the observed area distribution (right panel of Fig. 2.5). The right panel shows the accumulated distribution for a synthetic sunspot cycle obtained when considering the GW rule for all ranges of areas, illustrating the disagreement between synthetic and real data for the smallest groups (as mentioned in Sect. 2.1.3): the number of small groups in the synthetic accumulated distribution is lower than that found in the Sun and the peaks of the two distributions do not coincide.

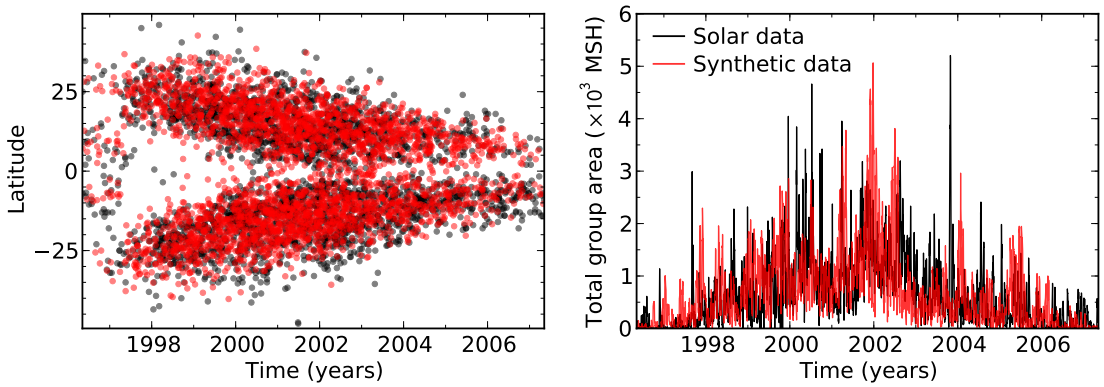

Fig. 2.10 – Comparison between synthetic (red) and solar (black) data. Left: Latitudinal distribution of sunspot groups. Right: Total area covered by sunspot groups.

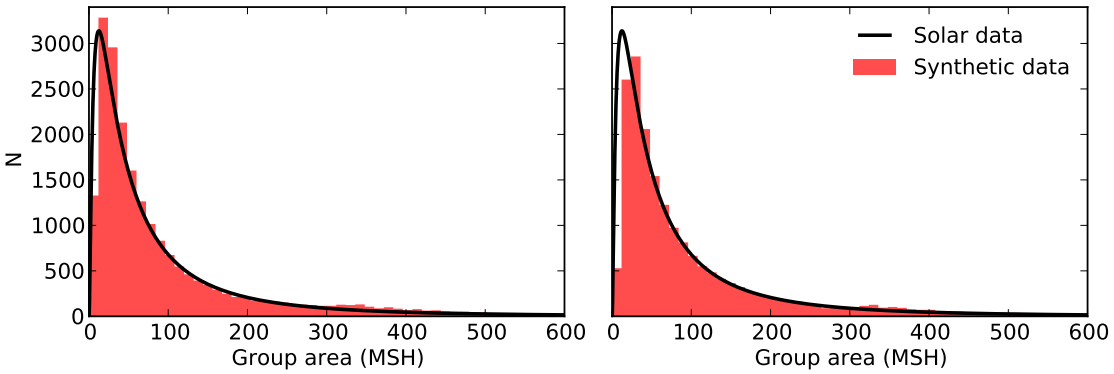

Fig. 2.11 – Accumulated area distribution for synthetic sunspot groups when assuming the modified area-lifetime relation (left) and when assuming the GW rule for all ranges of areas (right). The black line in both panels corresponds to the log-normal that best describes the observational data (Fig. 2.5; Table 2.3). We note that the bin for the smallest groups is incomplete, as the sunspot records are limited to areas larger than 10 MSH.

Comparison test: application of the Kolmogorov-Smirnov test

In order to test and improve our model we have quantified how closely related the observed and synthetic data sets are by applying the Kolmogorov-Smirnov (KS) test (Kolmogorov 1933; Smirnov 1939). This test compares the cumulative distribution functions of two samples, using the maximum deviation between them,

$$D_{n_1,n_2} = \max_x |F_{1,n_1}(x) - F_{2,n_2}(x)|, \tag{2.13}$$

where n_1 and n_2 are the number of elements of sample 1 and sample 2, respectively, and F_1 and F_2 are the corresponding cumulative distribution functions.

The null hypothesis – i.e. that both samples result from the same distribution – is rejected at significance level α if

$$D_{n_1,n_2} > c(\alpha)\sqrt{\frac{n_1+n_2}{n_1 n_2}}, \tag{2.14}$$

where $c(\alpha)$ is a constant that depends of the significance level to be considered.

More than to reject the null hypothesis at a given level α, in this work the KS-test was used to identify the aspects of the model which needed to be improved. The synthetic sunspot cycles obtained from early versions of the model resulted in large values of D_{n_1,n_2}, indicating that the model did not provide a good description of the observed properties of the sunspot cycle. By comparing the observed and synthetic cumulative distribution functions for the total area covered by sunspot groups and for the groups' latitudinal distribution, we could decide where and how to improve our model. An example of this is provided in Fig. 2.12, where we compare the cumulative distribution functions for the total group areas of the synthetic and real data. In this case, F corresponds to the fraction of days whose total area covered by sunspots is smaller than a given value, and $n_1 = n_2 = 4017$ is the total number of days considered in the real and synthetic data. The left panel corresponds to a sunspot cycle reconstruction obtained with the modified GW rule (Fig. 2.6), which corrects the area-lifetime relation for the smallest groups, while the right panel shows the results for a reconstruction obtained when adopting the GW rule for all group areas. Small groups from the former reconstruction live longer than groups with similar areas from the latter. This leads to an increase in the daily number of sunspot groups and, consequently, to a larger total area covered by the groups in the reconstruction obtained in the model that incorporates the corrected area-lifetime relation than with the other. The result is a shift of the cumulative distribution function towards larger areas and a better agreement with the observations.

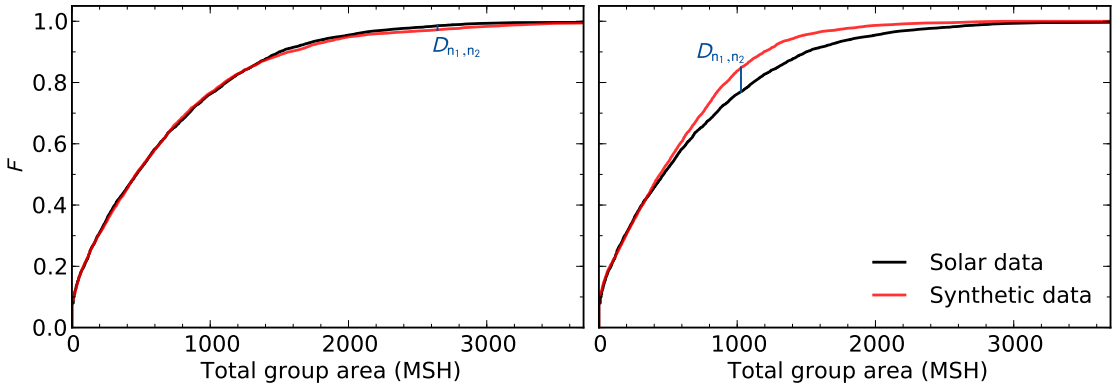

Fig. 2.12 – Cumulative distribution functions of the synthetic (red) and solar (black) data for the total area covered by sunspot groups. Left: Reconstruction obtained when assuming the modified GW rule to compute the group lifetimes, where $D_{n_1,n_2} \sim 0.0141$. Right: Reconstruction obtained when assuming the GW rule, where $D_{n_1,n_2} \sim 0.0798$.

The left panel of Fig. 2.13 compares the cumulative distribution functions for the real and synthetic latitudes resulting from the same reconstruction, obtained with the modified GW rule. Here, the cumulative distribution functions, F, represent the fraction of groups that become visible (first appearance) at a latitude lower than a given value, and $n_1 = 2801$ and $n_2 = 2919$ correspond to the total number of different observed groups in the real and synthetic data, respectively. Despite the small value of the statistics D_{n_1,n_2}, the difference between the two distributions is significant and its interpretation is relatively straightforward: the cumulative distribution function for the solar data indicates that the southern hemisphere retains almost 55% of the visible sunspot groups, while for the synthetic data the groups are more evenly distributed by the two hemispheres. This discrepancy results from the hemispheric asymmetry that is known to be present in the data, but that is not accounted for in our model (see Sect. 2.1.2). To verify this hypothesis, we compared the cumulative distribution functions for the absolute values of the latitude (right panel of Fig. 2.13), finding better agreement between them, which results in a lower value of the statistics D_{n_1,n_2}.

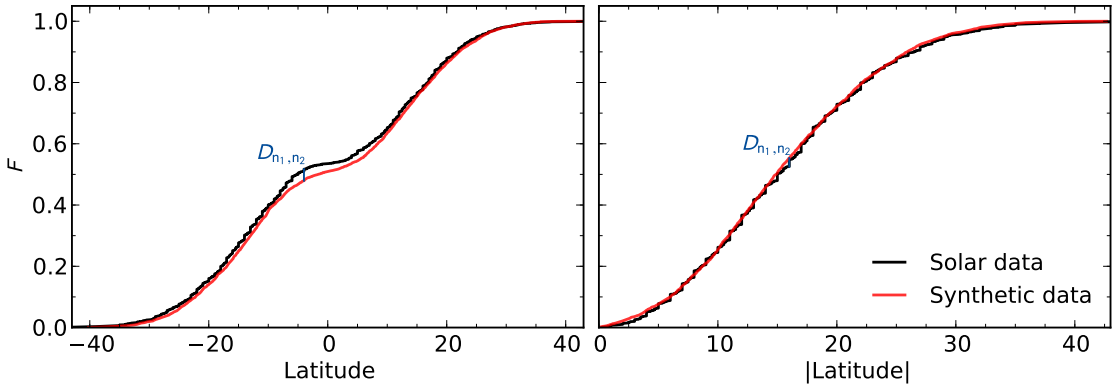

Fig. 2.13 – Cumulative distribution functions of the synthetic (red) and solar (black) data for the spot latitudes (left panel; $D_{n_1,n_2} \sim 0.0377$) and for the absolute values of the group latitudes (right panel; $D_{n_1,n_2} \sim 0.0283$.)

The results from the KS-test for the synthetic sunspot cycle discussed above are summarized in Table 2.4. At the significance level $\alpha = 0.1$ the null hypothesis for the total group area and absolute group latitudes is not rejected. Although the non-rejection of the null hypothesis does not allow us to conclude about its veracity, it certainly reinforces the expectation born from the direct inspection of Figs. 2.9 and 2.10 that the synthetic cycles obtained from the spot cycle model retain the main observed properties of the sunspot cycle.

The synthetic spot cycles obtained with our model are stochastic. Thus, we can perform Monte Carlo simulations to obtain the distributions for the statistics D_{n_1,n_2}. While n_2 is constant for the total area covered by sunspot groups (being the number of days), for the latitudinal distribution n_2 (number of spot groups) varies from reconstruction to reconstruction. Thus, rather than considering the distributions for D_{n_1,n_2}, we consider those for the quantity $C_{n_1,n_2} = D_{n_1,n_2}/\sqrt{(n_1+n_2)/(n_1 n_2)}$.

Figure 2.14 summarizes the results obtained from 5000 sunspot cycle reconstructions. The distribution of C_{n_1,n_2} obtained from the analysis of the total group area when the GW rule is assumed

for all ranges of area (left panel, blue histogram) is shifted towards larger values of C_{n_1,n_2} than while implementing the correction to the area-lifetime relation for small groups (left panel, red histogram). This confirms that the modified area-lifetime relation used in our model produces results that are statistically in better agreement with the solar data. Concerning the sunspot groups' latitudes (right panel of Fig. 2.14), the comparison of the distributions for C_{n_1,n_2} clearly confirms our earlier findings. The consequence of the non-inclusion of the hemispheric asymmetry in the model is that our synthetic cycles compare significantly better when considering the absolute values of the latitude.

	n_1	n_2	D_{n_1,n_2}	$\mathcal{D}(\alpha = 0.1)$
Total group area: Fig. 2.12, left	4017	4017	0.0141	0.0272
Latitudes: Fig. 2.13, left	2801	2919	0.0377	0.0323
Absolute Latitudes: Fig. 2.13, right			0.0283	

Table 2.4 – Results from the KS-test for the synthetic sunspot cycle discussed in the text. The n_1 and n_2 are the sample sizes for the real and synthetic data, respectively. $\mathcal{D} = c(0.1)\sqrt{(n_1+n_2)/(n_1 n_2)}$ is the right-hand side of equation (2.14) for a significance $\alpha = 0.1$.

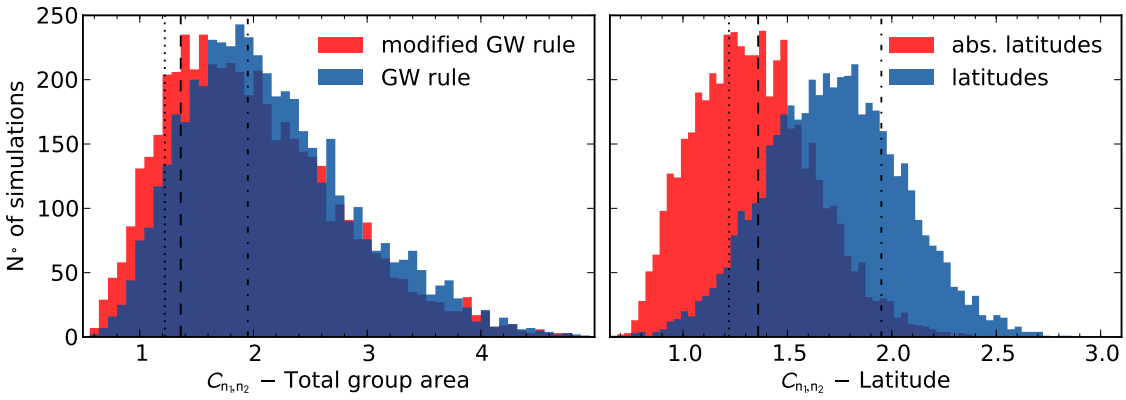

Fig. 2.14 – Distribution of $C_{n_1,n_2} = D_{n_1,n_2}/\sqrt{(n_1+n_2)/(n_1 n_2)}$ for the total area covered by sunspot groups (left) and for the latitudinal distribution (right). The vertical lines indicate the levels of significance $\alpha = 0.1$ (dotted), $\alpha = 0.05$ (dashed) and $\alpha = 0.001$ (dash-dotted). Left: Comparison between the synthetic cycles obtained when assuming the GW rule for all ranges of areas (blue) and the modified GW rule (red). Right: Distribution for the group latitudes (blue) and the absolute latitudes (red).

As mentioned in Sect. 2.1.1, we opted to use the function defined by Hathaway et al. (1994, equation 2.1) to determine a mean number of generated sunspot groups at each time step. Figure 2.15 shows the comparison of the distributions of C_{n_1,n_2} when using the functions defined by Du (2011, red histogram; equation 2.3) and Sabarinath & Anilkumar (2008, blue histogram; equation 2.2). The red distribution is similar to the one obtained using equation (2.1), which is consistent with the conclusions drawn from Fig. 2.1: the functional forms proposed by Hathaway et al. (1994) and Du (2011) yield similar fits to the observational data. The blue distribution is shifted towards larger values of C_{n_1,n_2} than the previous, illustrating that the function proposed by Sabarinath & Anilkumar (2008) is indeed a worse representation of the cycle, in particular of the rising phase (see also Fig. 2.1).

Concerning the latitudinal distribution, based on the agreement between synthetic and observa-

tional data, we opt to use an exponential function (Hathaway et al. 1994, equation 2.4) to describe the mean group latitude over the solar cycle and a polynomial function for the width of the sunspot formation zone (Jiang et al. 2011, equation 2.6). We also explored other possibilities for these two parameters, which lead to less successful representations of the solar cycle 23. The left panel of Fig. 2.16 shows the distribution of C_{n_1,n_2} for the group latitudes when assuming a polynomial function (Jiang et al. 2011, equation 2.5) for the main latitude. The right panel summarizes the results obtained while assuming σ_L to be a constant from minimum to maximum and a linear decreasing function from maximum to minimum.

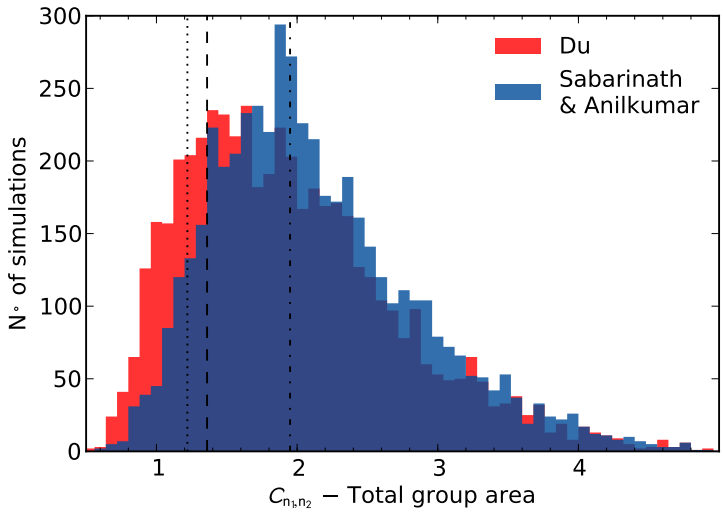

Fig. 2.15 – Distribution of C_{n_1,n_2} for the total area covered by sunspot groups when substituting the function N_S (equation 2.1) by the function defined by Du (2011, red; equation 2.3) and by Sabarinath & Anilkumar (2008, blue; equation 2.2). The vertical lines indicate the levels of significance $\alpha = 0.1$ (dotted), $\alpha = 0.05$ (dashed) and $\alpha = 0.001$ (dash-dotted).

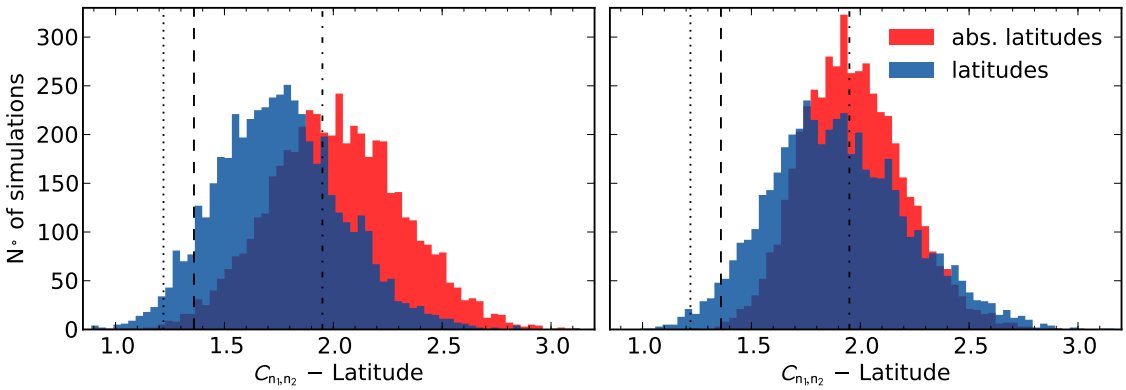

Fig. 2.16 – Distribution of C_{n_1,n_2} for the group latitudes when substituting the functions L_S and σ_L (equations 2.4 and 2.6) by other functional forms. Left: The mean latitude over the solar cycle is described by a polynomial function (equation 2.5; Jiang et al. 2011). Right: The width of the sunspot formation zone is assumed to be a constant from minimum to maximum and a linear decreasing function from maximum to minimum. The vertical lines indicate the levels of significance $\alpha = 0.1$ (dotted), $\alpha = 0.05$ (dashed) and $\alpha = 0.001$ (dash-dotted).

2.2.2 Results for solar cycle 22

The spot cycle model was first applied and calibrated to solar cycle 23. In this section, we present the results for solar cycle 22, which is stronger and shorter than solar cycle 23. The input parameters of the model are determined following the same procedure that was applied to cycle 23, described in Sect. 2.1. Table 2.5 list the parameters corresponding to the best fits obtained for cycle 22 with equations (2.1), (2.4), (2.6), and (2.7).

Mean number of groups (equation 2.1)	
a_1	4.17
t_0	1985.64
b_1	4.08
c_1	0.30

Maximum area distribution (equation 2.7)	
$H_{\mathrm{A_m}}$	0.29×10^5
$\sigma_{\mathrm{A_m}}$	1.25
$\mu_{\mathrm{A_m}}$	3.72

Mean Latitude (equation 2.4)	
L_0	30.20
t_0	1986.04

Accumulated area distribution (equation 2.7)	
$H_{\mathrm{A_{acc}}}$	2.50×10^5
$\sigma_{\mathrm{A_{acc}}}$	1.32
$\mu_{\mathrm{A_{acc}}}$	3.78

Width of the formation zone (equation 2.6)	
a_σ	0.12
b_σ	1.38
c_σ	-1.35

Table 2.5 – Approximate values of the parameters considered to describe the mean number of sunspot groups, group latitudes and areas over solar cycle 22.

Figure 2.17 compares the observational and synthetic data (from a given simulation) for cycle 22: number of sunspot groups, area coverage, latitudinal distribution, and accumulated area distribution. These results show that our model is able to reproduce reasonably well the properties of solar cycle 22.

Figures 2.18 and 2.19 show the cumulative distribution functions for the sunspot group areas and latitudes, respectively. Table 2.6 summarizes the results from the KS-test. Cycle 22 has a stronger hemispheric asymmetry than cycle 23, which results in larger values of $D_{\mathrm{n_1,n_2}}$ for the latitudes. However, the total area covered by spots and the absolute latitudes are in good agreement with the real sunspot data. This is also shown through the distributions of the quantity $C_{\mathrm{n_1,n_2}}$ obtained from 5000 simulations (Fig. 2.20).

	n_1	n_2	$D_{\mathrm{n_1,n_2}}$	$\mathcal{D}(\alpha = 0.1)$
Total group area: Fig. 2.18	3652	3652	0.0277	0.0285
Latitudes: Fig. 2.19, left	3016	3182	0.0573	0.0310
Absolute Latitudes: Fig. 2.19, right			0.0301	

Table 2.6 – Results from the KS-test for reconstruction of the solar cycle 22. $\mathcal{D}$ is the right-hand side of equation (2.14) for a significance $\alpha = 0.1$.

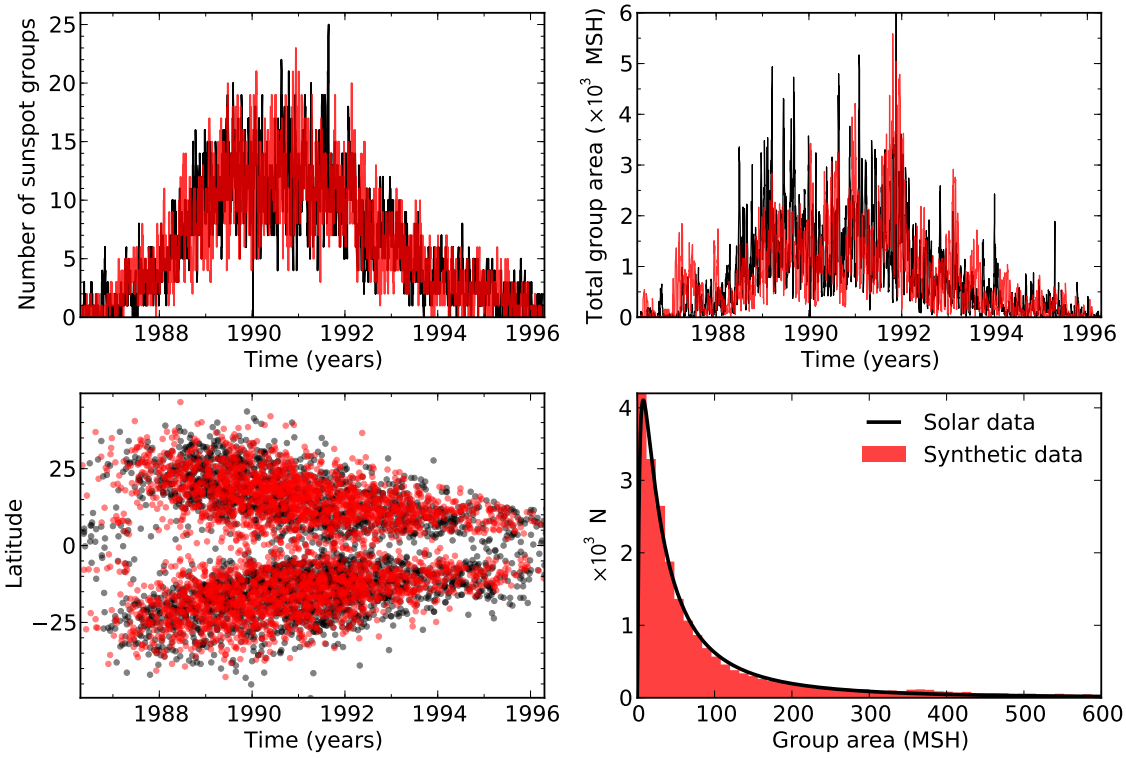

Fig. 2.17 – Comparison between observational (black) and synthetic (red) data for solar cycle 22: number of sunspot groups, total group area, group latitudes and accumulated area distribution.

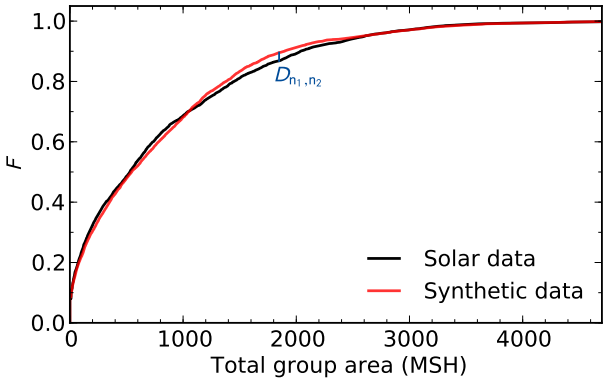

Fig. 2.18 – Cumulative distribution functions of the observational (black) and synthetic (red) data for the total area covered by sunspot groups, where $D_{n_1,n_2} = 0.0277$.

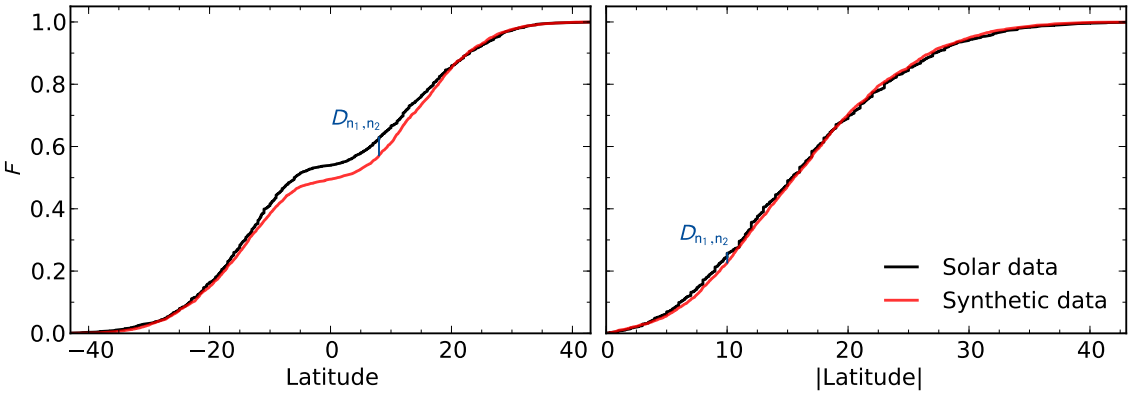

Fig. 2.19 – Cumulative distribution functions of the observational (black) and synthetic (red) data for the group latitudes (left; $D_{n_1,n_2} = 0.0573$) and absolute latitudes (right; where $D_{n_1,n_2} = 0.0301$).

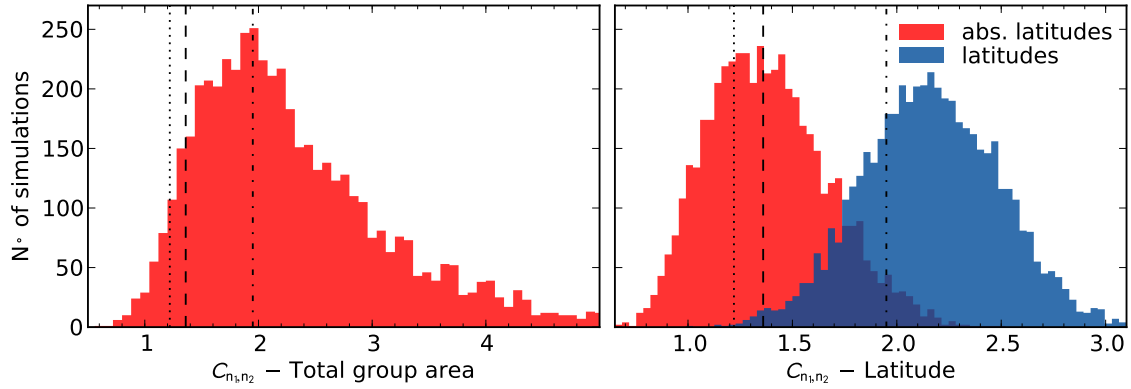

Fig. 2.20 – Distribution of C_{n_1,n_2} for the total area covered by sunspot groups (left), the group latitudes (red; right), and group absolute latitudes (blue; right). The vertical lines indicate the levels of significance $\alpha = 0.1$ (dotted), $\alpha = 0.05$ (dashed) and $\alpha = 0.001$ (dash-dotted).

2.3 Conclusions and applications

The main goal of the work presented in this chapter was to develop a simple tool able to simulate the main properties of a spot cycle, in particular the number of spot groups, the area coverage and lifetimes, and the latitudinal distribution.

A crucial assumption of our model is that different sunspot groups are generated independently. Despite evidence that sunspots tend to form within active longitudes (e.g. Bumba & Howard 1965; Bogart 1982; Jiang et al. 2011), pointing to possible correlations between their emergence, we found that the properties of the sunspot cycle are reasonably well reproduced under this model assumption.

An important by-product of this work was the verification that the GW rule is only appropriate for the largest sunspot groups. For the smallest groups, this rule seems to underestimate the groups' lifetime. We have proposed a modified area-lifetime relation for small groups which leads to a closer agreement of the synthetic sunspot cycle with observations.

The quantity, quality, and diversity of solar data, can only be adequately reproduced by a relatively complex model that includes a number of empirical parameters and functions describing the average observed properties of the sunspot number, area, latitude and solar rotation. The model can be easily adapted to simulate cycles of stars other than the Sun, characterized by different properties. However, for other stars the observational constraints are much more limited. Thus, the application of our tool to other stars may require the identification of the model parameters that have a significant impact on the activity-related stellar observables.

The spot cycle model has been used in the study of the activity-related frequency shifts (see Chapters 3 and 4; Santos et al. 2016, 2017a). Also, the spot cycle simulations can be used to study the spot signature on the stellar light curve, which enclose information about the starspot distribution (stellar magnetism) and stellar surface differential rotation. Another potential application of this kind of tool is related to the search for exoplanets, where new strategies for reducing activity signatures in the radial velocity and transit observations can be designed.

3. On the contribution from sunspots to the observed frequency shifts

Although the activity-related variations in the seismic properties of the Sun have been known for more than 30 years, the relative importance of the different contributions to those variations is not yet fully understood. In this chapter, we are interested in estimating the relative contribution from sunspots to the observed variations in the frequencies of the acoustic modes. To that end, we derive a model for the frequency shifts induced by sunspots (Sect. 3.1).

The model frequency shifts are computed by considering the sunspot data (number of sunspots, spot latitude, and size) from the NOAA/NGDC database[1]. In order to constrain the parameters of our model and to determine the contribution from spots to the total frequency shifts (Sect. 3.2), we compare the model predictions with observed frequency shifts obtained from the Global Oscillation Network Group (GONG) data and presented in Tripathy et al. (2011). Since sunspots usually last a few days only, the relatively short cadence of the frequency shifts is an important criteria for our choice of observations. In this case, Tripathy et al. (2011) obtained the acoustic frequencies from 36-day sub-series overlapped by 18 days. The authors used in their calculations the modes of degree between $l = 0$ and 100 with frequencies ranging from 2000 to 3300 μHz that are common to all the sub-datasets. The model frequency shifts are computed analogously to the observed frequency shifts (Sect. 3.2). In Sect. 3.3, we investigate the robustness of the model predictions and, in Sect. 3.4, we draw our main conclusions.[2]

3.1 Model for the spot-induced frequency shifts

The presence of sunspots on the solar photosphere can affect the propagation of acoustic waves, hence modifying the frequencies of global modes of oscillation. One way to quantify the sunspots' impact on the frequencies of global acoustic modes is by considering how the normal-mode solutions are locally perturbed by the presence of a sunspot. That perturbation can be expressed as a phase difference ($\Delta\delta$) between the solutions that would be obtained in the presence and in the absence of a spot. To fully incorporate the spot's effect, including both the direct and indirect effects, the phase must be computed at a fiducial depth, R^*, that is below the region of influence of the sunspot. R^* still needs to be sufficiently close to the surface, for the local plane-parallel approximation to be valid and above the lower turning point (r_1^l; equation 1.10) for the modes we consider in this study (Fig. 3.1). We note that $\Delta\delta$ represents a local shift in the phase of the normal modes and should not be confused with the phase shift determined in a local-helioseismic analysis (Cunha et al. 1998; Cunha & Gough 2000).

[1] http://www.ngdc.noaa.gov

[2] This chapter is focused on the work published in Santos et al. (2016).

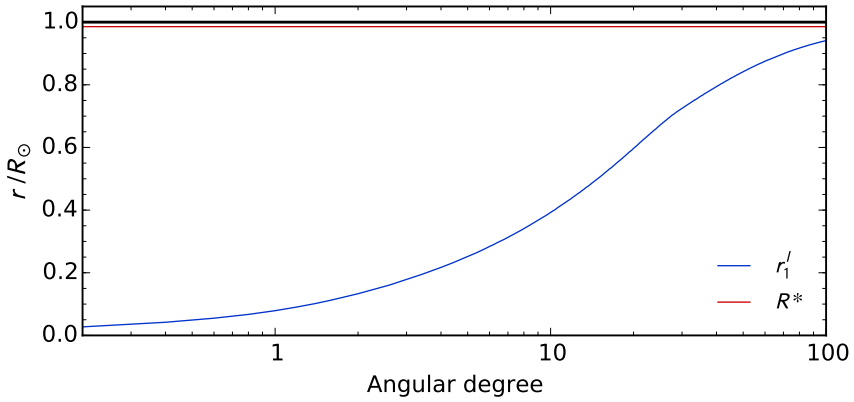

Fig. 3.1 – Lower turning point (r_1^l; blue) as a function of the mode angular degree l. The black and red lines mark the location of the solar surface and the depth R^*.

Based on the latter, Cunha & Gough (2000, see Sect. 1.3.1) (see also Cunha et al. 1998; Cunha 1999) for an application to sunspots) derived the following relation for the fractional spot-induced frequency shifts, in spherical coordinates (r,θ,ϕ),

$$\frac{\delta\omega}{\omega} \simeq -\frac{\overline{\Delta\delta}}{\omega^2 \int_{r_1^l}^{R^*} c^{-2}\kappa^{-1} dr}, \tag{3.1}$$

where $\overline{\Delta\delta}$ is the integral phase difference given by

$$\overline{\Delta\delta} = \frac{\int_0^{2\pi}\int_0^{\pi} \Delta\delta (Y_l^m)^2 \sin\theta d\theta d\phi}{\int_0^{2\pi}\int_0^{\pi} (Y_l^m)^2 \sin\theta d\theta d\phi}, \tag{3.2}$$

where $(Y_l^m)^2 = Y_l^m Y_l^{m*} = (P_l^m)^2$ and P_l^m are Legendre polynomials normalized such that the denominator is unity. The indice m indicate the mode azimuthal order ($m = -l..., 0, ...l$). At any given time, $\Delta\delta$ in equation (3.2) is non-zero only where spots are located. Since the phase difference is defined by comparing with the case when the spot is absent, the resulting frequency shifts are also defined with respect to the case when sunspots are absent from the solar surface.

Previous studies carried out in the context of strongly magnetic pulsating stars (e.g. Cunha & Gough 2000) show that the phase difference $\Delta\delta$ depends on the magnetic field strength and inclination, as well as on the mode frequency. This implies that the phase shift varies with the position within the spot. Nevertheless, the associated impact on the frequencies of the global oscillations is only an integrated one, as seen from equation 3.2. In addition, the phase difference was shown to depend on the mode frequency, which affects the phase with which the wave enters the region of influence of the sunspot. Nevertheless, the phase difference is not expected to depend significantly on the mode degree as the velocity fields of the modes of low and intermediate degree, and similar frequency, have a similar depth dependence in the very superficial layers, propagating almost vertically there, and thus interacting in a similar manner with the magnetic field. In order to test that, we use a sunspot model from Khomenko & Collados (2008) with parameters $\eta = 1.3$ (related with the inclination of the magnetic field), $a = 6$ Mm (related with the curvature of the magnetic field lines

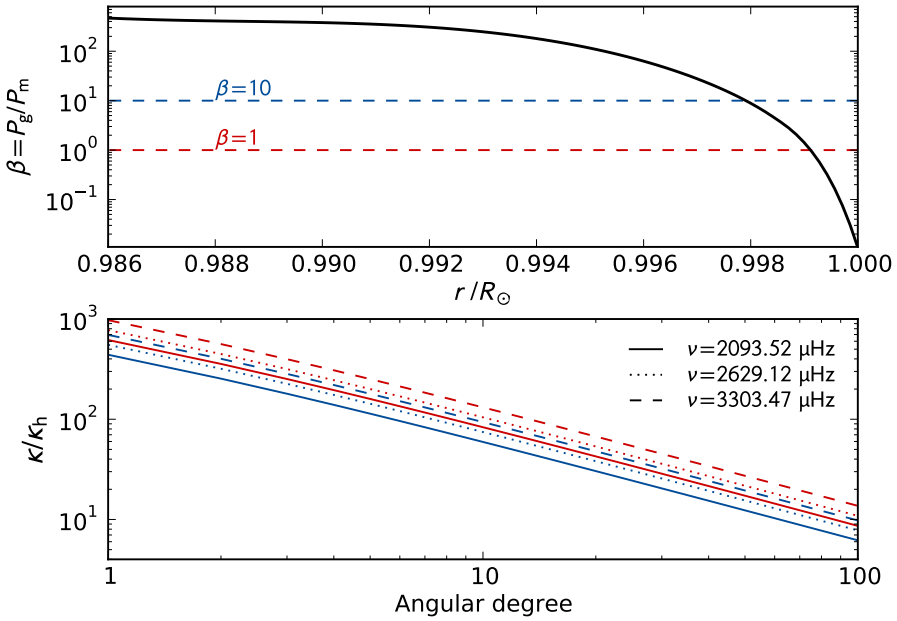

Fig. 3.2 – Top: Ratio between the gas and magnetic pressures for a given sunspot model. The red and blue lines mark $\beta = 1$ and $\beta = 10$. Bottom: Ratio between the vertical and horizontal components of the wavenumber at depths corresponding to $\beta = 1$ (red) and $\beta = 10$ (blue). The solid, dotted, and dashed lines correspond to $\nu = 2093.52\,\mu$Hz, $\nu = 2629.12\,\mu$Hz, and $\nu = 3303.47\,\mu$Hz, respectively.

and size of the magnetic flux tube at R^*), and $z_d = -1$ Mm (depth at which the models for the photosphere and deeper layers are merged). The top panel of Fig. 3.2 shows the ratio between the gas and magnetic pressures ($\beta = P_g/P_m = 4\pi P/B^2$) at the spot's axis. We then compare the vertical and horizontal components of the acoustic wavenumber of the modes at depths where $\beta = 1$ and $\beta = 10$. Far from the turning points of the mode the ratio between the two components of the wave number is given by (see equations 1.8 and 1.9)

$$\frac{\kappa}{\kappa_h} = \sqrt{\frac{\omega^2}{c^2} - \frac{l(l+1)}{r^2}} \Bigg/ \sqrt{\frac{l(l+1)}{r^2}}, \tag{3.3}$$

where ω and l correspond to the mode angular frequency and angular degree, c is the sound speed, and r is the distance from the solar centre. The bottom panel of Fig. 3.2 shows this ratio for three frequencies (low, intermediate, and high within the frequency range used by Tripathy et al. 2011). In the worst case scenario considered in this work ($l = 100$ and $\nu = \omega/(2\pi) = 2093.52\,\mu$Hz), the mode propagates with an inclination of only 6.6° at $\beta = 1$ and 9.2° at $\beta = 10$. This assures us that the dependence of the phase shift on the mode degree is weak for the range of mode degrees considered in the current work.

According to equations (3.1)-(3.2), the computation of the spot-induced frequency shifts from first principles would require the knowledge of the function $\Delta\delta$ within each individual sunspot. Mod-

elling each individual sunspot over a solar cycle is clearly an impossible task, but an estimate of the spot-induced frequency shifts may still be made by considering a characteristic phase difference, $\Delta\delta_{\rm ch}$, equal for all spots. This is accomplished by substituting $\Delta\delta$ in equation (3.2) by a function that is zero outside the sunspots and equal to a constant value $\Delta\delta_{\rm ch}$ inside the sunspots. In practice, this corresponds to assuming that the sunspot area and position on the solar surface are the only properties that distinguish the impact of different sunspots on the frequencies.

Two different approaches may be followed to estimate $\Delta\delta_{\rm ch}$. The first is to consider a model for the stratification and magnetic field of a characteristic sunspot and solve the pulsation equations adequate for a plasma permeated by a strong magnetic field. This was performed in part in an earlier work (Santos et al. 2012), where the authors considered an incomplete case in which only the indirect effect of the magnetic field on the oscillations (via the magnetically-induced changes in the stratification) was taken into account. They concluded that this indirect effect is small compared to the total spot's effect, in agreement with earlier findings by Cally et al. (2003) and Gordovskyy & Jain (2007). While this approach may have the advantage of determining the phase difference from first principles, including the presumably dominant direct effect of the magnetic field is a rather complex task. Moreover, the results will necessarily depend on our ability to correctly model a typical sunspot.

A second approach, which we will adopt in the current work, consists in taking $\Delta\delta_{\rm ch}$ as a parameter to be constrained by direct comparison of the frequency shifts derived from equations (3.1)-(3.2) and the observations. A potential difficulty in this case comes from the fact that the observed frequency shifts are not produced exclusively by the sunspots. Nevertheless, for observations with sufficient time resolution the short-term, stochastic-like frequency variations associated with the effect of the sunspots may be distinguished from the longer-term variations. This will be illustrated in Sect. 3.2 where the relative importance of the two contributions will be established.

To proceed, we substitute the phase difference in equations (3.1)-(3.2) by the characteristic parameter $\Delta\delta_{\rm ch}$. This parameter will be considered frequency-dependent, but, for the reasons explained previously, we shall neglect its dependence on mode degree. Taking the central colatitude (θ_i) and longitude (ϕ_i) of a given spot i, and having in mind that the spherical harmonic functions do not vary significantly within the spot, we approximate, for each spot, $\left(Y_l^m\right)_i = Y_l^m(\theta_i,\phi_i)$. Under these assumptions, equation (3.1) becomes

$$\frac{\delta\omega}{\omega} \simeq -\frac{\Delta\delta_{\rm ch}}{I_l}\sum_{i=1}^{N}\left[(P_l^m(\cos\theta_i))^2\int_{\phi_{\min_i}}^{\phi_{\max_i}}\int_{\theta_{\min_i}}^{\theta_{\max_i}}\sin\theta d\theta d\phi\right], \tag{3.4}$$

where $I_l = \omega^2\int_{r_1}^{R^*} c^{-2}\kappa^{-1}dr$ is related to the inertia of the mode, N is the number of sunspots on the solar surface, and $\phi_{\min_i}$, $\phi_{\max_i}$, $\theta_{\min_i}$, $\theta_{\max_i}$ define the limits of a given spot i.

Considering the temporal variation of the sunspot properties, equation (3.4) can be rewritten as

$$\frac{\delta\omega}{\omega}(t) \simeq -\frac{\Delta\delta_{\rm ch}}{I_l R^2}\sum_{i=1}^{N(t)}\left[(P_l^m(\cos\theta_i))^2 A_i\right], \tag{3.5}$$

where R is the solar radius and A_i the area of a given spot i. In addition to the temporal variation, the fractional frequency shifts given by equation (3.5) depend on mode frequency, due to the frequency

dependence of $\Delta\delta_{\rm ch}$, and on mode degree, due to the degree dependence of the Legendre polynomial and the degree dependence of the mode inertia (reflected in the integral I_l).

3.2 Results: comparison between the model and observed frequency shifts

In order to study the contribution of the sunspots to the observed activity-related frequency shifts, we have used the sunspot daily records from the NGDC/NOAA database. This database includes daily information about each observed sunspot group, such as latitude and area. With the sunspot group area and latitude in hand, equation (3.5) allows for the estimation of the spot-induced frequency shifts for different radial orders, angular degrees, and azimuthal orders, for any given characteristic phase difference.

In this work the model frequency shifts will be compared with the observational data from GONG presented in Tripathy et al. (2011). As summarized previously, the observed frequencies of the solar acoustic modes are measured from time-series of 36 days with 50% overlap. This means that consecutive data points are not independent. Later, we will separate the data into two samples of independent frequency shifts by taking only every second data point. Tripathy et al. (2011) used modes of degree between $l = 0$ and 100 with frequencies ranging from 2000 to 3300 μHz. For each multiplet the authors first derived a central frequency. The central frequency shifts, defined by comparison with a reference value, were then combined, weighted by the corresponding mode inertias, to establish a mean frequency shift for the observed frequency range.

Within the frequency range considered by Tripathy et al. (2011), the observed frequency shifts are almost a linear function of the frequency (e.g Libbrecht & Woodard 1990; Chaplin et al. 2001; Basu 2002). Therefore, the mean frequency shifts derived by the authors provides a good estimate of the frequency shifts of modes with frequencies close to the middle of the observed interval. With this in mind, in the computation of the model frequency shifts we will consider the frequency closest to the center of the frequency range used by Tripathy et al. (2011) (frequencies from Rabello-Soares & Appourchaux 1999). This implies that the phase difference $\Delta\delta_{\rm ch}$ that will be inferred from comparison of our model with the observations must be interpreted as the characteristic phase difference at that frequency.

The NGDC/NOAA data includes only the sunspots emerging on the visible side of the Sun. Since all sunspots on the solar surface, and not only the visible ones, contribute to the frequency shifts, we must make an assumption about the contribution of the invisible spots. As there is no reason to expect systematic differences between the two sides, it is reasonable to assume that on average the contributions are equal. Therefore, the fractional frequency shifts will be computed from equation (3.5) by taking twice the value obtained when only the visible spots are considered. The impact of doing so will be discussed at length in Sect. 3.3, where we will repeat our analysis using synthetic solar-cycle data. The model spot-induced frequency shifts, $\delta\nu_{lm} = \delta\omega_{lm}/2\pi$, are computed for $l = 0 - 100$ and the corresponding azimuthal orders. In this calculation we have taken R^* to correspond to a radius of 10 Mm below the photosphere. The model frequency shift associated to a

given angular degree, $\delta\nu_l$, is then calculated following the same procedure used for the observations by Tripathy et al. (2007, 2011). In particular, we fit the $\delta\nu_{lm}$ to a polynomial expansion of the form

$$\delta\nu_{lm} = \delta\nu_l + \sum_{j=1}^{j_{\max}} a_j(l) P_j(m/l), \tag{3.6}$$

where $j_{\max}$ is $2l$ for $l \leq 4$ and 9 for $l > 4$, a_j are the splitting coefficients and P_j is the Legendre polynomial of order j. Some examples (for $l = 1, ..., 12$) are shown in Fig. 3.3.

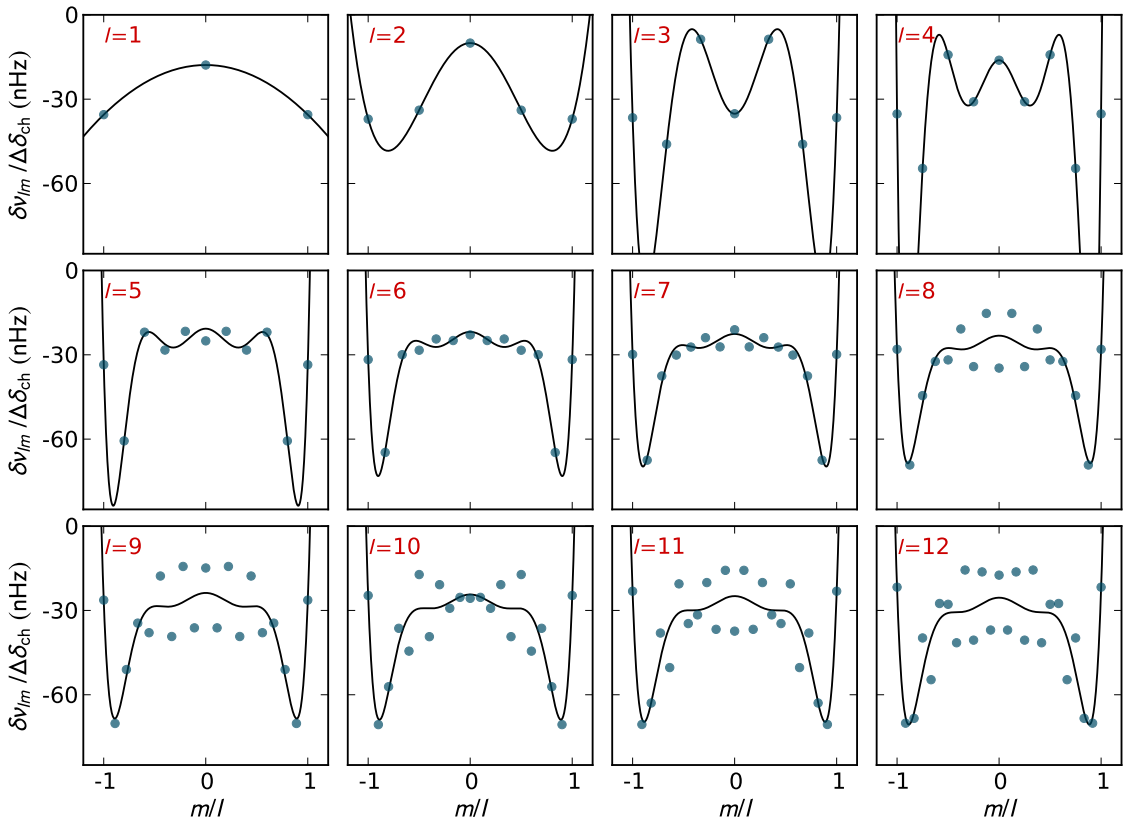

Fig. 3.3 – Comparison between the mode frequency shifts (blue), normalized by the constant phase difference, and the best fits obtained with equation (3.6; black solid lines) for a given time t.

The model mean frequency shifts $\delta\nu(t)$ are then defined as

$$\delta\nu(t) = \sum_l Q_l \delta\nu_l(t) \Big/ \sum_l Q_l \equiv \delta\nu_{\text{spots}}, \tag{3.7}$$

where Q_l is the inertia ratio ($E_l/E_0(\nu_l)$; equation 1.26; Christensen-Dalsgaard & Berthomieu 1991). $\delta\nu_{\text{spots}}$ is thus the model equivalent to the observable constructed by Tripathy et al. (2011) based on the GONG data, but including only the spot-induced part of the frequency shifts. For a known sunspot distribution, it depends on the single parameter $\Delta\delta_{\text{ch}}$. Figure 3.4 shows the daily model spot-induced frequency shifts obtained from the daily sunspot records, normalized to the characteristic phase difference, which is expected to be negative (see Sect. 1).

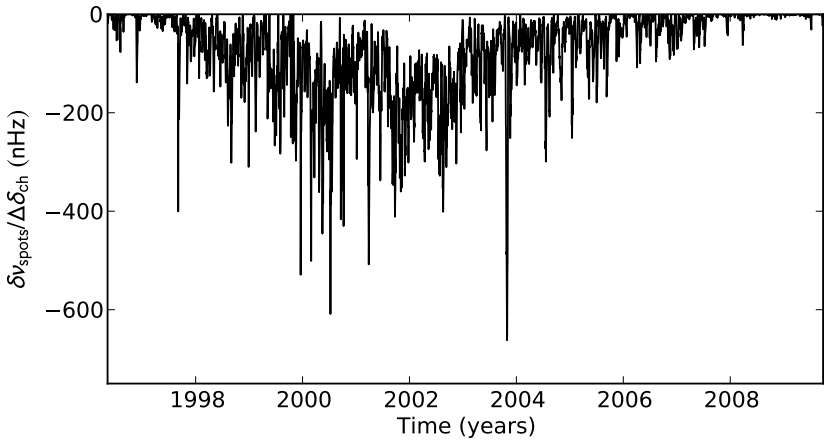

Fig. 3.4 – Spot-induced frequency shifts, normalized by the constant phase difference, obtained from the daily sunspot records.

It is well known that the observed frequency shifts do not result only from the effect of the sunspots (e.g. Tripathy et al. 2007; Chaplin et al. 2007b; Jain et al. 2009). Other effects, such as the variation of the global magnetic field and structural and thermal changes act on much longer timescales. As a consequence, in order to reproduce the observations it is necessary to add to our model an additional component of the frequency shifts, varying on longer timescales. That will be done later in this section. Nevertheless, it is instructive to consider, for a moment, the hypothetical case in which spots are the sole responsible source of the observed frequency shifts. In this case, the characteristic phase difference may be determined by fitting the model for the spot-induced frequency shifts to the observational data ($\delta\nu_{obs}$). To that end, we obtain the 36-day averages (with an overlap of 18 days) of the daily spot-induced frequency shifts. Then, using the consecutive independent data points, the best fit is obtained through a χ^2 minimization between the observational values and the model values, $\delta\nu_{spots}$. For each sample of independent frequency shifts, we find that $\Delta\delta_{ch} \sim -1.51$ and $\Delta\delta_{ch} \sim -1.52$, respectively. The model-data comparison is shown in Fig. 3.5. Note that the spot-induced frequency shifts are now relative to the minimum value in the observed frequency shifts.

As seen from Fig. 3.5, the scatter in the frequency shifts is about three times in the model data than in the observed data. This is a consequence of having taken the spots to be the sole responsible for the observed frequency shifts, which, as mentioned earlier, is well known not to be the case. In other words, while sunspots contribute both to the long and short-term variations in the oscillation frequencies, if they were the single cause for the frequency shifts, the observations would show a much more significant short-term variance. We can thus ask the question of how significant would a long-term-varying component originating from sources other than the sunspots have to be, in order to adequately fit the observations. To address this question, we add the long-term-varying component ($\delta\nu_{global}$) to the frequency shifts, which may be associated to the effect of the overall solar magnetic field and to global structural and thermal changes. Different approaches may be used to define the smooth component. Given that the long-term frequency shifts variations are well

correlated with the long-term variations in the sunspot number (e.g. Tripathy et al. 2007; Chaplin et al. 2007b; Jain et al. 2009, 2012), one option is to use the function that was proposed by Hathaway et al. (1994, equation 2.1) to fit the sunspot number. Accordingly, we fit the function $f(t)$, given by equation (2.1), to the observed frequency shifts. The values of the parameters found from the fit are: $a_1 \sim 6.76$, $b_1 \sim 4.71$, $c_1 \sim -0.46$, and $t_0 \sim 1995.06$.

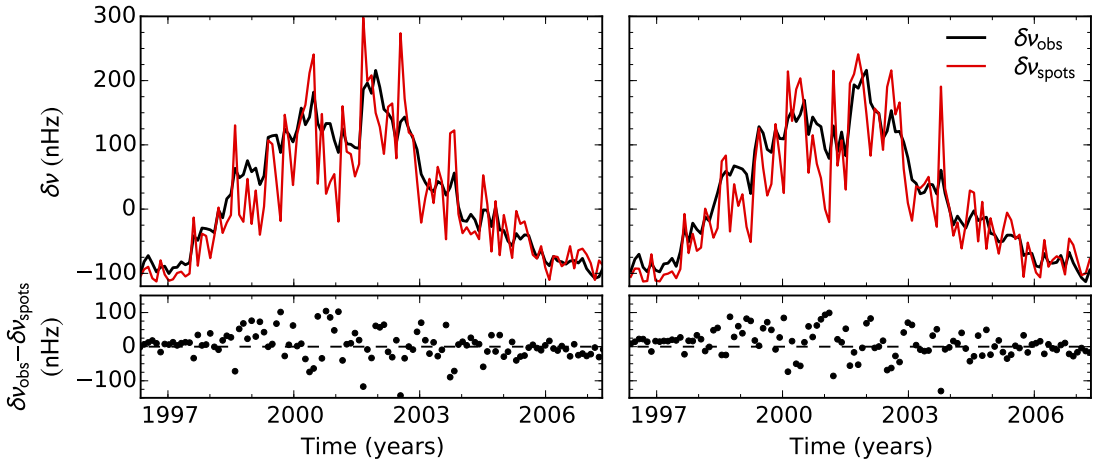

Fig. 3.5 – Left and right panels concern each sample of independent data points. Top panel: Observed (black; Tripathy et al. 2011) and model spot-induced frequency shifts (red) for the hypothetical case in which spots are taken to be the only contribution to the observed frequency shifts. The amplitude of the variations in $\delta\nu$ is much larger in our results than in the observational data, confirming that the spots are not the only contribution to the frequency shifts. Bottom panel: Residuals between the observed and model spot-induced frequency shifts.

The model frequency shifts are then given by

$$\delta\nu_{\rm model} = \delta\nu_{\rm global} + \delta\nu_{\rm spots}, \tag{3.8}$$

where $\delta\nu_{\rm global} = wf(t)$ and w is the weight of the smooth component to be defined by fitting the data. Thus, our model now contains two parameters, w and $\Delta\delta_{\rm ch}$.

From a χ^2 minimization between $\delta\nu_{\rm model}$ and the observations, for each sample of independent data points, we find $w \sim 0.71$ and $\Delta\delta_{\rm ch} \sim -0.47$, and $w \sim 0.69$ and $\Delta\delta_{\rm ch} \sim -0.50$. Figure 3.6 shows the comparison between the observed frequency shifts and the results for $\delta\nu_{\rm model}$. The resulting frequency shifts are in reasonable agreement with the observational data indicating that our simple, two-component model captures the main features contained in the observed frequency shifts. The weight of the smooth component, w, gives an estimate of the contribution resulting from the changes in the global magnetic field and associated structural and thermal variations, which is $\sim 70\%$. The remaining $\sim 30\%$ correspond then to the spot-induced contribution.

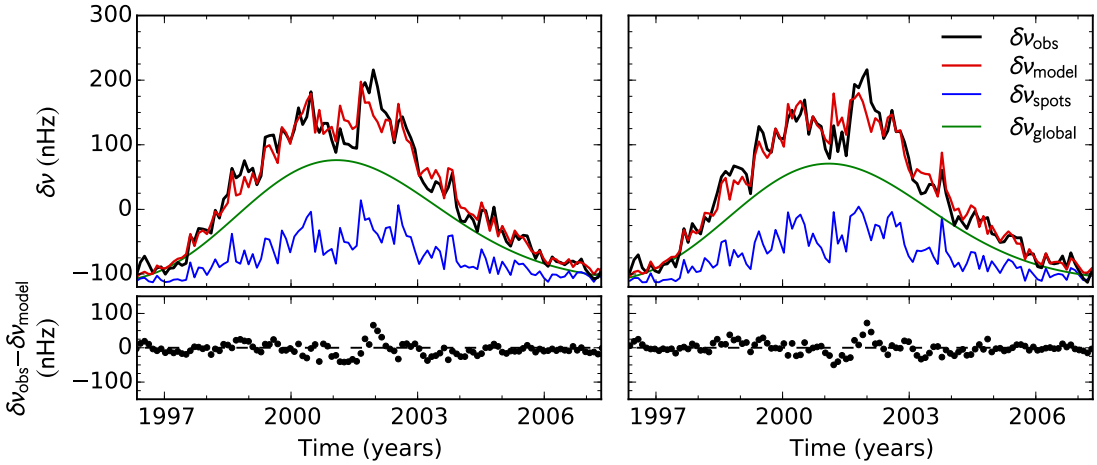

Fig. 3.6 – Left and right panels concern each sample of independent data points. Top panel: Observed (black; Tripathy et al. 2011) and model frequency shifts (red). The total model frequency shifts correspond to the combination of a global (green) and a spot-induced (blue) components. Bottom panel: Residuals between the observed and model frequency shifts.

3.3 Discussion: robustness of the model predictions

3.3.1 Global component

Different approaches may be considered to model the smooth component introduced in Sect. 3.2. While we have opted to use the function defined by Hathaway et al. (1994), we have also assessed the robustness of our results to changes in the modelling of the smooth component. We considered alternative approaches in which the function *f(t)* is defined by other functional forms (equations 2.2 and 2.3) or smoothed versions of the observed frequency shifts (obtained with 360-d, 468-d, and 540-d filters). Figure 3.7 compares the parameters w and $\Delta\delta_{ch}$ found when using each of these global components. Moreover, we have also considered an alternative approach to the model-data comparison, by which we have first subtracted a smooth component to both the observed and the spot-induced frequency shifts (obtained through the application of a 360-day filter to each set) and, then, fitted the residuals. In all cases the global and spot-induced fractional contributions were found to be similar to the values estimated in the original analysis, with the parameter w agreeing to better than $\sim 10\%$ with the value estimated in Sect. 3.2.

3.3.2 Far-side of the Sun

While the results from our two-parameter (w and $\Delta\delta_{ch}$) model reproduce reasonably well the observed frequency shifts, we see from the lower panel of Fig. 3.6 that some differences still exist between the two. Part of these residuals may be connected to the fact that only the visible sunspot groups are recorded in the NGDC/NOAA daily records. The observed frequency shifts are affected by the spots appearing throughout the whole solar surface. Thus, using the visible groups in the computation of the spot-induced frequency shifts from equation (3.5) and considering that the total spot-induced

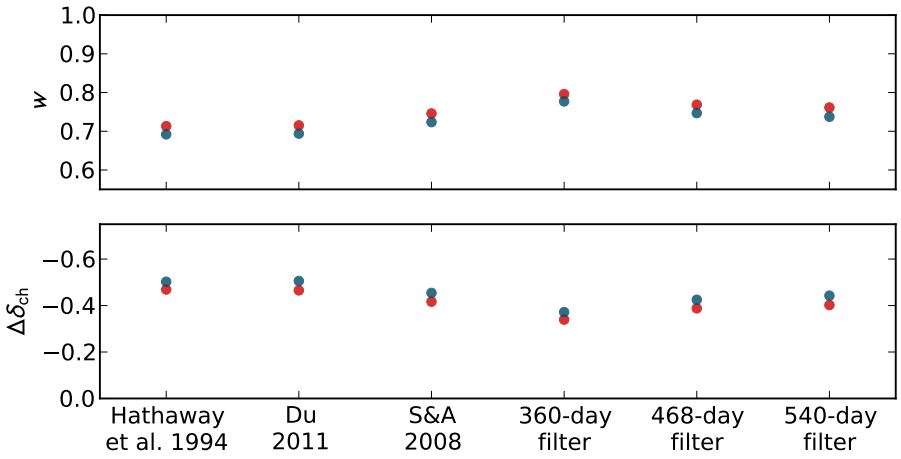

Fig. 3.7 – Parameters w and $\Delta\delta_{ch}$ obtained while considering the different functional forms for the global component given by: equations (2.1)-(2.3); 360-d, 468-d, and 570-d filter. Red and blue dots concern each sample of independent data points.

component is twice the value may introduce statistical differences between the model predictions and the observations. Since there is no data for the sunspots emerging on the invisible side of the Sun, the only way to check the impact of this limitation is to recur to simulations, which we will do by performing the same analysis as in Sect. 3.2 but using synthetic sunspot records obtained with the empirical tool developed by Santos et al. (2015, Chapter 2). With this tool we simulate the number of sunspot groups, the total area covered by them and their latitudinal distribution along one complete solar cycle. As mentioned previously, the output from this tool is analogous to that of the real daily records.

Following the methodology described in Sect. 3.2, we obtain the daily frequency shifts induced by all the groups on the solar surface (case 1) and by the visible groups alone assuming that they are a reasonable representation of both (visible and invisible) sides of the Sun (case 2). The first of these cases is used to simulate a model frequency-shift cycle, i.e. a model equivalent of the observations considered in the previous section (i.e. equivalent to $\delta\nu_{obs}$), while the second is used to estimate the error made when taking only the visible sunspot groups for the frequency shift calculations, with a factor of two to account for the far-side side (i.e. equivalent to $\delta\nu_{model}$).

In order to obtain synthetic data consistent with the observed frequency shifts, we follow a different approach to determine the parameters w and $\Delta\delta_{ch}$. In this case, we cannot compare directly the observed frequency shifts and the synthetic data, as done in Sect. 3.2 through a χ^2 minimization between the observed and model frequency shifts. Instead, for case 1, we start by determining $\Delta\delta_{ch}$ (and, thus, the synthetic spot-induced frequency shifts, $\delta\nu_{synt\text{-}spots}$) in such a way that the sum of the variations of the frequency shifts obtained from synthetic data coincides with the value found using the observed frequency shifts, i.e. $\sum_k |\Delta\delta\nu|_{obs,k} = \sum_k |\Delta\delta\nu|_{synt\text{-}spots,k}$, where $\Delta\delta\nu = \delta\nu_{k+1} - \delta\nu_k$ and different indices k correspond to the different data points. To the synthetic spot-induced frequency shifts we add the smooth global component, $\delta\nu_{global} = wf(t)$, to obtain the model frequency shifts

for case 1 (hereafter $\delta\nu_{\odot}$). The function $f(t)$ is that found in Sect. 3.2. The weight w is determined through a χ^2 minimization with the observed data, being $\Delta\delta_{\rm ch}$ fixed to the value found in the previous step. The frequency shifts $\delta\nu_{\odot}$ are now taken as the reference with which we compare the results obtained from the visible spots alone. We then, for case 2, proceed exactly as in Sect. 3.2, but substituting the observed frequency shifts by the reference-model frequency shifts $\delta\nu_{\odot}$, and the frequency shifts based on sunspot data from NGDC/NOAA by the frequency shifts obtained from simulated data for the visible side alone, hereafter $\delta\nu_{\rm visible\odot}$. Figure 3.8 shows the comparison between $\delta\nu_{\odot}$ and $\delta\nu_{\rm visible\odot}$ for a given simulation of the sunspot cycle.

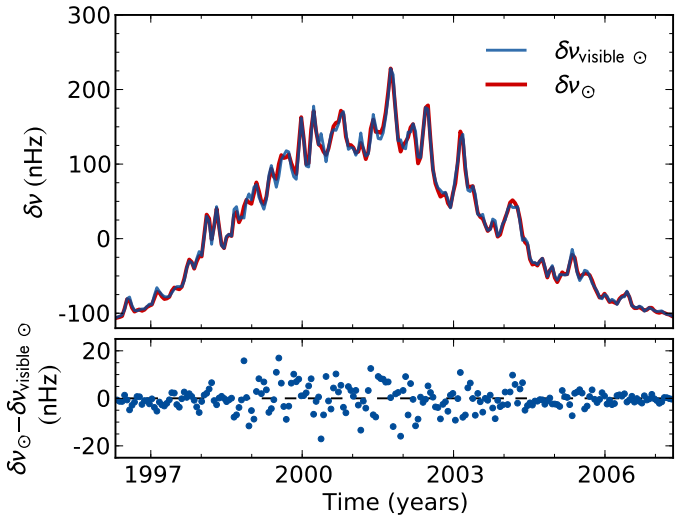

Fig. 3.8 – Top panel: Frequency shifts derived from synthetic sunspot data: when considering all synthetic sunspot groups at the solar surface (red) and when considering only the visible groups (blue). Bottom panel: Residuals between the frequency shifts shown in the top panel.

The differences between the model frequency shifts derived when considering all synthetic sunspot groups at the surface and when considering just the visible groups (in Fig. 3.8) are significantly smaller and more evenly distributed than the ones found in Sect. 3.2. We, therefore, conclude that the main differences seen in Fig. 3.6 are not explained by the fact that the sunspot data used for the computation of the model frequency shifts in Sect. 3.2 only contain information on the groups emerging on the near-side of the Sun.

Since the simulations of the sunspot cycles are stochastic, we repeat the procedure described above for a large number of synthetic data sets (500 simulations). Figure 3.9 shows the distribution of the difference between the parameter w (and consequently the weight of the spot-induced component) found for case 1 and case 2.

We found that the spot-induced contributions to the frequency shifts obtained when considering all synthetic sunspot groups and the visible groups alone, differ, on average, by less than 3% (dashed line in Fig. 3.9). The difference is small due to the 36-day averaging of the frequency shifts. This average dilutes the daily differences that may exist between the area and position of the spots in each side of the Sun. This reassures us that the estimated value for the spot-induced frequency shifts' contribution found in Sect. 3.2 is robust, even if computed from data for the visible sunspots only.

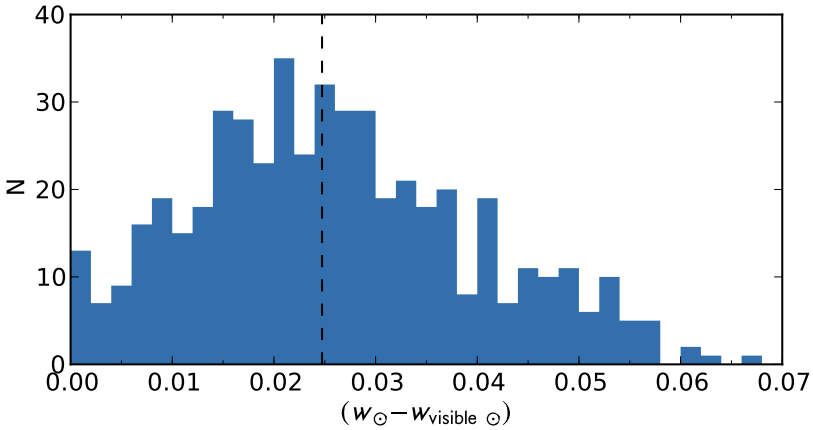

Fig. 3.9 – Distribution of the difference between the parameter w obtained when considering all the sunspots ($w_\odot$; case 1) and just the visible spots ($w_{\text{visible}\odot}$; case 2) for 500 simulations. This distribution also gives an indication on the error on the estimation of the spot-induced contribution computed as $1 - w$. The dashed line marks the average value.

3.3.3 Mid-term variation

A closer inspection of the residuals in Fig. 3.6 shows that these seem to be in phase with the quasi-biennial variations found in the frequency shifts by Fletcher et al. (2010) and Broomhall et al. (2012), having a significant periodicity of ∼1.5 years (Fig. 3.10).

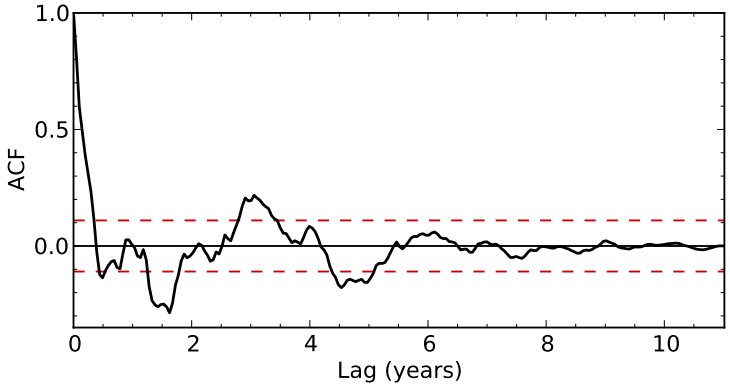

Fig. 3.10 – Autocorrelation function of the residuals shown in Fig. 3.6. Here, we do not consider the individual samples of independent data points. However, the results for the two samples are very similar. The red dashed lines indicate the 95% significance level.

A large number of activity indicators, including the sunspot areas used in our calculations of $\delta\nu_{\text{spots}}$, shows a quasi-biennial modulation (e.g. Bazilevskaya et al. 2014; Broomhall et al. 2012; Broomhall & Nakariakov 2015), but with slightly different periodicities. Similarly to what is done to the observed frequency shifts in Fletcher et al. (2010) and Broomhall et al. (2012), we compute smooth versions of $\delta\nu_{\text{obs}}$, $\delta\nu_{\text{spots}}$, and $\delta\nu_{\text{model}}$ by applying a boxcar filter with a 2.5-yr width and subtract them from the original data sets. Then, we compute the Lomb-Scargle periodogram for those residuals (Fig. 3.11).

The results for the model and spot-induced frequency shifts are very similar due to the fact that the short-term variations in our model (equation 3.8) are mainly determined by the spot contribution. We find a significant peak at $\sim$ 1.5-yr only for the observed frequency shifts. This indicates that the 1.5-yr periodicity is intrinsic to the observed frequency shifts.

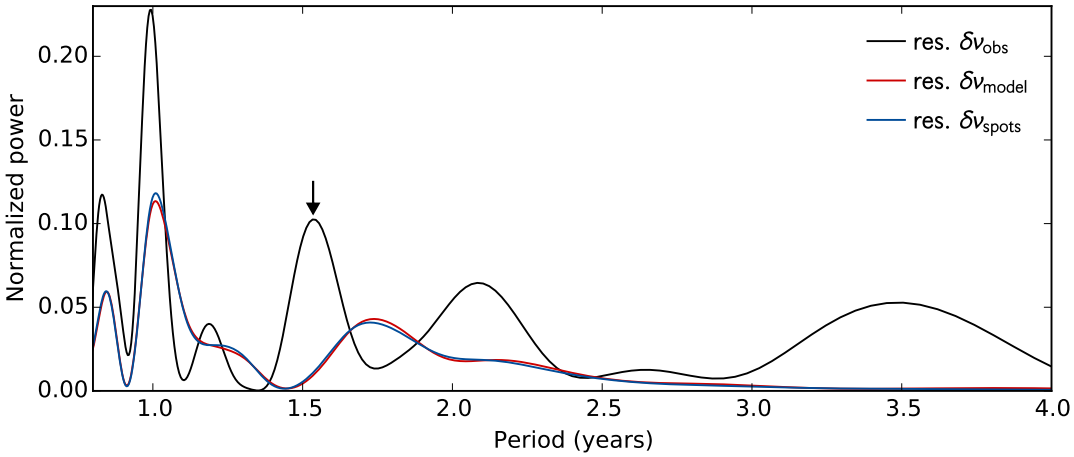

Fig. 3.11 – Lomb-Scargle periodogram of the residuals for the observed (black), model (red), and spot-induced (blue) frequency shifts. The arrow marks the 1.5-yr periodicity.

These results may point to a global contribution with structure in an intermediate time-scale, as opposed to one that varies only on the time-scale of the solar cycle, as considered in Sect. 3.2. In addition, the characteristic phase difference may vary during the solar cycle, e.g. as a result of changes in the typical structure and magnetic field within the sunspots. This could also contribute to the differences seen in Fig. 3.6.

3.4 Conclusions

Our results indicate that there are two main contributions to the total activity-related frequency shifts. A spot-induced contribution of about 30%, that is responsible for the stochastic behaviour of the frequency shifts as well as for part of their long-term variations, and a global contribution of about $\sim$70%, varying on the time-scale of the solar cycle, possibly related to the changes in the overall magnetic field. This is consistent with the results obtained by Jain et al. (2009) when studying the correlations between the frequency shifts and different activity indices.

We have checked that our results are robust against changes in the form adopted for the global component. Moreover, based on synthetic data, we have demonstrated that they would not change in any significant way, if all the sunspots emerging on the surface of the Sun could be considered, rather than just the visible ones.

Although, our model frequency shifts agree reasonably well with the observed frequency shifts, we find evidence for variations in the data at timescales not accounted for in our model. These

could either be associated with intermediate-term variations in the spot-induced phase shifts or with intermediate-term variations in the non-spot contributions. Despite these differences, we note that the contributions of 70% and 30% derived from our model are robust, as they depend essentially on the relative amplitudes of the stochastic and smooth components seen in the observations. In fact, we also verified by testing models with an additional intermediate-term component (see Sect. 4.6.1), that small corrections to the model associated to activity on intermediate timescales will not change the estimated fractional contribution of the spot-induced and global components in any significant way.

With the increasing number of solar-like stars with detected activity-related variations in the frequencies of the acoustic modes (García et al. 2010b; Salabert et al. 2016; Régulo et al. 2016; Kiefer et al. 2017, Chapter 5), the understanding of the different contributions to those variations becomes even more important. If the contribution from starspots to the frequency shifts in solar-like pulsators is comparable to that found in this work for the case of the Sun, the amplitude of those shifts can be used to estimate the surface coverage of starspots.

4. Short- and mid-term variations in the solar acoustic frequencies

The frequencies of the solar acoustic oscillations vary over the activity cycle (i.e. on a long, 11-yr timescale) and the variations in other activity proxies are found to be well correlated with the variations in the acoustic frequencies.

One of the difficulties in interpreting the correlations found between variations in the different activity proxies and variations in the oscillation frequencies comes from the fact that the latter result from the combination of different physical phenomena. In fact, the oscillation frequencies are sensitive to the direct effect of the magnetic field, which might be significant in active regions, but also to variations in the solar structure and dynamics that are induced both by the weak and strong magnetic field components. Luckily, these phenomena do not have the same characteristic timescale, and thus, by considering the behaviour of the frequency shifts on short- (timescale of days), mid- (quasi-biennial timescale), and long-terms (11-yr timescale) one may hope to move forward in the interpretation of the observed correlations.

In this chapter, our goal is to characterize the differences between the behaviour of the frequency shifts and the area covered by sunspots on the short and intermediate timescales. In particular, we are interested in identifying the times when the frequency shifts and the sunspot areas do not vary in a similar way. To do so, we propose a new observable, namely, the weighted sum of the frequency-shift differences, that is mostly sensitive to the short-term frequency variations, which we expect to be mainly determined by the spot component.

As in Chapter 3, we use the observed frequency shifts obtained by Tripathy et al. (2011) from GONG data. The observed frequency shifts are estimated from 36-d time-series overlapped by 18 days. These observations, thus, provide two datasets that we will analyse separately, each composed of a sequence of consecutive, independent, frequency shifts obtained from 36-d time-series: Sample 1 and Sample 2 – starting, respectively, on the first and second data point of the original dataset from Tripathy et al. (2011).

We also analyse the model frequency shifts, obtained with the parametrized model described in Santos et al. (2016, Chapter 3), and synthetic sunspot data from the empirical spot cycle model (Santos et al. 2015, Chapter 2).

Besides the relation between the sunspot areas and the observed frequency shifts, we also investigate the relation between the 10.7-cm flux and the frequency shifts, both modelled and observed.[1]

4.1 Method: weighted sum of the frequency-shift variations

The variations in the solar acoustic frequencies are known to be correlated with the variations in the solar activity indicators, in particular with the area covered by sunspots. The latter varies on a

[1] This chapter is mainly focused on the work published in Santos et al. (2017a).

timescale of days and induces frequency variations on a similar timescale. Unfortunately, it is not possible to derive accurate frequency shifts from time-series as short as a few days. Nevertheless, such short timescale variations are expected to be the main source of the 36-d frequency variations seen in the GONG data. To test this possibility and investigate more closely the short-term frequency shifts, we define a new observable

$$W_{\mathrm{D}} = \sum_k \Delta\delta\nu_k \times S_k, \tag{4.1}$$

as the weighted sum of the frequency shift differences. Here, $\Delta\delta\nu_k$ is the difference between the frequency shifts measured in two consecutive data bins (i.e. $\Delta\delta\nu_k = \delta\nu_k - \delta\nu_{k-1}$ with $k = 2,3,4,...$), thus corresponding to the bin-to-bin frequency variation. Also, S is a weight to be determined according to the variation of the area covered by sunspots (averaged over the respective bins of 36-d). At a given time t_k, if the total area covered by spots, A_{T}, increases with respect to its value at the time t_{k-1}, the weight, S_k, will be 1, otherwise $S_k = -1$, i.e.

$$S_k = \begin{cases} 1, & \text{if } \Delta A_{\mathrm{T},k} > 0 \\ -1, & \text{if } \Delta A_{\mathrm{T},k} < 0 \end{cases} \tag{4.2}$$

where $\Delta A_{\mathrm{T},k} = A_{\mathrm{T},k} - A_{\mathrm{T},k-1}$.

If the short-term frequency-shift differences are indeed strongly correlated with the variations in the area covered by spots, as predicted by the model for the spot-induced frequency shifts, they will be summed positively when performing this weighted sum. Thus, the new variable W_{D} is expected to be most sensitive to the short-term variation component of the frequency shifts, with the smooth, long-term component, being essentially cancelled due to the varying positive and negative weights. To show that this is indeed the case, we compute W_{D} using the spot-induced frequency shifts alone ($\delta\nu_{\mathrm{spots}}$; equation 3.7), derived from the observational sunspot data (NGDC/NOAA), and using the total model frequency shifts ($\delta\nu_{\mathrm{model}}$, which includes the spot contribution and the long-term smooth component; equation 3.8), where the weight S is determined from the observed sunspot areas (NGDC/NOAA).

The comparison between the two cases is shown in Fig. 4.1. The maximum difference between the two curves is one order of magnitude smaller than what would be found if the large-scale variations were summed positively, thus confirming that the smooth, long-term component almost cancels out when computing W_{D} for the 36-d cadence. The arrow marks the expected standard deviation at the end of the solar cycle for the case in which the frequency shift variations are described by a random walk, thus providing an indication of the interval where the maximum value of the curves would be expected to lie, if the frequency-shift differences were completely uncorrelated with the variations in the area covered by sunspots. The fact that the maxima of the two curves is so much greater than that value is a consequence of the almost perfect correlation between the spot-induced frequency-shift differences predicted by the model and the corresponding variations in the total sunspot area, as expected given the way the model is constructed.

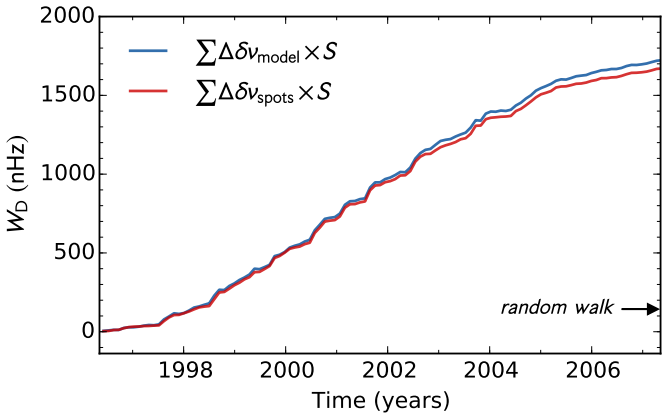

Fig. 4.1 – Weighted sum of the variations in the model (blue) and spot-induced (red) frequency shifts (derived from the observational sunspot data), where the weight S, in equation (4.1), is determined by the variation in the area covered by sunspots. The black arrow marks the expected standard deviation for a random walk.

We now compute W_D for the Samples 1 and 2 of the observed frequency shifts obtained from GONG data and compare the results with the hypothetical case of complete correlation, defined as the case in which the variations in the area covered by sunspots and in the frequency shifts always have the same sign (meaning that an increase (decrease) in one always correspond to an increase (decrease) in the other). In that case the weighted sum defined by equation (4.1) reduces to the sum of the absolute (modulus) values of the frequency-shift differences (M_D)

$$M_D = \sum_k |\Delta\delta\nu_k|. \tag{4.3}$$

The quantities W_D (black solid line) and M_D (black dashed line) obtained from Samples 1 and 2 (left and right panels, respectively) are shown in Fig. 4.2. The comparison between the maximum of the black solid line and the expected standard deviation for a random walk allows us to conclude that a significant correlation exists between the sunspot-area variations and the frequency-shift differences. In fact, in both cases the black continuous curve reaches a maximum value that is 7σ above that of a random walk, meaning that if the short-term variations in the frequency shifts and in the areas were uncorrelated, the probability of obtaining the deviation reached by the black solid lines would be less than 10^{-11}. For comparison we show in the same plot the the results for the model spot-induced frequency shifts derived from the observational sunspot data. The red solid and dashed lines correspond to the quantities W_D and M_D, respectively, obtained from Samples 1 and 2 (left and right panels, respectively). In this case, the correlation is perfect and, unlike in the case of the observed frequency shifts, the solid and dashed curves overlap.

We also verified to what extent the results for W_D are affected by the error associated with the observed frequency shifts. By taking the observational data points and assuming that the corresponding errors are Gaussian, we obtained random samples for the frequency shifts. We then estimated the standard deviation from W_D, which is represented by the grey area in Fig. 4.2. For some data

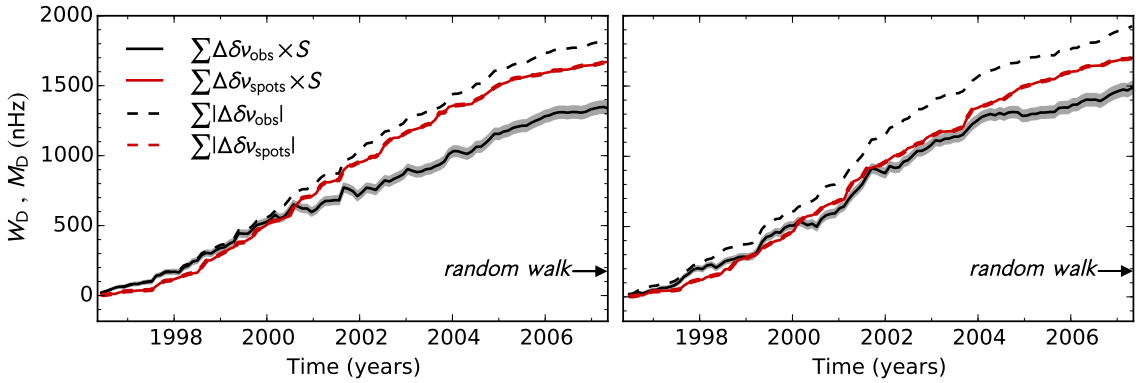

Fig. 4.2 – Left and right panels correspond to the results obtained for Samples 1 and 2, respectively. Weighted sum W_D of the variation in the observed (black solid line) and spot-induced (red solid line) frequency shifts (derived from the observational sunspot data), where the weight, S, is determined by the variation in the total observed area covered by sunspots. The grey region represents the 1σ confidence interval from the black continuous curve resulting from the errors in the observed frequency shifts. The dashed lines represent the sum, M_D, of the absolute (modulus) values of the frequency-shift differences. The arrow marks the expected standard deviation for a random walk.

points, the observational errors are of the same order as the frequency-shift differences. However, those data points do not contribute significantly to W_D. Clearly, the uncertainty in the black curve (grey region) associated to the observational errors in the frequency shifts does not explain the loss of correlation found.

We thus conclude that a strong, but not complete correlation exists between the short-term variations in the observed frequency shifts and in the spots' areas. The origin of the observed loss of correlation can be twofold: it may result from our inability to compute the true correlation between these two variations, or it may correspond to a genuine loss of correlation introduced either by changes in the effect that sunspots have on the frequencies or by the effect of other physical phenomena (besides spots) which may influence the solar frequency shifts on short timescales. In the next section we will discuss a potential source for that loss of correlation, associated with the lack of information about the sunspots on the far-side of the Sun.

4.2 Impact of the far-side of the Sun

Even if a complete correlation existed between the variations in the frequency shifts and in the total area covered by spots, we would still expect to see a significant loss of correlation when comparing the quantities W_D and M_D derived from the observations. The reason is that the sunspot areas we consider for the computation of W_D, obtained from the NGDC/NOAA databases, concern only the visible sunspot groups, while the acoustic frequencies are affected by sunspot groups emerging over the whole solar surface. In this section, we estimate the effect of having ignored the invisible sunspot groups in the computation of W_D of the previous section. To that end, we use synthetic sunspot data obtained with an empirical tool developed by Santos et al. (2015, Chapter 2). This tool generates

synthetic sunspot daily records analogous to the real sunspot data from NGDC/NOAA, starting from simulations of sunspot groups on both the near- and far-sides of the Sun.

Using the model presented in Chapter 3, we compute the spot-induced frequency shifts for the synthetic sunspot data, $\delta\nu_{\rm synthetic}$, taking into account all the spots, including those appearing on the near- and far-sides of the Sun. Since the model for the frequency shifts is parametrized, it needs to be calibrated by comparison with the observed data. In this case, we are interested in analysing the short-term variations in the frequency shifts. We, thus, calibrate the frequency shifts in such a way that their absolute sum is equal to the absolute sum of the observed counterparts, i.e. $\sum_k |\Delta\delta\nu_{\rm obs}|_k = \sum_k |\Delta\delta\nu_{\rm synthetic}|_k$ (as done in Sect. 3.3.2). We then compute $W_{\rm D}$ for the synthetic data, by combining the variations in the frequency shifts obtained from all the synthetic sunspot groups with the weights S_k computed only from the visible synthetic sunspot areas. Since the sunspot cycle simulations are stochastic, we repeated this exercise 1000 times, computing the values of $W_{\rm D}$ and $M_{\rm D}$ for all simulations.

The quantities $M_{\rm D}$ and $W_{\rm D}$ derived from the synthetic data are shown in the left panel of Fig. 4.3 for one particular simulation. The difference between these quantities gives an estimate of the loss of correlation that can be explained by our not accounting for the sunspot groups on the invisible side of the Sun when computing the weights S_k. The right panel of Fig. 4.3 shows the distribution of that difference at the end of the solar cycle (at $t_{\rm f}$). Taking the average of the distribution as an indicator and comparing it with the difference between $M_{\rm D}$ and $W_{\rm D}$ computed in Sect. 4.1 for the observations, we conclude that only about 30 per cent of the loss of correlation found in the analysis of the real data may be explained by this non-physical effect. Therefore, a significant part of the loss of correlation detected in Sect. 4.1 is expected to have its origin in physical effects other than sunspots that affect the short-term frequency shifts and that are not, themselves, fully correlated with the total area covered by sunspots.

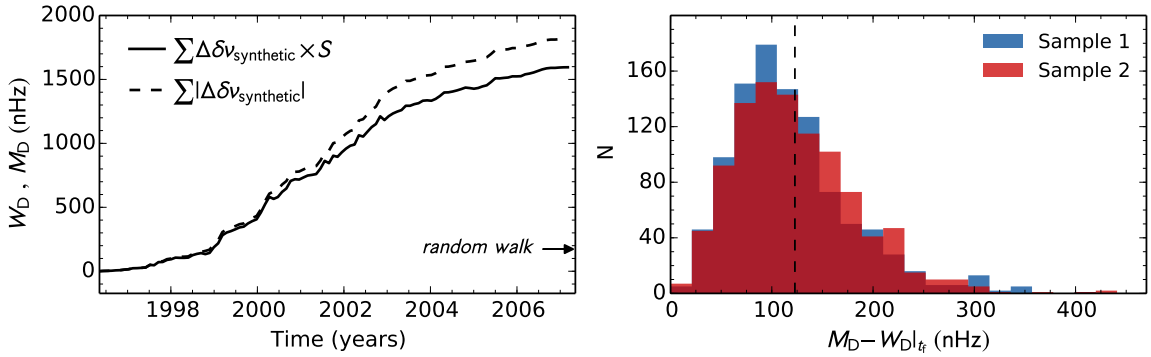

Fig. 4.3 – Left panel: Comparison between the quantities $M_{\rm D}$ (dashed line) and $W_{\rm D}$ (solid line) for a particular synthetic cycle. The arrow marks the expected standard deviation for a random walk. Right panel: Distribution of the difference between the quantities $M_{\rm D}$ and $W_{\rm D}$ at the end of the synthetic solar cycle (at $t_{\rm f}$). The dashed line marks the averaged difference found for both samples of independent frequency shifts.

4.3 Epochs of distinct behaviour between the observed frequency shifts and the sunspot areas

While the frequency-shift differences are found to be strongly correlated with the variations in the area covered by sunspots, there are particular epochs when the frequency shifts and the sunspot areas vary in the opposite way, leading to the loss of correlation found in Sect. 4.1. In this section, we identify those epochs.

The top panels of Fig. 4.4 show the difference between M_D (black dashed line in Fig. 4.2) and W_D (black solid line in Fig. 4.2) for the observed frequency shifts. The results for the two samples differ slightly. For Sample 1 (left panel) the differences have a larger amplitude around the solar maximum, while for Sample 2 they are more evenly spread. We recall that the two samples provide 36-d averages of the frequency shifts that are shifted by 18-d. The differences seen in the results for the two samples highlight that a significant loss of correlation takes place on shorter times scales than 18 d. In the discussion that follows we will, therefore, consider only aspects that are identified in both samples.

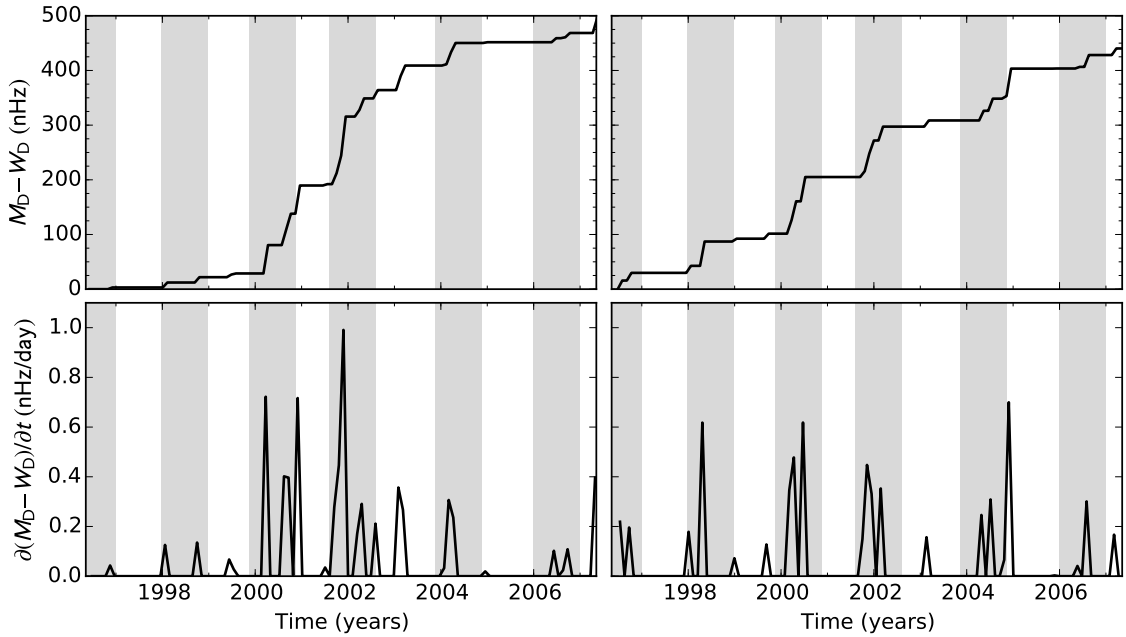

Fig. 4.4 – The left panel concerns Sample 1, while the right panel corresponds to Sample 2. Top panels: Difference between the absolute sum, M_D, and the weighted sum, W_D, of the observed frequency-shifts variations, i.e. between the black-dashed and solid lines in Fig. 4.2. Bottom panels: Time derivative of the difference shown in the top panels. The grey bars, with a width of one year, are centered around the approximate location of the maxima of the quasi-biennial signal detected by Broomhall et al. (2012).

The bottom panels of Fig. 4.4 show the derivative of the difference between M_D and W_D with respect to the time. This quantity is zero when the variations in the frequency shifts have the same sign as those in the sunspot areas, differing from zero when the two variations have an opposite

sign. The most significant correlation losses occur around the same times for the two samples of independent frequency shifts. The peaks are quasi-periodic, coinciding with the maxima of the quasi-biennial periodicity observed in the solar acoustic frequencies. This is illustrated by the grey bars in Fig. 4.4, which have a width of 1 year and are centered at the locations of maxima of the quasi-biennial signal found by Broomhall et al. (2012).

4.4 Short-term variations in the 10.7cm flux

The acoustic frequency shifts are found to be better correlated with the 10.7cm flux than with other activity proxies (e.g. Chaplin et al. 2007b; Tripathy et al. 2007; Jain et al. 2009). Besides the contribution from sunspots, the 10.7cm flux is also affected by radio plages and the quiet-Sun background in the upper chromosphere and lower corona (e.g. Covington 1969; Tapping 1987; Tapping & Detracey 1990). Given its sensitivity to both sunspots and plages, the 10.7cm flux may provide a more complete picture of the short-term variations in the solar activity than the sunspot areas alone. To test this possibility, we repeated our analysis using the variations in the 10.7cm flux (from NGDC/NOAA) instead of the sunspot area variations as the weight in equation (4.1). The results, shown in Fig. 4.5, confirm that the loss of correlation is less pronounced in this case than when the sunspot area variations are used (around 40 per cent smaller than that found in Figs. 4.2 and 4.4). Despite this, we still find that, in general, the loss of correlation is more significant around the maxima of the quasi-biennial variations.

The comparison between the results found for the area covered by sunspots and for the 10.7cm flux confirms that the latter contains contributions from additional activity-related features (besides sunspots) that vary on short timescales and that these features have a significant impact on the short-term variations of the frequency shifts. Still, the short-term variations in the 10.7cm flux are strongly correlated with the variations in the sunspot areas. This is shown in Fig. 4.6, where W_{D} corresponds to the weighted sum of the variations in the 10.7cm flux and the weight is determined by the variation in the sunspot areas. Finally, we may also conclude from the results for the 10.7cm that spots and plages alone do not fully explain the short-term variations in the observed frequency shifts.

4.5 Offset between the short-term variations in the frequency shifts and in the sunspot areas

One may expect that the frequency shifts can be better correlated with the observed sunspot areas corresponding to a slightly shifted time interval, as spots may affect the oscillation frequencies before and/or after becoming visible. In fact, the observed frequency shifts are found to be ahead of other activity indicators (e.g. Jain et al. 2009; Salabert et al. 2009, 2015). This suggests that the activity-related changes in the upper layers of the Sun affect the acoustic frequencies before becoming detectable in other activity proxies, including sunspot data. In this section, we explore that possibility

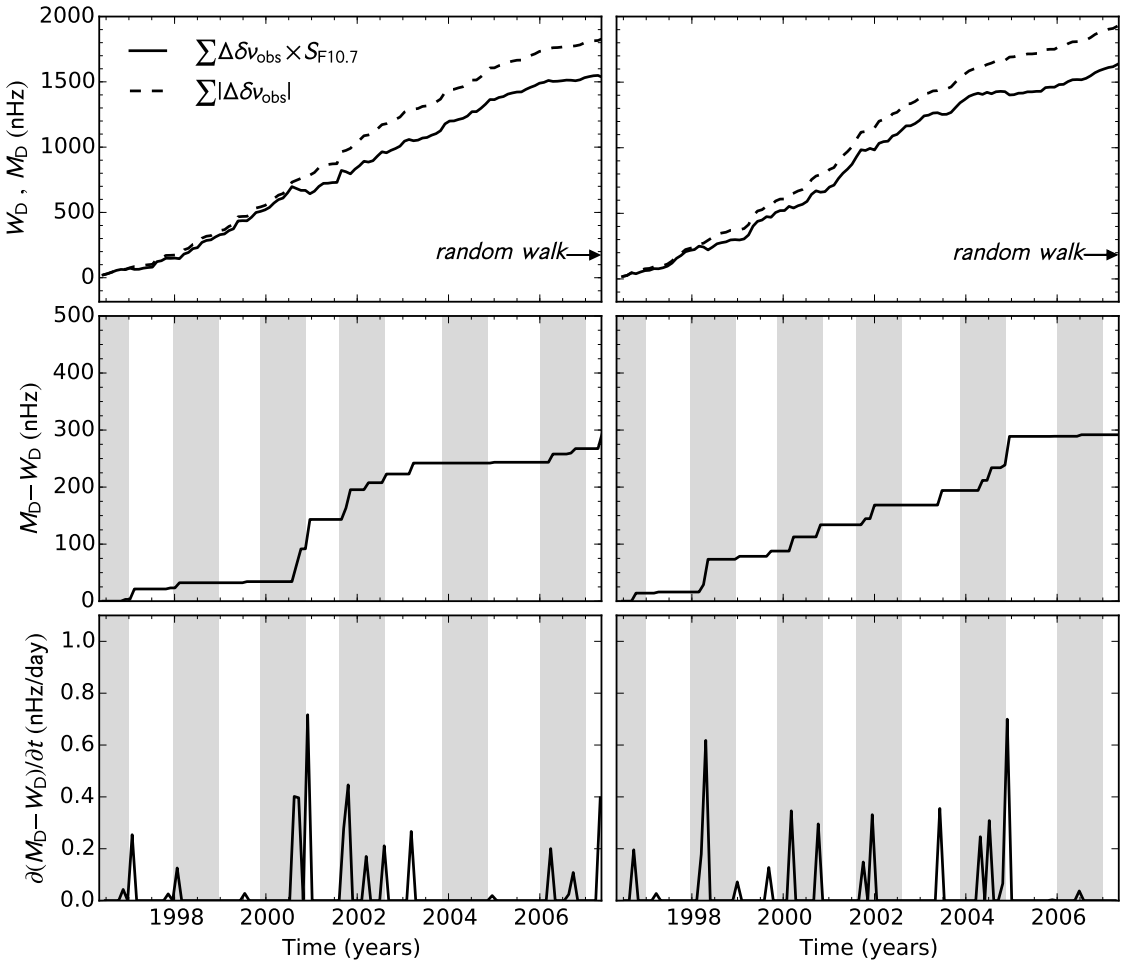

Fig. 4.5 – Left and right panel concern the Sample 1 and Sample 2, respectively. Top panels: Weighted sum of the variations in the observed frequency shifts (black solid line), where the weight S, in equation (4.1), is determined by the variation in the 10.7cm flux. The dashed line represents the sum of the absolute values of the frequency-shift differences, M_D. The arrow marks the expected standard deviation for a random walk. Middle panels: Difference between the dashed and solid lines in the top panels. Bottom panels: Derivative of the difference shown in the middle panels. The grey bars, with a width of one year, are centered around the approximate location of the maxima of the quasi-biennial signal detected by Broomhall et al. (2012).

by considering a temporal offset in the sunspot data, i.e. by computing the 36-d averages of the total sunspot area over bins shifted in time in relation to the observed frequency shifts. Figure 4.7 illustrates the offset introduced in the average sunspot areas. An offset of 0 days corresponds to the case of Fig. 4.2. A negative offset corresponds to using sunspot groups that are visible before the frequency shifts observed at a given time t_k, while a positive offset corresponds to using sunspot groups after $\delta\nu_k$.

We then compute the weighted sum of the frequency-shift differences, W_D (equation 4.1). The weight is determined by the variations in the sunspot areas now computed with a given temporal offset. The value of the quantity W_D at the end of the solar cycle, $W_D|_{t_f}$, is taken as the measure

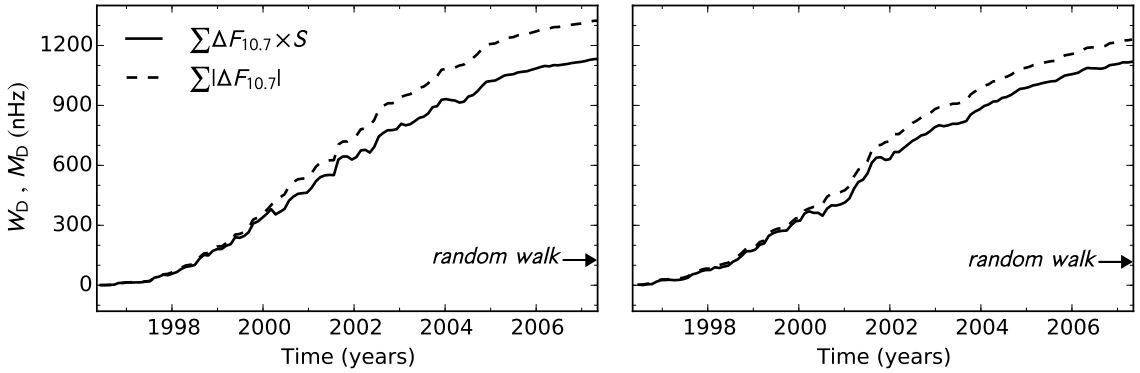

Fig. 4.6 – Comparison between the weighted sum of the variations in the 10.7cm flux (W_D; solid line) and the sum of the absolute values of those variations (M_D; dashed line). The weight is determined by the variation in the sunspot areas. Left and right panels concern the Sample 1 and Sample 2, respectively. The arrow marks the expected standard deviation for a random walk.

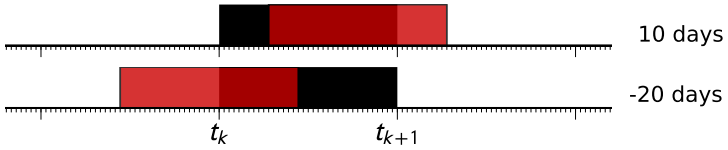

Fig. 4.7 – Illustration of the offset introduced in the sunspot data. The black bars represent the 36-d time-series used in the calculation of the frequency shift at a given time t_k. The red bar in the top panel illustrates the 36-d time-series, corresponding to an offset of 10 days, used to compute the total area covered by sunspots at a given time t_k. The red bar in the bottom panel corresponds to a negative offset of 20 days.

of the correlation level between the short-term variations in the frequency shifts and in the sunspot areas over the 11 years. Figure 4.8 shows the quantity $W_D|_{t_f}$ as a function of the offset introduced in the sunspot data.

For the spot-induced frequency shifts, $\delta\nu_{spots}$ (equation 3.7), as expected, the maximum correlation is found when there is no offset between the two data sets (frequency shifts and sunspot areas). For the observed frequency shifts, however, the maximum correlation corresponds to an offset of -2 days for Sample 1 and -7 days for Sample 2. To better estimate the offset on the maximum correlation, we fit $W_D|_{t_f}$ with a Ricker wavelet (negative second derivative of the Gaussian distribution). For the observed frequency shifts, the best fits are found for an offset of -5 and -6 days for Sample 1 and Sample 2, respectively. Due to the slightly asymmetry of $W_D|_{t_f}$ for the spot-induced frequency shifts, the corresponding best fits are found for an offset of 2 and -1 days.

These results are surprising because the negative offset for the observed frequency shifts suggests that the variations in the acoustic frequencies are better correlated with the sunspot areas observed prior to the moment when the frequency shifts are considered. This seems to contradict the previous findings, which suggest that the changes in the solar magnetism start affecting the propagation of the acoustic waves before they become visible.

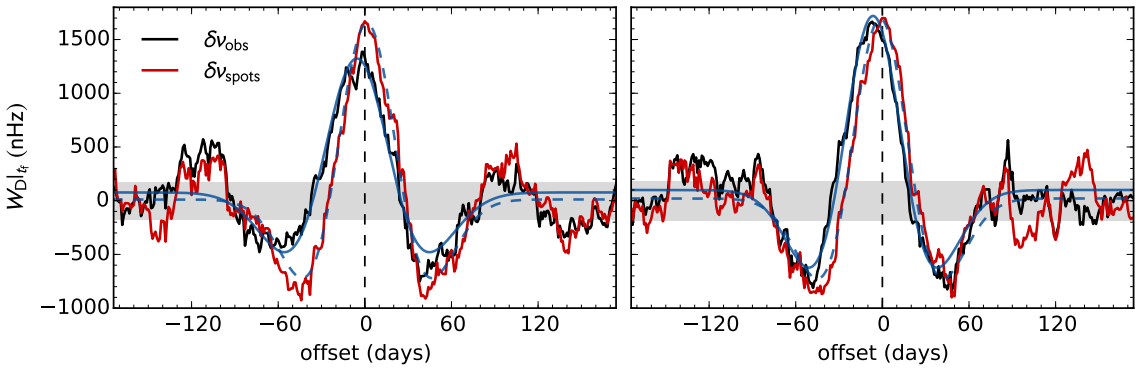

Fig. 4.8 – Weighted sum of the frequency-shift differences at the end of the solar cycle, $W_D|_{t_f}$, where the weight (equation 4.2) is determined by the sunspot areas while considering a given temporal offset with respect to the frequency shifts. The black and red lines correspond to the observed and spot-induced frequency shifts, respectively. The dashed and solid blue lines are the respective best fits with the Ricker wavelet. The dashed line marks the 0-lag and the grey area the expected standard deviation for a random walk. Left and right panels concern the Sample 1 and Sample 2, respectively.

We perform the same analysis to investigate the correlation between the short-term variations in the frequency shifts and in the 10.7cm flux (Fig. 4.9). For the spot-induced frequency shifts the maximum $W_D|_{t_f}$ is found for an offset of 0 and 1 days for Samples 1 and 2, respectively, while the best fits with the Ricker wavelet are found for offsets of 4 and 2 days. For the observed frequency shifts the maximum $W_D|_{t_f}$ is found for an offset of 1 and -2 days, while the best fits correspond to -2 and -4 days. Although smaller, the negative offsets for the maximum correlation between the short-term variations in the frequency shifts and in the 10.7cm flux still suggest that the frequency shifts are better correlated with the magnetic activity observed days before.

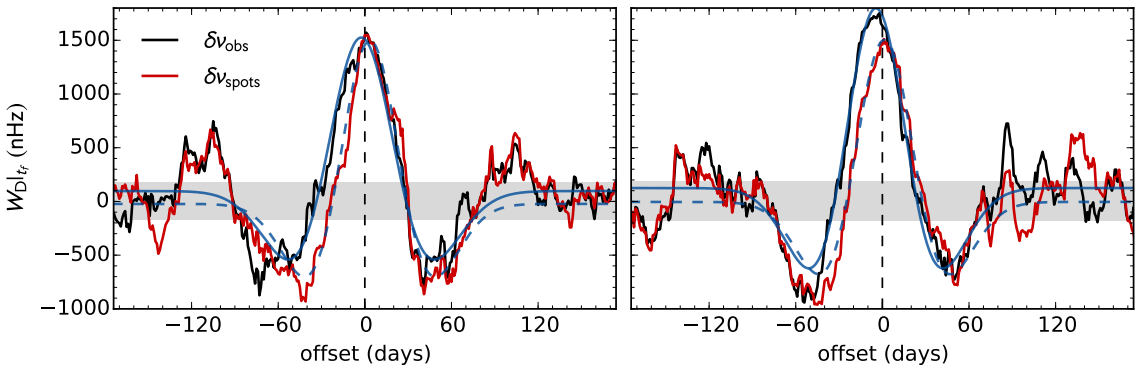

Fig. 4.9 – Weighted sum of the frequency-shift differences at the end of the solar cycle, $W_D|_{t_f}$, where the weight is determined by the 10.7cm flux while considering a given temporal offset with respect to the frequency shifts. The black and red lines correspond to the observed and spot-induced frequency shifts, respectively. The dashed and solid blue lines are the respective best fits with the Ricker wavelet. The dashed line marks the 0-lag and the grey area the expected standard deviation for a random walk. Left and right panels concern the Sample 1 and Sample 2, respectively.

Figure 4.10 shows the weighted sum of the variations in the 10.7cm flux at the end of the cycle as a function of the offset introduced in the sunspot data used to determine the weight. We find a small offset for the maximum $W_D|_{t_f}$ (offset of -3 and -2 days for each sample) and for the corresponding best fits (an offset of -2 days for both samples). A negative offset, in this case, suggests that the variations in the 10.7cm flux are correlated with the sunspots observed before, which is reasonable as the sunspots are a manifestation of the solar magnetism at the solar surface, while the 10.7cm flux is more sensitive to the chromosphere and lower corona. This offset of -2 days explains the smaller offset between the short-term variations in the frequency shifts and in the 10.7cm flux when compared with the offset between the short-term variations in the frequency shifts and in the sunspot areas.

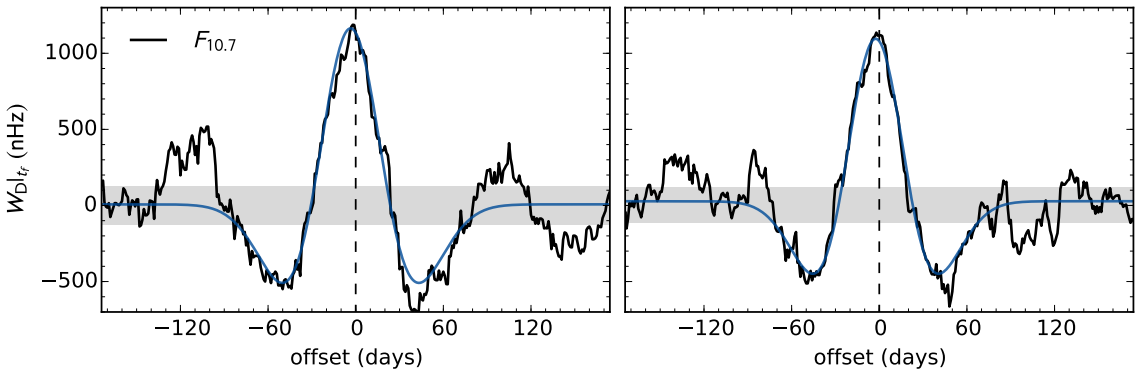

Fig. 4.10 – Weighted sum of the variations in the 10.7cm at the end of the solar cycle, $W_D|_{t_f}$, where the weight is determined by the sunspot areas while considering a given temporal offset with respect to the frequency shifts. The blue line shows the best fit with the Ricker wavelet. The dashed line marks the 0-lag and the grey area the expected standard deviation for a random walk. Left and right panels concern the Sample 1 and Sample 2, respectively.

The systematic offset found for the observed frequency shifts may lead to the suspicion that the quasi-periodic loss of correlation found for the 0-lag in Sect. 4.3 (Fig. 4.4) may be due to the fact that we are not considering the 36-d averages of the sunspot areas that are impacting more directly the observed frequency shifts. With this in mind, we have reconsidered the correlation computed in Sect. 4.3 for the cases of offsets between -6 and 6 days. However, we did not find evidences for a loss of correlation more equally spread in time for any of these offsets (i.e. the losses of correlation were still found concentrated around the maxima of the quasi-biennial signal).

4.5.1 Impact of the far-side of the Sun

For the model predictions of the spot-induced frequency shifts, we find a perfect correlation between the frequency-shift differences and the variations in the sunspot total area. Thus, the maximum correlation measured as $W_D|_{t_f}$ is found for an offset of 0 days between the frequency shifts and the sunspot data. While the Ricker wavelet that best describe $W_D|_{t_f}$ shows a small offset due to small asymmetries in the shape of $W_D|_{t_f}$, the offset found for the observed frequency shifts is, considerably larger (about -6 days).

The synthetic sunspot cycles obtained with the model developed by Santos et al. (2015, Chapter 2) allow us to estimate the impact of our ignoring of the far-side of the Sun on the inferred offset between the variations in the frequency shifts and in the sunspot area. Moreover, the simulations of the solar cycle also allow us to assess the significance of the offset found for the observed frequency shifts.

The synthetic frequency shifts are obtained while considering all the sunspots emerging on the solar surface (near- and far-sides of the Sun), averaged over bins of 36 days and calibrated to the short-term variations in the observed frequency shifts (see Sect. 4.2). We then compute W_D for the synthetic frequency shifts while considering a temporal offset on the sunspot areas (related to visible sunspots only), we take the value of W_D at the end of the cycle ($W_D|_{t_f}$), and we fit the results with a Ricker wavelet. Figure 4.11 shows $W_D|_{t_f}$ as a function of the offset introduced in the sunspot areas for a given simulation.

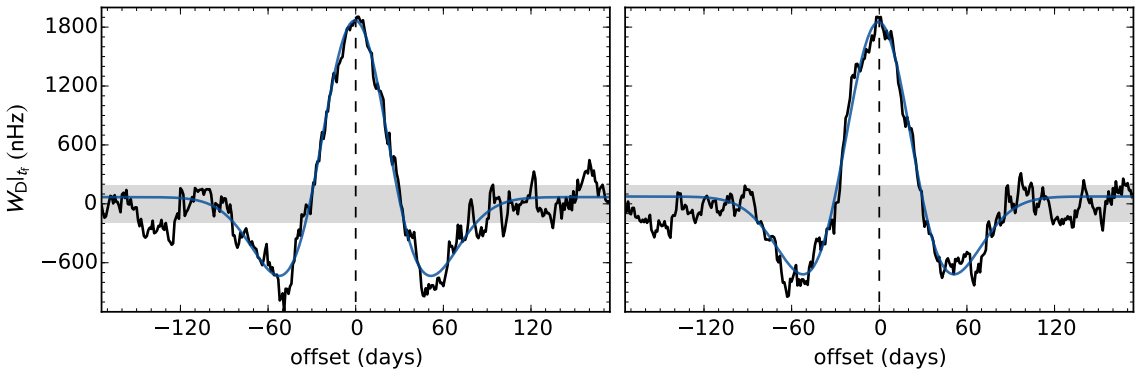

Fig. 4.11 – Weighted sum of the variations in the synthetic frequency shifts at the end of the solar cycle, $W_D|_{t_f}$, where the weight is determined by the sunspot areas while considering a given temporal offset with respect to the frequency shifts. The blue line shows the best fit with the Ricker wavelet. The dashed line marks the 0-lag and the grey area the expected standard deviation for a random walk. Left and right panels concern the Sample 1 and Sample 2, respectively.

We repeat the procedure described above for a large number of simulations (in this case, 500). Panel c) of Fig. 4.12 shows the distributions of the offset found for the maximum $W_D|_{t_f}$ and for the best fit obtained with the Ricker wavelet, while considering the 36-d time-series (consistent with the observed frequency shifts). These results show that the impact of our ignoring of the far-side of the Sun on the inferred offset is small and that the probability of obtaining an offset of -6 days (as found for the observed frequency shifts) is very low, in particular for the best fits to $W_D|_{t_f}$ with the Ricker wavelet. The remaining panels of Fig. 4.12 (panels a, b and d) show the distribution of the maximum correlation between the short-term variations in the synthetic frequency shifts and in the sunspot areas, while obtained from time-series of different lengths. It shows that it is more likely to find larger offsets as we consider longer time-series.

Finally, we note that, from the results shown above in this Chapter, it is not clear if the offset between the frequency shifts and the sunspot areas result from they being out of phase or if it is due to the non-inclusion of other contributions to the frequency shifts.

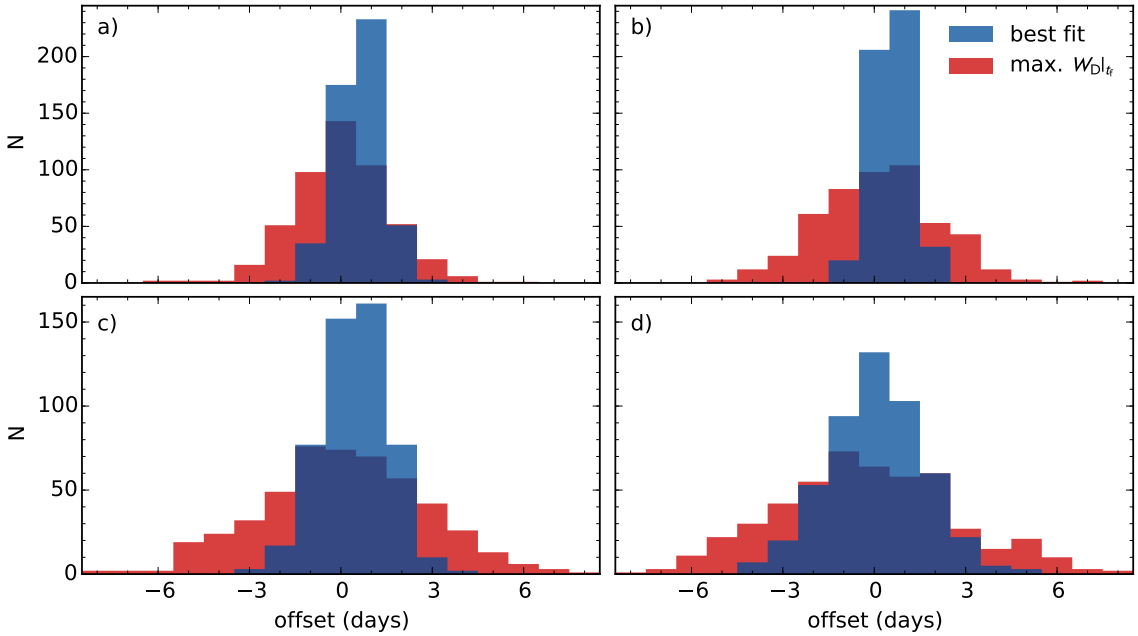

Fig. 4.12 – Distribution of the temporal offset found for the maximum $W_D|_{t_f}$ (red) and for the best fit obtained with the Ricker wavelet (blue) for different cadences: a) 10-d, b) 18-d, c) 36-d, and d) 46-d. For simplification, the results concern just one of the independent samples.

4.5.2 Width of the Ricker wavelet and sunspot properties

Since the frequency shifts are obtained from sub series of 36 days, one may expect to find a significant correlation between the seismic and sunspot data up to an offset of 36 days. Furthermore, depending on their lifetime, sunspots may affect the acoustic oscillations in more than one 36-d temporal bin. The width of the Ricker wavelet, measured as σ_{RW}, is related with the range of offsets for which that correlation is still significant.

Figure 4.13 compares the distribution of σ_{RW} for synthetic data (obtained with a cadence of 36 days) and the values for σ_{RW} found for the observed frequency shifts and for the spot-induced frequency shifts obtained using the NGDC/NOAA data. The results for observed, spot-induced, and synthetic frequency shifts agree reasonably well.

In this section, we try to understand the parameters on which σ_{RW} depends. First, we investigate the impact from the solar rotation on the width of the Ricker wavelet. Figure 4.14 shows the distributions of σ_{RW} found for a group of synthetic spot cycles where the rotation is ignored. The similarity between the distributions in Figs. 4.13 and 4.14 shows that the effect of the solar rotation is negligible (at least for a cadence of 36 d).

Figure 4.15 shows the distribution of the width of the width of the Ricker wavelet for spot cycle simulations where the solar rotation is assumed and the spot lifetime is reduced to one day for all the sunspot groups. In this case, the distributions are shifted towards smaller σ_{RW}. This leads to the conclusion that the spot lifetime has an important role on the width of the Ricker wavelet, thus on the range of temporal offsets over which a significant correlation between the short-term variations in the frequency shifts and in the sunspot areas is maintained.

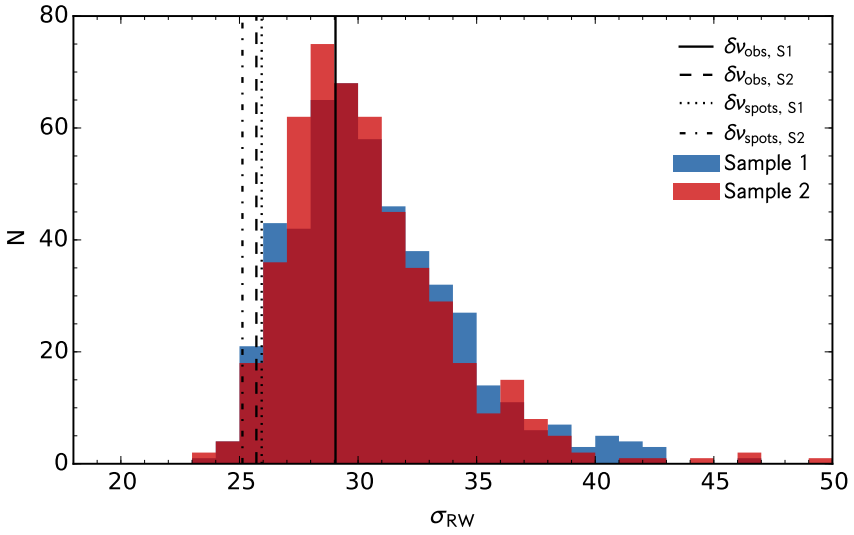

Fig. 4.13 – Distribution of the width of the Ricker wavelet found for a large number of spot cycle simulations. The frequency shifts are obtained with a cadence of 36 days. The blue and red histograms concern Sample 1 and Sample 2, respectively. The vertical black lines mark σ_{RW} found for the observed and the spot-induced frequency shifts (computed using the NGDC/NOAA data), where S1 and S2 indicate each sample.

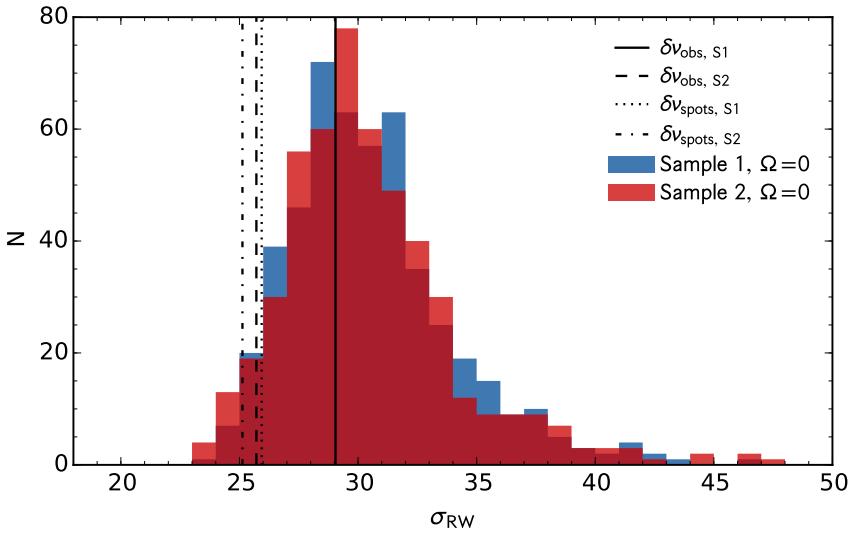

Fig. 4.14 – Same as Fig. 4.13 but for synthetic spot cycles with no rotation.

We consider now different cadences for the synthetic frequency shifts and corresponding averaged sunspot area (for spot lifetimes determined as in Chapter 2 and for solar rotation). As expected, Fig. 4.16 shows that the length of the time-series considered in the computation of the frequency shifts affects significantly the width of the resulting Ricker wavelet.

In summary, our results (Figs. 4.14 - 4.16) show that the time interval over which the correlation between the sunspot and seismic data is still significant is mainly determined by the sunspot lifetimes and the size of the time-series used to compute the frequency shifts and corresponding sunspot areas.

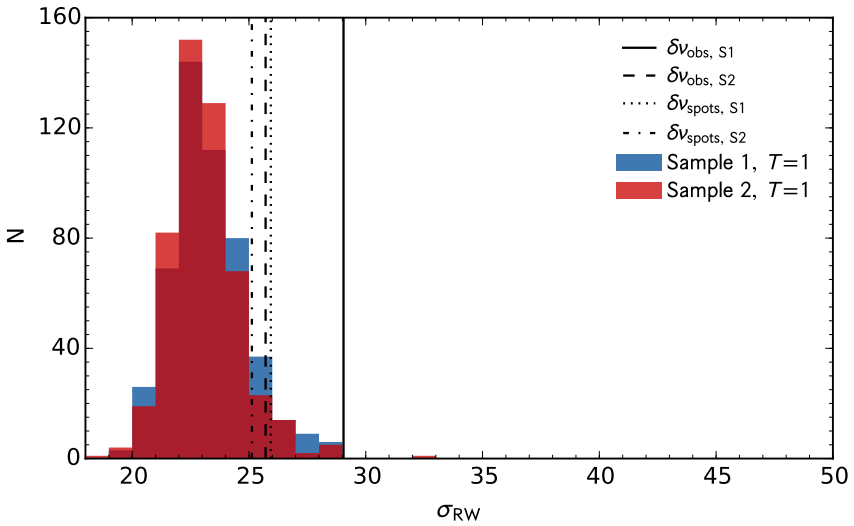

Fig. 4.15 – Sane as Fig. 4.13 but for a spot lifetime of one day independently of the spot size.

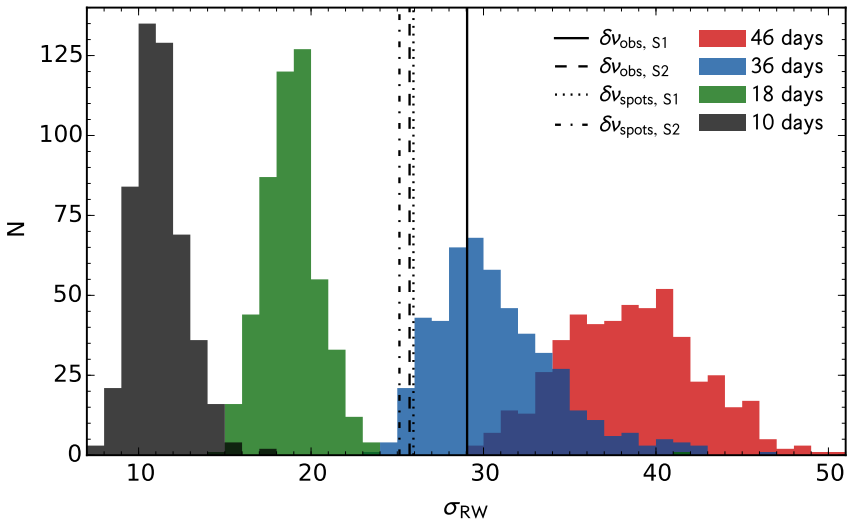

Fig. 4.16 – Distribution of the width of the Ricker wavelet found for a large number of simulations, where the frequency shifts and average sunspot areas are obtained with different cadences: cadence of 10 days (black), 18 days (green), 36 days (blue), and 46 days (red). For simplifications, only the results for one of the samples of independent data points are shown. The vertical black lines mark σ_{RW} found for the observed and the spot-induced frequency shifts.

4.6 On the mid-term contribution

Our results show that there is a strong correlation between the short-term variations in the frequency shifts and in the area covered by sunspots. However, the loss of correlation between the two is still significant and cannot be fully explained by the combined effect of the sunspot groups on the invisible side of the Sun and of the observational error in the observed frequency-shift differences. Moreover, the detailed analysis of the difference between the quantities W_D and M_D shows that

opposite variations in the frequency shifts and in the sunspot area are more significant around the times of maxima of the quasi-biennial signal. This clear signature of the quasi-biennial variations in the quantity W_D highlights the fact that the short timescale variations are modulated on a quasi-biennial timescale.

The above findings could point to a quasi-biennial change in the effect of the sunspots. However, we find this possibility difficult to understand on physical grounds because it would require that an increase in the sunspot area led to a decrease in the frequency shifts at the maximum of the quasi-biennial variations. According to the model for the spot-induced frequency shifts Santos et al. (2016, Chapter 3), this would imply that the phase shift induced by a sunspot on the acoustic wave travelling through it changed sign from the minimum to the maximum of the quasi-biennial variation. Another, perhaps more likely possibility is that other active-related features, such as plage, not accounted for in the computation of W_D, could contribute to the short-term variations in the frequency shifts. However, given the asymmetry found between the behaviour of the correlations at the maximum and minimum of the quasi-biennial variations, their effect would have to dominate the short-term frequency-shifts variations during the former, but be unimportant, compared to the effect of sunspots, during the latter. This possibility will be further investigated in the next sections.

4.6.1 Simple tests on the characteristics of the missing component

In this section, we explore the hypothesis of the global component inducing frequency shifts in other shorter timescales, besides being characterized by a smooth long-term variation in the 11-yr timescale.

First, we add a 1.5-yr periodic modulation to the so-called global component, $\delta\nu_{\rm global}$. Similarly to the quasi-periodic modulation found in the observed frequency shifts (Fletcher et al. 2010; Broomhall et al. 2012), the amplitude of the periodic signal is chosen to vary, being modulated by the 11-yr signal. Figure 4.17 compares the observed frequency shifts and the new model frequency shifts, $\delta\nu^*_{\rm model}$, where the spot-induced component accounts for $\sim 28\%$ (Sample 1) and $\sim 30\%$ (Sample 2) of the total frequency shifts. The comparison of the weighted sum of the frequency-shift differences and the sum of the absolute frequency-shift differences obtained for the observed frequency shifts with those obtained for $\delta\nu^*_{\rm model}$ shows that an extra smooth 1.5-yr periodic signal does not reproduce alone the loss of correlation found previously.

We now consider the residuals in the bottom panels of Fig. 3.6, which are characterized by a quasi-periodic signal of ~ 1.5 yr. Besides the 1.5-yr signal, those residuals vary in the shortest timescale ($\sim$days). We, therefore, divide the residuals in two components: one smooth component varying in the quasi-biennial timescale (red line in Fig. 4.18) obtained by filtering the residuals (for the example shown we used an 180-d filter), and a second component varying on the shortest timescale (blue dots in Fig. 4.18), obtained by subtracting the smooth component to the residuals of Fig. 3.6.

Figures 4.19 and 4.20 compare the observed frequency shifts and the new model predictions. In the case in Fig. 4.19, the spot-induced component accounts for $\sim 24\%$ (Sample 1) and $\sim 25\%$ (Sample 2) of the total frequency shifts, while in the case of Fig. 4.20, it accounts for $\sim 33\%$ and $\sim 34\%$, respectively. Both components (varying on the shortest and intermediate timescales)

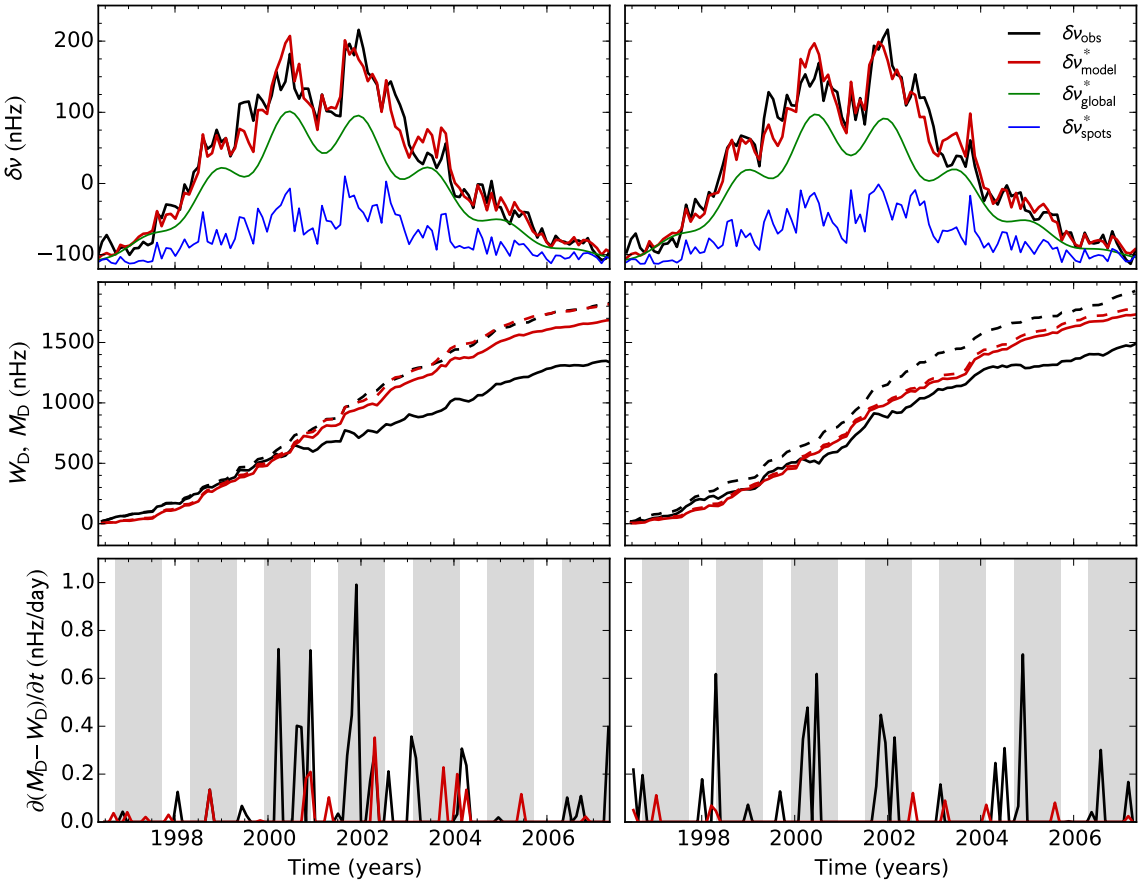

Fig. 4.17 – Top: Comparison between the observed frequency shifts (black; Tripathy et al. 2011) and the model frequency shifts (red) composed by a spot-induced component (blue) and a "global" component (green) varying on the long and intermediate timescales. Middle: Weighted sum of the frequency-shift differences (W_D; solid lines) for the observed (black) and model (red) frequency shifts. The dashed lines show the sum of the absolute values of the frequency-shift differences, M_D. Bottom: Time derivative if the difference between M_D and W_D. Left and right panels concern the Sample 1 and Sample 2, respectively.

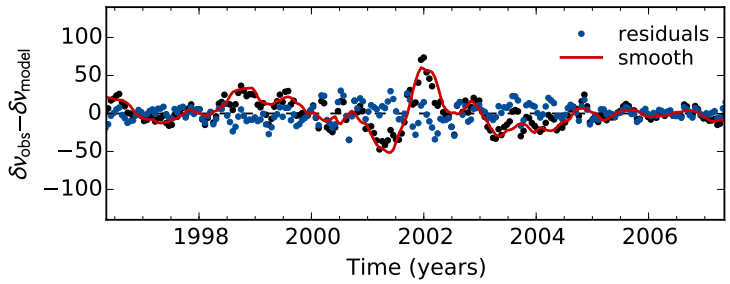

Fig. 4.18 – Residuals between the observed frequency shifts and model predictions from Chapter 3 (black). The residuals are use to compute a smooth component (red line) obtained by filtering the residuals and a component varying on a short timescale (blue dots) obtained by subtracting the smooth component to the residuals.

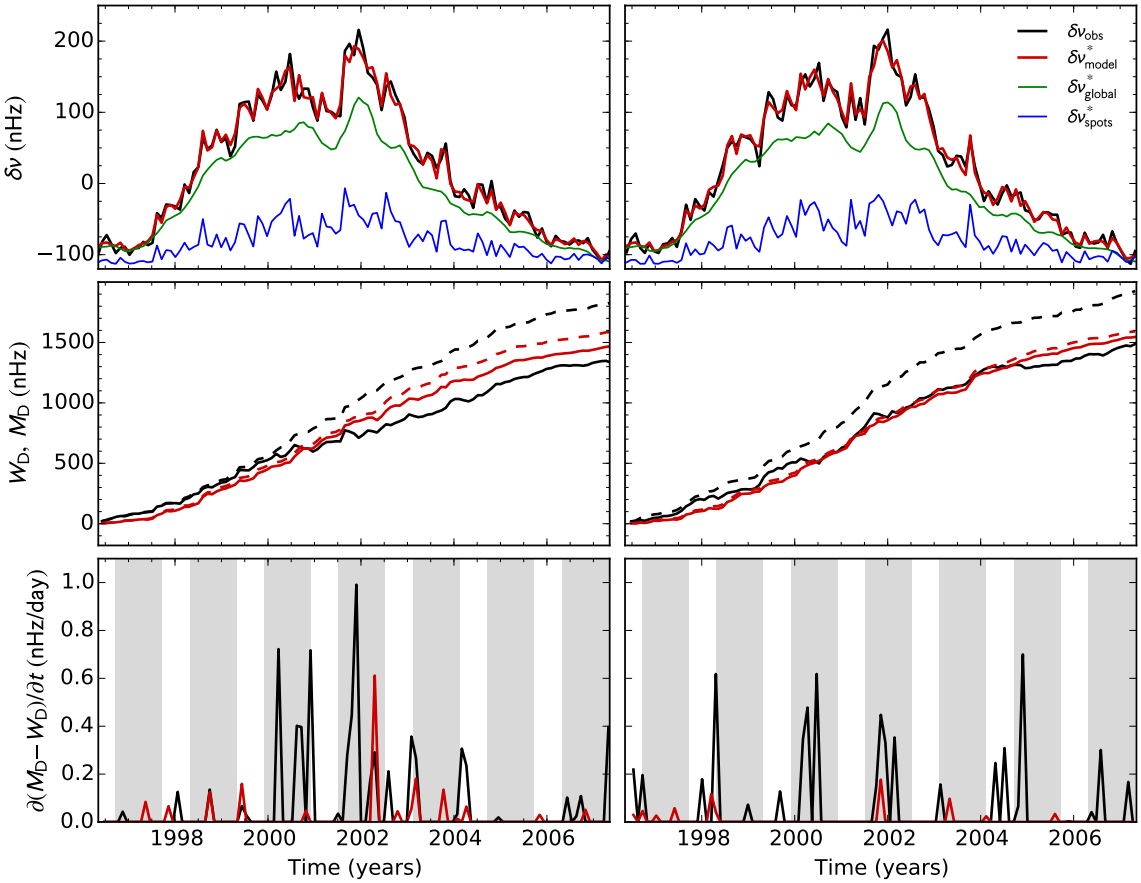

Fig. 4.19 – Same as in Fig. 4.17 but with the mid-term variation described through the smooth quasi-biennial variation in the residuals of Fig. 3.6.

contribute significantly to the loss of correlation between the short-term variations in the observed frequency shifts and in the sunspot areas, with the main contribution resulting from the shortest timescale (Fig. 4.20). This results corroborate our previous conclusions: the missing component should vary on the shortest timescale, while being modulated by the quasi-biennial signal.

4.6.2 Simulating a second short-term contribution

Our analysis shows that the short-term variations in the observed frequency shifts and in the visible (near-side) sunspot areas are strongly correlated. However, the epochs when the seismic and sunspot data behave differently seem to be quasi-periodic, taking place around the times of maximum of the quasi-biennial variation found previously in the observational seismic data (Fletcher et al. 2010; Broomhall et al. 2012). Our analysis, thus, suggests that there is a contribution that has not been accounted for in our model for the frequency shifts. This component should vary on the shortest timescale, being also modulated by the quasi-biennial signal. In this section, we consider in our synthetic frequency shifts an extra stochastic component, i.e. our synthetic "spot"-induced frequency shifts are now given by:

$$\delta\nu_{\rm spots} = \delta\nu_{\rm spots_1} + \delta\nu_{\rm spots_2}. \tag{4.4}$$

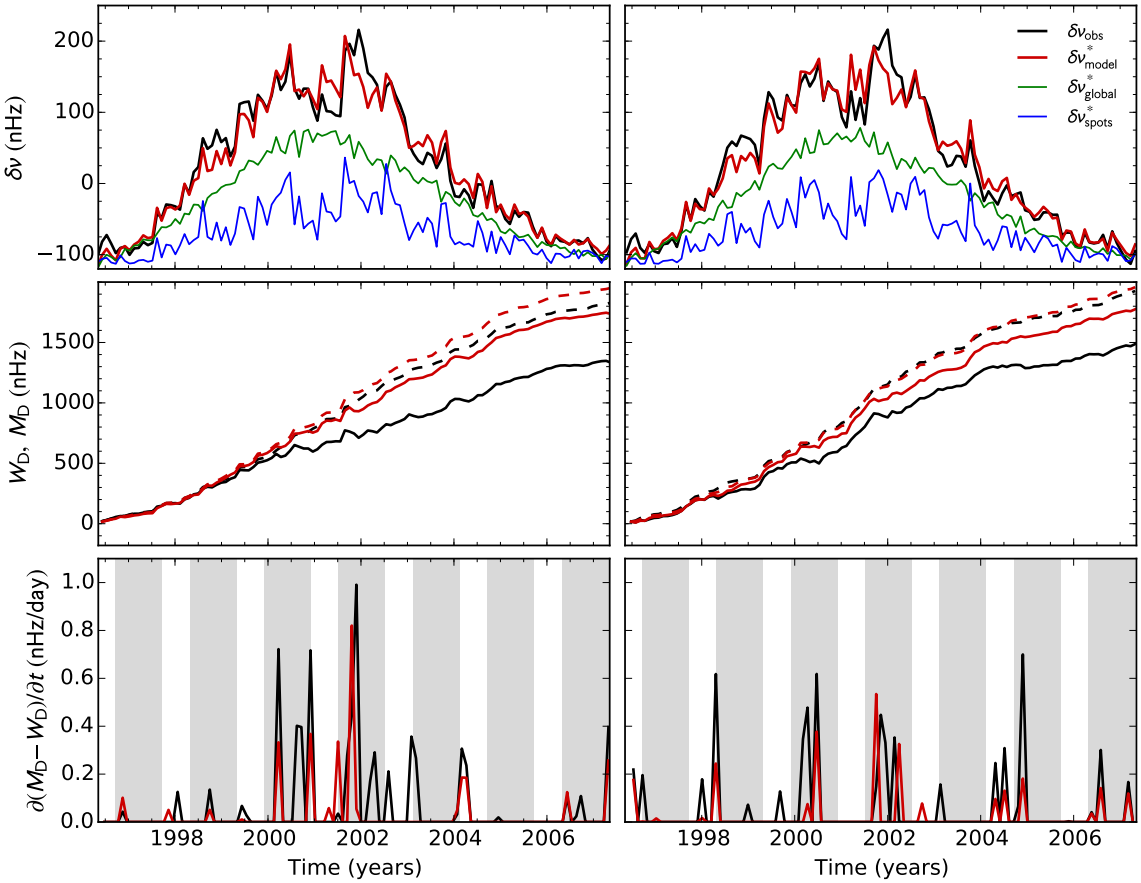

Fig. 4.20 – Same as Fig. 4.17 but instead of the quasi-biennial variation we consider the short-term variations of the residuals of Fig. 3.6.

The goal of simulating this second component is to understand the properties that we should expect for the mid-term contribution that is missing in our model, while reproducing the results for the observed frequency shifts, namely the quasi-periodic loss of correlation between the short-term variations in the frequency shifts and in the sunspot areas. Moreover, it would be particularly interesting if a second spot component was able to explain also the offset between the seismic and sunspot data, keeping the width of the Ricker wavelet unchanged.

The first spot component is obtained, as previously, by taking all the synthetic sunspots on the solar surface. The second spot component is obtained in the same way but now we introduce a periodic modulation of 1.5 yr and a given temporal offset in relation to the first spot component. We also vary its relative impact on the wave propagation. For the total area covered by sunspots we only consider the sunspots in the near-side of the Sun. In this way, the weighted sum of the frequency-shift differences accounts for both effects of the far-side of the Sun and of the extra component varying on the mid-term timescale.

Figures 4.21 and 4.22 show the results for one group of 500 simulations, where the second component has an offset of +10 d with respect to the first spot component (i.e. the second component

is ahead of the first, being equivalent to a frequency-shift component that affected by the sunspots before they become visible) and its characteristic phase shifts is $-0.7 \times \Delta\delta_{\mathrm{ch1}}$, where $\Delta\delta_{\mathrm{ch1}}$ is the characteristic phase shift of the first spot component. Figure 4.21 shows the distribution of the difference between the quantities M_{D} and W_{D} at the end of the cycle, which gives an estimate of the loss of correlation between the short-term variations in the frequency shifts and in the (near-side) sunspot areas: around the minimum (top) and maximum (middle) of the periodic modulation introduced in the second component, or for the full solar cycle (bottom). The left panel of Fig. 4.22 shows the distribution of the width of the Ricker wavelet found for each simulation, while the right panel shows the distribution of the offset found between the synthetic seismic and sunspot data. This particular set of simulations is able to reproduce reasonably well all the characteristics found for the relation between the short-term variations in the observed frequency shifts and in the visible sunspot areas, including the loss of correlation and offset discussed before.

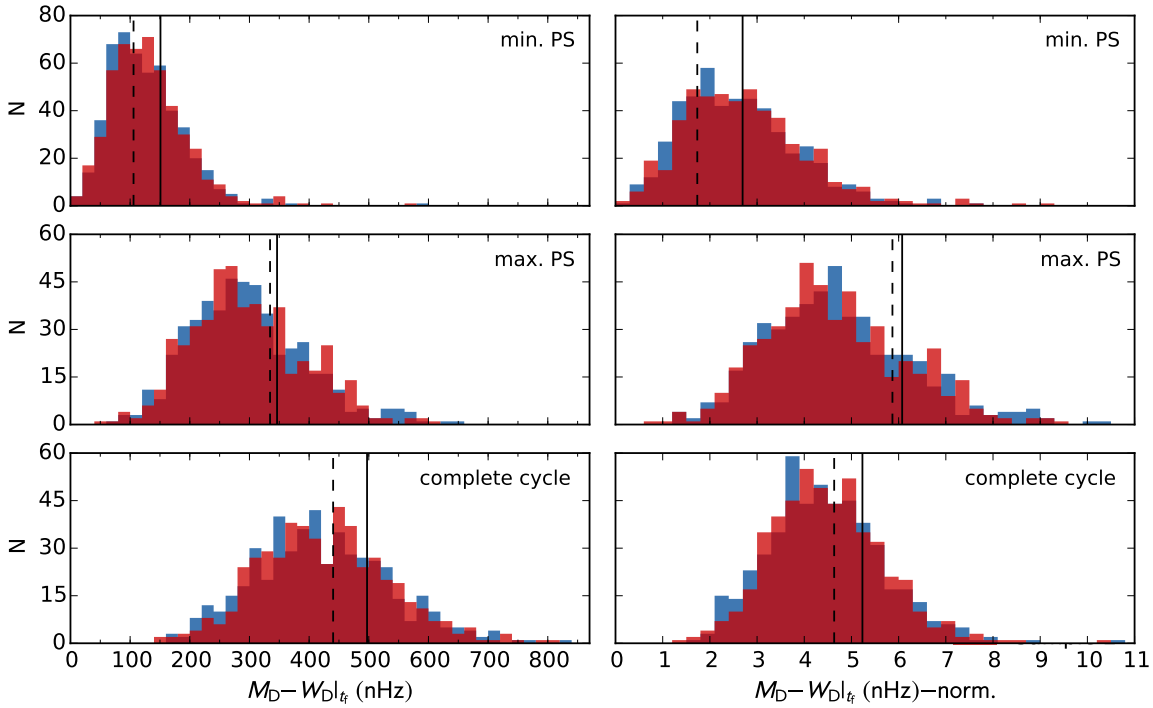

Fig. 4.21 – Distribution of $W_{\mathrm{D}} - M_{\mathrm{D}}|_{t_{\mathrm{f}}}$ for simulations that account for two "spot" contributions, one of them being modulated by a quasi-biennial modulation, having an offset of +10 d in relation to the first component, and a characteristic phase difference of $-0.7 \times \Delta\delta_{\mathrm{ch}}$. This difference measures the loss of correlation between the short-term variations in the frequency shifts and in the visible sunspot areas: around the minimum (top) and maximum (middle) of the periodic modulation or for the full solar cycle (bottom). The left and right panels show the distributions for the absolute values and the values normalized to the number of days, respectively. Blue and red concern Sample 1 and Sample 2. The solid and dashed lines mark the values found for the two samples of observed frequency shifts.

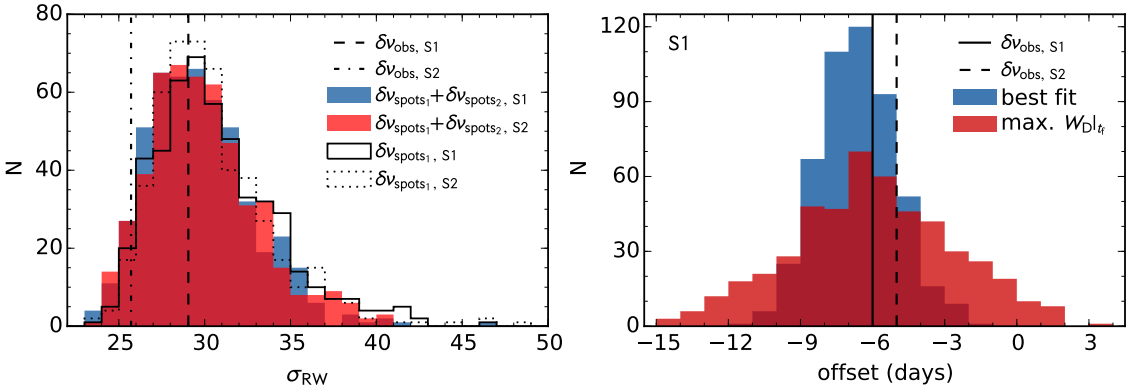

Fig. 4.22 – Left: Distribution of the width of the Ricker wavelet that best describes the relation between the seismic and sunspot data as a function of the offset between them, for Samples 1 and 2 of the same set of simulations as Fig. 4.21. The vertical lines and the transparent histograms show the values found for the observed frequency shifts and the distributions found for the synthetic data where only one spot-induced component was considered (Fig. 4.13), respectively. Right: Offset between the short-term variations in the frequency shifts and in the sunspot areas for Sample 1. The red histogram shows the distribution of the offset for the maximum $W_D|_{t_f}$ and the blue histrogram shows the distribution of the offset found for the corresponding Ricker wavelet. The vertical lines mark the offsets of Ricker wavelet found for the observed frequency shifts.

Figures 4.23 - 4.25 summarize the results for each set of simulations done so far. The y-labels indicate the properties of the second spot component that we are considering in the synthetic data. For each set of 500 simulations, we proceed in the same manner as before. We compute the loss of correlation between the short-term variations in the synthetic frequency shifts and in the synthetic visible sunspot areas over times of minimum and maximum of the mid-term modulation, and over the full solar cycle (analogous to Fig. 4.21). Then we consider the mean value of the distributions and compare with the values found for the observational data (marked by the vertical lines in Fig. 4.21). For the width and offset of the Ricker wavelet (see Fig. 4.22), we follow the same procedure. Figures 4.23 - 4.25, thus, show the difference between the average loss of correlation for each set of simulations and for the original data. For each set of simulations, these figures also identify the corresponding difference in the width and offset of the Ricker wavelet. The closer to zero are those values, the better is the agreement between synthetic and observational data, and thus the more likely are the second component with those specific properties (relative temporal offset and impact on the acoustic modes, and characteristic timescale).

Figure 4.23 shows the results for simulations where the second component is delayed in relation to the first spot component, having a negative offset. For negative offsets, in order to reproduce the observed loss of correlation and offset between the seismic and sunspot data, the relative impact of the second spot component must be large. Figure 4.24 shows the results for the simulations in which the second spot component is ahead of the first (i.e. positive offset). In this case, the characteristic phase difference of the second component has opposite sign and its relative importance is much smaller than in the first set of simulations, which is more reasonable. Some of the cases in this set of simulations are able to reproduce the observed loss of correlation and offset, while the width of the

Ricker wavelet remains almost unchanged. Finally, Fig. 4.25 summarizes the results for simulations with the same offset and relative impact of the spot component in Fig. 4.24 but now we apply a filter of 200 d, 100 d, and 50 d, which would be consistent with a component with longer lifetimes (longer characteristic timescale) than the sunspots. Most of the cases are not able to reproduce the loss of correlation and the offset between the seismic and sunspot data. Also, in some cases, the Ricker wavelet also becomes much wider than that of the observed frequency shifts.

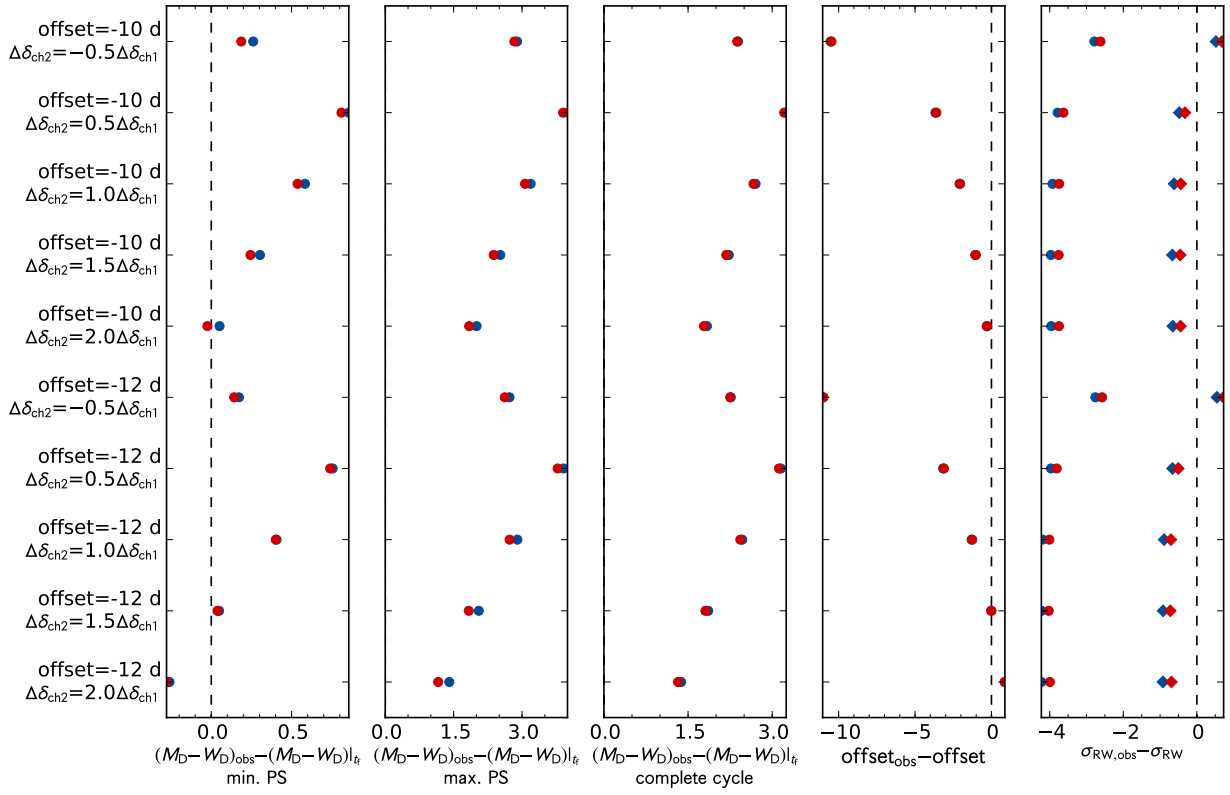

Fig. 4.23 – Comparison between the results found for the observed frequency shifts and those obtained for the synthetic frequency shifts that include two spot components. The y-labels indicate the temporal offset and relative impact of the second component with respect to the first. The first three columns show the difference between the average loss of correlation found for the synthetic data and that found for the observed frequency shifts: around times of minimum of the quasi-biennial modulation, around times of maximum of the quasi-biennial modulation, and for the full cycle, respectively. The dots in the last two columns show the difference between the average properties of the Ricker wavelet found for synthetic data and those found for the observed frequency shifts. The diamonds in the last column show the difference between the average width of the Ricker wavelet found for the synthetic data with two spot components and that found with only one spot-induced component (Fig. 4.13). Red and blue concern each sample of independent data points.

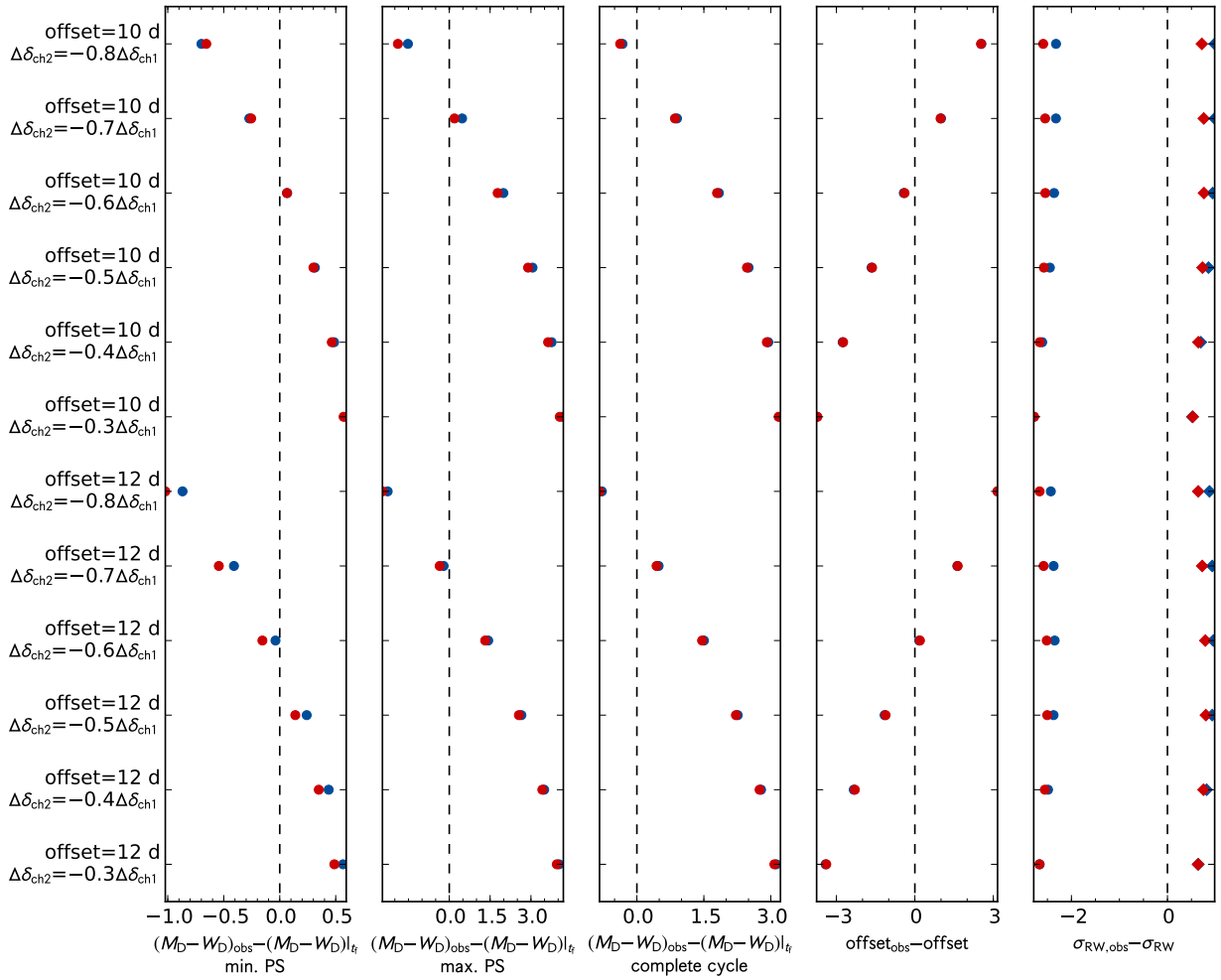

Fig. 4.24 – Same as in Fig. 4.23 but with a positive temporal offset for the second spot component.

4.7 Conclusions

In this work we investigated the correlation between the variation in the solar frequency shifts and in the area covered by sunspots. In particular, we proposed a new observable, consisting of the sum of the frequency shifts weighted by the variation of the sunspot area, which isolates and amplifies the signal from the short-term variations in the frequency shifts. Using this new observable, we found a strong correlation between the short-term variations in the area covered by sunspots and in the frequency shifts. Nevertheless, a significant loss of correlation is still observed, which cannot be explained by the far-side of the Sun and generally coincides with the times of maxima of the quasi-biennial variations seen in the solar acoustic frequencies. The loss of correlation on short timescales suggests that other physical phenomena, besides sunspots, acting on timescales shorter than 36 d contribute to the frequency shifts and that their relative importance changes in phase with the quasi-biennial signal.

We also considered the case in which the variation of the 10.7cm flux, rather than the visible

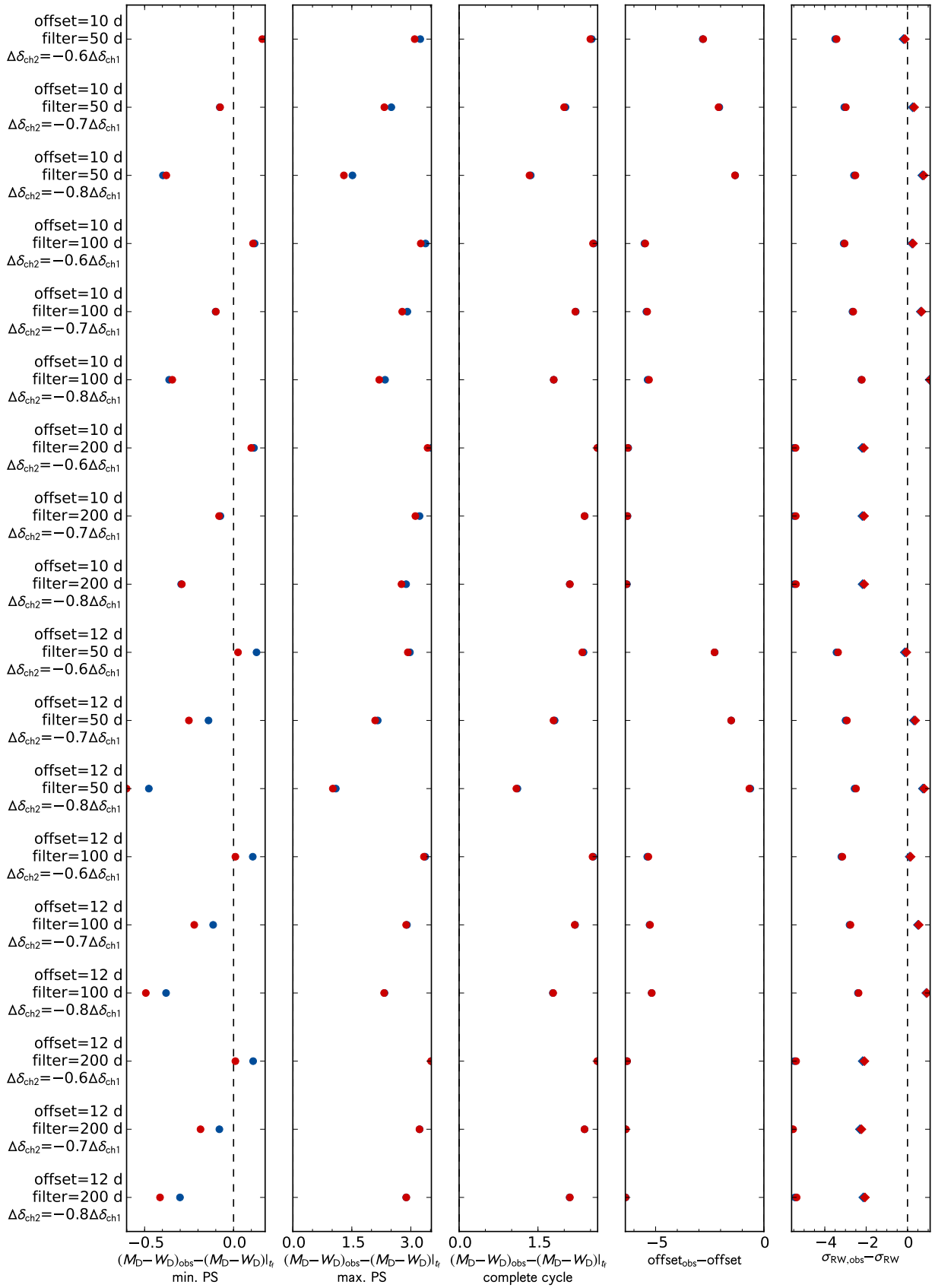

Fig. 4.25 – Same as in Fig. 4.24 but for a "spot" component with longer lifetimes, obtained by smoothing the first component with a filter of 200 d, 100 d, and 50 d.

sunspot area, is used as a weight in the computation of the new observable. The short-term variation in the frequency shifts was found to vary even more closely in line with the 10.7cm flux than with the sunspot areas, confirming that the 10.7cm flux contains information about additional activity-related features which contribute to the frequency shifts. Nevertheless, a significant loss of correlation, whose physical origin remains to be fully understood, is again observed around the times of maxima of the quasi-biennial signal.

When we compute the weighted sum of the frequency-shift differences while introducing an offset in the sunspot data, we find a negative offset for the maximum correlation between the short-term variations in the frequency shifts and in the visible sunspot areas, that once again cannot result from the impact of the far-side of the Sun. This would suggest that the observed frequency shifts are delayed in relation to the sunspots, which is in opposition with previous studies. However, by obtaining new synthetic data that account for a second stochastic component which is modulated by a periodic signal of 1.5 yr, we found that the second component may lead to the offset between the seismic and sunspot data at the same time that explains the periodic loss of correlation.

5. Detection and characterization of stellar magnetic cycles through seismic data

In the Sun, the frequencies of the acoustic modes are observed to vary in phase with the activity level. These frequency variations are expected to be common in solar-type stars and contain information about the activity-related changes that take place in their interior.

The first detection of activity-related changes in the seismic properties of a star other than the Sun was made by García et al. (2010b). The authors found evidence for an activity cycle in the photometric and seismic indicators of a solar-type star (HD 49933) observed by the CoRoT space telescope. Early in 2016, Salabert et al. successfully detected activity-related frequency shifts in an active (Mathur et al. 2014; García et al. 2014a) solar-type star observed by *Kepler*, KIC 10644253 (also known as Mowgli). Later, in spite of the large error bars, Régulo et al. (2016) found evidence for variations in the acoustic frequencies of the active (Mathur et al. 2014; García et al. 2014a) solar-type star KIC 3733735, also known as Shere Khan[1]. More recently, Kiefer et al. (2017) analysed 24 solar-type stars observed by *Kepler*. The authors reported significant frequency shifts in 23 stars and evidence for activity-related frequency shifts in six of those. The unprecedented high-quality long-term photometric time-series obtained by the *Kepler* satellite provide an unique opportunity to detect and characterize stellar magnetic cycles through asteroseismology. In this Chapter, we analyse the short-cadence data of a large sample of solar-type stars observed by *Kepler* and provide frequency shifts for them.

In order to search for temporal variations in the acoustic frequencies, each *Kepler* time-series is split in segments of 90 days overlapped by 45 days. For each sub-series the individual frequencies are obtained through a Bayesian peak-bagging tool, that we developed to perform the global fit to the acoustic modes of solar-type stars.

5.1 Target sample

The main goal of this work is to search for magnetic signatures on the acoustic frequencies of a large sample of *Kepler* targets. We analyse the short-cadence data of 87 *Kepler* solar-type stars (listed in Table 5.1), combining other two samples (with four common stars). 66 of those are high signal-to-noise Sun-like pulsators that constitute the LEGACY sample (Lund et al. 2017; Silva Aguirre et al. 2017). The second group of targets is composed by 25 solar-type *Kepler* Objects of Interest (KOIs), that were analysed by Campante et al. (2016) in the context of the spin-orbit alignment of exoplanet systems. These KOIs were also part of a larger sample analysed by Silva Aguirre et al. (2015) and Davies et al. (2016). The raw data was obtained from *Kepler* Asteroseismology Science Operations Center[2] (KASOC) and corrected using the KASOC filter (Handberg & Lund 2014). The respective power spectra are obtained as the periodogram of each time-series.

[1] Later, the *Kepler* data of the star Shere Khan (KIC 3733735) will be analysed in the context of the spot modulation in the light curve (Chapter 6.5.1).

[2] www.kasoc.phys.au.dk

KIC	KOI	Kp	ν_{max} (μHz)	$\Delta\nu$ (μHz)	T_{eff} (K)	P_{rot} (days)
1435467	–	8.88	1406±8	70.3±0.2	6326±77	6.68±0.89
2837475	–	8.48	1561±10	75.8±0.2	6614±77	3.7±0.1
3425851	268	10.56	2038±60	92.6±2.5	6343±85	7.873±0.001
3427720	–	9.11	2729±15	119.9±0.2	6045±7	13.94±2.15
3456181	–	9.66	971±8	52.0±0.2	6384±77	–
3544595	69	9.93	3366±81	147.7±0.5	5669±75	–
3632418	975	8.22	1168±4	60.7±0.2	6131±44	12.59±0.04
3656476	–	9.52	1926±8	93.1±0.2	5668±77	31.67±3.53
3735871	–	9.71	2862±28	122.8±0.2	6107±77	11.53±1.24
4141376	280	11.07	2928±97	128.8±1.3	6134±91	15.78±2.12
4349452	244	10.73	2106±50	98.27±0.4	6270±79	23.15±0.04
4914423	108	12.29	1663±56	81.5±1.6	6270±79	–
4914923	–	9.46	1813±6	88.5±0.2	5805±77	20.49±2.82
5184732	–	8.16	2092±5	95.5±0.2	5846±77	19.79±2.43
5773345	–	9.16	1102±7	57.1±0.2	6130±84	11.57±1.02
5866724	85	11.02	1880±60	89.6±0.5	6169±50	7.91±0.16
5950854	–	10.96	1923.9±26	96.6±0.2	5853±77	–
6106415	–	7.18	2257.2±5	104.1±0.2	6037±77	–
6116048	–	8.42	2138.4±5	100.8±0.2	6033±77	17.26±1.96
6225718	–	7.50	2369±5	105.7±0.2	6313±77	–
6278762	3158	8.73	4538±144	179.6±0.8	5046±74	–
6508366	–	8.97	965±5	51.4±0.2	6331±77	3.70±0.35
6521045	41	11.20	1502±31	77.0±1.1	5825±75	24.99±0.19
6603624	–	9.09	2380±6	100.0±0.2	5674±77	–
6679371	–	8.73	942.2±6	50.8±0.2	6479±77	5.48±0.50
6933899	–	9.62	1388±4	72.1±0.2	5832±77	–
7103006	–	8.86	1173±8	59.5±0.2	6344±77	4.73±0.06
7106245	–	10.79	2393±29	111.4±0.2	6068±102	–
7206837	–	9.77	1649±12	79.0±0.2	6305±77	4.072±0.005
7296438	364	10.09	1845±12	88.5±0.2	5775±77	25.16±0.16
7510397	–	7.77	1188±4	62.2±0.2	6171±77	–
7670943	269	10.93	1895±73	88.6±1.3	6463±110	5.27±0.03
7680114	–	10.07	1711±8	85.1±0.2	5811±77	26.31±1.86
7771282	–	10.77	1472±28	72.4±0.2	6248±77	11.744±0.23
7871531	–	9.25	3448±27	151.3±0.2	5501±77	35.36±0.22
7940546	–	7.40	1109±4	58.8±0.2	6235±77	11.36±0.95
7970740	–	7.78	4197±23	173.6±0.2	5309±77	17.97±3.09
8006161	–	7.36	3583±12	149.5±0.2	5488±77	29.79±3.09
8077137	274	11.39	1324±39	68.8±0.6	6072±75	–
8150065	–	10.74	1882±43	89.9±0.2	6173±106	–
8179536	–	9.46	2076±14	95.0±0.2	6343±77	24.55±1.61
8228742	–	9.37	1191±4	62.1±0.2	6122±77	20.23±2.16
8292840	260	10.50	1983±35	92.9±0.4	6239±94	–
8379927	–	6.96	2800±7	120.3±0.2	6067±120	17.26±0.03
⋮						

KIC	KOI	Kp	ν_{max} (μHz)	$\Delta\nu$ (μHz)	T_{eff} (K)	P_{rot} (days)
			⋮			
8394589	–	9.52	2397±11	109.3±0.2	6143±77	–
8424992	–	10.32	2529±35	120.8±0.3	5719±77	–
8478994	245	9.71	4660±50	178.7±1.4	5417±75	28.79±3.29
8494142	370	11.93	1133±81	61.8±0.8	6144±106	–
8694723	–	8.88	1474±5	75.2±0.2	6246±77	7.5±0.2
8760414	–	9.62	2470±10	117.3±0.2	5873±77	–
8866102	42	9.36	2014±32	94.5±0.3	6325±75	20.850±0.007
9098294	–	9.76	2311±10	108.9±0.2	5852±77	20.12±0.14
9139151	–	9.18	2686±13	117.1±0.2	6302±77	10.96±2.22
9139163	–	8.33	1724±7	81.0±0.2	6400±84	6.10±0.47
9206432	–	9.08	1864±15	84.7±0.2	6538±77	8.80±1.06
9353712	–	10.84	933±12	51.5±0.2	6278±77	11.30±1.12
9410862	–	10.71	2283±27	107.5±0.2	6047±7	22.77±2.37
9414417	974	9.58	1157±6	60.1±0.2	6253±5	10.847±0.002
9592705	288	11.02	1008±21	53.5±0.3	6174±92	13.38±0.10
9812850	–	9.47	1253±8	64.6±0.2	6321±77	5.19±0.79
9955598	1295	9.44	3614±30	153.2±0.2	5457±77	34.20±5.64
9965715	–	9.34	2079±11	97.2±0.2	5860±180	–
10068307	–	8.18	997±3	54.0±0.2	6132±77	18.60±2.07
10079226	–	10.07	2657±50	116.5±0.2	5949±77	15.69±0.17
10162436	–	8.61	1051±4	55.8±0.2	6146±77	12.33±0.33
10454113	–	8.62	2359±10	105.1±0.2	6177±77	14.45±0.23
10516096	–	9.46	1689±6	84.3±0.2	5964±77	–
10586004	275	11.70	1395±40	69.2±1.4	5770±83	29.79±1.02
10644253	–	9.16	2901±27	122.8±0.1	6045±77	10.91±0.87
10666592	2	10.46	1115±110	59.2±0.6	6350±80	–
10730618	–	10.45	1285±16	66.2±0.2	6150±180	–
10963065	1612	8.77	2205±7	103.1±0.2	6104±74	12.44±0.17
11081729	–	9.03	1969±14	90.2±0.2	6548±83	2.74±0.31
11253226	–	8.44	1593±10	77.2±0.2	6642±77	3.64±0.37
11295426	246	10.00	2154±13	101.6±0.1	5793±74	–
11401755	277	11.87	1250±44	67.9±1.2	5911±66	17.04±0.98
11772920	–	9.66	3683±51	157.8±0.2	5180±180	–
11807274	262	10.42	1496±56	75.7±0.3	6225±75	7.55±0.76
11904151	72	10.96	2730±280	118.2±0.2	5627±44	21.9±3.0
12009504	–	9.32	1869±7	88.2±0.2	6179±77	9.43±0.33
12069127	–	10.70	886±11	48.3±0.2	6276±77	0.92±0.05
12069424	–	5.86	2197±5	103.3±0.2	5825±50	–
12069449	–	6.09	2558±6	16.9±0.2	5750±50	–
12258514	–	8.08	514±3	74.8±0.2	5964±77	15.00±1.84
12317678	–	8.74	1202±7	63.7±0.2	6580±77	–

Table 5.1 – Stellar parameters of the target sample composed by 87 *Kepler* solar-type stars. References: Huber et al. (2013); McQuillan et al. (2013b, 2014); García et al. (2014a); Campante et al. (2015); Ceillier et al. (2016).

5.2 Bayesian peak-bagging tool for solar-type stars

The acoustic oscillations, stochastically excited by near-surface convection, lead to small fluctuations on the stellar brightness. Therefore, the power spectrum of a light curve encloses signatures of the acoustic modes that propagate inside the star. By fitting the power spectrum we can then determine the mode parameters and learn about the physics of the mode. This technique of analysing the individual oscillation modes is commonly called peak-bagging (Appourchaux 2003).

In our analysis, in order to perform the global (simultaneous) fit of the acoustic modes, we follow a Bayesian approach, through the implementation of the Affine Invariant Markov Chain Monte Carlo (MCMC) Ensemble sampler `emcee` (Goodman & Weare 2010; Foreman-Mackey et al. 2013). In the Bayesian framework, the posterior probability for a set of model parameters, $\mathbf{\Theta}$, given the observational data D and the available prior information I, is obtained through the Bayes' theorem

$$p(\mathbf{\Theta}|D,I) = \frac{p(\mathbf{\Theta}|I)p(D|\mathbf{\Theta},I)}{p(D|I)}, \tag{5.1}$$

being

$$\begin{aligned} p(\mathbf{\Theta}|D,I) &\equiv \text{posterior probability of the parameters;} \\ p(\mathbf{\Theta}|I) &\equiv \text{prior probability of the parameters;} \\ p(D|\mathbf{\Theta},I) &\equiv \text{likelihood function;} \\ p(D|I) &\equiv \text{evidence which is a normalization factor.} \end{aligned}$$

One of the most significant strengths of a Bayesian approach is the possibility of incorporating relevant prior information in the current analysis, which can improve in several orders of magnitude the parameter estimation (e.g. Gregory 2005b). Also, a Bayesian approach allows to obtain the probability density function for each parameter through marginalization, which, in the case of a MCMC sampling technique, is simply obtained by computing the histograms of the sample values. Furthermore, this approach also provides reliable error bars, which is particularly important to successfully detect the magnetic activity signature on the oscillation properties of stars.

In the following sections, we will describe the peak-bagging tool in detail: the model of the power density spectrum, the likelihood function, the prior probability for the model parameters, and the fitting strategy.

5.2.1 Modelling the power density spectrum

The power density spectrum of a solar-type star contains a number of oscillation modes characterized by the wave numbers n, l, and m (radial order, angular degree, and azimuthal order, respectively). The integrated light of a solar-like star (as observed by *Kepler*) is only sensitive to the lowest angular degree modes, i.e. $l \leq 3$.

To model the power density spectrum of each oscillation mode, we use a standard Lorentzian profile (Sect. 1.2) defined by

$$\mathcal{M}_{nlm}(\nu; S_{nlm}, \nu_{nlm}, \Gamma_{lmn}) = \frac{S_{nlm}}{1 + \frac{4}{\Gamma_{nlm}^2}(\nu - \nu_{nlm})^2}, \tag{5.2}$$

where ν_{nlm} is the resonance frequency of the mode, and S_{nlm} and Γ_{nlm} are the mode height and linewidth.

Due to the stellar rotation, for each (n, l) multiplet there are $2l+1$ visible peaks in the power density spectrum, differing on the azimuthal order m. However, for a spherically symmetric star, the frequencies of the different azimuthal components are degenerate within the (n, l) multiplet. Therefore, the Lorentzian profiles of the $2l+1$ components are combined into a single profile, corresponding to the (n, l) multiplet. For a slow rotator, assuming a rigid-body rotation, neglecting the effect of the Coriolis force and the splitting due to magnetic fields, the frequency of a mode is given by (Ledoux 1951, Sect. 1.2.1)

$$\nu_{nlm} = \nu_{nl} + m\nu_{\mathrm{s}}, \tag{5.3}$$

where ν_{s} represents the rotational splitting.

Assuming the energy equipartition between the azimuthal components of the multiplet, the power spectrum of the (n, l) multiplet is

$$\mathcal{M}_{nl}(\nu; S_{nl}, \nu_{nl}, \Gamma_{nlm}, \nu_{\mathrm{s}}, i) = \sum_{m=-l}^{l} \frac{\mathcal{E}_{lm}(i)\widetilde{V}_l^2 S_{nl}}{1 + \frac{4}{\Gamma_{nlm}^2}(\nu - \nu_{nl} - m\nu_{\mathrm{s}})^2}, \tag{5.4}$$

where $\widetilde{V}_l = V_l / V_0$ and V_l is related to the geometrical visibility of a (n, l) multiplet and results mainly from the limb-darkening. Table 5.2 summarizes the values of $\widetilde{V}_l$ that we use in our analysis. $\mathcal{E}_{lm}$ represents the relative mode visibility within the (n, l) multiplet, which depends on the inclination angle between the stellar rotation axis and the line of sight, i, and is given by (Gizon & Solanki 2003, Sect. 1.2.1)

$$\mathcal{E}_{lm}(i) = \frac{(l - |m|)!}{(l + |m|)!} \left[P_l^{|m|}(\cos i)^2 \right]. \tag{5.5}$$

The final model of the power density spectrum is

$$\mathcal{P}(\nu; \boldsymbol{\Theta}) = \sum_{n=n_0}^{n_{\max}} \sum_{l=0}^{l_{\max}} \sum_{m=-l}^{l} \frac{\mathcal{E}_{lm}(i)\widetilde{V}_l^2 S_{nl}}{1 + \frac{4}{\Gamma_{nlm}^2}(\nu - \nu_{nl} - m\nu_{\mathrm{s}})^2} + B(\nu), \tag{5.6}$$

where n_0 and $n_{\max}$ are the first and last radial order considered in the global fit, $l_{\max}$ is the highest angular degree that is visible (or considered) within the radial order n, $B(\nu)$ describes the acoustic background (see Sect. 5.4), and $\boldsymbol{\Theta}$ denotes the free parameters in the model.

In our analysis, only the linewidths and heights of the radial modes, Γ_{n0} and S_{n0}, are considered as free parameters. For the quadrupole modes, we consider the linewidth and height of the closest radial mode, since their frequencies do not differ by much. For the dipolar modes, we interpolate between the two closest radial orders. Thus, the final set of free parameters is

$$\boldsymbol{\Theta} = \{\nu_{nl}, S_{n0}, \Gamma_{n0}, \nu_{\rm s}, i\}. \tag{5.7}$$

This means that, for example, to perform the global fit of a stellar power spectrum with 10 detectable radial orders each with modes of angular degree $l \leq 2$, the final model is composed of 52 parameters.

	$\widetilde{V}_0^2$	$\widetilde{V}_1^2$	$\widetilde{V}_2^2$	$\widetilde{V}_3^2$	Reference
VIRGO	1.00	1.56	0.63	0.08	Lund et al. (2014)
BiSON	1.00	1.88	1.04	0.47	Kjeldsen et al. (2008)
Kepler	1.00	1.49	0.50	0.02	Handberg & Campante (2011)

Table 5.2 – Geometrical mode visibilities for VIRGO, BiSON, and *Kepler* data.

5.2.2 Likelihood function of a power spectrum

Assuming a χ^2 with two degrees of freedom statistic for the power spectrum (Gabriel 1994), at a fixed frequency ν_j, the probability density for a given observed power P_j is given by

$$f(P_j; \boldsymbol{\Theta}) = \frac{1}{\mathcal{P}(\nu_j; \boldsymbol{\Theta})} \exp\left[-\frac{P_j}{\mathcal{P}(\nu_j; \boldsymbol{\Theta})}\right], \tag{5.8}$$

where $\mathcal{P}(\nu_j; \boldsymbol{\Theta})$ corresponds to the mean power spectrum, which we model (equation 5.6). Assuming that the frequency bins are uncorrelated, the likelihood function becomes

$$L(\boldsymbol{\Theta}) = \prod_j f(P_j; \boldsymbol{\Theta}). \tag{5.9}$$

To ensure numerical stability, since we often deal with small values, the best approach is to use the logarithmic probabilities, i.e.

$$\mathcal{L}(\boldsymbol{\Theta}) \equiv \ln L(\boldsymbol{\Theta}) = -\sum_j \left\{ \ln \mathcal{P}(\nu_j; \boldsymbol{\Theta}) + \frac{P_j}{\mathcal{P}(\nu_j; \boldsymbol{\Theta})} \right\}. \tag{5.10}$$

5.2.3 Prior functions

One of the main strengths of a Bayesian approach is the possibility of using prior knowledge in the current analysis. Assuming that the prior on a given parameter Θ_k is independent on the priors on the remaining parameters and applying the product rule, the prior probability becomes

$$p(\boldsymbol{\Theta}|I) = \prod_k f_k(\Theta_k), \tag{5.11}$$

where $f_k(\Theta_k)$is the prior probability for Θ_k. The logarithmic prior probability becomes

$$\ln p(\boldsymbol{\Theta}|I) = \sum_k \ln f_k(\Theta_k). \tag{5.12}$$

When the prior information on the parameter is limited, one may assign an ignorance prior to Θ_k (e.g. Gregory 2005a,b; Handberg & Campante 2011). For the location parameters (e.g. ν_{nl}, ν_s, and i) one may use a uniform prior, being given by

$$f_k(\Theta_k) = \begin{cases} \dfrac{1}{\Theta_k^{\max} - \Theta_k^{\min}} & \text{if } \Theta_k^{\min} \leq \Theta_k \leq \Theta_k^{\max}, \\ 0 & \text{otherwise,} \end{cases} \tag{5.13}$$

where $\Theta_k^{\max}$ and $\Theta_k^{\min}$ are the upper and lower limits of Θ_k. In the case of scale parameters (e.g. Γ_{n0} and S_{n0}), that may range several orders of magnitude, one might use a Jeffreys' prior

$$f_k(\Theta_k) = \begin{cases} \dfrac{1}{\Theta_k \ln\left[\Theta_k^{\max}/\Theta_k^{\min}\right]} & \text{if } \Theta_k^{\min} \leq \Theta_k \leq \Theta_k^{\max}, \\ 0 & \text{otherwise.} \end{cases} \tag{5.14}$$

If the prior lower limit includes zero, to prevent for divergence at zero, one must use a modified Jeffreys' prior of the form

$$f_k(\Theta_k) = \begin{cases} \dfrac{1}{(\Theta_k + \Theta_k^{\text{uni}}) \ln\left[\left(\Theta_k^{\text{uni}} + \Theta_k^{\max}\right)/\Theta_k^{\text{uni}}\right]} & \text{if } 0 \leq \Theta_k \leq \Theta_k^{\max}, \\ 0 & \text{otherwise.} \end{cases} \tag{5.15}$$

This way, for $\Theta_k \gg \Theta_k^{\text{uni}}$, $f_k(\Theta_k)$ behaves like a Jeffreys' prior, while for $\Theta_k \ll \Theta_k^{\text{uni}}$ it behaves like a uniform prior.

In what follows, we summarize the prior functions that we assume for the model parameters: mode frequencies, heights and linewidths of the radial modes, rotational splitting, and inclination angle.

Mode frequencies

The mode frequencies are location parameters and, therefore, we use uniform priors (equation 5.13). For both solar and *Kepler* data, we use our prior knowledge on the mode frequencies to define the upper and lower limits. We take the values ν_{nl}^0 from the literature and consider that a given mode is located within $\nu_{nl}^0 \pm 4\,\mu$Hz.

For VIRGO/SPM data, ν_{nl}^0 are taken from Stahn (2010), while for BiSON data we use the frequencies estimated by Broomhall et al. (2009). For the *Kepler* data, we use the frequencies from Davies et al. (2016) and Lund et al. (2017).

For the *Kepler* targets, we further constrain the mode frequencies by using priors on the large and small frequency separations ($\Delta\nu$ and $d\nu$, respectively), as defined by Davies et al. (2016). Acoustic pulsations are characterized by approximately constant large and small separations, i.e. the derivatives of both quantities should be approximately equal to zero.

Assuming a Gaussian prior on the large separation of the form

$$f(\Delta\nu_l) = \frac{1}{\sqrt{2\pi}\sigma} \exp\left(-\frac{1}{2}\left(\frac{\Delta\nu_l(n) - \Delta\nu_l(n-1)}{\sigma}\right)^2\right), \tag{5.16}$$

where σ is related to the uncertainty in the prior knowledge. Rewriting equation (5.16) in terms of the second differences in the mode frequencies, one finds

$$\ln f(\Delta\nu_l) = -\lambda_\Delta \sum_{n=n_0}^{n_{\max}} \left(\frac{\partial^2 \nu_{nl}}{\partial n^2}\right)^2, \tag{5.17}$$

where λ_Δ is the tolerance, n_0 and $n_{\max}$ are, respectively, the minimum and maximum radial orders considered in the fit. To compute the second differences in the mode frequencies, at least five modes of angular degree l are needed. For this reason, the prior on the large separation is only applied when this condition is met.

Proceeding in the same manner for the small frequency separation, one finds

$$\ln f(d\nu_{l,l+2}) = -\lambda_d \sum_{n=n_0}^{n_{\max}} \left(\frac{\partial d\nu_{l,l+2}}{\partial n}\right)^2. \tag{5.18}$$

Following the approach by Davies et al. (2016), the prior on the small separation is only applied to $d\nu_{0,2}(n)$, which was found to be enough for a stable fit, and the tolerance values are fixed at $\lambda_\Delta = 0.125\,\mu\text{Hz}$ and $\lambda_d = 0.25\,\mu\text{Hz}$, which were found to be adequate.

Mode Heights

The mode heights may vary within several orders of magnitude. Therefore, they are often treated as scale parameters. In our analysis we follow two approaches, depending on the data we are dealing with: solar data or *Kepler* data.

For solar data, we consider a modified Jeffreys' prior (equation 5.15), with an upper limit of $20\,\text{ppm}^2/\mu\text{Hz}$ and transition between the uniform and the Jeffreys' prior at $0.2\,\text{ppm}^2/\mu\text{Hz}$.

For *Kepler* targets, we apply an uniform prior (equation 5.13), whose lower limit is fixed at $0\,\text{ppm}^2/\mu\text{Hz}$ and upper limit varies from power spectrum to power spectrum, being estimated as follows:

1. the frequency range of interest, the p-mode envelope, is defined as $[\nu^0_- - \Delta\nu/4, \nu^0_+ + \Delta\nu/4]$, where $\Delta\nu$ is the large separation, and ν^0_- and ν^0_+ are the minimum and maximum mode frequencies we consider (again 0 denotes the values from the literature);
2. the contribution of the acoustic background is removed from the power spectrum;
3. the resulting power spectrum is smoothed by applying an uniform filter with size equal to the reciprocal of the resolution of the spectrum;
4. finally, the height upper limit is defined as the maximum height of the smooth power spectrum.

Mode linewidths

Similarly to the mode heights, we also follow two approaches to define the priors on the mode linewidths depending on the data of interest.

For solar data, we consider a modified Jeffreys' prior (equation 5.15), whose upper limit and transition are set at 10 and 0.1 μHz, respectively.

For *Kepler* data, we apply an uniform prior (equation 5.13) with lower and upper limits of 0 and 12 μHz.

Rotational splitting and inclination angle

While studying solar data we use uniform priors (equation 5.13) for both parameters. The rotational splitting is allowed to vary between 0 and 5 μHz. In order to avoid boundary effects in the sampling (e.g. Lund et al. 2014, 2017; Campante et al. 2016), the inclination is sampled from $-90°$ to $180°$ and then folded onto the range $[0°, 90°]$.

For *Kepler* targets, we use the posterior distributions obtained by Davies et al. (2016) and Lund et al. (2017) as priors for the stellar rotational splitting and inclination angle.

5.2.4 Fitting method

The global fit to the acoustic modes is performed through the implementation of the algorithm `emcee` (Foreman-Mackey et al. 2013), based on the Affine Invariant Markov Chain Monte Carlo (MCMC) Ensemble sampler (Goodman & Weare 2010). `emcee` makes use of an interacting ensemble of the so-called "walkers". Each walker has its own separate MCMC chain but the proposal distribution, i.e. the next step in the chain, depends on the positions of the remaining walkers.

Furthermore, in order to ensure an efficient sampling of the parameter space, we also employ parallel tempering (Earl & Deem 2005), which is useful to avoid that a given walker gets trapped in a local maximum. Parallel chains at different temperatures, $\mathcal{T}$, are progressively flatter versions of the target distribution (with $\mathcal{T} = 1$). The higher temperature chains are able to access broader regions of the parameter sample and to exchange complete configurations with lower temperature chains. This way, parallel tempering allows to reach low-temperature regions which would be harder to reach through a standard MCMC algorithm. Note, that the parameter estimation is still based on the target distribution (with $\mathcal{T} = 1$).

For each power spectrum, we use 500 walkers (initialized by sampling the prior distributions) and 3 temperatures defined according to $\beta_i = 1/\mathcal{T}_i = 1.2^{1-i}$ (Benomar et al. 2009), with $i = 1, 2, 3$. Each chain runs for 10^4 steps after a burn-in phase, long enough to ensure the convergence of the chains and a swap acceptance rate between adjacent temperatures around 50%.

For each model parameter, the posterior distribution function is obtained directly by computing the histogram of the sample values. The final estimates are given by the median of the distribution and the uncertainty is based on the 68% credible region.

5.3 Frequency shift estimation

In order to search for temporal variations on the acoustic mode frequencies, the original time-series are segmented. For solar data, we have considered sub-series of 180 d with no overlap. For *Kepler* data, the time-series are segmented in 90-d sub-series overlapped by 45 d.

Having the mode frequencies, ν_{nl}, and the respective uncertainties (obtained with the peak-bagging tool described above) for each sub-series, one can then estimate the temporal frequency shifts. The reference mode frequencies, $\nu_{nl}^{\rm ref}$, are taken as the weighted time averages of the mode frequencies. Then, for each multiplet (n, l), we compute the variation in frequency with respect to the reference frequencies as

$$\delta\nu_{nl}(t) = \nu_{nl}^{\rm ref} - \nu_{nl}(t). \tag{5.19}$$

Finally, following the approach by, for example, Chaplin et al. (2007b) and Tripathy et al. (2007), we obtain the weighted mean frequency shifts as

$$\delta\nu(t) = \frac{\sum_{nl} Q_{nl}\delta\nu_{nl}(t)/\sigma_{nl}^2(t)}{\sum_{nl} Q_{nl}/\sigma_{nl}^2(t)}, \tag{5.20}$$

where Q_{nl} is the inertia ratio (Christensen-Dalsgaard & Berthomieu 1991). The uncertainty of the mean frequency shifts is

$$\sigma(t) = \left[\sum_{nl} \frac{Q_{nl}}{\sigma_{nl}^2(t)}\right]^{-1/2}. \tag{5.21}$$

Note that for the low-degree modes the degree dependence of the inertia ratio is not very significant. Therefore, for the *Kepler* targets, we neglect the inertia ratio, and the mean frequency shifts and the respective uncertainties are given by

$$\delta\nu(t) = \frac{\sum_{nl} \delta\nu_{nl}(t)/\sigma_{nl}^2}{\sum_{nl} 1/\sigma_{nl}^2(t)}, \tag{5.22}$$

$$\sigma(t) = \left[\sum_{nl} \frac{1}{\sigma_{nl}^2(t)}\right]^{-1/2}. \tag{5.23}$$

5.4 Acoustic Background

The power spectrum of solar-type stars may include signatures of different stellar phenomena, besides acoustic oscillations, which contribute to the variability of the stellar brightness. Figure 5.1 shows the solar power density spectrum and its different components. At very low frequencies (longer periods), the power spectrum is dominated by a stellar activity component, related with the rotational modulation and decay of active regions. Still at the low-frequency range, the contribution from granulation becomes important. Even at shorter timescales (higher frequencies), the signature of a second granular or facular component might be detected. Finally, at the high-frequency range, one can find the envelope of the acoustic modes (p-mode envelope).

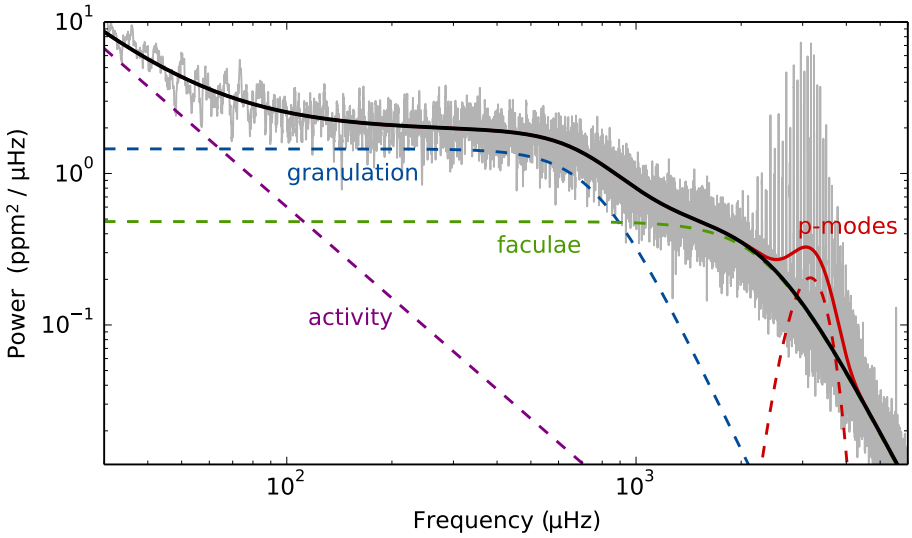

Fig. 5.1 – Solar power density spectrum obtained from VIRGO/SPM data (grey). The black solid line shows the best fit to the acoustic background, which includes an activity-related (purple), a granular (blue), and a facular (green) component. The red solid line shows the complete model of the power density spectrum which accounts for the p-mode envelope (dashed red).

The granular and facular components are commonly described by a Harvey profile (e.g. Harvey 1985; García et al. 2009; Mathur et al. 2011; Handberg & Campante 2011; Campante et al. 2011; Karoff 2012; Davies et al. 2016)

$$f(\nu) = \frac{H}{1+(2\pi\nu\tau)^{\alpha}}, \tag{5.24}$$

where $H = 4\sigma^2\tau$ is the amplitude of the component's power, σ and τ are, respectively, the characteristic amplitude and timescale, and α is the slope of the power law.

The activity component is described by power law of the form

$$f(\nu) = \frac{H_{\rm act}}{\nu^2}, \tag{5.25}$$

which results from considering a Harvey profile (equation 5.24) in the limit $2\pi\tau_{\rm act} \gg 1$ with $\alpha = 2$, that is found to be adequate to describe the exponential decay of active regions (e.g García et al. 2009; Campante et al. 2016).

The envelope of the acoustic modes can be modelled through a Gaussian function

$$f_{\rm p}(\nu) = H_{\rm p} \exp\left(-\frac{(\nu-\nu_{\rm max})^2}{2W_{\rm p}^2}\right), \tag{5.26}$$

where $H_{\rm p}$, $W_{\rm p}$, and $\nu_{\rm max}$ are respectively the height, width, and central frequency of the p-mode envelope.

Finally, to properly model the background signal, one needs to consider a flat component, N, related with the photon shot-noise.

Taking all the components, the final model of the background is

$$B(\nu) = \frac{H_{\rm act}}{\nu^2} + \frac{H_{\rm gran}}{1+(2\pi\nu\tau_{\rm gran})^{\alpha_{\rm gran}}} + \frac{H_{\rm fac}}{1+(2\pi\nu\tau_{\rm fac})^{\alpha_{\rm fac}}} + N. \quad (5.27)$$

Equation (5.27) corresponds to the general model for the stellar acoustic background. However, as it will be summarized below, we will consider variations of the background model in accordance to the target data: VIRGO, BiSON, or *Kepler* data.

The model parameters that best describe the acoustic background are obtained through Maximum Likelihood Estimation (MLE) and the formal errors are derived from the inverse Hessian matrix (tool developed by Campante et al. 2011; Campante 2012). The background parameters estimated in this process are then fixed in the subsequent peak-bagging analysis.

5.4.1 Background model for VIRGO/SPM data

To validate the peak-bagging tool, we first apply our method to solar real VIRGO/SPM and artificial BiSON data. Figure 5.1 compares the solar power density spectrum obtained from VIRGO/SPM data (the length of the corresponding time-series is 180 days) and the best model that accounts for the different contributions: activity, granulation, faculae, and acoustic modes (the photon shot-noise was also included in the fit, but is not significant in this case). Although the p-mode envelope is not part of the acoustic background, for VIRGO/SPM data, we model it simultaneously in order to improve the fit. Also, the low-frequency range of the solar power density spectrum (up to 100 μHz), which is dominated by the activity component, is not considered in the fit. However, to prevent any contamination (due to spectral leakage) into the frequency range where the granulation component becomes important, we still model the activity component. Finally, the faculae characteristic timescale is fixed at the value 65.8 s (Karoff 2012) in the fit.

Although different configurations of the background model were explored, the approach with the best performance corresponds to the one described above. In those tests, we verified that an overestimated/underestimated background results in underestimated/overestimated mode heights and linewidths (see also Appourchaux et al. 2012), while the mode frequencies were not affected.

5.4.2 Background model for artificial BiSON data

To further validate the efficiency of the peak-bagging tool, we also use two artificial BiSON time-series: BiSON 1 and BiSON 2. Figure 5.2 compares the power density spectrum of one 180-d sub-series of each artificial data set. The model of the power spectrum includes a granular component, the p-mode envelope, and the constant photon shot-noise component. All the model parameters are free. The p-mode envelope is excluded from the final background model.

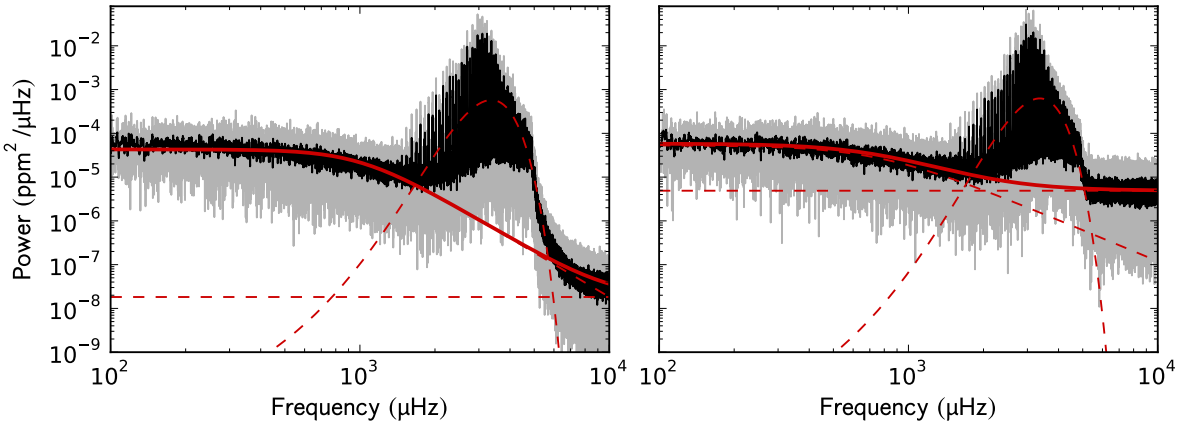

Fig. 5.2 – Power density spectrum (grey and black) of a given sub-series for both artificial BiSON data sets (left and right panels, BiSON 1 and BiSON 2, respectively). The red solid lines show the best background model composed by a granular and a photon shot-noise components. The dashed lines show the different background components and the p-mode envelope.

5.4.3 Background model for Kepler data

For *Kepler* data, we start by considering two competing background models. The first model only considers three components: activity, granulation, and photon shot-noise. Those three components are common to the second background model, which further includes the facular component.

To test the statistical significance of the model parameters, we compute the likelihood ratio (Appourchaux et al. 1998):

$$\ln \mathcal{L} = \ln L(\boldsymbol{\Theta}_p) - \ln L(\boldsymbol{\Theta}_{p+n}), \tag{5.28}$$

where $p = 5$ is the number of parameters in the first model and $p+n = 8$ is the number of parameters in the second model. When $\mathcal{L} \ll 1$, one can conclude that the additional parameters are not necessary to described the power density spectrum.

For most of the stellar sub-series, we find that the facular component is not significant enough. Therefore, the final background model, that we apply to all *Kepler* targets, is the first model, which accounts for the activity, granulation, and photon shot-noise. All the model parameters are free. Again, we exclude, in this step, the low-frequency range (defined as $200 \times \nu_{\rm max}/\nu_{\rm max,\odot}$ μHz) and the frequency range dominated by the acoustic oscillations (centred at $\nu_{\rm max}$ and has a width of $2/3\nu_{\rm max}$). As an example, Fig. 5.3 shows the power density spectrum of a 90-d sub-series for ten solar-type stars from our sample (an example for each star is presented in Appendix A), where the background model is consistent with the observational data.

As the convection is the mechanism behind both granulation and acoustic oscillations, the granulation timescale, one of the parameters in our model, is expected to be related with the timescale of the p-modes and, thus, with $\nu_{\rm max}$. The theoretical predictions of Huber et al. (2009) indicate that the granulation timescale, $\tau_{\rm gran}$, is related with $\nu_{\rm max}$ as

$$\tau_{\rm gran} = \tau_{\rm gran,\odot} \frac{\nu_{\rm max,\odot}}{\nu_{\rm max}}, \tag{5.29}$$

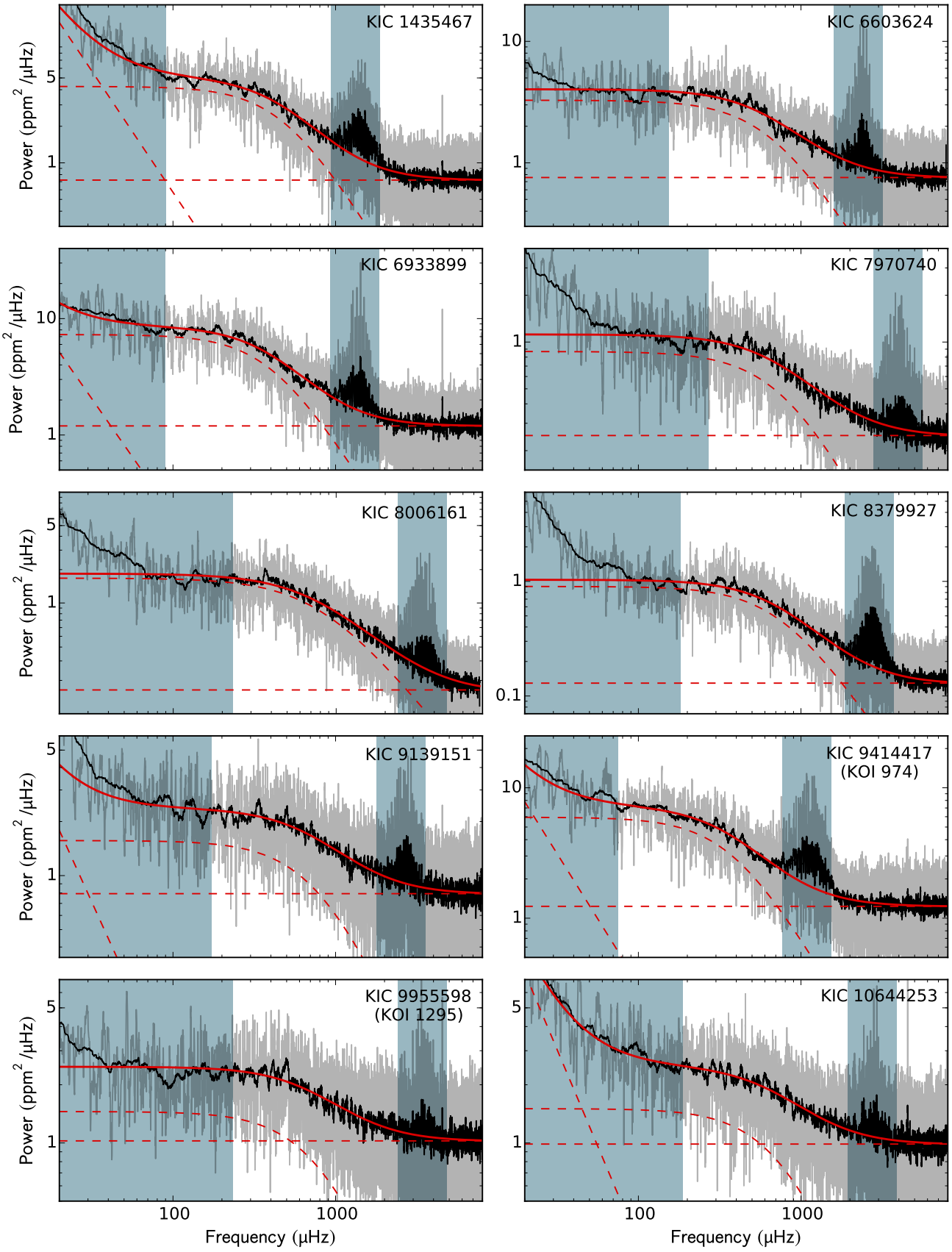

Fig. 5.3 – Power density spectrum (grey and black; with different smoothing for illustrative purpose) of 90-d sub-series of ten of the solar-type stars of our target sample. The red solid lines show the best background model. The dashed lines show the different background components: activity, granulation, and photon shot-noise. The blue areas mark the frequency intervals neglected from the fitting process.

which means that larger stars are expected to have longer granulation characteristic timescales than smaller stars (see also Kjeldsen & Bedding 2011). Later, while analysing observational data from CoRoT and *Kepler*, Kallinger & Matthews (2010) and Mathur et al. (2011) confirmed the theoretical prediction, finding that the granulation timescale scales with the inverse of $\nu_{\rm max}$.

Figure 5.4 shows the granulation timescale for each star in the sample, computed as the weighted average over all the sub-series, as a function of $\nu_{\rm max}$ (from the literature; Table 5.1). The yellow star marks the position of the Sun and the red line the best fit to the data. We find that $\tau_{\rm gran} \propto \nu_{\rm max}^{-1.1\pm0.2}$ which is in good agreement with the theoretical predictions and previous studies (Huber et al. 2009; Kjeldsen & Bedding 2011; Kallinger & Matthews 2010; Mathur et al. 2011). This further confirms that the background models we use are a good representation of the stellar power spectra.

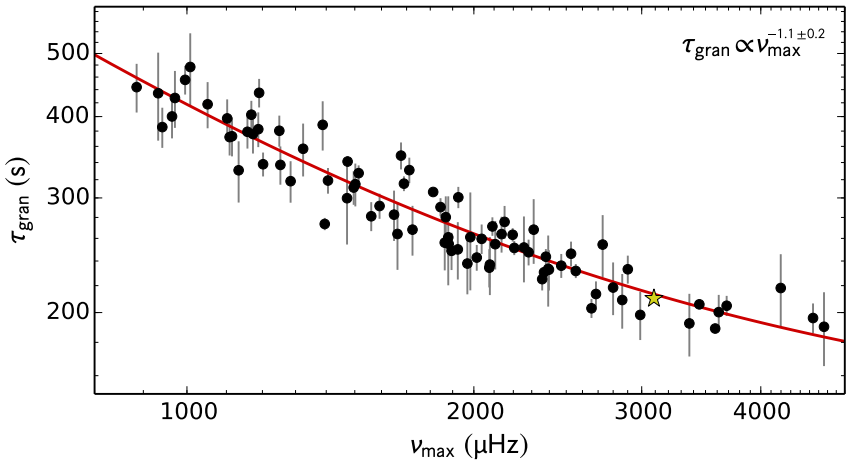

Fig. 5.4 – Granulation timescale as a function of $\nu_{\rm max}$ for the 87 stars in the sample. The red line shows the best fit ($\tau_{\rm gran} \propto \nu_{\rm max}^{-1.1\pm0.2}$) and the yellow star marks the position of the Sun.

5.5 Validation of the peak-bagging tool

Before using the peak-bagging tool (described in Sect. 5.2) to search for temporal variations in the acoustic frequencies of *Kepler* targets, we perform validation tests with solar data. The following sections summarize the results for VIRGO/SPM data and artificial BiSON data.

5.5.1 VIRGO/SPM solar data

The first validation test is performed with ∼12-yr VIRGO/SPM time-series. To estimate the temporal variations in the solar acoustic frequencies, the original light curve is divided in 180-d segments. Having the background model for each sub-series (Sect. 5.4), we apply the peak-bagging tool as described in Sect. 5.2, which performs the global fit to the acoustic modes. The parameters corresponding to the best fit (shown in Fig. 5.5 for a given sub-series) are estimated from respective posterior distribution[3] as described in Sect. 5.2.4.

[3]Examples of the posterior probability distributions will be shown in Sect. 5.6

With the acoustic frequencies in hand, we then compute the observed frequency shifts (following the procedure described in Sect. 5.3). Figure 5.6 shows the frequency shifts over the solar cycle 23. These results are consistent with those in the literature (e.g. Chaplin et al. 2007b; Tripathy et al. 2007; Jain et al. 2009; Tripathy et al. 2011; Salabert et al. 2011a). This shows that the peak-bagging tool is able to successfully recover the time behaviour of the solar acoustic frequencies. In particular, we recover the correct amplitude of the frequency shifts of $\sim 0.4\mu$Hz. Despite the long frequency-shift cadence, we also recover the signature of the quasi-biennial signal (Fletcher et al. 2010; Broomhall et al. 2012), in particular, the double peak at the solar maximum and the peak around 2004 (see Fig. 3.6 for reference).

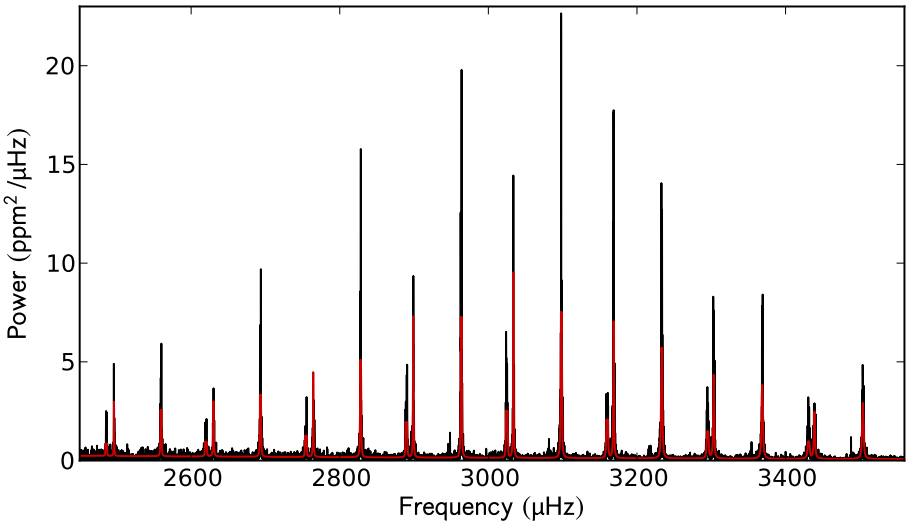

Fig. 5.5 – Solar power density spectrum (black) at the frequency range of the acoustic oscillations for an 180-d sub-series from the VIRGO/SPM data. The red line shows the best fit to the p-modes obtained with the peak-bagging tool.

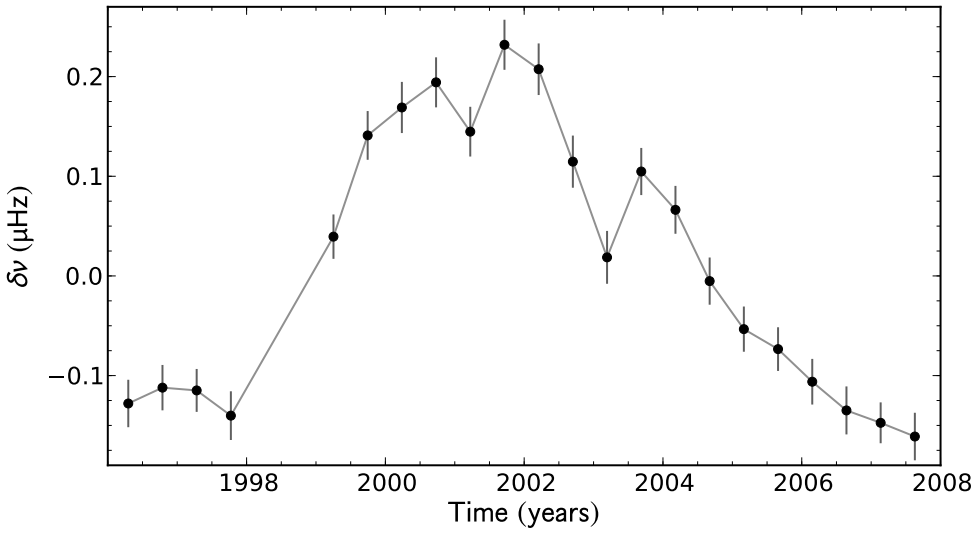

Fig. 5.6 – Solar average frequency shifts over the solar cycle 23, derived from VIRGO/SPM (instrument on-board of the SOHO stellite) data. Note that the time interval between 1998 and 1999 corresponds to the so-called SOHO vacations (e.g. Appourchaux 2005).

Figure 5.7 shows the frequency shifts for the individual angular degrees as a function of the observed 10.7-cm flux (from NOAA/NGDC) and the respective best linear fit (note that, as a first approximation, we neglect the magnetic hysteresis). The slope or shift gradient corresponds to the frequency shift per unit change in activity and is shown in Fig. 5.8. Our results are consistent with those from Chaplin et al. (2004b).

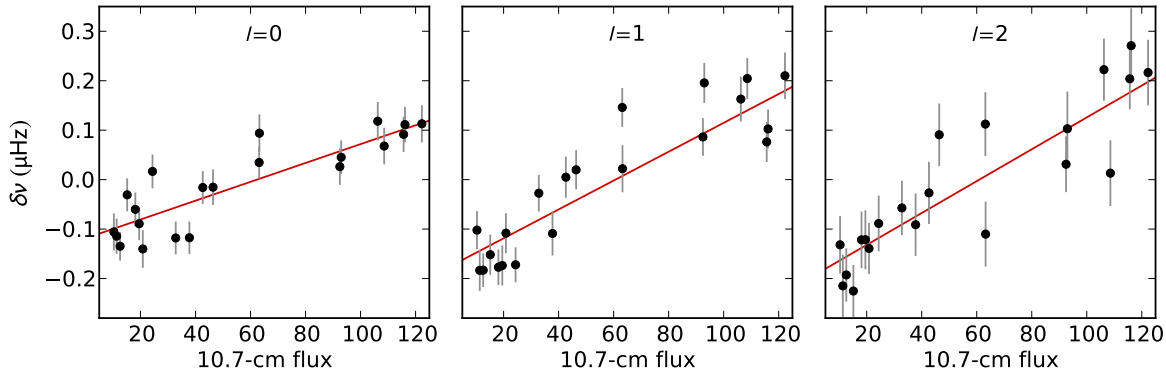

Fig. 5.7 – Frequency shifts for the VIRGO/SPM data (black) as a function of the 10.7-cm flux (from the NOAA/NGDC database) for the individual angular degrees: $l = 0$ (left), $l = 1$ (middle), and $l = 2$ (right). The red lines show the best fits to the data.

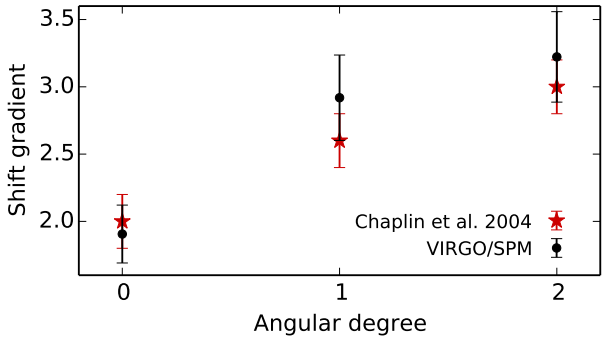

Fig. 5.8 – Frequency shift per unit change in activity, shift gradient (black), as a function of the angular degree for VIRGO/SPM data. For comparison, the red stars indicate the values for the shift gradient found by Chaplin et al. (2004b).

5.5.2 Artificial BiSON data

The efficiency of the peak-bagging tool was also tested with two artificial BiSON data sets (BiSON 1 and BiSON 2, with different realizations of the noise). Similarly to the VIRGO/SPM data, the original synthetic time-series are split in 180-d segments. Following the same procedure, we peak-bag the power density spectra obtained from each sub-series while assuming the background model derived in Sect. 5.4.2. Figure 5.9 shows the best fit to the p-modes for a given segment of each synthetic data set. Then, we compute the temporal variations in the acoustic frequencies (see Sect. 5.3) for each data set, shown in Fig. 5.10, and compare the average frequency shifts obtained for the individual angular degrees with the input activity level (Figs. 5.11 and 5.12). These results further confirm that our peak-bagging tool is able to successfully recover the magnetic signature on the acoustic frequencies.

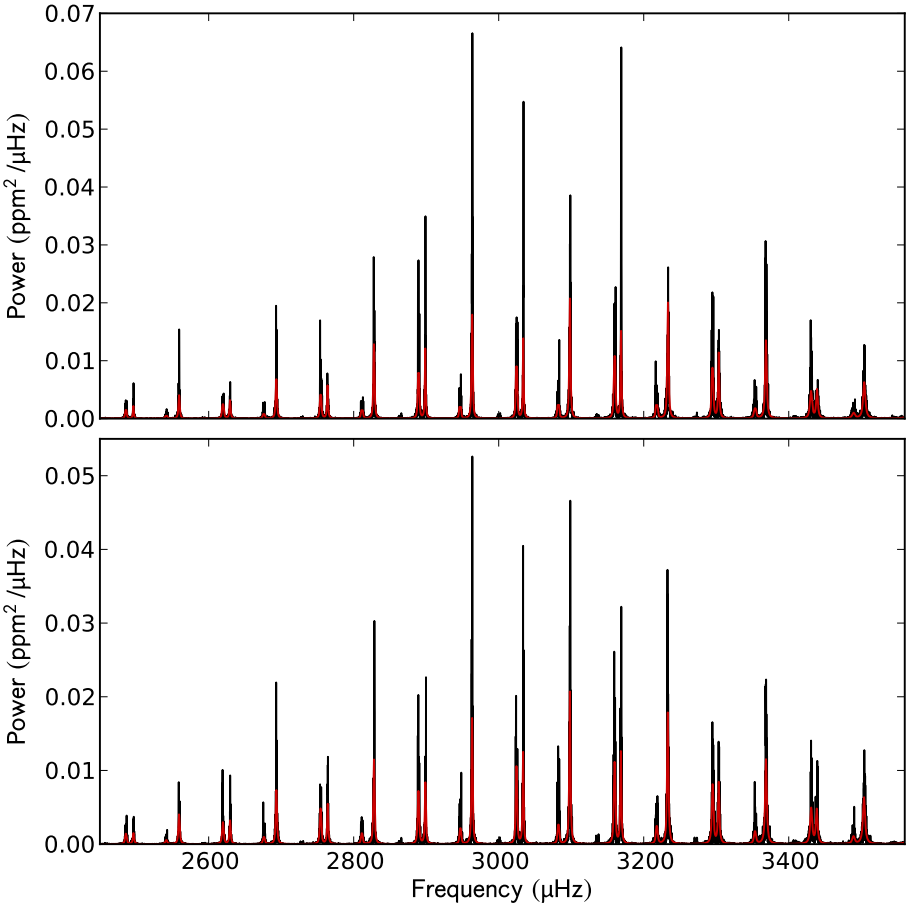

Fig. 5.9 – Power density spectrum (black) for a given 180-d segment from each (top and bottom panels) artificial BiSON time-series: BiSON 1 and BiSON 2, respectively. The red lines show the best fit to the p-modes obtained with the peak-bagging tool.

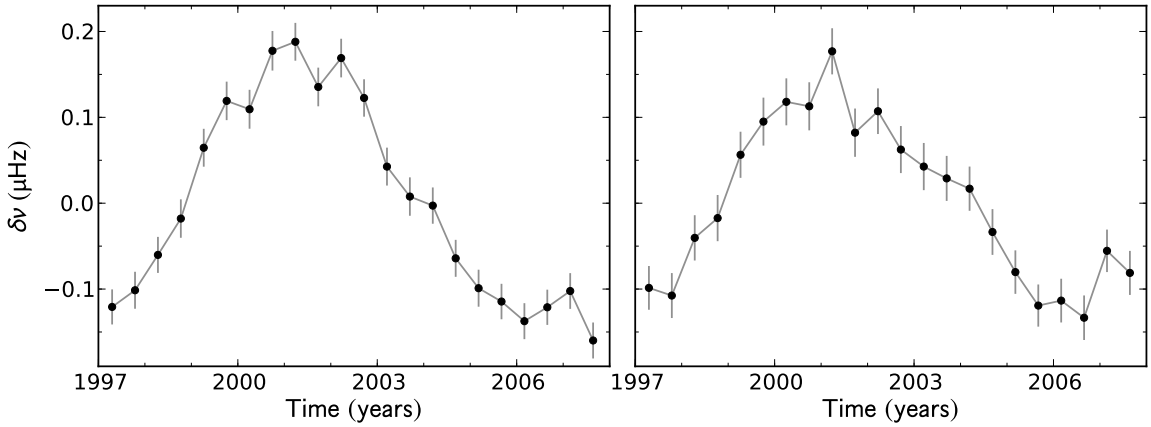

Fig. 5.10 – Solar average frequency shifts derived from two artificial BiSON time-series (left and right panels, BiSON 1 and BiSON 2, respectively).

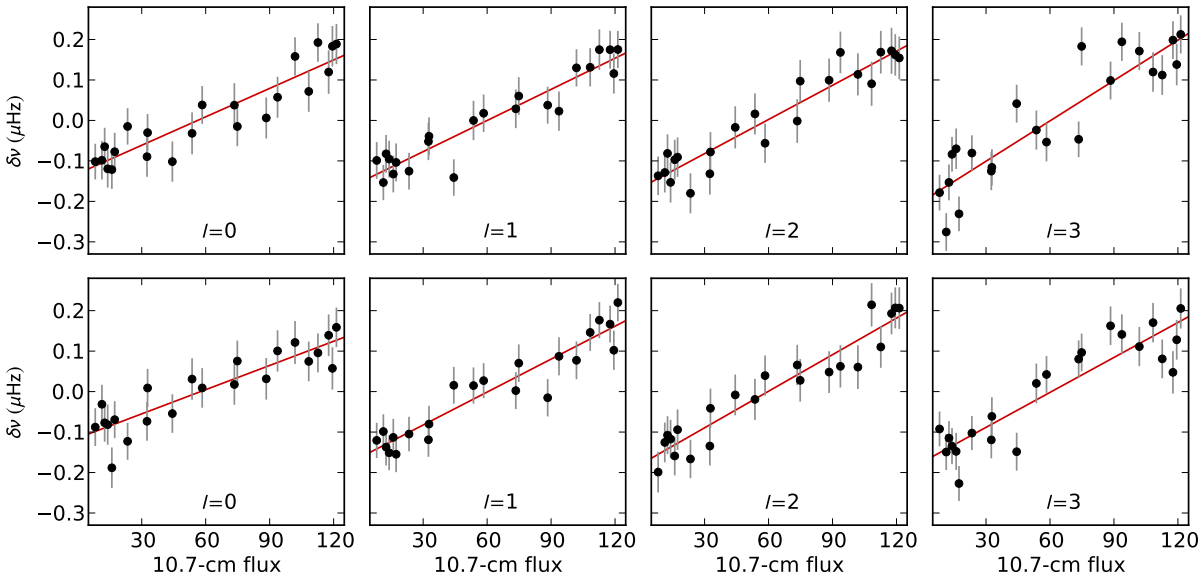

Fig. 5.11 – Frequency shifts for artificial BiSON data (black) as a function of the input 10.7-cm flux for the individual angular degrees: $l = 0$, $l = 1$, $l = 2$, and $l = 3$ (from left to right). Top and bottom rows concern each artificial data set (BiSON 1 and BiSON 2, respectively). The red lines show the best fits to the data.

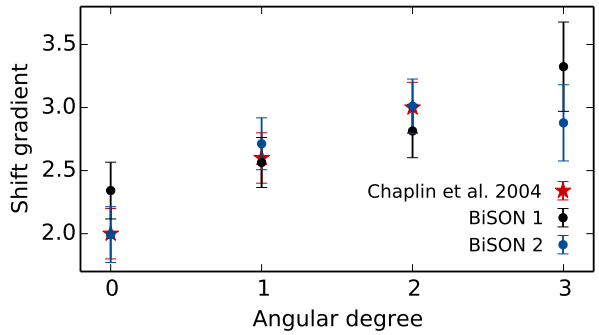

Fig. 5.12 – Frequency shift per unit change in activity, shift gradient, as a function of the angular degree for artificial BiSON data (black and blue, respectively). The red stars show the shift gradients found by Chaplin et al. (2004b).

5.6 Application to solar-type stars observed by Kepler

The high quality and quantity of data provided by *Kepler* give us an unique opportunity to search for the magnetic signatures on the seismic properties of stars and to better understand the stellar magnetism. With this in mind, we have been searching for temporal variations in the frequencies of a large sample of solar-type stars observed by *Kepler* (Sect. 5.1). To do so, we developed a Bayesian peak-bagging tool to estimate accurate mode frequencies from the stellar power density spectra.

This section summarizes the results for the *Kepler* targets. For each star, the original time-series is segmented in 90-d sub-series overlapped by 45 d. Considering the background model obtained in

Sect. 5.4 for each sub-series for each star, we apply the peak-bagging tool as described in Sect. 5.2, obtaining the marginal posterior probability distributions for the model parameters. As an example, Fig. 5.13 shows the posterior distributions of the mode parameters (i.e. ν_{nl}, S_{n0}, and Γ_{n0}) for the five central orders (closest to $\nu_{\rm max}$) obtained for a given sub-series of the star KIC 6933899. Figure 5.14 shows the posterior distributions for the rotational splitting and stellar inclination angle.

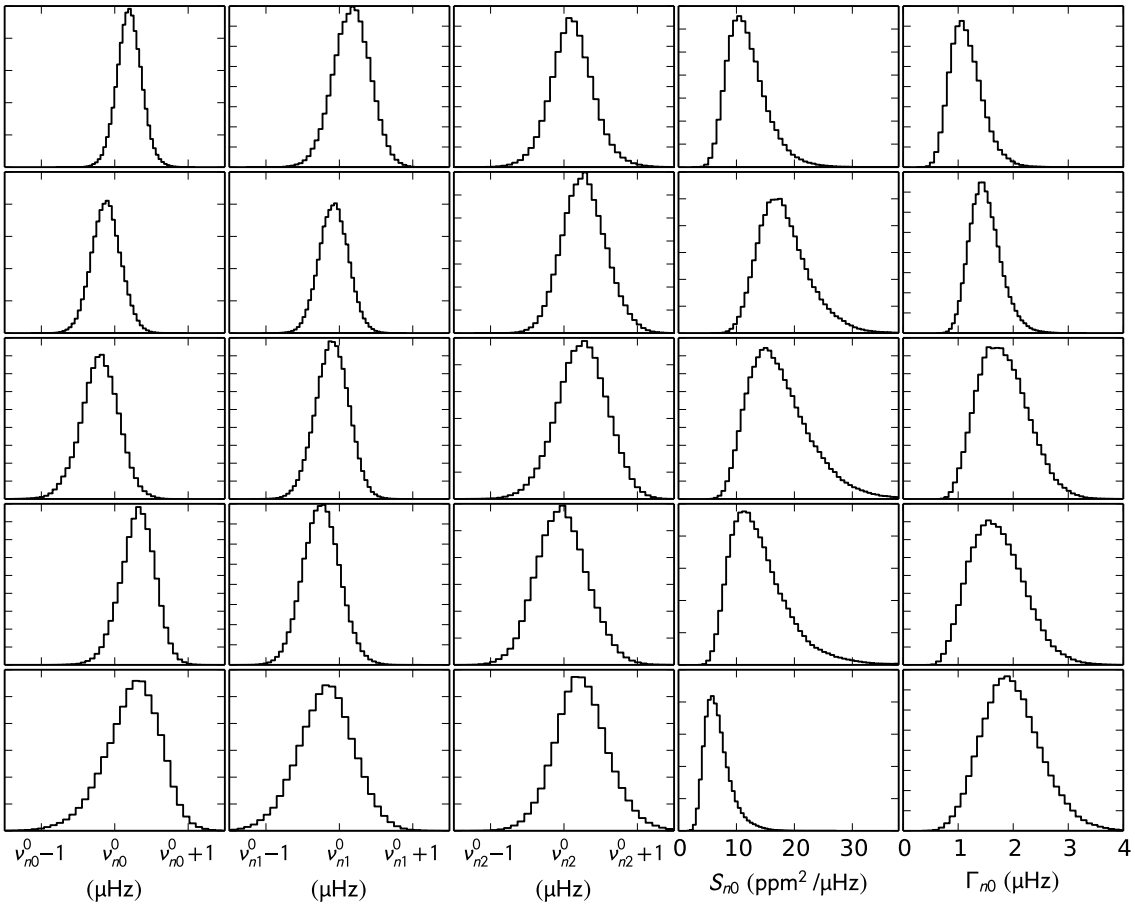

Fig. 5.13 – Posterior probability distributions for the mode parameters of KIC 6933899 for the five central orders (one row per order). The first 3 columns concern the mode frequencies for $l = 0$, $l = 1$, and $l = 2$, respectively. Note that the superscript "0" denotes the values from the literature (Lund et al. 2017, see Sect. 5.2.3). The last two columns concern the radial mode height and linewidth, respectively.

The final parameter estimates are given by the median of the posterior probability distribution and the uncertainties are determined base on the 68% credible region (see Sect. 5.2.4). Figure 5.15 compares the power density spectrum and the best fit obtained with the peak-bagging tool for a given sub-series of ten stars in the sample.

Having the mode frequencies for each sub-series, we then compute the weighted mean frequency shifts over time for each star (see Sect. 5.3 for details) and compare them with the results from a cross-correlation method (the latter are courtesy of René Kiefer; method described in Kiefer et al. 2017).

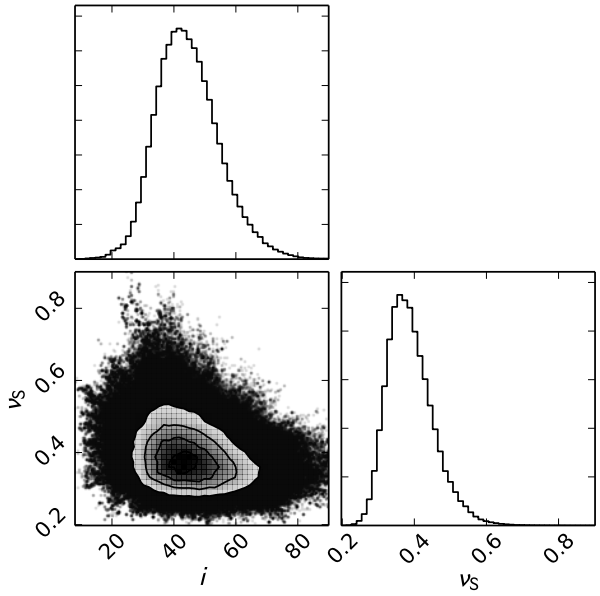

Fig. 5.14 – Top and bottom right: Posterior probability distributions for the stellar inclination angle and rotational splitting for KIC 6933899 (for the same 90-d sub-series of Fig. 5.13), respectively. Bottom left: Correlation map between the inclination and rotational splitting.

Table 5.3 summarizes the results for the star KIC 6933899. The frequency shifts presented here were obtained while considering only the five central orders, which usually have the largest signal-to-noise ratio in the p-modes. The tables for the remaining stars in the sample are presented in Appendix A.

Figure 5.16 compares the frequency shifts obtained with the Bayesian peak-bagging tool with those from the cross-correlation method for ten stars in the sample. These stars are some examples of stars for which we find significant temporal frequency shifts (see Appendix A for the remaining stars), that may be related with stellar magnetic activity. Note that the frequency shifts derived from our method are relative to the average value (see Sect. 5.3), while the frequency shifts from the cross-correlation method are estimated in relation to the first sub-series. In Fig. 5.16 and Table 5.3 (as well as on the Appendix A), the frequency shifts from the cross-correlation are shifted by their average value. First, this comparison shows that the results obtained with both methods agree very well. Second, the uncertainties on the estimated frequency shifts are smaller by a factor of a few for those obtained with the peak-bagging method than those obtained with the cross-correlation method. This reassures us that our peak-bagging tool is able to successfully recover accurate mode frequencies and, consequently, the temporal variations on those. Note that evidences for activity-related frequency shifts in five of those stars (shown in Fig. 5.16) were already reported in the literature (Salabert et al. 2016; Kiefer et al. 2017). Our results, thus confirm those evidences.

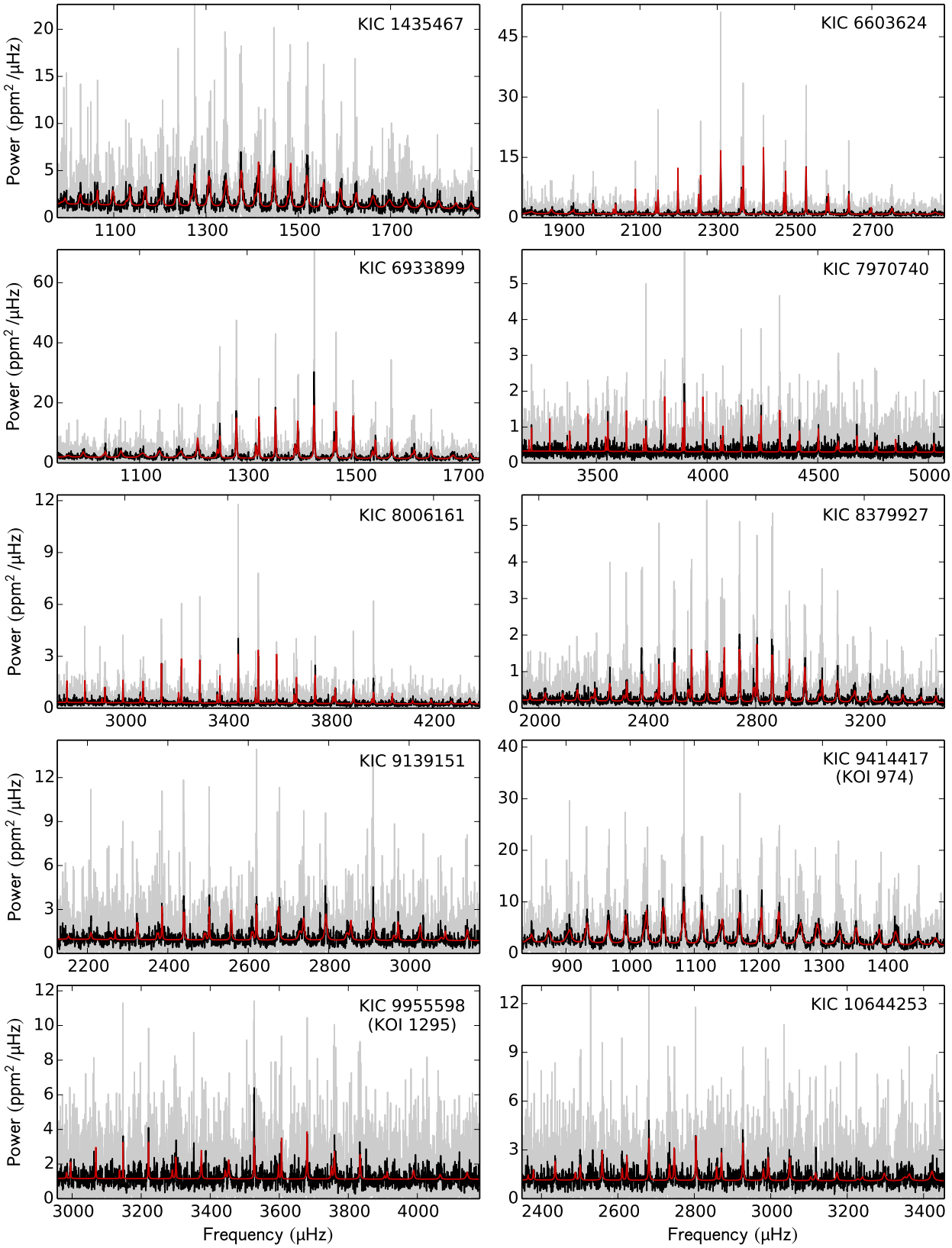

Fig. 5.15 – Power density spectrum (grey and black; with different smoothing for illustrative purpose) for a given 90-d sub-series of ten of the solar-type stars in our target sample. The red lines show the best fits to the respective power spectrum obtained with the Bayesian peak-bagging tool.

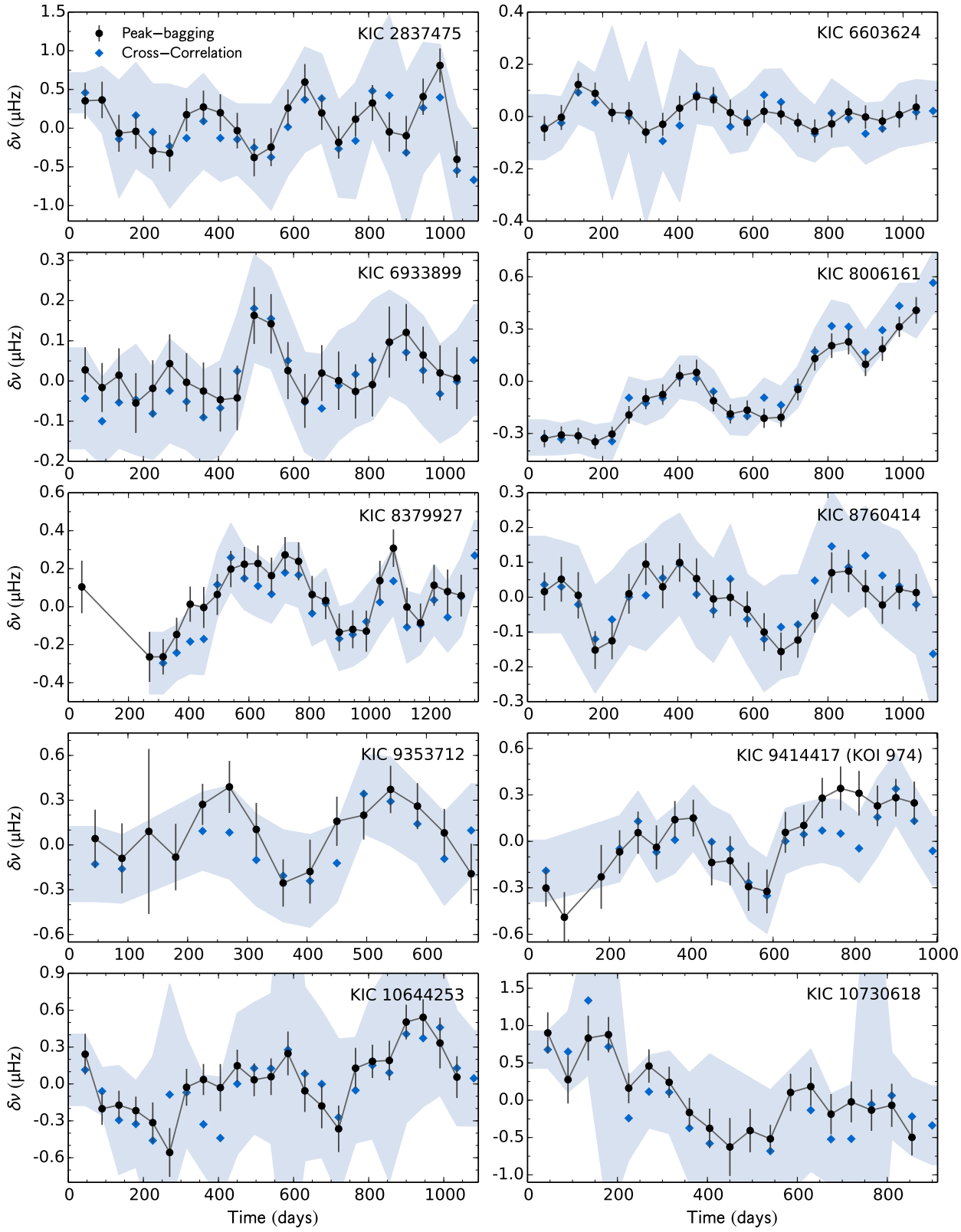

Fig. 5.16 – Comparison between the average frequency shifts obtained with the Bayesian peak-bagging tool (black) and those from the cross-correlation method (blue; described in Kiefer et al. 2017).

KIC 6933899

time (days)	d_c %	τ_{gran} (s)	Peak-bagging $\delta\nu_{l=0}$ (μHz)	$\delta\nu_{l=1}$ (μHz)	$\delta\nu_{l=2}$ (μHz)	$\delta\nu$ (μHz)	Cross-correlation $\delta\nu$ (μHz)
45	0.98	369.9 ± 1.7	0.06 ± 0.08	0.01 ± 0.08	-0.11 ± 0.12	0.04 ± 0.04	-0.04 ± 0.13
90	0.97	386.4 ± 20.3	0.07 ± 0.09	-0.07 ± 0.08	-0.32 ± 0.13	-0.00 ± -0.00	-0.10 ± 0.11
135	0.96	380.4 ± 20.6	0.05 ± 0.09	0.01 ± 0.09	-0.28 ± 0.12	0.03 ± 0.03	-0.05 ± 0.11
180	0.97	438.4 ± 24.8	0.03 ± 0.11	-0.10 ± 0.10	-0.02 ± 0.16	-0.04 ± -0.04	-0.05 ± 0.14
225	0.96	491.8 ± 30.7	0.11 ± 0.10	-0.12 ± 0.10	0.17 ± 0.15	-0.01 ± -0.01	-0.08 ± 0.11
270	0.80	511.2 ± 38.8	0.12 ± 0.10	-0.03 ± 0.11	0.18 ± 0.14	0.05 ± 0.05	-0.02 ± 0.13
315	0.78	428.8 ± 29.3	0.08 ± 0.09	-0.10 ± 0.12	0.01 ± 0.18	0.01 ± 0.01	-0.05 ± 0.12
360	0.89	396.7 ± 15.1	0.10 ± 0.09	-0.18 ± 0.11	-0.10 ± 0.14	-0.01 ± -0.01	-0.09 ± 0.12
405	0.93	402.5 ± 16.1	0.06 ± 0.10	-0.16 ± 0.12	-0.07 ± 0.14	-0.04 ± -0.04	-0.07 ± 0.12
450	0.97	385.5 ± 20.1	-0.06 ± 0.11	-0.01 ± 0.11	-0.15 ± 0.17	-0.03 ± -0.03	0.02 ± 0.14
495	0.97	399.9 ± 22.0	0.17 ± 0.11	0.18 ± 0.10	0.11 ± 0.16	0.17 ± 0.17	0.18 ± 0.13
540	0.98	464.5 ± 30.0	0.22 ± 0.10	0.08 ± 0.11	0.08 ± 0.14	0.15 ± 0.15	0.16 ± 0.13
585	0.94	469.5 ± 31.8	-0.01 ± 0.10	0.08 ± 0.10	0.02 ± 0.13	0.04 ± 0.04	0.05 ± 0.13
630	0.92	480.4 ± 35.4	-0.10 ± 0.10	0.00 ± 0.09	-0.24 ± 0.13	-0.05 ± -0.05	-0.05 ± 0.12
675	0.90	432.9 ± 26.5	0.11 ± 0.10	-0.04 ± 0.09	-0.14 ± 0.13	0.03 ± 0.03	-0.07 ± 0.13
720	0.91	376.1 ± 0.8	0.04 ± 0.11	-0.02 ± 0.10	0.03 ± 0.16	0.01 ± 0.01	-0.01 ± 0.14
765	0.95	377.5 ± 7.6	-0.06 ± 0.09	0.03 ± 0.10	0.03 ± 0.15	-0.02 ± -0.02	0.02 ± 0.13
810	0.90	377.0 ± 20.6	-0.16 ± 0.11	0.16 ± 0.11	0.36 ± 0.17	-0.00 ± -0.00	0.05 ± 0.15
855	0.89	370.4 ± 19.9	-0.13 ± 0.14	0.25 ± 0.11	0.15 ± 0.17	0.10 ± 0.10	0.10 ± 0.13
900	0.95	425.8 ± 24.4	0.07 ± 0.11	0.18 ± 0.10	-0.04 ± 0.16	0.13 ± 0.13	0.07 ± 0.13
945	0.90	546.8 ± 42.7	0.20 ± 0.10	-0.05 ± 0.10	-0.00 ± 0.16	0.08 ± 0.08	0.03 ± 0.14
990	0.89	535.3 ± 44.1	0.15 ± 0.10	-0.10 ± 0.10	-0.16 ± 0.14	0.03 ± 0.03	-0.03 ± 0.12
1035	0.85	407.4 ± 27.4	0.03 ± 0.11	0.00 ± 0.11	0.01 ± 0.15	0.02 ± 0.02	-0.00 ± 0.13
1080	0.85	340.3 ± 16.8	0.02 ± 0.12	0.08 ± 0.11	0.16 ± 0.17	0.05 ± 0.05	0.05 ± 0.14

Table 5.3 – Results for the solar-type star KIC 6933899. First column: corresponding time of the sub-series in relation to the starting time of the observations. Second column: duty-cycle for each sub-series. Third column: characteristic timescale of the granulation component (Sect. 5.4). Fourth-Seventh Columns: average frequency shifts obtained through the Bayesian peak-bagging tool for the radial ($\delta\nu_{l=0}$), dipolar($\delta\nu_{l=1}$), and quadrupolar ($\delta\nu_{l=2}$) modes, and the average frequency shifts obtained by combining the results for radial and dipolar modes ($\delta\nu$), respectively. Eighth column: frequency shifts obtained with the cross-correlation method described in Kiefer et al. (2017).

5.6.1 On the relation between the magnetic activity and the granulation

Although, it is still matter of debate in the literature, the properties of the solar granulation, namely amplitude and characteristic timescale, may be affected by magnetic activity. Muller et al. (2007) found evidences for a decrease in the granulation amplitude with the activity. However, other studies found no significant variation in this parameter (Pallé et al. 1995; Régulo et al. 2002, 2005; Lefebvre et al. 2008; Karoff 2012). Regarding the granulation characteristic timescale, while Lefebvre et al. (2008) claim no significant variation, Régulo et al. (2002, 2005) found that the granulation timescale increases with increasing activity. Moreover, although Lefebvre et al. (2008) and Karoff (2012) found that the granulation properties are mostly independent of the 11-yr solar cycle, these authors found evidences for shorter quasi-periodic (∼1-yr) variations, whose origin is still not understood. Lefebvre

et al. (2008), however, argued that they result from instrumental effects.

For stars other than the Sun, the relation between magnetic activity and the granulation properties is also not clear. García et al. (2010b) found no correlation between the observed activity-related frequency shifts and the granulation timescale for the solar-type star HD 49933 observed by CoRoT. Later, Karoff et al. (2013) analysed the variability of the granulation component on three solar-type stars observed by *Kepler*. For two of these stars (KIC 6603624 and KIC 6933899, both in our sample), the authors found quasi-annual/biennial periodicities on the granulation parameters, that resemble the quasi-biennial variations in the different solar activity indicators (Howe et al. 2000; Bazilevskaya et al. 2014; McIntosh et al. 2015), including frequency shifts (Fletcher et al. 2010; Broomhall et al. 2012; Broomhall & Nakariakov 2015). Finally, Kiefer et al. (2017) do not find evidence for a systematic correlation between the granulation timescale and the frequency shifts for their sample of 24 solar-type stars.

With the above in mind, we have been looking for correlations between the frequency shifts obtained through the Bayesian peak-bagging tool and the granulation characteristic timescale obtained in Sect. 5.4. This study is still in a preliminary stage and more tests need to be done in order to validate the variation that we found in the granulation timescale. In particular, one needs to exclude the possibility of any effects from the *Kepler*'s orbit.

Figure 5.17 compares the observed frequency shifts obtained from the peak-bagging method and the granulation timescale for some of the stars. For most of those stars, the variation in the acoustic frequencies seems to be associated to a variation in the characteristic timescales of the granulation. In particular, although with slightly different periodicities, we confirm the variation in the granulation for KIC 6603624 and KIC 69833899, previously reported by Karoff et al. (2013) based on shorter time-series (13-month time-series in comparison with the 4-yr time-series analysed in the current work). Moreover, for these two stars, that variation seems to be accompanied by a variation on the acoustic frequencies, perhaps with a slight offset: for example, by computing the cross-correlation function between the frequency shifts and the granulation timescale, for KIC 6933899 we find that the cross-correlation is maximal for an offset of +90 days (meaning that the frequency shifts are ahead of the variation in the granulation component), while for KIC 6603624 and KIC 9414417 we find that the cross-correlation is maximal for an offset of +45 days. Interestingly, for the Sun, Muller et al. (2007) also found evidence for a time lag of the granulation contrast in relation to the activity level.

5.6.2 Results for the ensemble

In this section, we look for correlations between the amplitude of the observed variations in the acoustic frequencies and the stellar effective temperature and rotation period.

Assuming that the frequency shifts scale linearly with the amplitude of the cycle, Chaplin et al. (2007a) predicted that the activity-related frequency shifts decrease with the stellar effective temperature. In opposition, the theoretical predictions of Metcalfe et al. (2007, that, besides the amplitude of the cycle, also consider in their scaling relation the depth of the source of the perturbations be-

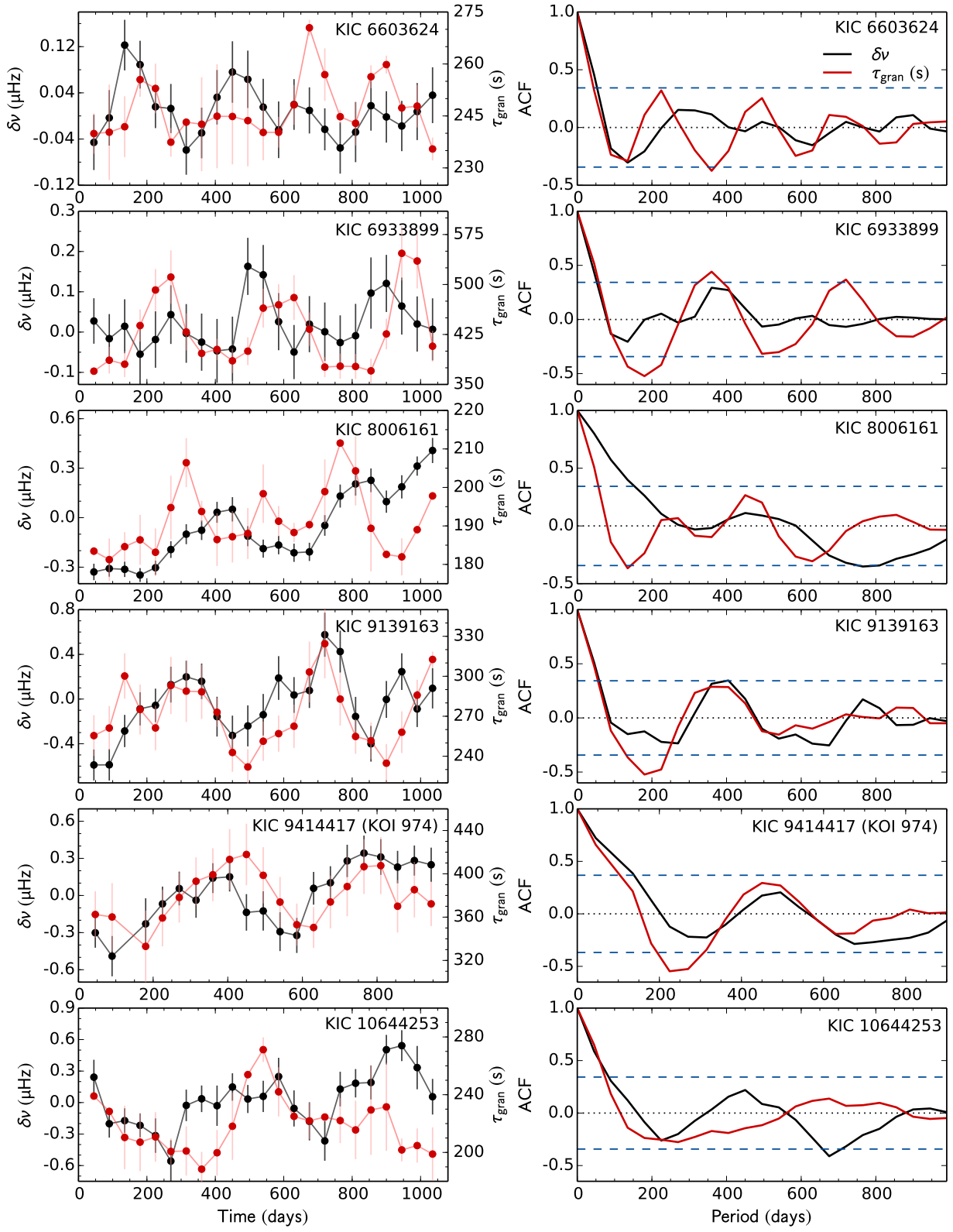

Fig. 5.17 – Comparison between the frequency shifts obtained with the peak-bagging tool (black) and the characteristic granulation timescale (red). The right panels show the autocorrelation function for the frequency shifts (black) and the granulation timescale (red). The blue dashed lines indicate the 95% significance level.

neath the photosphere and the mode inertia) show an increase in the frequency shifts with the stellar effective temperature.

Despite the large uncertainties, Kiefer et al. (2017) found evidences for an increase in the frequency-shift amplitude with increasing effective temperature and decreasing rotation period, which supports the scaling relation of Metcalfe et al. (2007). However, the authors have concluded that they could not exclude either of the opposing scenarios.

In the current work, we analyse a larger sample (more than three times larger than that of Kiefer et al. 2017), which covers a wider parameter space, namely higher temperatures and shorter rotation periods. Furthermore, as seen previously, the uncertainties in the frequency shifts estimated with the Bayesian peak-bagging tool are significantly smaller than those from the cross-correlation method (see Figs. 5.16 and 5.18).

Similarly to what is done in Kiefer et al. (2017), we compute the frequency-shift amplitudes as the difference between the maximum and minimum frequency shifts. Figure 5.18 compares the frequency-shift amplitudes as determined with our method with those from the cross-correlation method. The frequency-shift amplitudes determined from each method agree within the 1σ errors.

Figures 5.19 and 5.20 show the frequency-shift amplitudes (from the peak-bagging tool) as a function of the effective temperature and the rotation period (values from the literature; Table 5.1). Our results suggest that the frequency-shift amplitude increases with the stellar effective temperature (in agreement with the theoretical predictions of Metcalfe et al. 2007) and decreases with the surface rotation period (in agreement with stars with shorter rotation periods being more active; e.g. Wright et al. 2011; Metcalfe et al. 2016).

We note that only sub-series with duty cycle larger than 70% were considered in Figs. 5.18 - 5.20.

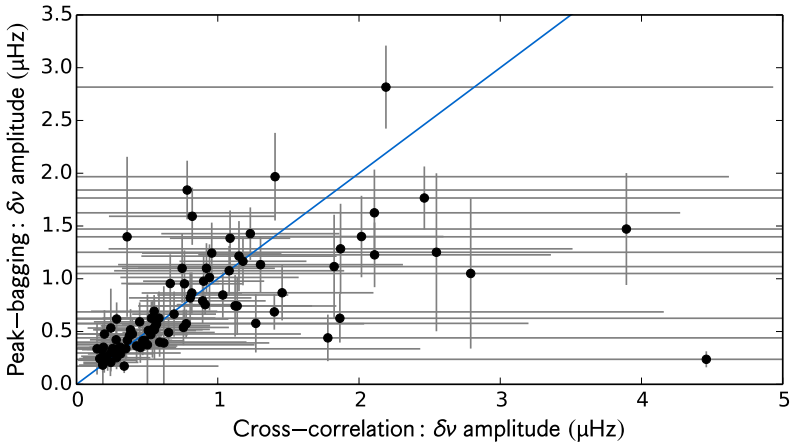

Fig. 5.18 – Comparison between the frequency-shift amplitudes from the peak-bagging tool and the cross-correlation method.

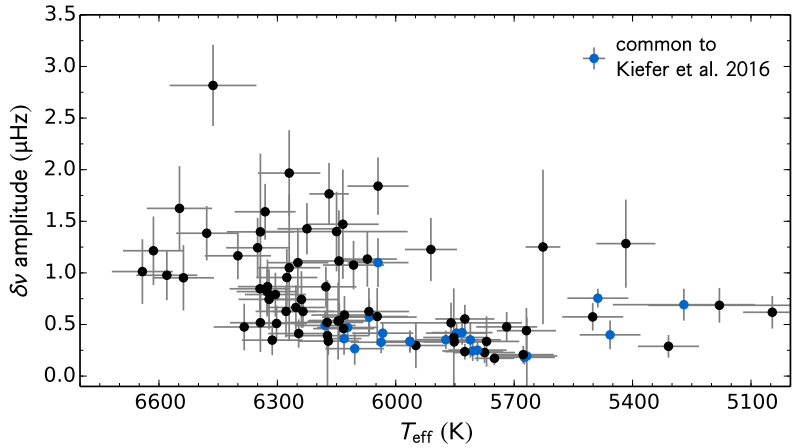

Fig. 5.19 – Amplitude of the frequency shifts (from the peak-bagging tool) as a function of the effective temperature for the stars in our sample. The blue dots mark the stars that are common to Kiefer et al. (2017).

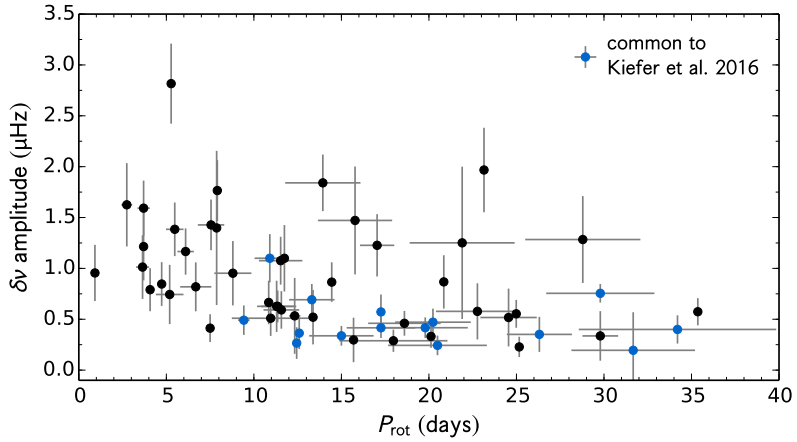

Fig. 5.20 – Amplitude of the frequency shifts (from the peak-bagging tool) as a function of the rotation period for the stars in our sample. The blue dots mark the stars that are common to Kiefer et al. (2017).

5.7 Conclusions

The solar oscillation frequencies are known to be sensitive to the changes in the solar activity (Woodard & Noyes 1985; Elsworth et al. 1990; Libbrecht & Woodard 1990; Chaplin et al. 1998; Howe et al. 2015, e.g.), varying in phase with the activity level. These activity-related variations are expected to be common among solar-type pulsators, enclosing the signatures of the magnetic changes taking place in the stellar interior. Asteroseismology, therefore, provides a unique way of studying stellar magnetism. With this in mind, we developed a Bayesian peak-bagging tool, which performs the global fit to the acoustic modes, being able to recover accurate mode parameters, in particular the mode frequencies.

The peak-bagging tool was first validated using solar real and artificial data. We verify that the

recovered activity-related frequency shifts were in good agreement with those in the literature. In particular, we were able to recover the correct amplitude of the frequency shifts, their angular degree dependence, and the signature of the quasi-biennial modulation.

Having validated the peak-bagging tool, we analyse a large sample of solar-type stars observed by the *Kepler* satellite. The original time-series are segmented in 90-d sub-series overlapped by 45 d. For each sub-series, we determine, first, the model for the acoustic background and, then, obtain the best fit to the acoustic modes with the peak-bagging tool. Finally, using the mode frequencies, we estimate the observed frequency shifts for each star in the sample and compare them with those obtained from a cross-correlation method. That comparison shows that our frequency shifts are consistent with those obtained from the cross-correlation method, which further confirms the efficacy of the Bayesian peak-bagging tool developed here. Moreover, the Bayesian approach we follow improves significantly the uncertainty on the estimated frequency shifts.

Some of the stars in the sample show evidences for (quasi-)period variations in the acoustic frequencies or for an ascending/descending phase of an activity cycle. We also find evidences for periodic variations in the characteristic timescale of the granulation for several stars. Some of those also show frequency variations consistent with the granulation timescale. However, in what concerns the comparison with the granulation timescale, we note that the results are preliminary as the work described in this Chapter is in progress and, thus, further investigation is needed.

Finally, our results suggest that the frequency shifts increase with the stellar effective temperature (which is consistent with the theoretical predictions of Metcalfe et al. 2007) and decrease with the surface rotation period (which is consistent with the fact that faster rotators are expected to be more active than slower rotators; e.g. Wright et al. 2011; Metcalfe et al. 2016).

6. Starspot signature on the light curve

Stellar rotation, in particular differential rotation, is a key ingredient of the dynamo mechanism, which is responsible for the generation of magnetic fields in the Sun and Sun-like stars.

In the Sun, the most direct evidence of magnetic activity is the emergence of dark spots at the solar surface. Although the surface of other stars cannot be resolved and, thus, starspots cannot be directly observed, one can still detect their indirect effect. Spots are regions of strong magnetic field that suppress the convection, resulting in a less efficient heat transport. Therefore, spots are cooler and, consequently, darker than the surroundings, having an impact on the stellar brightness. As the spots follow the stellar surface rotation and cross the visible disc, they induce quasi-periodic modulations on the stellar light curve. In turn, such modulations provide information about the stellar surface rotation and, also, magnetic activity (e.g. Mosser et al. 2009; Mathur et al. 2010; García et al. 2010a; Ballot et al. 2011; García et al. 2014a; Mathur et al. 2014).

Through the analysis of the spot modulation on the light curve, rotational periods have been determined for a large number of stars, in particular *Kepler* targets (e.g. Reinhold et al. 2013; Nielsen et al. 2013; McQuillan et al. 2013a,b, 2014; García et al. 2014a). The methods commonly used to estimate rotation periods are based on the Lomb-Scargle periodogram, the autocorrelation function and/or the wavelet transform. Furthermore, the high quality of these time-series provides a good opportunity to measure differential rotation, since the spot-induced modulations of the light curves enclose specific signatures of spots at different latitudes. The amplitude of the differential rotation can be recovered through spot modelling (e.g. Mosser et al. 2009; Huber et al. 2010; Lanza et al. 2011, 2014). By fitting a given model to the observed light curve, a number of stellar and spot parameters may be constrained, including the stellar surface rates at the spot latitudes. Differential rotation has also been measured through the periodogram analysis (e.g. Reinhold & Reiners 2013; Reinhold et al. 2013; Reinhold & Gizon 2015; Nagel et al. 2016; Distefano et al. 2016). In the periodogram, broad or multiple peaks associated with the stellar rotation are usually interpreted as evidence of the differential rotation. The analysis of individual sub-series of the full light curve, whose modulation might be dominated by spots at different latitudes, allows the identification of temporal variations in the recovered rotation period, which can also be an indication of differential rotation.

Recently, Reinhold & Arlt (2015) proposed a new and simple method, based on the periodogram analysis, to detect the sign of differential rotation, that is, whether the equatorial regions rotate faster or slower than the poles. The method consists on comparing the ratios between the height of the second and first harmonics (hereafter peak-height ratios) associated to different rotation periods. For a given rotation period P_j (first harmonic), the peak-height ratios are computed as

$$r_j = \frac{h(P'_j)}{h(P_j)}, \tag{6.1}$$

where P'_j is the second harmonic of the rotation period, and $h(P_j)$ and $h(P'_j)$ are the heights of the first and second harmonics, respectively (hereafter, h_j and h'_j).

The authors argued that spots at lower latitudes lead to less sine-shaped light curves than spots at higher latitudes, resulting in extra power on the second harmonic and, thus, larger peak-height ratios. While basing this argument/method on results for synthetic light curves with specific configurations, the authors do not provide any further explanation. Following their argument, one can attribute a relative latitude ("high" or "low") to each peak, P_j:

- if $r_j > r_{j+1} \Rightarrow P_{\rm low} = P_j$ and $P_{\rm high} = P_{j+1}$
- if $r_j < r_{j+1} \Rightarrow P_{\rm low} = P_{j+1}$ and $P_{\rm high} = P_j$.

With the relative latitudes in hand, one can then infer the sign of differential rotation. Reinhold & Arlt (2015) define the observed relative differential rotation as

$$\alpha_{\rm obs} = \frac{P_{\rm high} - P_{\rm low}}{P_{\rm high}}. \tag{6.2}$$

Here $\alpha_{\rm obs}$ is positive/negative when the equatorial regions rotate faster/slower than the polar regions (solar/antisolar differential rotation).

When Reinhold & Arlt (2015) applied the method to a particular set of synthetic light curves with solar differential rotation, a low false-positive rate (11.3%–20%) was recovered. The method was also applied to a sample of 50 stars observed by *Kepler*. Solar differential rotation was reported for 21–34 stars (depending on the criteria for the peak separation that they impose), while 5–10 stars were found to be consistent with anti-solar differential rotation (for details, see Reinhold & Arlt 2015).

In this chapter, we investigate the spot's signature on the light curve and, consequently, on the periodogram. To that end, we develop a simple tool to simulate the spot-induced modulation on the light curve (Sect. 6.1). We perform a detailed study of the peak-height ratios (equation 6.1) and their dependency on the spot and stellar properties (Sect. 6.2). In particular, we address the latitudinal dependence of the peak-height ratios. We are also interested in understanding the conditions that lead to the successful or unsuccessful detection of the sign of differential rotation. In section 6.3, we present the first source for false-positives/negatives of $\alpha_{\rm obs}$ (equation 6.2) and for observational bias.[1]

6.1 Synthetic light curves: simple tool

In order to study the modulation of the stellar light curves due to the presence of spots, we developed a tool to simulate the light curves of spotted stars based on the models of Lanza et al. (1993) and Eker (1994).

Each spot is assumed to be circular and is decomposed in a number of area elements, whose flux is given by

$$F_k = I_{\rm S}(\mu_k)\varpi_k, \tag{6.3}$$

[1] This chapter is focused on the work published in Santos et al. (2017b).

where I_S is the spot intensity, ϖ_k is the corresponding solid angle, and $\mu_k = \cos\psi_k$ where ψ_k is the angle between the line of sight and the normal to the surface element (see Fig. 6.1).

Figure 6.1 shows a schematic representation of a star. The dark spot represents a given element k marked by the position K. The stellar rotation axis is aligned with the z-axis and the position P marks the stellar northern pole. The red arrow indicates the line of sight and O indicates the center of the visible disc, while the position A marks the stellar center. Using the spherical triangle OKP, $\mu_k = \cos\psi_k$ can be written in terms of the element coordinates (colatitude, θ_k, and longitude, ϕ_k) and stellar inclination angle, i

$$\mu_k = \overline{\mathrm{AO}} \cdot \overline{\mathrm{AK}} = \cos i \cos\theta_k + \sin i \sin\theta_k \cos\phi_k . \tag{6.4}$$

The element k is visible whenever $0 \leq \mu_k \leq 1$.

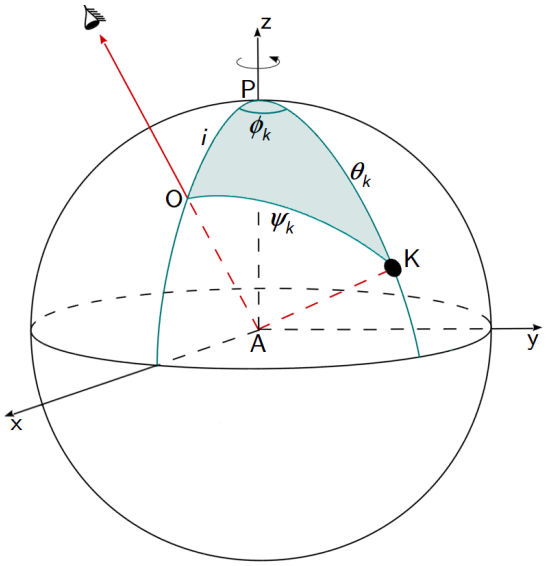

Fig. 6.1 – Representation of a star where the dark spot corresponds to the element k with a given colatitude, θ_k, and longitude, ϕ_k. The stellar inclination angle, i, corresponds to the angle between the stellar rotation axis and the line of sight, while the angle ψ_k is the angle between the normal to the element k and the line of sight.

The relative decrease in flux associated to an element k is

$$\left(\frac{\Delta F}{F}\right)_k = (1 - C_S)\frac{S_k}{\pi R_\star^2}\mu_k \frac{I(\mu_k)}{I(1)}, \tag{6.5}$$

where S_k is the element area, $R_\star$ is the stellar radius, $I(\mu_k)/I(1)$ is the relative photospheric intensity given by the limb-darkening law, $C_S = I_S/I(1)$ is the spot-to-photosphere intensity ratio, which, for simplicity, we shall assume to be a constant, not distinguishing the contributions from umbra and penumbra. F corresponds to the total stellar flux with no spots and while neglecting the limb darkening, i.e. assuming a constant stellar intensity of $I(1)$.

Finally, the total decrease in flux due to spots corresponds to the sum of the contributions from each element k

$$\frac{\Delta F}{F} = \sum_k \left(\frac{\Delta F}{F}\right)_k . \tag{6.6}$$

Each element is first defined in the spot's referential frame (r',θ'_k,ϕ'_k), which is rotated by θ_S in relation to the star's referential frame, where θ_S is the colatitude at the spot's center, i.e. the angle between the stellar rotation axis and the spot's axis. Thus, the two coordinate systems are related as (see Fig. 6.2)

$$\begin{cases} x = x'\cos\theta_S - z'\sin\theta_S \\ y = y' \\ z = x'\sin\theta_S + z'\cos\theta_S . \end{cases} \tag{6.7}$$

The coordinates of the element k on the star's and spot's referentials are, respectively

$$\begin{cases} x = \sin\theta_k\cos\phi_k \\ y = \sin\theta_k\sin\phi_k \\ z = \cos\theta_k \end{cases} \qquad \begin{cases} x' = \sin\theta'_k\cos\phi'_k \\ y' = \sin\theta'_k\sin\phi'_k \\ z' = \cos\phi'_k . \end{cases} \tag{6.8}$$

Combining equations (6.7) and (6.8), the coordinates of the element k in the star's referential correspond to

$$\begin{aligned} \cos\theta_k &= \cos\theta_S\cos\theta'_k + \sin\theta_S\sin\theta'_k\cos\phi'_k \\ \sin\theta_k &= \sqrt{1-\cos^2\theta_k} \\ \cos\phi_k &= (\cos\theta_S\sin\theta'_k\cos\phi'_k - \sin\theta_S\cos\theta'_k)/\sin\theta_k \\ \sin\phi_k &= \sin\phi'_k\sin\theta'_k/\sin\theta_k . \end{aligned} \tag{6.9}$$

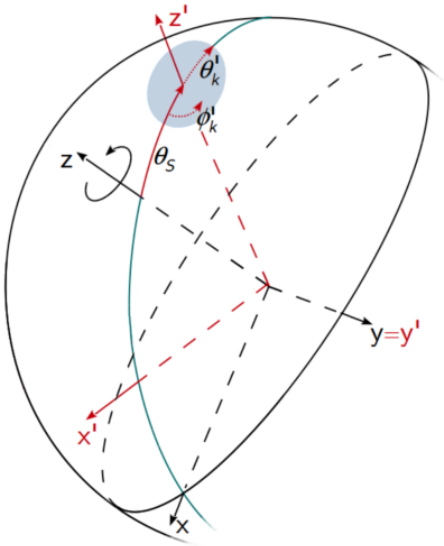

Fig. 6.2 – Comparison between the star's and spot's referential. The x'z'-plane in the spot's referential is rotated by θ_S (spot colatitude) in relation to the star's referential. θ'_k and ϕ'_k correspond to the colatitude and longitude of a given element k in the spot's referential.

6.2 Peak-height ratios: one-spot simulations

The modulation on the light curve induced by spots crossing the visible disc of the star depends on a number of stellar and spot parameters, e.g. the stellar inclination angle, rotation rate, limb-darkening law, spot size, latitude, and intensity contrast. In this section, we investigate how the resulting periodograms, in particular the peak-height ratios (equation 6.1), are affected by those properties.

We start by exploring to what extent the peak-height ratios, $r = h'/h$, are a measure of the sinusoidality of the spot modulation on the light curve. To do so, we start by considering the simplest case of one-spot simulations. We obtain the synthetic light curves for stars with different inclination angles, i, and a single spot at different latitudes, L. Figure 6.3 shows two light curves obtained from one-spot simulations with inclination $i = 50°$ and latitudes $L = 60°$ and $L = -20°$, respectively. The right panel illustrates the stellar visible disc, where the dark red and dark blue represent each of the spots at a given time. The light red and light blue mark the positions at different times, indicating the spots' trajectories and projected areas on the stellar visible disc.

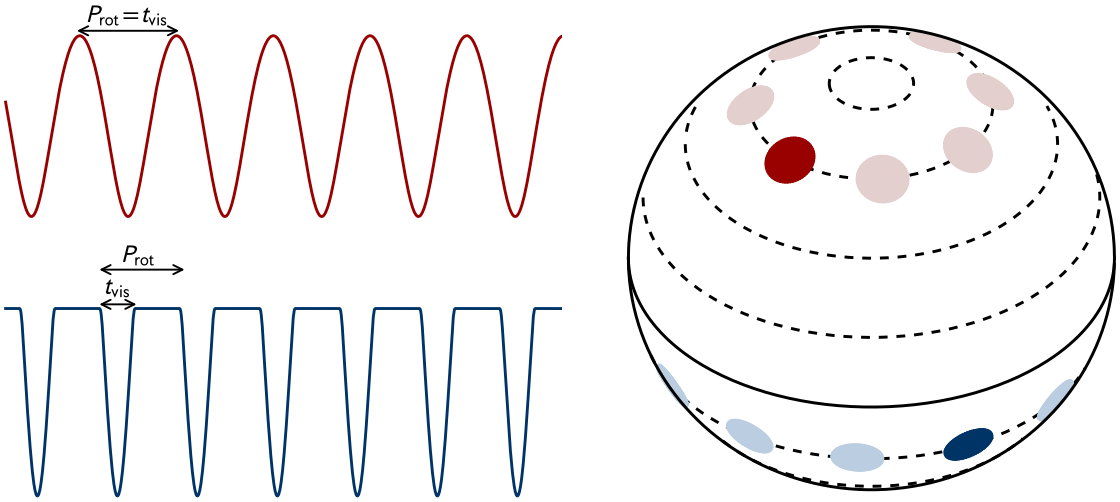

Fig. 6.3 – Left panel: Two light curves obtained from one-spot simulations. The stellar inclination angle is $i = 50°$, while the spot's latitude is $L = 60°$ in the first simulation and $L = -20°$ in the second (red and blue lines, respectively). The arrows indicate the visibility time of the spots and the rotation period. Right: Representation of the stellar visible disc, where the spots associated to each light curve are marked in red and blue. Dark red and dark blue show the spots at a given time, while the light colours show their positions and projected areas at different times. The stellar equator is represented by the solid line, while the dashed lines mark the corresponding parallels spaced by 20°.

For this first set of simulations we assume a circular spot of constant radius $R_S \sim 5.7°$ ($A = 5000\,\mu$Hem; about the area covered by sunspots at solar maximum), infinite lifetime, and an intensity contrast of $C_S = 0.67$, which is considered reasonable for the Sun and Sun-like stars (e.g. Sofia et al. 1982; Lanza et al. 2003; Walkowicz et al. 2013). Also, we assume a quadratic limb-darkening law

given by

$$\frac{I(\mu)}{I(1)} = 1 - a(1-\mu) + b(1-\mu)^2, \tag{6.10}$$

where $a = 0.5287$ and $b = 0.2175$, which is assumed to be adequate for solar-type stars observed by *Kepler* (Claret 2000; Reinhold & Reiners 2013). The differential rotation is assumed to be solar and is given by

$$\Omega(L) = \Omega_{\rm eq}(1 - \alpha \sin^2 L - \beta \sin^4 L), \tag{6.11}$$

where $\Omega_{\rm eq}$ is the angular velocity at the equator, and α and β are the parameters that determine the latitudinal dependency of the rotation rate. For this set of synthetic data, we have considered $\Omega_{\rm eq} = 0.2567\,{\rm rad\,d^{-1}}$, $\alpha = 0.1584$, and $\beta = 0.1210$ (Snodgrass 1983b; Snodgrass & Ulrich 1990a). The initial longitude of the spot for each simulation in this section is determined randomly.

Applying a rectangular window function, we compute the Lomb-Scargle periodogram (LSP) for each synthetic light curve. Then, we identify the peaks associated to the rotation period (first harmonic; P_j) and to its second harmonic (P'_j). Finally, we compute the corresponding peak-height ratio (equation 6.1).

We find that the peak-height ratios are essentially a function of a single parameter: the relative visibility time of the spot. Figure 6.4 shows how the peak-height ratios change as a function of the ratio between the visibility time and the rotation period (for comparison, in Fig. 6.3, the spots' visibility times and rotation periods are also indicated). Spots that are visible for most of the rotation period lead to more sine-shaped signals than spots that are visible for a smaller fraction of time. The spot is considered visible whenever there is a decrease in flux. Using this definition for the visibility time of the spot ($t_{\rm vis}$), we might be overestimating the true visibility time, especially for low inclination angles. Nevertheless, we can clearly conclude that the longer the spots are visible, the smaller the peak-height ratios are.

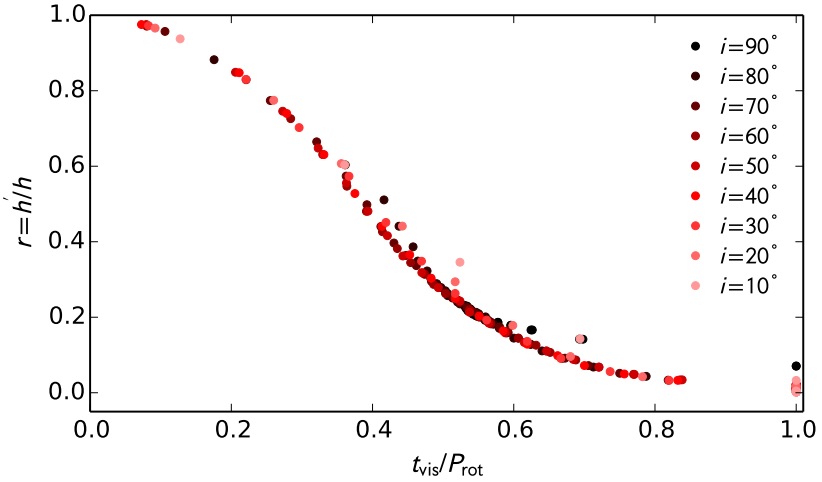

Fig. 6.4 – Peak-height ratios associated with spots at different latitudes (ranging from 0° to ±85°) as a function of the relative visibility time of the spots. Different colour shades indicate different stellar inclination angles, i.

Figure 6.5 shows the peak-height ratios as a function of the spot latitude. The spot latitude and the stellar inclination angle are the most determinant parameters for the spot visibility. As different combinations of i and L result in the same spot visibility time, there is a degeneracy between these two paremeters. Nevertheless, the peak-height ratios provide constraints on the possible solutions (i, L) that can lead to the spot signature on the observed light curve. If the stellar inclination is known, the spot latitude can be estimated.

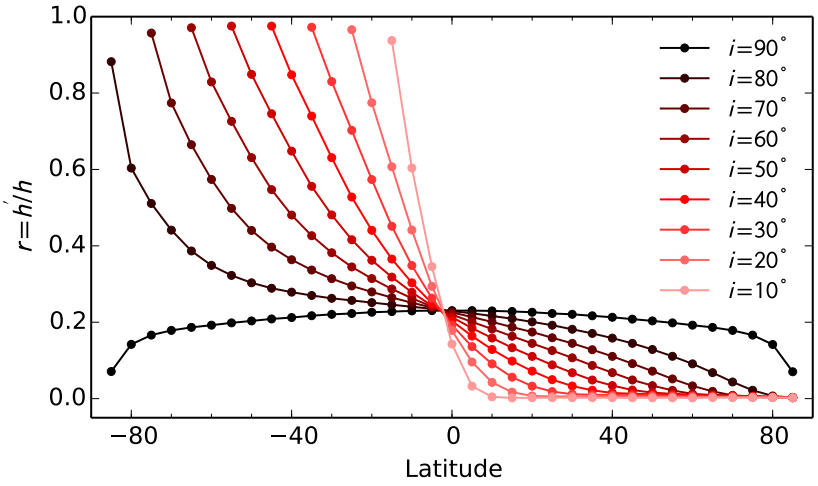

Fig. 6.5 – Peak-height ratios as a function of the spot latitude for different inclination angles, i. For a given inclination, it is shown that the peak-height ratios follow a well defined relation (that we call latitude-ratio relation).

The method proposed by Reinhold & Arlt (2015) for the determination of the sign of the surface differential rotation relies on the correct identification of a relative latitude (low/high) for at least two rotation periods (first harmonics) in the LSP. Implicit to their method is the assumption that spots at lower absolute latitudes are associated with higher peak-height ratios, $r = h'/h$, than are spots at higher absolute latitudes. Except for inclination angles very close to $i = 90°$, this is only true for spots on the same hemisphere as the observer (which we will call the northern hemisphere). Spots emerging at higher latitudes on the southern hemisphere are visible for a smaller fraction of time, thus, inducing a less sinusoidal signature and leading to higher peak-height ratios than spots at lower latitudes on the northern or southern hemispheres. Hence, for values of the inclination angle not too close to $i = 90°$, the method will suggest the wrong sign for the differential rotation when comparing the peak-height ratios of periods associated with spots on the southern hemisphere. A wrong sign will also be recovered when one of the spots is at L_1 on the northern hemisphere, the second is at L_2 on the southern, and $|L_2| > |L_1|$. Two examples are described below:

1. the target star is characterized by solar differential rotation ($\alpha > 0$)

2. we recover the rotation periods of two spots at $L_1 = -50°$ and $L_2 = -20°$ (example 1) or at $L_1 = -50°$ and $L_2 = +20°$ (example 2)

3. we compute the peak-height ratios (equation 6.1) and compare them, finding $r_1 > r_2$
4. the method proposed by (Reinhold & Arlt 2015) leads to $P_{\rm low} = P_1$ and $P_{\rm high} = P_2$
5. the relative differential rotation is determined as $\alpha_{\rm obs} = (P_2 - P_1)/P_2$ (equation 6.2) that yields $\alpha_{\rm obs} < 0$ while $\alpha > 0$.

For an inclination angle of $i = 90°$, the behaviour of the peak-height ratios is hemispheric symmetric and nearly independent on the latitude of the spot (except for $|L|$ very close to 90°). Therefore, for this inclination, the association of the detected rotation periods with different latitudes is difficult. Also, for small inclination angles, the ratios become saturated at high latitudes on the northern hemisphere as spots at that location are always visible.

Although our results show that the peak-height ratios are essentially a function of the visibility time of the spot, which is determined mainly by the stellar inclination angle and the spot latitude, the modulation on the light curves induced by spots also depends on other parameters. In what follows, we investigate the impact on the peak-height ratios of other spot and stellar properties, such as the spot area and relative intensity, rotation rate, and limb-darkening law.

The top panel of Fig. 6.6 shows the peak-height ratios as a function of latitude (left panel) and relative visibility time (right panel) for different inclination angles and spot sizes. The impact of the spot size on the recovered ratios is more significant for spots at higher latitudes on the southern hemisphere and lower inclinations. For a given latitude and inclination, a larger spot will be visible for a longer time than a smaller spot, thus larger spots lead to smaller ratios than smaller spots.

As the spot-to-photosphere intensity contrast does not affect the visibility time of the spot, it also does not have a significant impact on the peak-height ratios. This is shown in the second row of Fig. 6.6. As mentioned before, for these synthetic light curves the initial phase of the spot is determined randomly, taking into consideration that the light curve is discrete, this introduces a small effect on the estimated spot visibility time. The small differences seen in the right panel of the second row in Fig. 6.6 show that the phase of a given spot alone has little impact on the visibility time of the spot.

In order to investigate the impact of the rotation rate on the peak-height ratios, we have considered different rotation profiles in the synthetic data, including solar ($\alpha > 0$) and anti-solar ($\alpha < 0$) differential rotation. In this set of simulations, we consider the simplified version of equation (6.11) that is commonly used,

$$\Omega(L) = \Omega_{\rm eq}(1 - \alpha \sin^2 L). \tag{6.12}$$

The third row of Fig. 6.6 summarizes the results from this study, where $\Omega_{{\rm eq},\odot} = 0.2567\,{\rm rad\,d^{-1}}$ and $\alpha_\odot = 0.1584$ denote the solar values considered above. Since the rotation rate does not change the fraction of time the spot is visible, its impact on the peak-height ratios is not significant. However, small discrepancies are still visible, which result first from the random initial spot phases, and second from the fact that while the characteristic time-scale of the light curves changes when considering different rotation rates, the length and cadence of the light curves are unchanged.

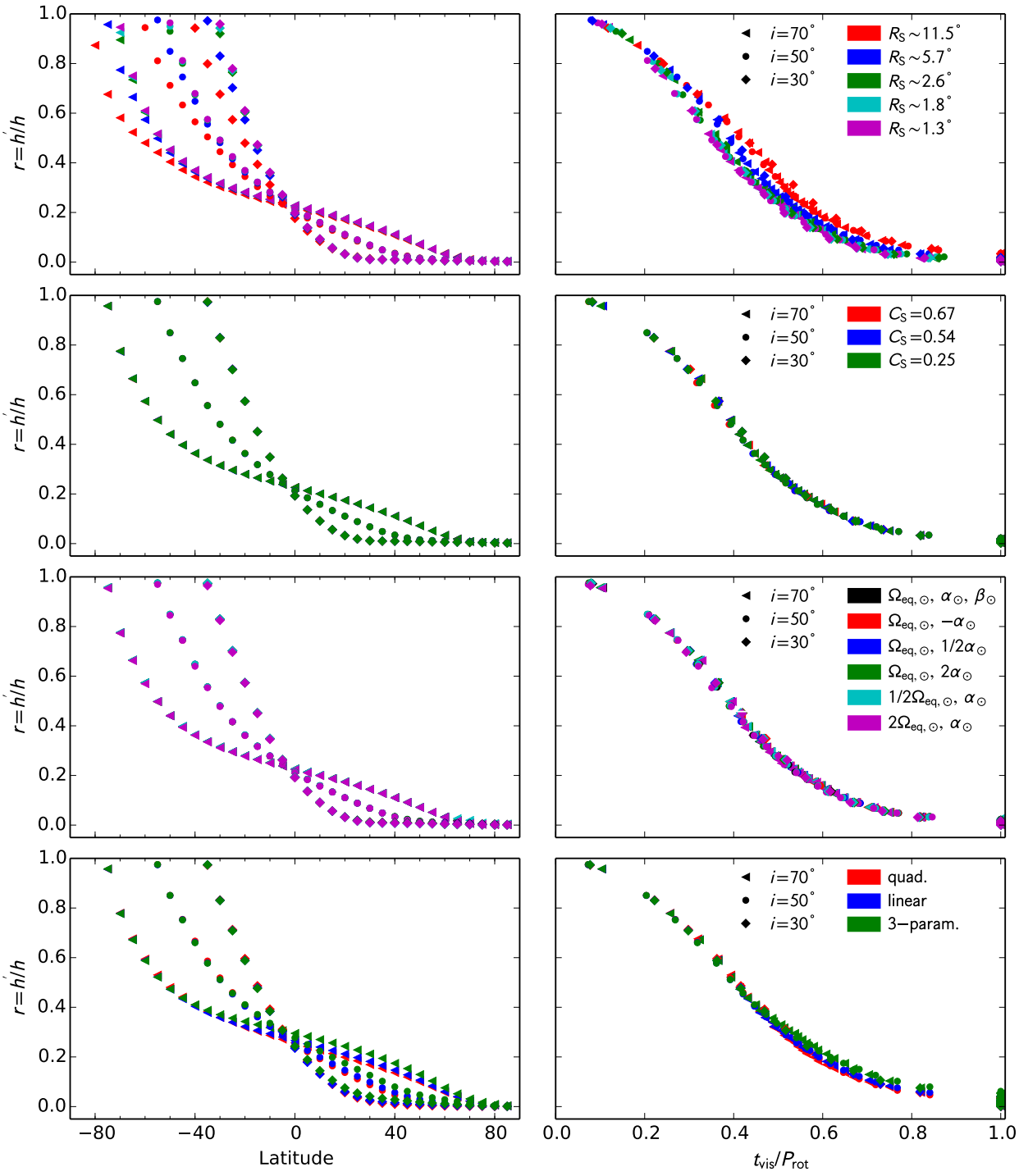

Fig. 6.6 – Peak-height ratios as a function of the spot latitude (left) and relative visibility time (right) for the inclination angles $i = 30°$, 50°, and 70° and for different spot areas (top panel), different spot-to-photosphere intensity ratios (second row), various differential rotation parameters (third row), and different limb-darkening laws (bottom panel). For these simulations, the default values of the spot radius and intensity contrast are $R_S \sim 5.7°$ and $C_S = 0.67$. We use the solar rotation ($\Omega_{eq,\odot}$, $\alpha_\odot$, and $\beta_\odot$) as the default rotation profile. Finally, the default limb-darkening law is the quadratic one with parameters $a = 0.5287$ and $b = 0.2175$. [$R_S \sim 11.5° \Leftrightarrow A_S = 20000\,\mu$Hem, $R_S \sim 5.7° \Leftrightarrow A_S = 5000\,\mu$Hem, $R_S \sim 2.6° \Leftrightarrow A_S = 1000\,\mu$Hem, $R_S \sim 1.8° \Leftrightarrow A_S = 500\,\mu$Hem, $R_S \sim 1.3° \Leftrightarrow A_S = 250\,\mu$Hem]

The bottom panel of Fig. 6.6 shows the results obtained from synthetic data considering different limb-darkening laws: the quadric limb-darkening law (equation 6.10), the linear limb-darkening law

$$\frac{I(\mu)}{I(1)} = 1 - u(1-\mu), \tag{6.13}$$

and the three-parameter non-linear limb-darkening law

$$\frac{I(\mu)}{I(1)} = 1 - c_2(1-\mu) - c_3\left(1-\mu^{3/2}\right) - c_4\left(1-\mu^2\right), \tag{6.14}$$

where u, c_2, c_3, and c_4 are the limb-darkening coefficients, which we take from the study by Sing (2010) for *Kepler* data. Since the effective temperature ($T_{\rm eff}$), the surface gravity ($\log g$), and the metallicity ([M/H]) are, in principle, known parameters, Fig. 6.6 shows the results for $T_{\rm eff} = 5750\,K$, $\log g = 4.50$ and [M/H] $= 0.00$. As the limb-darkening changes the shape of the spot modulation, it also affects the sinusoidality of the modulation seen through the peak-height ratios (bottom panel of Fig. 6.6). Also, for different inclinations, spots with the same relative visibility time ($t_{\rm vis}/P_{\rm rot}$) have different trajectories over the visible disc, corresponding to different limb-darkening and projected spot areas. In turn, the sinusoidality of the spot signature changes. This effect is small and can be seen through the differences between different inclinations (for example, second row of Fig. 6.6).

6.2.1 Choice of an appropriate window function

Sharp transitions and discontinuities in the light curve lead to spectral leakage in the periodogram, which in turn affects the heights of the peaks and, thus, the peak-height ratios. While the peridogram analysis assumes a periodic signal, often the spot modulation on the stellar light curves is not an integer number of periods. Thus the end points of the light curves are not continuous. To minimize that effect, an adequate window function (WF) must be applied to the light curve before computing the Lomb-Scargle periodogram.

In the case of one-spot simulations, we apply a rectangular WF to the light curves, which properly (and automatically) crops the time-series in order to make the signal as continuous as possible. However, for real data or more complex simulations, the application of such WF is not as simple as for one-spot simulations and may not be the most adequate.

There are several types of window functions used to reduce the amplitude of the discontinuities at the end points of the signal. In this section, we compare their performance on the one-spot simulations in order to chose the appropriate window function for our analysis.

In what follows, the window functions we tested are listed. M corresponds to the number of points in the time-series.

- **Bartlett window:** $f(t) = \frac{2}{M-1}\left(\frac{M-1}{2} - \left|t - \frac{M-1}{2}\right|\right)$ with $0 \leq t \leq M-1$

- **Blackman window:** $f(t) = 0.42 - 0.5\cos\left(\frac{2\pi t}{M}\right) + 0.08\cos\left(\frac{4\pi t}{M}\right)$ with $0 \leq t \leq M-1$
- **Kaiser window:** $f(t) = J_0\left(\beta\sqrt{1-\frac{4t^2}{(M-1)^2}}\right)/J_0(\beta)$, where $-\frac{M-1}{2} \leq t \leq \frac{M-1}{2}$ and J_0 is the modified 0-order Bessel function
  - $\beta = 0 \simeq$ Rectangular
  - $\beta = 5 \simeq$ Hamming
  - $\beta = 6 \simeq$ Hanning
  - $\beta = 8.6 \simeq$ Blackman
- **Hamming window:** $f(t) = 0.54 - 0.46\cos(2\pi t/(M-1))$ with $0 \leq t \leq M-1$
- **Hanning window:** $f(t) = 0.5 - 0.5\cos(2\pi t/(M-1))$ with $0 \leq t \leq M-1$
- **No window:** corresponds also to Rectangular window but with no proper cropping.

Figure 6.7 compares the different window functions and the reference case, which corresponds to the cropping rectangular WF mentioned before. The synthetic curves used in this test correspond to the inclination angles $i = 30°$, $i = 50°$, and $i = 70°$, and spot latitudes ranging from 0 to $\pm 85°$. The colour points indicate the average differences between peak-height ratios derived from each window function for a given inclination, while the black stars mark the final average difference. From this comparison, we can conclude that the WF with the best performance is the Hamming function. Therefore, we use the Hamming WF in the subsequent analysis.

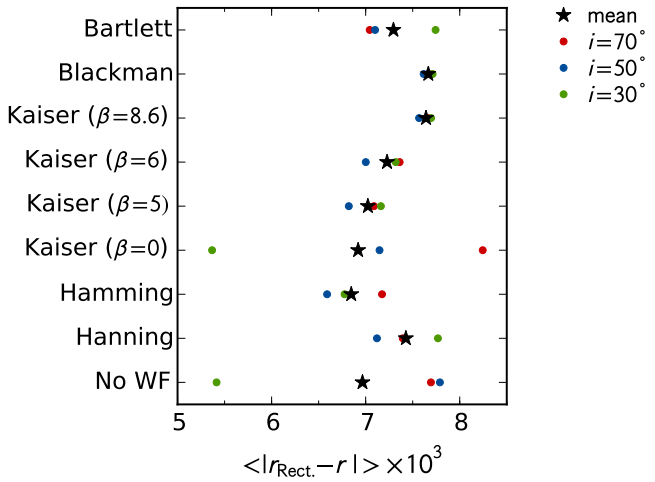

Fig. 6.7 – Average difference between the peak-height ratios derived from each window function and the reference case, corresponding to a rectangular window. The colour dots show the average differences over all spot latitudes for different inclinations. The black stars mark the average differences over all latitudes and inclinations.

6.3 Sign of the surface differential rotation: two-spot simulations

In this section, we analyse synthetic light curves obtained considering two spots on the stellar surface, in a broad range of latitudes, and we explore possible sources for contamination of the peak-height ratios.

For the first set of synthetic light curves, the rotation rate is defined by equation (6.12) with parameters $\Omega_{\mathrm{eq},\odot}$ and $\alpha_{\odot}$, and the spot radius is fixed at 5.7°. The length of the synthetic light curves is four years, consistent with the typical length of the *Kepler* light curves. The two spots have the same longitude at the beginning of the simulation.

The analysis performed in Sect. 6.2 will only be valid in cases for which at least two rotation periods are clearly detected in the Lomb-Scargle periodogram. As peaks in the LSP can interfere with each other, we impose a detectability limit for the period separation. Because of the non-infinite light curve, we fit a sinc function in frequency (being symmetric in frequency, not in period) to the main peak, P_1, and define the detectability limit to be equal to 1.5 times the width of the sinc function at half maximum. Figure 6.8 shows the LSP for three different cases: i) a case where there are two spots at different latitudes, but only one rotation period can be recovered (top panel), ii) a case where two rotation periods might be recovered but they do not fulfil the chosen criteria on the minimum distance between the two peaks (middle panel), and iii) a case where two rotation periods are clearly detected being separated by more than the imposed limit (bottom panel). Also, we discard peaks that may be significantly affected by the side lobes related to the first period.

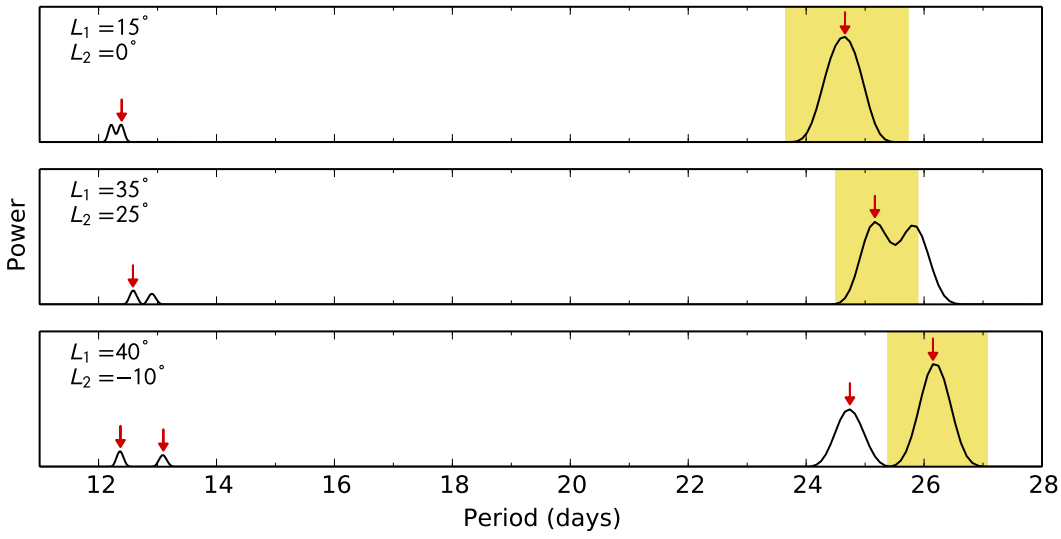

Fig. 6.8 – Lomb-Scargle periogram for three synthetic light curves from two-spot simulations. The spot latitudes, L_1 and L_2, are indicated in the top left corner of each panel. Top panel: Only one rotation period is detected. Middle panel: Two peaks associated with the surface rotation are seen but the second is not within the detectable period range. Bottom panel: The rotation periods associated with each spot latitude are successfully detected. The red arrows mark the first and second harmonics if detected. The yellow regions mark the detectability limit we impose.

6.3.1 Spots' latitude effect

The first source for false-positives/negatives for the sign of differential rotation was already identified from the one-spot simulations. The method proposed by Reinhold & Arlt (2015) is only fully valid for light curves whose spot modulation is induced by spots on the northern hemisphere. The method will also return the correct sign when the two spots are on opposite hemispheres, but only if the spot on the southern hemisphere is at a lower absolute latitude than the spot on the northern hemisphere. This is shown in Fig. 6.9, confirming that if the two surface rotation periods are successfully detected and distinguishable, the conclusions for one-spot simulations will be valid for two-spot simulations. Here, the sign of the surface differential rotation is determined by $\alpha_{\rm obs}$ (equation 6.2).

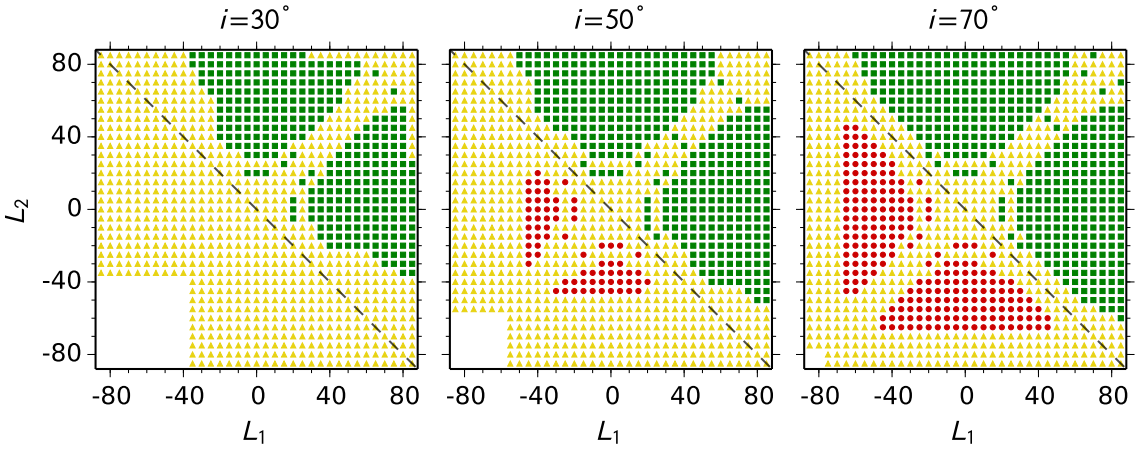

Fig. 6.9 – Sign of the surface differential rotation, $\alpha_{\rm obs}$, for two-spot simulations with stellar inclination angles of $i = 30°$ (left), $i = 50°$ (middle), and $i = 70°$ (right). The spot latitudes (L_1 and L_2) range from $-85°$ to $85°$ with steps of $5°$. The yellow triangles represent the cases where only one rotation period is detected according to the criteria we impose. The red dots represent the cases where the wrong sign of differential rotation ($\alpha_{\rm obs} < 0$) is found, while the green squares mark the cases where the correct sign ($\alpha_{\rm obs} > 0$) is recovered. The dashed line divides the regions where the correct (above) or wrong (below) sign of $\alpha_{\rm obs}$ is expected from the results of Sect. 6.2.

Figure 6.10 shows the errors on the recovered peak-height ratios and inferred latitudes as a function of L_2 for two particular cases with $i = 70°$. The left and right panels correspond to $L_1 = 40°$ and $L_1 = -10°$, respectively. The errors on the ratios are determined in relation to the reference values shown in Fig. 6.5. Taking the reference latitude-ratio relation and the peak-height ratios recovered from the two-spot simulations, the observed spot latitudes L can be inferred and then compared with the input latitudes. The yellow areas mark the latitude intervals where only one rotation period is successfully detected. For the cases shown, the error on the spot latitude is at most $\sim 15°$. If the stellar inclination angle is known and the spot modulation of the light curve is dominated by few spots that induce a stable signal (as the case of 2-spot simulations), this indicates that the observed peak-height ratios, together with the results from one-spot simulations (i.e. the latitude-ratio relation for the corresponding i), can be used to estimate the latitudinal distribution of spots.

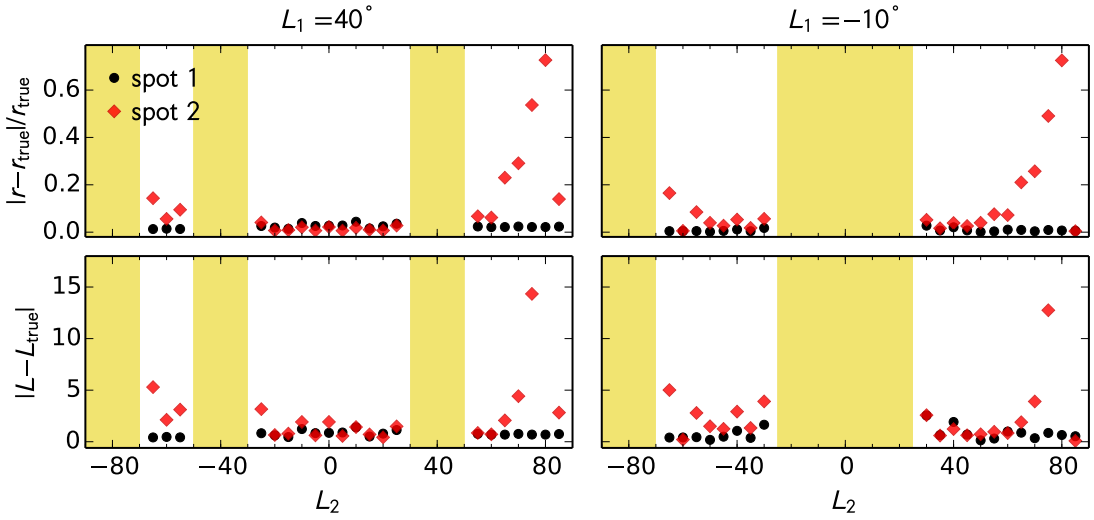

Fig. 6.10 – Error on the peak-height ratios (top) and latitudes (bottom) as a function of the latitude of the second spot. Black and red symbols concern spots 1 and 2, respectively. The left panels correspond to $L_1 = 40°$, while the right panels show the results for $L_1 = -10°$. The yellow areas mark the latitude intervals where only one rotation period was detected. Here we disregarded the cases in which the peak-height ratios were outside the one-spot peak-height ratio range given in Fig. 6.5.

6.3.2 Spot area effect

Figure 6.11 shows the errors on the peak-height ratios and latitudes as a function of the spot area ratio, A_2/A_1. For this set of simulations, the spot latitudes ($L_1 = 40°$ and $L_2 = 20°$), stellar inclination angle ($i = 70°$), and the surface rotation ($\Omega_{eq} = \Omega_{eq,\odot}$, $\alpha = \alpha_\odot$) are fixed. The spots at $L_1 = 40°$ have a constant radius of $R_1 = 5.7°$, while the radius of the spots at $L_2 = 20°$ varies between 1.8° and 11.5°. The results show that the errors in the inferred peak-height ratios and latitudes are not significantly affected by variations in the relative area of the spots. In this case, a solar differential rotation ($\alpha_{obs} > 0$) is correctly recovered for all the synthetic light curves.

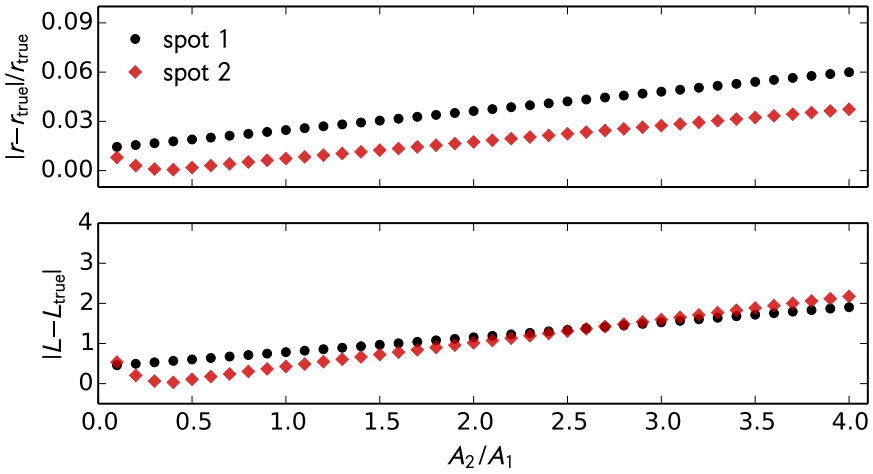

Fig. 6.11 – Error on the peak-height ratios (top) and latitudes (bottom) as a function of the ratio between the areas of spot 2 (red) and spot 1 (black). For all the cases, the correct sign of the surface differential rotation ($\alpha_{obs} > 0$) is recovered.

6.3.3 Spots phase effect

The phase of the spots also has an impact on the peak-height ratios. In particular, when spots have similar rotation rates and are in anti-phase, the LSP shows an excess of power on the second harmonic. In some cases the second harmonic can even be the main peak in the LSP, being wrongly identified as the rotation period of the star (e.g. McQuillan et al. 2013a; Reinhold & Reiners 2013). In these cases, the resulting peak-height ratios should not be used to infer the spot latitude or the sign of differential rotation.

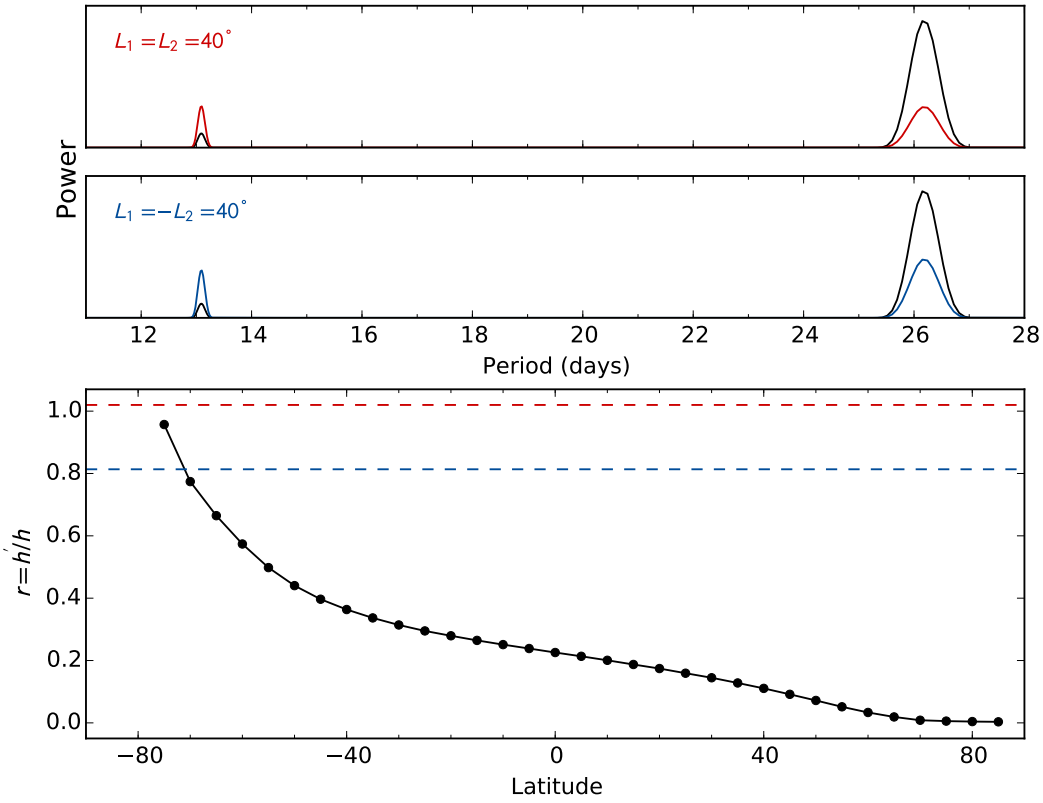

Fig. 6.12 – Top and middle panels: Lomb-Scargle periodogram of two synthetic light curves whose modulation is produced by two spots rotating with equal velocity and in anti-phase. In the first example (red) both spots are on the northern hemisphere, while in the second panel (blue) the spots are on opposite hemispheres. The black line corresponds to the reference case of one spot at $L_1 = 40°$. Bottom: Comparison between the peak-height ratios recovered from the top and middle panels (red and blue, respectively) and the reference ratios for $i = 70°$ (black).

Two examples are shown in Fig. 6.12, where we consider a stellar inclination angle of 70° and the spot latitudes $L_1 = 40°$ and $L_2 = \pm 40°$. If the spots have the same size and latitude, the modulations produced by each spot will have equal amplitude. In this case, the signature of the two spots rotating in anti-phase would be equivalent to the modulation of one spot rotating two times faster than the rotation period. This means that one would retrieve half of the rotation period. Thus, we have considered that when $L_1 = L_2$ the second spot is half the size of the first spot (i.e. $R_1 = 2 \times R_2 \sim 5.7°$), while when $L_1 = -L_2$ the two spots have the same size ($R_1 = R_2 \sim 5.7°$). For comparison, the black

line corresponds to the reference periodogram for one spot at 40°, with a radius of 5.7°. In both cases (top panel, red; middle panel, blue), the observer could be wrongly led to assume that the peak in the periodogram is being produced by a single spot, but the peak-height ratios in both cases would be very different from the case of a single spot (in black). This is also evident from the bottom panel, which compares the recovered ratios with the reference ratios from Fig. 6.5 for the inclination of 70°. If we still considered the higher period as the first harmonic, the peak-height ratio that would be inferred in the first case (red) would be outside the expected range for a single spot for the chosen inclination, while in the second case (blue) a very low latitude would be inferred if the single spot scenario were to be wrongly assumed. The longitude of the second spot (in both examples) is $\phi_2 = \phi_1 + \pi$.

Figure 6.13 shows the error on the estimated peak-height ratios and inferred latitudes as a function of the phase difference between the two spots rotating with equal velocities (for the same latitudes of Fig. 6.12, $L_1 = 40°$ and $L_2 = \pm 40°$). Clearly, for certain phase differences the inferred latitudes and peak-height ratios would be far from the true values. The results in both Figs. 6.12 and 6.13 thus confirm that caution is needed when using the analysis of light curves showing evidence of spots rotating in anti-phase.

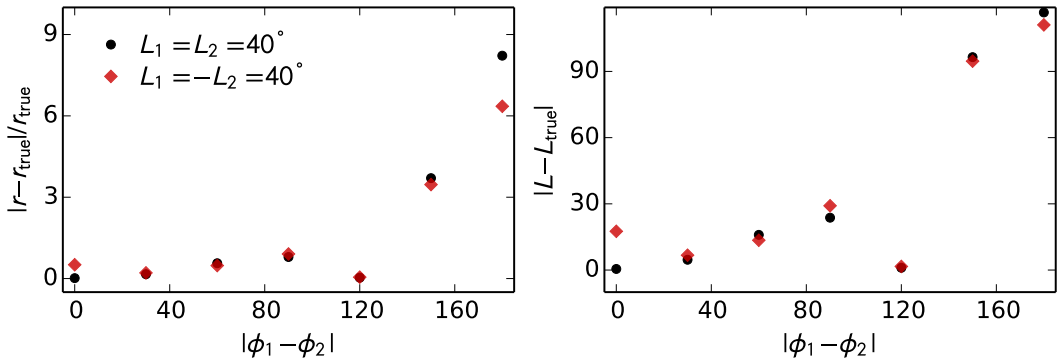

Fig. 6.13 – Error on the peak-height ratios (left) and latitudes (right) as a function of the phase difference between two spots rotating with equal velocity, both on the northern hemisphere (black) and on opposite hemispheres (red). The reference case corresponds to one spot at $L = 40°$.

6.4 Conclusions

The stellar surface rotation can be measured through the periodogram analysis of light curves of spotted stars. In particular, if the star is differentially rotating, one may use the Lomb-Scargle periodogram to learn about the amplitude and sign of the surface differential rotation (e.g. Reinhold & Reiners 2013; Reinhold et al. 2013; Reinhold & Gizon 2015; Reinhold & Arlt 2015; Nagel et al. 2016; Distefano et al. 2016).

The main goal of this work was to understand under what conditions the spot modulation on the light curve and its signature on the periodogram can provide insights into the latitudinal distribution of starspots and, consequently, into stellar surface differential rotation. In particular, we studied the dependence of the peak-height ratios in the periodogram (associated to the relative height of the harmonics of a given rotation period) on the spot and stellar parameters.

We found that the peak-height ratios depend essentially on the fraction of time the spot is visible. Spots that are visible for a longer time compared to $P_{\rm rot}$ produce smaller ratios than spots that are visible for a shorter time. In turn, the spot visibility time depends more significantly on the stellar inclination angle and spot latitude.

Our results from one-spot and two-spot simulations show that the method proposed by Reinhold & Arlt (2015) provides the wrong sign of surface differential rotation when the following conditions are met:

1. $i \neq 90^{\circ}$ and the peak-height ratios are associated with spots on the opposite hemisphere of the observer;
2. $i \neq 90^{\circ}$, one of the spots (spot 1) is on the opposite hemisphere while the second spot (spot 2) is on the same hemisphere of the observer and $|L_1| > |L_2|$;
3. the peak-height ratios are related to spots rotating with similar velocities and nearly in anti-phase.

Moreover, for low inclinations, the peak-height ratios become saturated as a result of spots being always visible for a wide range of latitudes. Also, for $i = 90^{\circ}$ the peak-height ratios are almost constant. In these cases, attributing a latitude to each rotation period and determining the sign of differential rotation will be difficult.

Despite the degeneracy between stellar inclination angle and spot latitude, we find that the peak-height ratios provide a simple and fast way to constrain these parameters. This is a clear advantage of this method in comparison with other time consuming methods (e.g. Mosser et al. 2009; Huber et al. 2010; Walkowicz et al. 2013; Lanza et al. 2014) where the inclination, spot latitude, area, and intensity contrast may be strongly degenerated. Moreover, if the inclination angle is known, the peak-height ratios can constrain the latitudinal distribution of starspots.

The spot signature on the light curves depends on a number of stellar and spot properties, such as the stellar surface rotation, limb-darkening law, spot size, and intensity contrast. We have investigated how the peak-height ratios depend on those parameters. We found that the effect of the spot size and limb-darkening on the peak-height ratios is small but not negligible.

We have also shown that when two rotation periods are successfully recovered, the conclusions taken from the one-spot simulations are also valid for two-spot simulations. Moreover, although the relative size of the spots (for two-spot simulations) affects the ratios, the effect is in general not strong enough to lead to an incorrect inference of the sign of differential rotation.

We have not considered spot evolution, which is beyond the scope of this study. However, we note that the multiple peaks in the periodogram can also result from spot evolution (e.g. Lanza et al. 2014; Aigrain et al. 2015; Reinhold & Gizon 2015; Nagel et al. 2016). For stars showing evidence of long-lived spot/active regions that induce stable signals, the LSP and the peak-height ratios will be less affected by the spot evolution. The analysis of different sub-series of the full light curve may also help in discriminating between periodic (or quasi-periodic) signals related to the stellar rotation and those resulting from other sources.

Finally, we note that there is an observational bias, which contributes to the small number of false-positives reported in Reinhold & Arlt (2015): the modulation induced by spots on the same hemisphere as the observer will be preferentially observed in comparison with spots on the opposite hemisphere, in particular for small inclination angles.

6.5 Application to observational data

Since starspots are darker than the surroundings and follow the stellar surface rotation, the light curves of spotted stars show quasi-periodic modulations. By studying those modulations, one can then learn about stellar rotation and also magnetic activity. In particular, as shown above, the peak-height ratios (equation 6.1) measured from the periodogram can be useful to determined the sign of the differential rotation. Furthermore, the peak-height ratios can also constraint the stellar inclination and latitudinal distribution of spots.

Above, we have analysed simple synthetic light curves, characterized by stable spot signals. Still, we have shown and mentioned the many limitations of the method. Due to the contamination of the peak-height ratios, one must be cautious when the stellar light curves show evidence for spots rotating in anti-phase or for short-lived spots.

The following sections show the preliminary results for two *Kepler* targets: KIC 3733735 and KIC 4918333. In here, we use KADACS (*Kepler* Asteroseismic Data Analysis and Calibration Software) light curves obtained from long-cadence data (29.42 min), being corrected following the approach described in García et al. (2011), interpolated using inpainting technique (García et al. 2014b; Pires et al. 2015), and high-pass filtered according to their rotation period (cut-off at 20 or 55 d).

Although the results shown below are only preliminary and further investigation is needed, these sections show what kind of studies we may perform in the future, in particular, for stars with known inclination angle.

6.5.1 KIC 3733735 (Shere Khan)

The F main-sequence star KIC 3733735 (Shere Khan) is a known active star (Mathur et al. 2014; García et al. 2014a; Régulo et al. 2016) with an inclination angle of $\sim 31.31°$ (Mathur et al. 2014). The spot modulation on the light curve suggests a relatively short rotation period of ~ 2.56 d (García et al. 2014a). Also, this star shows evidence for a cycle-like behaviour and long-lived spots or active regions (Mathur et al. 2014). More recently, Régulo et al. (2016) also found evidence for activity-related variations in the acoustic frequencies (obtained from the analysis of short-cadence data) consistent with the photometric activity proxy. Figure 6.14 shows the complete light curve of KIC 3733735 and two shorter segments, where one can recognize the spot modulation.

Aigrain et al. (2015) showed that for determining the average rotation period the best performance is achieved with a combination of auto-correlation and wavelet analysis, similar to the analysis performed in García et al. (2014a). Here, we first apply this method to the *Kepler* light curves and then we use the periodogram analysis to infer the sign of the differential rotation and the spot

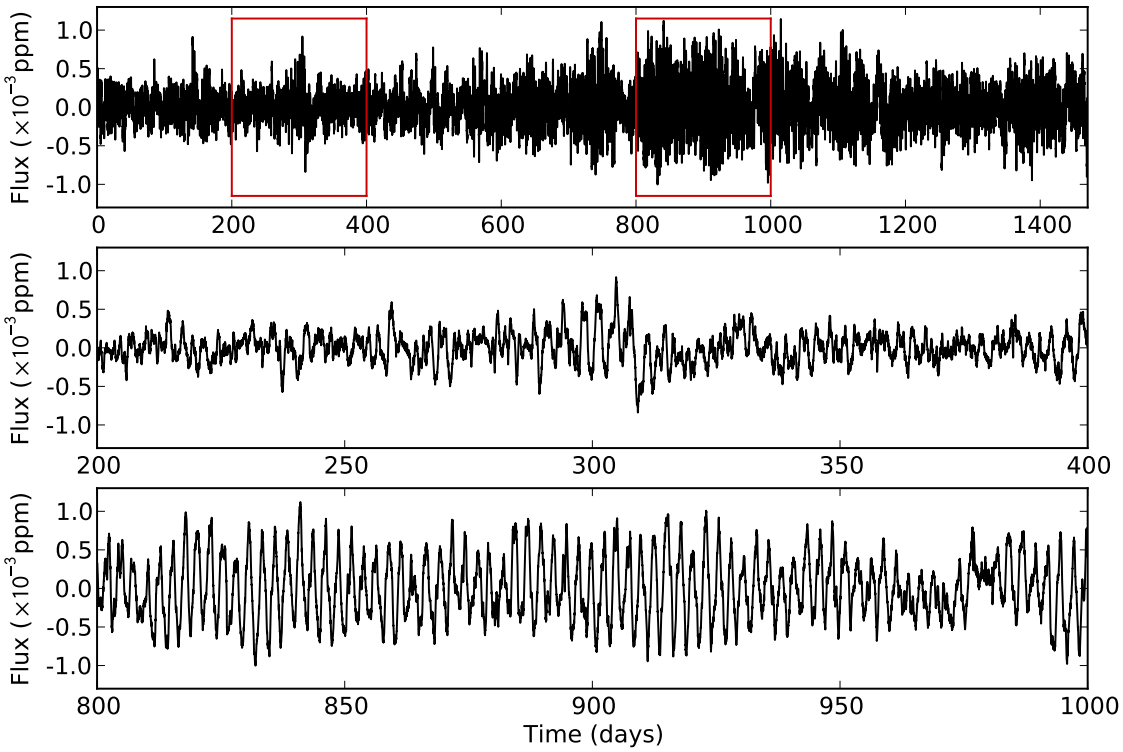

Fig. 6.14 – Complete KADACS light curve of KIC3733735 (top panel). The red rectangles indicate the segments that are zoomed in the middle and bottom panels.

latitudes. The top panels of Fig. 6.15 illustrate the results from the wavelet analysis. The left top panel corresponds to the wavelet power spectrum (WPS), where the highest and lowest power are represented in red and blue colours, respectively. The cone of influence (black-crossed area) marks the limit of four rotations imposed to increase the level of confidence in the rotation period estimate. The right top panel shows in the black the global wavelet power spectrum (GWPS), which corresponds to the WPS collapsed over the period axis. The red line is the best fit obtained with Gaussian functions. The rotation period corresponds to the highest fitted peak and the uncertainty is given by the half width at half maximum of the corresponding Gaussian function. Due to the relatively low resolution of the GWPS (lower than that of a periodogram), this uncertainty accounts for the possible differential rotation. The rotation period recovered from the GWPS is $P_{\mathrm{rot,\ GWPS}} = 2.57 \pm 0.18$ d. The middle panel shows the autocorrelation function (ACF), while the bottom panel shows the composite periodogram (CP) obtained by multiplying the AFC and the GWPS, which highlights the peaks that are common to both analysis. Similarly to the GWPS, the composite peridogram is fitted with Gaussian functions and the rotation period estimated in the same manner. The rotation periods recovered from the autocorrelation function and composite peridogram are $P_{\mathrm{rot,\ ACF}} = 2.62$ d and $P_{\mathrm{rot,\ CS}} = 2.60 \pm 0.14$ d, respectively.

Figure 6.16 shows the Lomb-Scargle periodogram obtained from the complete light curve. Besides the two main peaks related with the stellar rotation ($P_1 \simeq 2.56$ and $P_2 \simeq 2.63$ d), there is significant

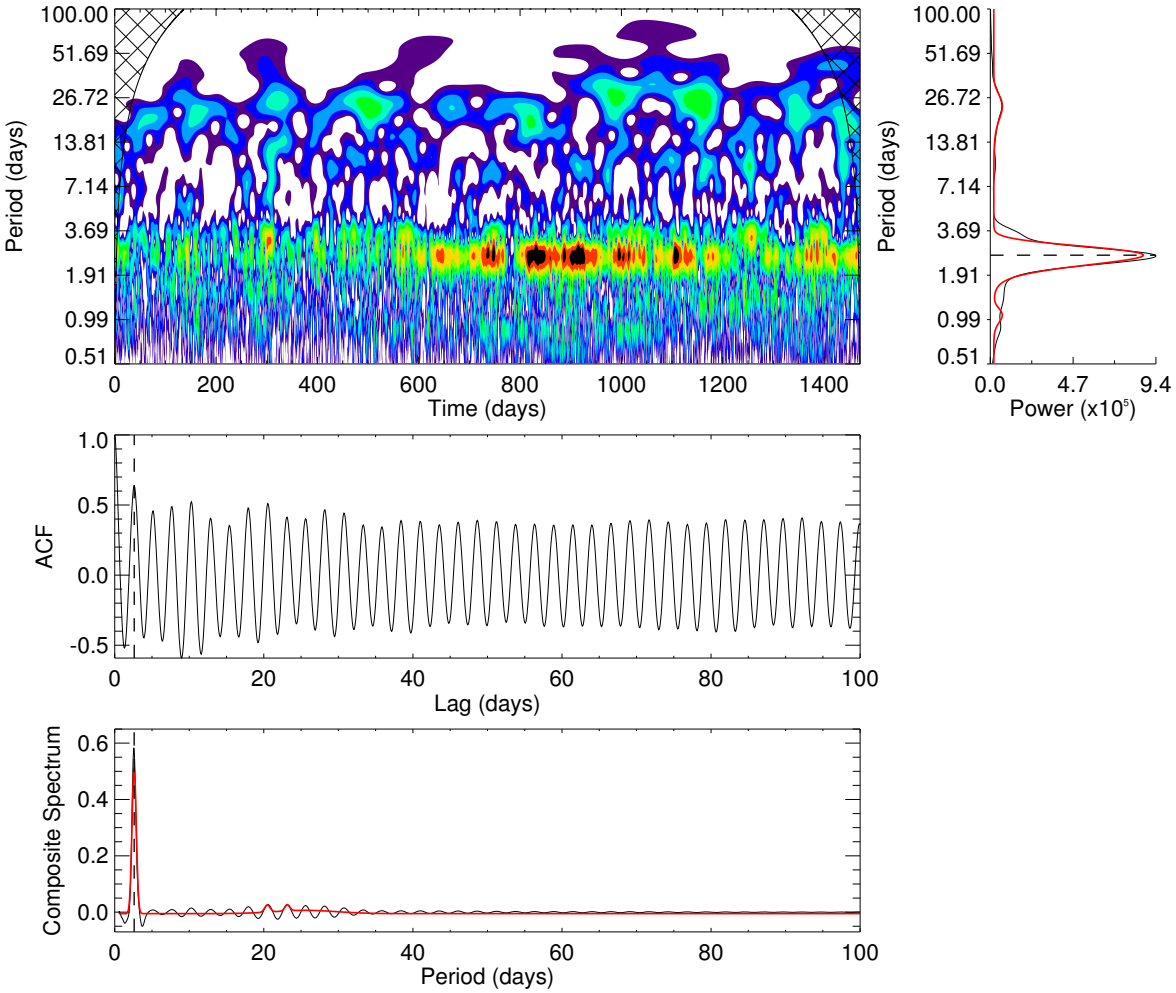

Fig. 6.15 – Top: Wavelet power spectrum (left) and global wavelet power spectrum (right) obtained from the light curve of KIC 3733735. Middle: Light curve autocorrelation function. Bottom: Composite periodogram resulting from the multiplication of GWPS and ACF. The red lines correspond to the best fits to the GWPS and CP obtained with Gaussian functions, and the dashed lines mark the retrieved rotation periods: $P_{\mathrm{rot,\ GWPS}} = 2.57 \pm 0.18$, $P_{\mathrm{rot,\ ACF}} = 2.62$, and $P_{\mathrm{rot,\ CS}} = 2.60 \pm 0.14$ d.

power around 3.5 d. These two different modulations can also be seen in the wavelet analysis (Fig. 6.15), where the first 600 days seem to be dominated by a weaker and longer periodicity than the remaining time-series (a zoom in each part is shown in Fig. 6.14). Because of that behaviour we also decided to analyse shorter segments of the light curve. Figure 6.17 shows the periods of the highest and second highest peaks in the periodogram (black and red, respectivelly), possibly related with the surface differential rotation, for the full time-series ("full lc"), the first 600 days of the light curve, the remaining time-series (excluding the first 600 days), and consecutive 200-d segments of the original time-series. The blue dashed line indicates the average rotation period recovered from the composite periodogram and the light blue area marks its uncertainty. Both distinct periodicities (~ 2.60 and ~ 3.50 d), detected in many of the segments, may suggest spot latitudinal migration as the magnetic cycle progress. Around the average rotation period, often two peaks are detected, which are within the uncertainty derived from the composite periodogram and are possibly related with different spots/active regions.

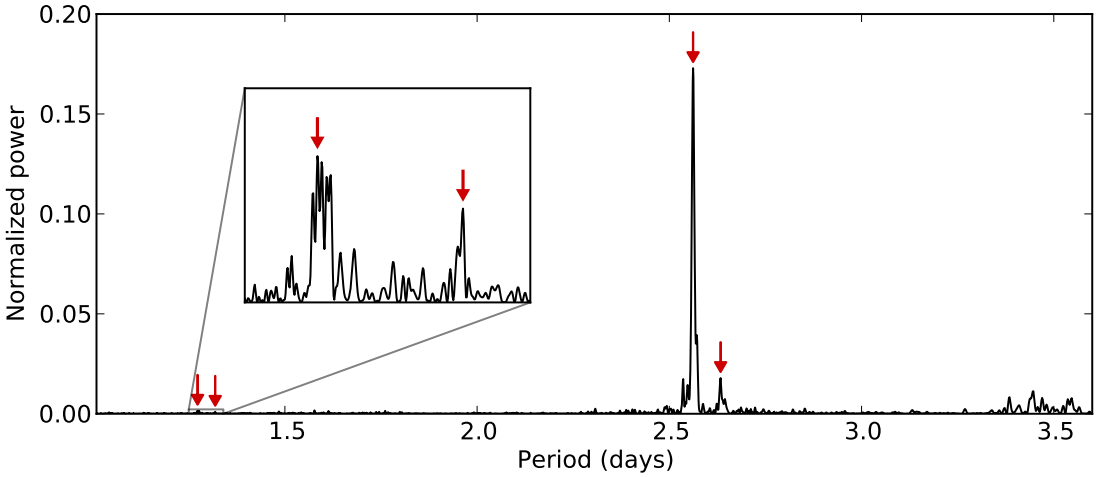

Fig. 6.16 – Lomb-Scargle periodogram of the full light-curve of KIC 3733735. The red arrows mark the first and second harmonics of the two main peaks related to the stellar surface rotation. A zoom in the period range of the second harmonics is also shown.

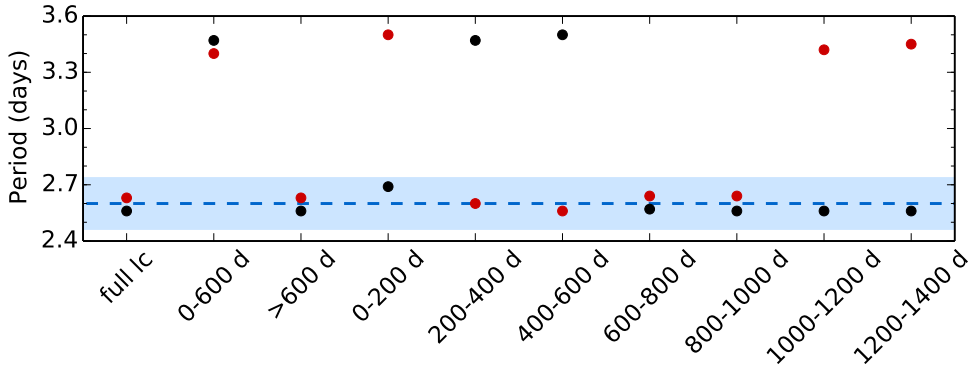

Fig. 6.17 – Rotation periods (highest and second highest peaks - black and red, respectively) detected in the periodogram of the full light curve and for different segments. The blue line and blue region mark the average rotation period and its uncertainty estimated from the composite periodogram.

The values found for the peak-height ratios (equation 6.1), corresponding to each detected rotation period, are small, which could already be expected due to the small inclination angle ($i = 31.41°$). Figure 6.18 shows the reference latitude-ratio relation for KIC 3733735 (thick solid line) and the recovered ratios (blue; for the 20 rotation periods in Fig. 6.17). For latitudes higher than $\sim 30°$ the peak-height ratios are mostly constant, which may hamper the task of attributing a corresponding latitude.

Figure 6.19 shows the peak-height ratios and the "observed" spot latitudes, obtained by interpolating the reference latitude-ratio relation, as a function of the rotation period. In general, from this figure, one may identify a trending where the ratios/latitudes increase/decrease with the period, which suggests anti-solar surface differential rotation for KIC 3733735. The light and dark blue dots

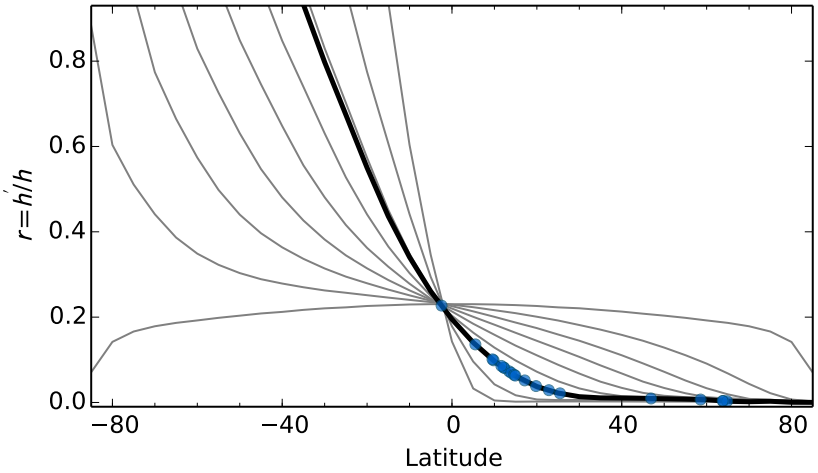

Fig. 6.18 – Comparison between the theoretical peak-height ratios for $i = 31.41°$ (thick line) and the values recovered for KIC 37333735 (blue dots). For reference, the grey thin lines show the relations for the different inclinations shown in Fig. 6.7.

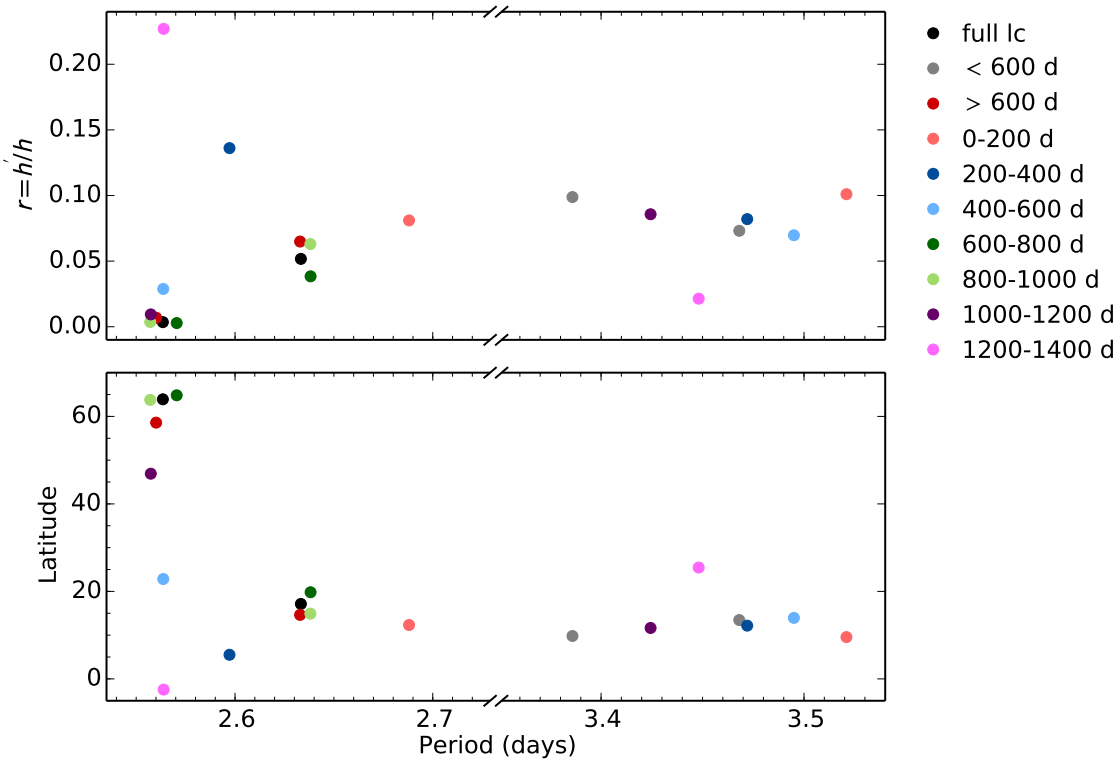

Fig. 6.19 – Peak-height ratios (top) and spot latitudes (bottom), inferred from the periodogram analysis for KIC 3733735, as a function of the rotation period.

at shorter period and both pink dots seem to be outliers on this trending. The blue dots correspond to sub-series where the dominant signal corresponds to the longest periodicity (~ 3.5 d). In the last 200-d segment (1200 - 1400 d; pink), the light curve shows evidence for spots rotating in anti-phase, which can contaminate the peak-height ratios as shown in Sect. 6.3.3. Table 6.1 summarizes the results from the periodogram analysis. We find solar differential rotation ($\alpha_{\rm obs} > 0$) only for three of the sub-series. For the remaining seven cases, we find anti-solar differential rotation ($\alpha_{\rm obs} < 0$).

Further investigation is needed, in particular, to test whether or not one can be confident on the recovered peak-height ratios and, thus, latitudes and sign for the surface differential rotation. The errors associated to the estimated peak-height ratios may affect the conclusions above.

	P_1	P_2	r_1	r_2	$\alpha_{\rm obs}$
full light cure	2.564	2.633	0.004	0.052	−
< 600 d	3.468	3.386	0.073	0.099	+
> 600 d	2.560	2.633	0.007	0.065	−
0 - 200 d	2.688	3.521	0.081	0.101	−
200 - 400 d	3.472	2.597	0.082	0.136	+
400 - 600 d	3.495	2.564	0.070	0.029	−
600 - 800 d	2.571	2.638	0.003	0.038	−
800 - 1000 d	2.557	2.638	0.004	0.063	−
1000 - 1200 d	2.557	3.424	0.009	0.086	−
1200 - 1400 d	2.564	3.448	0.227	0.021	+

Table 6.1 – Summary of the periodogram analysis for KIC 3733735. Each segment is indicated in the first column. The recovered rotation periods and the respective peak-height ratios are listed in the columns 2-5. The last column indicates the inferred sign for the differential rotation (equation 6.2).

6.5.2 KIC 4918333

The main sequence star KIC 4918333 is a known active star which shows a strong spot signature on its light curve. McQuillan et al. (2013a) estimated an average rotation period of ~ 19.85 d from the autocorrelation function of a 10-month time-series. The light curve in that particular time interval is dominated by a "double dip" modulation which is characteristic of two spots/active regions rotating with similar velocity but in anti-phase.

Figure 6.20 shows the 4-yr light curve of KIC 4918333. The spot modulation in the first 300 days is significantly distinct from the spot modulation in the remaining light curve.

Figure 6.21 shows the results from the wavelet and autocorrelation analysis. The average rotation periods estimated from the global wavelet spectrum, autocorrelation function, and composite periodogram are $P_{\rm rot,\ GWPS} = 19.7 \pm 1.4$ d, $P_{\rm rot,\ ACF} = 19.78$ d, and $P_{\rm rot,\ CP} = 19.71 \pm 0.89$ d, respectively. From the WPS of the complete time-series, it is clear that there are moments when the second harmonic of the rotation period becomes stronger.

The wavelet and the autocorrelation analysis for the first 300 days ($\sim$10-month time-series used in McQuillan et al. 2013a) are shown in Fig. 6.22. The wavelet analysis alone would suggest a rotation

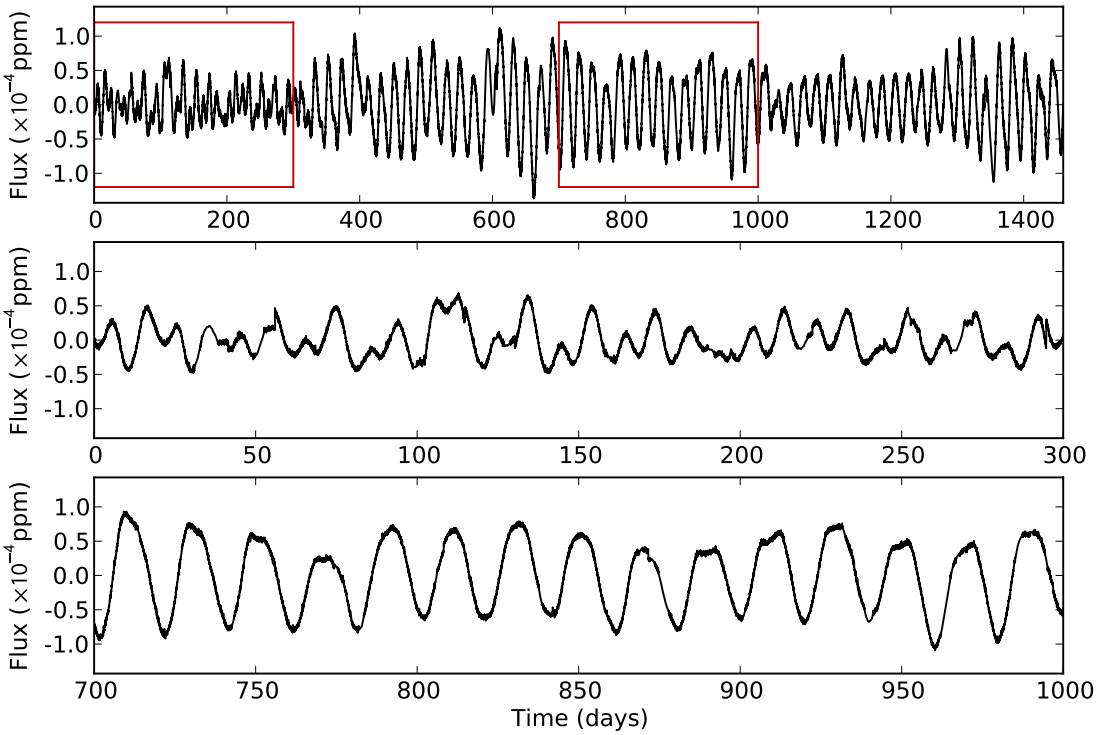

Fig. 6.20 – Complete light curve of KIC4918333 (top panel). The red rectangles indicate the segments that are zoomed in the middle and bottom panels.

period of $P_{\mathrm{rot,\ GWPS}} = 9.76 \pm 0.63$ d, half of the true period. Although still showing the signature at $P_{\mathrm{rot}}/2$, the ACF is able to recover the correct rotation period, $P_{\mathrm{rot,\ ACF}} = 19.70$ d. The composite periodogram highlights the common peaks in the WPS and ACF, recovering thus, the correct rotation period $P_{\mathrm{rot,\ CP}} = 19.60 \pm 0.69$ d.

Similarly to what we did previously, we also analyse different segments of the light curve. Figure 6.23 shows the Lomb-Scargle periodogram for three segments: the complete light curve, the first 300 days, and the remaining light curve (excluding the first 300 days). For the first 300 days, although the highest peak corresponds to $P_{\mathrm{rot}}/2$, we still consider the rotation period to be the first harmonic (as done in Sect. 6.3.3). Thus, the peak-height ratio in this case is larger than one. Figure 6.24 shows the rotation period and the peak-height ratio recovered for each segment of the light curve. Note that we only recover one rotation period per segment. Figure 6.25 compares the peak-height ratios with the reference latitude-ratio relations (Fig. 6.5), suggesting high spot latitudes (on the same hemisphere as the observer) and/or low stellar inclination angle, which is unknown for this star.

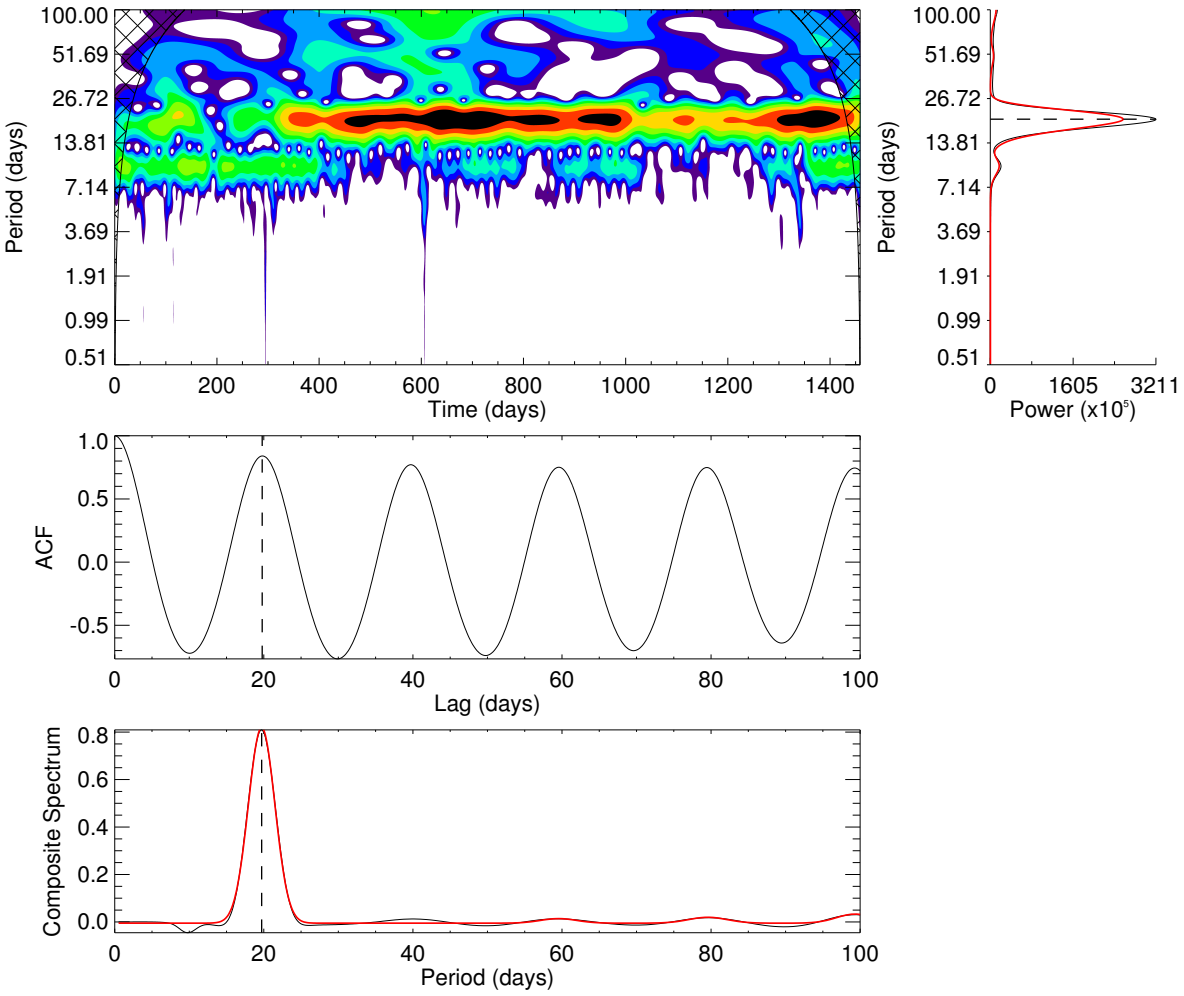

Fig. 6.21 – Top: Wavelet power spectrum (left) and global wavelet power spectrum (right) obtained from the light curve of KIC 4918333. Middle: Light curve autocorrelation function. Bottom: Composite periodogram. The red lines correspond to the best fits and the dashed lines mark the retrieved rotation periods: $P_{\mathrm{rot,\ GWPS}} = 19.7 \pm 1.4$, $P_{\mathrm{rot,\ ACF}} = 19.78$, and $P_{\mathrm{rot,\ CS}} = 19.71 \pm 0.89$ d.

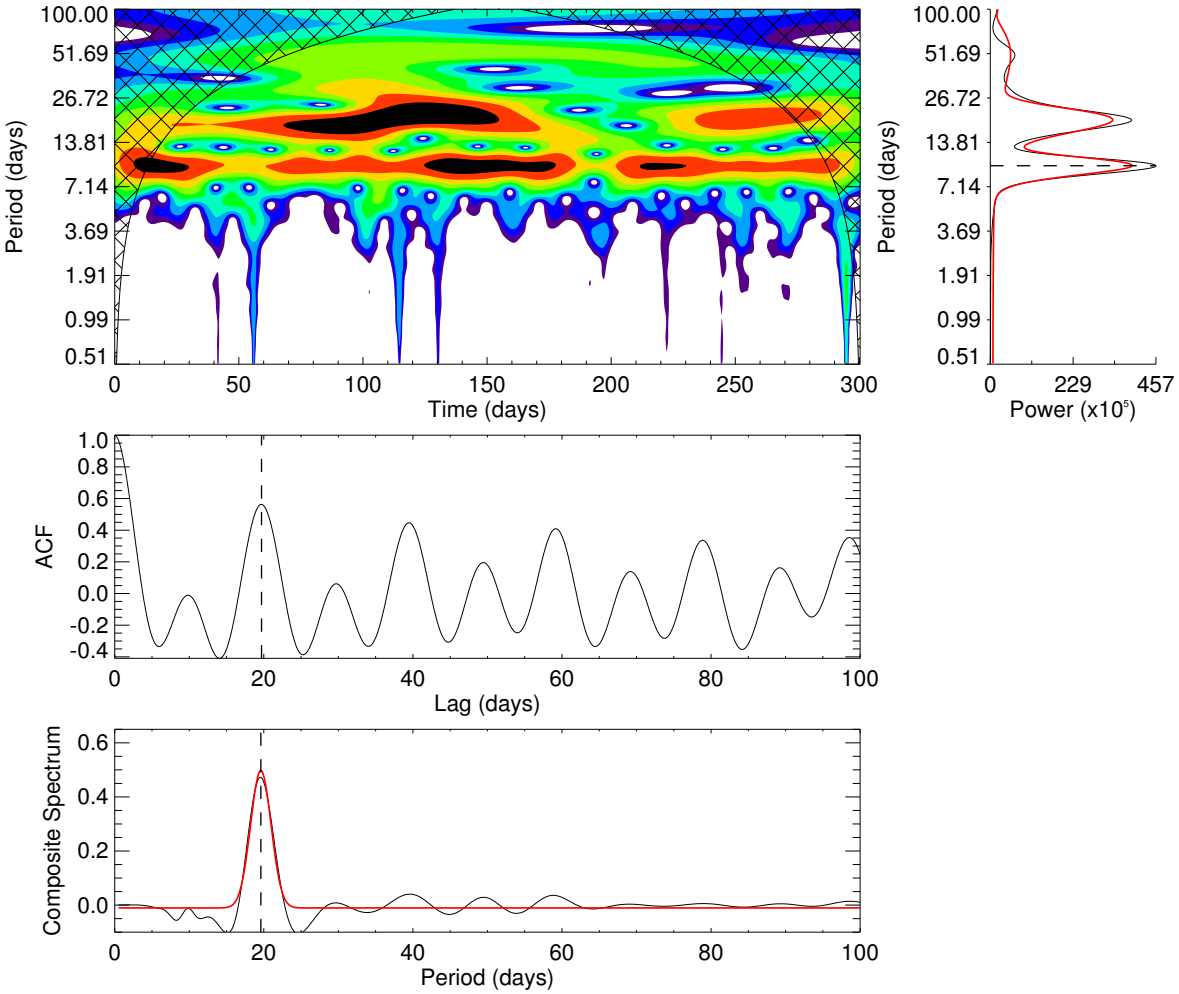

Fig. 6.22 – Top: Wavelet power spectrum (left) and global wavelet power spectrum (right) obtained from the first 300 days of data for KIC 4918333. Middle: Light curve autocorrelation function. Bottom: Composite periodogram. The red lines correspond to the best fits and the dashed lines mark the rotation periods: $P_{\mathrm{rot,\ GWPS}} = 9.76 \pm 0.63$, $P_{\mathrm{rot,\ ACF}} = 19.70$, and $P_{\mathrm{rot,\ CS}} = 19.60 \pm 0.69$ d.

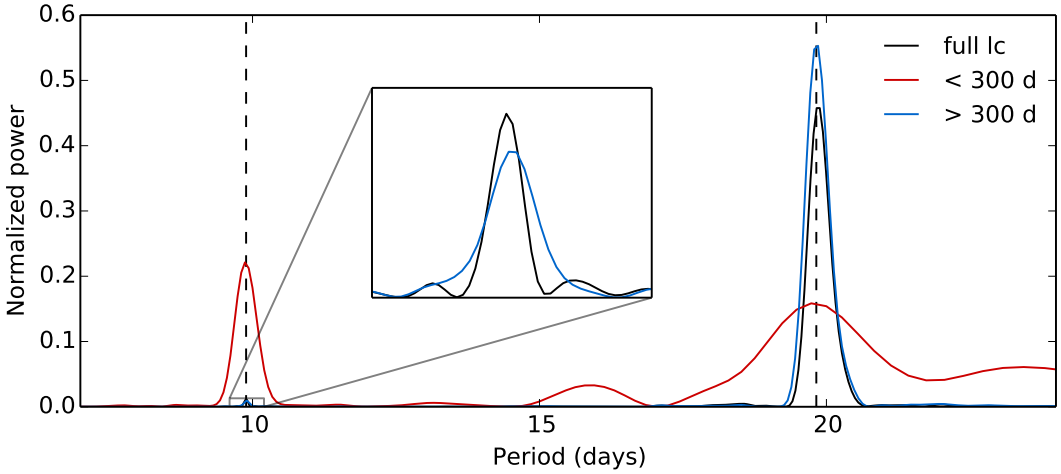

Fig. 6.23 – Lomb-Scargle periodogram of the full light-curve (black), the first 300 days (red), and the remaining time-series (excluding the first 300 days; blue) of KIC 4918333. The vertical dashed lines mark the position of the harmonics of the rotation period. A zoom in the period range of the second harmonics is also shown.

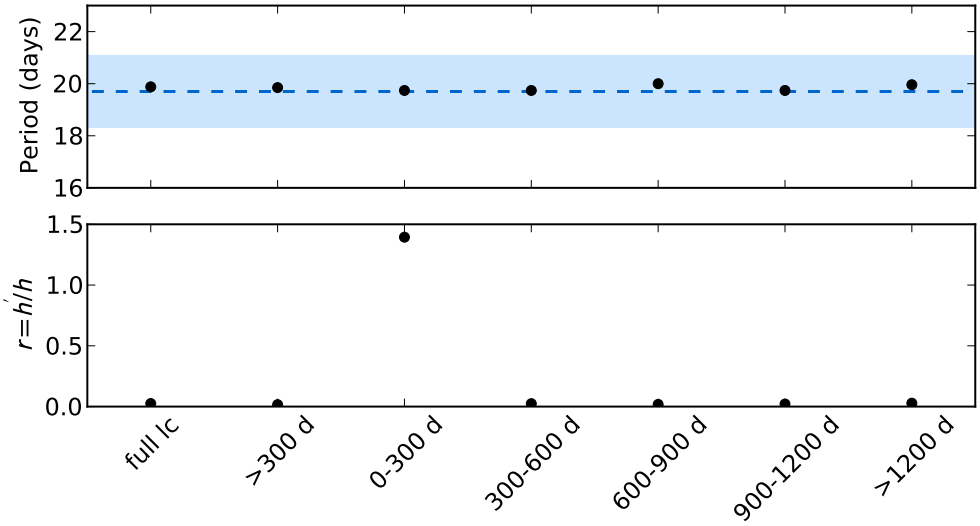

Fig. 6.24 – Rotation period and peak-height ratio detected in the periodogram of the full light curve and for different segments. The blue line and blue region mark the average rotation period and its uncertainty estimated from the composite periodogram.

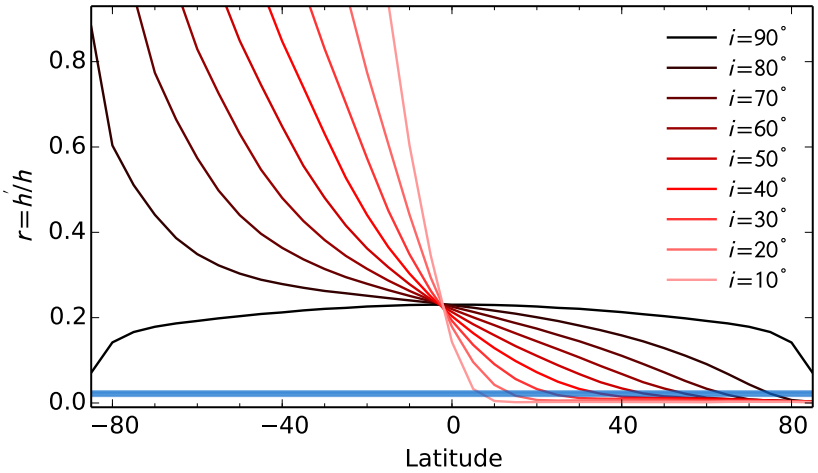

Fig. 6.25 – Comparison between the theoretical peak-height ratios (red shades) and the values recovered for KIC 4918333 (blue lines).

7. Conclusions

In the Sun, the most evident manifestation of the magnetic activity is the varying number of sunspots on the solar surface. For stars other than the Sun, the surface cannot be resolved and starspots, and other magnetic features, cannot be directly observed. However, one can still detect their effect, for example, in the stellar photometric flux and in the seismic properties.

With the above in mind and in order to investigate those magnetically-induced variations in the stellar properties, we have developed a parameterized tool able to simulate the spot properties (such as number of emerging spots, spot area, lifetime and evolution, latitudinal distribution of starspots) over a magnetic cycle. In particular, we have been using this tool to study the spots' impact on the solar oscillation frequencies.

The solar acoustic frequencies are known to be sensitive to the magnetic activity for three decades. Efforts have been made in order to understand the origin of the temporal frequency variations. Those variations are found to be better correlated with the weak component of the magnetic field (widely spread over the surface) than with the strong component (associated to active regions and, thus, confined to the so-called activity belts). However, different authors have been arguing that both components play an important role. Our results, shown here, point in the same direction. In particular, we find that the spot-induced frequency shifts (associated to the strong component of the solar magnetic field) account for $\sim 30\%$ of the total frequency shifts observed over the solar cycle 23. We also find that the short-term variations in the acoustic frequencies are closely related with the short-term variations in the visible sunspot areas. The remaining 70% result from a long-term variation that we interpret as being associated to the global solar magnetic field.

Interestingly, the epochs when the short-term variations in the sunspot areas and in the acoustic frequencies behave differently coincide with times of maxima of the quasi-biennial modulation that was previously identified in the solar seismic data. Quasi-biennial variations are also detected in other solar phenomena and activity indicators. However, we still lack knowledge on the physical mechanisms behind this mid-term modulation, as well as, on its impact on the different solar magnetic manifestations (including activity-related frequency shifts) and its relation with the most prominent 11-year cycle.

The activity-related variations in the frequencies of the acoustic modes are expected to be common in solar-type pulsators and enclose information about the activity-related changes that take place in the stellar interior. Here, we have performed a peak-bagging analysis of a large sample of solar-type stars observed by the *Kepler* satellite. The goal of this analysis was to search for temporal magnetically-induced variations in the stellar seismic properties, in particular in the frequencies of the acoustic modes. We have found evidence for periodic frequency shifts in some of the analysed stars. However, we must keep in mind that the *Kepler* time-series have a maximum length of about four years. Therefore, depending on the stellar rotation period, we will not be able to detect a full cycle for some stars. In fact, in the temporal frequency shifts of some stars we find evidence for an ascending/descending phase of a possible cycle. However, further investigation is needed in order to

effectively connect those shifts with a magnetic origin.

A quick look at the properties of the ensemble of stars already suggests that the amplitude of the observed frequency shifts depends on the stellar effective temperature and rotation period. Our results show that the frequency shifts increase with increasing temperature and decreasing rotation period.

We also may benefit from the synergy between different disciplines. One may combine the study of the stellar magnetism through Asteroseismology with spectroscopic studies and with the study of the spot modulation on the photometric light curves of active stars.

Here, we also have studied the spot signature on the light curve and in the subsequent periodogram analysis. We find that the peak-height ratios are a measure of the sinusoidality of the spot modulation, which in turn is mainly determined by the sunspot latitude and stellar inclination angle. Therefore, one may use the peak-height ratios to constrain the spot latitudes and/or stellar inclination. Knowing the spot latitudes associated to each detected rotation period, one may access to the amplitude and sign of the stellar surface differential rotation.

Helioseismology has contributed to a significant progress in our understanding of the dynamo theory and how magnetic fields are generated in the Sun. Asteroseismology of stellar cycles in stars with different physical and dynamical properties, can shed light on the relation between the stellar magnetic properties and the different stellar parameters, providing further constraints on dynamo models, leading to a better understanding on the origin of the stellar magnetism, and how magnetic fields evolve in stars, how they affect stellar evolution.

Bibliography

Abuzeid, B. & Marik, M. 1997, Sol. Phys., 173, 25
Aigrain, S., Llama, J., Ceillier, T., et al. 2015, MNRAS, 450, 3211
Aindow, A., Elsworth, Y. P., Isaak, G. R., et al. 1988, in
Anderson, E. R., Duvall, Jr., T. L., & Jefferies, S. M. 1990, ApJ, 364, 699
Appourchaux, T. 2003, Ap&SS, 284, 109
Appourchaux, T. 2005, in Payload and Mission Definition in Space Sciences, 185
Appourchaux, T., Chaplin, W. J., García, R. A., et al. 2012, A&A, 543, A54
Appourchaux, T., Gizon, L., & Rabello-Soares, M.-C. 1998, A&AS, 132, 107
Baglin, A., Michel, E., Auvergne, M., & COROT Team. 2006, in , 34.1
Baliunas, S. L., Nesme-Ribes, E., Sokoloff, D., & Soon, W. H. 1996, ApJ, 460, 848
Ballot, J., Gizon, L., Samadi, R., et al. 2011, A&A, 530, A97
Balthasar, H. & Woehl, H. 1983, Sol. Phys., 88, 71
Basu, S. 2002, in (ESA, Noordwijk: Wilson, A.), 508, 7–14
Basu, S., Broomhall, A.-M., Chaplin, W. J., & Elsworth, Y. 2012, ApJ, 758, 43
Baumann, I. & Solanki, S. K. 2005, A&A, 443, 1061
Bazilevskaya, G., Broomhall, A.-M., Elsworth, Y., & Nakariakov, V. M. 2014, Space Sci. Rev., 186, 359
Benomar, O., Appourchaux, T., & Baudin, F. 2009, A&A, 506, 15
Blanter, E. M., Le Mouël, J.-L., Perrier, F., & Shnirman, M. G. 2006, Sol. Phys., 237, 329
Bogart, R. S. 1982, Sol. Phys., 76, 155
Bogdan, T. J., Gilman, P. A., Lerche, I., & Howard, R. 1988, ApJ, 327, 451
Böhm-Vitense, E. 2007, ApJ, 657, 486
Borucki, W. J., Koch, D., Basri, G., et al. 2010, Science, 327, 977
Brandt, P. N., Schmidt, W., & Steinegger, M. 1990, Sol. Phys., 129, 191
Braun, D. C., Duvall, Jr., T. L., & Labonte, B. J. 1987, ApJL, 319, L27
Broomhall, A.-M., Chaplin, W. J., Davies, G. R., et al. 2009, MNRAS, 396, L100
Broomhall, A.-M., Chaplin, W. J., Elsworth, Y., & Simoniello, R. 2012, MNRAS, 420, 1405
Broomhall, A.-M., Chatterjee, P., Howe, R., Norton, A. A., & Thompson, M. J. 2014, Space Sci. Rev., 186, 191
Broomhall, A.-M. & Nakariakov, V. M. 2015, Sol. Phys., 290, 3095, broomhall2015
Bumba, V. & Howard, R. 1965, ApJ, 141, 1502
Cally, P. S., Crouch, A. D., & Braun, D. C. 2003, MNRAS, 346, 381
Campante, T. L. 2012, Ph.D. Thesis, Faculdade de Ciências da Universidade do Porto
Campante, T. L., Barclay, T., Swift, J. J., et al. 2015, ApJ, 799, 170
Campante, T. L., Handberg, R., Mathur, S., et al. 2011, A&A, 534, A6
Campante, T. L., Lund, M. N., Kuszlewicz, J. S., et al. 2016, ApJ, 819, 85
Campbell, C. G. & Papaloizou, J. C. B. 1986, MNRAS, 220, 577
Carrington, R. G. 1863, MNRAS, 23, 203
Ceillier, T., van Saders, J., García, R. A., et al. 2016, MNRAS, 456, 119
Chang, H.-Y. 2012, NewA, 17, 247
Chaplin, W. J., Appourchaux, T., Elsworth, Y., et al. 2004a, A&A, 424, 713
Chaplin, W. J., Appourchaux, T., Elsworth, Y., Isaak, G. R., & New, R. 2001, MNRAS, 324, 910

Chaplin, W. J., Elsworth, Y., Houdek, G., & New, R. 2007a, MNRAS, 377, 17
Chaplin, W. J., Elsworth, Y., Howe, R., et al. 1996, Sol. Phys., 168, 1
Chaplin, W. J., Elsworth, Y., Isaak, G. R., et al. 1998, MNRAS, 300, 1077
Chaplin, W. J., Elsworth, Y., Isaak, G. R., Miller, B. A., & New, R. 2000, MNRAS, 313, 32
Chaplin, W. J., Elsworth, Y., Isaak, G. R., Miller, B. A., & New, R. 2004b, MNRAS, 352, 1102
Chaplin, W. J., Elsworth, Y., Miller, B. A., Verner, G. A., & New, R. 2007b, ApJ, 659, 1749
Christensen-Dalsgaard, J. 1988, in (IAU Symposium: Christensen-Dalsgaard, J. and Frandsen, S.), 123, 295
Christensen-Dalsgaard, J. 2003, Lecture Notes on Stellar Oscillations, 5th edn. (Institut for Fysik og Astronomi, Aarhus Universitet, Teoretisk Astrofysik Center, Danmarks Grundforskningsfond)
Christensen-Dalsgaard, J. & Berthomieu, G. 1991, in Solar Interior and Atmosphere (University of Arizona Press, Tucson, AZ: Cox, A. N., Livingston, W. C., Mathews M.,), 401–478
Claret, A. 2000, A&A, 363, 1081
Covington, A. E. 1969, J. R. Astron. Soc. Canada, 63, 125
Cunha, M. S. 1999, PhD thesis, Cambrigde University, UK
Cunha, M. S., Aerts, C., Christensen-Dalsgaard, J., et al. 2007, A&AR, 14, 217
Cunha, M. S., Brüggen, M., & Gough, D. O. 1998, in (ESA, Noordwijk: Korzennik, S. G., Wilson, A.), 418, 905
Cunha, M. S. & Gough, D. 2000, MNRAS, 319, 1020
Czesla, S., Huber, K. F., Wolter, U., Schröter, S., & Schmitt, J. H. M. M. 2009, A&A, 505, 1277
Davies, G. R., Silva Aguirre, V., Bedding, T. R., et al. 2016, MNRAS, 456, 2183
Deubner, F.-L. & Gough, D. 1984, Ann. Rev. Astron. Astrophys., 22, 593
Distefano, E., Lanzafame, A. C., Lanza, A. F., Messina, S., & Spada, F. 2016, A&A, 591, A43
Du, Z. 2011, Sol. Phys., 273, 231
Dumusque, X., Santos, N. C., Udry, S., Lovis, C., & Bonfils, X. 2011, A&A, 527, A82
Duvall, Jr., T. L. & Harvey, J. W. 1986, in Proceedings of the NATO Advanced Research Workshop, Vol. 169 (Cambridge, England: Dordrecht, D. Reidel Publishing Co.), 105–116
Dziembowski, W. A. & Goode, P. R. 2005, ApJ, 625, 548
Earl, D. J. & Deem, M. W. 2005, PCCP, 7, 3910
Eker, Z. 1994, ApJ, 420, 373
Elling, W. & Schwentek, H. 1992, Sol. Phys., 137, 155
Elsworth, Y., Howe, R., Isaak, G. R., et al. 1994, ApJ, 434, 801
Elsworth, Y., Howe, R., Isaak, G. R., et al. 1995, A&AS, 113, 379
Elsworth, Y., Howe, R., Isaak, G. R., McLeod, C. P., & New, R. 1990, Nat., 345, 322
Figueira, P., Marmier, M., Bonfils, X., et al. 2010, A&A, 513, L8
Fletcher, S. T., Broomhall, A.-M., Salabert, D., et al. 2010, ApJ, 718, L19
Foreman-Mackey, D., Hogg, D. W., Lang, D., & Goodman, J. 2013, PASP, 125, 306
Fröhlich, C., Andersen, B. N., Appourchaux, T., et al. 1997, Sol. Phys., 170, 1
Fröhlich, C., Romero, J., Roth, H., et al. 1995, Sol. Phys., 162, 101
Gabriel, A. H., Grec, G., Charra, J., et al. 1995, Sol. Phys., 162, 61
Gabriel, M. 1994, A&A, 292, 281
García, R. A., Ballot, J., Mathur, S., Salabert, D., & Regulo, C. 2010a, ArXiv e-prints, 1012, arXiv:1012.0494
García, R. A., Ceillier, T., Salabert, D., et al. 2014a, A&A, 572, A34
García, R. A., Hekker, S., Stello, D., et al. 2011, MNRAS, 414, L6

García, R. A., Mathur, S., Pires, S., et al. 2014b, A&A, 568, A10
García, R. A., Mathur, S., Salabert, D., et al. 2010b, Science, 329, 1032
García, R. A., Régulo, C., Samadi, R., et al. 2009, A&A, 506, 41
Giovanelli, R. G. 1982, Sol. Phys., 80, 21
Gizon, L. & Solanki, S. K. 2003, ApJ, 589, 1009
Gleissberg, W. 1958, Z. Astrophys., 46, 219
Gnevyshev, M. N. 1938, zv. Gl. Astron. Obs. Pulkove, 16, B36
Gokhale, M. H. & Zwaan, C. 1972, Sol. Phys., 26, 52
Goldreich, P. & Keeley, D. A. 1977, ApJ, 212, 243
Goldreich, P. & Kumar, P. 1988, ApJ, 326, 462
Goodman, J. & Weare, J. 2010, Comm. App. Math. and Comp. Sci., 5, 65
Gordovskyy, M. & Jain, R. 2007, ApJ, 661, 586
Gough, D. O. 1993, Astrophysical Fluid Dynamics - Les Houches 1987, 399–560
Grec, G., Fossat, E., & Pomerantz, M. A. 1983, Sol. Phys., 82, 55
Gregory, P. C. 2005a, ApJ, 631, 1198
Gregory, P. C. 2005b, Bayesian Logical Data Analysis for the Physical Sciences: A Comparative Approach with 'Mathematica' Support, Edited by P. C. Gregory (Cambridge University Press, Cambridge, UK, 2005)
Haber, D., Jain, R., & Zweibel, E. G. 1999, ApJ, 515, 832
Handberg, R. & Campante, T. L. 2011, A&A, 527, A56
Handberg, R. & Lund, M. N. 2014, MNRAS, 445, 2698
Harvey, J. 1985, in Future Missions in Solar, Heliospheric & Space Plasma Physics, Vol. 235 (ESA, Noordwijk: Rolfe E. & Battrick B.), 199
Harvey, J. W., Hill, F., Hubbard, R. P., et al. 1996, Science, 272, 1284
Hathaway, D. H. 2010, Living Rev. Sol. Phys., 7, 1
Hathaway, D. H. 2011, Sol. Phys., 273, 221
Hathaway, D. H. & Choudhary, D. P. 2008, Sol. Phys., 250, 269
Hathaway, D. H., Wilson, R. M., & Reichmann, E. J. 1994, Sol. Phys., 151, 177
Henwood, R., Chapman, S. C., & Willis, D. M. 2009, Sol. Phys., 262, 299
Hindman, B., Haber, D., Toomre, J., & Bogart, R. 2000, Sol. Phys., 192, 363
Hoffleit, D. 1997, JAVSO, 25, 115
Houdek, G., Chaplin, W. J., Appourchaux, T., et al. 2001, MNRAS, 327, 483
Howard, R. F. 1992, Sol. Phys., 137, 51
Howe, R., Christensen-Dalsgaard, J., Hill, F., et al. 2000, Science, 287, 2456
Howe, R., Davies, G. R., Chaplin, W. J., Elsworth, Y. P., & Hale, S. J. 2015, MNRAS, 454, 4120
Howe, R., Komm, R., & Hill, F. 1999, ApJ, 524, 1084
Howe, R., Komm, R. W., & Hill, F. 2002, ApJ, 580, 1172
Huber, D., Chaplin, W. J., Christensen-Dalsgaard, J., et al. 2013, ApJ, 767, 127
Huber, D., Stello, D., Bedding, T. R., et al. 2009, Commun. Asteroseismol., 160, 74
Huber, K. F., Czesla, S., Wolter, U., & Schmitt, J. H. M. M. 2010, A&A, 514, A39
Ivanov, V. G. & Miletskii, E. V. 2011, Sol. Phys., 268, 231
Ivanov, V. G., Miletskii, E. V., & Nogovitsyn, Y. A. 2011, Astron. Rep., 55, 911
Jain, K., Tripathy, S. C., & Hill, F. 2009, ApJ, 695, 1567
Jain, R. & Haber, D. 2002, A&A, 387, 1092
Jain, R., Tripathy, S. C., Watson, F. T., et al. 2012, A&A, 545, A73

Javaraiah, J. 2012, Astrophys. Space Sci., 338, 217
Jiang, J., Cameron, R. H., Schmitt, D., & Schüssler, M. 2011, A&A, 528, A82
Jiménez, A., Roca Cortés, T., & Jiménez-Reyes, S. J. 2002, Sol. Phys., 209, 247
Jiménez-Reyes, S. J., Régulo, C., Pallé, P. L., & Roca Cortes, T. 1998, A&A, 329, 1119
Kallinger, T. & Matthews, J. M. 2010, ApJL, 711, L35
Karoff, C. 2012, MNRAS, 421, 3170
Karoff, C., Campante, T. L., Ballot, J., et al. 2013, ApJ, 767, 34
Khomenko, E. & Collados, M. 2008, ApJ, 689, 1379
Khomenko, E. & Collados, M. 2015, Living Rev. Solar Phys., 12, 6
Kiefer, R., Schad, A., Davies, G., & Roth, M. 2017, A&A, 598, A77
Kiess, C., Rezaei, R., & Schmidt, W. 2014, A&A, 565, A52
Kitchatinov, L. L. 2011, in Astronomical Society of India Conference Series, Vol. 2, 71–80
Kjeldsen, H. & Bedding, T. R. 2011, A&A, 529, L8
Kjeldsen, H., Bedding, T. R., Arentoft, T., et al. 2008, ApJ, 682, 1370
Kolmogorov, A. N. 1933, Giornale dell'Instituto Italiano degli Attuari, 4, 89
Lanza, A. F., Bonomo, A. S., Pagano, I., et al. 2011, A&A, 525, A14
Lanza, A. F., Das Chagas, M. L., & De Medeiros, J. R. 2014, A&A, 564, A50
Lanza, A. F., Rodonò, M., Pagano, I., Barge, P., & Llebaria, A. 2003, A&A, 403, 1135
Lanza, A. F., Rodono, M., & Zappala, R. A. 1993, A&A, 269, 351
Leavitt, H. S. 1908, Ann. Harvard College Observ., 60, 87
Leavitt, H. S. & Pickering, E. C. 1912, Harvard College Observ. Circular, 173, 1
Ledoux, P. 1951, ApJ, 114, 373
Lefebvre, S., García, R. A., Jiménez-Reyes, S. J., Turck-Chièze, S., & Mathur, S. 2008, A&A, 490, 1143
Leibacher, J. W. & Stein, R. F. 1971, Astrophysical Letters, 7, 191
Leighton, R. B., Noyes, R. W., & Simon, G. W. 1962, ApJ, 135, 474
Li, K. J., Gao, P. X., & Zhan, L. S. 2009, Sol. Phys., 255, 289
Li, K. J., Wang, J. X., Zhan, L. S., et al. 2003, Sol. Phys., 215, 99
Libbrecht, K. G. & Woodard, M. F. 1990, Nat., 345, 779
Lund, M. N., Lundkvist, M., Silva Aguirre, V., et al. 2014, A&A, 570, A54
Lund, M. N., Silva Aguirre, V., Davies, G. R., et al. 2017, ApJ, 835, 172
Mathur, S., García, R. A., Ballot, J., et al. 2014, A&A, 562, A124
Mathur, S., García, R. A., Catala, C., et al. 2010, A&A, 518, A53
Mathur, S., Hekker, S., Trampedach, R., et al. 2011, ApJ, 741, 119
Maunder, E. W. 1904, MNRAS, 64, 747
McIntosh, S. W., Leamon, R. J., Krista, L. D., et al. 2015, Nat. Commun., 6, 6491
McQuillan, A., Aigrain, S., & Mazeh, T. 2013a, MNRAS, 432, 1203
McQuillan, A., Mazeh, T., & Aigrain, S. 2013b, ApJ, 775, L11
McQuillan, A., Mazeh, T., & Aigrain, S. 2014, ApJS, 211, 24
Metcalfe, T. S., Dziembowski, W. A., Judge, P. G., & Snow, M. 2007, MNRAS, 379, L16
Metcalfe, T. S., Egeland, R., & van Saders, J. 2016, ApJL, 826, L2
Miletskii, E. V. & Ivanov, V. G. 2009, Astron. Rep., 53, 857
Moreno-Insertis, F. & Vázquez, M. 1988, A&A, 205, 289
Mosser, B., Baudin, F., Lanza, A. F., et al. 2009, A&A, 506, 245
Muller, R., Hanslmeier, A., & Saldaña-Muñoz, M. 2007, A&A, 475, 717

Nagel, E., Czesla, S., & Schmitt, J. H. M. M. 2016, A&A, 590, A47
Newton, H. W. & Milsom, A. S. 1955, MNRAS, 115, 398
Nielsen, M. B., Gizon, L., Schunker, H., & Karoff, C. 2013, A&A, 557, L10
Norton, A. A. & Gallagher, J. C. 2010, Sol. Phys., 261, 193
Oláh, K., Kolláth, Z., Granzer, T., et al. 2009, A&A, 501, 703
Oshagh, M., Santos, N. C., Boisse, I., et al. 2013, A&A, 556, A19
Oshagh, M., Santos, N. C., Ehrenreich, D., et al. 2014, A&A, 568, A99
Pallé, P. L., Jiménez, A., Perez Hernandez, F., et al. 1995, ApJ, 441, 952
Petrovay, K. & van Driel-Gesztelyi, L. 1997, Sol. Phys., 166, 249
Pires, S., Mathur, S., García, R. A., et al. 2015, A&A, 574, A18
Pont, F., Knutson, H., Gilliland, R. L., Moutou, C., & Charbonneau, D. 2008, MNRAS, 385, 109
Rabello-Soares, M. C. & Appourchaux, T. 1999, A&A, 345, 1027
Rabello-Soares, M. C., Bogart, R. S., & Scherrer, P. H. 2016, ApJ, 827, 140
Régulo, C., García, R. A., & Ballot, J. 2016, A&A, 589, A103
Régulo, C., Roca Cortés, T., & Vázquez Ramió, H. 2002, in (ESA, Noordwijk: Wilson, A.), 506, 889–892
Régulo, C., Vázquez Ramió, H., & Roca Cortés, T. 2005, A&A, 443, 1013
Reinhold, T. & Arlt, R. 2015, A&A, 576, A15
Reinhold, T. & Gizon, L. 2015, A&A, 583, A65
Reinhold, T. & Reiners, A. 2013, A&A, 557, A11
Reinhold, T., Reiners, A., & Basri, G. 2013, A&A, 560, A4
Roxburgh, I. W. & Vorontsov, S. V. 2003, A&A, 411, 215
Sabarinath, A. & Anilkumar, A. K. 2008, Sol. Phys., 250, 183
Salabert, D., García, R. A., Pallé, P. L., & Jiménez, A. 2011a, J. Phys. Conf. Ser., 271, 012030
Salabert, D., García, R. A., Pallé, P. L., & Jiménez-Reyes, S. J. 2009, A&A, 504, L1
Salabert, D., García, R. A., & Turck-Chièze, S. 2015, A&A, 578, A137
Salabert, D. & Jiménez-Reyes, S. J. 2006, ApJ, 650, 451
Salabert, D., Régulo, C., Ballot, J., García, R. A., & Mathur, S. 2011b, A&A, 530, A127
Salabert, D., Régulo, C., García, R. A., et al. 2016, A&A, 589, A118
Santos, A. R. G., Cunha, M. S., Avelino, P. P., & Campante, T. L. 2015, A&A, 580, A62
Santos, A. R. G., Cunha, M. S., Avelino, P. P., Chaplin, W. J., & Campante, T. L. 2016, MNRAS, 461, 224
Santos, A. R. G., Cunha, M. S., Avelino, P. P., Chaplin, W. J., & Campante, T. L. 2017a, MNRAS, 464, 4408
Santos, A. R. G., Cunha, M. S., Avelino, P. P., García, R. A., & Mathur, S. 2017b, A&A, 599, A1
Santos, A. R. G., Cunha, M. S., & Lima, J. J. G. 2012, Astron. Nachr., 333, 1032
Schou, J., Antia, H. M., Basu, S., et al. 1998, ApJ, 505, 390
Setwart, J. Q. & Panofsky, A. A. 1938, ApJ, 88, 385
Shapley, H. 1914, ApJ, 40, 448
Silva Aguirre, V., Davies, G. R., Basu, S., et al. 2015, MNRAS, 452, 2127
Silva Aguirre, V., Lund, M. N., Antia, H. M., et al. 2017, ApJ, 835, 173
Simoniello, R., Finsterle, W., Salabert, D., et al. 2012, A&A, 539, A135
Simoniello, R., Jain, K., Tripathy, S. C., et al. 2013, ApJ, 765, 100
Sing, D. K. 2010, A&A, 510, A21
Smirnov, N. V. 1939, Bulletin Moscow University, 2, 3

Snodgrass, H. B. 1983a, ApJ, 270, 288
Snodgrass, H. B. 1983b, ApJ, 270, 288
Snodgrass, H. B. & Ulrich, R. K. 1990a, ApJ, 351, 309
Snodgrass, H. B. & Ulrich, R. K. 1990b, ApJ, 351, 309
Sofia, S., Schatten, K., & Oster, L. 1982, Sol. Phys., 80, 87
Solanki, S. K. 2003, A&ARv, 11, 153
Solanki, S. K., Krivova, N. A., Schüssler, M., & Fligge, M. 2002, A&A, 396, 1029
Solanki, S. K., Wenzler, T., & Schmitt, D. 2008, A&A, 483, 623
Stahn, T. 2010, Ph.D. Thesis, Mathematisch-Naturwissenschaftlichen Fakultäten der Georg-August-Universität zu Göttingen
Tapping, K. F. 1987, J. Geophys. Res., 92, 829
Tapping, K. F. & Detracey, B. 1990, Sol. Phys., 127, 321
Tassoul, M. 1980, ApJS, 43, 469
Temmer, M., Rybák, J., Bendík, P., et al. 2006, A&A, 447, 735
Temmer, M., Veronig, A., & Hanslmeier, A. 2002, A&A, 390, 707
Tripathy, S. C., Hill, F., Jain, K., & Leibacher, J. W. 2007, Sol. Phys., 243, 105
Tripathy, S. C., Jain, K., Salabert, D., et al. 2011, J. Phys. Conf. Ser., 271, 012055
Tripathy, S. C., Kumar, B., Jain, K., & Bhatnagar, A. 2000, J. Astrophys. Atr., 21, 357
Ulrich, R. K. 1970, ApJ, 162, 993
Vandakurov, Y. V. 1967, Astron. Zh., 44, 786
Vaquero, M. J., Gordillo, A., Gallego, M. C., Sánchez-Bajo, F., & García, J. A. 2005, Observatory, 125, 152
Volobuev, D. M. 2009, Sol. Phys., 258, 319
Waldmeier, M. 1955, Ergebnisse und Probleme der Sonnenforschung (Leipzig: Geest & Portig)
Waldmeier, M. 1971, Sol. Phys., 20, 332
Walkowicz, L. M., Basri, G., & Valenti, J. A. 2013, ApJS, 205, 17
Woodard, M. F. & Noyes, R. W. 1985, Nat., 318, 449
Wright, N. J., Drake, J. J., Mamajek, E. E., & Henry, G. W. 2011, ApJ, 743, 48
Zappalà, R. A. & Zuccarello, F. 1991, A&A, 242, 480
Zhao, H. & Chou, D.-Y. 2016, ApJ, 822, 23
Zuccarello, F. 1993, A&A, 272, 587

A. Peak-bagging of solar-type stars

The following sections summarize the results from the peak-bagging analysis of the 87 solar-type stars in our target sample (Table 5.1).

In order to search for temporal variations in the acoustic frequencies we segment the original time-series in sub-series of 90 days. For each sub-series we obtain the power density spectrum and determine the corresponding background model (top panels in the following figures). Then, taking into consideration the acoustic background we perform a global fit of the p-modes with our peak-bagging tool (bottom left panels). Having the mode frequencies for each sub-series, we compute the temporal frequency shifts in relation to an average value (black circles in the top right panels), and we compare them with those obtained from a correlation method (displaced by their average value; see Sect. 5.6; courtesy of René Kiefer; blue diamonds in the top right panels) and with the granulation timescale (bottom right panels), that we obtain from the fit to the background.

For further details please consult Chapter 5.

KIC 1435467

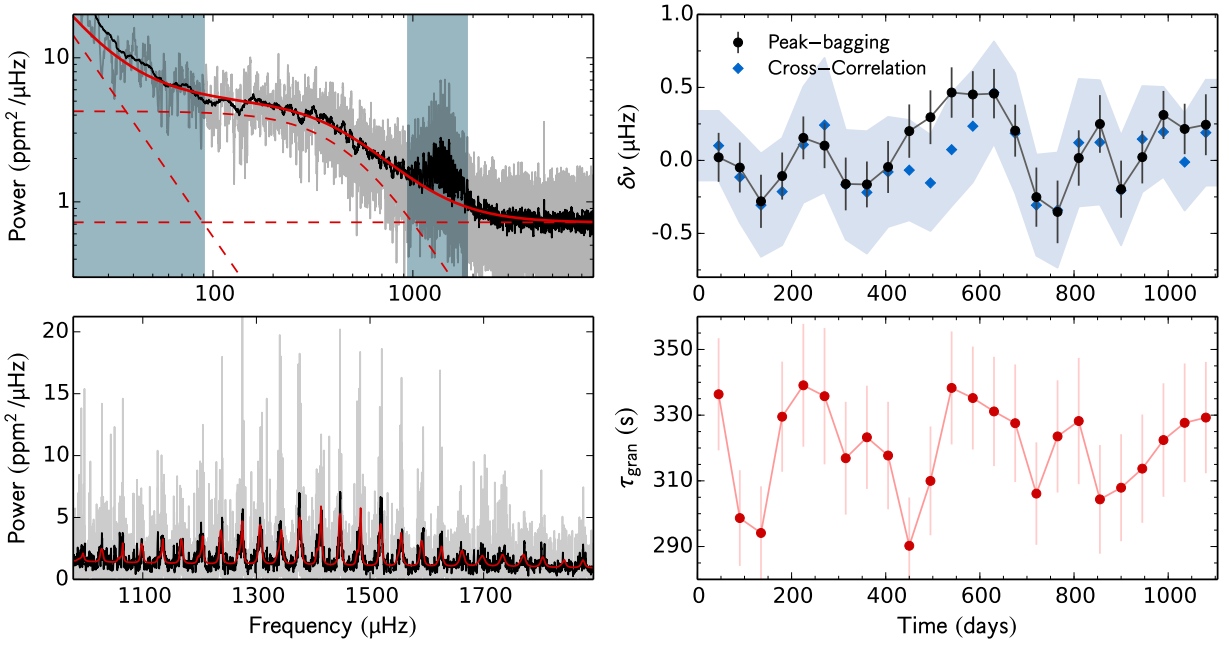

Fig. A.1 – Left: Power density spectrum (grey and black) of one 90-d sub-series of KIC1435467 and the corresponding fits (red lines) to the background (top) and to the p-modes (bottom). Right: Temporal variations in the acoustic frequencies (top) and in the granulation timescale (bottom).

time (days)	d_c %	τ_{gran} (s)	Peak-bagging $\delta\nu_{l=0}$ (μHz)	$\delta\nu_{l=1}$ (μHz)	$\delta\nu_{l=2}$ (μHz)	$\delta\nu$ (μHz)	Cross-correlation $\delta\nu$ (μHz)
45	0.98	336.4 ± 17.1	0.38 ± 0.24	-0.30 ± 0.23	-0.06 ± 0.46	0.02 ± 0.02	0.10 ± 0.24
90	0.97	298.7 ± 14.6	0.35 ± 0.25	-0.42 ± 0.24	-0.34 ± 0.44	-0.05 ± -0.05	-0.11 ± 0.31
135	0.96	294.1 ± 14.2	-0.28 ± 0.27	-0.28 ± 0.25	0.26 ± 0.44	-0.28 ± -0.28	-0.31 ± 0.35
180	0.97	329.5 ± 16.8	-0.42 ± 0.25	0.12 ± 0.21	-0.50 ± 0.34	-0.11 ± -0.11	-0.21 ± 0.37
225	0.96	339.1 ± 18.7	-0.06 ± 0.22	0.34 ± 0.20	-0.93 ± 0.38	0.15 ± 0.15	0.11 ± 0.40
270	0.81	335.8 ± 20.7	0.01 ± 0.24	0.17 ± 0.20	-0.53 ± 0.51	0.10 ± 0.10	0.24 ± 0.46
315	0.78	316.9 ± 17.2	-0.34 ± 0.29	-0.04 ± 0.23	0.54 ± 0.57	-0.16 ± -0.16	-0.17 ± 0.38
360	0.89	323.3 ± 15.7	-0.32 ± 0.24	-0.05 ± 0.21	-1.47 ± 0.48	-0.16 ± -0.16	-0.22 ± 0.42
405	0.93	317.7 ± 16.4	-0.05 ± 0.27	-0.04 ± 0.23	0.02 ± 0.47	-0.05 ± -0.05	-0.08 ± 0.38
450	0.97	290.2 ± 14.7	0.28 ± 0.29	0.15 ± 0.24	0.06 ± 0.37	0.20 ± 0.20	-0.07 ± 0.34
495	0.97	310.0 ± 16.6	0.47 ± 0.28	0.17 ± 0.24	-0.28 ± 0.39	0.30 ± 0.30	-0.15 ± 0.33
540	0.98	338.3 ± 17.2	0.66 ± 0.26	0.31 ± 0.23	-0.44 ± 0.41	0.46 ± 0.46	0.07 ± 0.39
585	0.94	335.2 ± 15.7	0.70 ± 0.24	0.25 ± 0.21	0.01 ± 0.41	0.45 ± 0.45	0.23 ± 0.38
630	0.92	331.1 ± 16.6	0.43 ± 0.28	0.47 ± 0.21	-0.45 ± 0.41	0.46 ± 0.46	0.46 ± 0.35
675	0.90	327.5 ± 17.9	-0.25 ± 0.29	0.47 ± 0.23	-1.17 ± 0.44	0.20 ± 0.20	0.19 ± 0.41
720	0.90	306.1 ± 15.6	-0.76 ± 0.30	0.18 ± 0.27	-0.65 ± 0.48	-0.25 ± -0.25	-0.31 ± 0.35
765	0.95	323.5 ± 17.1	-1.17 ± 0.35	0.14 ± 0.27	1.47 ± 0.57	-0.35 ± -0.35	-0.34 ± 0.39
810	0.90	328.2 ± 19.2	0.09 ± 0.31	-0.03 ± 0.24	1.59 ± 0.48	0.02 ± 0.02	0.12 ± 0.44
855	0.89	304.4 ± 16.5	0.82 ± 0.31	-0.13 ± 0.25	1.20 ± 0.52	0.25 ± 0.25	0.12 ± 0.43
900	0.95	307.9 ± 16.3	-0.13 ± 0.32	-0.24 ± 0.25	0.36 ± 0.52	-0.20 ± -0.20	-0.21 ± 0.38
945	0.90	313.7 ± 16.5	0.02 ± 0.28	0.03 ± 0.23	0.25 ± 0.43	0.02 ± 0.02	0.15 ± 0.36
990	0.89	322.4 ± 17.3	0.61 ± 0.23	0.02 ± 0.23	-0.49 ± 0.36	0.31 ± 0.31	0.20 ± 0.31
1035	0.85	327.7 ± 18.1	0.51 ± 0.25	-0.04 ± 0.24	-0.15 ± 0.41	0.22 ± 0.22	-0.01 ± 0.33
1080	0.85	329.3 ± 17.0	0.45 ± 0.34	0.12 ± 0.27	0.25 ± 0.61	0.24 ± 0.24	0.19 ± 0.36

Table A.1 – Results for the solar-type star KIC 1435467. First column: corresponding time of the sub-series in relation to the starting time of the observations. Second column: duty-cycle for each sub-series. Third column: characteristic timescale of the granulation component. Fourth-Seventh Columns: average frequency shifts obtained through the Bayesian peak-bagging tool for the radial ($\delta\nu_{l=0}$), dipolar($\delta\nu_{l=1}$), and quadrupolar ($\delta\nu_{l=2}$) modes, and the average frequency shifts obtained by combining the results for radial and dipolar modes ($\delta\nu$), respectively. Eighth column: frequency shifts obtained with the cross-correlation method described in Kiefer et al. (2017).

KIC 2837475

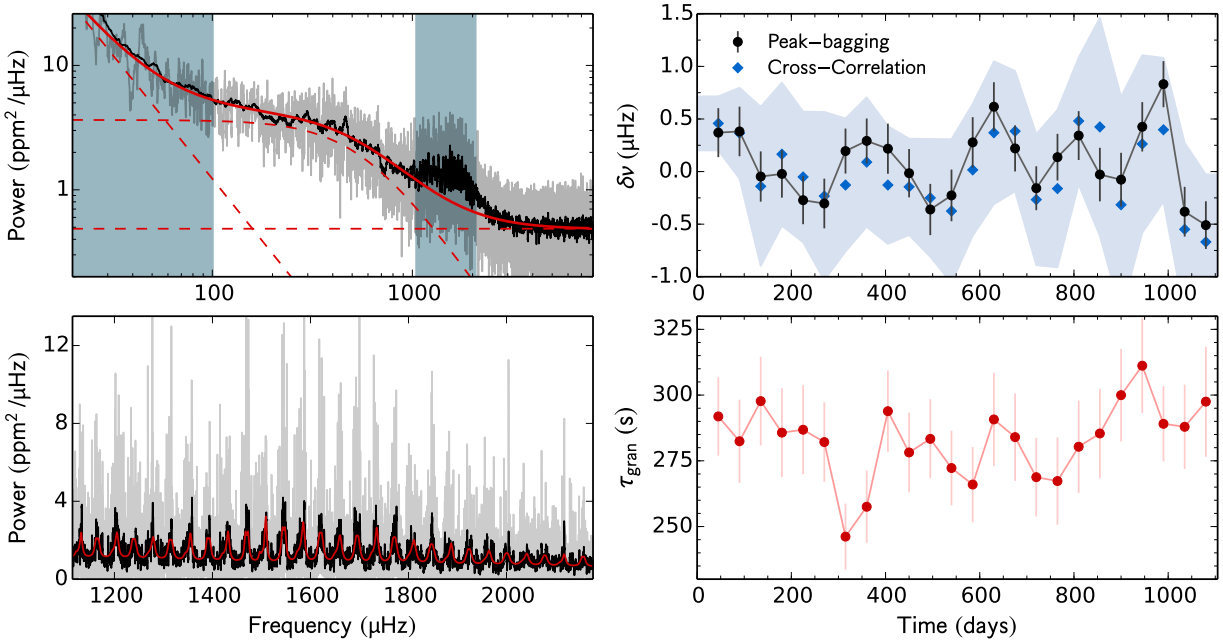

Fig. A.2 – Same as in Fig. A.1, but for KIC 2837475.

time (days)	d_c %	τ_{gran} (s)	Peak-bagging $\delta\nu_{l=0}$ (μHz)	$\delta\nu_{l=1}$ (μHz)	$\delta\nu_{l=2}$ (μHz)	$\delta\nu$ (μHz)	Cross-correlation $\delta\nu$ (μHz)
45	0.98	291.9 ± 14.9	0.01 ± 0.34	0.71 ± 0.32	0.57 ± 0.61	0.37 ± 0.37	0.46 ± 0.26
90	0.97	282.4 ± 15.8	0.00 ± 0.37	0.64 ± 0.31	0.11 ± 0.59	0.38 ± 0.38	0.37 ± 0.43
135	0.96	297.7 ± 16.9	0.29 ± 0.35	-0.33 ± 0.32	-0.40 ± 0.58	-0.05 ± -0.05	-0.14 ± 0.76
180	0.97	285.7 ± 16.9	0.55 ± 0.29	-0.90 ± 0.36	-0.56 ± 0.65	-0.02 ± -0.02	0.16 ± 0.68
225	0.96	286.8 ± 16.9	-0.14 ± 0.31	-0.43 ± 0.33	1.11 ± 0.51	-0.27 ± -0.27	-0.05 ± 0.62
270	0.81	282.1 ± 15.1	-0.69 ± 0.34	0.07 ± 0.33	1.38 ± 0.46	-0.30 ± -0.30	-0.23 ± 0.80
315	0.78	246.2 ± 12.6	0.34 ± 0.31	0.07 ± 0.29	-0.45 ± 0.72	0.19 ± 0.19	-0.13 ± 0.63
360	0.89	257.5 ± 13.7	0.02 ± 0.34	0.46 ± 0.27	-1.38 ± 0.49	0.29 ± 0.29	0.09 ± 0.62
405	0.93	293.9 ± 15.5	0.05 ± 0.36	0.34 ± 0.31	-0.85 ± 0.54	0.22 ± 0.22	-0.13 ± 0.56
450	0.97	278.2 ± 15.1	0.39 ± 0.34	-0.37 ± 0.31	-0.79 ± 0.55	-0.02 ± -0.02	-0.15 ± 0.46
495	0.97	283.4 ± 15.1	-0.34 ± 0.34	-0.38 ± 0.35	-0.06 ± 0.62	-0.36 ± -0.36	-0.25 ± 0.56
540	0.98	272.3 ± 14.2	-0.33 ± 0.33	-0.10 ± 0.37	-0.25 ± 0.60	-0.23 ± -0.23	-0.38 ± 0.68
585	0.94	266.0 ± 14.3	0.25 ± 0.32	0.32 ± 0.36	-0.30 ± 0.56	0.28 ± 0.28	0.02 ± 0.63
630	0.92	290.7 ± 17.7	0.57 ± 0.33	0.67 ± 0.33	-0.17 ± 0.59	0.62 ± 0.62	0.37 ± 0.68
675	0.90	284.0 ± 16.6	0.69 ± 0.30	-0.29 ± 0.32	0.14 ± 0.55	0.22 ± 0.22	0.38 ± 0.57
720	0.91	268.8 ± 15.0	0.08 ± 0.29	-0.40 ± 0.30	-0.15 ± 0.49	-0.16 ± -0.16	-0.27 ± 0.62
765	0.95	267.3 ± 16.6	0.22 ± 0.32	0.06 ± 0.30	0.53 ± 0.47	0.14 ± 0.14	-0.16 ± 0.75
810	0.90	280.4 ± 17.6	0.27 ± 0.34	0.41 ± 0.32	1.19 ± 0.42	0.34 ± 0.34	0.48 ± 0.60
855	0.89	285.4 ± 17.0	-0.21 ± 0.38	0.11 ± 0.34	0.49 ± 0.55	-0.03 ± -0.03	0.42 ± 1.04
900	0.95	300.0 ± 17.6	0.52 ± 0.37	-0.62 ± 0.35	-0.29 ± 0.56	-0.08 ± -0.08	-0.32 ± 1.03
945	0.90	311.2 ± 18.1	0.61 ± 0.34	0.24 ± 0.33	0.81 ± 0.54	0.43 ± 0.43	0.26 ± 0.84
990	0.89	289.1 ± 14.3	0.06 ± 0.36	1.30 ± 0.28	0.31 ± 0.63	0.83 ± 0.83	0.40 ± 0.68
1035	0.85	287.9 ± 16.0	-1.24 ± 0.35	0.34 ± 0.32	-0.41 ± 0.55	-0.38 ± -0.38	-0.55 ± 0.82
1080	0.85	297.5 ± 20.9	-0.70 ± 0.33	-0.34 ± 0.31	0.29 ± 0.47	-0.51 ± -0.51	-0.67 ± 0.64

Table A.2 – Same as in Table A.1, but for KIC 2837475.

KIC 3425851

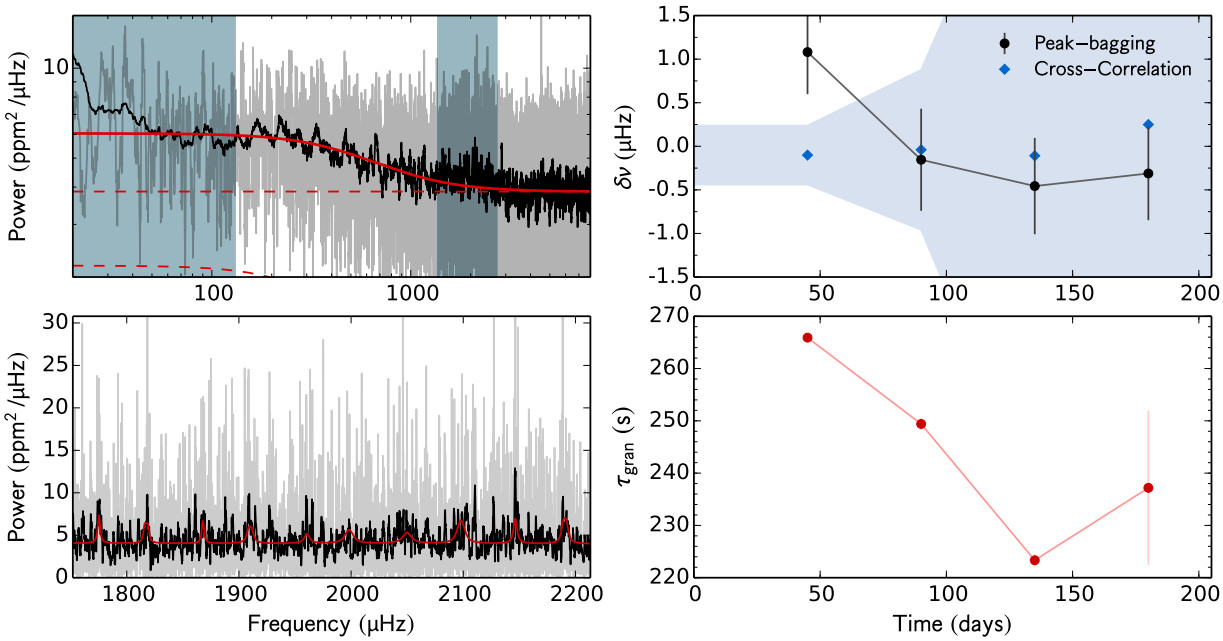

Fig. A.3 – Same as in Fig. A.1, but for KIC 3425851.

time (days)	d_c %	τ_{gran} (s)	Peak-bagging $\delta\nu_{l=0}$ (μHz)	$\delta\nu_{l=1}$ (μHz)	$\delta\nu_{l=2}$ (μHz)	$\delta\nu$ (μHz)	Cross-correlation $\delta\nu$ (μHz)
45	0.98	265.9 ± 0.2	1.23 ± 0.61	0.83 ± 0.80	0.00 ± 0.00	1.08 ± 1.08	-0.10 ± 0.34
90	0.97	249.4 ± 1.1	0.14 ± 0.81	-0.48 ± 0.85	0.00 ± 0.00	-0.15 ± -0.15	-0.04 ± 0.92
135	0.96	223.3 ± 1.2	-0.43 ± 0.76	-0.48 ± 0.80	0.00 ± 0.00	-0.46 ± -0.46	-0.11 ± 3.97
180	0.78	237.2 ± 14.8	-0.69 ± 0.66	0.42 ± 0.92	0.00 ± 0.00	-0.31 ± -0.31	0.25 ± 4.83

Table A.3 – Same as in Table A.1, but for KIC 3425851.

KIC 3427720

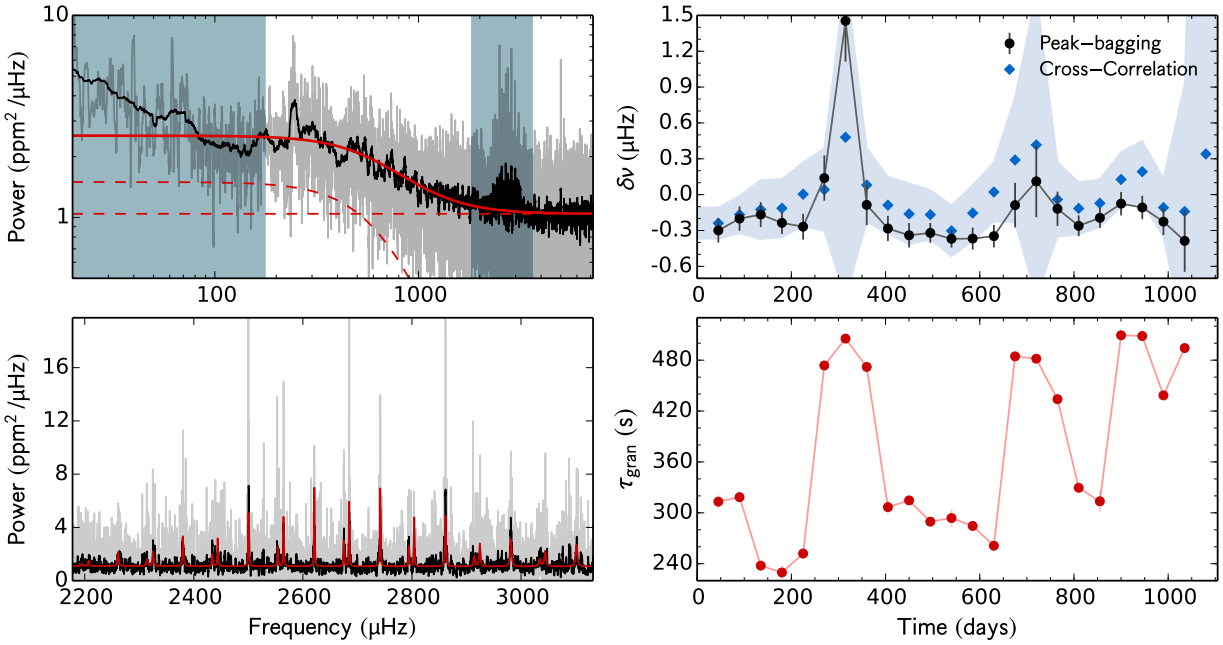

Fig. A.4 – Same as in Fig. A.1, but for KIC 3427720.

time (days)	d_c %	τ_{gran} (s)	Peak-bagging $\delta\nu_{l=0}$ (μHz)	$\delta\nu_{l=1}$ (μHz)	$\delta\nu_{l=2}$ (μHz)	$\delta\nu$ (μHz)	Cross-correlation $\delta\nu$ (μHz)
45	0.97	313.2 ± 7.5	-0.37 ± 0.14	-0.22 ± 0.15	0.12 ± 0.17	-0.30 ± -0.30	-0.24 ± 0.13
90	0.97	318.5 ± 3.5	-0.44 ± 0.14	0.04 ± 0.15	-0.14 ± 0.19	-0.20 ± -0.20	-0.17 ± 0.16
135	0.96	237.8 ± 0.6	-0.39 ± 0.16	-0.01 ± 0.14	0.16 ± 0.21	-0.17 ± -0.17	-0.12 ± 0.25
180	0.97	229.6 ± 7.9	-0.40 ± 0.15	-0.14 ± 0.12	0.52 ± 0.20	-0.24 ± -0.24	-0.11 ± 0.24
225	0.96	252.1 ± 6.3	-0.25 ± 0.17	-0.28 ± 0.14	0.10 ± 0.24	-0.27 ± -0.27	0.00 ± 0.27
270	0.80	473.7 ± 3.4	0.61 ± 0.34	-0.08 ± 0.23	-0.48 ± 0.36	0.14 ± 0.14	0.04 ± 0.34
315	0.78	505.4 ± 0.1	1.98 ± 0.48	0.90 ± 0.49	-1.82 ± 0.52	1.45 ± 1.45	0.48 ± 1.34
360	0.89	472.0 ± 3.5	0.01 ± 0.26	-0.16 ± 0.22	-0.30 ± 0.39	-0.09 ± -0.09	0.08 ± 0.31
405	0.93	306.7 ± 8.3	-0.28 ± 0.17	-0.28 ± 0.13	0.23 ± 0.18	-0.28 ± -0.28	-0.09 ± 0.24
450	0.97	314.6 ± 0.7	-0.51 ± 0.20	-0.28 ± 0.12	-0.14 ± 0.17	-0.34 ± -0.34	-0.16 ± 0.26
495	0.97	289.6 ± 0.8	-0.44 ± 0.12	-0.23 ± 0.11	0.04 ± 0.33	-0.32 ± -0.32	-0.17 ± 0.21
540	0.98	293.8 ± 10.6	-0.56 ± 0.10	-0.15 ± 0.11	0.49 ± 0.34	-0.37 ± -0.37	-0.30 ± 0.21
585	0.94	284.5 ± 0.6	-0.68 ± 0.16	-0.21 ± 0.11	0.19 ± 0.27	-0.37 ± -0.37	-0.15 ± 0.23
630	0.92	261.2 ± 4.0	-0.49 ± 0.16	-0.27 ± 0.12	0.26 ± 0.19	-0.35 ± -0.35	0.02 ± 0.25
675	0.90	484.5 ± 2.6	-0.19 ± 0.28	-0.01 ± 0.25	0.93 ± 0.32	-0.09 ± -0.09	0.29 ± 0.53
720	0.90	481.7 ± 2.7	0.05 ± 0.51	0.14 ± 0.37	0.35 ± 0.69	0.11 ± 0.11	0.42 ± 1.27
765	0.95	434.0 ± 0.5	-0.14 ± 0.29	-0.11 ± 0.17	0.24 ± 0.44	-0.12 ± -0.12	-0.04 ± 0.31
810	0.90	329.6 ± 0.9	-0.33 ± 0.12	-0.18 ± 0.13	0.42 ± 0.22	-0.26 ± -0.26	-0.12 ± 0.22
855	0.89	313.6 ± 12.6	-0.30 ± 0.11	-0.06 ± 0.13	0.07 ± 0.20	-0.19 ± -0.19	-0.07 ± 0.20
900	0.95	509.3 ± 0.1	-0.04 ± 0.15	-0.11 ± 0.13	0.15 ± 0.16	-0.08 ± -0.08	0.13 ± 0.23
945	0.90	508.5 ± 0.2	-0.20 ± 0.13	0.02 ± 0.15	0.35 ± 0.22	-0.11 ± -0.11	0.19 ± 0.26
990	0.89	438.5 ± 0.4	-0.38 ± 0.17	-0.10 ± 0.15	-0.20 ± 0.24	-0.23 ± -0.23	-0.11 ± 0.24
1035	0.85	494.3 ± 1.4	-0.34 ± 0.47	-0.41 ± 0.31	0.01 ± 0.50	-0.39 ± -0.39	-0.14 ± 1.06
1080	–	–	–	–	–	–	0.34 ± 6.54

Table A.4 – Same as in Table A.1, but for KIC 3427720.

KIC 3456181

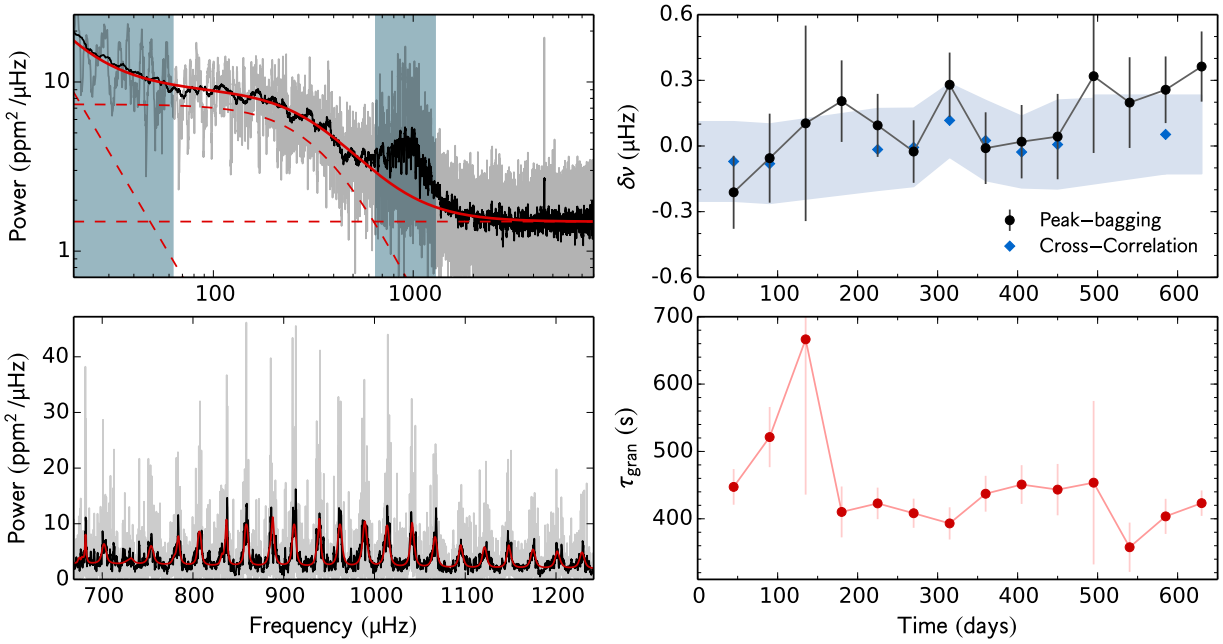

Fig. A.5 – Same as in Fig. A.1, but for KIC 3456181.

time (days)	d_c %	τ_{gran} (s)	Peak-bagging $\delta\nu_{l=0}$ (μHz)	$\delta\nu_{l=1}$ (μHz)	$\delta\nu_{l=2}$ (μHz)	$\delta\nu$ (μHz)	Cross-correlation $\delta\nu$ (μHz)
45	0.98	447.3 ± 26.5	-0.75 ± 0.35	-0.05 ± 0.19	1.66 ± 0.60	-0.21 ± -0.21	-0.07 ± 0.18
90	0.54	521.3 ± 44.7	-0.30 ± 0.37	0.05 ± 0.24	0.02 ± 0.66	-0.06 ± -0.06	-0.08 ± 0.18
135	0.05	666.4 ± 230.6	0.11 ± 0.60	0.10 ± 0.66	0.12 ± 0.67	0.10 ± 0.10	–
180	0.42	410.2 ± 37.8	0.12 ± 0.36	0.24 ± 0.22	-0.91 ± 0.36	0.20 ± 0.20	–
225	0.90	422.9 ± 23.4	0.21 ± 0.24	0.03 ± 0.18	-1.17 ± 0.32	0.09 ± 0.09	-0.02 ± 0.19
270	0.80	408.2 ± 21.6	0.14 ± 0.23	-0.14 ± 0.18	-0.45 ± 0.38	-0.03 ± -0.03	-0.01 ± 0.18
315	0.78	393.1 ± 23.9	0.30 ± 0.25	0.27 ± 0.18	-0.19 ± 0.37	0.28 ± 0.28	0.12 ± 0.17
360	0.89	437.2 ± 26.6	-0.35 ± 0.30	0.14 ± 0.20	0.05 ± 0.46	-0.01 ± -0.01	0.03 ± 0.18
405	0.93	450.8 ± 28.8	-0.12 ± 0.30	0.08 ± 0.20	-0.13 ± 0.37	0.02 ± 0.02	-0.03 ± 0.16
450	0.63	443.3 ± 38.1	0.27 ± 0.32	-0.09 ± 0.25	0.14 ± 0.41	0.04 ± 0.04	0.01 ± 0.20
495	0.14	453.6 ± 121.4	0.60 ± 0.48	0.01 ± 0.51	0.14 ± 0.55	0.32 ± 0.32	–
540	0.30	357.7 ± 36.6	0.44 ± 0.30	-0.02 ± 0.28	-0.24 ± 0.45	0.20 ± 0.20	–
585	0.76	403.6 ± 26.1	0.44 ± 0.22	0.08 ± 0.21	-0.12 ± 0.38	0.26 ± 0.26	0.05 ± 0.18
630	0.73	423.2 ± 18.9	0.44 ± 0.23	0.29 ± 0.23	-0.42 ± 0.42	0.36 ± 0.36	–

Table A.5 – Same as in Table A.1, but for KIC 3456181.

KIC 3544595

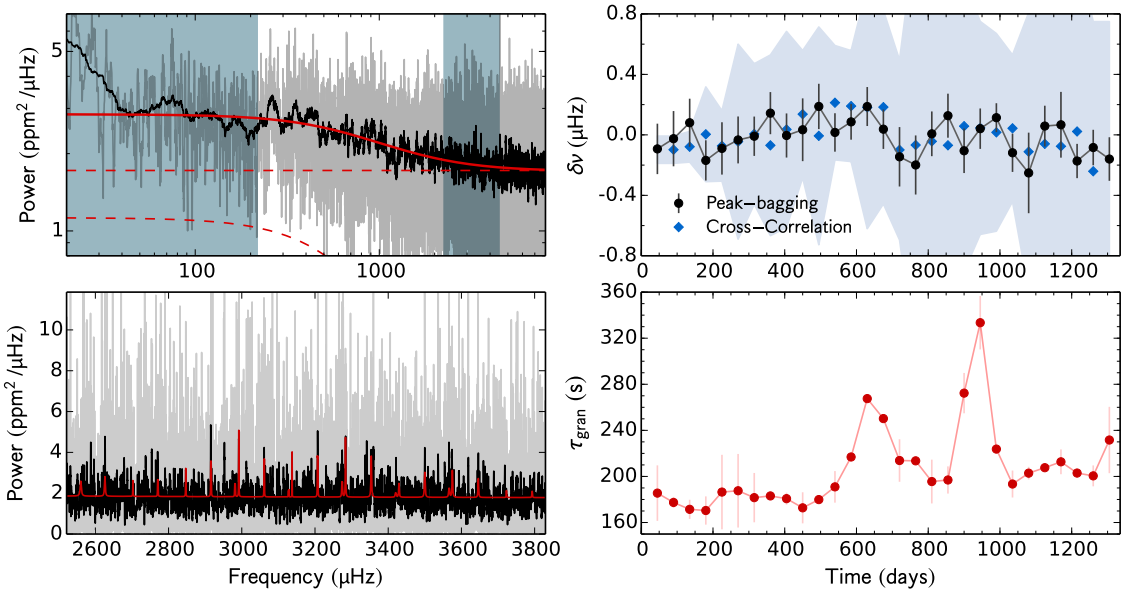

Fig. A.6 – Same as in Fig. A.1, but for KIC 3544595. Due to the extremely large error bars, the results from the cross-correlation method, that are shown here, were obtained from 180-d sub-series.

time (days)	d_c %	τ_{gran} (s)	Peak-bagging $\delta\nu_{l=0}$ (μHz)	$\delta\nu_{l=1}$ (μHz)	$\delta\nu_{l=2}$ (μHz)	$\delta\nu$ (μHz)	Cross-correlation $\delta\nu$ (μHz)
45	0.95	185.5 ± 24.1	-0.05 ± 0.23	-0.14 ± 0.24	-0.47 ± 0.65	-0.09 ± -0.09	–
90	0.92	177.4 ± 4.8	-0.08 ± 0.25	0.04 ± 0.26	0.53 ± 0.72	-0.03 ± -0.03	-0.10 ± 0.09
135	0.89	171.4 ± 8.3	0.02 ± 0.19	0.22 ± 0.29	-0.43 ± 0.68	0.08 ± 0.08	-0.08 ± 0.10
180	0.93	170.4 ± 12.3	-0.18 ± 0.16	-0.14 ± 0.23	-0.57 ± 0.50	-0.17 ± -0.17	0.00 ± 0.31
225	0.97	186.4 ± 32.3	-0.05 ± 0.24	-0.13 ± 0.25	-0.67 ± 0.52	-0.09 ± -0.09	-0.07 ± 0.23
270	0.96	187.6 ± 31.9	0.19 ± 0.24	-0.21 ± 0.21	0.28 ± 0.50	-0.03 ± -0.03	-0.05 ± 0.64
315	0.97	181.6 ± 21.4	0.15 ± 0.20	-0.12 ± 0.17	0.13 ± 0.38	-0.01 ± -0.01	0.01 ± 0.46
360	0.97	183.1 ± 0.1	0.13 ± 0.25	0.15 ± 0.17	0.35 ± 0.40	0.14 ± 0.14	-0.07 ± 0.60
405	0.97	180.7 ± 5.1	0.06 ± 0.24	-0.04 ± 0.18	0.27 ± 0.52	-0.00 ± -0.00	0.04 ± 0.65
450	0.90	172.8 ± 13.5	0.20 ± 0.39	-0.03 ± 0.24	-0.46 ± 0.63	0.03 ± 0.03	0.14 ± 0.42
495	0.78	179.9 ± 0.4	0.30 ± 0.28	0.14 ± 0.18	-0.56 ± 0.48	0.19 ± 0.19	-0.01 ± 0.72
540	0.80	190.9 ± 13.7	0.13 ± 0.20	-0.07 ± 0.17	0.08 ± 0.41	0.02 ± 0.02	0.21 ± 0.38
585	0.92	216.9 ± 1.0	0.15 ± 0.14	-0.05 ± 0.21	0.31 ± 0.45	0.09 ± 0.09	0.19 ± 0.37
630	0.98	267.6 ± 3.2	0.16 ± 0.16	0.24 ± 0.21	0.64 ± 0.70	0.19 ± 0.19	0.18 ± 0.80
675	0.97	250.2 ± 2.9	-0.07 ± 0.18	0.17 ± 0.19	0.31 ± 0.55	0.04 ± 0.04	0.18 ± 0.64
720	0.97	213.8 ± 18.5	-0.07 ± 0.31	-0.19 ± 0.25	0.59 ± 0.66	-0.15 ± -0.15	-0.10 ± 0.60
765	0.97	213.5 ± 1.6	0.15 ± 0.30	-0.47 ± 0.26	-0.23 ± 0.76	-0.20 ± -0.20	-0.07 ± 1.40
810	0.94	195.6 ± 19.0	0.02 ± 0.18	-0.02 ± 0.26	-0.16 ± 0.62	0.01 ± 0.01	-0.04 ± 1.27
855	0.91	196.9 ± 11.8	-0.04 ± 0.19	0.39 ± 0.23	0.27 ± 0.70	0.13 ± 0.13	-0.07 ± 1.44
900	0.88	272.3 ± 17.5	-0.44 ± 0.21	0.20 ± 0.20	0.59 ± 0.80	-0.11 ± -0.11	0.06 ± 0.96
945	0.92	333.4 ± 23.2	-0.09 ± 0.21	0.13 ± 0.17	-1.14 ± 0.43	0.04 ± 0.04	0.05 ± 0.70
990	0.97	223.7 ± 3.2	0.27 ± 0.13	-0.09 ± 0.14	-1.06 ± 0.40	0.11 ± 0.11	0.02 ± 0.65
1035	0.89	193.4 ± 11.7	0.14 ± 0.21	-0.27 ± 0.16	-0.41 ± 0.51	-0.12 ± -0.12	0.04 ± 0.49
1080	0.89	202.8 ± 5.5	-0.28 ± 0.37	-0.22 ± 0.39	0.42 ± 0.66	-0.25 ± -0.25	-0.11 ± 0.92
1125	0.96	207.6 ± 3.0	0.06 ± 0.16	0.05 ± 0.23	-0.06 ± 0.51	0.06 ± 0.06	-0.06 ± 1.32
1170	0.89	212.7 ± 10.8	0.40 ± 0.40	-0.07 ± 0.26	0.29 ± 0.64	0.07 ± 0.07	-0.08 ± 1.37
1215	0.78	202.9 ± 3.7	-0.21 ± 0.19	-0.15 ± 0.14	0.28 ± 0.47	-0.17 ± -0.17	0.02 ± 1.19
1260	0.84	200.5 ± 9.1	-0.05 ± 0.16	-0.12 ± 0.17	0.26 ± 0.49	-0.08 ± -0.08	-0.24 ± 0.99
1305	0.96	231.6 ± 28.8	-0.11 ± 0.20	-0.21 ± 0.20	-1.18 ± 0.73	-0.16 ± -0.16	–

Table A.6 – Same as in Table A.1, but for KIC 3544595. Due to the extremely large error bars, the results from the cross-correlation method, that are shown here, were obtained from 180-d sub-series.

KIC 3632418

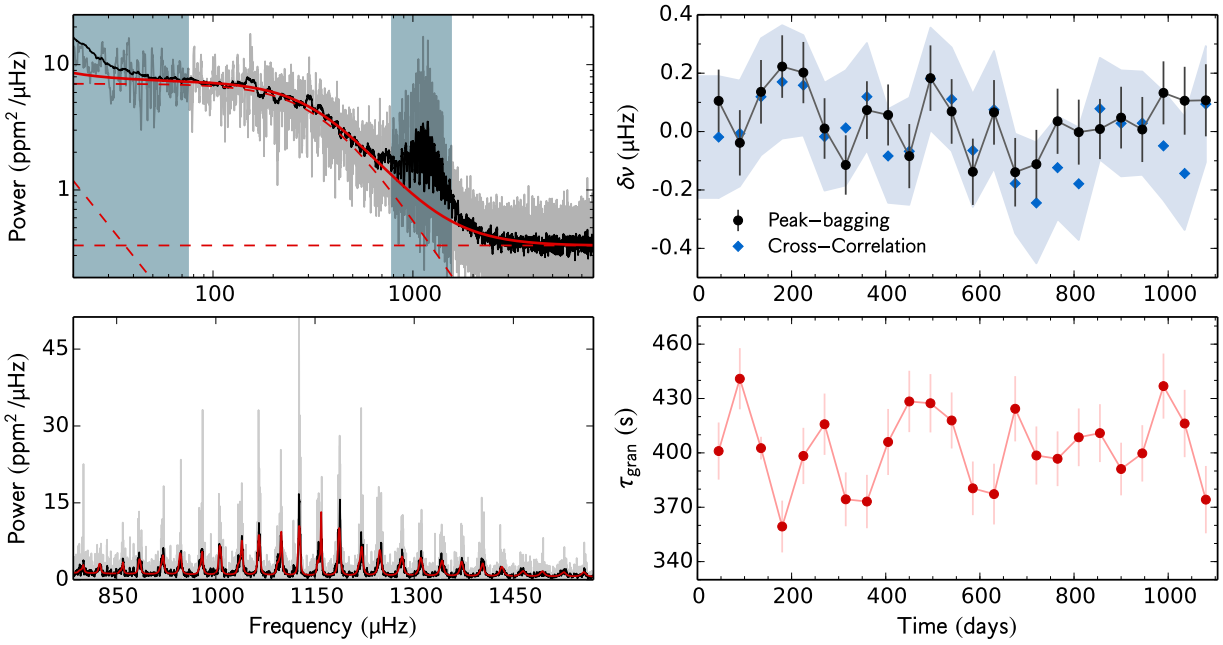

Fig. A.7 – Same as in Fig. A.1, but for KIC 3632418.

time (days)	d_c %	τ_{gran} (s)	Peak-bagging $\delta\nu_{l=0}$ (μHz)	$\delta\nu_{l=1}$ (μHz)	$\delta\nu_{l=2}$ (μHz)	$\delta\nu$ (μHz)	Cross-correlation $\delta\nu$ (μHz)
45	0.98	401.0 ± 15.8	0.02 ± 0.16	0.18 ± 0.15	-0.34 ± 0.27	0.11 ± 0.11	-0.02 ± 0.21
90	0.97	440.9 ± 16.9	-0.33 ± 0.18	0.16 ± 0.15	0.04 ± 0.30	-0.04 ± -0.04	-0.01 ± 0.18
135	0.96	402.6 ± 6.3	0.18 ± 0.17	0.10 ± 0.14	0.31 ± 0.29	0.14 ± 0.14	0.12 ± 0.20
180	0.97	359.4 ± 14.3	0.34 ± 0.15	0.11 ± 0.15	0.21 ± 0.29	0.22 ± 0.22	0.17 ± 0.19
225	0.96	398.3 ± 15.5	0.36 ± 0.15	0.07 ± 0.14	0.05 ± 0.28	0.20 ± 0.20	0.16 ± 0.17
270	0.80	415.8 ± 16.9	0.06 ± 0.17	-0.02 ± 0.13	-0.19 ± 0.23	0.01 ± 0.01	-0.02 ± 0.18
315	0.78	374.4 ± 14.9	-0.15 ± 0.16	-0.09 ± 0.13	0.12 ± 0.25	-0.11 ± -0.11	0.01 ± 0.20
360	0.89	373.1 ± 14.7	0.12 ± 0.14	0.03 ± 0.14	0.08 ± 0.28	0.07 ± 0.07	0.12 ± 0.18
405	0.93	406.0 ± 18.2	0.11 ± 0.15	0.00 ± 0.15	-0.05 ± 0.26	0.06 ± 0.06	-0.08 ± 0.16
450	0.97	428.4 ± 16.9	-0.32 ± 0.16	0.12 ± 0.15	0.23 ± 0.29	-0.08 ± -0.08	-0.07 ± 0.18
495	0.97	427.4 ± 16.1	-0.03 ± 0.16	0.37 ± 0.15	-0.07 ± 0.28	0.18 ± 0.18	0.18 ± 0.18
540	0.98	417.9 ± 15.5	-0.05 ± 0.16	0.17 ± 0.15	-0.23 ± 0.29	0.07 ± 0.07	0.11 ± 0.18
585	0.94	380.4 ± 14.8	0.11 ± 0.18	-0.31 ± 0.15	0.34 ± 0.27	-0.14 ± -0.14	-0.06 ± 0.19
630	0.92	377.3 ± 16.8	0.26 ± 0.16	-0.10 ± 0.15	0.48 ± 0.26	0.07 ± 0.07	0.07 ± 0.20
675	0.90	424.3 ± 18.0	-0.08 ± 0.18	-0.18 ± 0.16	0.11 ± 0.27	-0.14 ± -0.14	-0.18 ± 0.17
720	0.90	398.6 ± 16.0	-0.14 ± 0.19	-0.09 ± 0.15	0.09 ± 0.31	-0.11 ± -0.11	-0.24 ± 0.21
765	0.95	396.8 ± 15.1	0.09 ± 0.19	0.00 ± 0.14	-0.16 ± 0.26	0.04 ± 0.04	-0.12 ± 0.18
810	0.90	408.6 ± 15.9	0.04 ± 0.17	-0.03 ± 0.15	-0.35 ± 0.24	-0.00 ± -0.00	-0.18 ± 0.19
855	0.89	410.9 ± 16.0	0.01 ± 0.16	0.01 ± 0.13	-0.35 ± 0.26	0.01 ± 0.01	0.08 ± 0.17
900	0.95	391.1 ± 14.5	0.13 ± 0.17	-0.01 ± 0.14	-0.03 ± 0.25	0.05 ± 0.05	0.03 ± 0.18
945	0.90	399.7 ± 15.5	-0.05 ± 0.16	0.06 ± 0.15	-0.57 ± 0.28	0.01 ± 0.01	0.03 ± 0.18
990	0.89	436.9 ± 18.0	-0.03 ± 0.16	0.27 ± 0.15	-0.77 ± 0.28	0.13 ± 0.13	-0.05 ± 0.19
1035	0.85	416.2 ± 18.6	-0.01 ± 0.18	0.19 ± 0.15	-0.29 ± 0.30	0.11 ± 0.11	-0.14 ± 0.19
1080	0.85	374.2 ± 18.6	0.44 ± 0.18	-0.17 ± 0.17	0.41 ± 0.32	0.11 ± 0.11	0.09 ± 0.20

Table A.7 – Same as in Table A.1, but for KIC 3632418.

KIC 3656476

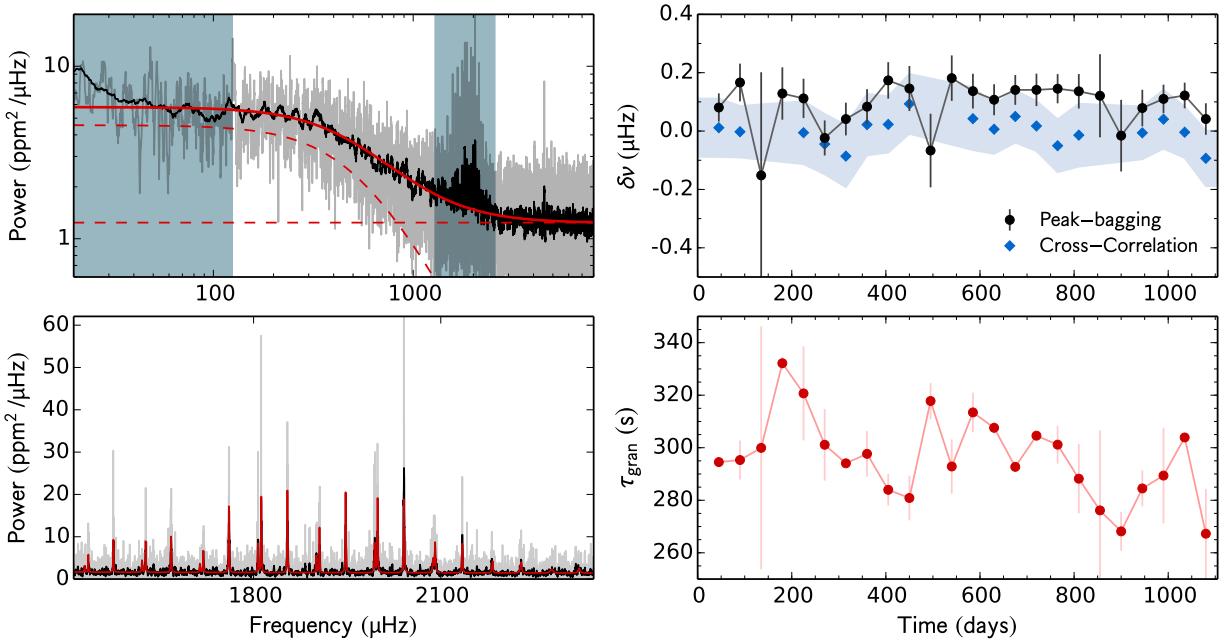

Fig. A.8 – Same as in Fig. A.1, but for KIC 3656476.

time (days)	d_c %	τ_{gran} (s)	Peak-bagging $\delta\nu_{l=0}$ (μHz)	$\delta\nu_{l=1}$ (μHz)	$\delta\nu_{l=2}$ (μHz)	$\delta\nu$ (μHz)	Cross-correlation $\delta\nu$ (μHz)
45	0.98	294.5 ± 2.0	0.01 ± 0.07	0.16 ± 0.07	0.01 ± 0.11	0.08 ± 0.08	0.01 ± 0.10
90	0.54	295.3 ± 7.4	0.10 ± 0.10	0.22 ± 0.09	-0.18 ± 0.11	0.17 ± 0.17	-0.00 ± 0.09
135	0.05	299.9 ± 46.2	-0.08 ± 0.45	-0.26 ± 0.57	0.49 ± 0.57	-0.15 ± -0.15	–
180	0.42	332.2 ± 2.3	-0.02 ± 0.13	0.29 ± 0.13	-0.39 ± 0.14	0.13 ± 0.13	–
225	0.90	320.7 ± 17.9	0.12 ± 0.09	0.11 ± 0.10	-0.28 ± 0.10	0.11 ± 0.11	-0.01 ± 0.11
270	0.80	301.1 ± 13.6	-0.03 ± 0.09	-0.02 ± 0.08	-0.03 ± 0.10	-0.02 ± -0.02	-0.04 ± 0.10
315	0.78	294.1 ± 0.0	-0.01 ± 0.08	0.10 ± 0.08	-0.06 ± 0.11	0.04 ± 0.04	-0.09 ± 0.11
360	0.89	297.7 ± 8.7	0.02 ± 0.08	0.15 ± 0.09	-0.03 ± 0.13	0.08 ± 0.08	0.02 ± 0.11
405	0.93	284.0 ± 6.0	0.17 ± 0.09	0.18 ± 0.09	-0.02 ± 0.12	0.17 ± 0.17	0.02 ± 0.10
450	0.63	280.9 ± 8.5	0.10 ± 0.11	0.19 ± 0.11	0.07 ± 0.11	0.15 ± 0.15	0.09 ± 0.10
495	0.14	317.8 ± 6.8	-0.27 ± 0.19	0.10 ± 0.17	0.08 ± 0.25	-0.07 ± -0.07	–
540	0.30	292.9 ± 10.3	0.15 ± 0.10	0.24 ± 0.13	0.05 ± 0.19	0.18 ± 0.18	–
585	0.76	313.5 ± 7.6	0.10 ± 0.08	0.17 ± 0.09	-0.12 ± 0.13	0.14 ± 0.14	0.04 ± 0.11
630	0.92	307.6 ± 2.2	0.09 ± 0.08	0.12 ± 0.07	-0.16 ± 0.10	0.11 ± 0.11	0.01 ± 0.08
675	0.90	292.7 ± 0.6	0.15 ± 0.08	0.13 ± 0.07	-0.19 ± 0.09	0.14 ± 0.14	0.05 ± 0.09
720	0.90	304.6 ± 0.6	0.18 ± 0.08	0.11 ± 0.08	-0.28 ± 0.12	0.14 ± 0.14	0.02 ± 0.09
765	0.95	301.2 ± 7.2	0.17 ± 0.07	0.12 ± 0.07	-0.20 ± 0.15	0.15 ± 0.15	-0.05 ± 0.09
810	0.70	288.2 ± 13.2	0.11 ± 0.07	0.18 ± 0.10	-0.05 ± 0.12	0.14 ± 0.14	-0.01 ± 0.11
855	0.22	276.1 ± 30.4	0.20 ± 0.20	0.03 ± 0.21	0.01 ± 0.24	0.12 ± 0.12	–
900	0.17	268.2 ± 7.4	0.05 ± 0.14	-0.22 ± 0.25	-0.81 ± 0.33	-0.02 ± -0.02	–
945	0.59	284.5 ± 6.8	0.10 ± 0.08	0.04 ± 0.10	-0.07 ± 0.12	0.08 ± 0.08	-0.01 ± 0.09
990	0.89	289.4 ± 18.2	0.10 ± 0.06	0.12 ± 0.08	-0.04 ± 0.10	0.11 ± 0.11	0.04 ± 0.10
1035	0.85	303.9 ± 0.6	0.16 ± 0.06	0.09 ± 0.06	-0.01 ± 0.10	0.12 ± 0.12	-0.00 ± 0.09
1080	0.85	267.3 ± 17.1	0.08 ± 0.07	-0.01 ± 0.08	-0.03 ± 0.11	0.04 ± 0.04	-0.09 ± 0.10

Table A.8 – Same as in Table A.1, but for KIC 3656476.

KIC 3735871

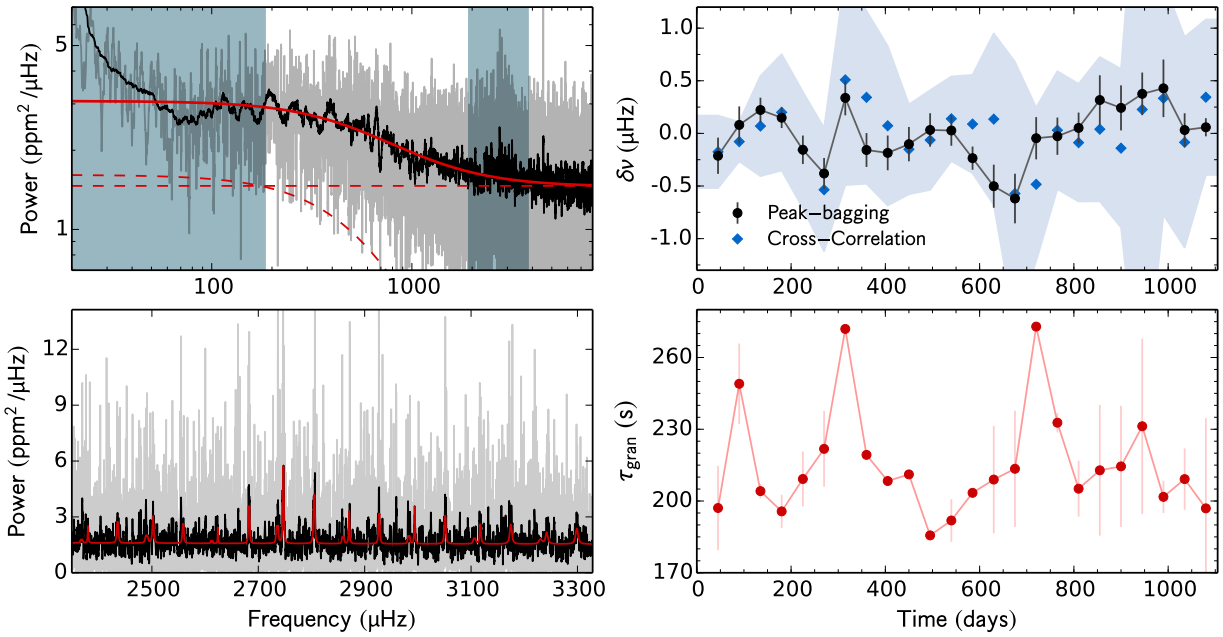

Fig. A.9 – Same as in Fig. A.1, but for KIC 3735871.

time (days)	d_c %	τ_{gran} (s)	Peak-bagging $\delta\nu_{l=0}$ (μHz)	$\delta\nu_{l=1}$ (μHz)	$\delta\nu_{l=2}$ (μHz)	$\delta\nu$ (μHz)	Cross-correlation $\delta\nu$ (μHz)
45	0.98	197.1 ± 17.6	-0.04 ± 0.23	-0.45 ± 0.27	0.05 ± 0.49	-0.21 ± -0.21	-0.18 ± 0.34
90	0.97	249.0 ± 16.8	0.08 ± 0.26	0.08 ± 0.24	-0.13 ± 0.43	0.08 ± 0.08	-0.08 ± 0.19
135	0.96	204.1 ± 3.1	0.25 ± 0.14	0.16 ± 0.21	0.64 ± 0.37	0.22 ± 0.22	0.07 ± 0.48
180	0.97	195.7 ± 6.9	0.02 ± 0.12	0.43 ± 0.17	-0.31 ± 0.32	0.15 ± 0.15	0.20 ± 0.55
225	0.96	209.2 ± 11.5	-0.43 ± 0.18	0.24 ± 0.21	-0.58 ± 0.42	-0.16 ± -0.16	-0.16 ± 0.55
270	0.80	221.8 ± 15.8	-0.63 ± 0.18	0.06 ± 0.25	0.08 ± 0.36	-0.38 ± -0.38	-0.54 ± 0.59
315	0.78	271.9 ± 1.5	-0.21 ± 0.21	1.18 ± 0.26	0.09 ± 0.33	0.34 ± 0.34	0.51 ± 1.00
360	0.89	219.3 ± 0.7	-0.35 ± 0.20	0.22 ± 0.28	0.03 ± 0.30	-0.16 ± -0.16	0.34 ± 0.82
405	0.93	208.4 ± 0.1	-0.12 ± 0.23	-0.26 ± 0.24	0.20 ± 0.33	-0.19 ± -0.19	0.07 ± 0.76
450	0.97	211.1 ± 1.0	-0.12 ± 0.22	-0.09 ± 0.25	0.21 ± 0.46	-0.10 ± -0.10	-0.15 ± 0.43
495	0.97	185.6 ± 0.2	0.04 ± 0.25	0.03 ± 0.21	-0.22 ± 0.40	0.03 ± 0.03	-0.06 ± 0.47
540	0.98	191.9 ± 8.9	0.32 ± 0.23	-0.17 ± 0.19	0.10 ± 0.39	0.03 ± 0.03	0.14 ± 0.40
585	0.94	203.4 ± 0.8	-0.18 ± 0.12	-0.47 ± 0.25	-0.58 ± 0.46	-0.24 ± -0.24	0.09 ± 0.47
630	0.92	209.0 ± 22.5	-0.36 ± 0.26	-0.74 ± 0.33	-0.17 ± 0.63	-0.50 ± -0.50	0.14 ± 0.81
675	0.90	213.5 ± 24.3	-0.02 ± 0.32	-1.30 ± 0.34	-0.13 ± 0.59	-0.62 ± -0.62	-0.57 ± 1.25
720	0.91	272.9 ± 0.9	-0.14 ± 0.28	0.05 ± 0.29	0.05 ± 0.56	-0.05 ± -0.05	-0.48 ± 0.73
765	0.95	232.7 ± 4.1	-0.23 ± 0.27	0.14 ± 0.24	-0.25 ± 0.40	-0.03 ± -0.03	0.03 ± 0.56
810	0.90	205.2 ± 11.7	-0.02 ± 0.20	0.13 ± 0.21	-0.65 ± 0.42	0.05 ± 0.05	-0.09 ± 0.56
855	0.89	212.8 ± 27.3	0.17 ± 0.36	0.43 ± 0.31	-0.58 ± 0.55	0.32 ± 0.32	0.04 ± 0.69
900	0.95	214.5 ± 25.4	0.31 ± 0.29	0.16 ± 0.32	-0.17 ± 0.50	0.24 ± 0.24	-0.14 ± 0.75
945	0.90	231.3 ± 36.6	0.63 ± 0.27	0.07 ± 0.30	0.22 ± 0.49	0.38 ± 0.38	0.23 ± 2.96
990	0.89	201.7 ± 6.8	-0.46 ± 0.55	0.72 ± 0.32	0.81 ± 0.53	0.43 ± 0.43	0.33 ± 1.11
1035	0.85	209.2 ± 12.8	0.07 ± 0.20	-0.05 ± 0.27	0.31 ± 0.43	0.03 ± 0.03	-0.08 ± 1.00
1080	0.85	196.9 ± 37.7	0.12 ± 0.09	-0.46 ± 0.26	0.02 ± 0.48	0.06 ± 0.06	0.34 ± 0.74

Table A.9 – Same as in Table A.1, but for KIC 3735871.

KIC 4141376

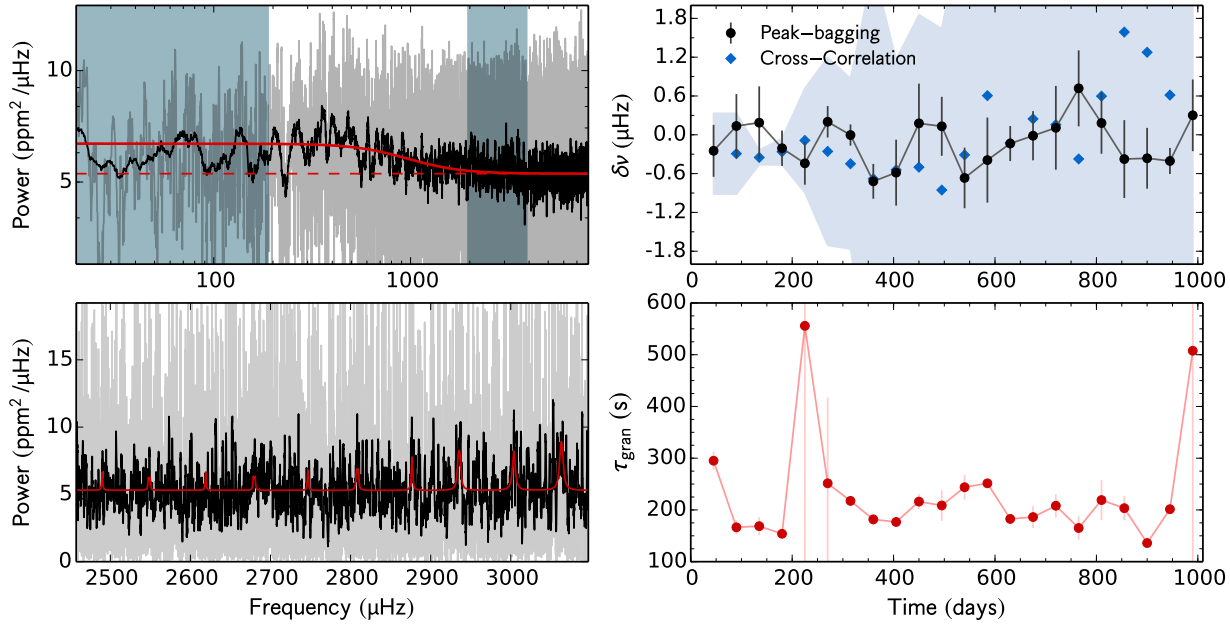

Fig. A.10 – Same as in Fig. A.1, but for KIC 4141376. Due to the extremely large error bars, the results from the cross-correlation method, that are shown here, were obtained from 180-d sub-series.

time (days)	d_c %	τ_{gran} (s)	Peak-bagging $\delta\nu_{l=0}$ (μHz)	$\delta\nu_{l=1}$ (μHz)	$\delta\nu_{l=2}$ (μHz)	$\delta\nu$ (μHz)	Cross-correlation $\delta\nu$ (μHz)
45	0.98	295.1 ± 17.8	-0.58 ± 0.65	-0.05 ± 0.51	0.00 ± 0.00	-0.25 ± -0.25	–
90	0.97	166.4 ± 13.6	0.14 ± 0.83	0.13 ± 0.62	0.00 ± 0.00	0.14 ± 0.14	-0.29 ± 0.62
135	0.96	168.7 ± 17.2	0.59 ± 0.85	-0.13 ± 0.75	0.00 ± 0.00	0.19 ± 0.19	-0.35 ± 0.11
180	0.78	153.9 ± 1.2	-0.18 ± 0.30	-0.35 ± 0.71	0.00 ± 0.00	-0.21 ± -0.21	-0.26 ± 0.20
225	0.72	555.8 ± 703.6	-0.61 ± 0.40	-0.10 ± 0.57	0.00 ± 0.00	-0.44 ± -0.44	-0.09 ± 0.80
270	0.92	251.4 ± 166.0	-0.39 ± 0.52	0.36 ± 0.27	0.00 ± 0.00	0.20 ± 0.20	-0.26 ± 1.45
315	0.98	217.5 ± 6.6	-0.61 ± 0.33	0.19 ± 0.19	0.00 ± 0.00	-0.00 ± -0.00	-0.45 ± 1.32
360	0.97	181.7 ± 10.6	-0.77 ± 0.31	-0.54 ± 0.55	0.00 ± 0.00	-0.72 ± -0.72	-0.68 ± 3.26
405	0.97	176.7 ± 3.0	-0.65 ± 0.79	-0.54 ± 0.67	0.00 ± 0.00	-0.59 ± -0.59	-0.54 ± 1.71
450	0.97	216.1 ± 14.4	0.01 ± 0.88	0.33 ± 0.86	0.00 ± 0.00	0.18 ± 0.18	-0.50 ± 2.36
495	0.94	208.6 ± 29.6	-0.90 ± 0.80	0.63 ± 0.56	0.00 ± 0.00	0.13 ± 0.13	-0.85 ± 2.49
540	0.91	243.9 ± 24.1	-1.27 ± 0.68	-0.11 ± 0.65	0.00 ± 0.00	-0.67 ± -0.67	-0.31 ± 3.76
585	0.88	251.4 ± 2.0	-0.71 ± 0.93	-0.08 ± 0.93	0.00 ± 0.00	-0.39 ± -0.39	0.61 ± 11.58
630	0.92	182.6 ± 1.9	-0.17 ± 0.29	0.13 ± 0.79	0.00 ± 0.00	-0.14 ± -0.14	-0.13 ± 3.34
675	0.97	186.2 ± 21.1	-0.00 ± 0.50	-0.03 ± 0.59	0.00 ± 0.00	-0.01 ± -0.01	0.25 ± 5.08
720	0.90	208.1 ± 22.8	0.64 ± 1.04	-0.23 ± 0.83	0.00 ± 0.00	0.11 ± 0.11	0.16 ± 8.75
765	0.89	165.1 ± 22.5	0.86 ± 0.90	0.61 ± 0.78	0.00 ± 0.00	0.72 ± 0.72	-0.37 ± 11.90
810	0.95	219.1 ± 38.4	0.14 ± 0.67	0.22 ± 0.67	0.00 ± 0.00	0.18 ± 0.18	0.60 ± 4.05
855	0.89	203.4 ± 23.4	-0.41 ± 0.89	-0.35 ± 0.82	0.00 ± 0.00	-0.38 ± -0.38	1.59 ± 6.32
900	0.82	136.0 ± 0.0	-0.66 ± 0.54	0.59 ± 0.96	0.00 ± 0.00	-0.36 ± -0.36	1.28 ± 16.59
945	0.84	201.5 ± 3.9	-0.57 ± 0.21	1.11 ± 0.65	0.00 ± 0.00	-0.40 ± -0.40	0.61 ± 4.13
990	0.92	507.6 ± 811.4	0.32 ± 0.81	0.28 ± 0.76	0.00 ± 0.00	0.30 ± 0.30	–

Table A.10 – Same as in Table A.1, but for KIC 4141376. Due to the extremely large error bars, the results from the cross-correlation method, that are shown here, were obtained from 180-d sub-series.

KIC 4349452

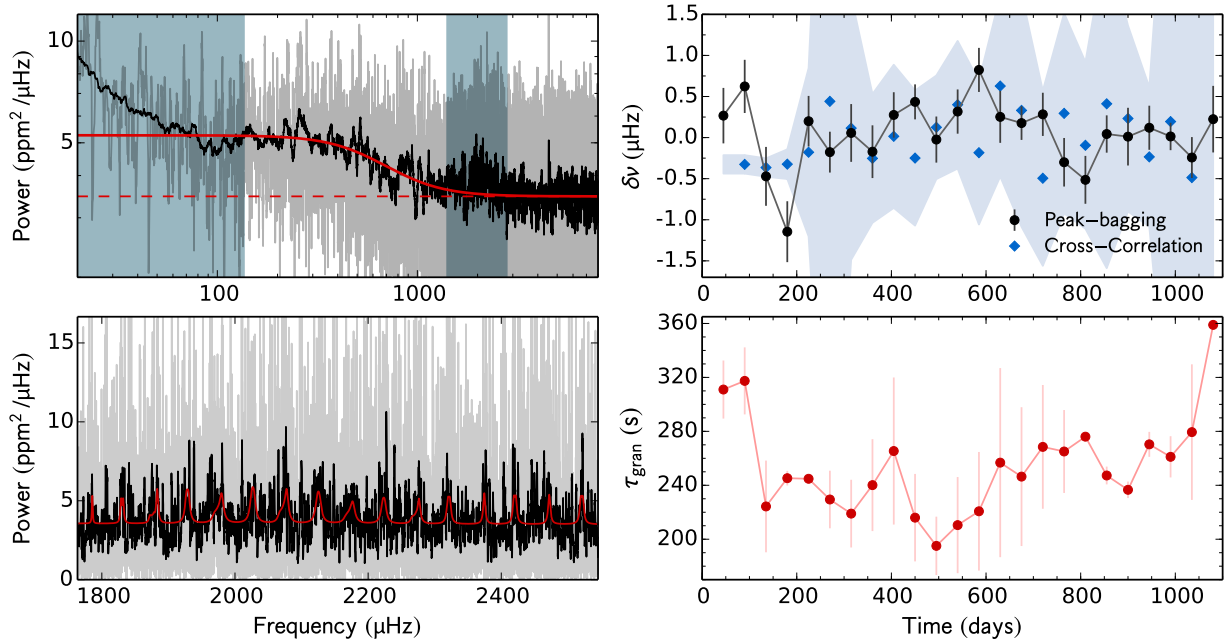

Fig. A.11 – Same as in Fig. A.1, but for KIC 4349452. Due to the extremely large error bars, the results from the cross-correlation method, that are shown here, were obtained from 180-d sub-series.

time (days)	d_c %	τ_{gran} (s)	Peak-bagging $\delta\nu_{l=0}$ (μHz)	$\delta\nu_{l=1}$ (μHz)	$\delta\nu_{l=2}$ (μHz)	$\delta\nu$ (μHz)	Cross-correlation $\delta\nu$ (μHz)
45	0.97	311.0 ± 21.5	0.54 ± 0.43	-0.19 ± 0.55	0.06 ± 0.91	0.27 ± 0.27	–
90	0.97	317.4 ± 24.9	1.05 ± 0.44	0.11 ± 0.48	0.15 ± 0.85	0.62 ± 0.62	-0.33 ± 0.11
135	0.96	224.3 ± 34.0	-0.48 ± 0.46	-0.46 ± 0.56	-0.76 ± 0.88	-0.47 ± -0.47	-0.36 ± 0.11
180	0.97	245.3 ± 5.4	-1.42 ± 0.49	-0.76 ± 0.57	-0.90 ± 0.92	-1.15 ± -1.15	-0.32 ± 0.18
225	0.96	244.8 ± 1.4	-0.27 ± 0.41	0.84 ± 0.47	0.66 ± 0.89	0.20 ± 0.20	-0.18 ± 1.02
270	0.80	229.5 ± 21.4	-0.14 ± 0.27	-0.38 ± 0.61	0.21 ± 0.84	-0.18 ± -0.18	0.44 ± 5.91
315	0.78	219.0 ± 25.1	-0.02 ± 0.46	0.16 ± 0.54	-0.03 ± 0.83	0.06 ± 0.06	0.11 ± 1.60
360	0.89	240.1 ± 34.1	-0.25 ± 0.42	-0.06 ± 0.50	0.57 ± 0.80	-0.17 ± -0.17	-0.25 ± 0.78
405	0.93	265.4 ± 54.5	0.32 ± 0.34	0.18 ± 0.48	0.61 ± 0.87	0.28 ± 0.28	0.02 ± 0.87
450	0.97	216.0 ± 32.4	0.55 ± 0.30	0.32 ± 0.30	0.79 ± 0.82	0.43 ± 0.43	-0.25 ± 0.82
495	0.97	195.1 ± 21.7	-0.08 ± 0.58	-0.01 ± 0.32	-0.06 ± 0.90	-0.02 ± -0.02	0.13 ± 0.63
540	0.98	210.5 ± 35.7	0.86 ± 0.41	-0.10 ± 0.36	-0.56 ± 0.73	0.32 ± 0.32	0.40 ± 0.78
585	0.94	220.7 ± 44.0	1.32 ± 0.36	0.24 ± 0.40	0.16 ± 0.72	0.82 ± 0.82	-0.18 ± 0.87
630	0.92	256.8 ± 70.1	0.87 ± 0.44	-0.41 ± 0.45	0.01 ± 0.75	0.25 ± 0.25	0.63 ± 1.10
675	0.90	246.4 ± 51.5	0.36 ± 0.32	0.05 ± 0.27	-0.64 ± 0.79	0.18 ± 0.18	0.33 ± 1.42
720	0.90	268.5 ± 45.9	0.27 ± 0.34	0.30 ± 0.42	0.11 ± 0.90	0.28 ± 0.28	-0.49 ± 1.07
765	0.95	265.1 ± 30.8	-0.30 ± 0.36	-0.30 ± 0.53	0.60 ± 0.86	-0.30 ± -0.30	0.29 ± 1.22
810	0.90	276.0 ± 1.5	-0.48 ± 0.38	-0.57 ± 0.45	-0.05 ± 0.79	-0.51 ± -0.51	-0.09 ± 1.02
855	0.89	247.3 ± 6.6	0.42 ± 0.32	-0.32 ± 0.32	-0.86 ± 0.65	0.04 ± 0.04	0.41 ± 2.00
900	0.95	236.6 ± 6.1	0.27 ± 0.53	-0.19 ± 0.47	-0.41 ± 0.81	0.01 ± 0.01	0.23 ± 1.13
945	0.90	270.4 ± 9.3	-0.37 ± 0.43	0.42 ± 0.34	-0.39 ± 0.86	0.12 ± 0.12	-0.23 ± 0.85
990	0.89	261.1 ± 15.3	-0.09 ± 0.27	0.07 ± 0.21	-0.37 ± 0.74	0.01 ± 0.01	0.19 ± 4.07
1035	0.85	279.4 ± 50.3	-0.41 ± 0.36	-0.09 ± 0.34	0.28 ± 0.73	-0.24 ± -0.24	-0.49 ± 4.62
1080	0.85	359.0 ± 1.9	-0.17 ± 0.60	0.56 ± 0.55	0.49 ± 0.77	0.22 ± 0.22	–

Table A.11 – Same as in Table A.1, but for KIC 4349452. Due to the extremely large error bars, the results from the cross-correlation method, that are shown here, were obtained from 180-d sub-series.

KIC 4914423

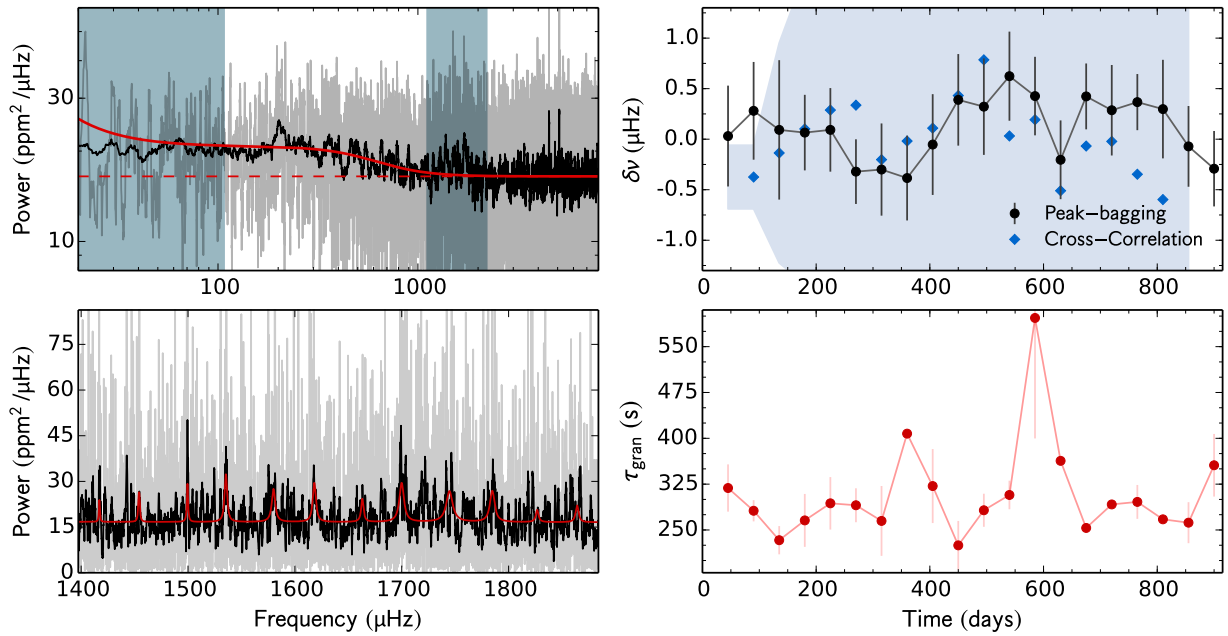

Fig. A.12 – Same as in Fig. A.1, but for KIC 4914423. Due to the extremely large error bars, the results from the cross-correlation method, that are shown here, were obtained from 180-d sub-series.

time (days)	d_c %	τ_{gran} (s)	Peak-bagging $\delta\nu_{l=0}$ (μHz)	$\delta\nu_{l=1}$ (μHz)	$\delta\nu_{l=2}$ (μHz)	$\delta\nu$ (μHz)	Cross-correlation $\delta\nu$ (μHz)
45	0.95	318.7 ± 38.7	-0.75 ± 0.89	0.39 ± 0.60	0.00 ± 0.00	0.03 ± 0.03	–
90	0.93	281.4 ± 17.4	-0.95 ± 1.01	0.65 ± 0.55	0.00 ± 0.00	0.28 ± 0.28	-0.37 ± 0.31
135	0.92	233.3 ± 23.1	0.10 ± 1.07	0.09 ± 0.90	0.00 ± 0.00	0.09 ± 0.09	-0.14 ± 1.09
180	0.92	265.7 ± 43.3	-0.30 ± 0.54	0.42 ± 0.52	0.00 ± 0.00	0.07 ± 0.07	0.10 ± 1.53
225	0.96	293.6 ± 43.0	-0.56 ± 0.78	0.35 ± 0.49	0.00 ± 0.00	0.09 ± 0.09	0.29 ± 1.77
270	0.97	290.5 ± 27.8	-0.53 ± 0.58	-0.23 ± 0.38	0.00 ± 0.00	-0.32 ± -0.32	0.34 ± 5.81
315	0.96	264.8 ± 57.2	0.25 ± 0.95	-0.47 ± 0.52	0.00 ± 0.00	-0.30 ± -0.30	-0.20 ± 2.46
360	0.97	407.6 ± 6.6	0.24 ± 0.94	-0.54 ± 0.47	0.00 ± 0.00	-0.38 ± -0.38	-0.02 ± 4.93
405	0.97	321.9 ± 60.6	-0.52 ± 0.91	0.15 ± 0.60	0.00 ± 0.00	-0.05 ± -0.05	0.11 ± 3.37
450	0.80	224.8 ± 40.0	-0.06 ± 0.90	0.54 ± 0.52	0.00 ± 0.00	0.39 ± 0.39	0.43 ± 1.82
495	0.78	282.3 ± 27.1	-0.13 ± 0.69	0.73 ± 0.66	0.00 ± 0.00	0.32 ± 0.32	0.79 ± 8.35
540	0.90	307.3 ± 23.4	0.70 ± 0.54	0.47 ± 0.77	0.00 ± 0.00	0.62 ± 0.62	0.03 ± 2.42
585	0.91	597.0 ± 197.2	0.96 ± 0.53	-0.19 ± 0.57	0.00 ± 0.00	0.43 ± 0.43	0.19 ± 4.06
630	0.97	363.1 ± 2.5	0.24 ± 0.60	-0.52 ± 0.51	0.00 ± 0.00	-0.20 ± -0.20	-0.51 ± 3.13
675	0.97	253.3 ± 0.1	0.80 ± 0.52	0.18 ± 0.42	0.00 ± 0.00	0.42 ± 0.42	-0.07 ± 3.55
720	0.97	291.8 ± 2.6	0.65 ± 0.69	0.02 ± 0.59	0.00 ± 0.00	0.29 ± 0.29	-0.02 ± 4.11
765	0.97	295.9 ± 27.7	0.61 ± 0.35	-0.02 ± 0.45	0.00 ± 0.00	0.37 ± 0.37	-0.35 ± 3.53
810	0.94	267.4 ± 2.7	0.23 ± 0.58	0.46 ± 0.89	0.00 ± 0.00	0.30 ± 0.30	-0.60 ± 8.19
855	0.91	261.9 ± 33.6	0.18 ± 0.69	-0.20 ± 0.49	0.00 ± 0.00	-0.07 ± -0.07	–
900	0.64	355.9 ± 51.3	0.28 ± 0.77	-0.47 ± 0.43	0.00 ± 0.00	-0.29 ± -0.29	–

Table A.12 – Same as in Table A.1, but for KIC 4914423. Due to the extremely large error bars, the results from the cross-correlation method, that are shown here, were obtained from 180-d sub-series.

KIC 4914923

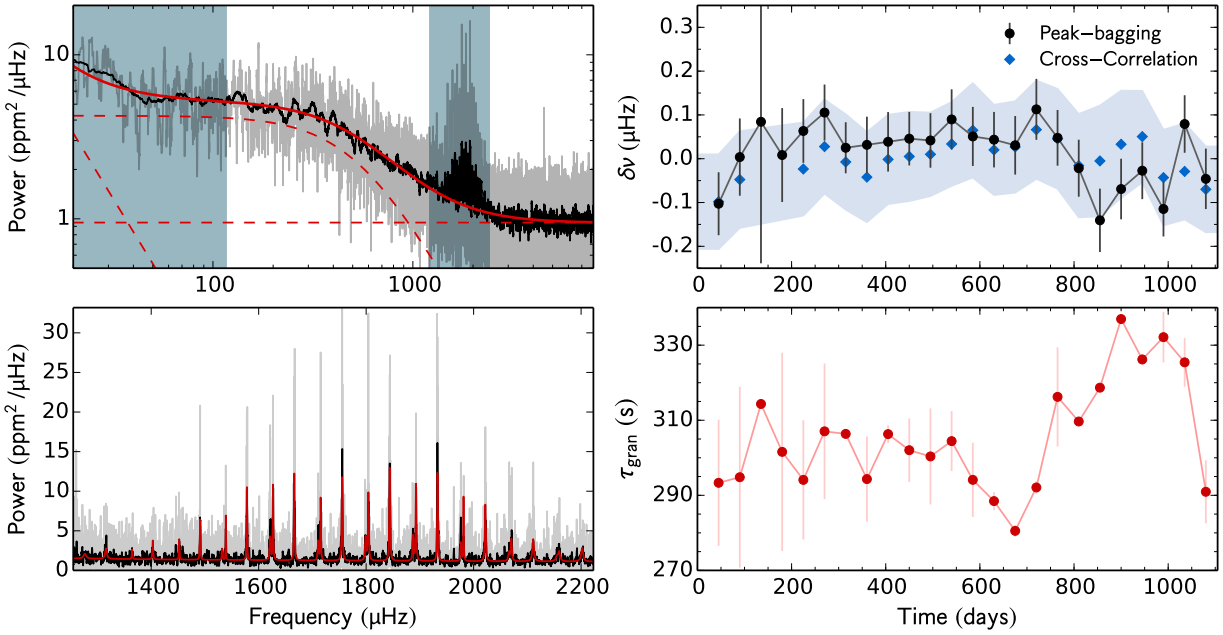

Fig. A.13 – Same as in Fig. A.1, but for KIC 4914923.

time (days)	d_c %	τ_{gran} (s)	Peak-bagging $\delta\nu_{l=0}$ (μHz)	$\delta\nu_{l=1}$ (μHz)	$\delta\nu_{l=2}$ (μHz)	$\delta\nu$ (μHz)	Cross-correlation $\delta\nu$ (μHz)
45	0.98	293.3 ± 16.8	-0.12 ± 0.11	-0.09 ± 0.09	-0.13 ± 0.14	-0.10 ± -0.10	-0.10 ± 0.11
90	0.54	294.8 ± 24.1	0.04 ± 0.14	-0.02 ± 0.11	-0.08 ± 0.19	0.00 ± 0.00	-0.05 ± 0.11
135	0.05	314.3 ± 1.1	-0.02 ± 0.47	0.17 ± 0.44	0.47 ± 0.74	0.08 ± 0.08	–
180	0.41	301.6 ± 26.4	0.05 ± 0.15	-0.03 ± 0.15	0.23 ± 0.27	0.01 ± 0.01	–
225	0.90	294.1 ± 15.9	0.17 ± 0.11	-0.01 ± 0.09	-0.32 ± 0.19	0.06 ± 0.06	-0.02 ± 0.11
270	0.81	307.0 ± 18.1	0.17 ± 0.10	0.06 ± 0.08	-0.23 ± 0.12	0.11 ± 0.11	0.03 ± 0.11
315	0.78	306.4 ± 0.0	0.12 ± 0.07	-0.14 ± 0.10	-0.14 ± 0.11	0.03 ± 0.03	-0.01 ± 0.11
360	0.89	294.3 ± 11.4	0.14 ± 0.08	-0.11 ± 0.10	-0.23 ± 0.14	0.03 ± 0.03	-0.04 ± 0.10
405	0.93	306.3 ± 2.3	0.06 ± 0.10	0.02 ± 0.09	0.06 ± 0.18	0.04 ± 0.04	-0.00 ± 0.10
450	0.97	302.0 ± 8.5	0.07 ± 0.08	0.02 ± 0.09	0.11 ± 0.17	0.05 ± 0.05	0.01 ± 0.10
495	0.97	300.4 ± 12.8	0.13 ± 0.09	-0.03 ± 0.08	0.16 ± 0.14	0.04 ± 0.04	0.01 ± 0.10
540	0.98	304.4 ± 8.0	0.18 ± 0.11	0.03 ± 0.09	0.20 ± 0.16	0.09 ± 0.09	0.03 ± 0.10
585	0.94	294.1 ± 9.9	-0.05 ± 0.09	0.17 ± 0.10	-0.18 ± 0.18	0.05 ± 0.05	0.06 ± 0.11
630	0.92	288.5 ± 2.4	-0.04 ± 0.09	0.14 ± 0.09	-0.29 ± 0.14	0.04 ± 0.04	0.02 ± 0.10
675	0.90	280.5 ± 1.6	0.07 ± 0.09	-0.02 ± 0.10	-0.15 ± 0.14	0.03 ± 0.03	0.03 ± 0.10
720	0.90	292.1 ± 1.6	0.18 ± 0.10	0.05 ± 0.10	0.07 ± 0.18	0.11 ± 0.11	0.07 ± 0.11
765	0.95	316.2 ± 13.2	0.05 ± 0.09	0.05 ± 0.10	-0.18 ± 0.14	0.05 ± 0.05	0.05 ± 0.11
810	0.90	309.7 ± 0.5	-0.10 ± 0.09	0.08 ± 0.10	-0.17 ± 0.14	-0.02 ± -0.02	-0.02 ± 0.12
855	0.89	318.7 ± 0.6	-0.13 ± 0.10	-0.15 ± 0.11	-0.18 ± 0.19	-0.14 ± -0.14	-0.01 ± 0.13
900	0.95	337.0 ± 0.6	-0.02 ± 0.09	-0.13 ± 0.10	-0.08 ± 0.18	-0.07 ± -0.07	0.03 ± 0.12
945	0.90	326.2 ± 1.4	-0.03 ± 0.09	-0.02 ± 0.09	-0.10 ± 0.15	-0.03 ± -0.03	0.05 ± 0.10
990	0.89	332.1 ± 6.7	-0.17 ± 0.09	-0.06 ± 0.09	-0.58 ± 0.08	-0.11 ± -0.11	-0.04 ± 0.11
1035	0.85	325.4 ± 6.5	0.04 ± 0.10	0.11 ± 0.09	-0.41 ± 0.13	0.08 ± 0.08	-0.03 ± 0.11
1080	0.85	290.9 ± 8.4	-0.06 ± 0.10	-0.04 ± 0.10	-0.08 ± 0.17	-0.05 ± -0.05	-0.07 ± 0.10

Table A.13 – Same as in Table A.1, but for KIC 4914923.

KIC 5184732

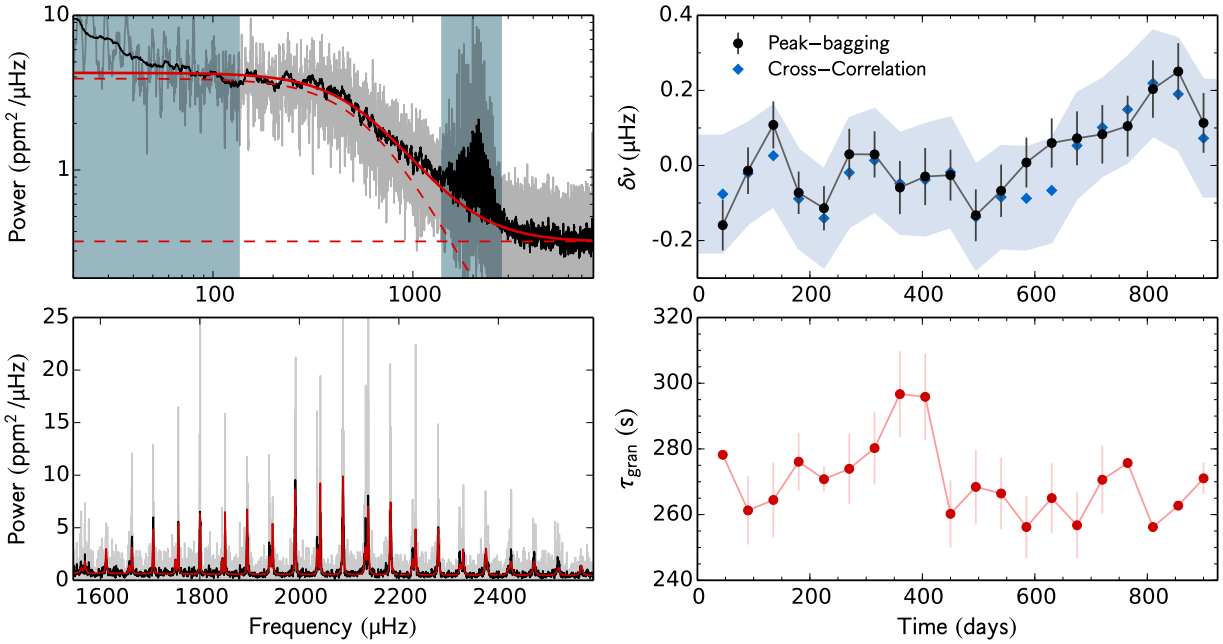

Fig. A.14 – Same as in Fig. A.1, but for KIC 5184732.

time (days)	d_c %	τ_{gran} (s)	Peak-bagging $\delta\nu_{l=0}$ (μHz)	$\delta\nu_{l=1}$ (μHz)	$\delta\nu_{l=2}$ (μHz)	$\delta\nu$ (μHz)	Cross-correlation $\delta\nu$ (μHz)
45	0.96	278.2 ± 0.4	-0.25 ± 0.09	-0.05 ± 0.10	-0.07 ± 0.13	-0.16 ± -0.16	-0.08 ± 0.16
90	0.78	261.3 ± 10.4	-0.09 ± 0.08	0.09 ± 0.10	-0.00 ± 0.13	-0.01 ± -0.01	-0.02 ± 0.14
135	0.73	264.5 ± 11.3	0.11 ± 0.08	0.10 ± 0.10	0.01 ± 0.13	0.11 ± 0.11	0.03 ± 0.14
180	0.92	276.1 ± 8.8	-0.07 ± 0.08	-0.07 ± 0.08	-0.13 ± 0.11	-0.07 ± -0.07	-0.09 ± 0.13
225	0.98	270.8 ± 3.8	-0.08 ± 0.08	-0.15 ± 0.09	-0.24 ± 0.12	-0.11 ± -0.11	-0.14 ± 0.13
270	0.97	273.9 ± 10.8	0.08 ± 0.09	-0.02 ± 0.10	-0.26 ± 0.14	0.03 ± 0.03	-0.02 ± 0.15
315	0.97	280.3 ± 11.0	0.05 ± 0.08	0.01 ± 0.09	0.07 ± 0.11	0.03 ± 0.03	0.01 ± 0.14
360	0.97	296.7 ± 13.0	-0.04 ± 0.11	-0.08 ± 0.10	-0.08 ± 0.14	-0.06 ± -0.06	-0.05 ± 0.13
405	0.94	295.9 ± 13.1	-0.07 ± 0.11	0.00 ± 0.11	-0.22 ± 0.15	-0.03 ± -0.03	-0.04 ± 0.15
450	0.91	260.2 ± 10.2	-0.05 ± 0.09	0.00 ± 0.10	-0.20 ± 0.15	-0.03 ± -0.03	-0.02 ± 0.15
495	0.88	268.4 ± 11.2	-0.06 ± 0.09	-0.22 ± 0.10	0.06 ± 0.14	-0.13 ± -0.13	-0.14 ± 0.14
540	0.92	266.4 ± 10.9	0.03 ± 0.09	-0.19 ± 0.11	-0.06 ± 0.13	-0.07 ± -0.07	-0.08 ± 0.14
585	0.97	256.2 ± 9.5	0.07 ± 0.09	-0.06 ± 0.10	-0.39 ± 0.14	0.01 ± 0.01	-0.09 ± 0.14
630	0.89	265.0 ± 10.6	0.12 ± 0.09	-0.00 ± 0.09	-0.28 ± 0.15	0.06 ± 0.06	-0.07 ± 0.14
675	0.89	256.8 ± 10.0	0.08 ± 0.10	0.06 ± 0.10	0.41 ± 0.15	0.07 ± 0.07	0.05 ± 0.14
720	0.95	270.6 ± 10.4	0.14 ± 0.11	0.02 ± 0.11	0.38 ± 0.17	0.08 ± 0.08	0.10 ± 0.13
765	0.89	275.7 ± 0.2	0.09 ± 0.11	0.12 ± 0.12	0.14 ± 0.16	0.10 ± 0.10	0.15 ± 0.14
810	0.81	256.2 ± 0.5	0.14 ± 0.11	0.28 ± 0.11	0.22 ± 0.15	0.20 ± 0.20	0.22 ± 0.14
855	0.84	262.7 ± 1.3	0.24 ± 0.11	0.26 ± 0.10	0.08 ± 0.13	0.25 ± 0.25	0.19 ± 0.15
900	0.92	271.0 ± 4.8	0.16 ± 0.12	0.08 ± 0.11	0.12 ± 0.17	0.11 ± 0.11	0.07 ± 0.16

Table A.14 – Same as in Table A.1, but for KIC 5184732.

KIC 5773345

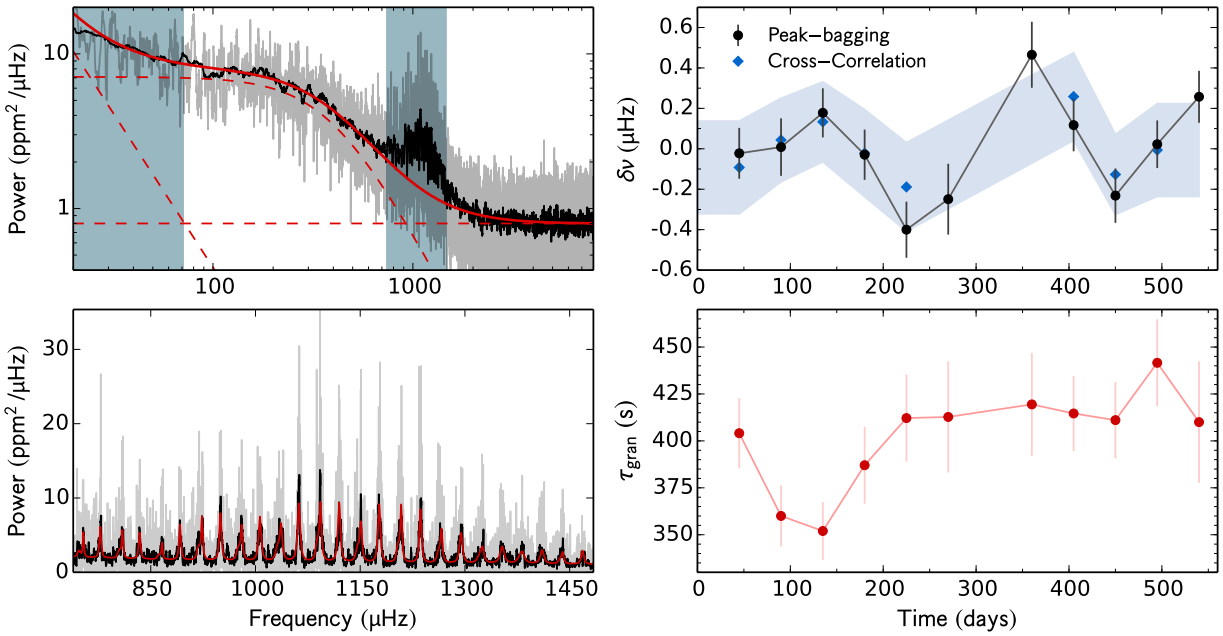

Fig. A.15 – Same as in Fig. A.1, but for KIC 5773345.

time (days)	d_c %	τ_{gran} (s)	Peak-bagging $\delta\nu_{l=0}$ (μHz)	$\delta\nu_{l=1}$ (μHz)	$\delta\nu_{l=2}$ (μHz)	$\delta\nu$ (μHz)	Cross-correlation $\delta\nu$ (μHz)
45	0.98	404.1 ± 18.7	0.08 ± 0.20	-0.10 ± 0.16	-1.02 ± 0.35	-0.02 ± -0.02	-0.09 ± 0.23
90	0.97	360.0 ± 16.2	-0.16 ± 0.23	0.12 ± 0.18	-0.51 ± 0.41	0.01 ± 0.01	0.04 ± 0.21
135	0.96	352.0 ± 15.5	0.12 ± 0.19	0.22 ± 0.16	-0.61 ± 0.30	0.18 ± 0.18	0.13 ± 0.20
180	0.78	387.0 ± 20.5	0.08 ± 0.19	-0.11 ± 0.17	-0.00 ± 0.33	-0.03 ± -0.03	-0.02 ± 0.22
225	0.71	412.1 ± 23.3	-0.34 ± 0.24	-0.43 ± 0.17	0.88 ± 0.35	-0.40 ± -0.40	-0.19 ± 0.22
270	0.42	412.7 ± 29.6	-0.26 ± 0.29	-0.24 ± 0.22	0.59 ± 0.41	-0.25 ± -0.25	–
360	0.41	419.4 ± 27.4	0.41 ± 0.24	0.51 ± 0.22	-0.04 ± 0.45	0.47 ± 0.47	–
405	0.90	414.6 ± 20.0	-0.01 ± 0.18	0.24 ± 0.18	0.09 ± 0.36	0.12 ± 0.12	0.26 ± 0.22
450	0.97	411.1 ± 20.4	-0.41 ± 0.21	-0.11 ± 0.18	0.22 ± 0.36	-0.23 ± -0.23	-0.13 ± 0.20
495	0.94	441.6 ± 23.2	0.25 ± 0.18	-0.15 ± 0.16	-0.04 ± 0.34	0.02 ± 0.02	-0.01 ± 0.23
540	0.00	410.0 ± 32.4	0.75 ± 0.18	-0.24 ± 0.18	0.29 ± 0.44	0.26 ± 0.26	–

Table A.15 – Same as in Table A.1, but for KIC 5773345.

KIC 5866724

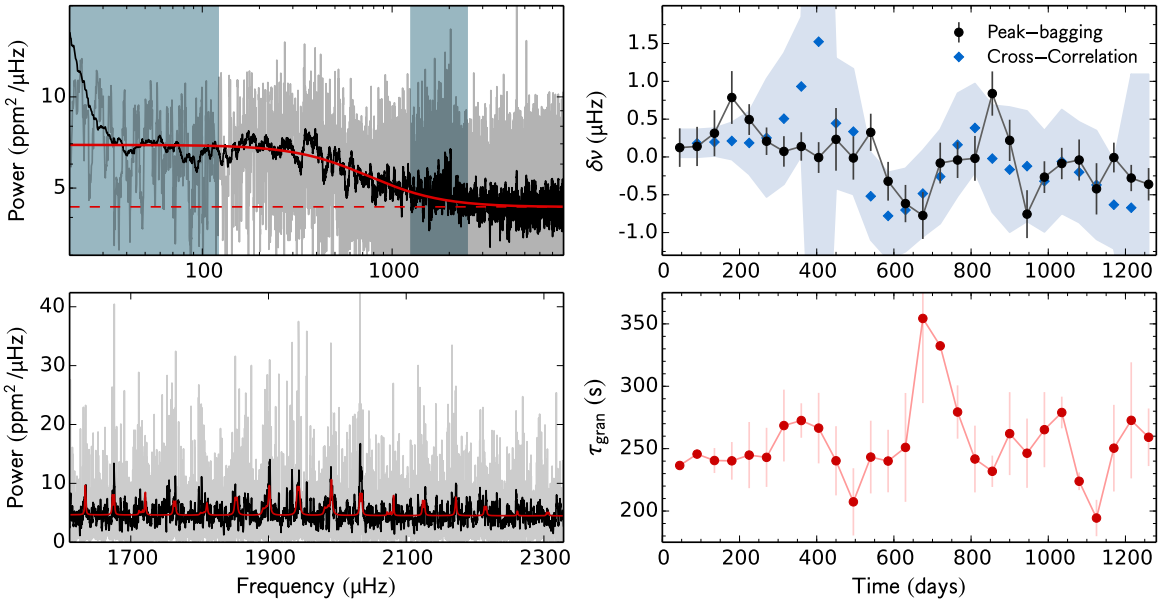

Fig. A.16 – Same as in Fig. A.1, but for KIC 5866724. Due to the extremely large error bars, the results from the cross-correlation method, that are shown here, were obtained from 180-d sub-series.

time (days)	d_c %	τ_{gran} (s)	Peak-bagging $\delta\nu_{l=0}$ (μHz)	$\delta\nu_{l=1}$ (μHz)	$\delta\nu_{l=2}$ (μHz)	$\delta\nu$ (μHz)	Cross-correlation $\delta\nu$ (μHz)
45	0.95	236.5 ± 1.0	-0.20 ± 0.41	0.33 ± 0.32	0.30 ± 0.78	0.12 ± 0.12	–
90	0.93	245.6 ± 0.0	0.05 ± 0.40	0.21 ± 0.34	-0.01 ± 0.83	0.14 ± 0.14	0.18 ± 0.18
135	0.92	240.5 ± 10.0	0.23 ± 0.36	0.51 ± 0.56	-0.06 ± 0.84	0.31 ± 0.31	0.20 ± 0.18
180	0.92	240.2 ± 15.1	1.05 ± 0.44	0.35 ± 0.57	0.39 ± 0.81	0.79 ± 0.79	0.21 ± 0.25
225	0.96	244.8 ± 26.5	0.68 ± 0.29	0.32 ± 0.28	1.12 ± 0.76	0.49 ± 0.49	0.19 ± 0.42
270	0.97	243.0 ± 23.7	0.34 ± 0.24	0.02 ± 0.28	0.77 ± 0.73	0.21 ± 0.21	0.25 ± 0.78
315	0.96	268.5 ± 28.8	0.07 ± 0.25	0.09 ± 0.33	0.09 ± 0.65	0.07 ± 0.07	0.51 ± 0.87
360	0.97	272.5 ± 13.8	0.48 ± 0.30	-0.08 ± 0.24	0.31 ± 0.72	0.14 ± 0.14	0.93 ± 0.92
405	0.97	266.5 ± 28.3	0.66 ± 0.41	-0.23 ± 0.23	0.83 ± 0.89	-0.01 ± -0.01	1.52 ± 6.81
450	0.80	240.3 ± 27.7	0.58 ± 0.59	-0.11 ± 0.58	-0.74 ± 0.87	0.23 ± 0.23	0.45 ± 0.86
495	0.79	207.4 ± 26.9	0.16 ± 0.44	-0.14 ± 0.38	-0.88 ± 0.72	-0.01 ± -0.01	0.33 ± 0.83
540	0.90	243.2 ± 29.1	0.62 ± 0.31	-0.15 ± 0.40	-0.41 ± 0.74	0.33 ± 0.33	-0.52 ± 0.58
585	0.91	240.1 ± 25.1	-0.51 ± 0.34	-0.08 ± 0.39	-0.49 ± 0.78	-0.32 ± -0.32	-0.78 ± 0.58
630	0.97	251.0 ± 43.6	-0.79 ± 0.32	-0.37 ± 0.38	-0.21 ± 0.70	-0.62 ± -0.62	-0.70 ± 0.55
675	0.97	354.3 ± 67.8	-0.36 ± 0.46	-1.11 ± 0.42	0.23 ± 0.88	-0.77 ± -0.77	-0.48 ± 0.57
720	0.97	332.4 ± 1.7	-0.04 ± 0.39	-0.12 ± 0.38	0.36 ± 0.89	-0.08 ± -0.08	-0.26 ± 0.62
765	0.97	279.4 ± 21.4	-0.07 ± 0.32	-0.01 ± 0.36	0.29 ± 0.80	-0.04 ± -0.04	0.16 ± 0.68
810	0.94	241.7 ± 26.7	0.22 ± 0.38	-0.37 ± 0.47	-0.34 ± 0.85	-0.02 ± -0.02	0.38 ± 0.59
855	0.91	231.9 ± 12.6	1.09 ± 0.37	0.43 ± 0.47	0.43 ± 0.91	0.84 ± 0.84	-0.02 ± 0.71
900	0.88	262.0 ± 33.3	-0.10 ± 0.36	0.63 ± 0.41	1.57 ± 0.79	0.22 ± 0.22	-0.17 ± 0.83
945	0.92	246.3 ± 27.8	-1.19 ± 0.40	-0.04 ± 0.52	0.61 ± 0.81	-0.76 ± -0.76	-0.12 ± 0.73
990	0.90	265.2 ± 30.1	-0.44 ± 0.26	0.07 ± 0.36	0.18 ± 0.80	-0.27 ± -0.27	-0.32 ± 0.67
1035	0.89	279.0 ± 12.7	-0.24 ± 0.29	0.08 ± 0.30	-0.51 ± 0.78	-0.09 ± -0.09	-0.06 ± 0.69
1080	0.94	223.9 ± 7.1	-0.08 ± 0.40	-0.01 ± 0.37	-1.03 ± 0.79	-0.04 ± -0.04	-0.20 ± 0.67
1125	0.90	194.4 ± 14.6	-0.64 ± 0.63	-0.33 ± 0.40	-1.55 ± 0.73	-0.42 ± -0.42	-0.37 ± 0.72
1170	0.90	250.4 ± 34.7	0.11 ± 0.27	-0.13 ± 0.28	-0.87 ± 0.84	-0.01 ± -0.01	-0.63 ± 0.58
1215	0.85	272.7 ± 46.5	-0.27 ± 0.20	-0.31 ± 0.35	0.52 ± 0.82	-0.28 ± -0.28	-0.67 ± 1.76
1260	0.84	259.1 ± 23.1	-0.07 ± 0.30	-0.68 ± 0.31	-0.44 ± 0.88	-0.36 ± -0.36	–

Table A.16 – Same as in Table A.1, but for KIC 5866724. Due to the extremely large error bars, the results from the cross-correlation method, that are shown here, were obtained from 180-d sub-series.

KIC 5950854

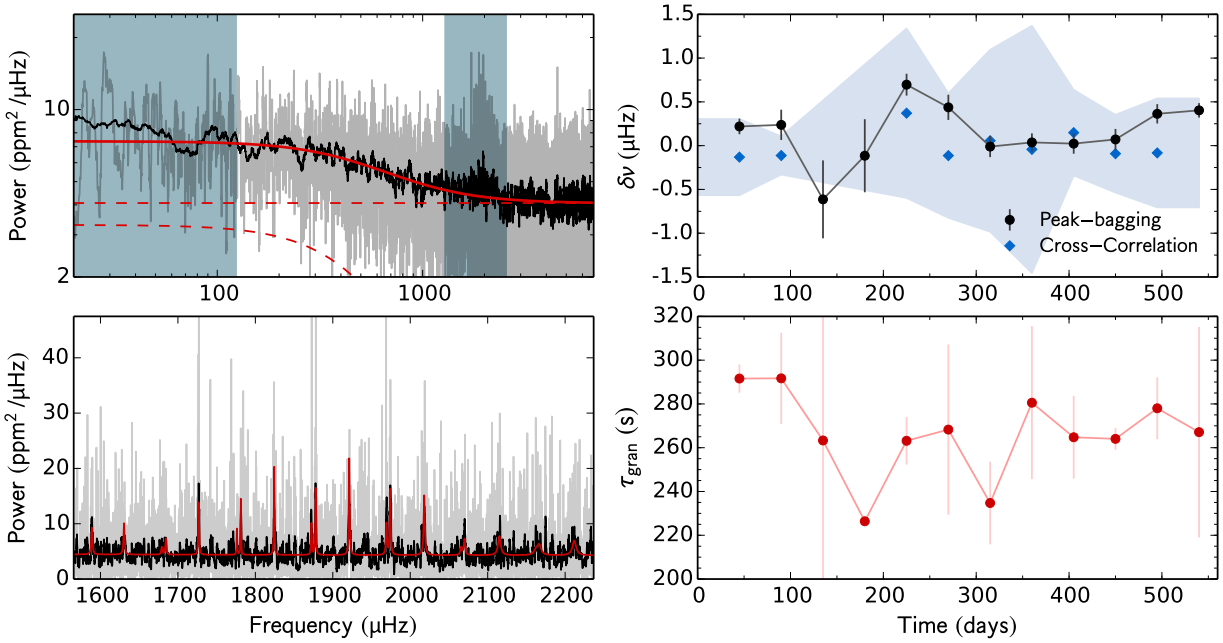

Fig. A.17 – Same as in Fig. A.1, but for KIC 5950854.

time (days)	d_c %	τ_{gran} (s)	Peak-bagging $\delta\nu_{l=0}$ (μHz)	$\delta\nu_{l=1}$ (μHz)	$\delta\nu_{l=2}$ (μHz)	$\delta\nu$ (μHz)	Cross-correlation $\delta\nu$ (μHz)
45	0.97	291.6 ± 6.5	0.73 ± 0.13	-0.19 ± 0.12	0.13 ± 0.37	0.22 ± 0.22	-0.13 ± 0.43
90	0.54	291.7 ± 20.8	0.70 ± 0.25	-0.16 ± 0.24	0.01 ± 0.66	0.24 ± 0.24	-0.11 ± 0.22
135	0.05	263.3 ± 139.9	-0.66 ± 0.71	-0.58 ± 0.57	0.28 ± 0.94	-0.61 ± -0.61	–
180	0.33	226.4 ± 1.5	-0.60 ± 0.61	0.31 ± 0.57	-0.29 ± 0.76	-0.12 ± -0.12	–
225	0.58	263.2 ± 10.8	1.05 ± 0.16	0.18 ± 0.20	0.65 ± 0.46	0.70 ± 0.70	0.37 ± 0.97
270	0.56	268.3 ± 38.9	0.88 ± 0.22	0.12 ± 0.19	0.30 ± 0.45	0.44 ± 0.44	-0.11 ± 0.71
315	0.78	234.7 ± 18.9	0.22 ± 0.22	-0.12 ± 0.15	-0.21 ± 0.22	-0.01 ± -0.01	0.06 ± 1.04
360	0.89	280.6 ± 34.9	0.36 ± 0.22	-0.06 ± 0.12	-0.28 ± 0.21	0.04 ± 0.04	-0.04 ± 1.41
405	0.93	264.8 ± 18.9	0.51 ± 0.32	-0.05 ± 0.12	0.42 ± 0.37	0.02 ± 0.02	0.15 ± 0.49
450	0.97	264.0 ± 5.0	0.28 ± 0.18	-0.09 ± 0.16	-0.09 ± 0.25	0.07 ± 0.07	-0.09 ± 0.44
495	0.97	278.0 ± 14.1	0.53 ± 0.13	0.00 ± 0.20	-0.15 ± 0.24	0.36 ± 0.36	-0.08 ± 0.62
540	0.67	267.1 ± 48.1	0.58 ± 0.11	0.15 ± 0.13	-0.38 ± 0.32	0.40 ± 0.40	–

Table A.17 – Same as in Table A.1, but for KIC 5950854.

KIC 6106415

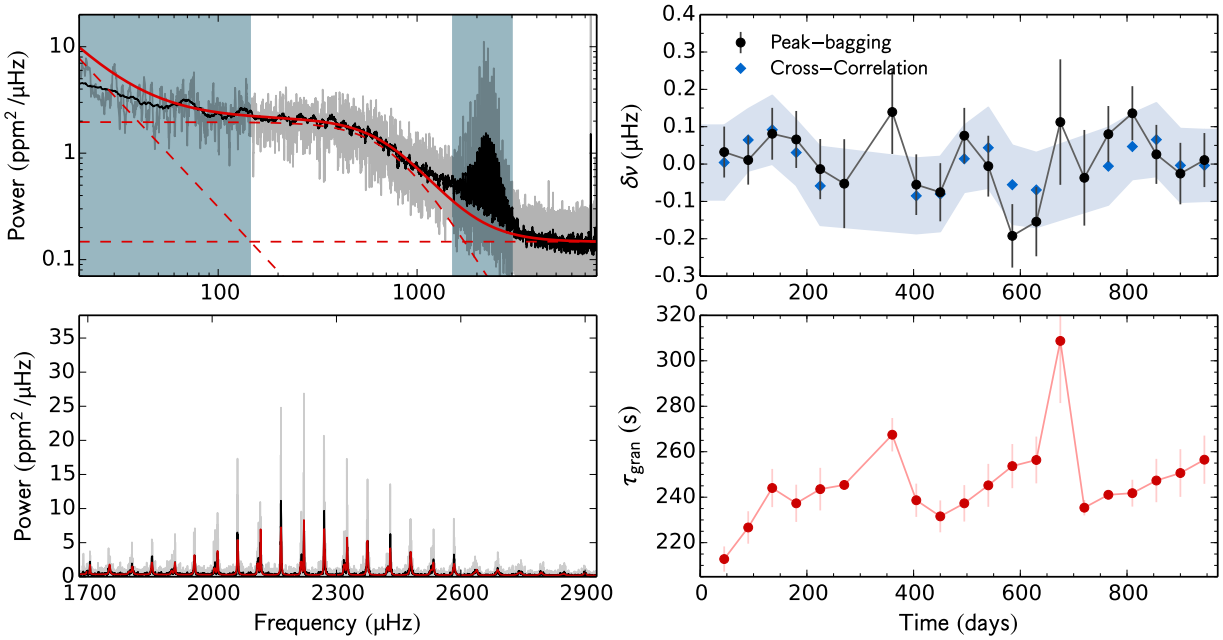

Fig. A.18 – Same as in Fig. A.1, but for KIC 6106415.

time (days)	d_c %	τ_{gran} (s)	Peak-bagging $\delta\nu_{l=0}$ (μHz)	$\delta\nu_{l=1}$ (μHz)	$\delta\nu_{l=2}$ (μHz)	$\delta\nu$ (μHz)	Cross-correlation $\delta\nu$ (μHz)
45	0.97	205.5 ± 5.7	-0.07 ± 0.09	0.17 ± 0.11	0.11 ± 0.13	0.03 ± 0.03	0.00 ± 0.10
90	0.97	220.0 ± 6.9	-0.05 ± 0.09	0.10 ± 0.10	0.07 ± 0.13	0.01 ± 0.01	0.06 ± 0.08
135	0.96	237.9 ± 8.3	0.04 ± 0.09	0.15 ± 0.11	-0.06 ± 0.13	0.08 ± 0.08	0.09 ± 0.09
180	0.77	234.1 ± 8.6	0.05 ± 0.10	0.09 ± 0.12	0.27 ± 0.15	0.07 ± 0.07	0.03 ± 0.09
225	0.71	237.1 ± 9.3	0.07 ± 0.11	-0.12 ± 0.12	0.27 ± 0.16	-0.01 ± -0.01	-0.06 ± 0.11
270	0.42	237.3 ± 0.5	0.02 ± 0.17	-0.12 ± 0.17	0.11 ± 0.25	-0.05 ± -0.05	–
360	0.41	262.8 ± 1.3	-0.01 ± 0.16	0.28 ± 0.16	0.25 ± 0.19	0.14 ± 0.14	–
405	0.90	231.8 ± 7.5	-0.17 ± 0.11	0.06 ± 0.12	0.06 ± 0.14	-0.06 ± -0.06	-0.09 ± 0.10
450	0.97	228.7 ± 7.3	-0.14 ± 0.11	-0.01 ± 0.11	-0.23 ± 0.16	-0.08 ± -0.08	-0.08 ± 0.10
495	0.94	224.2 ± 7.4	0.00 ± 0.10	0.16 ± 0.11	-0.08 ± 0.15	0.08 ± 0.08	0.01 ± 0.09
540	0.91	226.6 ± 8.6	-0.07 ± 0.11	0.07 ± 0.12	0.13 ± 0.14	-0.01 ± -0.01	0.04 ± 0.11
585	0.88	244.8 ± 10.1	-0.18 ± 0.11	-0.21 ± 0.13	0.07 ± 0.16	-0.19 ± -0.19	-0.06 ± 0.11
630	0.57	255.4 ± 11.7	-0.04 ± 0.12	-0.34 ± 0.15	-0.14 ± 0.18	-0.15 ± -0.15	-0.07 ± 0.10
675	0.14	310.8 ± 1.1	0.38 ± 0.23	-0.22 ± 0.25	-0.41 ± 0.27	0.11 ± 0.11	–
720	0.26	235.1 ± 5.6	-0.03 ± 0.18	-0.04 ± 0.19	-0.10 ± 0.23	-0.04 ± -0.04	–
765	0.74	237.0 ± 7.3	0.10 ± 0.11	0.07 ± 0.10	0.01 ± 0.14	0.08 ± 0.08	-0.01 ± 0.10
810	0.95	236.2 ± 6.8	0.07 ± 0.11	0.18 ± 0.09	0.27 ± 0.12	0.14 ± 0.14	0.05 ± 0.09
855	0.89	245.1 ± 10.0	-0.15 ± 0.12	0.16 ± 0.10	0.10 ± 0.15	0.03 ± 0.03	0.07 ± 0.10
900	0.82	252.6 ± 11.0	-0.12 ± 0.12	0.06 ± 0.11	-0.37 ± 0.16	-0.03 ± -0.03	-0.00 ± 0.10
945	0.84	261.2 ± 11.6	-0.04 ± 0.10	0.07 ± 0.11	-0.34 ± 0.16	0.01 ± 0.01	-0.00 ± 0.10

Table A.18 – Same as in Table A.1, but for KIC 6106415.

KIC 6116048

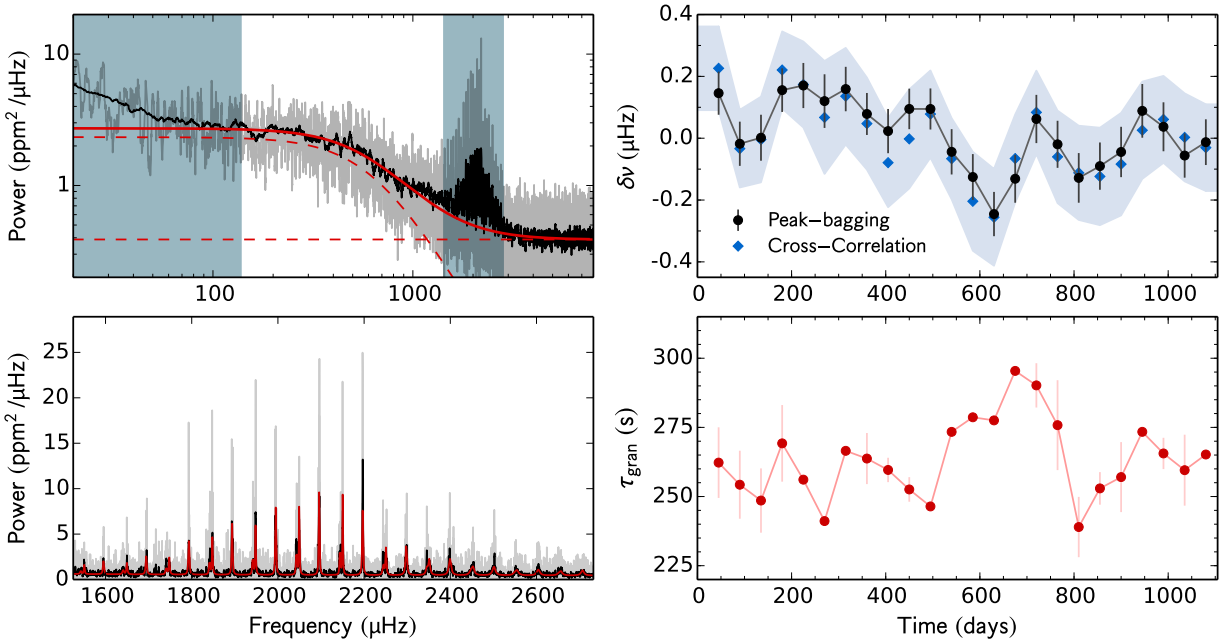

Fig. A.19 – Same as in Fig. A.1, but for KIC 6116048.

time (days)	d_c %	τ_{gran} (s)	Peak-bagging $\delta\nu_{l=0}$ (μHz)	$\delta\nu_{l=1}$ (μHz)	$\delta\nu_{l=2}$ (μHz)	$\delta\nu$ (μHz)	Cross-correlation $\delta\nu$ (μHz)
45	0.98	262.3 ± 12.8	0.04 ± 0.10	0.26 ± 0.10	-0.01 ± 0.15	0.15 ± 0.15	0.23 ± 0.14
90	0.97	254.3 ± 12.3	0.02 ± 0.10	-0.05 ± 0.10	0.11 ± 0.14	-0.02 ± -0.02	-0.03 ± 0.13
135	0.96	248.6 ± 11.6	-0.05 ± 0.11	0.05 ± 0.10	0.12 ± 0.14	0.00 ± 0.00	-0.00 ± 0.14
180	0.97	269.2 ± 13.9	0.04 ± 0.10	0.28 ± 0.10	0.20 ± 0.16	0.16 ± 0.16	0.22 ± 0.12
225	0.96	256.1 ± 1.6	0.19 ± 0.10	0.15 ± 0.11	0.46 ± 0.15	0.17 ± 0.17	0.17 ± 0.14
270	0.80	241.1 ± 0.2	0.20 ± 0.13	0.05 ± 0.12	0.15 ± 0.18	0.12 ± 0.12	0.07 ± 0.18
315	0.78	266.5 ± 0.0	0.23 ± 0.10	0.07 ± 0.11	-0.13 ± 0.15	0.16 ± 0.16	0.14 ± 0.16
360	0.89	263.7 ± 9.2	0.13 ± 0.09	0.02 ± 0.10	-0.18 ± 0.18	0.08 ± 0.08	0.05 ± 0.15
405	0.93	259.6 ± 4.4	0.08 ± 0.10	-0.04 ± 0.10	0.02 ± 0.16	0.02 ± 0.02	-0.08 ± 0.14
450	0.97	252.6 ± 4.4	0.16 ± 0.09	0.03 ± 0.09	-0.03 ± 0.15	0.09 ± 0.09	-0.00 ± 0.16
495	0.97	246.4 ± nan	0.13 ± 0.09	0.05 ± 0.10	-0.14 ± 0.12	0.09 ± 0.09	0.08 ± 0.14
540	0.98	273.4 ± nan	-0.03 ± 0.11	-0.05 ± 0.10	-0.29 ± 0.17	-0.04 ± -0.04	-0.07 ± 0.13
585	0.94	278.7 ± 0.4	-0.06 ± 0.12	-0.17 ± 0.10	-0.27 ± 0.17	-0.13 ± -0.13	-0.20 ± 0.16
630	0.92	277.5 ± 0.2	-0.20 ± 0.11	-0.28 ± 0.10	0.04 ± 0.16	-0.25 ± -0.25	-0.26 ± 0.16
675	0.90	295.4 ± nan	-0.09 ± 0.11	-0.17 ± 0.11	-0.09 ± 0.18	-0.13 ± -0.13	-0.07 ± 0.14
720	0.90	290.2 ± 8.0	0.00 ± 0.11	0.12 ± 0.11	-0.10 ± 0.19	0.06 ± 0.06	0.08 ± 0.14
765	0.95	275.8 ± 16.3	-0.10 ± 0.11	0.07 ± 0.11	0.35 ± 0.19	-0.02 ± -0.02	-0.06 ± 0.15
810	0.90	239.0 ± 10.9	-0.18 ± 0.11	-0.08 ± 0.11	0.20 ± 0.19	-0.13 ± -0.13	-0.11 ± 0.15
855	0.89	252.9 ± 5.9	-0.02 ± 0.11	-0.16 ± 0.11	0.16 ± 0.17	-0.09 ± -0.09	-0.12 ± 0.16
900	0.95	257.0 ± 12.7	0.06 ± 0.12	-0.13 ± 0.11	0.13 ± 0.18	-0.04 ± -0.04	-0.08 ± 0.17
945	0.90	273.4 ± 1.2	0.27 ± 0.13	-0.07 ± 0.12	-0.09 ± 0.16	0.09 ± 0.09	0.03 ± 0.16
990	0.89	265.6 ± 5.7	0.04 ± 0.11	0.03 ± 0.12	-0.32 ± 0.16	0.04 ± 0.04	0.06 ± 0.14
1035	0.85	259.5 ± 12.8	-0.19 ± 0.10	0.10 ± 0.10	-0.22 ± 0.15	-0.06 ± -0.06	0.00 ± 0.14
1080	0.85	265.2 ± 0.5	-0.07 ± 0.10	0.06 ± 0.11	-0.09 ± 0.17	-0.01 ± -0.01	-0.03 ± 0.14

Table A.19 – Same as in Table A.1, but for KIC 6116048.

KIC 6225718

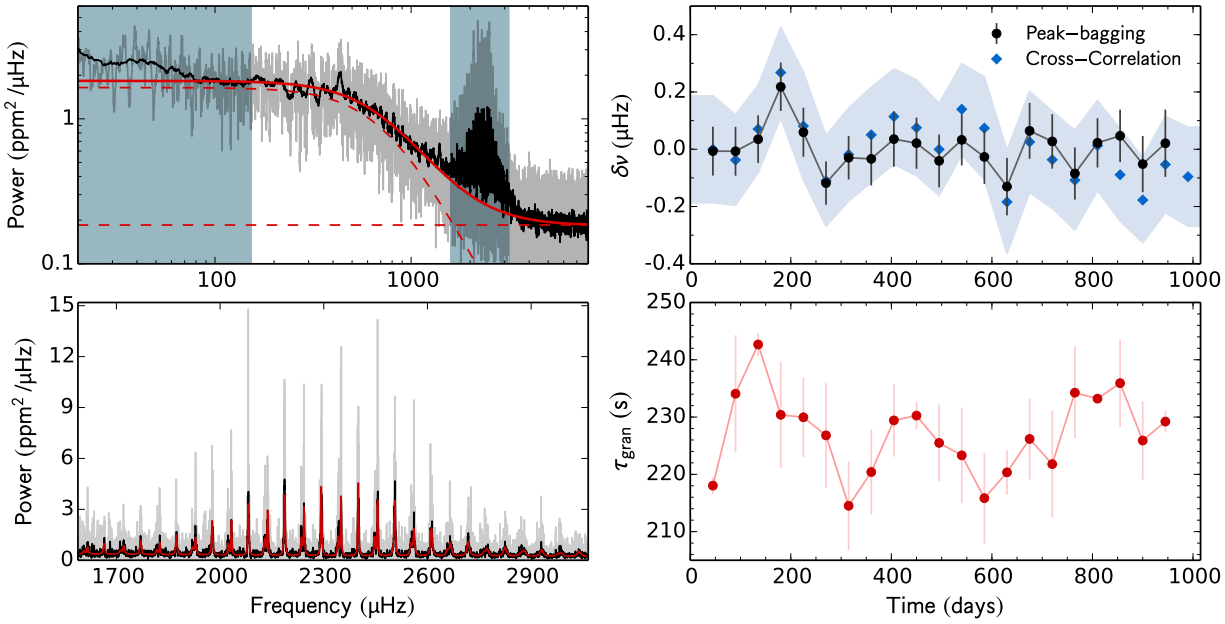

Fig. A.20 – Same as in Fig. A.1, but for KIC 6225718.

time (days)	d_c %	τ_{gran} (s)	Peak-bagging $\delta\nu_{l=0}$ (μHz)	$\delta\nu_{l=1}$ (μHz)	$\delta\nu_{l=2}$ (μHz)	$\delta\nu$ (μHz)	Cross-correlation $\delta\nu$ (μHz)
45	0.98	218.0 ± 6.8	-0.01 ± 0.12	-0.00 ± 0.12	0.40 ± 0.18	-0.01 ± -0.01	-0.00 ± 0.19
90	0.97	234.1 ± 10.9	0.06 ± 0.12	-0.07 ± 0.12	0.25 ± 0.18	-0.01 ± -0.01	-0.04 ± 0.16
135	0.96	242.7 ± 0.5	-0.07 ± 0.12	0.13 ± 0.12	-0.08 ± 0.18	0.04 ± 0.04	0.07 ± 0.15
180	0.78	230.4 ± 8.3	0.04 ± 0.12	0.39 ± 0.12	-0.00 ± 0.19	0.22 ± 0.22	0.27 ± 0.16
225	0.72	230.0 ± 0.0	0.06 ± 0.12	0.06 ± 0.12	0.03 ± 0.18	0.06 ± 0.06	0.08 ± 0.19
270	0.92	226.8 ± 1.4	-0.14 ± 0.10	-0.09 ± 0.11	0.29 ± 0.18	-0.12 ± -0.12	-0.11 ± 0.16
315	0.98	214.5 ± 7.8	0.08 ± 0.10	-0.16 ± 0.11	0.42 ± 0.19	-0.03 ± -0.03	-0.02 ± 0.16
360	0.97	220.4 ± 6.8	0.03 ± 0.13	-0.09 ± 0.13	0.06 ± 0.19	-0.03 ± -0.03	0.05 ± 0.17
405	0.97	229.4 ± 0.4	-0.08 ± 0.14	0.14 ± 0.13	-0.12 ± 0.20	0.04 ± 0.04	0.11 ± 0.17
450	0.97	230.3 ± 0.1	0.02 ± 0.12	0.03 ± 0.13	-0.01 ± 0.18	0.02 ± 0.02	0.08 ± 0.17
495	0.94	225.5 ± 0.8	-0.01 ± 0.13	-0.08 ± 0.13	-0.21 ± 0.17	-0.04 ± -0.04	-0.00 ± 0.16
540	0.91	223.3 ± 10.1	-0.05 ± 0.13	0.11 ± 0.12	-0.38 ± 0.19	0.03 ± 0.03	0.14 ± 0.16
585	0.88	215.8 ± 9.1	-0.15 ± 0.14	0.08 ± 0.13	-0.17 ± 0.21	-0.03 ± -0.03	0.07 ± 0.18
630	0.92	220.3 ± 7.3	-0.08 ± 0.15	-0.17 ± 0.13	0.05 ± 0.21	-0.13 ± -0.13	-0.18 ± 0.18
675	0.97	226.2 ± 7.0	0.20 ± 0.15	-0.05 ± 0.13	0.15 ± 0.21	0.06 ± 0.06	0.03 ± 0.18
720	0.89	221.8 ± 10.9	0.02 ± 0.14	0.03 ± 0.13	-0.03 ± 0.21	0.03 ± 0.03	-0.04 ± 0.17
765	0.88	234.3 ± 4.3	-0.08 ± 0.13	-0.09 ± 0.13	-0.17 ± 0.22	-0.08 ± -0.08	-0.11 ± 0.17
810	0.94	233.2 ± 1.0	0.04 ± 0.12	0.01 ± 0.12	-0.09 ± 0.19	0.02 ± 0.02	0.01 ± 0.16
855	0.88	235.9 ± 1.4	-0.01 ± 0.13	0.10 ± 0.12	-0.28 ± 0.19	0.05 ± 0.05	-0.09 ± 0.16
900	0.82	225.9 ± 8.1	0.05 ± 0.15	-0.13 ± 0.13	-0.09 ± 0.19	-0.05 ± -0.05	-0.18 ± 0.15
945	0.84	229.2 ± 2.8	0.08 ± 0.17	-0.04 ± 0.17	0.04 ± 0.23	0.02 ± 0.02	-0.05 ± 0.17
990	–	–	–	–	–	–	-0.10 ± 0.17

Table A.20 – Same as in Table A.1, but for KIC 6225718.

KIC 6278762

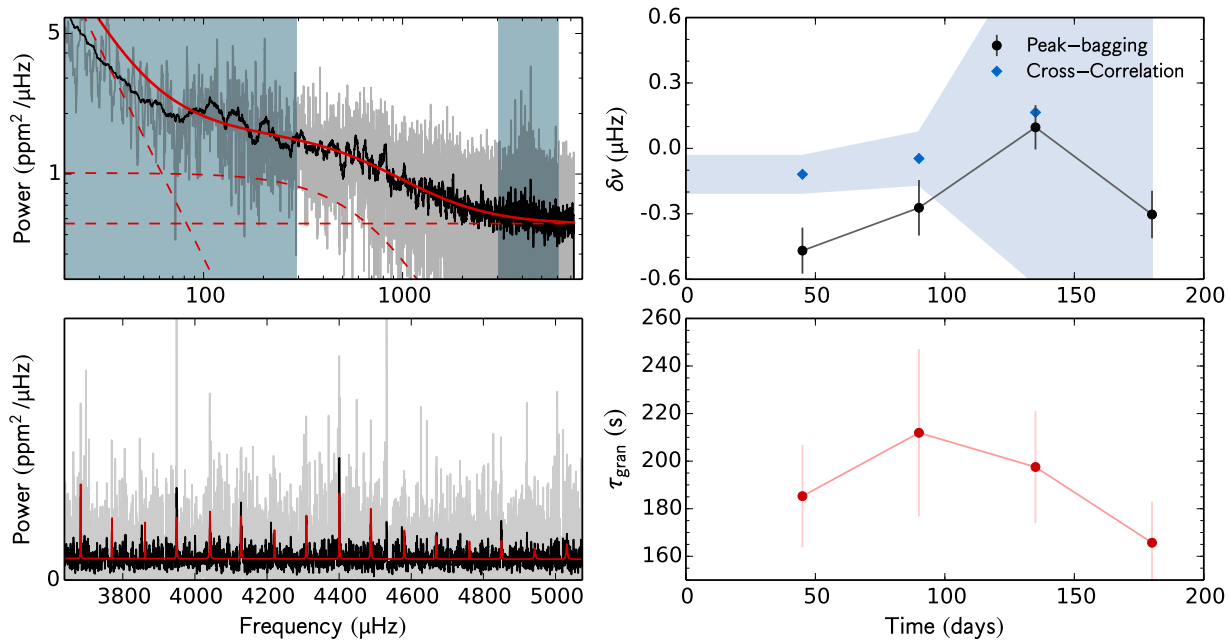

Fig. A.21 – Same as in Fig. A.1, but for KIC 6278762.

time (days)	d_c %	τ_{gran} (s)	Peak-bagging $\delta\nu_{l=0}$ (μHz)	$\delta\nu_{l=1}$ (μHz)	$\delta\nu_{l=2}$ (μHz)	$\delta\nu$ (μHz)	Cross-correlation $\delta\nu$ (μHz)
45	0.91	185.3 ± 21.5	-0.55 ± 0.15	-0.39 ± 0.15	0.00 ± 0.00	-0.47 ± -0.47	-0.12 ± 0.09
90	0.85	211.9 ± 35.2	-0.56 ± 0.16	0.24 ± 0.21	0.00 ± 0.00	-0.27 ± -0.27	-0.05 ± 0.12
135	0.84	197.5 ± 23.6	-0.07 ± 0.14	0.30 ± 0.15	0.00 ± 0.00	0.10 ± 0.10	0.17 ± 0.79
180	0.82	165.7 ± 17.2	-0.36 ± 0.16	-0.25 ± 0.15	0.00 ± 0.00	-0.30 ± -0.30	–

Table A.21 – Same as in Table A.1, but for KIC 6278762.

KIC 6508366

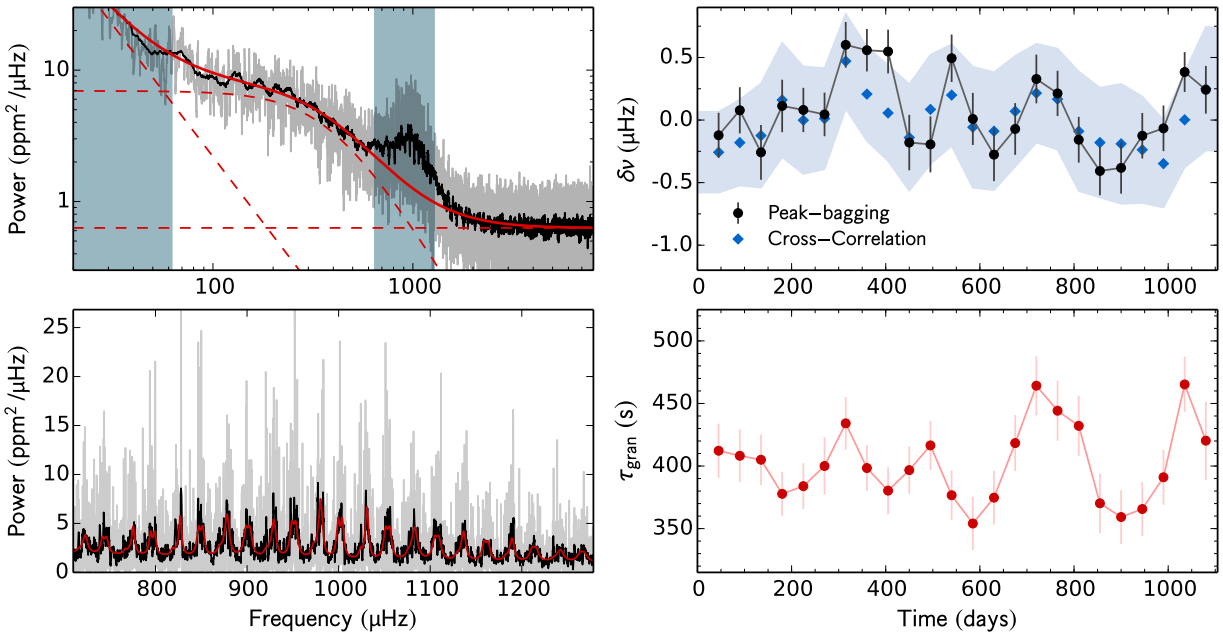

Fig. A.22 – Same as in Fig. A.1, but for KIC 6508366.

time (days)	d_c %	τ_{gran} (s)	Peak-bagging $\delta\nu_{l=0}$ (μHz)	$\delta\nu_{l=1}$ (μHz)	$\delta\nu_{l=2}$ (μHz)	$\delta\nu$ (μHz)	Cross-correlation $\delta\nu$ (μHz)
45	0.98	412.2 ± 21.6	0.16 ± 0.27	-0.36 ± 0.24	-0.60 ± 0.44	-0.12 ± -0.12	-0.26 ± 0.32
90	0.97	408.2 ± 21.1	0.21 ± 0.28	-0.02 ± 0.24	-0.12 ± 0.48	0.08 ± 0.08	-0.18 ± 0.34
135	0.96	405.0 ± 20.3	-0.41 ± 0.33	-0.13 ± 0.30	-0.36 ± 0.52	-0.26 ± -0.26	-0.12 ± 0.42
180	0.97	377.8 ± 17.6	-0.05 ± 0.29	0.30 ± 0.31	-0.67 ± 0.48	0.11 ± 0.11	0.16 ± 0.46
225	0.96	383.9 ± 18.3	-0.28 ± 0.25	0.47 ± 0.26	0.14 ± 0.40	0.08 ± 0.08	-0.00 ± 0.43
270	0.81	400.0 ± 22.9	0.00 ± 0.24	0.09 ± 0.25	0.67 ± 0.48	0.04 ± 0.04	0.01 ± 0.40
315	0.78	434.1 ± 21.0	0.87 ± 0.27	0.37 ± 0.25	0.56 ± 0.60	0.60 ± 0.60	0.47 ± 0.38
360	0.89	398.4 ± 18.2	0.83 ± 0.25	0.31 ± 0.23	-0.35 ± 0.47	0.56 ± 0.56	0.21 ± 0.37
405	0.93	380.3 ± 18.7	0.79 ± 0.27	0.37 ± 0.23	-0.72 ± 0.54	0.55 ± 0.55	0.06 ± 0.38
450	0.97	396.8 ± 18.9	-0.34 ± 0.36	-0.09 ± 0.28	-0.27 ± 0.57	-0.18 ± -0.18	-0.14 ± 0.43
495	0.97	416.5 ± 19.8	-0.18 ± 0.37	-0.20 ± 0.28	0.21 ± 0.53	-0.19 ± -0.19	0.09 ± 0.44
540	0.98	376.7 ± 19.8	0.84 ± 0.29	0.23 ± 0.25	-0.28 ± 0.55	0.49 ± 0.49	0.20 ± 0.41
585	0.94	354.1 ± 21.3	-0.35 ± 0.31	0.31 ± 0.28	1.28 ± 0.42	0.01 ± 0.01	-0.06 ± 0.48
630	0.92	374.7 ± 21.5	-0.40 ± 0.33	-0.18 ± 0.28	0.95 ± 0.48	-0.28 ± -0.28	-0.09 ± 0.47
675	0.90	418.3 ± 22.3	0.35 ± 0.32	-0.37 ± 0.27	0.18 ± 0.54	-0.07 ± -0.07	0.07 ± 0.44
720	0.91	464.2 ± 23.5	0.63 ± 0.30	0.11 ± 0.26	-0.25 ± 0.50	0.33 ± 0.33	0.22 ± 0.39
765	0.95	444.2 ± 24.0	0.08 ± 0.29	0.30 ± 0.23	-0.10 ± 0.43	0.21 ± 0.21	0.17 ± 0.40
810	0.90	432.1 ± 24.0	-0.62 ± 0.31	0.09 ± 0.23	-0.41 ± 0.48	-0.16 ± -0.16	-0.09 ± 0.48
855	0.89	370.2 ± 23.9	-0.77 ± 0.32	-0.20 ± 0.24	0.19 ± 0.47	-0.41 ± -0.41	-0.18 ± 0.44
900	0.95	359.2 ± 21.5	-0.38 ± 0.32	-0.39 ± 0.27	0.31 ± 0.45	-0.38 ± -0.38	-0.19 ± 0.48
945	0.90	365.7 ± 21.5	-0.12 ± 0.26	-0.13 ± 0.25	-0.20 ± 0.46	-0.13 ± -0.13	-0.24 ± 0.43
990	0.89	391.0 ± 21.8	0.23 ± 0.24	-0.50 ± 0.29	-0.16 ± 0.46	-0.07 ± -0.07	-0.35 ± 0.35
1035	0.85	465.2 ± 22.2	0.54 ± 0.20	0.10 ± 0.27	0.73 ± 0.67	0.38 ± 0.38	0.00 ± 0.38
1080	0.85	420.3 ± 31.3	0.04 ± 0.28	0.40 ± 0.26	-0.28 ± 0.60	0.24 ± 0.24	0.25 ± 0.49

Table A.22 – Same as in Table A.1, but for KIC 6508366.

KIC 6521045

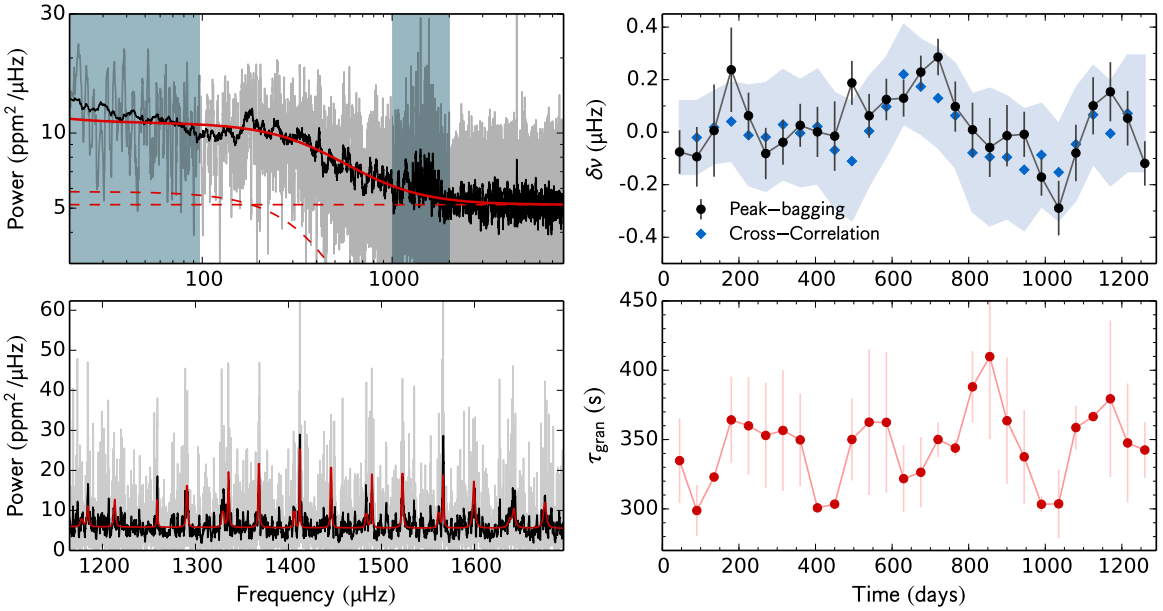

Fig. A.23 – Same as in Fig. A.1, but for KIC 6521045. Due to the extremely large error bars, the results from the cross-correlation method, that are shown here, were obtained from 180-d sub-series.

time (days)	d_c %	τ_{gran} (s)	Peak-bagging $\delta\nu_{l=0}$ (μHz)	$\delta\nu_{l=1}$ (μHz)	$\delta\nu_{l=2}$ (μHz)	$\delta\nu$ (μHz)	Cross-correlation $\delta\nu$ (μHz)
45	0.95	334.8 ± 30.7	-0.13 ± 0.09	0.01 ± 0.17	-0.26 ± 0.29	-0.08 ± -0.08	–
90	0.93	298.8 ± 18.5	-0.05 ± 0.13	-0.27 ± 0.20	-0.18 ± 0.27	-0.09 ± -0.09	-0.02 ± 0.14
135	0.92	323.0 ± nan	0.04 ± 0.26	-0.10 ± 0.23	-0.03 ± 0.46	0.01 ± 0.01	0.02 ± 0.14
180	0.92	364.2 ± 31.2	0.18 ± 0.23	0.29 ± 0.21	-0.63 ± 0.44	0.24 ± 0.24	0.04 ± 0.15
225	0.96	359.9 ± 35.1	0.08 ± 0.14	0.05 ± 0.11	-0.18 ± 0.22	0.06 ± 0.06	-0.01 ± 0.19
270	0.97	353.0 ± 38.0	-0.14 ± 0.14	-0.03 ± 0.13	0.04 ± 0.26	-0.08 ± -0.08	-0.02 ± 0.21
315	0.96	356.6 ± 43.6	-0.13 ± 0.10	0.26 ± 0.14	0.01 ± 0.24	-0.04 ± -0.04	0.03 ± 0.21
360	0.97	349.8 ± 33.4	-0.01 ± 0.11	0.16 ± 0.13	-0.42 ± 0.33	0.03 ± 0.03	-0.00 ± 0.20
405	0.97	300.7 ± 1.2	-0.02 ± 0.12	0.07 ± 0.14	-0.13 ± 0.34	0.00 ± 0.00	0.02 ± 0.22
450	0.80	303.4 ± 0.2	-0.11 ± 0.19	0.06 ± 0.18	-0.21 ± 0.38	-0.02 ± -0.02	-0.07 ± 0.22
495	0.78	350.1 ± 29.5	0.32 ± 0.12	0.07 ± 0.11	-0.04 ± 0.26	0.19 ± 0.19	-0.11 ± 0.23
540	0.89	362.6 ± 52.5	0.06 ± 0.15	0.05 ± 0.11	0.06 ± 0.36	0.06 ± 0.06	0.00 ± 0.21
585	0.91	362.4 ± 50.7	0.10 ± 0.11	0.09 ± 0.11	0.55 ± 0.28	0.12 ± 0.12	0.10 ± 0.19
630	0.97	321.8 ± 24.3	0.08 ± 0.09	0.22 ± 0.11	0.63 ± 0.26	0.13 ± 0.13	0.22 ± 0.19
675	0.97	326.4 ± 25.3	0.22 ± 0.08	0.24 ± 0.10	0.47 ± 0.24	0.23 ± 0.23	0.17 ± 0.18
720	0.97	350.1 ± 12.6	0.21 ± 0.10	0.29 ± 0.10	0.49 ± 0.20	0.29 ± 0.29	0.13 ± 0.19
765	0.97	343.9 ± 5.5	0.12 ± 0.15	0.07 ± 0.12	0.59 ± 0.35	0.10 ± 0.10	0.06 ± 0.20
810	0.94	388.0 ± 25.7	0.02 ± 0.16	0.08 ± 0.13	0.84 ± 0.26	0.01 ± 0.01	-0.08 ± 0.22
855	0.91	409.9 ± 59.5	-0.26 ± 0.16	0.04 ± 0.13	0.40 ± 0.25	-0.06 ± -0.06	-0.09 ± 0.26
900	0.88	363.6 ± 45.5	-0.03 ± 0.18	0.02 ± 0.14	0.03 ± 0.44	-0.01 ± -0.01	-0.10 ± 0.23
945	0.92	337.6 ± 33.8	-0.11 ± 0.11	0.06 ± 0.12	0.19 ± 0.42	-0.01 ± -0.01	-0.14 ± 0.23
990	0.90	303.3 ± 5.6	-0.32 ± 0.09	-0.02 ± 0.10	-0.36 ± 0.37	-0.17 ± -0.17	-0.09 ± 0.20
1035	0.89	303.7 ± 24.7	-0.38 ± 0.12	-0.01 ± 0.17	-0.21 ± 0.32	-0.29 ± -0.29	-0.15 ± 0.19
1080	0.94	358.7 ± 15.7	-0.27 ± 0.13	0.20 ± 0.16	0.07 ± 0.29	-0.08 ± -0.08	-0.05 ± 0.21
1125	0.90	366.6 ± 1.3	0.06 ± 0.15	0.00 ± 0.16	0.04 ± 0.28	0.10 ± 0.10	0.07 ± 0.19
1170	0.90	379.4 ± 56.4	0.37 ± 0.17	-0.09 ± 0.15	-0.23 ± 0.29	0.15 ± 0.15	-0.01 ± 0.20
1215	0.85	347.6 ± 43.0	0.24 ± 0.18	-0.07 ± 0.12	0.21 ± 0.27	0.05 ± 0.05	0.07 ± 0.22
1260	0.84	342.5 ± 20.1	-0.28 ± 0.11	0.08 ± 0.13	0.77 ± 0.35	-0.12 ± -0.12	–

Table A.23 – Same as in Table A.1, but for KIC 6521045. Due to the extremely large error bars, the results from the cross-correlation method, that are shown here, were obtained from 180-d sub-series.

KIC 6603624

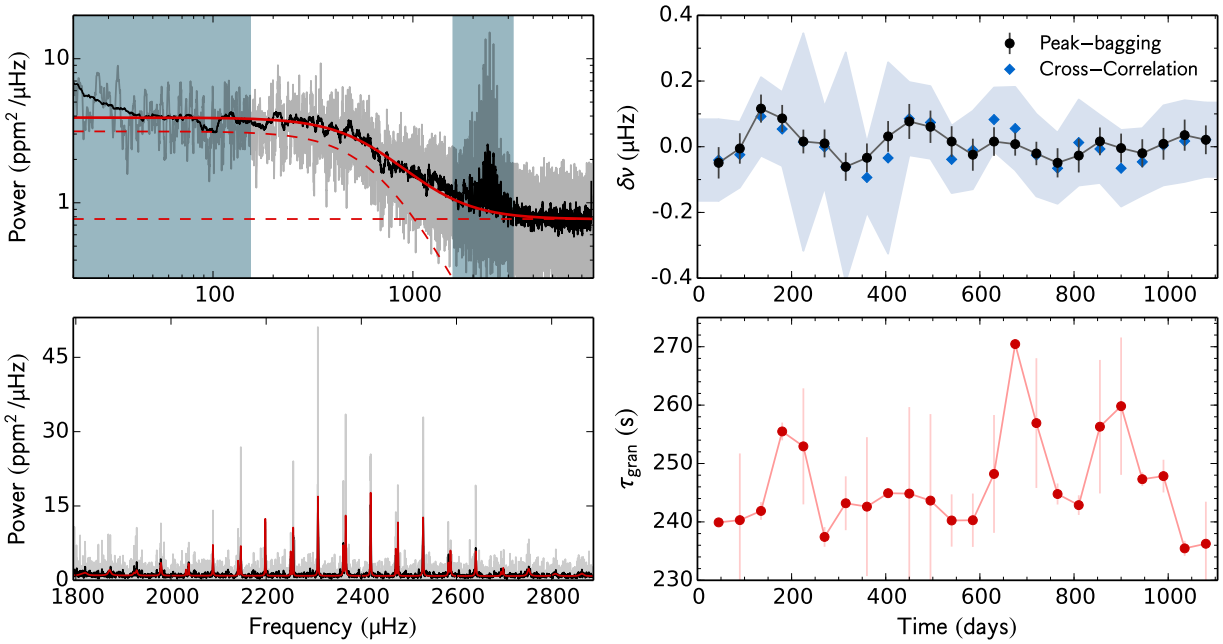

Fig. A.24 – Same as in Fig. A.1, but for KIC 6603624.

time (days)	d_c %	τ_{gran} (s)	Peak-bagging $\delta\nu_{l=0}$ (μHz)	$\delta\nu_{l=1}$ (μHz)	$\delta\nu_{l=2}$ (μHz)	$\delta\nu$ (μHz)	Cross-correlation $\delta\nu$ (μHz)
45	0.98	239.9 ± 0.4	-0.07 ± 0.07	-0.03 ± 0.07	0.05 ± 0.06	-0.05 ± -0.05	-0.04 ± 0.12
90	0.97	240.3 ± 11.4	-0.05 ± 0.07	0.03 ± 0.06	0.04 ± 0.07	-0.01 ± -0.01	-0.02 ± 0.10
135	0.96	241.9 ± 1.5	0.05 ± 0.06	0.17 ± 0.06	-0.01 ± 0.06	0.12 ± 0.12	0.09 ± 0.12
180	0.97	255.5 ± 1.5	0.06 ± 0.07	0.10 ± 0.05	-0.09 ± 0.07	0.09 ± 0.09	0.05 ± 0.11
225	0.96	252.9 ± 9.9	0.05 ± 0.05	-0.02 ± 0.05	-0.12 ± 0.06	0.02 ± 0.02	0.01 ± 0.33
270	0.80	237.4 ± 1.7	0.04 ± 0.06	-0.02 ± 0.06	-0.04 ± 0.06	0.01 ± 0.01	-0.00 ± 0.12
315	0.78	243.2 ± 4.6	-0.03 ± 0.06	-0.09 ± 0.06	-0.17 ± 0.07	-0.06 ± -0.06	-0.06 ± 0.35
360	0.89	242.6 ± 11.9	-0.03 ± 0.06	-0.04 ± 0.07	-0.09 ± 0.06	-0.03 ± -0.03	-0.09 ± 0.11
405	0.93	244.9 ± 0.0	0.08 ± 0.07	-0.01 ± 0.06	-0.10 ± 0.06	0.03 ± 0.03	-0.03 ± 0.29
450	0.97	244.8 ± 14.8	0.06 ± 0.08	0.10 ± 0.07	-0.13 ± 0.07	0.08 ± 0.08	0.09 ± 0.11
495	0.97	243.6 ± 14.8	-0.04 ± 0.07	0.17 ± 0.07	0.00 ± 0.07	0.06 ± 0.06	0.07 ± 0.11
540	0.98	240.2 ± 4.5	-0.04 ± 0.06	0.09 ± 0.07	-0.04 ± 0.07	0.02 ± 0.02	-0.04 ± 0.10
585	0.94	240.3 ± 4.6	-0.03 ± 0.06	-0.01 ± 0.08	0.01 ± 0.07	-0.02 ± -0.02	-0.01 ± 0.12
630	0.92	248.2 ± 10.1	0.01 ± 0.06	0.03 ± 0.07	0.00 ± 0.07	0.02 ± 0.02	0.08 ± 0.10
675	0.90	270.5 ± nan	0.03 ± 0.05	-0.00 ± 0.05	0.00 ± 0.07	0.01 ± 0.01	0.06 ± 0.13
720	0.90	256.9 ± 11.1	0.05 ± 0.06	-0.07 ± 0.05	-0.01 ± 0.07	-0.02 ± -0.02	-0.03 ± 0.13
765	0.95	244.8 ± 1.8	-0.01 ± 0.07	-0.08 ± 0.06	-0.10 ± 0.07	-0.05 ± -0.05	-0.07 ± 0.11
810	0.90	242.9 ± 1.7	-0.07 ± 0.07	0.01 ± 0.07	-0.07 ± 0.08	-0.03 ± -0.03	0.01 ± 0.13
855	0.89	256.3 ± 11.4	0.04 ± 0.06	-0.02 ± 0.06	0.03 ± 0.07	0.02 ± 0.02	-0.01 ± 0.10
900	0.95	259.8 ± 11.8	0.10 ± 0.07	-0.09 ± 0.06	-0.03 ± 0.06	-0.00 ± -0.00	-0.07 ± 0.12
945	0.90	247.3 ± 1.2	0.02 ± 0.06	-0.06 ± 0.06	0.07 ± 0.05	-0.02 ± -0.02	-0.05 ± 0.10
990	0.89	247.8 ± 2.8	-0.05 ± 0.07	0.07 ± 0.07	0.08 ± 0.08	0.01 ± 0.01	0.00 ± 0.12
1035	0.85	235.5 ± 1.3	0.01 ± 0.07	0.05 ± 0.06	-0.13 ± 0.06	0.04 ± 0.04	0.02 ± 0.12
1080	0.85	236.3 ± 7.2	0.04 ± 0.06	-0.00 ± 0.06	-0.09 ± 0.06	0.02 ± 0.02	0.02 ± 0.11

Table A.24 – Same as in Table A.1, but for KIC 6603624.

KIC 6679371

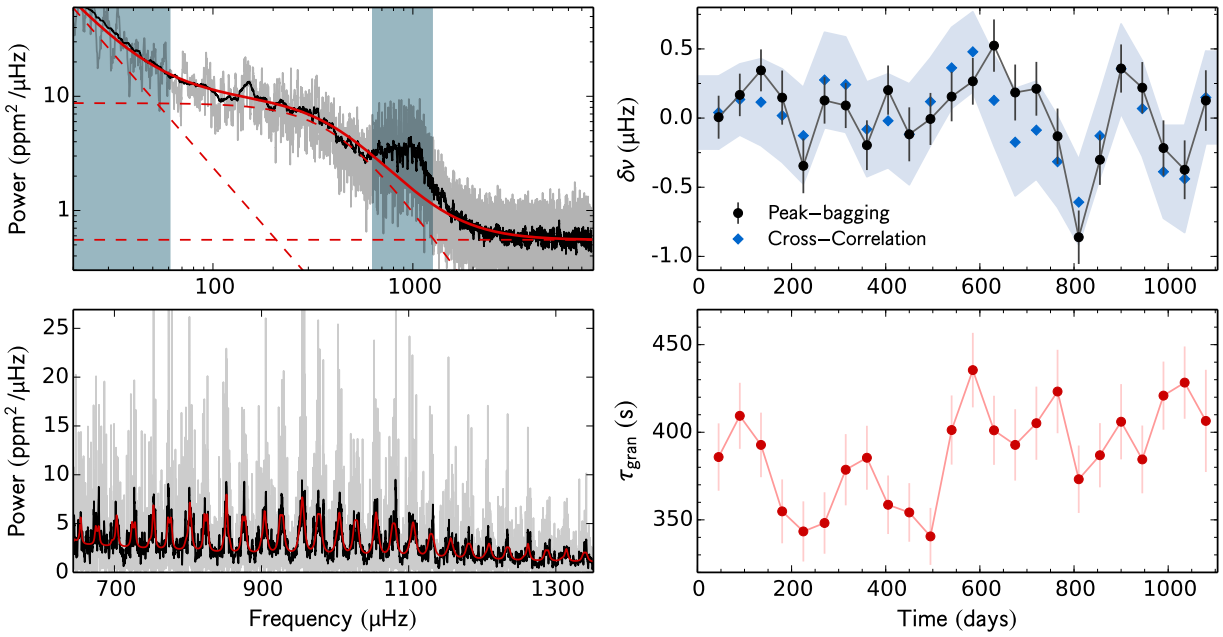

Fig. A.25 – Same as in Fig. A.1, but for KIC 6679371.

time (days)	d_c %	τ_{gran} (s)	Peak-bagging $\delta\nu_{l=0}$ (μHz)	$\delta\nu_{l=1}$ (μHz)	$\delta\nu_{l=2}$ (μHz)	$\delta\nu$ (μHz)	Cross-correlation $\delta\nu$ (μHz)
45	0.98	385.8 ± 19.2	0.07 ± 0.20	-0.08 ± 0.24	0.63 ± 0.60	0.01 ± 0.01	0.04 ± 0.26
90	0.97	409.4 ± 18.9	0.31 ± 0.21	0.00 ± 0.22	-0.90 ± 0.50	0.17 ± 0.17	0.13 ± 0.26
135	0.96	392.8 ± 18.4	0.70 ± 0.21	-0.05 ± 0.22	-0.79 ± 0.52	0.34 ± 0.34	0.11 ± 0.31
180	0.97	354.8 ± 18.2	0.31 ± 0.28	-0.02 ± 0.28	0.74 ± 0.47	0.15 ± 0.15	0.02 ± 0.34
225	0.96	343.4 ± 17.2	-0.14 ± 0.28	-0.56 ± 0.28	0.35 ± 0.60	-0.35 ± -0.35	-0.13 ± 0.35
270	0.80	348.2 ± 17.5	0.02 ± 0.25	0.22 ± 0.23	-0.20 ± 0.58	0.13 ± 0.13	0.28 ± 0.34
315	0.78	378.6 ± 20.3	-0.14 ± 0.25	0.26 ± 0.22	1.06 ± 0.35	0.09 ± 0.09	0.24 ± 0.34
360	0.89	385.4 ± 18.3	-0.51 ± 0.27	0.05 ± 0.24	0.94 ± 0.46	-0.20 ± -0.20	-0.08 ± 0.34
405	0.93	358.6 ± 16.7	0.26 ± 0.25	0.14 ± 0.25	-0.92 ± 0.51	0.20 ± 0.20	-0.02 ± 0.34
450	0.97	354.2 ± 16.7	-0.36 ± 0.30	0.05 ± 0.25	0.40 ± 0.43	-0.12 ± -0.12	-0.12 ± 0.36
495	0.97	340.5 ± 16.3	-0.96 ± 0.33	0.43 ± 0.23	0.54 ± 0.43	-0.01 ± -0.01	0.12 ± 0.32
540	0.98	401.3 ± 19.7	-0.14 ± 0.27	0.38 ± 0.24	-0.03 ± 0.48	0.16 ± 0.16	0.36 ± 0.29
585	0.94	435.5 ± 21.3	0.42 ± 0.24	0.10 ± 0.24	-0.13 ± 0.48	0.27 ± 0.27	0.48 ± 0.29
630	0.92	401.1 ± 19.7	0.71 ± 0.25	0.27 ± 0.29	-0.73 ± 0.47	0.52 ± 0.52	0.13 ± 0.33
675	0.90	392.8 ± 20.4	0.32 ± 0.28	0.03 ± 0.30	-0.73 ± 0.46	0.18 ± 0.18	-0.17 ± 0.39
720	0.91	405.2 ± 20.9	0.49 ± 0.30	0.02 ± 0.25	-0.57 ± 0.50	0.21 ± 0.21	-0.09 ± 0.35
765	0.95	423.3 ± 23.8	0.11 ± 0.32	-0.29 ± 0.26	0.31 ± 0.60	-0.13 ± -0.13	-0.32 ± 0.33
810	0.90	373.2 ± 19.2	-1.07 ± 0.27	-0.63 ± 0.28	1.20 ± 0.42	-0.86 ± -0.86	-0.61 ± 0.31
855	0.89	386.9 ± 18.3	-0.50 ± 0.25	-0.09 ± 0.26	0.83 ± 0.43	-0.30 ± -0.30	-0.13 ± 0.31
900	0.95	406.0 ± 21.5	0.40 ± 0.24	0.31 ± 0.25	-0.23 ± 0.48	0.36 ± 0.36	0.36 ± 0.32
945	0.90	384.5 ± 19.4	0.30 ± 0.28	0.15 ± 0.25	-0.37 ± 0.59	0.22 ± 0.22	0.07 ± 0.34
990	0.89	420.9 ± 19.4	-0.05 ± 0.30	-0.34 ± 0.27	-1.37 ± 0.59	-0.22 ± -0.22	-0.39 ± 0.34
1035	0.85	428.3 ± 20.6	-0.42 ± 0.31	-0.34 ± 0.29	0.02 ± 0.62	-0.37 ± -0.37	-0.44 ± 0.39
1080	0.85	406.5 ± 29.2	-0.19 ± 0.34	0.36 ± 0.29	0.90 ± 0.51	0.13 ± 0.13	0.15 ± 0.33

Table A.25 – Same as in Table A.1, but for KIC 6679371.

KIC 6933899

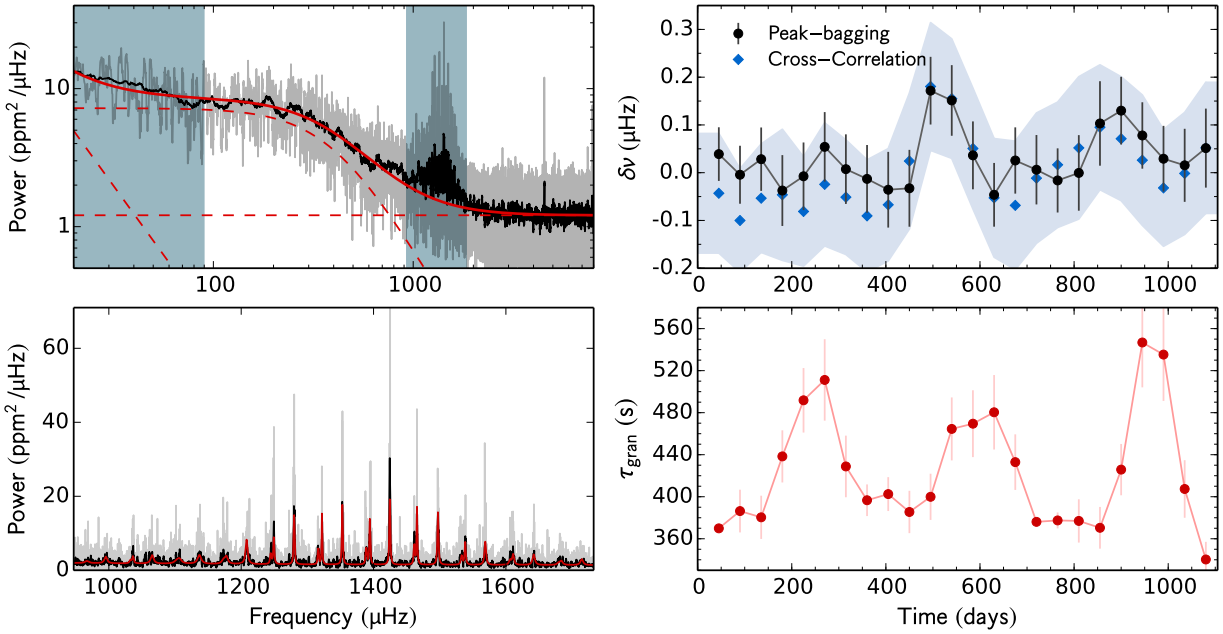

Fig. A.26 – Same as in Fig. A.1, but for KIC 6933899.

time (days)	d_c %	τ_{gran} (s)	Peak-bagging $\delta\nu_{l=0}$ (μHz)	$\delta\nu_{l=1}$ (μHz)	$\delta\nu_{l=2}$ (μHz)	$\delta\nu$ (μHz)	Cross-correlation $\delta\nu$ (μHz)
45	0.98	369.9 ± 1.7	0.06 ± 0.08	0.01 ± 0.08	-0.11 ± 0.12	0.04 ± 0.04	-0.04 ± 0.13
90	0.97	386.4 ± 20.3	0.07 ± 0.09	-0.07 ± 0.08	-0.32 ± 0.13	-0.00 ± -0.00	-0.10 ± 0.11
135	0.96	380.4 ± 20.6	0.05 ± 0.09	0.01 ± 0.09	-0.28 ± 0.12	0.03 ± 0.03	-0.05 ± 0.11
180	0.97	438.4 ± 24.8	0.03 ± 0.11	-0.10 ± 0.10	-0.02 ± 0.16	-0.04 ± -0.04	-0.05 ± 0.14
225	0.96	491.8 ± 30.7	0.11 ± 0.10	-0.12 ± 0.10	0.17 ± 0.15	-0.01 ± -0.01	-0.08 ± 0.11
270	0.80	511.2 ± 38.8	0.12 ± 0.10	-0.03 ± 0.11	0.18 ± 0.14	0.05 ± 0.05	-0.02 ± 0.13
315	0.78	428.8 ± 29.3	0.08 ± 0.09	-0.10 ± 0.12	0.01 ± 0.18	0.01 ± 0.01	-0.05 ± 0.12
360	0.89	396.7 ± 15.1	0.10 ± 0.09	-0.18 ± 0.11	-0.10 ± 0.14	-0.01 ± -0.01	-0.09 ± 0.12
405	0.93	402.5 ± 16.1	0.06 ± 0.10	-0.16 ± 0.12	-0.07 ± 0.14	-0.04 ± -0.04	-0.07 ± 0.12
450	0.97	385.5 ± 20.1	-0.06 ± 0.11	-0.01 ± 0.11	-0.15 ± 0.17	-0.03 ± -0.03	0.02 ± 0.14
495	0.97	399.9 ± 22.0	0.17 ± 0.11	0.18 ± 0.10	0.11 ± 0.16	0.17 ± 0.17	0.18 ± 0.13
540	0.98	464.5 ± 30.0	0.22 ± 0.10	0.08 ± 0.11	0.08 ± 0.14	0.15 ± 0.15	0.16 ± 0.13
585	0.94	469.5 ± 31.8	-0.01 ± 0.10	0.08 ± 0.10	0.02 ± 0.13	0.04 ± 0.04	0.05 ± 0.13
630	0.92	480.4 ± 35.4	-0.10 ± 0.10	0.00 ± 0.09	-0.24 ± 0.13	-0.05 ± -0.05	-0.05 ± 0.12
675	0.90	432.9 ± 26.5	0.11 ± 0.10	-0.04 ± 0.09	-0.14 ± 0.13	0.03 ± 0.03	-0.07 ± 0.13
720	0.91	376.1 ± 0.8	0.04 ± 0.11	-0.02 ± 0.10	0.03 ± 0.16	0.01 ± 0.01	-0.01 ± 0.14
765	0.95	377.5 ± 7.6	-0.06 ± 0.09	0.03 ± 0.10	0.03 ± 0.15	-0.02 ± -0.02	0.02 ± 0.13
810	0.90	377.0 ± 20.6	-0.16 ± 0.11	0.16 ± 0.11	0.36 ± 0.17	-0.00 ± -0.00	0.05 ± 0.15
855	0.89	370.4 ± 19.9	-0.13 ± 0.14	0.25 ± 0.11	0.15 ± 0.17	0.10 ± 0.10	0.10 ± 0.13
900	0.95	425.8 ± 24.4	0.07 ± 0.11	0.18 ± 0.10	-0.04 ± 0.16	0.13 ± 0.13	0.07 ± 0.13
945	0.90	546.8 ± 42.7	0.20 ± 0.10	-0.05 ± 0.10	-0.00 ± 0.16	0.08 ± 0.08	0.03 ± 0.14
990	0.89	535.3 ± 44.1	0.15 ± 0.10	-0.10 ± 0.10	-0.16 ± 0.14	0.03 ± 0.03	-0.03 ± 0.12
1035	0.85	407.4 ± 27.4	0.03 ± 0.11	0.00 ± 0.11	0.01 ± 0.15	0.02 ± 0.02	-0.00 ± 0.13
1080	0.85	340.3 ± 16.8	0.02 ± 0.12	0.08 ± 0.11	0.16 ± 0.17	0.05 ± 0.05	0.05 ± 0.14

Table A.26 – Same as in Table A.1, but for KIC 6933899.

KIC 7103006

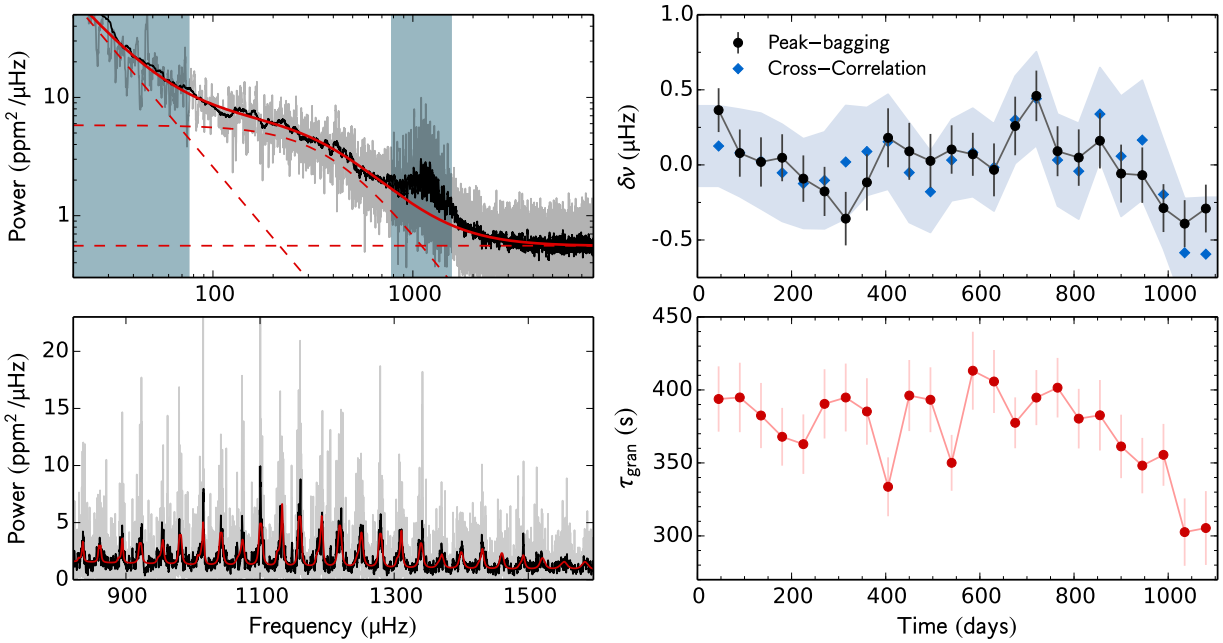

Fig. A.27 – Same as in Fig. A.1, but for KIC 7103006.

time (days)	d_c %	τ_{gran} (s)	Peak-bagging $\delta\nu_{l=0}$ (μHz)	$\delta\nu_{l=1}$ (μHz)	$\delta\nu_{l=2}$ (μHz)	$\delta\nu$ (μHz)	Cross-correlation $\delta\nu$ (μHz)
45	0.98	393.8 ± 22.4	0.54 ± 0.21	0.21 ± 0.20	-0.59 ± 0.44	0.36 ± 0.36	0.13 ± 0.27
90	0.97	394.8 ± 23.8	0.21 ± 0.25	-0.01 ± 0.20	0.09 ± 0.50	0.08 ± 0.08	0.08 ± 0.29
135	0.96	382.5 ± 22.3	0.32 ± 0.22	-0.32 ± 0.24	-0.71 ± 0.47	0.02 ± 0.02	0.03 ± 0.32
180	0.97	367.9 ± 19.8	0.43 ± 0.23	-0.28 ± 0.21	-0.95 ± 0.44	0.05 ± 0.05	-0.05 ± 0.32
225	0.96	362.9 ± 20.4	0.03 ± 0.25	-0.17 ± 0.20	-0.20 ± 0.49	-0.09 ± -0.09	-0.12 ± 0.30
270	0.81	390.5 ± 23.7	-0.04 ± 0.25	-0.28 ± 0.22	1.02 ± 0.49	-0.18 ± -0.18	-0.10 ± 0.32
315	0.78	394.8 ± 23.3	-0.28 ± 0.25	-0.43 ± 0.25	1.27 ± 0.45	-0.36 ± -0.36	0.02 ± 0.38
360	0.89	385.2 ± 22.8	-0.31 ± 0.28	0.04 ± 0.25	0.66 ± 0.49	-0.12 ± -0.12	0.09 ± 0.29
405	0.93	333.6 ± 20.2	-0.01 ± 0.34	0.28 ± 0.24	0.47 ± 0.48	0.18 ± 0.18	0.15 ± 0.32
450	0.97	396.2 ± 24.4	-0.26 ± 0.31	0.30 ± 0.24	-0.02 ± 0.46	0.09 ± 0.09	-0.05 ± 0.33
495	0.97	393.3 ± 22.2	-0.15 ± 0.28	0.15 ± 0.24	-0.13 ± 0.52	0.03 ± 0.03	-0.18 ± 0.27
540	0.98	350.1 ± 19.1	0.23 ± 0.24	-0.00 ± 0.22	-0.41 ± 0.48	0.10 ± 0.10	0.03 ± 0.27
585	0.94	413.2 ± 26.7	0.18 ± 0.20	-0.04 ± 0.20	-0.64 ± 0.38	0.07 ± 0.07	0.08 ± 0.29
630	0.92	405.8 ± 21.6	-0.29 ± 0.27	0.17 ± 0.24	0.61 ± 0.49	-0.03 ± -0.03	-0.02 ± 0.29
675	0.90	377.5 ± 17.4	0.25 ± 0.30	0.27 ± 0.26	1.06 ± 0.54	0.26 ± 0.26	0.30 ± 0.29
720	0.91	394.7 ± 18.9	0.70 ± 0.23	0.18 ± 0.25	0.69 ± 0.55	0.46 ± 0.46	0.44 ± 0.31
765	0.95	401.5 ± 20.4	0.44 ± 0.25	-0.17 ± 0.22	-0.17 ± 0.52	0.09 ± 0.09	0.03 ± 0.31
810	0.90	380.3 ± 20.4	0.32 ± 0.30	-0.13 ± 0.24	0.14 ± 0.58	0.05 ± 0.05	-0.04 ± 0.32
855	0.89	382.6 ± 24.2	0.08 ± 0.28	0.23 ± 0.25	-0.13 ± 0.55	0.16 ± 0.16	0.34 ± 0.31
900	0.95	361.3 ± 21.7	-0.23 ± 0.30	0.07 ± 0.25	-1.00 ± 0.44	-0.06 ± -0.06	0.06 ± 0.40
945	0.90	348.2 ± 19.0	-0.15 ± 0.27	-0.00 ± 0.25	-0.04 ± 0.53	-0.07 ± -0.07	0.17 ± 0.40
990	0.89	355.5 ± 21.2	-0.10 ± 0.23	-0.46 ± 0.22	-0.18 ± 0.47	-0.29 ± -0.29	-0.20 ± 0.36
1035	0.85	302.6 ± 23.1	-0.34 ± 0.25	-0.42 ± 0.20	-1.01 ± 0.45	-0.39 ± -0.39	-0.59 ± 0.36
1080	0.85	305.4 ± 25.3	-0.54 ± 0.24	-0.10 ± 0.21	-0.30 ± 0.41	-0.29 ± -0.29	-0.59 ± 0.38

Table A.27 – Same as in Table A.1, but for KIC 7103006.

KIC 7106245

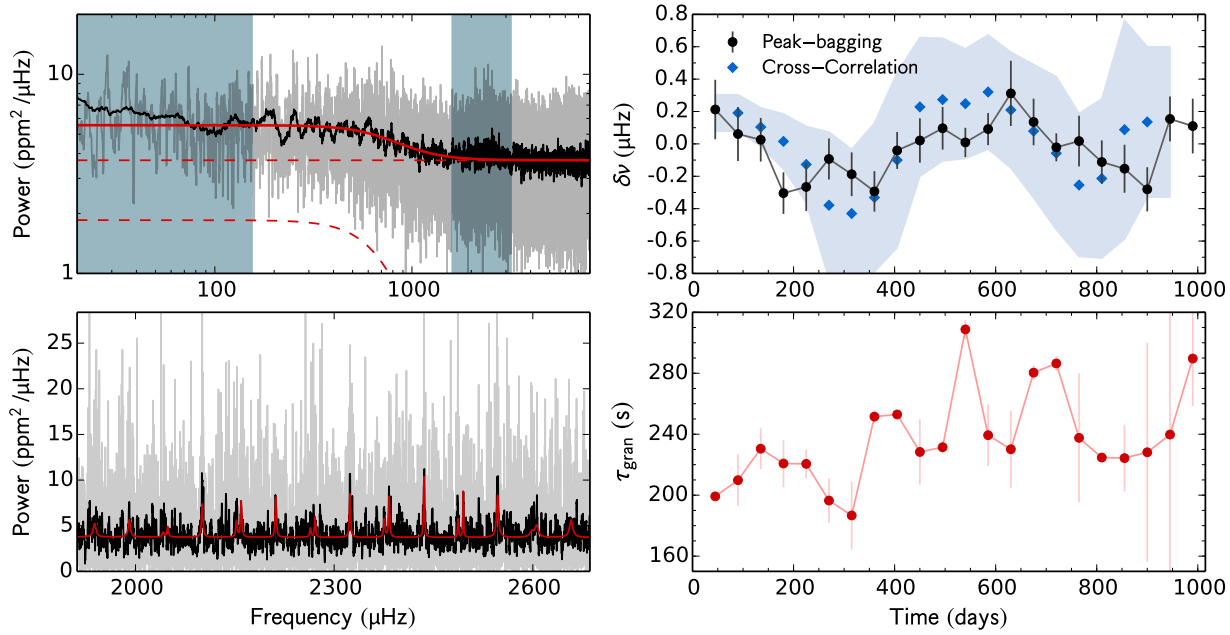

Fig. A.28 – Same as in Fig. A.1, but for KIC 7106245. Due to the extremely large error bars, the results from the cross-correlation method, that are shown here, were obtained from 180-d sub-series.

time (days)	d_c %	τ_{gran} (s)	Peak-bagging $\delta\nu_{l=0}$ (μHz)	$\delta\nu_{l=1}$ (μHz)	$\delta\nu_{l=2}$ (μHz)	$\delta\nu$ (μHz)	Cross-correlation $\delta\nu$ (μHz)
45	0.98	199.2 ± 0.8	0.30 ± 0.31	0.17 ± 0.23	-0.43 ± 0.41	0.21 ± 0.21	–
90	0.97	209.8 ± 16.9	-0.02 ± 0.21	0.19 ± 0.27	-0.00 ± 0.65	0.06 ± 0.06	0.19 ± 0.11
135	0.96	230.5 ± 13.5	-0.16 ± 0.18	0.25 ± 0.20	0.35 ± 0.47	0.03 ± 0.03	0.10 ± 0.12
180	0.97	220.8 ± 15.5	-0.56 ± 0.20	-0.11 ± 0.17	0.32 ± 0.47	-0.30 ± -0.30	0.02 ± 0.17
225	0.96	220.5 ± 9.3	-0.57 ± 0.28	-0.15 ± 0.18	0.16 ± 0.65	-0.27 ± -0.27	-0.13 ± 0.23
270	0.80	196.5 ± 14.6	-0.20 ± 0.22	-0.04 ± 0.16	-0.23 ± 0.33	-0.09 ± -0.09	-0.38 ± 0.45
315	0.78	186.7 ± 22.3	-0.14 ± 0.19	-0.23 ± 0.19	-0.54 ± 0.27	-0.19 ± -0.19	-0.43 ± 0.40
360	0.89	251.6 ± 4.2	-0.05 ± 0.17	-0.57 ± 0.18	-0.90 ± 0.34	-0.29 ± -0.29	-0.33 ± 0.46
405	0.93	253.0 ± 0.9	0.02 ± 0.13	-0.23 ± 0.24	0.82 ± 0.99	-0.04 ± -0.04	-0.10 ± 0.54
450	0.97	228.4 ± 21.3	0.10 ± 0.20	-0.05 ± 0.19	0.72 ± 0.70	0.02 ± 0.02	0.23 ± 0.43
495	0.97	231.5 ± 4.1	0.02 ± 0.22	0.14 ± 0.16	-0.05 ± 0.27	0.10 ± 0.10	0.27 ± 0.38
540	0.98	308.8 ± 6.4	0.21 ± 0.15	-0.11 ± 0.12	-0.06 ± 0.15	0.01 ± 0.01	0.25 ± 0.34
585	0.94	239.4 ± 20.2	0.30 ± 0.13	-0.23 ± 0.16	0.01 ± 0.26	0.09 ± 0.09	0.32 ± 0.35
630	0.92	230.1 ± 25.2	0.28 ± 0.24	0.37 ± 0.36	-0.39 ± 0.47	0.31 ± 0.31	0.21 ± 0.36
675	0.90	280.4 ± 4.8	0.26 ± 0.23	0.06 ± 0.18	0.04 ± 0.44	0.14 ± 0.14	0.08 ± 0.41
720	0.90	286.4 ± 5.0	0.02 ± 0.17	-0.04 ± 0.10	0.47 ± 0.45	-0.02 ± -0.02	-0.06 ± 0.47
765	0.95	237.6 ± 42.3	0.05 ± 0.26	-0.00 ± 0.20	-0.57 ± 0.46	0.02 ± 0.02	-0.25 ± 0.44
810	0.90	224.7 ± 1.2	-0.05 ± 0.21	-0.15 ± 0.17	-0.84 ± 0.42	-0.11 ± -0.11	-0.21 ± 0.49
855	0.89	224.3 ± 21.8	-0.33 ± 0.26	-0.07 ± 0.18	0.16 ± 0.33	-0.15 ± -0.15	0.09 ± 0.68
900	0.78	228.1 ± 71.9	-0.59 ± 0.18	0.15 ± 0.21	0.45 ± 0.39	-0.28 ± -0.28	0.14 ± 0.46
945	0.56	239.8 ± 134.3	0.04 ± 0.36	0.17 ± 0.15	-0.18 ± 0.42	0.15 ± 0.15	–
990	0.66	289.7 ± 31.2	0.14 ± 0.28	0.09 ± 0.21	-1.31 ± 0.38	0.11 ± 0.11	–

Table A.28 – Same as in Table A.1, but for KIC 7106245. Due to the extremely large error bars, the results from the cross-correlation method, that are shown here, were obtained from 180-d sub-series.

KIC 7206837

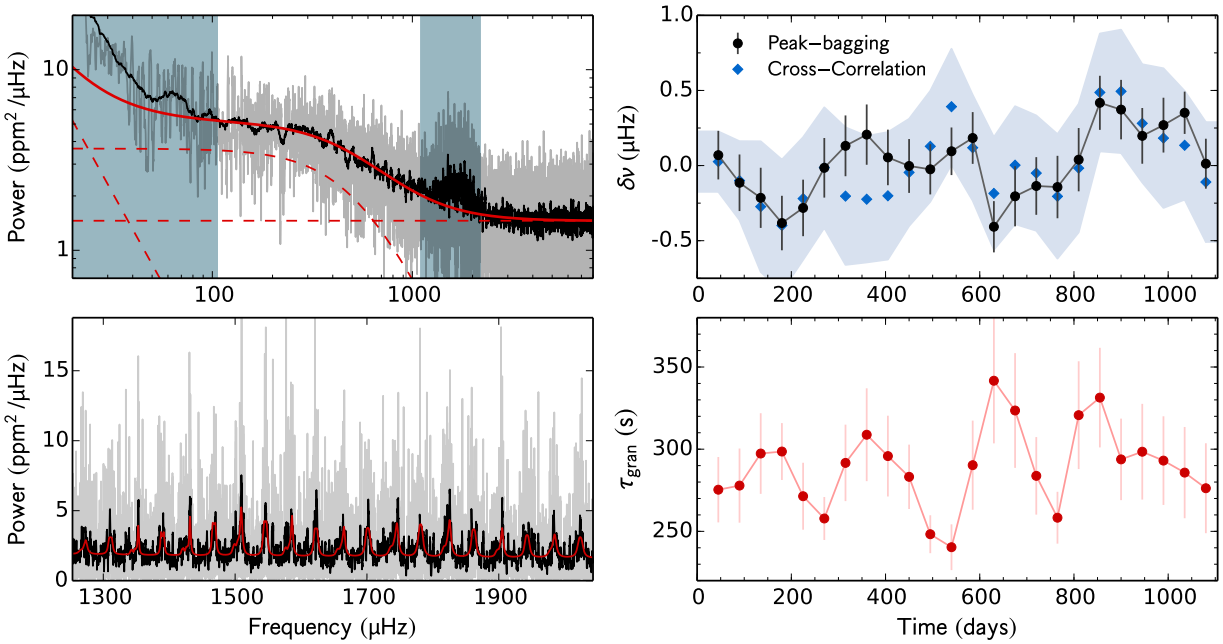

Fig. A.29 – Same as in Fig. A.1, but for KIC 7206837.

time (days)	d_c %	τ_{gran} (s)	Peak-bagging $\delta\nu_{l=0}$ (μHz)	$\delta\nu_{l=1}$ (μHz)	$\delta\nu_{l=2}$ (μHz)	$\delta\nu$ (μHz)	Cross-correlation $\delta\nu$ (μHz)
45	0.98	275.3 ± 19.9	-0.02 ± 0.23	0.15 ± 0.23	0.33 ± 0.45	0.07 ± 0.07	0.03 ± 0.20
90	0.97	277.8 ± 22.6	-0.23 ± 0.26	0.02 ± 0.28	-0.45 ± 0.55	-0.11 ± -0.11	-0.10 ± 0.26
135	0.96	297.4 ± 24.5	0.06 ± 0.25	-0.73 ± 0.34	-0.88 ± 0.63	-0.21 ± -0.21	-0.27 ± 0.44
180	0.97	298.6 ± 17.3	-0.12 ± 0.22	-0.90 ± 0.31	0.03 ± 0.53	-0.38 ± -0.38	-0.40 ± 0.44
225	0.96	271.4 ± 20.4	-0.57 ± 0.25	0.07 ± 0.28	-0.55 ± 0.55	-0.28 ± -0.28	-0.22 ± 0.41
270	0.81	257.8 ± 13.1	-0.48 ± 0.30	0.36 ± 0.27	-1.18 ± 0.46	-0.01 ± -0.01	-0.01 ± 0.40
315	0.78	291.7 ± 23.3	0.54 ± 0.31	-0.17 ± 0.27	0.22 ± 0.50	0.13 ± 0.13	-0.20 ± 0.46
360	0.89	308.8 ± 28.2	0.98 ± 0.33	-0.24 ± 0.25	0.78 ± 0.46	0.21 ± 0.21	-0.22 ± 0.42
405	0.93	295.8 ± 24.6	0.55 ± 0.26	-0.48 ± 0.27	-0.21 ± 0.54	0.05 ± 0.05	-0.20 ± 0.42
450	0.97	283.2 ± 19.6	0.23 ± 0.26	-0.22 ± 0.25	0.17 ± 0.44	-0.00 ± -0.00	-0.05 ± 0.36
495	0.97	248.3 ± 11.5	-0.33 ± 0.23	0.34 ± 0.25	1.34 ± 0.34	-0.02 ± -0.02	0.13 ± 0.37
540	0.98	240.3 ± 13.9	-0.30 ± 0.22	0.55 ± 0.23	1.47 ± 0.40	0.10 ± 0.10	0.39 ± 0.39
585	0.94	290.3 ± 27.1	0.16 ± 0.24	0.20 ± 0.24	1.02 ± 0.52	0.18 ± 0.18	0.12 ± 0.35
630	0.92	341.7 ± 38.1	-0.36 ± 0.22	-0.47 ± 0.26	-0.54 ± 0.61	-0.41 ± -0.41	-0.19 ± 0.38
675	0.90	323.5 ± 34.9	-0.38 ± 0.30	-0.06 ± 0.27	0.62 ± 0.44	-0.20 ± -0.20	0.00 ± 0.39
720	0.90	283.8 ± 23.6	-0.32 ± 0.26	0.09 ± 0.29	0.28 ± 0.54	-0.14 ± -0.14	-0.05 ± 0.38
765	0.95	258.3 ± 15.8	-0.11 ± 0.28	-0.19 ± 0.31	-0.11 ± 0.62	-0.14 ± -0.14	-0.20 ± 0.41
810	0.90	320.7 ± 32.8	0.11 ± 0.32	-0.02 ± 0.28	-0.56 ± 0.63	0.04 ± 0.04	-0.02 ± 0.43
855	0.89	331.4 ± 30.3	0.32 ± 0.25	0.52 ± 0.26	-0.44 ± 0.60	0.42 ± 0.42	0.49 ± 0.39
900	0.95	293.8 ± 24.8	-0.15 ± 0.30	0.77 ± 0.26	-0.59 ± 0.53	0.37 ± 0.37	0.49 ± 0.41
945	0.90	298.5 ± 29.1	-0.16 ± 0.26	0.57 ± 0.26	-1.46 ± 0.48	0.20 ± 0.20	0.28 ± 0.39
990	0.89	293.0 ± 27.0	-0.03 ± 0.25	0.63 ± 0.27	-0.21 ± 0.62	0.27 ± 0.27	0.18 ± 0.46
1035	0.85	285.7 ± 27.8	0.33 ± 0.18	0.38 ± 0.22	1.39 ± 0.43	0.35 ± 0.35	0.13 ± 0.36
1080	0.85	276.2 ± 27.4	0.15 ± 0.20	-0.36 ± 0.32	0.99 ± 0.51	0.01 ± 0.01	-0.11 ± 0.40

Table A.29 – Same as in Table A.1, but for KIC 7206837.

KIC 7296438

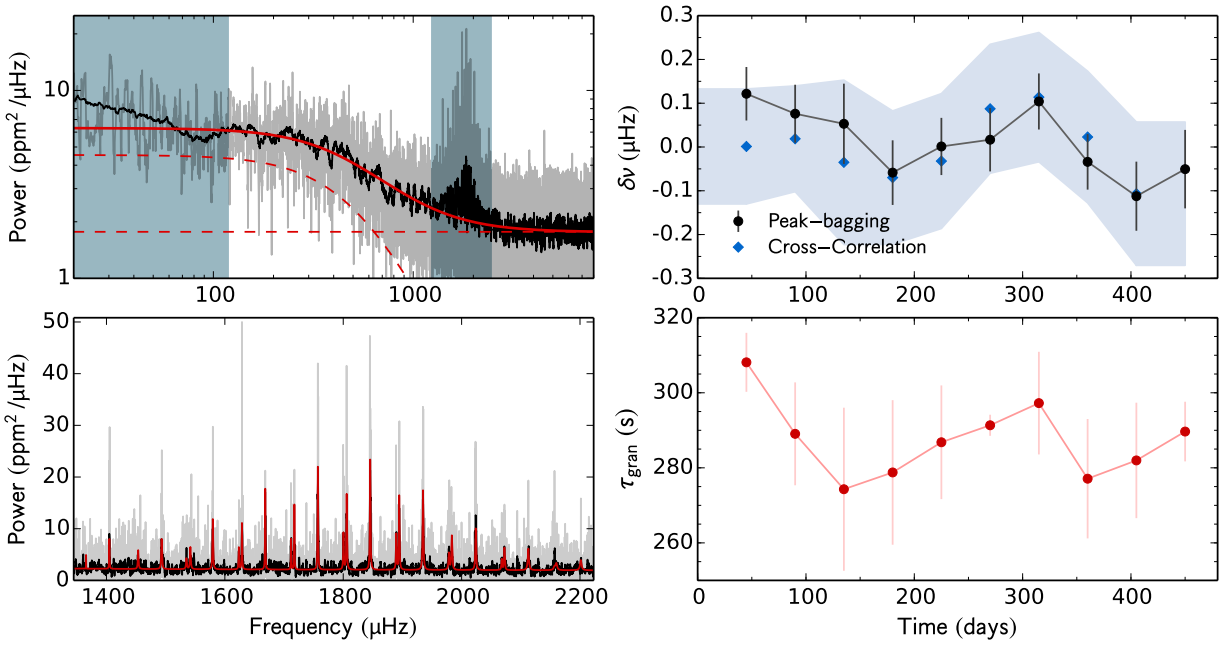

Fig. A.30 – Same as in Fig. A.1, but for KIC 7296438.

time (days)	d_c %	τ_{gran} (s)	Peak-bagging $\delta\nu_{l=0}$ (μHz)	$\delta\nu_{l=1}$ (μHz)	$\delta\nu_{l=2}$ (μHz)	$\delta\nu$ (μHz)	Cross-correlation $\delta\nu$ (μHz)
45	0.97	308.1 ± 7.9	0.11 ± 0.09	0.13 ± 0.08	-0.11 ± 0.15	0.12 ± 0.12	0.00 ± 0.13
90	0.78	289.1 ± 13.7	0.04 ± 0.10	0.10 ± 0.09	-0.22 ± 0.17	0.08 ± 0.08	0.02 ± 0.12
135	0.73	274.3 ± 21.7	0.12 ± 0.13	-0.01 ± 0.13	0.16 ± 0.18	0.05 ± 0.05	-0.04 ± 0.19
180	0.92	278.8 ± 19.3	-0.10 ± 0.11	-0.03 ± 0.10	-0.06 ± 0.16	-0.06 ± -0.06	-0.07 ± 0.15
225	0.98	286.8 ± 15.2	-0.03 ± 0.09	0.04 ± 0.09	-0.26 ± 0.19	0.00 ± 0.00	-0.03 ± 0.15
270	0.97	291.3 ± 2.8	0.01 ± 0.09	0.02 ± 0.11	0.12 ± 0.18	0.02 ± 0.02	0.09 ± 0.15
315	0.97	297.2 ± 13.7	0.12 ± 0.09	0.09 ± 0.09	-0.08 ± 0.17	0.10 ± 0.10	0.11 ± 0.15
360	0.97	277.1 ± 15.9	-0.07 ± 0.08	0.02 ± 0.10	-0.13 ± 0.16	-0.03 ± -0.03	0.02 ± 0.15
405	0.94	282.0 ± 15.4	-0.17 ± 0.11	-0.06 ± 0.11	0.01 ± 0.22	-0.11 ± -0.11	-0.11 ± 0.16
450	0.66	289.7 ± 7.9	0.18 ± 0.14	-0.23 ± 0.12	-0.04 ± 0.23	-0.05 ± -0.05	–

Table A.30 – Same as in Table A.1, but for KIC 7296438.

KIC 7510397

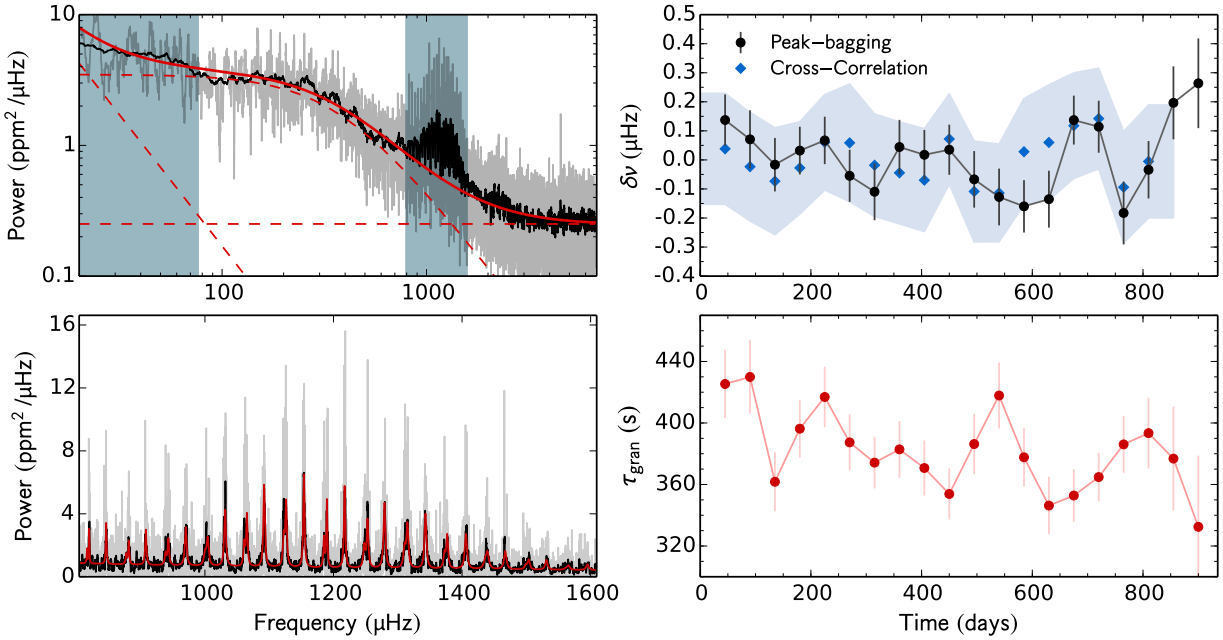

Fig. A.31 – Same as in Fig. A.1, but for KIC 7510397.

time (days)	d_c %	τ_{gran} (s)	Peak-bagging $\delta\nu_{l=0}$ (μHz)	$\delta\nu_{l=1}$ (μHz)	$\delta\nu_{l=2}$ (μHz)	$\delta\nu$ (μHz)	Cross-correlation $\delta\nu$ (μHz)
45	0.96	425.3 ± 22.1	0.11 ± 0.14	0.16 ± 0.12	0.17 ± 0.15	0.14 ± 0.14	0.04 ± 0.19
90	0.77	429.9 ± 24.0	0.03 ± 0.15	0.10 ± 0.13	0.01 ± 0.18	0.07 ± 0.07	-0.02 ± 0.19
135	0.73	361.8 ± 19.1	0.06 ± 0.14	-0.07 ± 0.12	0.03 ± 0.18	-0.02 ± -0.02	-0.07 ± 0.18
180	0.92	396.3 ± 18.7	0.13 ± 0.13	-0.04 ± 0.11	-0.05 ± 0.16	0.03 ± 0.03	-0.03 ± 0.16
225	0.98	416.9 ± 19.7	0.24 ± 0.12	-0.09 ± 0.11	0.13 ± 0.15	0.07 ± 0.07	0.06 ± 0.16
270	0.97	387.4 ± 18.2	0.06 ± 0.13	-0.16 ± 0.12	0.25 ± 0.20	-0.05 ± -0.05	0.06 ± 0.20
315	0.97	374.2 ± 16.8	0.03 ± 0.15	-0.21 ± 0.13	0.23 ± 0.18	-0.11 ± -0.11	-0.02 ± 0.18
360	0.97	382.8 ± 18.5	0.13 ± 0.14	-0.02 ± 0.12	0.10 ± 0.15	0.04 ± 0.04	-0.04 ± 0.18
405	0.94	370.7 ± 17.8	-0.10 ± 0.13	0.11 ± 0.12	-0.29 ± 0.18	0.02 ± 0.02	-0.07 ± 0.18
450	0.91	353.8 ± 16.6	-0.07 ± 0.13	0.12 ± 0.12	-0.35 ± 0.21	0.04 ± 0.04	0.07 ± 0.16
495	0.88	386.3 ± 19.6	-0.01 ± 0.15	-0.11 ± 0.13	-0.19 ± 0.18	-0.07 ± -0.07	-0.11 ± 0.17
540	0.92	417.8 ± 21.4	-0.18 ± 0.16	-0.10 ± 0.12	-0.15 ± 0.19	-0.13 ± -0.13	-0.11 ± 0.17
585	0.97	377.7 ± 19.1	-0.16 ± 0.14	-0.16 ± 0.12	-0.24 ± 0.22	-0.16 ± -0.16	0.03 ± 0.18
630	0.89	346.3 ± 18.7	-0.06 ± 0.15	-0.20 ± 0.13	0.13 ± 0.22	-0.14 ± -0.14	0.06 ± 0.20
675	0.89	352.8 ± 17.2	-0.10 ± 0.14	0.28 ± 0.11	0.19 ± 0.18	0.14 ± 0.14	0.12 ± 0.18
720	0.95	364.8 ± 15.9	-0.01 ± 0.14	0.19 ± 0.11	0.18 ± 0.21	0.11 ± 0.11	0.14 ± 0.17
765	0.89	386.1 ± 18.5	-0.08 ± 0.17	-0.25 ± 0.14	0.12 ± 0.18	-0.18 ± -0.18	-0.09 ± 0.19
810	0.76	393.4 ± 23.0	-0.08 ± 0.13	0.03 ± 0.15	0.01 ± 0.16	-0.03 ± -0.03	-0.01 ± 0.19
855	0.34	376.8 ± 33.9	0.08 ± 0.16	0.38 ± 0.20	0.45 ± 0.24	0.20 ± 0.20	–
900	0.17	332.5 ± 46.3	0.50 ± 0.20	-0.10 ± 0.24	0.04 ± 0.33	0.26 ± 0.26	–

Table A.31 – Same as in Table A.1, but for KIC 7510397.

KIC 7670943

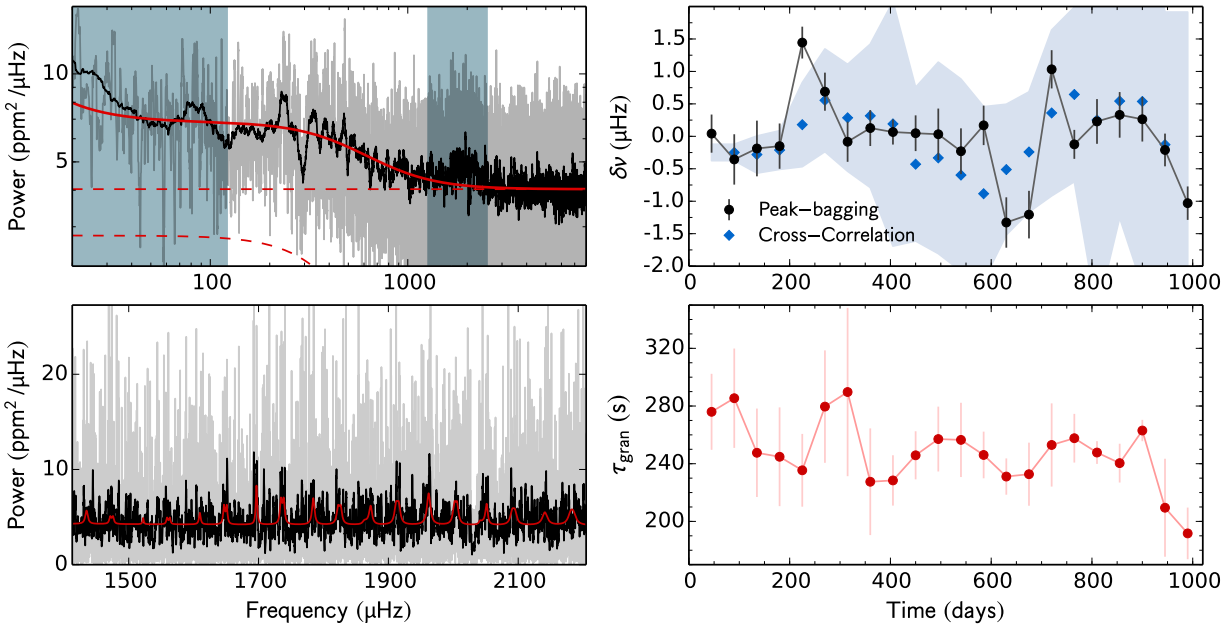

Fig. A.32 – Same as in Fig. A.1, but for KIC 7670943. Due to the extremely large error bars, the results from the cross-correlation method, that are shown here, were obtained from 180-d sub-series.

time (days)	d_c %	τ_{gran} (s)	Peak-bagging $\delta\nu_{l=0}$ (μHz)	$\delta\nu_{l=1}$ (μHz)	$\delta\nu_{l=2}$ (μHz)	$\delta\nu$ (μHz)	Cross-correlation $\delta\nu$ (μHz)
45	0.98	276.0 ± 26.3	0.35 ± 0.39	-0.36 ± 0.45	0.28 ± 1.66	0.04 ± 0.04	–
90	0.97	285.4 ± 34.4	-0.19 ± 0.50	-0.62 ± 0.62	0.19 ± 1.68	-0.36 ± -0.36	-0.25 ± 0.13
135	0.96	247.6 ± 30.7	0.24 ± 0.56	-0.77 ± 0.66	-0.04 ± 1.83	-0.19 ± -0.19	-0.28 ± 0.29
180	0.78	244.8 ± 34.2	0.16 ± 0.44	-0.66 ± 0.56	-0.06 ± 1.71	-0.15 ± -0.15	-0.21 ± 0.30
225	0.72	235.4 ± 25.2	1.42 ± 0.32	1.47 ± 0.39	-1.18 ± 1.65	1.44 ± 1.44	0.18 ± 0.65
270	0.92	279.6 ± 39.0	0.74 ± 0.38	0.61 ± 0.46	-0.77 ± 1.66	0.69 ± 0.69	0.56 ± 0.79
315	0.98	289.7 ± 58.4	-0.12 ± 0.44	-0.05 ± 0.43	-0.67 ± 1.68	-0.08 ± -0.08	0.29 ± 0.82
360	0.97	227.5 ± 37.0	0.05 ± 0.34	0.27 ± 0.47	-1.22 ± 1.44	0.13 ± 0.13	0.32 ± 1.10
405	0.97	228.4 ± 17.5	0.35 ± 0.26	-0.29 ± 0.29	-1.19 ± 1.21	0.07 ± 0.07	0.19 ± 1.88
450	0.97	245.8 ± 16.7	0.66 ± 0.39	-0.54 ± 0.38	-0.26 ± 1.49	0.05 ± 0.05	-0.43 ± 1.18
495	0.94	257.1 ± 22.5	0.43 ± 0.56	-0.38 ± 0.56	0.26 ± 1.57	0.03 ± 0.03	-0.33 ± 1.47
540	0.91	256.5 ± 25.8	0.08 ± 0.43	-0.91 ± 0.63	-0.16 ± 1.71	-0.23 ± -0.23	-0.60 ± 1.48
585	0.88	246.1 ± 16.2	0.22 ± 0.35	0.02 ± 0.61	0.29 ± 1.75	0.17 ± 0.17	-0.88 ± 1.34
630	0.92	231.1 ± 12.6	-1.83 ± 0.48	-0.36 ± 0.66	0.14 ± 1.70	-1.33 ± -1.33	-0.51 ± 1.01
675	0.97	232.7 ± 21.9	-2.20 ± 0.48	0.25 ± 0.58	0.95 ± 1.54	-1.21 ± -1.21	-0.24 ± 0.93
720	0.90	253.0 ± 28.9	0.41 ± 0.44	1.56 ± 0.40	1.77 ± 1.10	1.03 ± 1.03	0.36 ± 1.28
765	0.89	257.7 ± 16.9	-0.56 ± 0.27	0.91 ± 0.41	1.07 ± 1.32	-0.12 ± -0.12	0.65 ± 1.34
810	0.95	247.8 ± 7.9	-0.11 ± 0.46	0.65 ± 0.52	0.43 ± 1.54	0.23 ± 0.23	0.25 ± 2.96
855	0.89	240.4 ± 13.4	0.16 ± 0.45	0.60 ± 0.56	0.43 ± 1.77	0.33 ± 0.33	0.54 ± 1.80
900	0.82	263.0 ± 7.4	0.44 ± 0.41	-0.12 ± 0.62	-0.13 ± 1.83	0.26 ± 0.26	0.54 ± 2.84
945	0.84	209.5 ± 34.0	-0.26 ± 0.29	-0.05 ± 0.53	0.34 ± 1.82	-0.21 ± -0.21	-0.13 ± 2.04
990	0.92	191.7 ± 17.9	-1.51 ± 0.30	0.42 ± 0.52	-0.12 ± 1.82	-1.03 ± -1.03	–

Table A.32 – Same as in Table A.1, but for KIC 7670943. Due to the extremely large error bars, the results from the cross-correlation method, that are shown here, were obtained from 180-d sub-series.

KIC 7680114

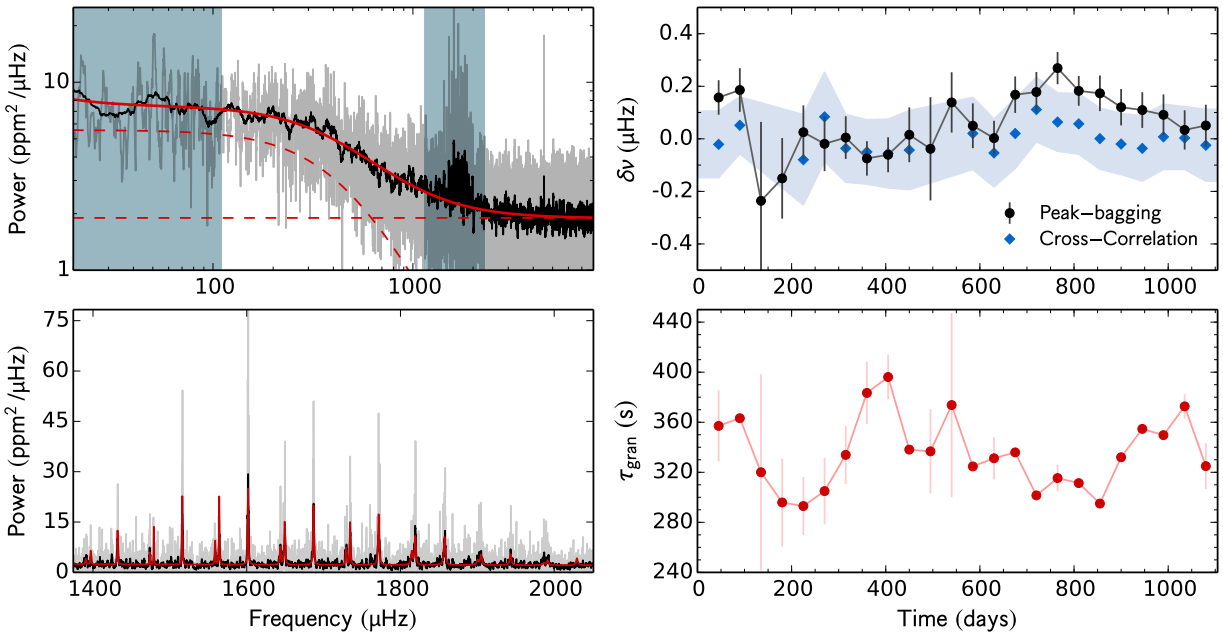

Fig. A.33 – Same as in Fig. A.1, but for KIC 7680114.

time (days)	d_c %	τ_{gran} (s)	Peak-bagging $\delta\nu_{l=0}$ (μHz)	$\delta\nu_{l=1}$ (μHz)	$\delta\nu_{l=2}$ (μHz)	$\delta\nu$ (μHz)	Cross-correlation $\delta\nu$ (μHz)
45	0.98	357.1 ± 28.5	0.11 ± 0.10	0.19 ± 0.09	-0.14 ± 0.15	0.16 ± 0.16	-0.02 ± 0.13
90	0.54	363.2 ± 2.7	-0.03 ± 0.15	0.29 ± 0.10	-0.24 ± 0.16	0.19 ± 0.19	0.05 ± 0.11
135	0.05	320.0 ± 78.5	-0.21 ± 0.44	-0.26 ± 0.41	0.33 ± 0.72	-0.24 ± -0.24	–
180	0.33	295.9 ± 35.2	-0.08 ± 0.22	-0.22 ± 0.22	-0.81 ± 0.28	-0.15 ± -0.15	–
225	0.58	293.0 ± 23.2	0.01 ± 0.14	0.04 ± 0.15	-0.60 ± 0.19	0.03 ± 0.03	-0.08 ± 0.17
270	0.56	305.0 ± 26.6	-0.05 ± 0.15	0.00 ± 0.14	0.47 ± 0.29	-0.02 ± -0.02	0.08 ± 0.17
315	0.78	333.9 ± 23.2	0.04 ± 0.12	-0.03 ± 0.11	0.13 ± 0.20	0.00 ± 0.00	-0.04 ± 0.13
360	0.89	383.4 ± 24.9	-0.12 ± 0.09	-0.02 ± 0.10	0.09 ± 0.17	-0.07 ± -0.07	-0.05 ± 0.12
405	0.93	396.1 ± 17.9	-0.16 ± 0.09	0.10 ± 0.11	-0.02 ± 0.17	-0.06 ± -0.06	-0.06 ± 0.13
450	0.63	338.1 ± 0.9	-0.12 ± 0.16	0.12 ± 0.14	0.03 ± 0.21	0.02 ± 0.02	-0.04 ± 0.15
495	0.14	336.7 ± 33.7	0.12 ± 0.26	-0.24 ± 0.30	0.24 ± 0.44	-0.04 ± -0.04	–
540	0.30	373.7 ± 73.5	0.15 ± 0.14	0.12 ± 0.20	0.19 ± 0.34	0.14 ± 0.14	–
585	0.76	324.7 ± 0.2	0.01 ± 0.11	0.11 ± 0.13	0.21 ± 0.21	0.05 ± 0.05	0.02 ± 0.14
630	0.92	331.2 ± 16.9	-0.01 ± 0.09	0.02 ± 0.09	0.20 ± 0.11	0.00 ± 0.00	-0.05 ± 0.13
675	0.90	335.9 ± 0.2	0.13 ± 0.11	0.19 ± 0.09	-0.02 ± 0.11	0.17 ± 0.17	0.02 ± 0.13
720	0.90	301.5 ± 0.7	-0.08 ± 0.11	0.39 ± 0.10	0.03 ± 0.10	0.18 ± 0.18	0.11 ± 0.12
765	0.95	315.4 ± 10.4	0.19 ± 0.10	0.32 ± 0.08	0.14 ± 0.09	0.27 ± 0.27	0.06 ± 0.11
810	0.90	311.4 ± 2.3	0.04 ± 0.08	0.33 ± 0.08	-0.33 ± 0.18	0.18 ± 0.18	0.06 ± 0.11
855	0.89	295.0 ± 0.0	0.01 ± 0.09	0.37 ± 0.10	-0.14 ± 0.15	0.17 ± 0.17	0.00 ± 0.12
900	0.95	332.0 ± 0.9	0.06 ± 0.10	0.17 ± 0.09	0.15 ± 0.16	0.12 ± 0.12	-0.02 ± 0.12
945	0.90	354.7 ± 2.6	0.08 ± 0.11	0.13 ± 0.09	0.10 ± 0.19	0.11 ± 0.11	-0.04 ± 0.12
990	0.89	349.7 ± 0.8	0.05 ± 0.14	0.11 ± 0.09	0.07 ± 0.16	0.09 ± 0.09	0.01 ± 0.12
1035	0.85	372.7 ± 9.6	-0.16 ± 0.12	0.17 ± 0.10	0.10 ± 0.13	0.03 ± 0.03	0.00 ± 0.12
1080	0.85	324.9 ± 18.3	-0.19 ± 0.13	0.19 ± 0.10	-0.10 ± 0.12	0.05 ± 0.05	-0.02 ± 0.14

Table A.33 – Same as in Table A.1, but for KIC 7680114.

KIC 7771282

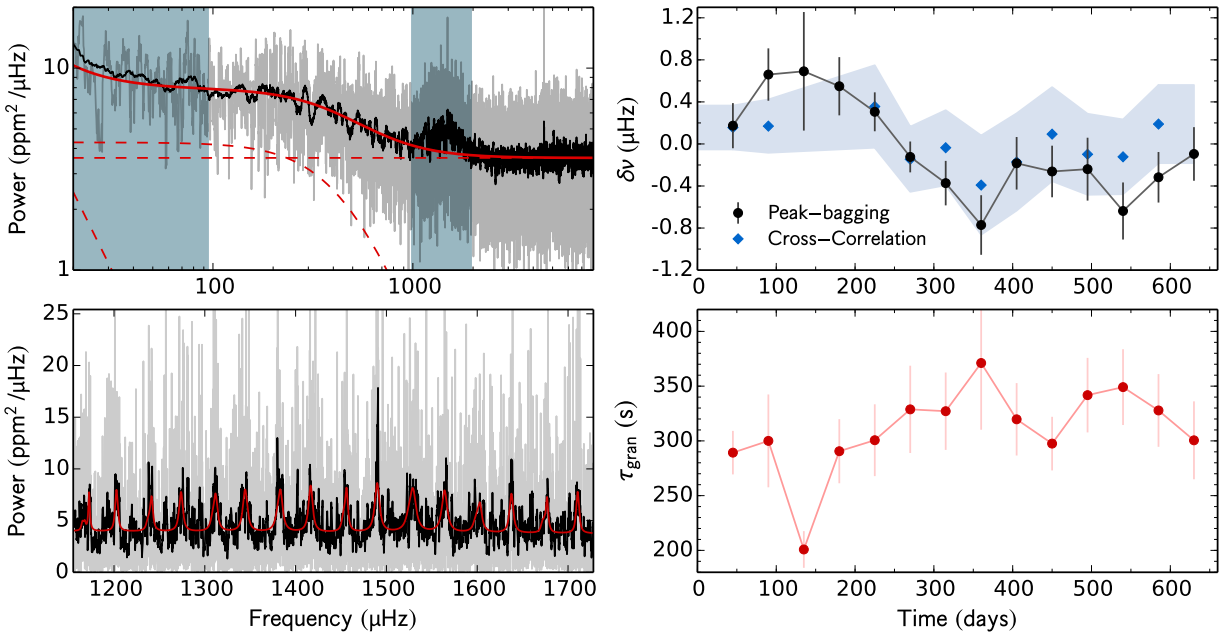

Fig. A.34 – Same as in Fig. A.1, but for KIC 7771282.

time (days)	d_c %	τ_{gran} (s)	Peak-bagging $\delta\nu_{l=0}$ (μHz)	$\delta\nu_{l=1}$ (μHz)	$\delta\nu_{l=2}$ (μHz)	$\delta\nu$ (μHz)	Cross-correlation $\delta\nu$ (μHz)
45	0.97	289.3 ± 19.9	0.38 ± 0.29	-0.07 ± 0.31	-1.39 ± 0.49	0.17 ± 0.17	0.16 ± 0.21
90	0.54	300.0 ± 42.4	1.11 ± 0.33	0.07 ± 0.38	-0.82 ± 0.73	0.66 ± 0.66	0.17 ± 0.25
135	0.05	200.8 ± 16.8	0.34 ± 0.84	0.98 ± 0.76	0.21 ± 0.78	0.69 ± 0.69	–
180	0.42	290.6 ± 29.3	0.13 ± 0.34	1.40 ± 0.48	1.41 ± 0.66	0.55 ± 0.55	–
225	0.90	300.6 ± 32.8	0.23 ± 0.24	0.42 ± 0.30	1.15 ± 0.65	0.31 ± 0.31	0.36 ± 0.39
270	0.81	328.8 ± 39.9	-0.10 ± 0.24	-0.14 ± 0.19	-0.78 ± 0.43	-0.12 ± -0.12	-0.15 ± 0.31
315	0.78	327.1 ± 35.3	-0.86 ± 0.30	0.09 ± 0.29	-0.30 ± 0.58	-0.37 ± -0.37	-0.04 ± 0.36
360	0.89	371.1 ± 60.9	-0.86 ± 0.44	-0.71 ± 0.37	-0.77 ± 0.54	-0.77 ± -0.77	-0.39 ± 0.47
405	0.93	319.7 ± 33.1	0.24 ± 0.37	-0.56 ± 0.34	-1.06 ± 0.56	-0.18 ± -0.18	-0.17 ± 0.46
450	0.97	297.5 ± 24.5	-0.25 ± 0.32	-0.28 ± 0.38	0.18 ± 0.65	-0.26 ± -0.26	0.09 ± 0.45
495	0.97	341.8 ± 34.0	-0.64 ± 0.46	0.04 ± 0.39	0.74 ± 0.61	-0.24 ± -0.24	-0.10 ± 0.39
540	0.98	349.1 ± 34.6	-0.86 ± 0.44	-0.50 ± 0.34	0.55 ± 0.63	-0.64 ± -0.64	-0.12 ± 0.36
585	0.94	327.8 ± 33.2	0.08 ± 0.41	-0.52 ± 0.30	-0.39 ± 0.54	-0.32 ± -0.32	0.19 ± 0.37
630	0.73	300.5 ± 35.6	0.59 ± 0.41	-0.53 ± 0.33	0.62 ± 0.67	-0.10 ± -0.10	–

Table A.34 – Same as in Table A.1, but for KIC 7771282.

KIC 7871531

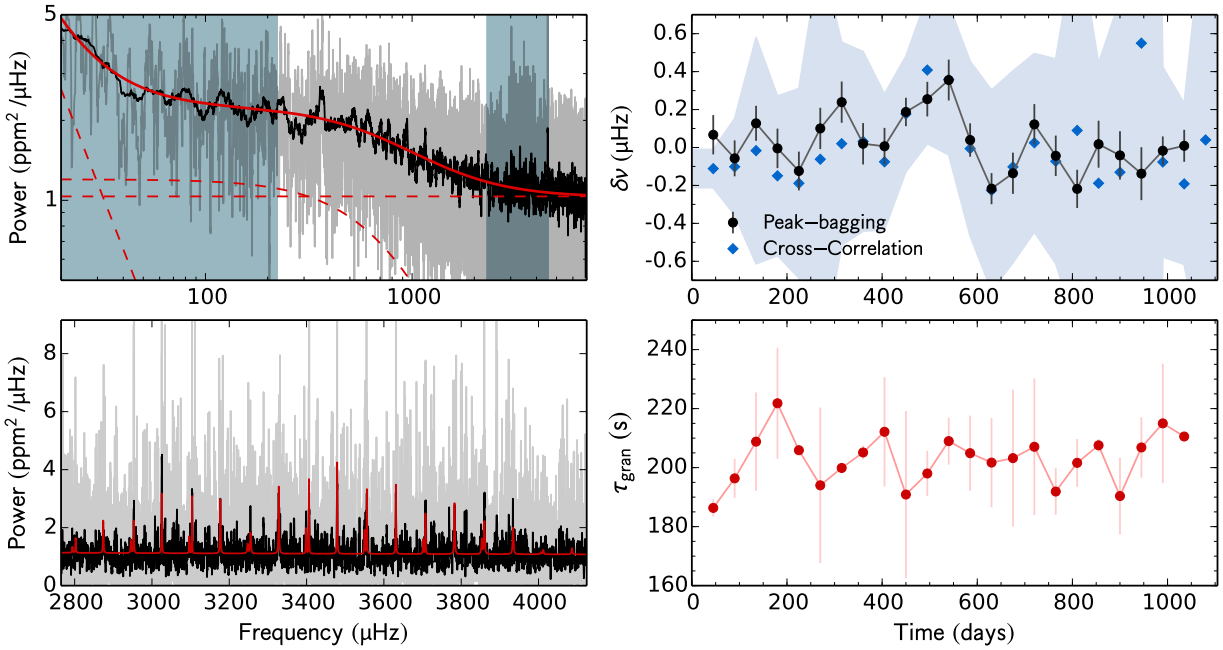

Fig. A.35 – Same as in Fig. A.1, but for KIC 7871531.

time (days)	d_c %	τ_{gran} (s)	Peak-bagging $\delta\nu_{l=0}$ (μHz)	$\delta\nu_{l=1}$ (μHz)	$\delta\nu_{l=2}$ (μHz)	$\delta\nu$ (μHz)	Cross-correlation $\delta\nu$ (μHz)
45	0.98	186.3 ± 2.9	0.15 ± 0.17	0.02 ± 0.13	0.31 ± 0.29	0.07 ± 0.07	-0.11 ± 0.10
90	0.97	196.4 ± 6.6	0.02 ± 0.13	-0.15 ± 0.14	0.37 ± 0.28	-0.06 ± -0.06	-0.10 ± 0.25
135	0.96	208.8 ± 16.7	0.06 ± 0.11	0.27 ± 0.16	0.67 ± 0.27	0.13 ± 0.13	-0.02 ± 0.60
180	0.97	221.8 ± 18.8	-0.17 ± 0.15	0.15 ± 0.14	0.59 ± 0.32	-0.00 ± -0.00	-0.15 ± 0.42
225	0.96	205.9 ± 0.0	-0.28 ± 0.14	0.05 ± 0.15	-0.34 ± 0.38	-0.12 ± -0.12	-0.19 ± 0.50
270	0.80	194.0 ± 26.4	0.01 ± 0.14	0.21 ± 0.17	0.34 ± 0.38	0.10 ± 0.10	-0.06 ± 1.09
315	0.78	199.9 ± 0.8	0.39 ± 0.15	0.09 ± 0.15	0.55 ± 0.37	0.24 ± 0.24	0.02 ± 0.53
360	0.89	205.1 ± 2.3	0.20 ± 0.17	-0.11 ± 0.14	0.05 ± 0.25	0.02 ± 0.02	0.03 ± 0.47
405	0.93	212.1 ± 18.5	0.14 ± 0.13	-0.16 ± 0.15	-0.11 ± 0.27	0.01 ± 0.01	-0.08 ± 0.36
450	0.97	190.9 ± 28.3	0.28 ± 0.09	0.02 ± 0.12	-0.22 ± 0.24	0.19 ± 0.19	0.18 ± 0.30
495	0.97	198.0 ± 7.7	0.22 ± 0.13	0.29 ± 0.13	-1.11 ± 0.40	0.25 ± 0.25	0.41 ± 0.39
540	0.98	209.0 ± 7.9	0.31 ± 0.15	0.41 ± 0.16	-0.59 ± 0.46	0.36 ± 0.36	0.36 ± 0.40
585	0.94	204.9 ± 12.7	0.03 ± 0.11	0.05 ± 0.16	-0.01 ± 0.32	0.04 ± 0.04	-0.01 ± 0.46
630	0.92	201.7 ± 15.1	-0.16 ± 0.11	-0.29 ± 0.12	-0.08 ± 0.28	-0.22 ± -0.22	-0.23 ± 0.53
675	0.90	203.2 ± 23.2	-0.02 ± 0.16	-0.24 ± 0.15	0.41 ± 0.29	-0.14 ± -0.14	-0.10 ± 0.51
720	0.91	207.1 ± 23.2	0.17 ± 0.17	0.09 ± 0.14	0.36 ± 0.39	0.12 ± 0.12	0.02 ± 0.47
765	0.95	191.9 ± 7.9	-0.46 ± 0.18	0.20 ± 0.13	-0.42 ± 0.41	-0.04 ± -0.04	-0.07 ± 0.54
810	0.90	201.6 ± 8.1	-0.25 ± 0.13	-0.18 ± 0.15	0.65 ± 0.57	-0.22 ± -0.22	0.09 ± 1.05
855	0.89	207.6 ± 2.1	0.12 ± 0.16	-0.14 ± 0.20	-0.63 ± 0.49	0.02 ± 0.02	-0.19 ± 0.63
900	0.95	190.4 ± 13.0	0.18 ± 0.21	-0.16 ± 0.16	-0.75 ± 0.43	-0.04 ± -0.04	-0.13 ± 0.91
945	0.90	206.8 ± 10.3	-0.09 ± 0.22	-0.17 ± 0.18	-0.19 ± 0.38	-0.14 ± -0.14	0.55 ± 7.63
990	0.89	215.0 ± 20.2	-0.11 ± 0.10	0.09 ± 0.11	0.02 ± 0.19	-0.02 ± -0.02	-0.08 ± 0.50
1035	0.85	210.5 ± 0.8	-0.19 ± 0.14	0.13 ± 0.11	0.33 ± 0.14	0.01 ± 0.01	-0.19 ± 0.42
1080	–	–	–	–	–	–	0.04 ± 1.26

Table A.35 – Same as in Table A.1, but for KIC 7871531.

KIC 7940546

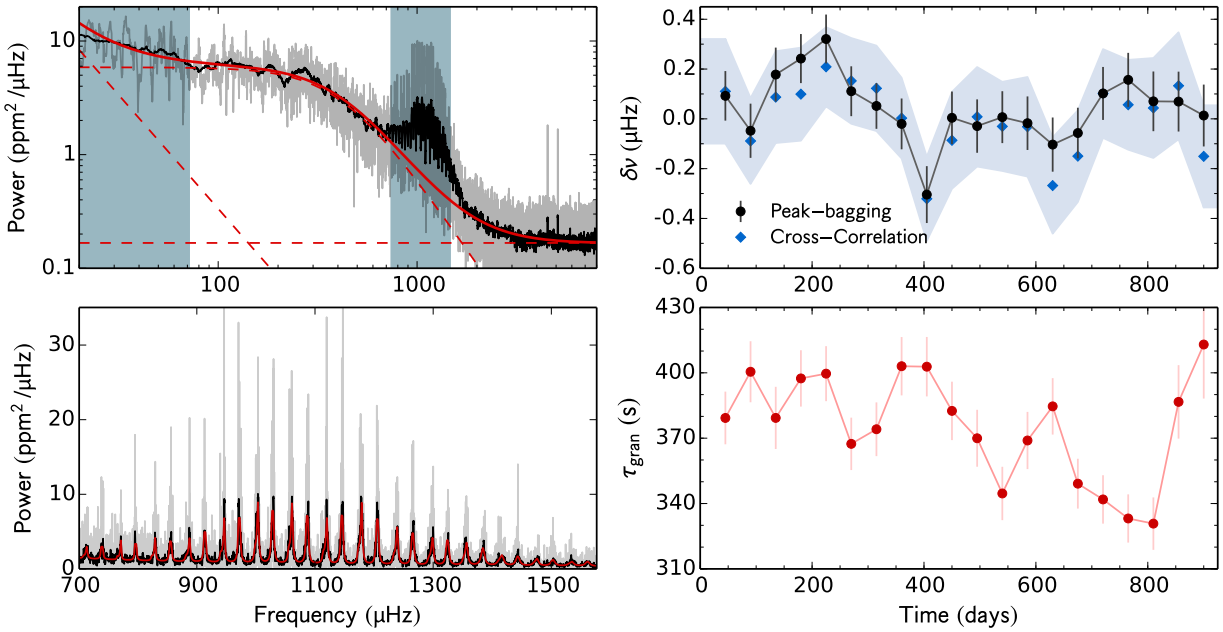

Fig. A.36 – Same as in Fig. A.1, but for KIC 7940546.

time (days)	d_c %	τ_{gran} (s)	Peak-bagging $\delta\nu_{l=0}$ (μHz)	$\delta\nu_{l=1}$ (μHz)	$\delta\nu_{l=2}$ (μHz)	$\delta\nu$ (μHz)	Cross-correlation $\delta\nu$ (μHz)
45	0.97	379.3 ± 12.1	0.11 ± 0.14	0.07 ± 0.14	0.54 ± 0.28	0.09 ± 0.09	0.11 ± 0.21
90	0.77	400.5 ± 14.0	-0.01 ± 0.16	-0.08 ± 0.15	0.36 ± 0.29	-0.05 ± -0.05	-0.09 ± 0.17
135	0.73	379.3 ± 14.3	0.09 ± 0.17	0.24 ± 0.14	-0.04 ± 0.31	0.18 ± 0.18	0.09 ± 0.18
180	0.92	397.4 ± 12.9	0.28 ± 0.14	0.20 ± 0.14	-0.67 ± 0.26	0.24 ± 0.24	0.10 ± 0.19
225	0.98	399.6 ± 12.6	0.56 ± 0.14	0.10 ± 0.14	-0.44 ± 0.26	0.32 ± 0.32	0.21 ± 0.16
270	0.97	367.4 ± 12.0	0.20 ± 0.15	0.05 ± 0.13	-0.01 ± 0.30	0.11 ± 0.11	0.15 ± 0.17
315	0.97	374.1 ± 12.3	-0.02 ± 0.14	0.10 ± 0.12	0.25 ± 0.27	0.05 ± 0.05	0.12 ± 0.17
360	0.97	403.0 ± 13.4	-0.08 ± 0.17	0.02 ± 0.13	0.41 ± 0.33	-0.02 ± -0.02	0.00 ± 0.16
405	0.94	402.8 ± 13.6	-0.34 ± 0.19	-0.28 ± 0.14	0.47 ± 0.33	-0.30 ± -0.30	-0.32 ± 0.17
450	0.91	382.5 ± 13.4	0.06 ± 0.17	-0.03 ± 0.14	0.13 ± 0.28	0.00 ± 0.00	-0.09 ± 0.19
495	0.88	370.0 ± 13.1	0.04 ± 0.17	-0.08 ± 0.14	0.69 ± 0.30	-0.03 ± -0.03	0.01 ± 0.20
540	0.91	344.6 ± 12.2	0.13 ± 0.15	-0.11 ± 0.14	0.20 ± 0.24	0.01 ± 0.01	-0.03 ± 0.18
585	0.97	368.9 ± 13.1	0.02 ± 0.16	-0.05 ± 0.15	-0.45 ± 0.27	-0.02 ± -0.02	-0.03 ± 0.20
630	0.90	384.6 ± 13.0	-0.15 ± 0.18	-0.07 ± 0.14	-0.58 ± 0.23	-0.10 ± -0.10	-0.27 ± 0.19
675	0.89	349.1 ± 11.4	-0.01 ± 0.15	-0.09 ± 0.14	-0.63 ± 0.26	-0.06 ± -0.06	-0.15 ± 0.18
720	0.95	341.9 ± 11.1	0.19 ± 0.15	0.02 ± 0.15	-0.35 ± 0.27	0.10 ± 0.10	0.10 ± 0.18
765	0.89	333.1 ± 11.1	0.19 ± 0.16	0.13 ± 0.15	-0.66 ± 0.25	0.16 ± 0.16	0.06 ± 0.18
810	0.81	330.8 ± 12.0	0.15 ± 0.16	-0.02 ± 0.17	-0.24 ± 0.31	0.07 ± 0.07	0.04 ± 0.20
855	0.83	386.7 ± 16.9	0.20 ± 0.17	-0.07 ± 0.17	0.24 ± 0.28	0.07 ± 0.07	0.13 ± 0.21
900	0.91	413.0 ± 24.8	-0.03 ± 0.19	0.04 ± 0.16	0.04 ± 0.27	0.01 ± 0.01	-0.15 ± 0.21

Table A.36 – Same as in Table A.1, but for KIC 7940546.

KIC 7970740

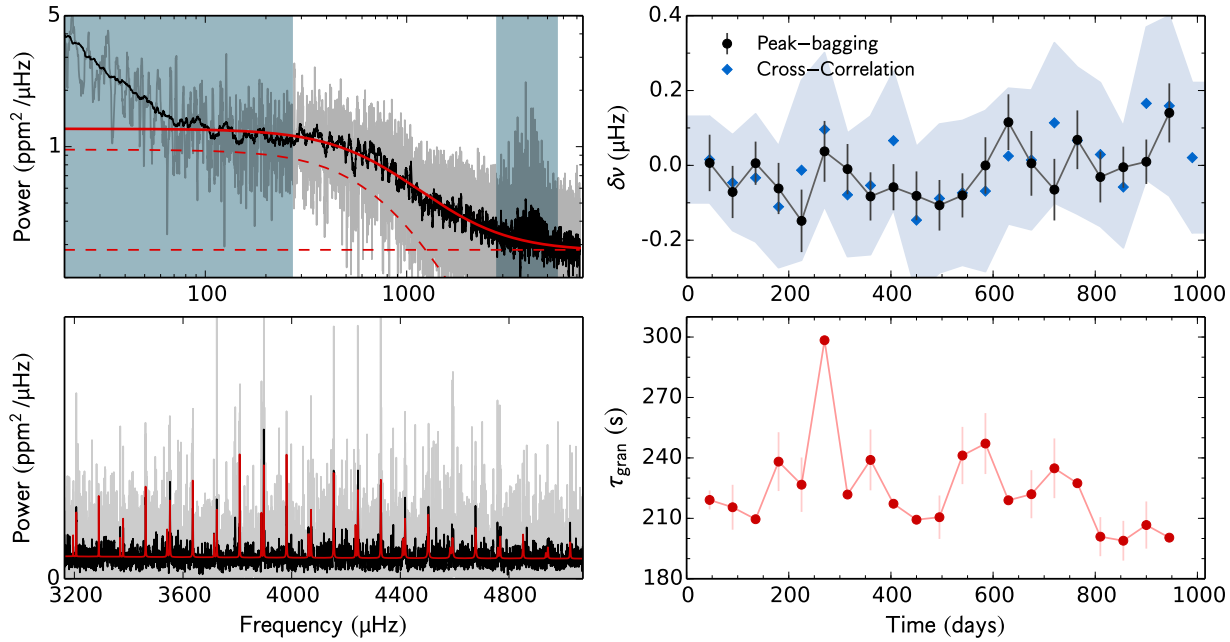

Fig. A.37 – Same as in Fig. A.1, but for KIC 7970740.

time (days)	d_c %	τ_{gran} (s)	Peak-bagging $\delta\nu_{l=0}$ (μHz)	$\delta\nu_{l=1}$ (μHz)	$\delta\nu_{l=2}$ (μHz)	$\delta\nu$ (μHz)	Cross-correlation $\delta\nu$ (μHz)
45	0.97	219.1 ± 4.7	0.07 ± 0.09	-0.11 ± 0.13	-0.19 ± 0.21	0.01 ± 0.01	0.02 ± 0.12
90	0.97	215.5 ± 11.1	-0.01 ± 0.09	-0.16 ± 0.11	0.21 ± 0.24	-0.07 ± -0.07	-0.05 ± 0.13
135	0.96	209.6 ± 0.3	-0.01 ± 0.08	0.02 ± 0.08	-0.09 ± 0.14	0.01 ± 0.01	-0.03 ± 0.17
180	0.77	238.2 ± 14.6	-0.11 ± 0.10	-0.01 ± 0.10	-0.07 ± 0.15	-0.06 ± -0.06	-0.11 ± 0.16
225	0.72	226.7 ± 13.5	-0.24 ± 0.10	0.04 ± 0.14	-0.08 ± 0.17	-0.15 ± -0.15	-0.01 ± 0.24
270	0.92	298.4 ± 0.4	-0.03 ± 0.11	0.13 ± 0.12	-0.25 ± 0.16	0.04 ± 0.04	0.10 ± 0.21
315	0.98	221.8 ± 1.0	0.06 ± 0.09	-0.10 ± 0.10	-0.23 ± 0.14	-0.01 ± -0.01	-0.08 ± 0.16
360	0.97	239.0 ± 15.1	-0.08 ± 0.08	-0.09 ± 0.11	0.02 ± 0.17	-0.08 ± -0.08	-0.05 ± 0.19
405	0.97	217.2 ± 0.3	-0.07 ± 0.07	-0.02 ± 0.12	0.05 ± 0.17	-0.06 ± -0.06	0.07 ± 0.18
450	0.97	209.3 ± 0.0	-0.12 ± 0.08	-0.02 ± 0.10	-0.21 ± 0.22	-0.08 ± -0.08	-0.15 ± 0.20
495	0.94	210.6 ± 10.8	-0.16 ± 0.09	-0.03 ± 0.11	-0.14 ± 0.18	-0.11 ± -0.11	-0.09 ± 0.20
540	0.91	241.2 ± 14.2	-0.13 ± 0.07	0.02 ± 0.11	-0.31 ± 0.18	-0.08 ± -0.08	-0.07 ± 0.19
585	0.88	247.1 ± 15.1	-0.03 ± 0.09	0.06 ± 0.14	-0.32 ± 0.21	-0.00 ± -0.00	-0.07 ± 0.22
630	0.92	219.0 ± 0.5	0.18 ± 0.09	-0.06 ± 0.15	0.09 ± 0.23	0.12 ± 0.12	0.02 ± 0.18
675	0.97	222.0 ± 11.9	0.02 ± 0.11	-0.02 ± 0.14	0.36 ± 0.27	0.01 ± 0.01	0.01 ± 0.19
720	0.89	234.8 ± 14.8	0.02 ± 0.12	-0.14 ± 0.11	-0.48 ± 0.34	-0.06 ± -0.06	0.11 ± 0.21
765	0.89	227.4 ± 0.5	0.19 ± 0.11	-0.05 ± 0.11	0.01 ± 0.19	0.07 ± 0.07	0.07 ± 0.20
810	0.95	200.9 ± 9.7	-0.04 ± 0.10	-0.02 ± 0.10	-0.01 ± 0.22	-0.03 ± -0.03	0.03 ± 0.19
855	0.88	198.9 ± 9.9	-0.08 ± 0.07	0.10 ± 0.09	0.24 ± 0.20	-0.00 ± -0.00	-0.06 ± 0.16
900	0.82	206.7 ± 11.7	-0.04 ± 0.07	0.14 ± 0.12	0.05 ± 0.18	0.01 ± 0.01	0.17 ± 0.20
945	0.84	200.4 ± 0.1	0.13 ± 0.09	0.17 ± 0.14	-0.20 ± 0.21	0.14 ± 0.14	0.16 ± 0.24
990	–	–	–	–	–	–	0.02 ± 0.20

Table A.37 – Same as in Table A.1, but for KIC 7970740.

KIC 8006161

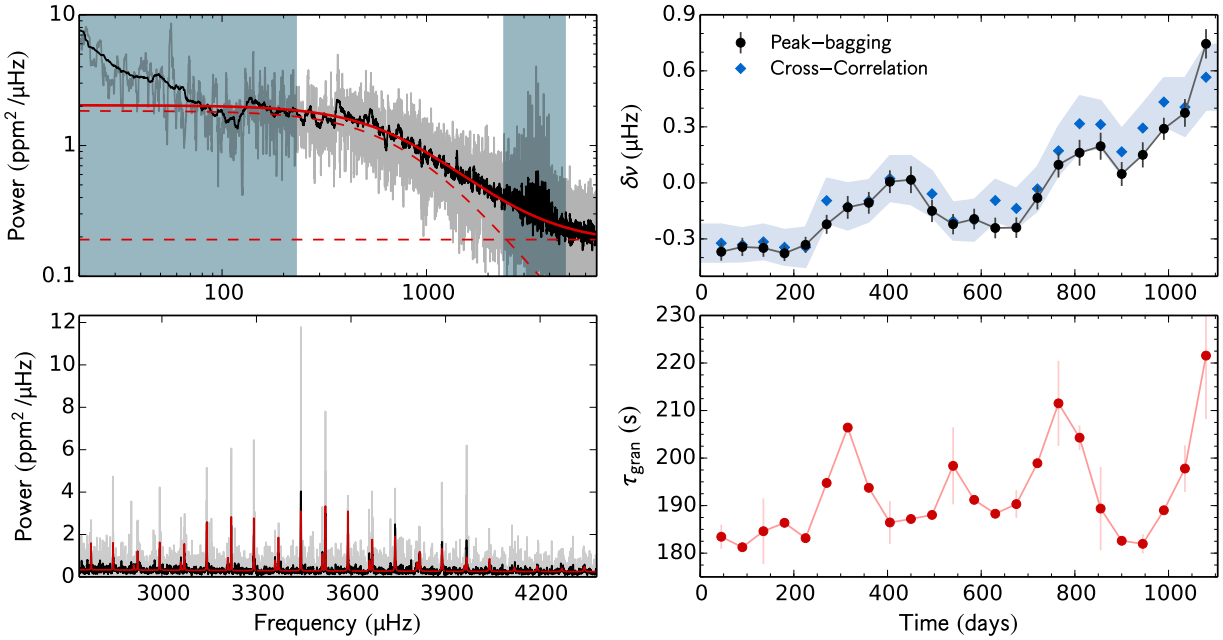

Fig. A.38 – Same as in Fig. A.1, but for KIC 8006161.

time (days)	d_c %	τ_{gran} (s)	Peak-bagging $\delta\nu_{l=0}$ (μHz)	$\delta\nu_{l=1}$ (μHz)	$\delta\nu_{l=2}$ (μHz)	$\delta\nu$ (μHz)	Cross-correlation $\delta\nu$ (μHz)
45	0.97	183.4 ± 2.6	-0.38 ± 0.06	-0.35 ± 0.07	-0.32 ± 0.13	-0.37 ± -0.37	-0.32 ± 0.10
90	0.97	181.2 ± 0.3	-0.26 ± 0.06	-0.45 ± 0.07	-0.44 ± 0.15	-0.34 ± -0.34	-0.33 ± 0.09
135	0.96	184.6 ± 6.9	-0.32 ± 0.06	-0.39 ± 0.08	-0.45 ± 0.14	-0.35 ± -0.35	-0.32 ± 0.09
180	0.97	186.4 ± 0.2	-0.35 ± 0.05	-0.43 ± 0.07	-0.30 ± 0.12	-0.38 ± -0.38	-0.35 ± 0.09
225	0.96	183.2 ± 0.6	-0.28 ± 0.05	-0.44 ± 0.08	-0.36 ± 0.12	-0.33 ± -0.33	-0.34 ± 0.11
270	0.80	194.8 ± 0.6	-0.22 ± 0.06	-0.23 ± 0.09	-0.17 ± 0.15	-0.22 ± -0.22	-0.10 ± 0.12
315	0.78	206.4 ± 0.4	-0.10 ± 0.08	-0.17 ± 0.09	-0.13 ± 0.18	-0.13 ± -0.13	-0.13 ± 0.13
360	0.89	193.7 ± 0.0	-0.03 ± 0.08	-0.21 ± 0.09	-0.14 ± 0.17	-0.11 ± -0.11	-0.10 ± 0.11
405	0.93	186.5 ± 4.5	0.12 ± 0.09	-0.10 ± 0.09	-0.12 ± 0.17	0.01 ± 0.01	0.02 ± 0.12
450	0.97	187.2 ± 0.2	0.16 ± 0.10	-0.13 ± 0.10	-0.18 ± 0.14	0.02 ± 0.02	0.01 ± 0.13
495	0.97	188.0 ± 0.3	-0.16 ± 0.08	-0.14 ± 0.09	-0.35 ± 0.15	-0.15 ± -0.15	-0.06 ± 0.12
540	0.98	198.4 ± 8.1	-0.12 ± 0.07	-0.40 ± 0.09	-0.57 ± 0.15	-0.22 ± -0.22	-0.20 ± 0.10
585	0.94	191.2 ± 0.3	-0.18 ± 0.07	-0.22 ± 0.09	-0.69 ± 0.13	-0.19 ± -0.19	-0.20 ± 0.11
630	0.92	188.3 ± 0.8	-0.33 ± 0.07	-0.10 ± 0.09	-0.17 ± 0.18	-0.24 ± -0.24	-0.09 ± 0.11
675	0.90	190.3 ± 2.9	-0.27 ± 0.07	-0.20 ± 0.09	-0.05 ± 0.14	-0.24 ± -0.24	-0.14 ± 0.11
720	0.90	198.9 ± 0.2	-0.09 ± 0.09	-0.07 ± 0.09	0.00 ± 0.15	-0.08 ± -0.08	-0.03 ± 0.12
765	0.95	211.5 ± 8.9	0.06 ± 0.09	0.15 ± 0.11	-0.30 ± 0.17	0.10 ± 0.10	0.17 ± 0.13
810	0.89	204.3 ± 2.6	0.12 ± 0.09	0.23 ± 0.11	-0.01 ± 0.22	0.16 ± 0.16	0.32 ± 0.15
855	0.89	189.4 ± 8.7	0.12 ± 0.11	0.25 ± 0.09	0.39 ± 0.18	0.20 ± 0.20	0.31 ± 0.13
900	0.95	182.6 ± 0.9	-0.03 ± 0.09	0.14 ± 0.09	0.20 ± 0.14	0.05 ± 0.05	0.17 ± 0.12
945	0.90	182.0 ± 2.0	0.09 ± 0.09	0.22 ± 0.10	0.38 ± 0.17	0.15 ± 0.15	0.29 ± 0.13
990	0.89	189.0 ± 0.0	0.13 ± 0.08	0.51 ± 0.09	0.49 ± 0.20	0.29 ± 0.29	0.43 ± 0.13
1035	0.84	197.8 ± 4.9	0.21 ± 0.10	0.59 ± 0.11	0.47 ± 0.23	0.37 ± 0.37	0.41 ± 0.16
1080	0.84	221.6 ± 13.4	0.78 ± 0.09	0.65 ± 0.15	0.80 ± 0.18	0.74 ± 0.74	0.57 ± 0.17

Table A.38 – Same as in Table A.1, but for KIC 8006161.

KIC 8077137

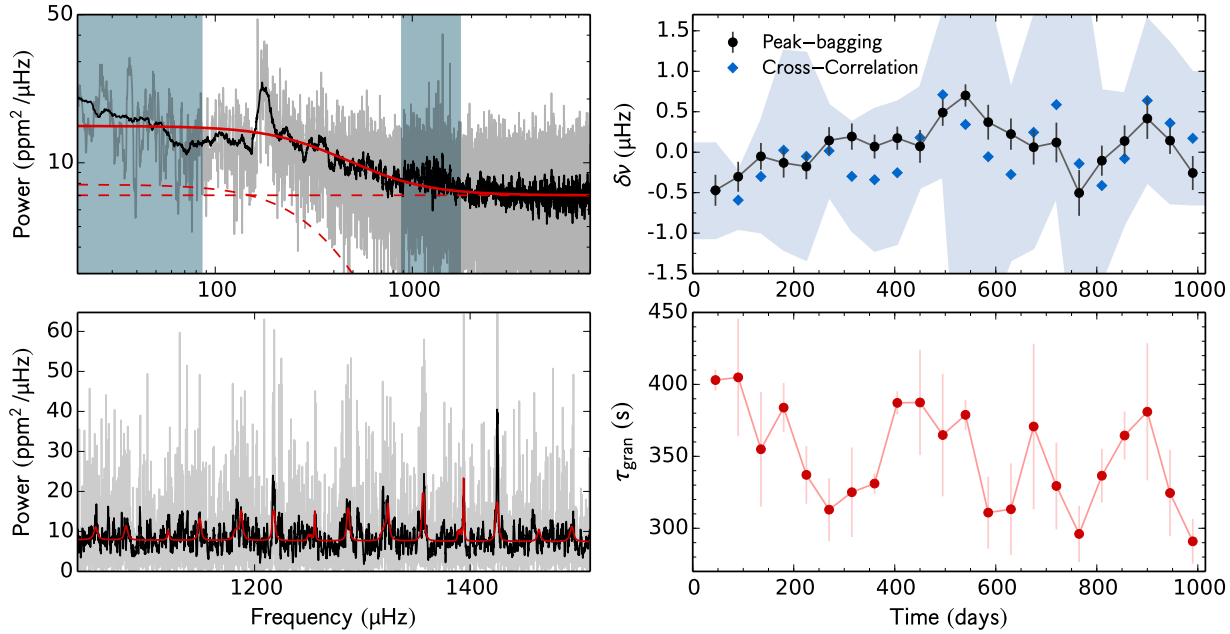

Fig. A.39 – Same as in Fig. A.1, but for KIC 8077137.

time (days)	d_c %	τ_{gran} (s)	Peak-bagging $\delta\nu_{l=0}$ (μHz)	$\delta\nu_{l=1}$ (μHz)	$\delta\nu_{l=2}$ (μHz)	$\delta\nu$ (μHz)	Cross-correlation $\delta\nu$ (μHz)
45	0.98	403.0 ± 7.3	-1.24 ± 0.33	-0.09 ± 0.23	-0.26 ± 0.74	-0.47 ± -0.47	-0.48 ± 0.59
90	0.97	404.9 ± 40.7	-0.07 ± 0.27	-0.51 ± 0.25	1.07 ± 0.68	-0.30 ± -0.30	-0.59 ± 0.36
135	0.96	354.9 ± 39.8	0.11 ± 0.22	-0.27 ± 0.26	1.04 ± 0.70	-0.05 ± -0.05	-0.30 ± 0.69
180	0.78	383.9 ± 17.1	0.23 ± 0.27	-0.44 ± 0.25	0.07 ± 0.68	-0.13 ± -0.13	0.02 ± 1.23
225	0.72	337.1 ± 20.0	-0.09 ± 0.21	-0.29 ± 0.24	-0.84 ± 0.51	-0.18 ± -0.18	-0.05 ± 1.28
270	0.92	312.9 ± 21.9	0.31 ± 0.24	0.01 ± 0.22	-0.34 ± 0.56	0.15 ± 0.15	0.02 ± 0.57
315	0.98	325.0 ± 31.1	0.79 ± 0.24	-0.35 ± 0.22	0.69 ± 0.61	0.19 ± 0.19	-0.30 ± 0.67
360	0.97	331.1 ± 7.1	0.39 ± 0.24	-0.12 ± 0.19	0.27 ± 0.84	0.07 ± 0.07	-0.34 ± 0.88
405	0.97	387.2 ± 8.0	-0.08 ± 0.22	0.35 ± 0.19	-0.70 ± 0.86	0.17 ± 0.17	-0.25 ± 0.88
450	0.97	387.4 ± 36.6	-0.06 ± 0.31	0.17 ± 0.27	1.40 ± 0.70	0.07 ± 0.07	0.18 ± 0.62
495	0.94	364.8 ± 42.6	0.48 ± 0.22	0.50 ± 0.24	1.61 ± 0.67	0.49 ± 0.49	0.71 ± 1.02
540	0.91	378.8 ± 10.4	0.69 ± 0.18	0.72 ± 0.21	-0.57 ± 0.87	0.70 ± 0.70	0.34 ± 4.47
585	0.88	310.9 ± 25.0	0.20 ± 0.29	0.59 ± 0.32	-1.88 ± 0.65	0.37 ± 0.37	-0.06 ± 1.98
630	0.92	313.2 ± 31.9	0.42 ± 0.24	-0.10 ± 0.32	-0.41 ± 0.75	0.22 ± 0.22	-0.28 ± 1.06
675	0.97	370.7 ± 57.6	0.01 ± 0.31	0.11 ± 0.30	-0.14 ± 0.97	0.06 ± 0.06	0.25 ± 1.43
720	0.90	329.4 ± 30.1	-0.25 ± 0.34	0.52 ± 0.35	-1.17 ± 0.90	0.12 ± 0.12	0.59 ± 1.14
765	0.89	296.1 ± 19.6	-0.87 ± 0.37	-0.02 ± 0.43	-0.62 ± 0.78	-0.50 ± -0.50	-0.14 ± 2.77
810	0.95	336.5 ± 18.7	-0.09 ± 0.26	-0.12 ± 0.27	-0.87 ± 0.61	-0.10 ± -0.10	-0.41 ± 1.18
855	0.89	364.5 ± 16.7	0.40 ± 0.27	-0.16 ± 0.28	-0.42 ± 0.73	0.14 ± 0.14	-0.08 ± 0.81
900	0.82	381.0 ± 47.7	0.45 ± 0.42	0.40 ± 0.32	0.72 ± 0.73	0.42 ± 0.42	0.64 ± 1.01
945	0.84	324.5 ± 30.0	0.31 ± 0.25	0.01 ± 0.22	1.14 ± 0.55	0.14 ± 0.14	0.36 ± 0.99
990	0.92	290.9 ± 15.6	-0.12 ± 0.34	-0.34 ± 0.27	1.10 ± 0.69	-0.26 ± -0.26	0.17 ± 0.82

Table A.39 – Same as in Table A.1, but for KIC 8077137.

KIC 8150065

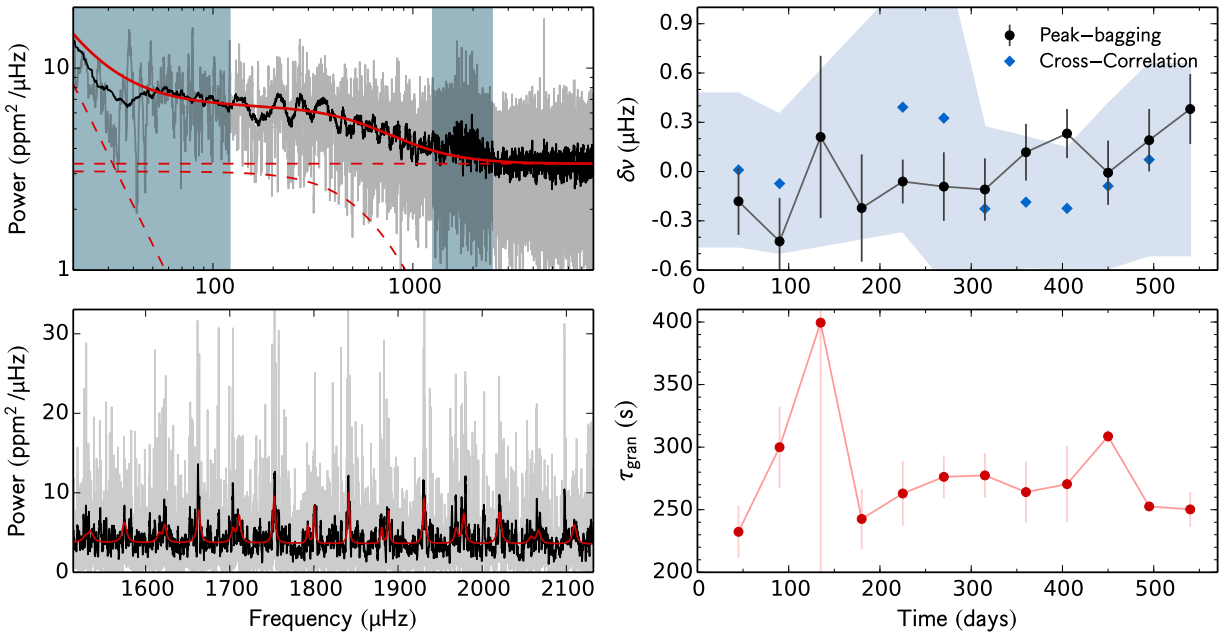

Fig. A.40 – Same as in Fig. A.1, but for KIC 8150065.

time (days)	d_c %	τ_{gran} (s)	Peak-bagging $\delta\nu_{l=0}$ (μHz)	$\delta\nu_{l=1}$ (μHz)	$\delta\nu_{l=2}$ (μHz)	$\delta\nu$ (μHz)	Cross-correlation $\delta\nu$ (μHz)
45	0.97	232.4 ± 21.0	-0.22 ± 0.38	-0.17 ± 0.24	-1.43 ± 0.40	-0.18 ± -0.18	0.01 ± 0.47
90	0.54	299.9 ± 32.7	-0.74 ± 0.45	-0.26 ± 0.33	-1.27 ± 0.61	-0.43 ± -0.43	-0.07 ± 0.42
135	0.05	399.5 ± 460.4	0.26 ± 0.68	0.16 ± 0.72	-0.32 ± 0.80	0.21 ± 0.21	–
180	0.33	242.6 ± 23.9	-0.43 ± 0.52	-0.08 ± 0.42	0.36 ± 0.68	-0.22 ± -0.22	–
225	0.58	263.0 ± 25.9	-0.19 ± 0.16	0.20 ± 0.23	0.34 ± 0.35	-0.06 ± -0.06	0.39 ± 0.75
270	0.56	276.3 ± 17.2	0.43 ± 0.33	-0.45 ± 0.27	-0.14 ± 0.40	-0.09 ± -0.09	0.33 ± 0.99
315	0.78	277.4 ± 17.9	0.54 ± 0.33	-0.42 ± 0.23	1.17 ± 0.38	-0.11 ± -0.11	-0.23 ± 0.50
360	0.89	264.1 ± 24.5	0.25 ± 0.28	0.04 ± 0.22	0.78 ± 0.30	0.12 ± 0.12	-0.19 ± 0.40
405	0.93	270.4 ± 30.6	0.23 ± 0.21	0.23 ± 0.22	0.24 ± 0.38	0.23 ± 0.23	-0.22 ± 0.37
450	0.97	308.6 ± 5.1	0.18 ± 0.27	-0.22 ± 0.29	-0.28 ± 0.37	-0.01 ± -0.01	-0.09 ± 0.50
495	0.97	252.6 ± 0.2	0.33 ± 0.26	0.03 ± 0.27	-0.04 ± 0.41	0.19 ± 0.19	0.07 ± 0.58
540	0.68	250.3 ± 13.8	0.23 ± 0.29	0.55 ± 0.31	0.38 ± 0.57	0.38 ± 0.38	–

Table A.40 – Same as in Table A.1, but for KIC 8150065.

KIC 8179536

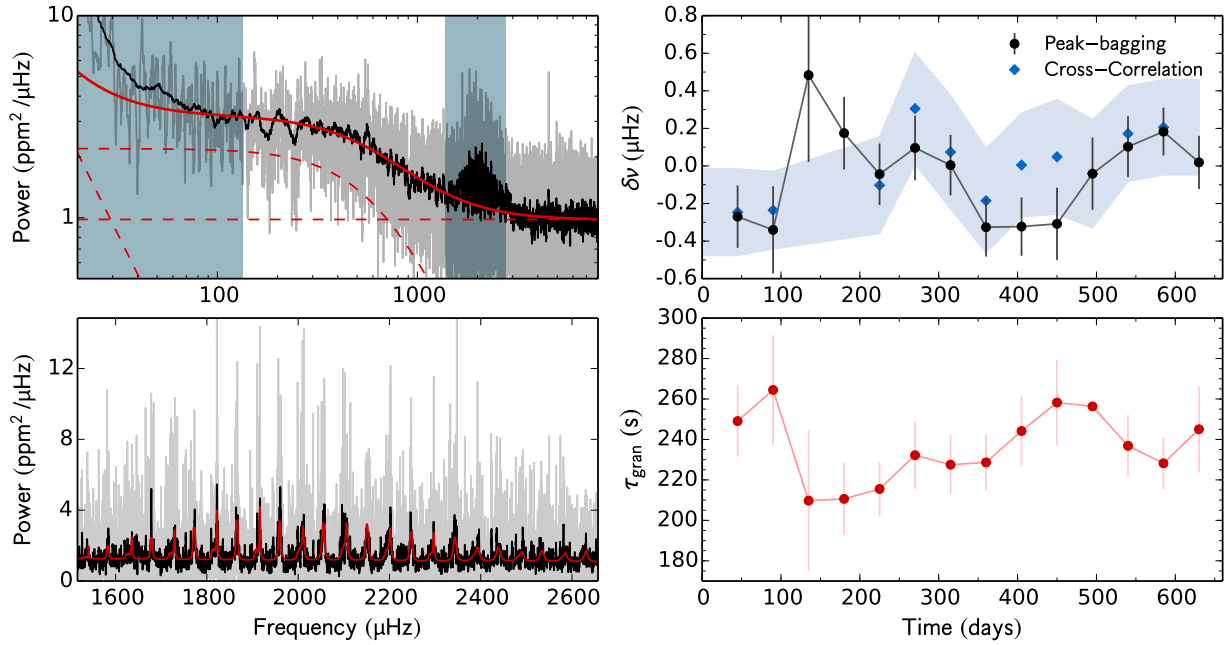

Fig. A.41 – Same as in Fig. A.1, but for KIC 8179536.

time (days)	d_c %	τ_{gran} (s)	Peak-bagging $\delta\nu_{l=0}$ (μHz)	$\delta\nu_{l=1}$ (μHz)	$\delta\nu_{l=2}$ (μHz)	$\delta\nu$ (μHz)	Cross-correlation $\delta\nu$ (μHz)
45	0.98	249.1 ± 17.5	-0.21 ± 0.21	-0.37 ± 0.27	-0.13 ± 0.48	-0.27 ± -0.27	-0.25 ± 0.23
90	0.54	264.5 ± 27.0	-0.14 ± 0.30	-0.64 ± 0.37	0.35 ± 0.55	-0.34 ± -0.34	-0.24 ± 0.21
135	0.05	209.7 ± 34.6	0.68 ± 0.62	0.23 ± 0.69	0.10 ± 0.66	0.48 ± 0.48	–
180	0.42	210.6 ± 17.9	0.09 ± 0.25	0.30 ± 0.30	-0.05 ± 0.53	0.17 ± 0.17	–
225	0.90	215.5 ± 13.2	0.02 ± 0.21	-0.13 ± 0.25	0.31 ± 0.41	-0.04 ± -0.04	-0.10 ± 0.26
270	0.81	232.2 ± 16.6	0.03 ± 0.23	0.18 ± 0.26	0.11 ± 0.50	0.10 ± 0.10	0.31 ± 0.29
315	0.78	227.5 ± 14.7	0.10 ± 0.25	-0.06 ± 0.21	-0.23 ± 0.48	0.00 ± 0.00	0.07 ± 0.30
360	0.89	228.6 ± 13.9	-0.42 ± 0.21	-0.22 ± 0.23	0.22 ± 0.39	-0.33 ± -0.33	-0.19 ± 0.28
405	0.93	244.2 ± 17.5	-0.55 ± 0.20	0.04 ± 0.25	-0.10 ± 0.45	-0.32 ± -0.32	0.00 ± 0.28
450	0.97	258.2 ± 21.1	-0.71 ± 0.25	0.32 ± 0.31	-0.85 ± 0.52	-0.31 ± -0.31	0.05 ± 0.30
495	0.97	256.3 ± nan	-0.44 ± 0.27	0.40 ± 0.28	-0.23 ± 0.49	-0.04 ± -0.04	-0.04 ± 0.29
540	0.98	236.9 ± 15.2	0.20 ± 0.24	0.01 ± 0.22	-0.12 ± 0.37	0.10 ± 0.10	0.17 ± 0.25
585	0.94	228.2 ± 12.7	0.57 ± 0.17	-0.30 ± 0.19	-0.31 ± 0.35	0.18 ± 0.18	0.21 ± 0.25
630	0.73	245.0 ± 21.0	0.08 ± 0.17	-0.12 ± 0.25	0.56 ± 0.49	0.02 ± 0.02	–

Table A.41 – Same as in Table A.1, but for KIC 8179536.

KIC 8228742

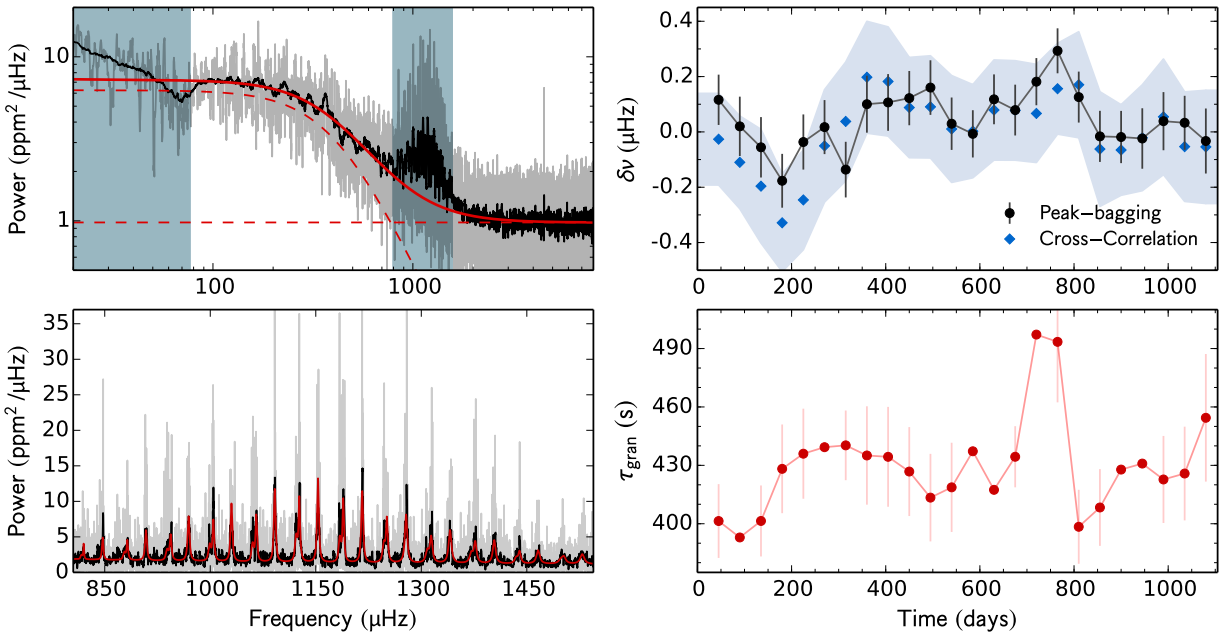

Fig. A.42 – Same as in Fig. A.1, but for KIC 8228742.

time (days)	d_c %	τ_{gran} (s)	Peak-bagging $\delta\nu_{l=0}$ (μHz)	$\delta\nu_{l=1}$ (μHz)	$\delta\nu_{l=2}$ (μHz)	$\delta\nu$ (μHz)	Cross-correlation $\delta\nu$ (μHz)
45	0.98	401.4 ± 19.0	0.23 ± 0.13	0.01 ± 0.13	0.28 ± 0.18	0.12 ± 0.12	-0.03 ± 0.17
90	0.97	393.0 ± 1.9	0.11 ± 0.16	-0.06 ± 0.15	-0.25 ± 0.22	0.02 ± 0.02	-0.11 ± 0.17
135	0.96	401.4 ± 18.2	0.08 ± 0.17	-0.15 ± 0.14	-0.14 ± 0.23	-0.06 ± -0.06	-0.20 ± 0.21
180	0.97	428.2 ± 22.8	-0.04 ± 0.16	-0.26 ± 0.12	-0.55 ± 0.22	-0.18 ± -0.18	-0.33 ± 0.18
225	0.96	436.0 ± 23.1	-0.08 ± 0.16	-0.01 ± 0.13	-0.42 ± 0.21	-0.04 ± -0.04	-0.25 ± 0.18
270	0.80	439.3 ± 2.5	-0.29 ± 0.15	0.22 ± 0.13	-0.29 ± 0.21	0.02 ± 0.02	-0.05 ± 0.20
315	0.78	440.3 ± 17.9	-0.32 ± 0.14	0.04 ± 0.14	-0.83 ± 0.30	-0.14 ± -0.14	0.04 ± 0.21
360	0.89	435.1 ± 25.3	-0.06 ± 0.15	0.24 ± 0.14	-0.46 ± 0.26	0.10 ± 0.10	0.20 ± 0.20
405	0.93	434.4 ± 25.7	-0.05 ± 0.16	0.22 ± 0.13	-0.22 ± 0.24	0.11 ± 0.11	0.18 ± 0.20
450	0.97	426.8 ± 22.9	-0.08 ± 0.15	0.27 ± 0.13	0.00 ± 0.25	0.12 ± 0.12	0.09 ± 0.18
495	0.97	413.4 ± 22.5	-0.04 ± 0.14	0.36 ± 0.14	-0.17 ± 0.23	0.16 ± 0.16	0.09 ± 0.18
540	0.98	418.7 ± 22.9	0.12 ± 0.13	-0.07 ± 0.14	-0.10 ± 0.23	0.03 ± 0.03	0.01 ± 0.19
585	0.94	437.2 ± 0.3	0.11 ± 0.13	-0.09 ± 0.11	0.34 ± 0.22	-0.01 ± -0.01	0.00 ± 0.17
630	0.92	417.4 ± 0.7	0.22 ± 0.14	0.05 ± 0.12	0.53 ± 0.26	0.12 ± 0.12	0.08 ± 0.18
675	0.90	434.4 ± 15.7	0.14 ± 0.13	0.02 ± 0.13	0.11 ± 0.27	0.08 ± 0.08	0.08 ± 0.18
720	0.90	497.2 ± 0.9	0.24 ± 0.12	0.13 ± 0.12	0.19 ± 0.20	0.18 ± 0.18	0.07 ± 0.18
765	0.95	493.4 ± 31.1	0.43 ± 0.11	0.15 ± 0.12	0.29 ± 0.19	0.29 ± 0.29	0.16 ± 0.16
810	0.90	398.4 ± 19.0	0.33 ± 0.13	-0.10 ± 0.13	0.47 ± 0.24	0.13 ± 0.13	0.17 ± 0.19
855	0.89	408.3 ± 19.7	0.23 ± 0.14	-0.21 ± 0.12	0.18 ± 0.20	-0.02 ± -0.02	-0.06 ± 0.21
900	0.95	427.8 ± 0.9	-0.01 ± 0.15	-0.03 ± 0.12	0.17 ± 0.22	-0.02 ± -0.02	-0.07 ± 0.16
945	0.90	430.9 ± 0.3	-0.22 ± 0.18	0.09 ± 0.14	0.19 ± 0.27	-0.02 ± -0.02	-0.02 ± 0.19
990	0.89	422.7 ± 22.4	-0.00 ± 0.17	0.06 ± 0.13	0.71 ± 0.26	0.04 ± 0.04	0.05 ± 0.21
1035	0.85	425.8 ± 24.1	0.28 ± 0.15	-0.15 ± 0.13	0.37 ± 0.23	0.03 ± 0.03	-0.05 ± 0.20
1080	0.85	454.4 ± 32.8	0.03 ± 0.19	-0.07 ± 0.15	-0.15 ± 0.27	-0.03 ± -0.03	-0.05 ± 0.20

Table A.42 – Same as in Table A.1, but for KIC 8228742.

KIC 8292840

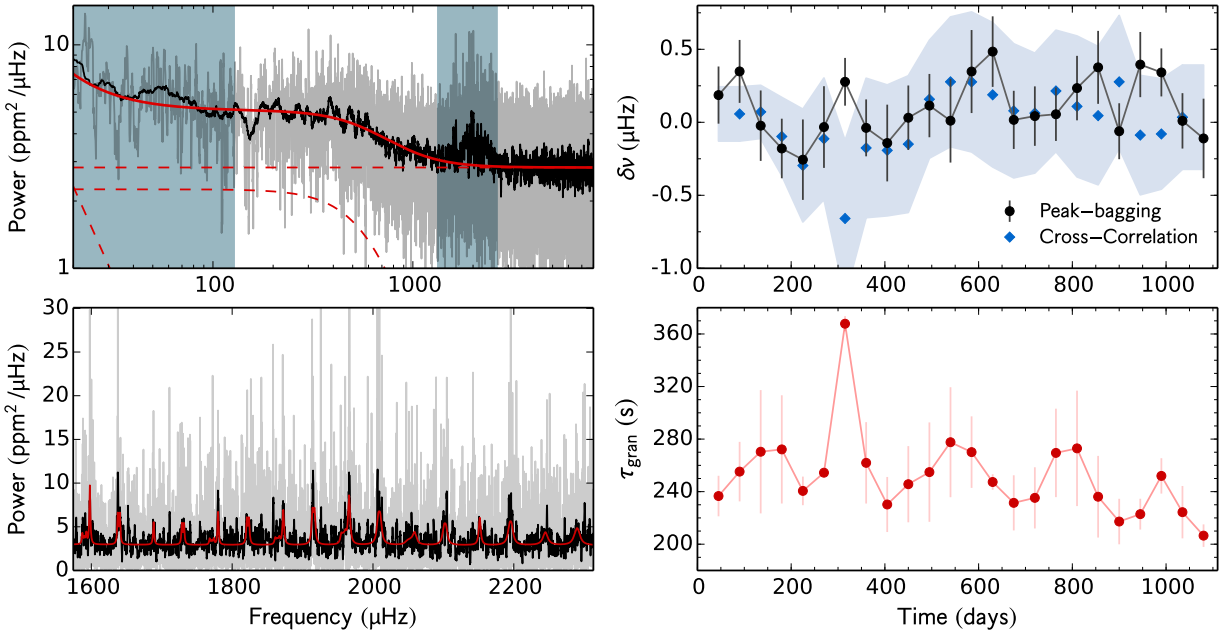

Fig. A.43 – Same as in Fig. A.1, but for KIC 8292840. Due to the extremely large error bars, the results from the cross-correlation method, that are shown here, were obtained from 180-d sub-series.

			Peak-bagging				Cross-
time	d_c	τ_{gran}	$\delta\nu_{l=0}$	$\delta\nu_{l=1}$	$\delta\nu_{l=2}$	$\delta\nu$	correlation
(days)	%	(s)	(μHz)	(μHz)	(μHz)	(μHz)	$\delta\nu$ (μHz)
45	0.97	236.7 ± 15.4	0.19 ± 0.26	0.18 ± 0.30	-0.22 ± 0.92	0.19 ± 0.19	–
90	0.97	255.2 ± 22.6	0.53 ± 0.29	0.13 ± 0.32	0.75 ± 0.71	0.35 ± 0.35	0.06 ± 0.19
135	0.96	270.4 ± 46.9	0.06 ± 0.32	-0.14 ± 0.37	0.94 ± 0.70	-0.02 ± -0.02	0.07 ± 0.18
180	0.97	272.2 ± 41.2	-0.33 ± 0.26	0.08 ± 0.34	0.23 ± 0.73	-0.18 ± -0.18	-0.10 ± 0.27
225	0.96	240.6 ± 10.9	-0.07 ± 0.34	-0.62 ± 0.47	0.02 ± 0.84	-0.26 ± -0.26	-0.30 ± 0.39
270	0.80	254.4 ± 0.0	0.43 ± 0.35	-0.86 ± 0.47	0.86 ± 0.73	-0.03 ± -0.03	-0.11 ± 0.42
315	0.78	367.8 ± 5.8	0.03 ± 0.25	0.46 ± 0.22	0.68 ± 0.49	0.28 ± 0.28	-0.66 ± 0.53
360	0.89	261.9 ± 31.0	0.03 ± 0.26	-0.13 ± 0.30	-1.04 ± 0.52	-0.04 ± -0.04	-0.18 ± 0.48
405	0.93	230.2 ± 21.0	0.04 ± 0.38	-0.31 ± 0.37	-1.04 ± 0.81	-0.14 ± -0.14	-0.19 ± 0.45
450	0.97	245.7 ± 29.0	-0.07 ± 0.29	0.17 ± 0.34	-0.35 ± 0.85	0.03 ± 0.03	-0.15 ± 0.47
495	0.97	254.9 ± 37.8	0.18 ± 0.28	0.02 ± 0.34	0.35 ± 0.85	0.11 ± 0.11	0.16 ± 0.40
540	0.98	277.6 ± 41.9	0.28 ± 0.39	-0.30 ± 0.42	0.29 ± 0.86	0.01 ± 0.01	0.28 ± 0.44
585	0.94	270.1 ± 27.2	0.51 ± 0.39	0.16 ± 0.41	-0.18 ± 0.84	0.35 ± 0.35	0.28 ± 0.48
630	0.92	247.3 ± 5.9	0.22 ± 0.35	0.73 ± 0.33	-0.41 ± 0.85	0.48 ± 0.48	0.19 ± 0.49
675	0.90	231.5 ± 21.0	-0.31 ± 0.27	0.43 ± 0.30	0.21 ± 0.84	0.02 ± 0.02	0.08 ± 0.46
720	0.90	235.3 ± 23.3	0.16 ± 0.24	-0.27 ± 0.39	0.38 ± 0.69	0.04 ± 0.04	0.06 ± 0.41
765	0.95	269.5 ± 33.7	0.35 ± 0.22	-0.64 ± 0.34	0.07 ± 0.67	0.06 ± 0.06	0.21 ± 0.42
810	0.90	272.9 ± 43.9	-0.10 ± 0.29	0.66 ± 0.34	-0.05 ± 0.75	0.23 ± 0.23	0.11 ± 0.48
855	0.89	236.1 ± 31.1	-0.16 ± 0.36	0.85 ± 0.34	0.12 ± 0.92	0.38 ± 0.38	0.05 ± 0.47
900	0.95	217.2 ± 17.3	-0.02 ± 0.22	-0.19 ± 0.37	-0.09 ± 0.92	-0.06 ± -0.06	0.28 ± 0.46
945	0.90	222.9 ± 11.7	0.36 ± 0.29	0.45 ± 0.35	-1.12 ± 0.83	0.40 ± 0.40	-0.09 ± 0.41
990	0.89	252.0 ± 13.5	0.16 ± 0.21	0.61 ± 0.26	-0.29 ± 0.66	0.34 ± 0.34	-0.08 ± 0.38
1035	0.85	224.4 ± 19.9	0.07 ± 0.21	-0.23 ± 0.41	0.41 ± 0.54	0.01 ± 0.01	0.03 ± 0.36
1080	0.85	206.5 ± 8.6	-0.31 ± 0.38	0.10 ± 0.39	0.32 ± 0.87	-0.11 ± -0.11	–

Table A.43 – Same as in Table A.1, but for KIC 8292840. Due to the extremely large error bars, the results from the cross-correlation method, that are shown here, were obtained from 180-d sub-series.

KIC 8379927

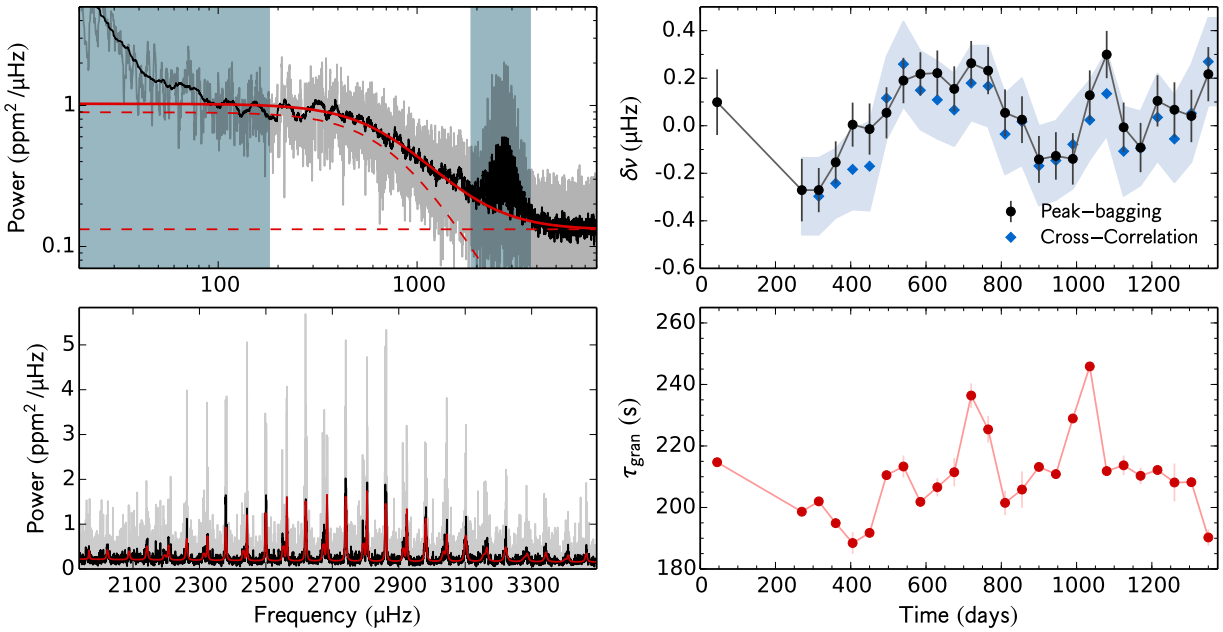

Fig. A.44 – Same as in Fig. A.1, but for KIC 8379927.

time (days)	d_c %	τ_{gran} (s)	Peak-bagging $\delta\nu_{l=0}$ (μHz)	$\delta\nu_{l=1}$ (μHz)	$\delta\nu_{l=2}$ (μHz)	$\delta\nu$ (μHz)	Cross-correlation $\delta\nu$ (μHz)
45	0.32	214.7 ± 0.4	0.02 ± 0.18	0.21 ± 0.22	0.14 ± 0.31	0.10 ± 0.10	–
270	0.44	198.6 ± 0.2	-0.23 ± 0.17	-0.32 ± 0.20	0.70 ± 0.33	-0.27 ± -0.27	–
315	0.93	202.0 ± 0.0	-0.25 ± 0.12	-0.30 ± 0.15	0.15 ± 0.22	-0.27 ± -0.27	-0.30 ± 0.16
360	0.96	194.9 ± 0.6	-0.13 ± 0.11	-0.18 ± 0.14	-0.15 ± 0.19	-0.15 ± -0.15	-0.24 ± 0.15
405	0.96	188.4 ± 3.5	-0.00 ± 0.13	0.01 ± 0.14	0.09 ± 0.20	0.00 ± 0.00	-0.18 ± 0.17
450	0.97	191.8 ± 0.2	0.05 ± 0.15	-0.08 ± 0.15	0.09 ± 0.23	-0.01 ± -0.01	-0.17 ± 0.19
495	0.97	210.5 ± 1.0	0.01 ± 0.15	0.10 ± 0.16	-0.04 ± 0.22	0.05 ± 0.05	0.12 ± 0.17
540	0.80	213.3 ± 3.6	0.01 ± 0.13	0.43 ± 0.15	0.16 ± 0.21	0.19 ± 0.19	0.26 ± 0.18
585	0.78	201.8 ± 1.3	0.29 ± 0.12	0.11 ± 0.14	0.31 ± 0.17	0.22 ± 0.22	0.15 ± 0.17
630	0.90	206.6 ± 3.0	0.41 ± 0.12	-0.09 ± 0.15	0.35 ± 0.17	0.22 ± 0.22	0.11 ± 0.16
675	0.91	211.5 ± 4.6	0.23 ± 0.13	0.05 ± 0.14	-0.58 ± 0.24	0.15 ± 0.15	0.07 ± 0.15
720	0.97	236.4 ± 3.9	0.30 ± 0.12	0.21 ± 0.14	-0.07 ± 0.19	0.26 ± 0.26	0.18 ± 0.16
765	0.96	225.4 ± 4.3	0.30 ± 0.14	0.16 ± 0.15	0.25 ± 0.19	0.23 ± 0.23	0.17 ± 0.17
810	0.97	201.5 ± 4.0	0.19 ± 0.14	-0.09 ± 0.14	-0.13 ± 0.20	0.05 ± 0.05	-0.04 ± 0.17
855	0.97	205.8 ± 5.9	0.09 ± 0.13	-0.05 ± 0.15	-0.28 ± 0.20	0.03 ± 0.03	0.02 ± 0.18
900	0.94	213.2 ± 1.1	-0.13 ± 0.13	-0.16 ± 0.15	-0.18 ± 0.21	-0.14 ± -0.14	-0.17 ± 0.17
945	0.90	210.9 ± 0.9	-0.10 ± 0.14	-0.16 ± 0.15	-0.23 ± 0.21	-0.13 ± -0.13	-0.15 ± 0.17
990	0.88	228.9 ± 0.2	-0.06 ± 0.15	-0.22 ± 0.16	-0.07 ± 0.23	-0.14 ± -0.14	-0.08 ± 0.19
1035	0.91	245.9 ± 0.1	0.27 ± 0.14	-0.07 ± 0.16	0.40 ± 0.26	0.13 ± 0.13	0.02 ± 0.17
1080	0.90	211.8 ± 0.0	0.37 ± 0.13	0.19 ± 0.16	-0.01 ± 0.18	0.30 ± 0.30	0.13 ± 0.18
1125	0.89	213.7 ± 3.2	0.14 ± 0.14	-0.18 ± 0.15	-0.02 ± 0.20	-0.01 ± -0.01	-0.11 ± 0.19
1170	0.93	210.3 ± 2.7	-0.11 ± 0.14	-0.07 ± 0.15	-0.06 ± 0.24	-0.09 ± -0.09	-0.09 ± 0.16
1215	0.89	212.2 ± 1.0	0.26 ± 0.14	-0.08 ± 0.16	-0.31 ± 0.23	0.10 ± 0.10	0.04 ± 0.18
1260	0.90	208.1 ± 6.2	0.14 ± 0.16	-0.00 ± 0.16	-0.02 ± 0.25	0.07 ± 0.07	-0.06 ± 0.18
1305	0.84	208.2 ± 1.2	-0.08 ± 0.15	0.20 ± 0.17	-0.02 ± 0.26	0.04 ± 0.04	0.05 ± 0.21
1350	0.00	190.2 ± 2.6	0.06 ± 0.15	0.43 ± 0.18	-0.37 ± 0.24	0.22 ± 0.22	0.27 ± 0.18

Table A.44 – Same as in Table A.1, but for KIC 8379927.

KIC 8394589

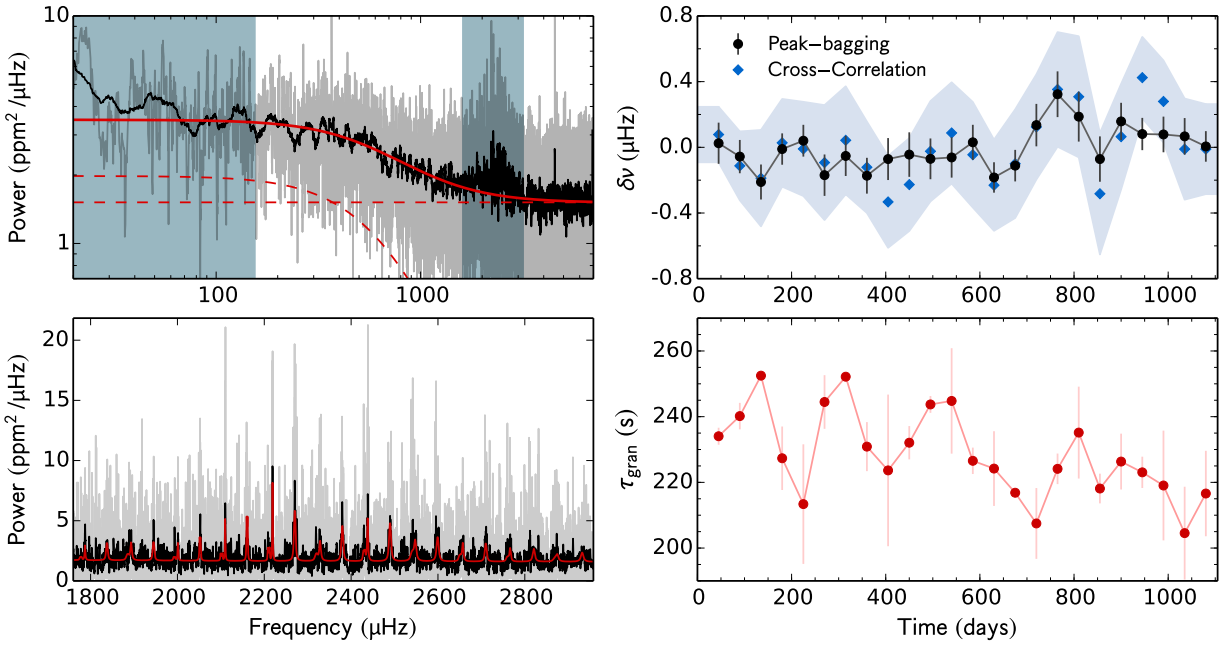

Fig. A.45 – Same as in Fig. A.1, but for KIC 8394589.

time (days)	d_c %	τ_{gran} (s)	Peak-bagging $\delta\nu_{l=0}$ (μHz)	$\delta\nu_{l=1}$ (μHz)	$\delta\nu_{l=2}$ (μHz)	$\delta\nu$ (μHz)	Cross-correlation $\delta\nu$ (μHz)
45	0.98	234.0 ± 2.6	-0.11 ± 0.18	0.15 ± 0.17	-0.55 ± 0.35	0.02 ± 0.02	0.08 ± 0.17
90	0.97	240.2 ± 4.0	-0.11 ± 0.14	0.01 ± 0.15	-0.14 ± 0.35	-0.06 ± -0.06	-0.11 ± 0.21
135	0.96	252.5 ± 0.7	-0.22 ± 0.12	-0.20 ± 0.21	0.27 ± 0.28	-0.21 ± -0.21	-0.19 ± 0.29
180	0.97	227.3 ± 9.7	-0.01 ± 0.12	-0.01 ± 0.16	0.14 ± 0.28	-0.01 ± -0.01	0.03 ± 0.27
225	0.96	213.4 ± 18.2	0.04 ± 0.13	0.04 ± 0.15	-0.04 ± 0.35	0.04 ± 0.04	-0.01 ± 0.29
270	0.81	244.5 ± 8.2	-0.15 ± 0.14	-0.25 ± 0.29	-0.21 ± 0.43	-0.17 ± -0.17	-0.09 ± 0.35
315	0.78	252.2 ± 0.2	-0.12 ± 0.14	0.13 ± 0.23	-0.04 ± 0.37	-0.05 ± -0.05	0.04 ± 0.33
360	0.89	230.9 ± 7.5	-0.19 ± 0.14	-0.15 ± 0.17	-0.15 ± 0.41	-0.17 ± -0.17	-0.12 ± 0.28
405	0.93	223.6 ± 23.1	0.09 ± 0.17	-0.27 ± 0.19	0.60 ± 0.33	-0.07 ± -0.07	-0.33 ± 0.28
450	0.97	232.1 ± 5.1	-0.02 ± 0.19	-0.08 ± 0.20	0.12 ± 0.36	-0.04 ± -0.04	-0.23 ± 0.28
495	0.97	243.7 ± 2.6	-0.03 ± 0.18	-0.11 ± 0.17	-0.68 ± 0.33	-0.07 ± -0.07	-0.02 ± 0.31
540	0.98	244.8 ± 16.0	0.16 ± 0.17	-0.30 ± 0.18	-0.03 ± 0.30	-0.06 ± -0.06	0.09 ± 0.31
585	0.94	226.6 ± 4.0	0.16 ± 0.14	-0.17 ± 0.17	0.16 ± 0.24	0.03 ± 0.03	-0.05 ± 0.32
630	0.92	224.2 ± 11.4	-0.08 ± 0.13	-0.30 ± 0.13	0.47 ± 0.28	-0.18 ± -0.18	-0.23 ± 0.28
675	0.90	216.8 ± 0.1	-0.01 ± 0.13	-0.23 ± 0.14	-0.15 ± 0.39	-0.11 ± -0.11	-0.10 ± 0.33
720	0.90	207.5 ± 10.8	0.12 ± 0.17	0.16 ± 0.21	-0.33 ± 0.38	0.14 ± 0.14	0.12 ± 0.32
765	0.95	224.1 ± 4.7	0.33 ± 0.19	0.31 ± 0.20	0.34 ± 0.33	0.32 ± 0.32	0.35 ± 0.35
810	0.90	235.2 ± 14.0	-0.04 ± 0.20	0.47 ± 0.23	0.08 ± 0.33	0.19 ± 0.19	0.31 ± 0.37
855	0.89	218.1 ± 4.5	-0.16 ± 0.18	0.06 ± 0.22	-0.12 ± 0.39	-0.07 ± -0.07	-0.28 ± 0.37
900	0.95	226.3 ± 8.5	0.08 ± 0.14	0.34 ± 0.21	0.50 ± 0.50	0.16 ± 0.16	0.06 ± 0.32
945	0.90	223.0 ± 4.8	0.02 ± 0.11	0.24 ± 0.19	-0.29 ± 0.39	0.08 ± 0.08	0.42 ± 0.25
990	0.89	219.0 ± 16.7	0.09 ± 0.14	0.06 ± 0.16	0.53 ± 0.31	0.08 ± 0.08	0.28 ± 0.25
1035	0.85	204.5 ± 14.1	0.12 ± 0.14	-0.02 ± 0.18	0.44 ± 0.44	0.07 ± 0.07	-0.01 ± 0.31
1080	0.85	216.6 ± 13.0	0.11 ± 0.13	-0.11 ± 0.14	0.16 ± 0.38	0.01 ± 0.01	-0.01 ± 0.27

Table A.45 – Same as in Table A.1, but for KIC 8394589.

KIC 8424992

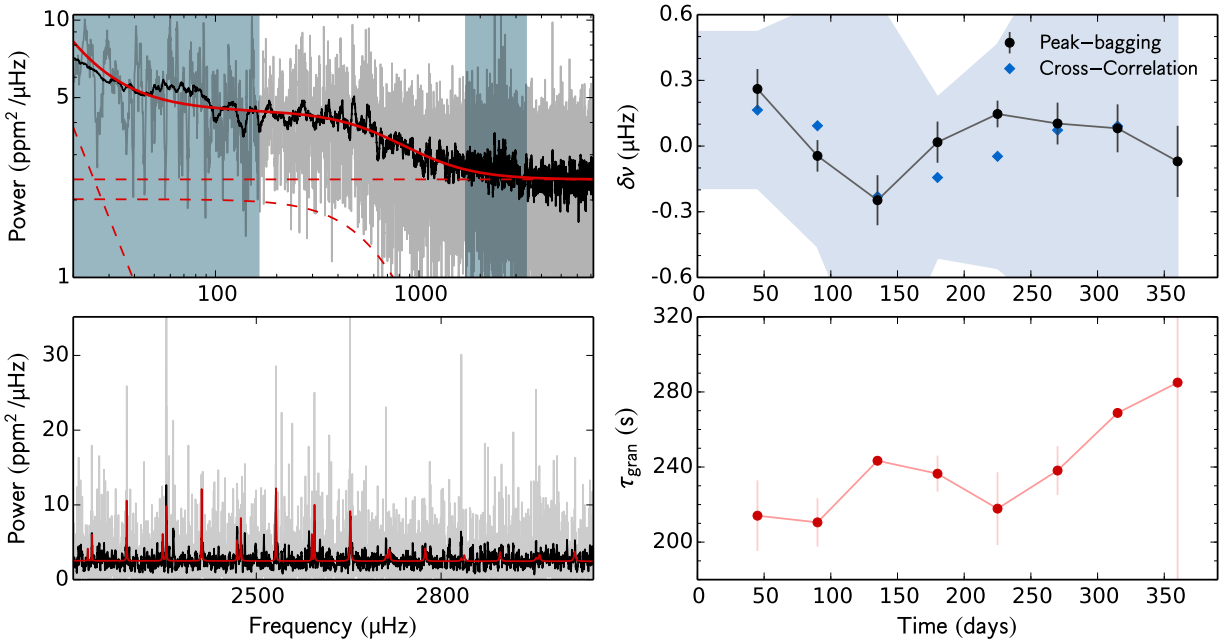

Fig. A.46 – Same as in Fig. A.1, but for KIC 8424992.

time (days)	d_c %	τ_{gran} (s)	Peak-bagging $\delta\nu_{l=0}$ (μHz)	$\delta\nu_{l=1}$ (μHz)	$\delta\nu_{l=2}$ (μHz)	$\delta\nu$ (μHz)	Cross-correlation $\delta\nu$ (μHz)
45	0.96	214.1 ± 18.8	0.23 ± 0.12	0.31 ± 0.15	0.31 ± 0.23	0.26 ± 0.26	0.16 ± 0.36
90	0.78	210.5 ± 12.8	0.18 ± 0.09	-0.36 ± 0.11	0.00 ± 0.12	-0.04 ± -0.04	0.09 ± 0.55
135	0.73	243.4 ± 0.2	0.02 ± 0.18	-0.42 ± 0.15	-0.11 ± 0.22	-0.25 ± -0.25	-0.23 ± 0.90
180	0.92	236.5 ± 9.6	0.10 ± 0.13	-0.06 ± 0.13	0.06 ± 0.17	0.02 ± 0.02	-0.14 ± 0.37
225	0.98	217.8 ± 19.4	0.18 ± 0.08	0.10 ± 0.09	0.03 ± 0.15	0.15 ± 0.15	-0.05 ± 0.51
270	0.97	238.1 ± 13.0	0.05 ± 0.15	0.14 ± 0.13	0.46 ± 0.22	0.10 ± 0.10	0.07 ± 0.86
315	0.97	268.8 ± 1.0	0.07 ± 0.16	0.09 ± 0.15	-0.03 ± 0.19	0.08 ± 0.08	0.09 ± 1.14
360	0.60	285.0 ± 133.6	-0.20 ± 0.26	0.01 ± 0.21	-0.28 ± 0.25	-0.07 ± -0.07	–

Table A.46 – Same as in Table A.1, but for KIC 8424992.

KIC 8478994

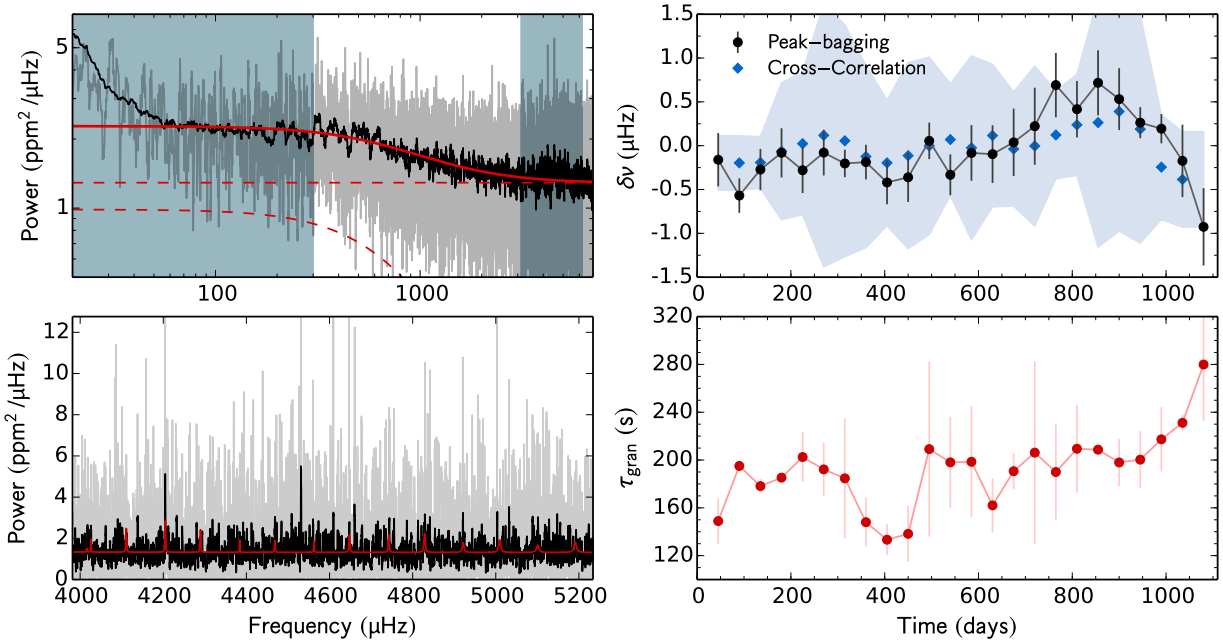

Fig. A.47 – Same as in Fig. A.1, but for KIC 8478994. Due to the extremely large error bars, the results from the cross-correlation method, that are shown here, were obtained from 180-d sub-series.

time (days)	d_c %	τ_{gran} (s)	Peak-bagging $\delta\nu_{l=0}$ (μHz)	$\delta\nu_{l=1}$ (μHz)	$\delta\nu_{l=2}$ (μHz)	$\delta\nu$ (μHz)	Cross-correlation $\delta\nu$ (μHz)
45	0.97	148.9 ± 18.9	0.03 ± 0.44	-0.33 ± 0.42	0.00 ± 0.00	-0.16 ± -0.16	–
90	0.97	195.1 ± nan	-0.65 ± 0.25	-0.44 ± 0.31	0.00 ± 0.00	-0.57 ± -0.57	-0.20 ± 0.31
135	0.96	178.2 ± 5.8	-0.88 ± 0.50	-0.10 ± 0.27	0.00 ± 0.00	-0.27 ± -0.27	-0.19 ± 0.29
180	0.97	185.3 ± 3.3	0.04 ± 0.78	-0.10 ± 0.30	0.00 ± 0.00	-0.08 ± -0.08	-0.06 ± 0.78
225	0.96	202.5 ± 20.6	0.08 ± 0.34	-0.80 ± 0.40	0.00 ± 0.00	-0.28 ± -0.28	0.02 ± 0.81
270	0.80	192.2 ± 22.5	0.01 ± 0.35	-0.19 ± 0.39	0.00 ± 0.00	-0.08 ± -0.08	0.12 ± 1.50
315	0.78	184.7 ± 50.1	-0.40 ± 0.21	0.04 ± 0.23	0.00 ± 0.00	-0.20 ± -0.20	0.06 ± 1.32
360	0.89	148.0 ± 20.8	-0.47 ± 0.25	0.24 ± 0.31	0.00 ± 0.00	-0.19 ± -0.19	-0.12 ± 1.04
405	0.93	133.3 ± 13.0	-0.71 ± 0.36	-0.16 ± 0.34	0.00 ± 0.00	-0.42 ± -0.42	-0.20 ± 0.71
450	0.97	138.2 ± 23.5	-0.51 ± 0.52	-0.30 ± 0.33	0.00 ± 0.00	-0.36 ± -0.36	-0.11 ± 1.06
495	0.97	209.1 ± 73.2	0.68 ± 0.43	-0.13 ± 0.24	0.00 ± 0.00	0.06 ± 0.06	-0.00 ± 1.01
540	0.98	198.1 ± 38.0	0.44 ± 0.42	-0.69 ± 0.28	0.00 ± 0.00	-0.33 ± -0.33	0.07 ± 0.63
585	0.94	198.5 ± 46.4	0.07 ± 0.55	-0.16 ± 0.39	0.00 ± 0.00	-0.08 ± -0.08	-0.02 ± 1.05
630	0.92	162.1 ± 22.7	-0.76 ± 0.56	0.26 ± 0.41	0.00 ± 0.00	-0.10 ± -0.10	0.12 ± 0.81
675	0.90	190.7 ± 14.9	0.16 ± 0.63	-0.03 ± 0.49	0.00 ± 0.00	0.04 ± 0.04	-0.04 ± 0.65
720	0.91	206.2 ± 76.7	0.25 ± 0.62	0.19 ± 0.62	0.00 ± 0.00	0.22 ± 0.22	-0.00 ± 0.91
765	0.95	190.0 ± 40.5	-0.01 ± 0.58	1.16 ± 0.47	0.00 ± 0.00	0.69 ± 0.69	0.12 ± 0.50
810	0.90	209.4 ± 36.7	0.36 ± 0.48	0.47 ± 0.44	0.00 ± 0.00	0.42 ± 0.42	0.24 ± 0.58
855	0.89	208.7 ± 3.2	0.56 ± 0.56	0.84 ± 0.49	0.00 ± 0.00	0.72 ± 0.72	0.26 ± 1.42
900	0.95	198.0 ± 19.8	0.64 ± 0.56	0.46 ± 0.46	0.00 ± 0.00	0.53 ± 0.53	0.39 ± 1.36
945	0.90	200.3 ± 23.8	0.24 ± 0.21	0.32 ± 0.32	0.00 ± 0.00	0.26 ± 0.26	0.19 ± 1.30
990	0.89	217.3 ± 26.9	0.12 ± 0.22	0.30 ± 0.26	0.00 ± 0.00	0.19 ± 0.19	-0.24 ± 0.60
1035	0.85	231.1 ± 7.0	-0.16 ± 0.69	-0.18 ± 0.52	0.00 ± 0.00	-0.17 ± -0.17	-0.38 ± 0.54
1080	0.00	279.9 ± 47.1	-0.39 ± 0.75	-1.21 ± 0.55	0.00 ± 0.00	-0.93 ± -0.93	–

Table A.47 – Same as in Table A.1, but for KIC 8478994. Due to the extremely large error bars, the results from the cross-correlation method, that are shown here, were obtained from 180-d sub-series.

KIC 8494142

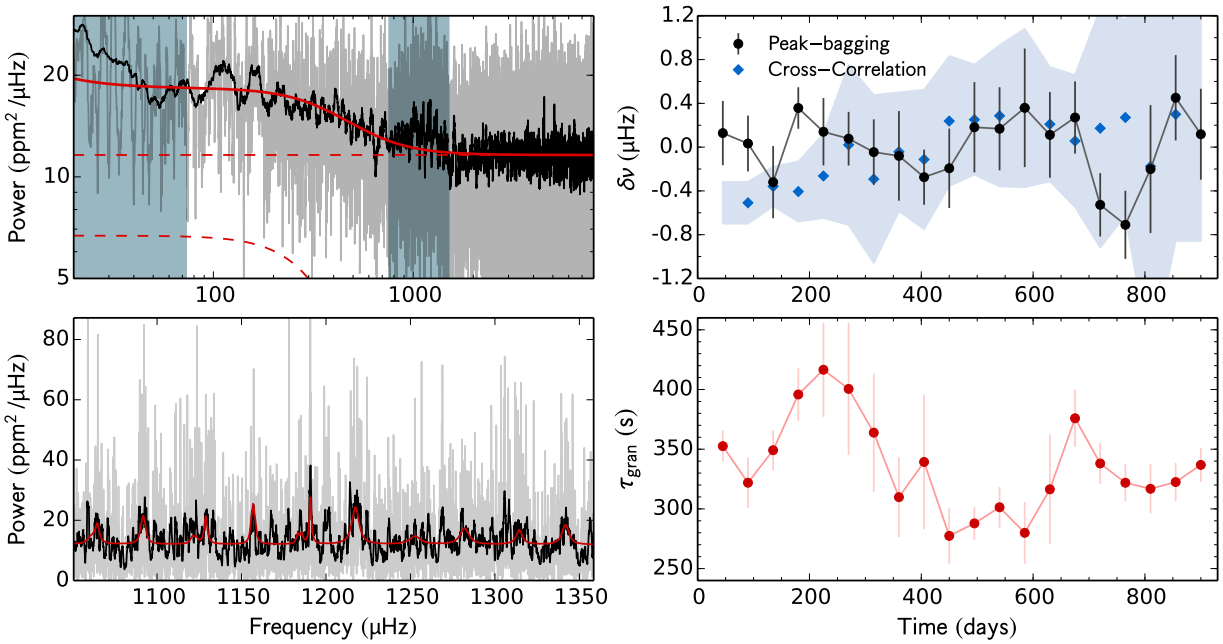

Fig. A.48 – Same as in Fig. A.1, but for KIC 8494142. Due to the extremely large error bars, the results from the cross-correlation method, that are shown here, were obtained from 180-d sub-series.

time (days)	d_c %	τ_{gran} (s)	Peak-bagging $\delta\nu_{l=0}$ (μHz)	$\delta\nu_{l=1}$ (μHz)	$\delta\nu_{l=2}$ (μHz)	$\delta\nu$ (μHz)	Cross-correlation $\delta\nu$ (μHz)
45	0.97	352.6 ± 13.0	0.21 ± 0.34	-0.14 ± 0.61	1.09 ± 1.28	0.13 ± 0.13	–
90	0.78	321.9 ± 21.0	0.17 ± 0.30	-0.32 ± 0.49	0.11 ± 1.37	0.03 ± 0.03	-0.51 ± 0.19
135	0.73	349.2 ± 16.8	-0.11 ± 0.39	-0.87 ± 0.62	0.24 ± 1.38	-0.32 ± -0.32	-0.36 ± 0.18
180	0.92	395.8 ± 21.9	0.63 ± 0.21	-1.12 ± 0.48	-0.02 ± 1.45	0.36 ± 0.36	-0.41 ± 0.27
225	0.98	416.5 ± 39.3	0.94 ± 0.44	-0.62 ± 0.43	-0.28 ± 1.34	0.14 ± 0.14	-0.26 ± 0.38
270	0.97	400.5 ± 55.3	0.11 ± 0.29	-0.00 ± 0.45	-0.84 ± 1.09	0.08 ± 0.08	0.02 ± 0.73
315	0.97	363.8 ± 49.6	0.05 ± 0.37	-0.24 ± 0.51	-0.75 ± 1.29	-0.05 ± -0.05	-0.29 ± 0.77
360	0.97	309.8 ± 33.4	0.03 ± 0.60	-0.18 ± 0.56	-0.14 ± 1.43	-0.08 ± -0.08	-0.04 ± 0.54
405	0.94	339.3 ± 56.3	-0.58 ± 0.36	0.00 ± 0.35	-0.61 ± 1.52	-0.27 ± -0.27	-0.11 ± 0.64
450	0.91	277.4 ± 23.4	-0.62 ± 0.50	0.29 ± 0.53	-0.56 ± 1.40	-0.19 ± -0.19	0.24 ± 0.59
495	0.88	287.9 ± 13.6	-0.80 ± 0.62	0.96 ± 0.55	-0.40 ± 1.30	0.18 ± 0.18	0.25 ± 0.50
540	0.92	301.4 ± 17.1	-0.18 ± 0.59	0.41 ± 0.50	0.67 ± 1.22	0.17 ± 0.17	0.29 ± 0.64
585	0.97	280.0 ± 25.8	0.45 ± 0.91	0.31 ± 0.67	0.56 ± 1.38	0.36 ± 0.36	0.36 ± 0.72
630	0.90	316.4 ± 45.8	-0.24 ± 0.82	0.22 ± 0.45	0.33 ± 0.91	0.11 ± 0.11	0.21 ± 0.52
675	0.89	375.9 ± 24.1	0.13 ± 0.55	0.35 ± 0.41	0.67 ± 1.21	0.27 ± 0.27	0.06 ± 0.60
720	0.95	338.1 ± 17.3	-0.98 ± 0.38	0.12 ± 0.45	1.13 ± 1.26	-0.53 ± -0.53	0.17 ± 1.09
765	0.89	321.9 ± 15.6	-0.62 ± 0.35	-1.01 ± 0.65	0.61 ± 1.35	-0.71 ± -0.71	0.27 ± 0.89
810	0.82	316.8 ± 20.5	-0.74 ± 0.73	0.77 ± 0.98	0.21 ± 1.52	-0.20 ± -0.20	-0.18 ± 1.78
855	0.85	322.5 ± 16.1	0.50 ± 0.65	0.42 ± 0.49	-0.17 ± 1.47	0.45 ± 0.45	0.30 ± 1.16
900	0.93	336.8 ± 14.2	1.15 ± 0.67	-0.53 ± 0.53	-0.86 ± 1.43	0.12 ± 0.12	–

Table A.48 – Same as in Table A.1, but for KIC 8494142. Due to the extremely large error bars, the results from the cross-correlation method, that are shown here, were obtained from 180-d sub-series.

KIC 8694723

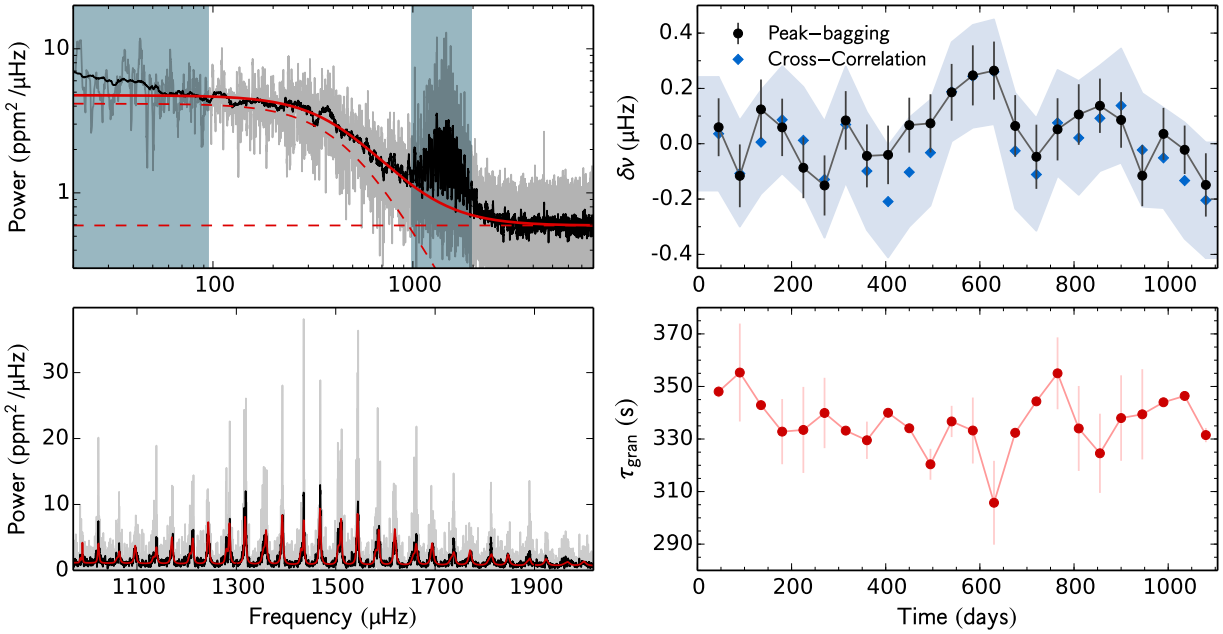

Fig. A.49 – Same as in Fig. A.1, but for KIC 8694723.

time (days)	d_c %	τ_{gran} (s)	Peak-bagging $\delta\nu_{l=0}$ (μHz)	$\delta\nu_{l=1}$ (μHz)	$\delta\nu_{l=2}$ (μHz)	$\delta\nu$ (μHz)	Cross-correlation $\delta\nu$ (μHz)
45	0.98	348.0 ± 2.2	0.00 ± 0.15	0.11 ± 0.15	0.18 ± 0.26	0.06 ± 0.06	0.04 ± 0.21
90	0.97	355.3 ± 18.6	-0.26 ± 0.18	-0.01 ± 0.15	0.08 ± 0.26	-0.12 ± -0.12	-0.11 ± 0.19
135	0.96	342.9 ± 0.3	0.02 ± 0.17	0.20 ± 0.14	0.05 ± 0.25	0.12 ± 0.12	0.01 ± 0.19
180	0.97	332.8 ± 12.4	-0.13 ± 0.16	0.21 ± 0.14	-0.13 ± 0.26	0.06 ± 0.06	0.09 ± 0.19
225	0.96	333.5 ± 16.4	-0.21 ± 0.16	0.03 ± 0.15	-0.59 ± 0.25	-0.09 ± -0.09	0.01 ± 0.19
270	0.80	339.9 ± 13.4	-0.17 ± 0.15	-0.14 ± 0.15	-0.68 ± 0.24	-0.15 ± -0.15	-0.13 ± 0.21
315	0.78	333.2 ± 1.7	0.16 ± 0.14	-0.01 ± 0.16	-0.25 ± 0.28	0.08 ± 0.08	0.07 ± 0.21
360	0.89	329.5 ± 7.1	0.02 ± 0.16	-0.10 ± 0.16	0.06 ± 0.29	-0.04 ± -0.04	-0.10 ± 0.21
405	0.93	340.0 ± nan	-0.20 ± 0.17	0.07 ± 0.14	-0.28 ± 0.21	-0.04 ± -0.04	-0.21 ± 0.20
450	0.97	334.1 ± 1.7	-0.11 ± 0.15	0.21 ± 0.13	-0.41 ± 0.22	0.07 ± 0.07	-0.10 ± 0.20
495	0.97	320.4 ± 5.9	0.18 ± 0.16	-0.01 ± 0.14	-0.10 ± 0.27	0.07 ± 0.07	-0.03 ± 0.19
540	0.98	336.7 ± 5.9	0.41 ± 0.15	-0.03 ± 0.14	0.31 ± 0.27	0.19 ± 0.19	0.19 ± 0.18
585	0.94	333.2 ± 12.6	0.33 ± 0.16	0.18 ± 0.15	0.50 ± 0.30	0.25 ± 0.25	0.24 ± 0.19
630	0.92	305.7 ± 16.0	0.35 ± 0.16	0.20 ± 0.14	0.49 ± 0.26	0.26 ± 0.26	0.26 ± 0.19
675	0.90	332.4 ± 1.9	0.18 ± 0.17	-0.03 ± 0.15	0.05 ± 0.28	0.06 ± 0.06	-0.03 ± 0.21
720	0.90	344.3 ± 0.4	0.02 ± 0.17	-0.10 ± 0.16	-0.13 ± 0.27	-0.05 ± -0.05	-0.11 ± 0.20
765	0.95	355.0 ± 13.7	0.18 ± 0.17	-0.05 ± 0.15	-0.14 ± 0.28	0.05 ± 0.05	0.08 ± 0.19
810	0.89	334.0 ± 16.2	0.23 ± 0.17	0.02 ± 0.14	-0.01 ± 0.32	0.11 ± 0.11	0.02 ± 0.21
855	0.89	324.6 ± 15.1	0.15 ± 0.15	0.13 ± 0.13	0.75 ± 0.32	0.14 ± 0.14	0.09 ± 0.19
900	0.95	338.0 ± 16.3	0.09 ± 0.14	0.08 ± 0.14	-0.43 ± 0.28	0.09 ± 0.09	0.14 ± 0.21
945	0.89	339.4 ± 17.2	-0.11 ± 0.16	-0.12 ± 0.15	-0.35 ± 0.25	-0.12 ± -0.12	-0.02 ± 0.20
990	0.89	344.0 ± 0.0	0.17 ± 0.13	-0.10 ± 0.13	0.26 ± 0.21	0.04 ± 0.04	-0.05 ± 0.18
1035	0.85	346.4 ± 0.7	0.13 ± 0.13	-0.14 ± 0.12	0.47 ± 0.24	-0.02 ± -0.02	-0.13 ± 0.21
1080	0.85	331.5 ± 2.7	-0.08 ± 0.18	-0.19 ± 0.15	0.19 ± 0.32	-0.15 ± -0.15	-0.20 ± 0.21

Table A.49 – Same as in Table A.1, but for KIC 8694723.

KIC 8760414

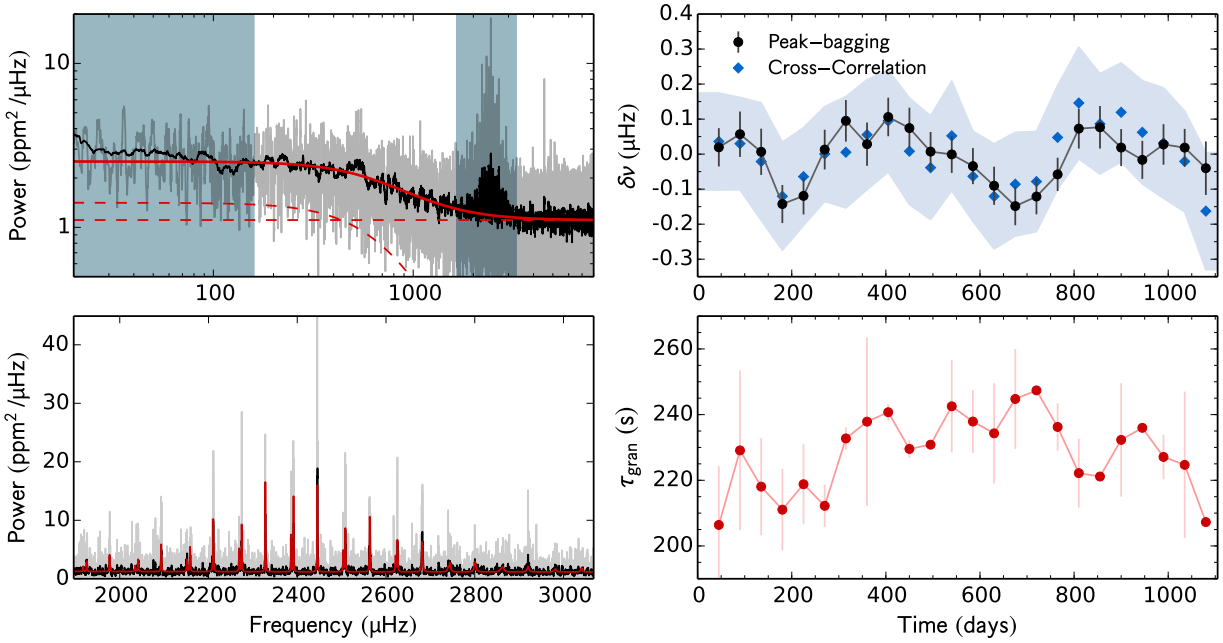

Fig. A.50 – Same as in Fig. A.1, but for KIC 8760414.

time (days)	d_c %	τ_{gran} (s)	Peak-bagging $\delta\nu_{l=0}$ (μHz)	$\delta\nu_{l=1}$ (μHz)	$\delta\nu_{l=2}$ (μHz)	$\delta\nu$ (μHz)	Cross-correlation $\delta\nu$ (μHz)
45	0.97	206.4 ± 17.9	0.02 ± 0.09	0.02 ± 0.10	0.18 ± 0.10	0.02 ± 0.02	0.04 ± 0.14
90	0.97	229.1 ± 24.3	0.04 ± 0.11	0.08 ± 0.11	0.14 ± 0.12	0.06 ± 0.06	0.03 ± 0.13
135	0.96	218.1 ± 14.8	0.07 ± 0.11	-0.05 ± 0.11	0.18 ± 0.13	0.01 ± 0.01	-0.02 ± 0.17
180	0.97	211.0 ± 12.4	-0.09 ± 0.09	-0.18 ± 0.08	0.08 ± 0.12	-0.14 ± -0.14	-0.12 ± 0.15
225	0.96	218.8 ± 12.2	-0.12 ± 0.08	-0.12 ± 0.08	-0.10 ± 0.15	-0.12 ± -0.12	-0.06 ± 0.14
270	0.80	212.2 ± 6.5	0.05 ± 0.08	-0.03 ± 0.09	-0.26 ± 0.15	0.01 ± 0.01	0.00 ± 0.14
315	0.78	232.7 ± 3.4	-0.01 ± 0.11	0.17 ± 0.09	-0.10 ± 0.11	0.10 ± 0.10	0.01 ± 0.16
360	0.89	237.9 ± 25.7	-0.13 ± 0.10	0.16 ± 0.09	0.03 ± 0.13	0.03 ± 0.03	0.06 ± 0.16
405	0.93	240.7 ± 2.6	-0.03 ± 0.10	0.19 ± 0.08	0.26 ± 0.10	0.11 ± 0.11	0.09 ± 0.15
450	0.97	229.5 ± 2.7	0.05 ± 0.10	0.10 ± 0.09	0.17 ± 0.12	0.07 ± 0.07	0.01 ± 0.15
495	0.97	230.8 ± 0.2	0.03 ± 0.09	-0.01 ± 0.08	0.03 ± 0.15	0.01 ± 0.01	-0.04 ± 0.15
540	0.98	242.5 ± 14.1	-0.02 ± 0.09	0.01 ± 0.08	0.13 ± 0.12	-0.00 ± -0.00	0.05 ± 0.16
585	0.94	237.9 ± 9.6	-0.09 ± 0.08	0.02 ± 0.08	0.01 ± 0.11	-0.03 ± -0.03	-0.06 ± 0.13
630	0.92	234.3 ± 15.3	-0.13 ± 0.10	-0.06 ± 0.09	-0.08 ± 0.10	-0.09 ± -0.09	-0.12 ± 0.15
675	0.90	244.8 ± 15.2	-0.16 ± 0.09	-0.14 ± 0.09	-0.12 ± 0.11	-0.15 ± -0.15	-0.09 ± 0.15
720	0.90	247.4 ± 0.2	-0.18 ± 0.08	-0.06 ± 0.08	0.18 ± 0.11	-0.12 ± -0.12	-0.08 ± 0.14
765	0.95	236.2 ± 7.2	-0.11 ± 0.07	-0.00 ± 0.08	0.23 ± 0.10	-0.06 ± -0.06	0.05 ± 0.15
810	0.90	222.2 ± 10.5	0.06 ± 0.10	0.09 ± 0.10	0.05 ± 0.10	0.07 ± 0.07	0.15 ± 0.16
855	0.89	221.1 ± 0.6	0.07 ± 0.11	0.08 ± 0.09	-0.00 ± 0.12	0.08 ± 0.08	0.09 ± 0.14
900	0.95	232.3 ± 17.3	-0.06 ± 0.09	0.11 ± 0.09	-0.07 ± 0.09	0.02 ± 0.02	0.12 ± 0.14
945	0.89	236.0 ± 0.0	0.04 ± 0.09	-0.08 ± 0.09	-0.01 ± 0.10	-0.02 ± -0.02	0.06 ± 0.15
990	0.89	227.1 ± 6.8	0.15 ± 0.09	-0.12 ± 0.09	0.07 ± 0.14	0.03 ± 0.03	0.03 ± 0.16
1035	0.85	224.7 ± 22.3	0.08 ± 0.09	-0.04 ± 0.08	-0.06 ± 0.11	0.02 ± 0.02	-0.02 ± 0.14
1080	0.85	207.3 ± 1.1	0.05 ± 0.14	-0.11 ± 0.12	0.18 ± 0.14	-0.04 ± -0.04	-0.16 ± 0.17

Table A.50 – Same as in Table A.1, but for KIC 8760414.

KIC 8866102

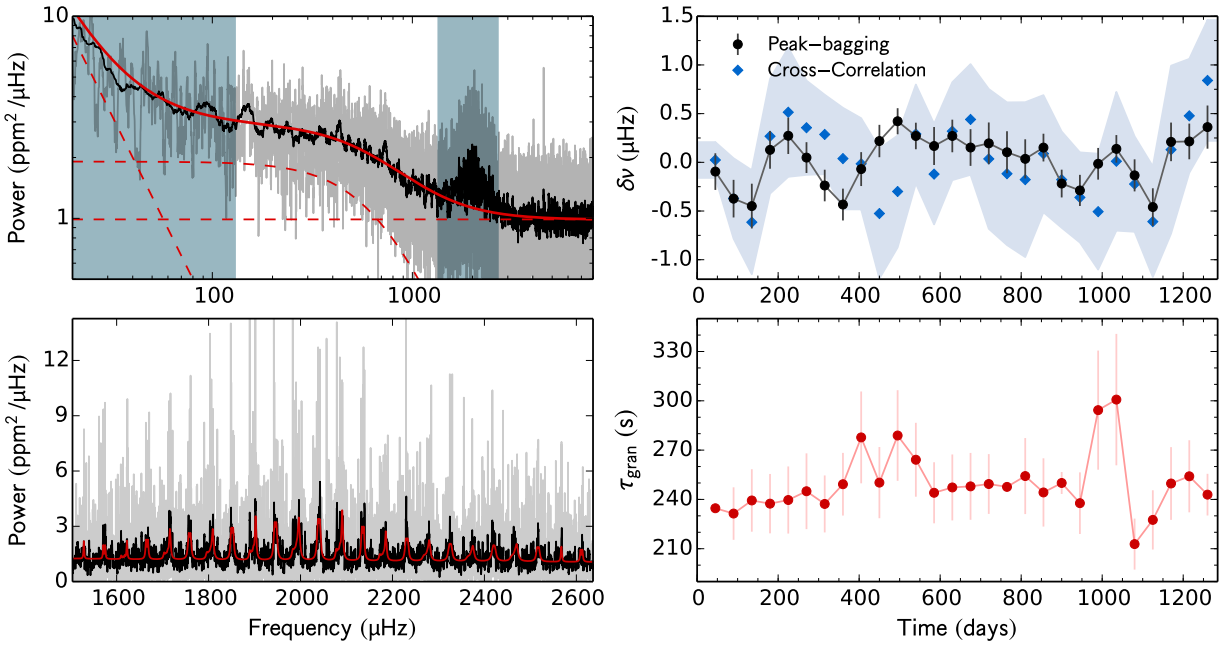

Fig. A.51 – Same as in Fig. A.1, but for KIC 8866102.

time (days)	d_c %	τ_{gran} (s)	Peak-bagging $\delta\nu_{l=0}$ (μHz)	$\delta\nu_{l=1}$ (μHz)	$\delta\nu_{l=2}$ (μHz)	$\delta\nu$ (μHz)	Cross-correlation $\delta\nu$ (μHz)
45	0.95	234.6 ± 0.7	-0.14 ± 0.29	-0.06 ± 0.25	0.72 ± 0.57	-0.10 ± -0.10	0.02 ± 0.18
90	0.93	231.4 ± 16.0	-0.60 ± 0.27	-0.14 ± 0.28	-0.98 ± 0.41	-0.37 ± -0.37	-0.37 ± 0.41
135	0.92	239.4 ± 19.0	-0.58 ± 0.32	-0.32 ± 0.33	-0.79 ± 0.45	-0.45 ± -0.45	-0.62 ± 0.53
180	0.92	237.4 ± 18.1	0.20 ± 0.31	0.08 ± 0.25	0.69 ± 0.48	0.13 ± 0.13	0.27 ± 0.59
225	0.96	239.6 ± 20.4	0.10 ± 0.31	0.37 ± 0.24	0.59 ± 0.42	0.27 ± 0.27	0.51 ± 0.66
270	0.97	245.0 ± 23.1	-0.07 ± 0.21	0.21 ± 0.24	-0.16 ± 0.49	0.05 ± 0.05	0.36 ± 0.48
315	0.96	237.2 ± 17.3	-0.18 ± 0.23	-0.30 ± 0.23	-1.30 ± 0.51	-0.24 ± -0.24	0.29 ± 0.41
360	0.97	249.2 ± 19.1	-0.25 ± 0.24	-0.59 ± 0.22	-1.27 ± 0.35	-0.43 ± -0.43	0.04 ± 0.52
405	0.97	277.7 ± 27.9	0.15 ± 0.25	-0.29 ± 0.25	-0.44 ± 0.42	-0.07 ± -0.07	-0.02 ± 0.47
450	0.81	250.2 ± 21.7	0.01 ± 0.25	0.38 ± 0.22	0.21 ± 0.35	0.22 ± 0.22	-0.53 ± 0.67
495	0.78	278.9 ± 27.6	0.49 ± 0.18	0.35 ± 0.19	0.21 ± 0.26	0.42 ± 0.42	-0.30 ± 0.57
540	0.90	264.1 ± 22.5	0.17 ± 0.18	0.42 ± 0.22	0.02 ± 0.35	0.27 ± 0.27	0.29 ± 0.51
585	0.91	244.0 ± 18.6	0.06 ± 0.26	0.29 ± 0.29	-0.99 ± 0.54	0.17 ± 0.17	-0.12 ± 0.52
630	0.97	247.3 ± 20.1	0.27 ± 0.23	0.27 ± 0.25	0.26 ± 0.43	0.27 ± 0.27	0.32 ± 0.50
675	0.97	247.9 ± 20.3	0.11 ± 0.24	0.23 ± 0.31	1.45 ± 0.56	0.15 ± 0.15	0.44 ± 0.57
720	0.97	249.4 ± 18.2	0.25 ± 0.31	0.15 ± 0.29	0.37 ± 0.51	0.19 ± 0.19	0.04 ± 0.72
765	0.97	247.6 ± 0.7	0.13 ± 0.35	0.09 ± 0.27	-0.40 ± 0.50	0.10 ± 0.10	-0.12 ± 0.73
810	0.94	254.2 ± 23.1	0.26 ± 0.27	-0.23 ± 0.29	-0.32 ± 0.49	0.04 ± 0.04	-0.18 ± 0.79
855	0.91	244.2 ± 20.8	0.27 ± 0.19	-0.01 ± 0.22	0.51 ± 0.55	0.15 ± 0.15	0.09 ± 0.60
900	0.89	250.0 ± 6.7	-0.38 ± 0.22	-0.09 ± 0.19	0.93 ± 0.42	-0.22 ± -0.22	-0.18 ± 0.49
945	0.92	237.7 ± 18.7	-0.27 ± 0.23	-0.30 ± 0.22	0.64 ± 0.34	-0.29 ± -0.29	-0.36 ± 0.46
990	0.90	294.3 ± 36.2	0.44 ± 0.23	-0.47 ± 0.23	0.49 ± 0.39	-0.01 ± -0.01	-0.51 ± 0.59
1035	0.89	300.7 ± 40.0	0.22 ± 0.19	0.02 ± 0.22	0.08 ± 0.37	0.14 ± 0.14	0.01 ± 0.71
1080	0.94	212.8 ± 15.5	-0.10 ± 0.24	-0.16 ± 0.22	-0.50 ± 0.51	-0.13 ± -0.13	-0.22 ± 0.49
1125	0.90	227.5 ± 18.0	-0.24 ± 0.29	-0.63 ± 0.26	-0.54 ± 0.59	-0.46 ± -0.46	-0.61 ± 0.57
1170	0.90	249.7 ± 22.1	0.46 ± 0.26	-0.14 ± 0.31	0.43 ± 0.40	0.21 ± 0.21	0.13 ± 0.86
1215	0.85	254.1 ± 21.9	0.53 ± 0.24	-0.20 ± 0.28	0.31 ± 0.36	0.21 ± 0.21	0.48 ± 0.58
1260	0.84	242.9 ± 12.7	0.36 ± 0.30	0.36 ± 0.32	0.20 ± 0.49	0.36 ± 0.36	0.84 ± 0.62

Table A.51 – Same as in Table A.1, but for KIC 8866102.

KIC 8938364

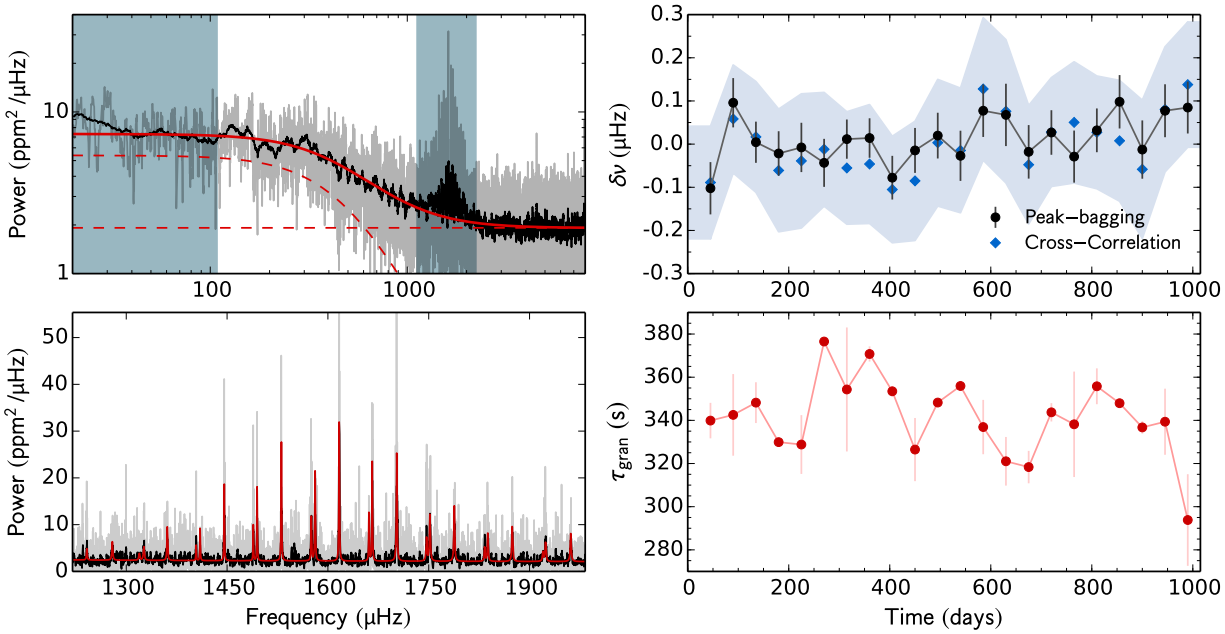

Fig. A.52 – Same as in Fig. A.1, but for KIC 8938364.

time (days)	d_c %	τ_{gran} (s)	Peak-bagging $\delta\nu_{l=0}$ (μHz)	$\delta\nu_{l=1}$ (μHz)	$\delta\nu_{l=2}$ (μHz)	$\delta\nu$ (μHz)	Cross-correlation $\delta\nu$ (μHz)
45	0.98	339.9 ± 8.2	-0.06 ± 0.09	-0.14 ± 0.08	0.01 ± 0.11	-0.10 ± -0.10	-0.09 ± 0.13
90	0.97	342.5 ± 18.9	0.06 ± 0.08	0.14 ± 0.09	-0.17 ± 0.10	0.10 ± 0.10	0.06 ± 0.13
135	0.96	348.2 ± 9.5	-0.10 ± 0.07	0.12 ± 0.07	-0.20 ± 0.07	0.00 ± 0.00	0.02 ± 0.13
180	0.78	329.9 ± 0.8	-0.13 ± 0.08	0.06 ± 0.07	-0.27 ± 0.07	-0.02 ± -0.02	-0.06 ± 0.14
225	0.72	328.8 ± 13.6	-0.03 ± 0.09	0.01 ± 0.07	-0.23 ± 0.12	-0.01 ± -0.01	-0.04 ± 0.16
270	0.92	376.5 ± 1.0	-0.03 ± 0.08	-0.06 ± 0.08	0.04 ± 0.10	-0.04 ± -0.04	-0.01 ± 0.13
315	0.98	354.3 ± 28.7	0.04 ± 0.06	-0.04 ± 0.08	-0.04 ± 0.10	0.01 ± 0.01	-0.06 ± 0.13
360	0.97	370.8 ± 3.5	0.03 ± 0.06	-0.00 ± 0.07	0.13 ± 0.08	0.01 ± 0.01	-0.05 ± 0.14
405	0.97	353.5 ± 2.4	-0.14 ± 0.07	-0.02 ± 0.07	-0.16 ± 0.08	-0.08 ± -0.08	-0.11 ± 0.12
450	0.97	326.5 ± 14.6	-0.10 ± 0.08	0.06 ± 0.07	-0.27 ± 0.08	-0.01 ± -0.01	-0.09 ± 0.14
495	0.94	348.3 ± 0.0	0.03 ± 0.08	0.01 ± 0.07	-0.08 ± 0.10	0.02 ± 0.02	0.00 ± 0.15
540	0.91	355.9 ± 2.2	-0.05 ± 0.08	-0.00 ± 0.09	-0.06 ± 0.10	-0.03 ± -0.03	-0.01 ± 0.14
585	0.88	336.9 ± 12.6	-0.02 ± 0.09	0.15 ± 0.08	-0.18 ± 0.10	0.08 ± 0.08	0.13 ± 0.17
630	0.92	321.0 ± 11.3	0.06 ± 0.12	0.07 ± 0.09	-0.15 ± 0.15	0.07 ± 0.07	0.08 ± 0.17
675	0.97	318.4 ± 7.5	0.05 ± 0.09	-0.09 ± 0.09	-0.17 ± 0.12	-0.02 ± -0.02	-0.05 ± 0.14
720	0.90	343.7 ± 4.2	0.09 ± 0.07	-0.04 ± 0.08	-0.07 ± 0.11	0.03 ± 0.03	0.03 ± 0.13
765	0.89	338.2 ± 24.4	0.03 ± 0.09	-0.08 ± 0.08	0.13 ± 0.14	-0.03 ± -0.03	0.05 ± 0.14
810	0.95	355.8 ± 8.3	0.07 ± 0.07	-0.02 ± 0.07	0.09 ± 0.13	0.03 ± 0.03	0.03 ± 0.13
855	0.89	347.9 ± 0.9	0.16 ± 0.09	0.03 ± 0.09	-0.08 ± 0.14	0.10 ± 0.10	0.01 ± 0.14
900	0.82	336.7 ± 2.9	0.09 ± 0.10	-0.09 ± 0.09	0.24 ± 0.18	-0.01 ± -0.01	-0.06 ± 0.16
945	0.84	339.4 ± 15.3	0.06 ± 0.09	0.09 ± 0.09	0.20 ± 0.14	0.08 ± 0.08	0.08 ± 0.14
990	0.92	293.8 ± 21.2	-0.02 ± 0.09	0.16 ± 0.08	0.22 ± 0.10	0.08 ± 0.08	0.14 ± 0.15

Table A.52 – Same as in Table A.1, but for KIC 8938364.

KIC 9025370

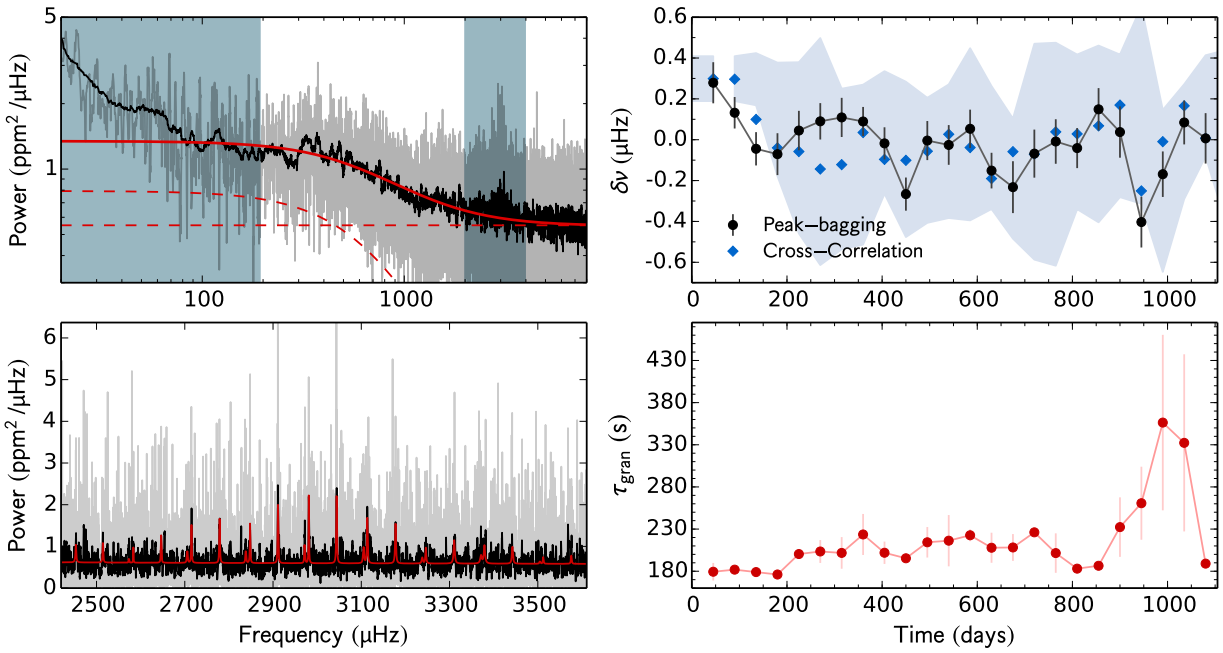

Fig. A.53 – Same as in Fig. A.1, but for KIC 9025370.

time (days)	d_c %	τ_{gran} (s)	Peak-bagging $\delta\nu_{l=0}$ (μHz)	$\delta\nu_{l=1}$ (μHz)	$\delta\nu_{l=2}$ (μHz)	$\delta\nu$ (μHz)	Cross-correlation $\delta\nu$ (μHz)
45	0.97	179.4 ± 10.4	0.26 ± 0.12	0.33 ± 0.19	0.40 ± 0.28	0.28 ± 0.28	0.30 ± 0.11
90	0.96	181.9 ± 5.0	0.02 ± 0.09	0.54 ± 0.17	0.07 ± 0.31	0.13 ± 0.13	0.30 ± 0.13
135	0.96	179.0 ± 5.3	-0.04 ± 0.09	-0.07 ± 0.16	-0.71 ± 0.29	-0.04 ± -0.04	0.10 ± 0.28
180	0.97	176.1 ± 6.2	0.00 ± 0.12	-0.27 ± 0.20	-0.38 ± 0.33	-0.07 ± -0.07	-0.04 ± 0.42
225	0.96	200.4 ± 0.5	0.04 ± 0.12	0.05 ± 0.16	0.16 ± 0.34	0.04 ± 0.04	-0.06 ± 0.56
270	0.80	203.4 ± 13.6	0.20 ± 0.11	-0.08 ± 0.14	0.76 ± 0.30	0.09 ± 0.09	-0.14 ± 0.39
315	0.78	201.7 ± 18.8	0.20 ± 0.13	-0.01 ± 0.14	0.37 ± 0.24	0.11 ± 0.11	-0.12 ± 0.39
360	0.89	223.6 ± 24.3	0.11 ± 0.08	-0.00 ± 0.17	0.20 ± 0.23	0.09 ± 0.09	0.04 ± 0.30
405	0.93	201.9 ± 13.3	0.07 ± 0.09	-0.33 ± 0.16	0.01 ± 0.33	-0.02 ± -0.02	-0.10 ± 0.38
450	0.97	195.4 ± 2.1	-0.20 ± 0.12	-0.32 ± 0.11	0.33 ± 0.21	-0.27 ± -0.27	-0.10 ± 0.31
495	0.97	214.3 ± 18.1	0.21 ± 0.14	-0.19 ± 0.13	0.34 ± 0.27	-0.00 ± -0.00	-0.06 ± 0.33
540	0.98	216.2 ± 30.4	0.11 ± 0.17	-0.10 ± 0.12	0.41 ± 0.34	-0.03 ± -0.03	0.03 ± 0.42
585	0.94	222.7 ± 7.0	-0.06 ± 0.18	0.10 ± 0.11	-0.32 ± 0.27	0.05 ± 0.05	-0.04 ± 0.30
630	0.92	207.9 ± 17.8	-0.18 ± 0.14	-0.13 ± 0.11	-0.58 ± 0.37	-0.15 ± -0.15	-0.19 ± 0.29
675	0.90	208.2 ± 15.9	-0.41 ± 0.18	-0.04 ± 0.18	-0.16 ± 0.49	-0.23 ± -0.23	-0.06 ± 0.53
720	0.90	226.1 ± 1.0	-0.06 ± 0.15	-0.07 ± 0.18	0.03 ± 0.32	-0.07 ± -0.07	-0.07 ± 0.55
765	0.95	201.5 ± 23.4	0.07 ± 0.13	-0.21 ± 0.21	0.21 ± 0.34	-0.01 ± -0.01	0.04 ± 0.38
810	0.89	183.1 ± 2.3	-0.00 ± 0.12	-0.11 ± 0.16	0.52 ± 0.52	-0.04 ± -0.04	0.03 ± 0.43
855	0.89	186.5 ± 0.5	0.06 ± 0.13	0.30 ± 0.17	-0.48 ± 0.46	0.15 ± 0.15	0.07 ± 0.35
900	0.95	232.3 ± 35.3	0.06 ± 0.17	0.01 ± 0.18	0.15 ± 0.41	0.04 ± 0.04	0.17 ± 0.48
945	0.90	260.7 ± 43.3	-0.43 ± 0.17	-0.37 ± 0.18	0.18 ± 0.32	-0.40 ± -0.40	-0.25 ± 0.40
990	0.89	356.3 ± 104.1	-0.22 ± 0.15	-0.10 ± 0.17	-0.04 ± 0.26	-0.17 ± -0.17	-0.01 ± 0.28
1035	0.85	332.3 ± 105.1	-0.34 ± 0.17	0.39 ± 0.14	-0.18 ± 0.22	0.08 ± 0.08	0.17 ± 0.25
1080	0.85	189.0 ± 1.8	-0.11 ± 0.21	0.07 ± 0.15	0.02 ± 0.46	0.01 ± 0.01	0.01 ± 0.43

Table A.53 – Same as in Table A.1, but for KIC 9025370.

KIC 9098294

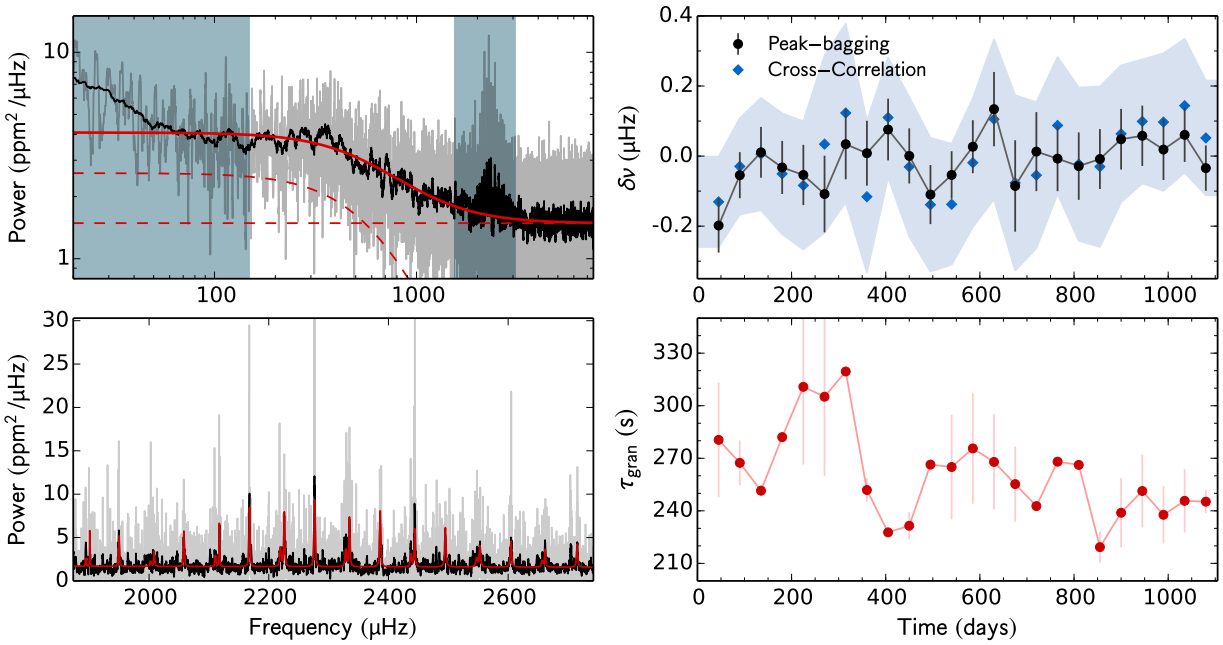

Fig. A.54 – Same as in Fig. A.1, but for KIC 9098294.

time (days)	d_c %	τ_{gran} (s)	Peak-bagging $\delta\nu_{l=0}$ (μHz)	$\delta\nu_{l=1}$ (μHz)	$\delta\nu_{l=2}$ (μHz)	$\delta\nu$ (μHz)	Cross-correlation $\delta\nu$ (μHz)
45	0.98	280.5 ± 32.7	-0.36 ± 0.11	-0.04 ± 0.11	-0.26 ± 0.20	-0.20 ± -0.20	-0.13 ± 0.13
90	0.97	267.4 ± 12.8	-0.11 ± 0.08	0.05 ± 0.11	-0.38 ± 0.24	-0.05 ± -0.05	-0.03 ± 0.14
135	0.96	251.5 ± 3.2	-0.02 ± 0.10	0.05 ± 0.11	-0.26 ± 0.22	0.01 ± 0.01	0.01 ± 0.16
180	0.97	282.1 ± 2.9	-0.11 ± 0.10	0.06 ± 0.11	-0.08 ± 0.16	-0.03 ± -0.03	-0.05 ± 0.17
225	0.96	310.8 ± 44.4	-0.14 ± 0.11	0.07 ± 0.13	-0.39 ± 0.20	-0.05 ± -0.05	-0.08 ± 0.18
270	0.81	305.1 ± 45.2	-0.13 ± 0.14	-0.07 ± 0.18	-0.32 ± 0.26	-0.11 ± -0.11	0.03 ± 0.25
315	0.78	319.5 ± 0.8	0.07 ± 0.12	-0.03 ± 0.17	-0.47 ± 0.26	0.03 ± 0.03	0.12 ± 0.25
360	0.89	251.9 ± 6.8	0.14 ± 0.13	-0.15 ± 0.14	-0.78 ± 0.31	0.01 ± 0.01	-0.12 ± 0.22
405	0.93	227.7 ± 0.0	0.14 ± 0.12	0.01 ± 0.13	0.39 ± 0.32	0.08 ± 0.08	0.11 ± 0.17
450	0.97	231.5 ± 7.9	0.02 ± 0.10	-0.04 ± 0.13	0.32 ± 0.24	0.00 ± 0.00	-0.03 ± 0.20
495	0.97	266.4 ± 3.1	-0.05 ± 0.11	-0.19 ± 0.13	-0.22 ± 0.18	-0.11 ± -0.11	-0.14 ± 0.19
540	0.98	265.0 ± 29.8	0.05 ± 0.08	-0.24 ± 0.11	0.14 ± 0.16	-0.05 ± -0.05	-0.14 ± 0.17
585	0.94	275.6 ± 31.5	0.06 ± 0.10	-0.03 ± 0.12	0.29 ± 0.18	0.03 ± 0.03	-0.02 ± 0.18
630	0.92	267.9 ± 27.2	0.06 ± 0.15	0.20 ± 0.15	0.11 ± 0.24	0.13 ± 0.13	0.11 ± 0.23
675	0.90	255.3 ± 21.5	-0.05 ± 0.19	-0.12 ± 0.18	0.26 ± 0.31	-0.09 ± -0.09	-0.08 ± 0.25
720	0.90	242.7 ± 0.6	0.11 ± 0.18	-0.06 ± 0.15	0.44 ± 0.28	0.01 ± 0.01	-0.05 ± 0.21
765	0.95	268.1 ± 2.5	-0.08 ± 0.14	0.06 ± 0.13	0.42 ± 0.18	-0.01 ± -0.01	0.09 ± 0.20
810	0.90	266.2 ± 2.1	-0.19 ± 0.15	0.08 ± 0.12	0.14 ± 0.23	-0.03 ± -0.03	-0.02 ± 0.22
855	0.89	219.3 ± 8.8	-0.02 ± 0.11	0.01 ± 0.13	0.39 ± 0.24	-0.01 ± -0.01	-0.03 ± 0.23
900	0.95	238.9 ± 19.8	0.08 ± 0.12	0.02 ± 0.12	0.64 ± 0.29	0.05 ± 0.05	0.06 ± 0.20
945	0.90	251.3 ± 20.7	0.07 ± 0.12	0.05 ± 0.13	-0.06 ± 0.33	0.06 ± 0.06	0.10 ± 0.18
990	0.89	237.7 ± 16.3	-0.01 ± 0.12	0.05 ± 0.13	-0.27 ± 0.25	0.02 ± 0.02	0.10 ± 0.20
1035	0.85	245.7 ± 18.0	-0.09 ± 0.10	0.26 ± 0.12	0.02 ± 0.20	0.06 ± 0.06	0.14 ± 0.19
1080	0.85	245.2 ± 6.6	-0.16 ± 0.09	0.12 ± 0.10	0.11 ± 0.15	-0.03 ± -0.03	0.05 ± 0.16

Table A.54 – Same as in Table A.1, but for KIC 9098294.

KIC 9139151

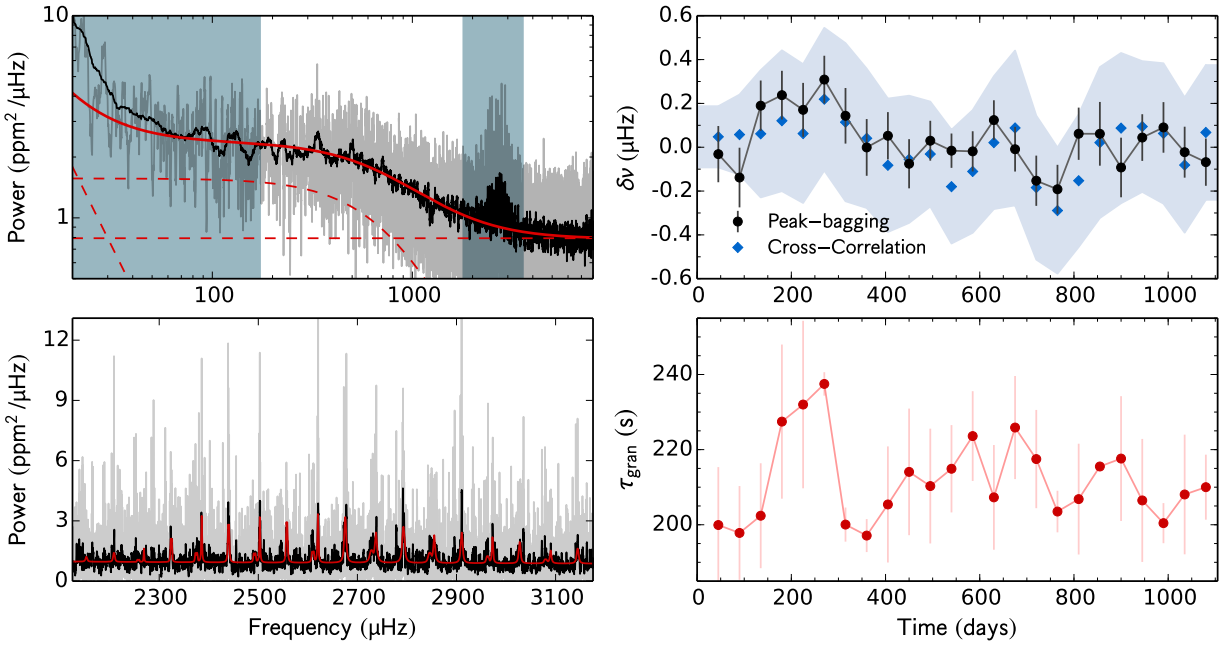

Fig. A.55 – Same as in Fig. A.1, but for KIC 9139151.

time (days)	d_c %	τ_{gran} (s)	Peak-bagging $\delta\nu_{l=0}$ (μHz)	$\delta\nu_{l=1}$ (μHz)	$\delta\nu_{l=2}$ (μHz)	$\delta\nu$ (μHz)	Cross-correlation $\delta\nu$ (μHz)
45	0.98	199.9 ± 15.4	0.10 ± 0.17	-0.22 ± 0.20	0.23 ± 0.43	-0.03 ± -0.03	0.05 ± 0.14
90	0.97	197.8 ± 12.5	-0.30 ± 0.19	0.06 ± 0.20	-0.32 ± 0.38	-0.14 ± -0.14	0.06 ± 0.18
135	0.96	202.4 ± 14.0	0.07 ± 0.16	0.32 ± 0.17	-0.20 ± 0.29	0.19 ± 0.19	0.06 ± 0.29
180	0.97	227.5 ± 20.5	0.23 ± 0.14	0.25 ± 0.18	0.03 ± 0.29	0.24 ± 0.24	0.12 ± 0.32
225	0.96	232.0 ± 22.3	0.17 ± 0.15	0.17 ± 0.20	0.23 ± 0.28	0.17 ± 0.17	0.06 ± 0.32
270	0.80	237.5 ± 3.1	0.38 ± 0.14	0.19 ± 0.18	-0.19 ± 0.28	0.31 ± 0.31	0.22 ± 0.33
315	0.78	200.0 ± 4.5	0.13 ± 0.17	0.17 ± 0.20	-0.97 ± 0.48	0.14 ± 0.14	0.11 ± 0.36
360	0.89	197.1 ± 4.4	-0.24 ± 0.18	0.27 ± 0.19	-0.90 ± 0.43	-0.00 ± -0.00	0.04 ± 0.32
405	0.93	205.4 ± 15.5	-0.04 ± 0.15	0.14 ± 0.15	-1.16 ± 0.32	0.05 ± 0.05	-0.08 ± 0.30
450	0.97	214.1 ± 16.9	0.00 ± 0.15	-0.18 ± 0.17	0.11 ± 0.46	-0.08 ± -0.08	-0.06 ± 0.29
495	0.97	210.3 ± 15.3	0.04 ± 0.11	-0.00 ± 0.18	0.16 ± 0.36	0.03 ± 0.03	-0.03 ± 0.24
540	0.98	214.9 ± 11.6	0.02 ± 0.09	-0.11 ± 0.15	-0.10 ± 0.27	-0.02 ± -0.02	-0.18 ± 0.26
585	0.94	223.6 ± 11.9	0.08 ± 0.12	-0.16 ± 0.14	-0.26 ± 0.23	-0.02 ± -0.02	-0.11 ± 0.28
630	0.92	207.3 ± 13.9	0.20 ± 0.11	0.01 ± 0.15	-0.07 ± 0.45	0.12 ± 0.12	0.02 ± 0.30
675	0.90	225.9 ± 13.7	-0.05 ± 0.13	0.06 ± 0.16	-0.14 ± 0.47	-0.01 ± -0.01	0.09 ± 0.35
720	0.91	217.5 ± 13.1	-0.26 ± 0.14	0.03 ± 0.19	0.43 ± 0.42	-0.15 ± -0.15	-0.18 ± 0.33
765	0.95	203.5 ± 5.5	-0.28 ± 0.17	-0.12 ± 0.15	0.68 ± 0.37	-0.19 ± -0.19	-0.29 ± 0.29
810	0.90	206.8 ± 14.7	0.14 ± 0.17	-0.02 ± 0.17	0.33 ± 0.40	0.06 ± 0.06	-0.15 ± 0.30
855	0.89	215.5 ± 0.4	0.22 ± 0.21	-0.09 ± 0.20	1.16 ± 0.43	0.06 ± 0.06	0.02 ± 0.34
900	0.95	217.6 ± 16.6	-0.03 ± 0.19	-0.15 ± 0.19	0.91 ± 0.49	-0.09 ± -0.09	0.09 ± 0.34
945	0.90	206.5 ± 16.4	0.13 ± 0.13	-0.12 ± 0.18	0.53 ± 0.32	0.04 ± 0.04	0.09 ± 0.30
990	0.89	200.4 ± 5.3	0.08 ± 0.14	0.11 ± 0.20	0.57 ± 0.34	0.09 ± 0.09	0.06 ± 0.32
1035	0.85	208.1 ± 15.9	0.07 ± 0.14	-0.21 ± 0.20	-0.93 ± 0.36	-0.02 ± -0.02	-0.08 ± 0.31
1080	0.85	210.0 ± 8.7	-0.09 ± 0.13	-0.03 ± 0.19	-0.01 ± 0.28	-0.07 ± -0.07	0.07 ± 0.31

Table A.55 – Same as in Table A.1, but for KIC 9139151.

KIC 9139163

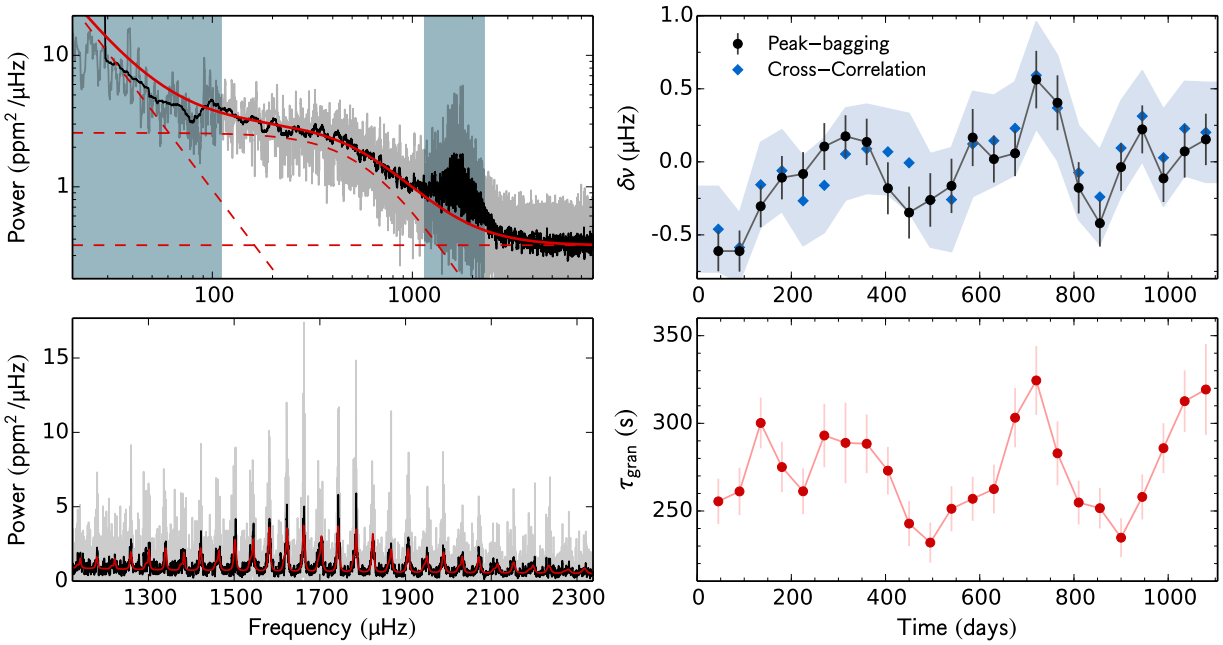

Fig. A.56 – Same as in Fig. A.1, but for KIC 9139163.

time (days)	d_c %	τ_{gran} (s)	Peak-bagging $\delta\nu_{l=0}$ (μHz)	$\delta\nu_{l=1}$ (μHz)	$\delta\nu_{l=2}$ (μHz)	$\delta\nu$ (μHz)	Cross-correlation $\delta\nu$ (μHz)
45	0.97	255.5 ± 13.0	-0.81 ± 0.20	-0.42 ± 0.19	-0.94 ± 0.43	-0.61 ± -0.61	-0.46 ± 0.29
90	0.96	261.2 ± 13.5	-0.77 ± 0.20	-0.46 ± 0.20	-1.23 ± 0.40	-0.61 ± -0.61	-0.59 ± 0.23
135	0.96	300.2 ± 14.5	-0.33 ± 0.21	-0.28 ± 0.20	0.75 ± 0.39	-0.30 ± -0.30	-0.16 ± 0.29
180	0.97	275.1 ± 14.4	0.01 ± 0.22	-0.22 ± 0.20	0.66 ± 0.40	-0.11 ± -0.11	-0.06 ± 0.28
225	0.96	261.2 ± 13.1	0.35 ± 0.23	-0.41 ± 0.20	-0.44 ± 0.40	-0.08 ± -0.08	-0.27 ± 0.31
270	0.80	293.1 ± 18.1	0.46 ± 0.24	-0.20 ± 0.22	-0.45 ± 0.41	0.10 ± 0.10	-0.16 ± 0.32
315	0.78	288.9 ± 22.9	0.17 ± 0.20	0.18 ± 0.21	0.17 ± 0.40	0.17 ± 0.17	0.05 ± 0.31
360	0.89	288.3 ± 16.8	0.16 ± 0.24	0.11 ± 0.22	0.85 ± 0.42	0.14 ± 0.14	0.09 ± 0.30
405	0.93	273.0 ± 13.6	-0.69 ± 0.28	0.18 ± 0.23	0.81 ± 0.44	-0.18 ± -0.18	0.07 ± 0.29
450	0.97	242.8 ± 12.8	-0.77 ± 0.26	0.03 ± 0.24	0.07 ± 0.41	-0.35 ± -0.35	-0.01 ± 0.34
495	0.97	232.0 ± 11.5	-0.23 ± 0.28	-0.29 ± 0.24	-0.11 ± 0.43	-0.26 ± -0.26	-0.26 ± 0.32
540	0.98	251.3 ± 12.9	0.35 ± 0.29	-0.51 ± 0.24	0.29 ± 0.45	-0.16 ± -0.16	-0.26 ± 0.36
585	0.94	257.0 ± 12.6	0.77 ± 0.31	-0.24 ± 0.25	0.36 ± 0.47	0.17 ± 0.17	0.12 ± 0.36
630	0.92	262.5 ± 13.9	0.32 ± 0.22	-0.29 ± 0.23	-0.52 ± 0.45	0.02 ± 0.02	0.14 ± 0.31
675	0.90	303.2 ± 16.9	0.35 ± 0.20	-0.35 ± 0.24	-0.87 ± 0.43	0.06 ± 0.06	0.23 ± 0.32
720	0.90	324.5 ± 19.6	0.74 ± 0.29	0.41 ± 0.27	0.06 ± 0.50	0.56 ± 0.56	0.59 ± 0.37
765	0.95	282.9 ± 18.2	-0.05 ± 0.27	0.84 ± 0.26	0.12 ± 0.48	0.40 ± 0.40	0.37 ± 0.36
810	0.89	254.8 ± 12.5	-0.20 ± 0.24	-0.15 ± 0.26	-0.23 ± 0.49	-0.18 ± -0.18	-0.07 ± 0.32
855	0.89	251.6 ± 11.6	-0.12 ± 0.22	-0.78 ± 0.24	0.84 ± 0.43	-0.42 ± -0.42	-0.24 ± 0.32
900	0.95	234.8 ± 11.1	-0.18 ± 0.23	0.12 ± 0.24	0.71 ± 0.44	-0.04 ± -0.04	0.09 ± 0.32
945	0.90	258.0 ± 12.8	-0.16 ± 0.24	0.58 ± 0.23	-0.57 ± 0.46	0.22 ± 0.22	0.31 ± 0.31
990	0.89	285.8 ± 14.3	-0.51 ± 0.24	0.22 ± 0.22	-0.42 ± 0.42	-0.11 ± -0.11	0.03 ± 0.33
1035	0.85	312.6 ± 17.6	-0.27 ± 0.25	0.45 ± 0.26	-0.28 ± 0.49	0.07 ± 0.07	0.23 ± 0.32
1080	0.85	319.3 ± 25.9	0.04 ± 0.24	0.30 ± 0.26	0.37 ± 0.55	0.15 ± 0.15	0.20 ± 0.34

Table A.56 – Same as in Table A.1, but for KIC 9139163.

KIC 9206432

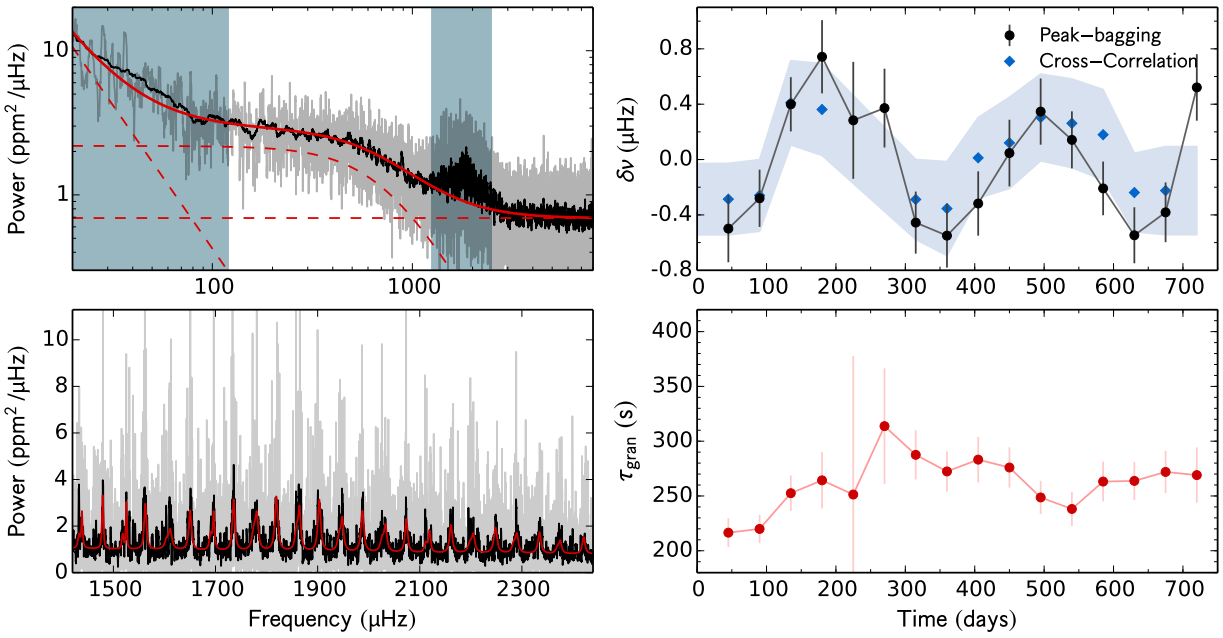

Fig. A.57 – Same as in Fig. A.1, but for KIC 9206432.

time (days)	d_c %	τ_{gran} (s)	Peak-bagging $\delta\nu_{l=0}$ (μHz)	$\delta\nu_{l=1}$ (μHz)	$\delta\nu_{l=2}$ (μHz)	$\delta\nu$ (μHz)	Cross-correlation $\delta\nu$ (μHz)
45	0.98	216.5 ± 13.2	-1.08 ± 0.37	-0.06 ± 0.32	-0.14 ± 0.51	-0.50 ± -0.50	-0.29 ± 0.26
90	0.97	219.9 ± 12.9	-0.36 ± 0.31	-0.22 ± 0.28	0.62 ± 0.43	-0.28 ± -0.28	-0.26 ± 0.26
135	0.96	252.5 ± 16.1	0.34 ± 0.29	0.45 ± 0.27	1.49 ± 0.54	0.40 ± 0.40	0.41 ± 0.30
180	0.55	264.3 ± 25.7	0.76 ± 0.37	0.73 ± 0.38	1.04 ± 0.64	0.74 ± 0.74	0.36 ± 0.33
225	0.06	251.3 ± 126.5	0.26 ± 0.53	0.32 ± 0.70	0.19 ± 0.69	0.28 ± 0.28	–
270	0.26	313.7 ± 52.8	0.80 ± 0.41	-0.03 ± 0.39	0.31 ± 0.51	0.37 ± 0.37	–
315	0.71	287.5 ± 22.4	-0.94 ± 0.33	-0.02 ± 0.31	-0.25 ± 0.45	-0.46 ± -0.46	-0.29 ± 0.29
360	0.89	272.4 ± 18.4	-0.63 ± 0.32	-0.45 ± 0.34	-0.04 ± 0.50	-0.55 ± -0.55	-0.35 ± 0.34
405	0.93	283.2 ± 20.8	0.30 ± 0.35	-0.79 ± 0.31	0.12 ± 0.62	-0.32 ± -0.32	0.01 ± 0.29
450	0.97	276.0 ± 18.4	0.31 ± 0.39	-0.11 ± 0.30	0.79 ± 0.66	0.05 ± 0.05	0.12 ± 0.33
495	0.97	248.7 ± 15.1	0.68 ± 0.36	0.08 ± 0.32	-0.09 ± 0.63	0.35 ± 0.35	0.30 ± 0.31
540	0.98	238.1 ± 15.5	0.11 ± 0.29	0.18 ± 0.30	-0.72 ± 0.56	0.14 ± 0.14	0.26 ± 0.32
585	0.94	263.2 ± 18.2	-0.40 ± 0.26	0.02 ± 0.29	-0.99 ± 0.49	-0.21 ± -0.21	0.18 ± 0.33
630	0.92	263.8 ± 17.5	-0.89 ± 0.27	-0.11 ± 0.30	-1.33 ± 0.48	-0.55 ± -0.55	-0.24 ± 0.28
675	0.90	271.9 ± 19.2	-0.63 ± 0.30	-0.12 ± 0.31	-0.87 ± 0.50	-0.38 ± -0.38	-0.22 ± 0.32
720	0.62	269.0 ± 25.2	1.19 ± 0.34	-0.17 ± 0.34	-0.41 ± 0.67	0.52 ± 0.52	–

Table A.57 – Same as in Table A.1, but for KIC 9206432.

KIC 9353712

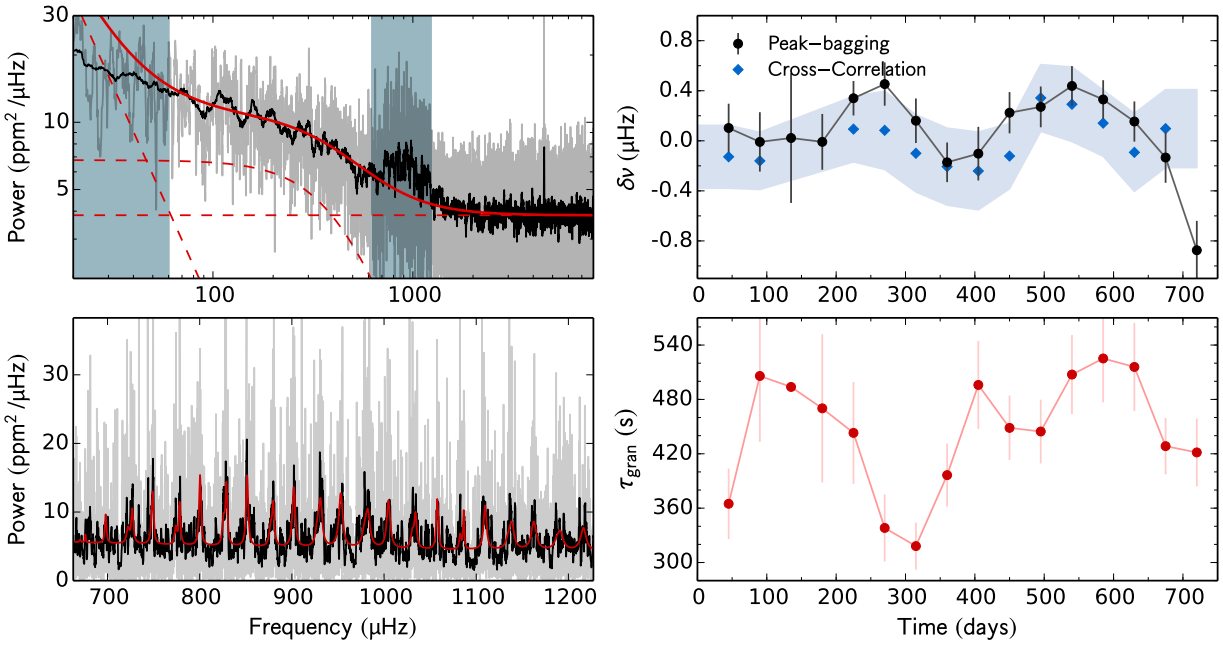

Fig. A.58 – Same as in Fig. A.1, but for KIC 9353712.

time (days)	d_c %	τ_{gran} (s)	Peak-bagging $\delta\nu_{l=0}$ (μHz)	$\delta\nu_{l=1}$ (μHz)	$\delta\nu_{l=2}$ (μHz)	$\delta\nu$ (μHz)	Cross-correlation $\delta\nu$ (μHz)
45	0.98	364.8 ± 38.9	0.09 ± 0.29	0.12 ± 0.26	0.57 ± 0.43	0.10 ± 0.10	-0.13 ± 0.25
90	0.54	505.9 ± 72.6	-0.39 ± 0.34	0.35 ± 0.33	0.74 ± 0.46	-0.01 ± -0.01	-0.16 ± 0.23
135	0.05	493.8 ± 0.0	0.21 ± 0.69	-0.22 ± 0.79	0.35 ± 0.73	0.02 ± 0.02	–
180	0.33	470.2 ± 81.7	0.08 ± 0.34	-0.07 ± 0.30	0.03 ± 0.52	-0.01 ± -0.01	–
225	0.58	443.1 ± 56.2	0.54 ± 0.20	0.16 ± 0.19	0.35 ± 0.37	0.34 ± 0.34	0.09 ± 0.26
270	0.56	338.2 ± 37.0	0.64 ± 0.24	0.24 ± 0.25	0.19 ± 0.57	0.45 ± 0.45	0.08 ± 0.31
315	0.78	318.1 ± 26.0	0.41 ± 0.31	0.03 ± 0.22	0.40 ± 0.52	0.16 ± 0.16	-0.10 ± 0.31
360	0.89	396.4 ± 34.9	-0.25 ± 0.22	-0.09 ± 0.23	-0.21 ± 0.58	-0.17 ± -0.17	-0.21 ± 0.31
405	0.93	496.0 ± 48.6	0.12 ± 0.31	-0.29 ± 0.29	-0.46 ± 0.59	-0.10 ± -0.10	-0.24 ± 0.31
450	0.97	448.6 ± 35.6	0.18 ± 0.24	0.26 ± 0.23	-0.08 ± 0.51	0.22 ± 0.22	-0.12 ± 0.26
495	0.97	444.6 ± 35.1	0.21 ± 0.26	0.31 ± 0.21	0.07 ± 0.46	0.27 ± 0.27	0.34 ± 0.27
540	0.98	507.4 ± 43.6	0.43 ± 0.28	0.44 ± 0.19	0.81 ± 0.42	0.44 ± 0.44	0.29 ± 0.30
585	0.94	525.2 ± 48.5	0.24 ± 0.27	0.37 ± 0.19	0.65 ± 0.45	0.33 ± 0.33	0.14 ± 0.26
630	0.92	515.8 ± 48.6	-0.01 ± 0.26	0.25 ± 0.20	-0.70 ± 0.42	0.15 ± 0.15	-0.09 ± 0.31
675	0.90	428.4 ± 31.1	0.05 ± 0.32	-0.26 ± 0.26	-0.57 ± 0.61	-0.13 ± -0.13	0.10 ± 0.31
720	0.62	421.5 ± 37.5	-1.42 ± 0.34	-0.39 ± 0.32	-0.80 ± 0.69	-0.87 ± -0.87	–

Table A.58 – Same as in Table A.1, but for KIC 9353712.

KIC 9410862

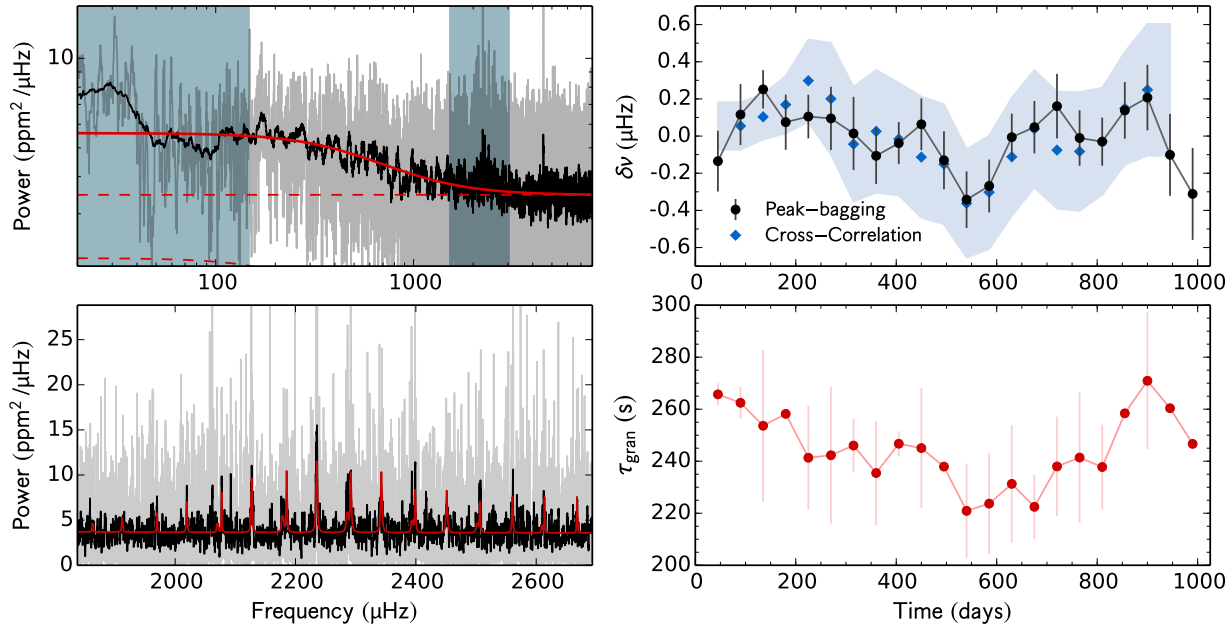

Fig. A.59 – Same as in Fig. A.1, but for KIC 9410862. Due to the extremely large error bars, the results from the cross-correlation method, that are shown here, were obtained from 180-d sub-series.

time (days)	d_c %	τ_{gran} (s)	Peak-bagging $\delta\nu_{l=0}$ (μHz)	$\delta\nu_{l=1}$ (μHz)	$\delta\nu_{l=2}$ (μHz)	$\delta\nu$ (μHz)	Cross-correlation $\delta\nu$ (μHz)
45	0.98	265.7 ± 4.3	0.23 ± 0.24	-0.47 ± 0.23	-0.72 ± 0.44	-0.14 ± -0.14	–
90	0.97	262.5 ± 6.0	0.48 ± 0.22	-0.32 ± 0.24	-1.03 ± 0.52	0.12 ± 0.12	0.05 ± 0.13
135	0.96	253.6 ± 29.2	0.31 ± 0.13	0.16 ± 0.16	-0.72 ± 0.50	0.25 ± 0.25	0.10 ± 0.12
180	0.97	258.2 ± 1.1	-0.19 ± 0.19	0.55 ± 0.25	0.19 ± 0.44	0.07 ± 0.07	0.17 ± 0.15
225	0.96	241.3 ± 19.9	0.10 ± 0.13	0.12 ± 0.25	0.01 ± 0.39	0.10 ± 0.10	0.30 ± 0.22
270	0.80	242.3 ± 26.3	0.26 ± 0.24	-0.06 ± 0.24	0.23 ± 0.36	0.09 ± 0.09	0.20 ± 0.30
315	0.78	246.0 ± 10.3	-0.37 ± 0.33	0.23 ± 0.25	0.28 ± 0.41	0.01 ± 0.01	-0.04 ± 0.31
360	0.89	235.5 ± 20.0	0.01 ± 0.25	-0.17 ± 0.19	-0.34 ± 0.37	-0.11 ± -0.11	0.03 ± 0.33
405	0.93	246.7 ± 4.8	0.19 ± 0.18	-0.20 ± 0.15	-0.07 ± 0.25	-0.04 ± -0.04	-0.02 ± 0.30
450	0.97	245.0 ± 23.2	0.19 ± 0.20	-0.06 ± 0.19	0.21 ± 0.24	0.06 ± 0.06	-0.11 ± 0.33
495	0.97	237.9 ± 0.1	-0.21 ± 0.23	-0.06 ± 0.21	0.55 ± 0.34	-0.13 ± -0.13	-0.15 ± 0.32
540	0.98	220.9 ± 18.2	-0.30 ± 0.20	-0.41 ± 0.24	0.32 ± 0.33	-0.34 ± -0.34	-0.36 ± 0.29
585	0.94	223.7 ± 19.5	-0.08 ± 0.19	-0.48 ± 0.21	0.29 ± 0.28	-0.27 ± -0.27	-0.30 ± 0.31
630	0.92	231.3 ± 22.6	0.04 ± 0.20	-0.04 ± 0.16	-0.22 ± 0.40	-0.01 ± -0.01	-0.11 ± 0.32
675	0.90	222.5 ± 12.4	-0.14 ± 0.22	0.18 ± 0.18	-0.06 ± 0.95	0.05 ± 0.05	0.04 ± 0.32
720	0.90	238.0 ± 19.2	0.16 ± 0.26	0.16 ± 0.23	0.53 ± 0.65	0.16 ± 0.16	-0.08 ± 0.31
765	0.95	241.4 ± 25.0	0.21 ± 0.19	-0.35 ± 0.24	0.37 ± 0.60	-0.01 ± -0.01	-0.08 ± 0.32
810	0.90	237.8 ± 16.2	-0.02 ± 0.16	-0.04 ± 0.21	-0.41 ± 0.53	-0.03 ± -0.03	-0.03 ± 0.29
855	0.89	258.4 ± 1.3	-0.00 ± 0.22	0.28 ± 0.21	0.19 ± 0.41	0.14 ± 0.14	0.15 ± 0.30
900	0.78	270.9 ± 26.3	0.46 ± 0.37	0.13 ± 0.20	0.68 ± 0.44	0.21 ± 0.21	0.25 ± 0.35
945	0.56	260.4 ± 0.2	-0.16 ± 0.33	-0.05 ± 0.30	0.21 ± 0.35	-0.10 ± -0.10	–
990	0.66	246.7 ± 0.9	-0.10 ± 0.33	-0.57 ± 0.37	-0.66 ± 0.56	-0.31 ± -0.31	–

Table A.59 – Same as in Table A.1, but for KIC 9410862. Due to the extremely large error bars, the results from the cross-correlation method, that are shown here, were obtained from 180-d sub-series.

KIC 9414417

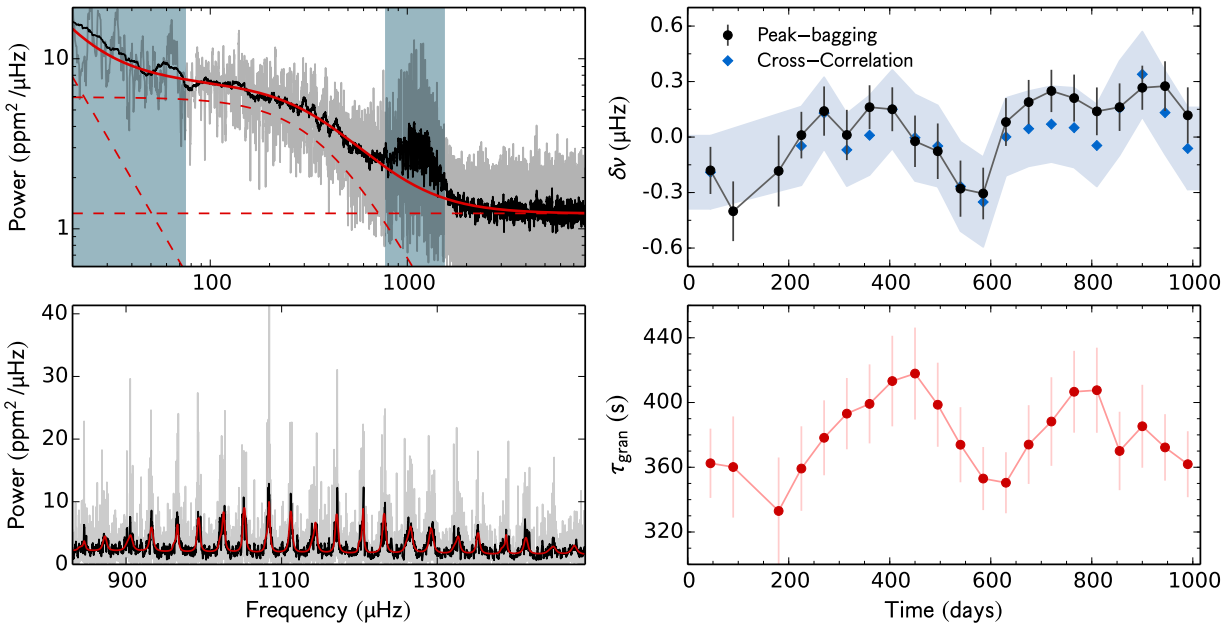

Fig. A.60 – Same as in Fig. A.1, but for KIC 9414417.

time (days)	d_c %	τ_{gran} (s)	Peak-bagging $\delta\nu_{l=0}$ (μHz)	$\delta\nu_{l=1}$ (μHz)	$\delta\nu_{l=2}$ (μHz)	$\delta\nu$ (μHz)	Cross-correlation $\delta\nu$ (μHz)
45	0.98	362.5 ± 21.4	-0.06 ± 0.18	-0.30 ± 0.18	-0.30 ± 0.36	-0.18 ± -0.18	-0.19 ± 0.20
90	0.49	360.1 ± 31.2	-0.40 ± 0.21	-0.40 ± 0.25	0.47 ± 0.50	-0.40 ± -0.40	–
180	0.29	333.0 ± 33.1	0.09 ± 0.26	-0.51 ± 0.29	-0.11 ± 0.46	-0.18 ± -0.18	–
225	0.72	359.2 ± 26.1	-0.03 ± 0.19	0.04 ± 0.17	0.53 ± 0.36	0.01 ± 0.01	-0.05 ± 0.21
270	0.92	378.2 ± 23.2	0.03 ± 0.21	0.22 ± 0.17	0.27 ± 0.38	0.14 ± 0.14	0.13 ± 0.19
315	0.98	393.1 ± 22.0	0.01 ± 0.21	0.01 ± 0.18	-0.67 ± 0.32	0.01 ± 0.01	-0.07 ± 0.20
360	0.97	399.2 ± 24.4	0.25 ± 0.17	0.08 ± 0.16	-0.52 ± 0.31	0.16 ± 0.16	0.01 ± 0.21
405	0.97	413.3 ± 28.0	-0.04 ± 0.17	0.35 ± 0.17	-0.14 ± 0.33	0.15 ± 0.15	0.15 ± 0.21
450	0.97	417.9 ± 28.4	-0.29 ± 0.19	0.26 ± 0.20	0.47 ± 0.38	-0.02 ± -0.02	-0.00 ± 0.23
495	0.94	398.6 ± 26.0	-0.16 ± 0.22	-0.01 ± 0.20	0.39 ± 0.42	-0.08 ± -0.08	-0.05 ± 0.22
540	0.91	373.9 ± 23.2	-0.29 ± 0.22	-0.27 ± 0.21	-0.43 ± 0.43	-0.28 ± -0.28	-0.27 ± 0.24
585	0.88	353.0 ± 19.5	-0.28 ± 0.21	-0.33 ± 0.18	-0.30 ± 0.29	-0.31 ± -0.31	-0.35 ± 0.24
630	0.92	350.4 ± 18.9	0.14 ± 0.20	0.03 ± 0.17	-0.39 ± 0.33	0.08 ± 0.08	0.00 ± 0.21
675	0.97	374.0 ± 24.3	0.42 ± 0.18	0.01 ± 0.16	-0.41 ± 0.38	0.19 ± 0.19	0.05 ± 0.20
720	0.90	388.2 ± 27.4	0.65 ± 0.16	-0.13 ± 0.16	-0.11 ± 0.43	0.25 ± 0.25	0.07 ± 0.20
765	0.89	406.6 ± 25.3	0.46 ± 0.19	-0.01 ± 0.17	0.18 ± 0.39	0.21 ± 0.21	0.05 ± 0.22
810	0.95	407.6 ± 26.3	0.14 ± 0.18	0.14 ± 0.18	-0.34 ± 0.32	0.14 ± 0.14	-0.05 ± 0.22
855	0.89	370.1 ± 24.2	0.10 ± 0.17	0.24 ± 0.20	0.12 ± 0.33	0.16 ± 0.16	0.16 ± 0.25
900	0.82	385.3 ± 25.6	0.20 ± 0.16	0.35 ± 0.18	0.18 ± 0.43	0.27 ± 0.27	0.34 ± 0.23
945	0.85	372.3 ± 20.5	0.10 ± 0.19	0.45 ± 0.19	-0.03 ± 0.38	0.28 ± 0.28	0.13 ± 0.23
990	0.00	361.9 ± 20.4	-0.00 ± 0.22	0.23 ± 0.21	0.23 ± 0.39	0.12 ± 0.12	-0.06 ± 0.22

Table A.60 – Same as in Table A.1, but for KIC 9414417.

KIC 9592705

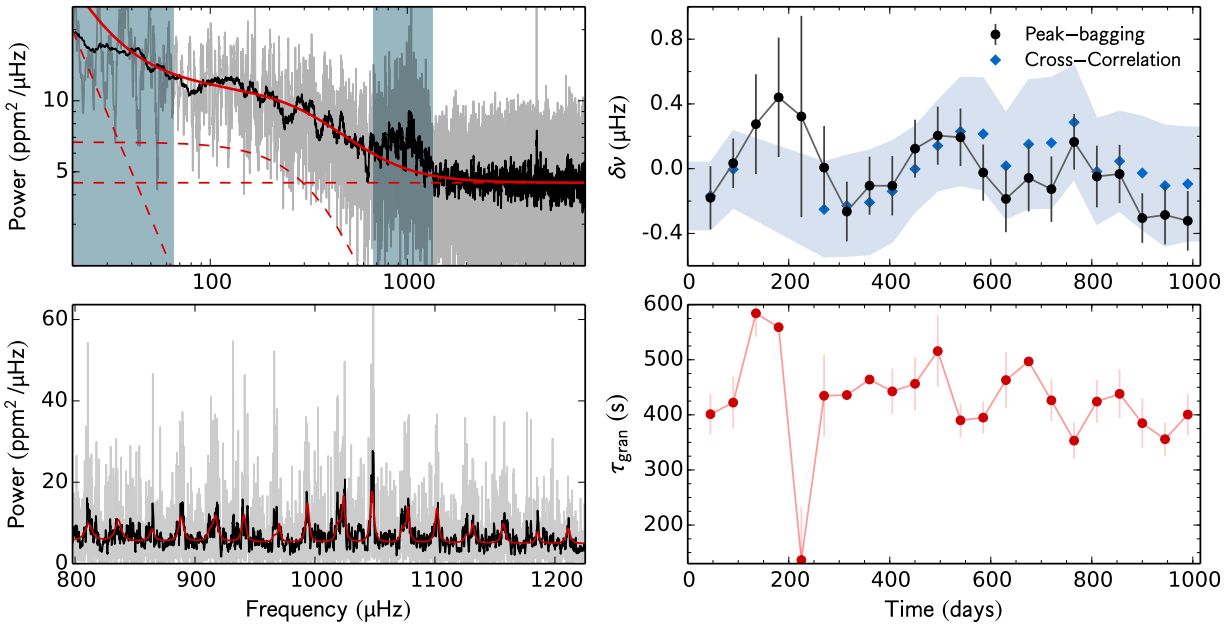

Fig. A.61 – Same as in Fig. A.1, but for KIC 9592705.

time (days)	d_c %	τ_{gran} (s)	Peak-bagging $\delta\nu_{l=0}$ (μHz)	$\delta\nu_{l=1}$ (μHz)	$\delta\nu_{l=2}$ (μHz)	$\delta\nu$ (μHz)	Cross-correlation $\delta\nu$ (μHz)
45	0.98	401.2 ± 36.7	-0.57 ± 0.34	0.01 ± 0.24	-0.49 ± 0.47	-0.18 ± -0.18	-0.17 ± 0.21
90	0.63	422.2 ± 46.9	-0.05 ± 0.24	0.09 ± 0.20	0.23 ± 0.34	0.03 ± 0.03	-0.00 ± 0.24
135	0.32	584.3 ± 42.5	0.11 ± 0.43	0.45 ± 0.44	0.12 ± 0.91	0.28 ± 0.28	–
180	0.17	559.1 ± 4.4	0.35 ± 0.49	0.56 ± 0.56	-0.33 ± 0.92	0.44 ± 0.44	–
225	0.01	136.4 ± 95.9	0.50 ± 0.83	0.10 ± 0.94	-0.29 ± 0.95	0.32 ± 0.32	–
270	0.50	434.7 ± 74.1	0.06 ± 0.45	-0.02 ± 0.31	0.10 ± 0.71	0.01 ± 0.01	-0.25 ± 0.29
315	0.98	436.0 ± 7.8	-0.14 ± 0.27	-0.38 ± 0.26	-0.24 ± 0.65	-0.26 ± -0.26	-0.23 ± 0.31
360	0.97	464.2 ± 7.6	-0.10 ± 0.23	-0.12 ± 0.29	-1.13 ± 0.54	-0.11 ± -0.11	-0.21 ± 0.32
405	0.97	442.5 ± 41.4	-0.33 ± 0.25	0.14 ± 0.27	-1.00 ± 0.50	-0.11 ± -0.11	-0.14 ± 0.31
450	0.97	456.4 ± 47.7	0.07 ± 0.26	0.18 ± 0.25	-0.55 ± 0.72	0.12 ± 0.12	-0.00 ± 0.26
495	0.94	515.7 ± 65.2	0.43 ± 0.25	-0.02 ± 0.25	0.59 ± 0.63	0.20 ± 0.20	0.14 ± 0.28
540	0.91	390.0 ± 30.7	0.36 ± 0.25	0.03 ± 0.25	0.78 ± 0.55	0.19 ± 0.19	0.23 ± 0.33
585	0.88	395.0 ± 29.0	-0.19 ± 0.22	0.22 ± 0.27	0.04 ± 0.70	-0.02 ± -0.02	0.21 ± 0.34
630	0.92	463.1 ± 50.5	0.15 ± 0.27	-0.63 ± 0.31	0.77 ± 0.64	-0.19 ± -0.19	0.02 ± 0.33
675	0.97	496.9 ± 1.5	0.21 ± 0.30	-0.31 ± 0.29	0.78 ± 0.66	-0.06 ± -0.06	0.15 ± 0.40
720	0.90	426.3 ± 37.6	-0.29 ± 0.27	0.08 ± 0.31	0.12 ± 0.73	-0.13 ± -0.13	0.16 ± 0.40
765	0.89	353.2 ± 32.9	-0.22 ± 0.24	0.60 ± 0.25	-0.20 ± 0.73	0.17 ± 0.17	0.29 ± 0.35
810	0.95	424.1 ± 38.8	-0.04 ± 0.28	-0.06 ± 0.26	-0.53 ± 0.63	-0.05 ± -0.05	-0.02 ± 0.33
855	0.89	438.1 ± 44.1	-0.20 ± 0.32	0.05 ± 0.22	0.11 ± 0.56	-0.03 ± -0.03	0.05 ± 0.31
900	0.82	384.8 ± 44.8	-0.20 ± 0.22	-0.41 ± 0.22	0.46 ± 0.46	-0.31 ± -0.31	-0.03 ± 0.35
945	0.84	355.8 ± 30.3	0.05 ± 0.25	-0.66 ± 0.27	0.54 ± 0.51	-0.29 ± -0.29	-0.11 ± 0.37
990	0.92	400.6 ± 38.2	-0.68 ± 0.26	0.01 ± 0.26	0.53 ± 0.68	-0.32 ± -0.32	-0.09 ± 0.35

Table A.61 – Same as in Table A.1, but for KIC 9592705.

KIC 9812850

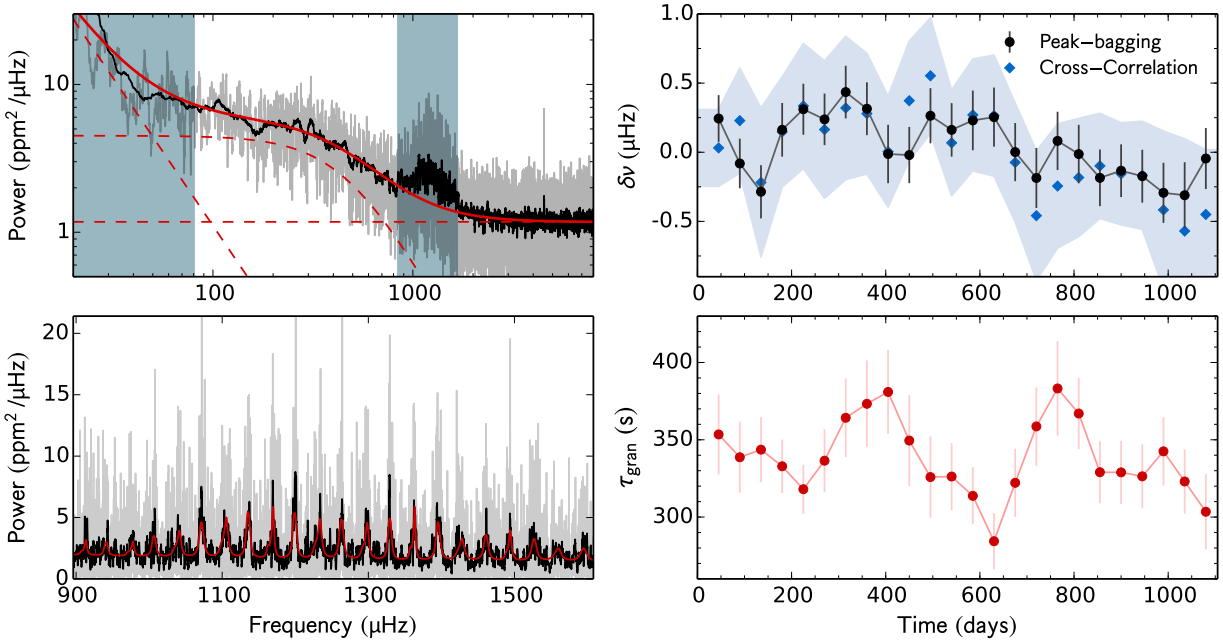

Fig. A.62 – Same as in Fig. A.1, but for KIC 9812850.

time (days)	d_c %	τ_{gran} (s)	Peak-bagging $\delta\nu_{l=0}$ (μHz)	$\delta\nu_{l=1}$ (μHz)	$\delta\nu_{l=2}$ (μHz)	$\delta\nu$ (μHz)	Cross-correlation $\delta\nu$ (μHz)
45	0.98	353.5 ± 25.9	0.41 ± 0.24	0.08 ± 0.24	-0.09 ± 0.52	0.24 ± 0.24	0.03 ± 0.28
90	0.97	338.7 ± 23.0	-0.50 ± 0.26	0.28 ± 0.25	-0.06 ± 0.59	-0.08 ± -0.08	0.23 ± 0.38
135	0.96	343.6 ± 21.1	-0.82 ± 0.25	0.51 ± 0.30	0.61 ± 0.49	-0.29 ± -0.29	-0.22 ± 0.54
180	0.97	332.9 ± 17.3	0.06 ± 0.27	0.27 ± 0.28	-0.15 ± 0.48	0.16 ± 0.16	0.15 ± 0.40
225	0.96	318.0 ± 15.7	0.29 ± 0.27	0.33 ± 0.25	-0.37 ± 0.44	0.31 ± 0.31	0.33 ± 0.45
270	0.80	336.5 ± 20.3	0.06 ± 0.26	0.41 ± 0.26	-0.60 ± 0.47	0.24 ± 0.24	0.16 ± 0.50
315	0.78	364.2 ± 25.4	0.65 ± 0.28	0.23 ± 0.26	0.05 ± 0.51	0.43 ± 0.43	0.32 ± 0.52
360	0.89	373.3 ± 28.1	0.41 ± 0.27	0.22 ± 0.27	0.20 ± 0.44	0.31 ± 0.31	0.28 ± 0.44
405	0.93	380.9 ± 27.0	0.07 ± 0.30	-0.09 ± 0.29	0.03 ± 0.54	-0.01 ± -0.01	0.00 ± 0.40
450	0.97	349.5 ± 29.4	-0.27 ± 0.30	0.19 ± 0.28	0.60 ± 0.61	-0.02 ± -0.02	0.37 ± 0.43
495	0.97	325.9 ± 26.3	0.05 ± 0.29	0.45 ± 0.28	1.42 ± 0.56	0.26 ± 0.26	0.55 ± 0.42
540	0.98	326.2 ± 21.7	0.49 ± 0.28	-0.13 ± 0.27	1.06 ± 0.52	0.16 ± 0.16	0.07 ± 0.38
585	0.94	313.7 ± 18.4	0.15 ± 0.33	0.29 ± 0.29	-0.27 ± 0.59	0.23 ± 0.23	0.27 ± 0.40
630	0.92	284.4 ± 18.2	-0.63 ± 0.34	0.86 ± 0.28	-0.22 ± 0.55	0.25 ± 0.25	0.26 ± 0.44
675	0.90	322.2 ± 22.1	-0.03 ± 0.33	0.02 ± 0.27	-0.07 ± 0.54	0.00 ± 0.00	-0.07 ± 0.43
720	0.91	358.6 ± 25.3	0.22 ± 0.31	-0.57 ± 0.30	0.57 ± 0.55	-0.19 ± -0.19	-0.46 ± 0.47
765	0.95	383.2 ± 30.6	0.28 ± 0.29	-0.13 ± 0.30	0.29 ± 0.55	0.08 ± 0.08	-0.24 ± 0.45
810	0.90	367.0 ± 23.1	0.27 ± 0.30	-0.28 ± 0.30	-1.31 ± 0.58	-0.01 ± -0.01	-0.18 ± 0.43
855	0.89	329.0 ± 20.1	-0.06 ± 0.29	-0.32 ± 0.29	-0.31 ± 0.51	-0.19 ± -0.19	-0.10 ± 0.38
900	0.95	328.9 ± 20.5	-0.14 ± 0.28	-0.13 ± 0.26	0.09 ± 0.48	-0.13 ± -0.13	-0.16 ± 0.37
945	0.90	326.4 ± 20.7	-0.24 ± 0.27	-0.10 ± 0.28	-0.32 ± 0.51	-0.17 ± -0.17	-0.17 ± 0.39
990	0.89	342.5 ± 22.1	-0.03 ± 0.29	-0.64 ± 0.33	-0.44 ± 0.61	-0.29 ± -0.29	-0.42 ± 0.57
1035	0.85	323.0 ± 20.8	-0.04 ± 0.34	-0.58 ± 0.34	-0.55 ± 0.67	-0.31 ± -0.31	-0.57 ± 0.67
1080	0.85	303.4 ± 24.3	0.13 ± 0.32	-0.20 ± 0.30	0.01 ± 0.52	-0.05 ± -0.05	-0.45 ± 0.47

Table A.62 – Same as in Table A.1, but for KIC 9812850.

KIC 9955598

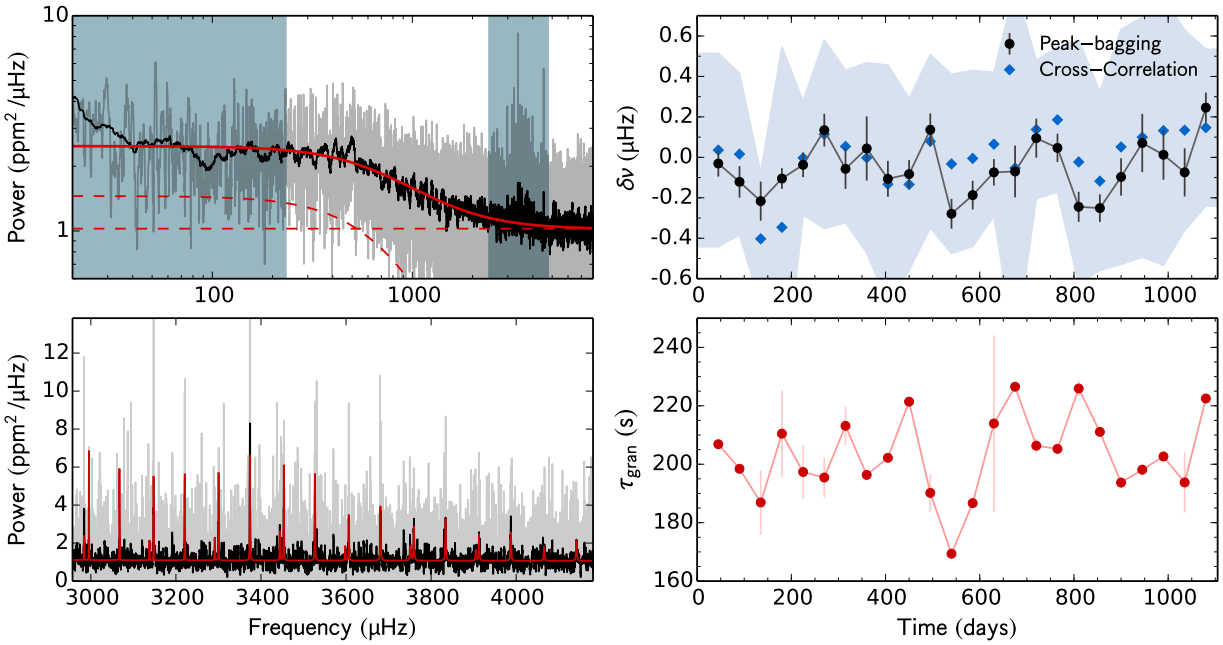

Fig. A.63 – Same as in Fig. A.1, but for KIC 9955598.

time (days)	d_c %	τ_{gran} (s)	Peak-bagging $\delta\nu_{l=0}$ (μHz)	$\delta\nu_{l=1}$ (μHz)	$\delta\nu_{l=2}$ (μHz)	$\delta\nu$ (μHz)	Cross-correlation $\delta\nu$ (μHz)
45	0.98	206.9 ± 0.0	0.06 ± 0.10	-0.10 ± 0.09	0.25 ± 0.18	-0.03 ± -0.03	0.04 ± 0.48
90	0.97	198.4 ± 0.5	-0.16 ± 0.12	-0.09 ± 0.11	0.03 ± 0.23	-0.12 ± -0.12	0.02 ± 0.40
135	0.96	186.9 ± 11.0	-0.20 ± 0.12	-0.25 ± 0.16	0.39 ± 0.64	-0.22 ± -0.22	-0.40 ± 0.33
180	0.97	210.5 ± 14.8	-0.10 ± 0.05	-0.17 ± 0.15	0.00 ± 0.34	-0.10 ± -0.10	-0.35 ± 0.89
225	0.96	197.3 ± 9.2	-0.04 ± 0.07	-0.04 ± 0.12	-0.48 ± 0.21	-0.04 ± -0.04	-0.00 ± 0.28
270	0.80	195.5 ± 6.8	0.21 ± 0.10	0.01 ± 0.13	-0.47 ± 0.21	0.13 ± 0.13	0.11 ± 0.47
315	0.78	213.2 ± 6.6	-0.10 ± 0.13	0.01 ± 0.16	-0.22 ± 0.33	-0.06 ± -0.06	0.05 ± 0.38
360	0.89	196.3 ± 0.2	-0.18 ± 0.23	0.24 ± 0.22	-0.73 ± 0.52	0.04 ± 0.04	-0.00 ± 0.47
405	0.93	202.2 ± 0.0	-0.05 ± 0.11	-0.22 ± 0.16	-0.64 ± 0.39	-0.11 ± -0.11	-0.13 ± 0.59
450	0.97	221.4 ± 1.1	-0.08 ± 0.09	-0.09 ± 0.11	-0.04 ± 0.29	-0.08 ± -0.08	-0.13 ± 0.42
495	0.97	190.2 ± 6.4	0.04 ± 0.12	0.23 ± 0.11	0.10 ± 0.24	0.14 ± 0.14	0.08 ± 0.43
540	0.98	169.4 ± 1.9	-0.41 ± 0.10	-0.13 ± 0.11	0.02 ± 0.21	-0.28 ± -0.28	-0.03 ± 0.44
585	0.94	186.7 ± 0.4	-0.28 ± 0.08	0.06 ± 0.14	-0.11 ± 0.30	-0.19 ± -0.19	-0.01 ± 0.44
630	0.92	213.9 ± 30.2	-0.13 ± 0.08	0.08 ± 0.12	-0.25 ± 0.31	-0.07 ± -0.07	0.07 ± 0.35
675	0.90	226.5 ± 0.9	0.18 ± 0.20	-0.25 ± 0.17	-0.35 ± 0.33	-0.07 ± -0.07	-0.05 ± 0.90
720	0.90	206.3 ± 2.4	0.10 ± 0.13	0.08 ± 0.15	-0.32 ± 0.29	0.09 ± 0.09	0.14 ± 0.34
765	0.95	205.3 ± 1.7	0.01 ± 0.09	0.11 ± 0.12	0.12 ± 0.32	0.05 ± 0.05	0.19 ± 0.36
810	0.90	225.9 ± 2.5	-0.24 ± 0.09	-0.25 ± 0.14	0.22 ± 0.33	-0.24 ± -0.24	-0.02 ± 0.60
855	0.89	211.1 ± 1.0	-0.31 ± 0.08	0.02 ± 0.16	0.28 ± 0.40	-0.25 ± -0.25	-0.12 ± 0.44
900	0.95	193.7 ± 1.9	-0.29 ± 0.12	0.22 ± 0.15	0.52 ± 0.28	-0.10 ± -0.10	0.05 ± 0.58
945	0.90	198.1 ± 1.9	0.30 ± 0.22	-0.09 ± 0.19	-0.84 ± 0.75	0.07 ± 0.07	0.10 ± 0.59
990	0.89	202.7 ± 1.7	0.02 ± 0.18	0.01 ± 0.17	0.88 ± 0.32	0.01 ± 0.01	0.13 ± 0.66
1035	0.85	193.8 ± 10.3	-0.29 ± 0.21	0.02 ± 0.14	0.86 ± 0.34	-0.07 ± -0.07	0.13 ± 0.50
1080	0.85	222.5 ± 1.7	0.28 ± 0.10	0.20 ± 0.11	0.94 ± 0.49	0.25 ± 0.25	0.15 ± 0.39

Table A.63 – Same as in Table A.1, but for KIC 9955598.

KIC 9965715

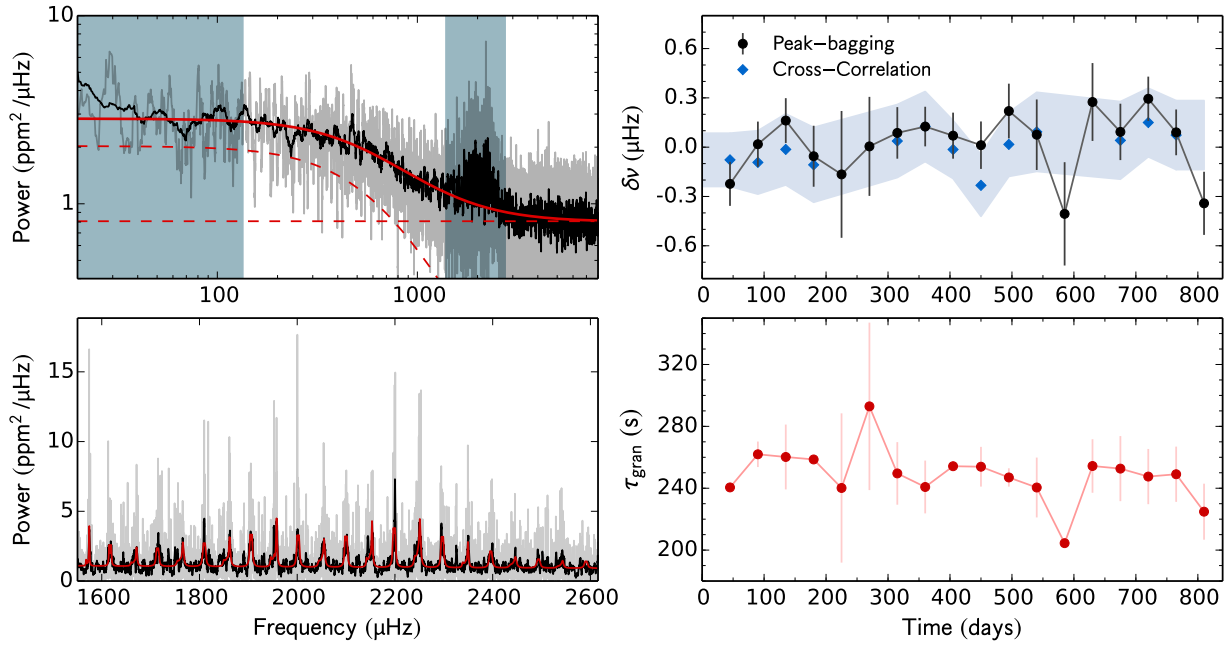

Fig. A.64 – Same as in Fig. A.1, but for KIC 9965715.

time (days)	d_c %	τ_{gran} (s)	Peak-bagging $\delta\nu_{l=0}$ (μHz)	$\delta\nu_{l=1}$ (μHz)	$\delta\nu_{l=2}$ (μHz)	$\delta\nu$ (μHz)	Cross-correlation $\delta\nu$ (μHz)
45	0.98	240.5 ± 2.6	-0.03 ± 0.19	-0.42 ± 0.19	0.35 ± 0.33	-0.22 ± -0.22	-0.08 ± 0.16
90	0.97	261.9 ± 8.2	0.03 ± 0.20	0.01 ± 0.19	-0.40 ± 0.40	0.02 ± 0.02	-0.09 ± 0.19
135	0.96	260.2 ± 21.0	0.28 ± 0.19	0.04 ± 0.20	-0.28 ± 0.37	0.16 ± 0.16	-0.01 ± 0.22
180	0.55	258.6 ± 0.6	0.11 ± 0.26	-0.23 ± 0.27	0.09 ± 0.49	-0.06 ± -0.06	-0.11 ± 0.23
225	0.06	240.2 ± 48.3	-0.14 ± 0.54	-0.19 ± 0.56	-0.29 ± 0.71	-0.17 ± -0.17	–
270	0.26	292.9 ± 54.1	0.44 ± 0.54	-0.19 ± 0.36	0.40 ± 0.58	0.00 ± 0.00	–
315	0.71	249.6 ± 20.2	-0.04 ± 0.20	0.28 ± 0.25	-0.17 ± 0.41	0.09 ± 0.09	0.04 ± 0.22
360	0.89	240.8 ± 17.1	-0.01 ± 0.15	0.37 ± 0.20	-0.18 ± 0.39	0.13 ± 0.13	0.13 ± 0.21
405	0.93	254.2 ± 0.8	0.20 ± 0.20	-0.06 ± 0.20	0.31 ± 0.43	0.07 ± 0.07	-0.01 ± 0.18
450	0.97	253.9 ± 12.8	-0.01 ± 0.20	0.03 ± 0.21	0.11 ± 0.35	0.01 ± 0.01	-0.23 ± 0.19
495	0.97	247.0 ± 5.9	0.35 ± 0.24	0.10 ± 0.23	0.18 ± 0.48	0.22 ± 0.22	0.02 ± 0.19
540	0.67	240.5 ± 19.4	0.38 ± 0.31	-0.20 ± 0.30	0.66 ± 0.66	0.08 ± 0.08	0.09 ± 0.24
585	0.19	204.5 ± 0.5	-0.39 ± 0.39	-0.44 ± 0.54	0.15 ± 0.77	-0.41 ± -0.41	–
630	0.19	254.4 ± 17.3	0.05 ± 0.29	0.76 ± 0.42	0.38 ± 0.59	0.27 ± 0.27	–
675	0.62	252.7 ± 21.0	-0.00 ± 0.25	0.17 ± 0.23	-0.48 ± 0.43	0.09 ± 0.09	0.04 ± 0.24
720	0.90	247.5 ± 17.9	0.25 ± 0.20	0.33 ± 0.19	-0.86 ± 0.34	0.29 ± 0.29	0.15 ± 0.21
765	0.95	249.0 ± 17.9	-0.10 ± 0.20	0.28 ± 0.20	-0.50 ± 0.45	0.09 ± 0.09	0.07 ± 0.21
810	0.70	224.8 ± 18.1	-0.75 ± 0.29	-0.03 ± 0.26	-0.21 ± 0.51	-0.34 ± -0.34	–

Table A.64 – Same as in Table A.1, but for KIC 9965715.

KIC 10068307

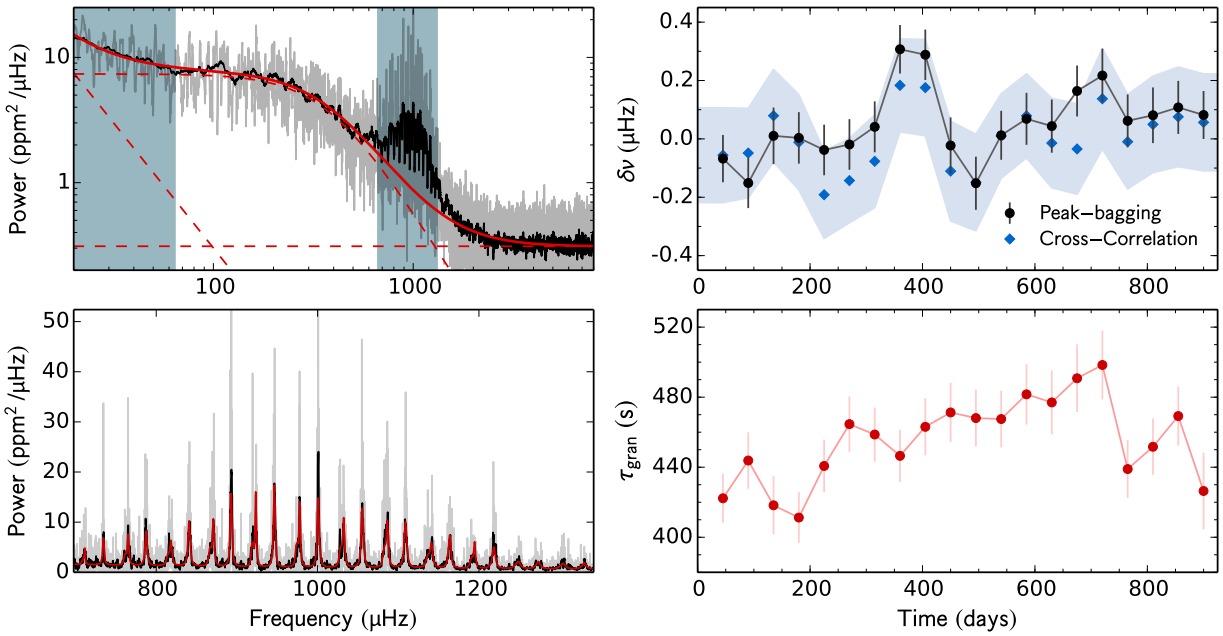

Fig. A.65 – Same as in Fig. A.1, but for KIC 10068307.

time (days)	d_c %	τ_{gran} (s)	Peak-bagging $\delta\nu_{l=0}$ (μHz)	$\delta\nu_{l=1}$ (μHz)	$\delta\nu_{l=2}$ (μHz)	$\delta\nu$ (μHz)	Cross-correlation $\delta\nu$ (μHz)
45	0.97	422.3 ± 14.0	0.01 ± 0.13	-0.12 ± 0.11	-0.10 ± 0.22	-0.07 ± -0.07	-0.06 ± 0.16
90	0.78	443.8 ± 16.1	-0.12 ± 0.12	-0.18 ± 0.12	0.03 ± 0.22	-0.15 ± -0.15	-0.05 ± 0.15
135	0.73	418.2 ± 16.6	0.10 ± 0.14	-0.08 ± 0.14	0.25 ± 0.25	0.01 ± 0.01	0.08 ± 0.16
180	0.92	411.2 ± 14.4	0.07 ± 0.13	-0.06 ± 0.12	0.12 ± 0.19	0.00 ± 0.00	-0.01 ± 0.16
225	0.98	440.7 ± 15.0	0.01 ± 0.14	-0.07 ± 0.11	-0.04 ± 0.17	-0.04 ± -0.04	-0.19 ± 0.15
270	0.97	464.6 ± 15.8	0.10 ± 0.13	-0.12 ± 0.12	-0.26 ± 0.19	-0.02 ± -0.02	-0.14 ± 0.14
315	0.97	458.7 ± 15.4	0.07 ± 0.13	0.02 ± 0.12	-0.40 ± 0.19	0.04 ± 0.04	-0.08 ± 0.16
360	0.97	446.5 ± 15.0	0.25 ± 0.13	0.35 ± 0.11	-0.18 ± 0.16	0.31 ± 0.31	0.18 ± 0.16
405	0.94	463.1 ± 16.3	0.31 ± 0.13	0.27 ± 0.12	0.01 ± 0.19	0.29 ± 0.29	0.18 ± 0.16
450	0.91	471.3 ± 16.9	0.09 ± 0.15	-0.10 ± 0.12	0.00 ± 0.21	-0.02 ± -0.02	-0.11 ± 0.17
495	0.88	468.1 ± 16.3	-0.16 ± 0.13	-0.14 ± 0.12	-0.56 ± 0.22	-0.15 ± -0.15	-0.15 ± 0.17
540	0.92	467.5 ± 16.2	0.02 ± 0.13	0.01 ± 0.11	-0.48 ± 0.22	0.01 ± 0.01	0.01 ± 0.14
585	0.97	481.6 ± 17.2	0.14 ± 0.14	0.02 ± 0.11	0.52 ± 0.22	0.07 ± 0.07	0.08 ± 0.14
630	0.89	477.0 ± 18.2	0.11 ± 0.15	0.00 ± 0.12	0.51 ± 0.20	0.04 ± 0.04	-0.01 ± 0.15
675	0.89	490.8 ± 19.3	0.18 ± 0.15	0.16 ± 0.11	0.13 ± 0.18	0.16 ± 0.16	-0.03 ± 0.15
720	0.95	498.4 ± 19.6	0.15 ± 0.15	0.26 ± 0.12	0.11 ± 0.19	0.22 ± 0.22	0.14 ± 0.17
765	0.89	439.0 ± 16.5	0.06 ± 0.14	0.06 ± 0.12	0.24 ± 0.21	0.06 ± 0.06	-0.01 ± 0.16
810	0.82	451.7 ± 16.2	0.04 ± 0.15	0.10 ± 0.12	0.19 ± 0.21	0.08 ± 0.08	0.05 ± 0.16
855	0.84	469.2 ± 16.8	0.04 ± 0.15	0.15 ± 0.11	-0.13 ± 0.20	0.11 ± 0.11	0.08 ± 0.17
900	0.92	426.4 ± 21.9	0.13 ± 0.13	0.05 ± 0.11	0.09 ± 0.19	0.08 ± 0.08	0.06 ± 0.17

Table A.65 – Same as in Table A.1, but for KIC 10068307.

KIC 10079226

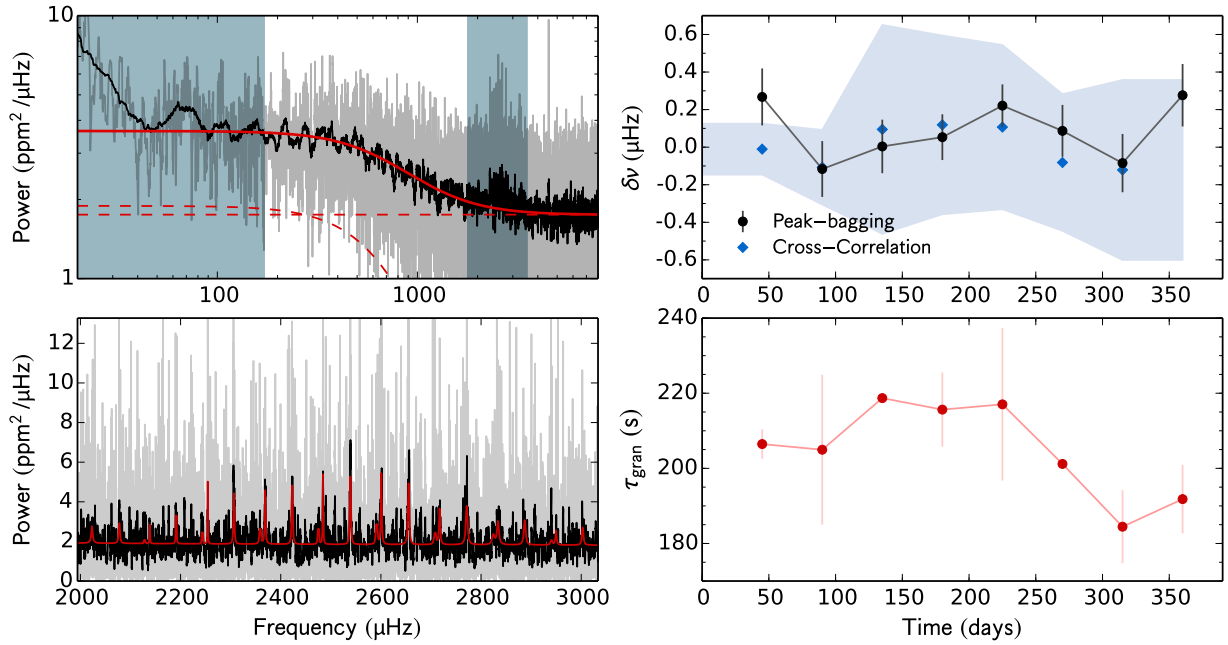

Fig. A.66 – Same as in Fig. A.1, but for KIC 10079226.

time (days)	d_c %	τ_{gran} (s)	Peak-bagging $\delta\nu_{l=0}$ (μHz)	$\delta\nu_{l=1}$ (μHz)	$\delta\nu_{l=2}$ (μHz)	$\delta\nu$ (μHz)	Cross-correlation $\delta\nu$ (μHz)
45	0.96	206.5 ± 3.9	0.61 ± 0.20	-0.20 ± 0.23	0.12 ± 0.52	0.27 ± 0.27	-0.01 ± 0.14
90	0.78	205.0 ± 19.9	0.08 ± 0.19	-0.40 ± 0.24	0.39 ± 0.51	-0.12 ± -0.12	-0.11 ± 0.20
135	0.73	218.7 ± nan	0.05 ± 0.19	-0.05 ± 0.21	-0.09 ± 0.42	0.00 ± 0.00	0.09 ± 0.56
180	0.92	215.6 ± 9.9	0.02 ± 0.16	0.11 ± 0.19	-0.26 ± 0.44	0.05 ± 0.05	0.12 ± 0.48
225	0.98	217.0 ± 20.3	0.27 ± 0.15	0.15 ± 0.17	-0.66 ± 0.38	0.22 ± 0.22	0.11 ± 0.44
270	0.97	201.2 ± 0.8	0.14 ± 0.19	0.03 ± 0.20	-0.52 ± 0.39	0.09 ± 0.09	-0.08 ± 0.36
315	0.97	184.5 ± 9.7	-0.21 ± 0.24	0.01 ± 0.20	0.47 ± 0.39	-0.08 ± -0.08	-0.12 ± 0.48
360	0.60	191.8 ± 9.1	0.01 ± 0.30	0.40 ± 0.20	0.59 ± 0.27	0.28 ± 0.28	–

Table A.66 – Same as in Table A.1, but for KIC 10079226.

KIC 10162436

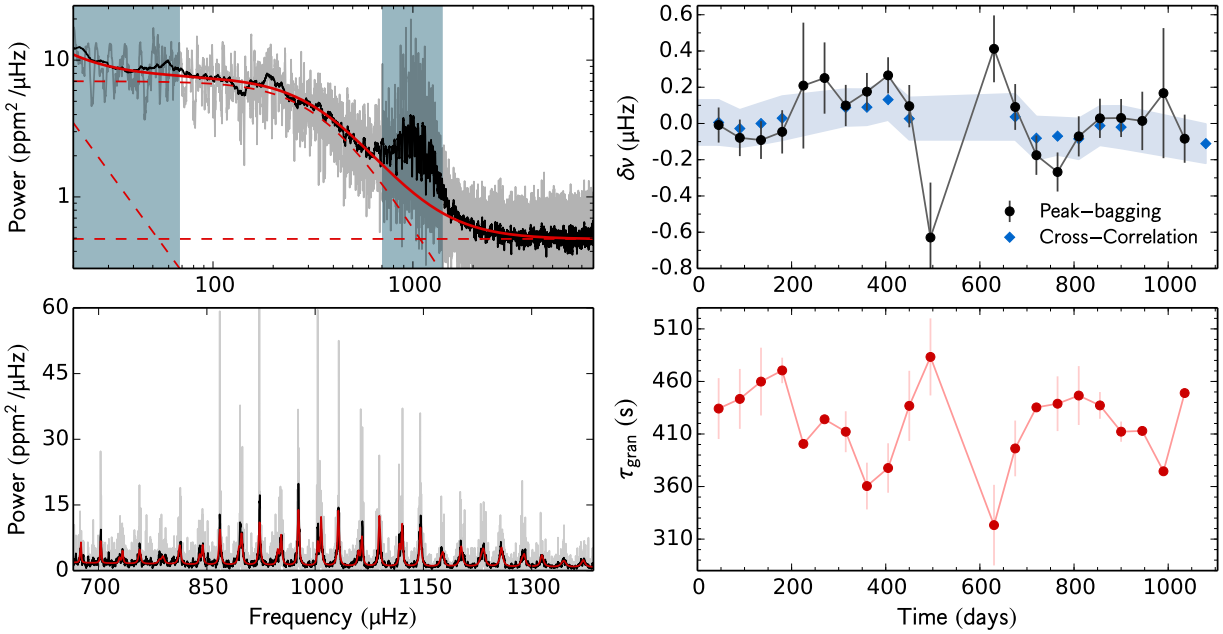

Fig. A.67 – Same as in Fig. A.1, but for KIC 10162436.

time (days)	d_c %	τ_{gran} (s)	Peak-bagging $\delta\nu_{l=0}$ (μHz)	$\delta\nu_{l=1}$ (μHz)	$\delta\nu_{l=2}$ (μHz)	$\delta\nu$ (μHz)	Cross-correlation $\delta\nu$ (μHz)
45	0.98	434.2 ± 19.1	0.02 ± 0.15	-0.03 ± 0.13	-0.71 ± 0.21	-0.01 ± -0.01	0.01 ± 0.12
90	0.97	443.4 ± 18.7	-0.14 ± 0.16	-0.04 ± 0.13	-1.04 ± 0.22	-0.08 ± -0.08	-0.03 ± 0.10
135	0.96	459.9 ± 19.2	0.23 ± 0.17	-0.28 ± 0.13	-0.07 ± 0.25	-0.09 ± -0.09	-0.00 ± 0.11
180	0.55	470.5 ± 26.0	0.33 ± 0.17	-0.40 ± 0.17	0.49 ± 0.29	-0.05 ± -0.05	0.03 ± 0.12
225	0.06	400.6 ± 5.4	0.39 ± 0.47	-0.01 ± 0.51	-0.16 ± 0.50	0.21 ± 0.21	–
270	0.26	424.0 ± 34.2	0.24 ± 0.33	0.25 ± 0.25	0.14 ± 0.35	0.25 ± 0.25	–
315	0.71	412.2 ± 18.5	-0.14 ± 0.19	0.24 ± 0.14	0.11 ± 0.21	0.10 ± 0.10	0.09 ± 0.10
360	0.89	360.5 ± 14.5	-0.10 ± 0.18	0.32 ± 0.13	0.31 ± 0.23	0.18 ± 0.18	0.09 ± 0.10
405	0.93	377.6 ± 15.5	0.06 ± 0.16	0.39 ± 0.13	0.14 ± 0.23	0.27 ± 0.27	0.13 ± 0.11
450	0.63	436.8 ± 22.0	-0.09 ± 0.19	0.22 ± 0.15	-0.03 ± 0.23	0.10 ± 0.10	0.03 ± 0.12
495	0.14	483.3 ± 26.8	-0.75 ± 0.55	-0.58 ± 0.36	-0.30 ± 0.42	-0.63 ± -0.63	–
630	0.19	323.3 ± 31.7	0.38 ± 0.26	0.44 ± 0.26	1.04 ± 0.41	0.41 ± 0.41	–
675	0.62	396.3 ± 21.1	0.15 ± 0.17	0.03 ± 0.18	0.37 ± 0.32	0.09 ± 0.09	0.04 ± 0.13
720	0.90	435.3 ± 18.3	0.03 ± 0.16	-0.36 ± 0.15	-0.02 ± 0.26	-0.18 ± -0.18	-0.08 ± 0.12
765	0.95	438.8 ± 19.3	-0.13 ± 0.17	-0.37 ± 0.14	-0.19 ± 0.25	-0.27 ± -0.27	-0.07 ± 0.10
810	0.89	446.6 ± 20.4	-0.04 ± 0.16	-0.09 ± 0.15	-0.52 ± 0.25	-0.07 ± -0.07	-0.08 ± 0.11
855	0.89	437.2 ± 17.6	0.06 ± 0.16	0.00 ± 0.15	-0.37 ± 0.30	0.03 ± 0.03	-0.01 ± 0.11
900	0.78	412.2 ± 17.9	0.07 ± 0.16	0.00 ± 0.14	-0.42 ± 0.26	0.03 ± 0.03	-0.02 ± 0.12
945	0.31	412.9 ± 28.1	-0.08 ± 0.25	0.08 ± 0.21	-0.29 ± 0.31	0.01 ± 0.01	–
990	0.06	374.5 ± 38.6	0.17 ± 0.50	0.17 ± 0.51	0.37 ± 0.64	0.17 ± 0.17	–
1035	0.44	448.9 ± 27.1	-0.13 ± 0.18	-0.03 ± 0.19	-0.01 ± 0.23	-0.08 ± -0.08	–
1080	–	–	–	–	–	–	-0.11 ± 0.11

Table A.67 – Same as in Table A.1, but for KIC 10162436.

KIC 10454113

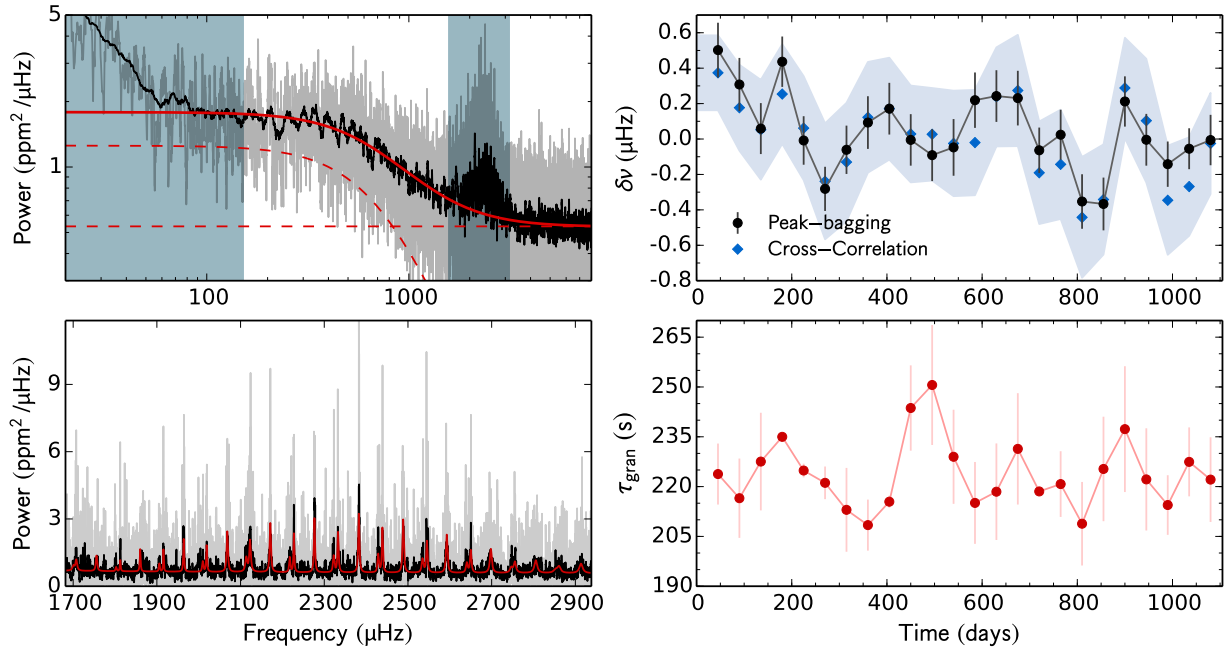

Fig. A.68 – Same as in Fig. A.1, but for KIC 10454113.

time (days)	d_c %	τ_{gran} (s)	Peak-bagging $\delta\nu_{l=0}$ (μHz)	$\delta\nu_{l=1}$ (μHz)	$\delta\nu_{l=2}$ (μHz)	$\delta\nu$ (μHz)	Cross-correlation $\delta\nu$ (μHz)
45	0.98	223.8 ± 9.2	0.53 ± 0.22	0.48 ± 0.21	0.21 ± 0.33	0.50 ± 0.50	0.37 ± 0.21
90	0.97	216.5 ± 12.0	0.49 ± 0.22	0.16 ± 0.20	0.24 ± 0.30	0.31 ± 0.31	0.18 ± 0.24
135	0.96	227.5 ± 14.7	-0.16 ± 0.20	0.31 ± 0.21	0.10 ± 0.34	0.06 ± 0.06	0.05 ± 0.28
180	0.97	235.0 ± 0.4	0.58 ± 0.20	0.28 ± 0.21	0.69 ± 0.33	0.44 ± 0.44	0.25 ± 0.28
225	0.96	224.8 ± 2.1	0.10 ± 0.19	-0.13 ± 0.20	0.42 ± 0.27	-0.01 ± -0.01	0.06 ± 0.29
270	0.80	221.1 ± 4.9	-0.17 ± 0.16	-0.44 ± 0.19	0.26 ± 0.29	-0.28 ± -0.28	-0.24 ± 0.33
315	0.78	213.0 ± 12.6	0.02 ± 0.19	-0.16 ± 0.20	-0.05 ± 0.34	-0.06 ± -0.06	-0.13 ± 0.33
360	0.89	208.4 ± 7.7	-0.15 ± 0.21	0.35 ± 0.21	-0.24 ± 0.33	0.09 ± 0.09	0.12 ± 0.31
405	0.93	215.5 ± 1.8	0.17 ± 0.20	0.17 ± 0.22	-0.33 ± 0.30	0.17 ± 0.17	0.17 ± 0.29
450	0.97	243.7 ± 12.8	0.14 ± 0.20	-0.17 ± 0.21	-0.12 ± 0.30	-0.01 ± -0.01	0.03 ± 0.27
495	0.97	250.6 ± 18.1	-0.05 ± 0.22	-0.12 ± 0.20	0.30 ± 0.33	-0.09 ± -0.09	0.03 ± 0.26
540	0.98	229.0 ± 14.2	-0.09 ± 0.25	-0.02 ± 0.21	-0.07 ± 0.33	-0.05 ± -0.05	-0.02 ± 0.30
585	0.94	215.1 ± 12.3	0.43 ± 0.23	0.03 ± 0.22	0.09 ± 0.33	0.22 ± 0.22	-0.02 ± 0.30
630	0.92	218.5 ± 14.5	0.42 ± 0.21	0.07 ± 0.20	0.54 ± 0.34	0.24 ± 0.24	0.24 ± 0.28
675	0.90	231.4 ± 16.8	0.38 ± 0.22	0.09 ± 0.21	-0.38 ± 0.32	0.23 ± 0.23	0.27 ± 0.31
720	0.90	218.5 ± 0.5	0.20 ± 0.18	-0.37 ± 0.19	-0.38 ± 0.27	-0.06 ± -0.06	-0.19 ± 0.29
765	0.95	220.8 ± 9.9	0.20 ± 0.19	-0.18 ± 0.21	0.18 ± 0.32	0.02 ± 0.02	-0.14 ± 0.31
810	0.89	208.8 ± 12.6	-0.19 ± 0.20	-0.58 ± 0.24	0.08 ± 0.35	-0.35 ± -0.35	-0.44 ± 0.34
855	0.89	225.3 ± 15.7	-0.41 ± 0.21	-0.33 ± 0.21	0.02 ± 0.34	-0.37 ± -0.37	-0.34 ± 0.31
900	0.95	237.3 ± 18.9	-0.20 ± 0.21	0.57 ± 0.19	-0.23 ± 0.33	0.21 ± 0.21	0.29 ± 0.28
945	0.90	222.2 ± 15.4	-0.37 ± 0.21	0.33 ± 0.20	-0.30 ± 0.29	-0.00 ± -0.00	0.10 ± 0.35
990	0.89	214.4 ± 9.0	0.07 ± 0.18	-0.34 ± 0.18	-0.15 ± 0.28	-0.14 ± -0.14	-0.35 ± 0.31
1035	0.85	227.4 ± 10.4	0.06 ± 0.16	-0.18 ± 0.17	-0.01 ± 0.19	-0.05 ± -0.05	-0.27 ± 0.28
1080	0.85	222.1 ± 12.8	-0.30 ± 0.21	0.24 ± 0.19	-0.32 ± 0.34	-0.01 ± -0.01	-0.03 ± 0.29

Table A.68 – Same as in Table A.1, but for KIC 10454113.

KIC 10516096

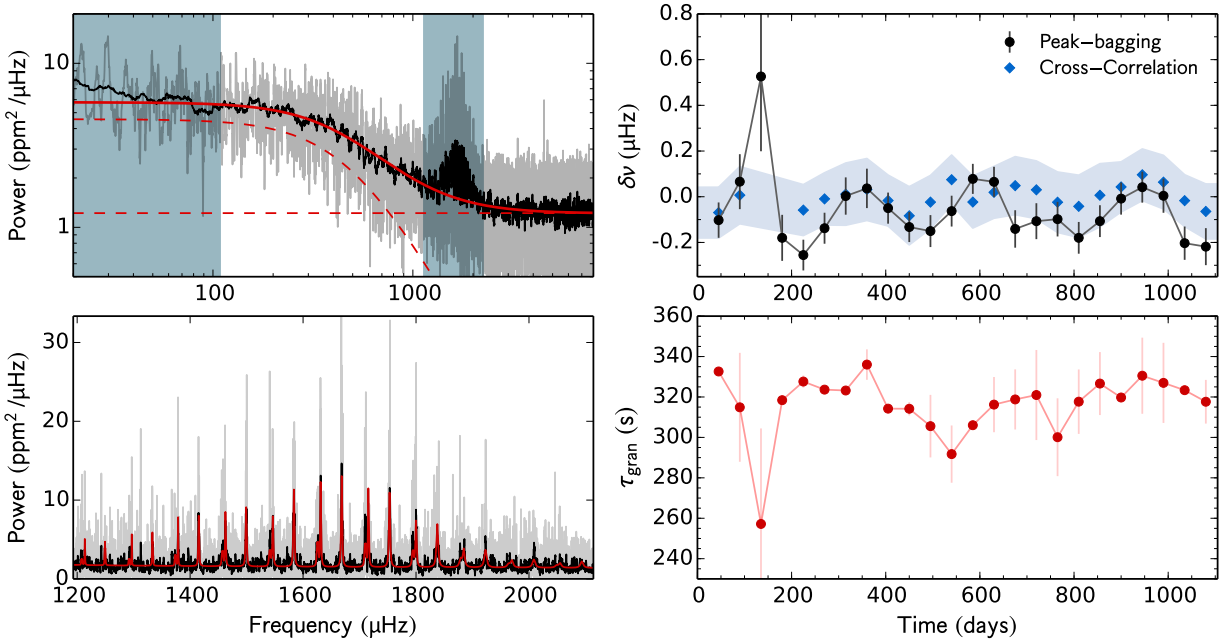

Fig. A.69 – Same as in Fig. A.1, but for KIC 10516096.

time (days)	d_c %	τ_{gran} (s)	Peak-bagging $\delta\nu_{l=0}$ (μHz)	$\delta\nu_{l=1}$ (μHz)	$\delta\nu_{l=2}$ (μHz)	$\delta\nu$ (μHz)	Cross-correlation $\delta\nu$ (μHz)
45	0.98	332.6 ± 2.0	-0.11 ± 0.12	-0.09 ± 0.13	-0.12 ± 0.18	-0.10 ± -0.10	-0.07 ± 0.11
90	0.54	314.9 ± 26.9	0.02 ± 0.18	0.12 ± 0.20	-0.32 ± 0.30	0.07 ± 0.07	0.01 ± 0.13
135	0.05	257.2 ± 47.3	0.30 ± 0.54	0.76 ± 0.54	0.22 ± 0.65	0.53 ± 0.53	–
180	0.42	318.4 ± 0.3	-0.08 ± 0.15	-0.32 ± 0.17	0.14 ± 0.25	-0.18 ± -0.18	–
225	0.90	327.6 ± 3.0	-0.12 ± 0.10	-0.40 ± 0.11	-0.09 ± 0.15	-0.26 ± -0.26	-0.06 ± 0.11
270	0.80	323.6 ± 0.6	0.04 ± 0.11	-0.30 ± 0.10	-0.32 ± 0.15	-0.14 ± -0.14	-0.01 ± 0.11
315	0.78	323.2 ± 0.6	0.26 ± 0.12	-0.32 ± 0.14	-0.13 ± 0.18	0.00 ± 0.00	0.01 ± 0.14
360	0.89	336.0 ± 7.5	0.24 ± 0.14	-0.15 ± 0.13	0.18 ± 0.20	0.04 ± 0.04	0.03 ± 0.14
405	0.93	314.2 ± 0.4	0.11 ± 0.11	-0.21 ± 0.11	0.20 ± 0.16	-0.05 ± -0.05	-0.02 ± 0.11
450	0.64	314.2 ± 3.3	0.06 ± 0.10	-0.35 ± 0.11	0.23 ± 0.15	-0.13 ± -0.13	-0.08 ± 0.13
495	0.63	305.6 ± 15.5	0.02 ± 0.10	-0.35 ± 0.11	-0.15 ± 0.17	-0.15 ± -0.15	-0.02 ± 0.12
540	0.98	291.7 ± 14.2	0.03 ± 0.10	-0.17 ± 0.11	-0.08 ± 0.16	-0.06 ± -0.06	0.07 ± 0.11
585	0.94	306.0 ± 0.2	0.19 ± 0.09	-0.06 ± 0.11	-0.08 ± 0.17	0.08 ± 0.08	-0.02 ± 0.11
630	0.92	316.2 ± 13.7	0.19 ± 0.10	-0.07 ± 0.10	-0.30 ± 0.15	0.07 ± 0.07	0.02 ± 0.11
675	0.90	318.8 ± 14.9	-0.22 ± 0.12	-0.05 ± 0.13	0.37 ± 0.23	-0.14 ± -0.14	0.05 ± 0.13
720	0.90	321.0 ± 22.3	-0.00 ± 0.12	-0.22 ± 0.12	0.24 ± 0.20	-0.11 ± -0.11	0.03 ± 0.13
765	0.95	300.1 ± 19.3	-0.09 ± 0.11	-0.11 ± 0.12	0.01 ± 0.19	-0.10 ± -0.10	-0.02 ± 0.13
810	0.90	317.7 ± 15.9	-0.30 ± 0.10	-0.02 ± 0.11	-0.28 ± 0.17	-0.18 ± -0.18	-0.04 ± 0.14
855	0.89	326.6 ± 15.6	-0.26 ± 0.10	0.10 ± 0.12	0.07 ± 0.18	-0.11 ± -0.11	0.01 ± 0.14
900	0.95	319.7 ± 2.4	-0.02 ± 0.10	0.00 ± 0.12	0.02 ± 0.19	-0.01 ± -0.01	0.04 ± 0.11
945	0.90	330.5 ± 18.8	0.06 ± 0.09	0.02 ± 0.12	-0.15 ± 0.18	0.04 ± 0.04	0.10 ± 0.11
990	0.89	327.0 ± 19.8	0.10 ± 0.12	-0.07 ± 0.11	0.49 ± 0.19	0.00 ± 0.00	0.06 ± 0.12
1035	0.85	323.4 ± 2.2	-0.31 ± 0.12	-0.13 ± 0.10	0.10 ± 0.19	-0.20 ± -0.20	-0.02 ± 0.11
1080	0.85	317.6 ± 10.8	-0.28 ± 0.12	-0.16 ± 0.13	-0.58 ± 0.20	-0.22 ± -0.22	-0.06 ± 0.12

Table A.69 – Same as in Table A.1, but for KIC 10516096.

KIC 10586004

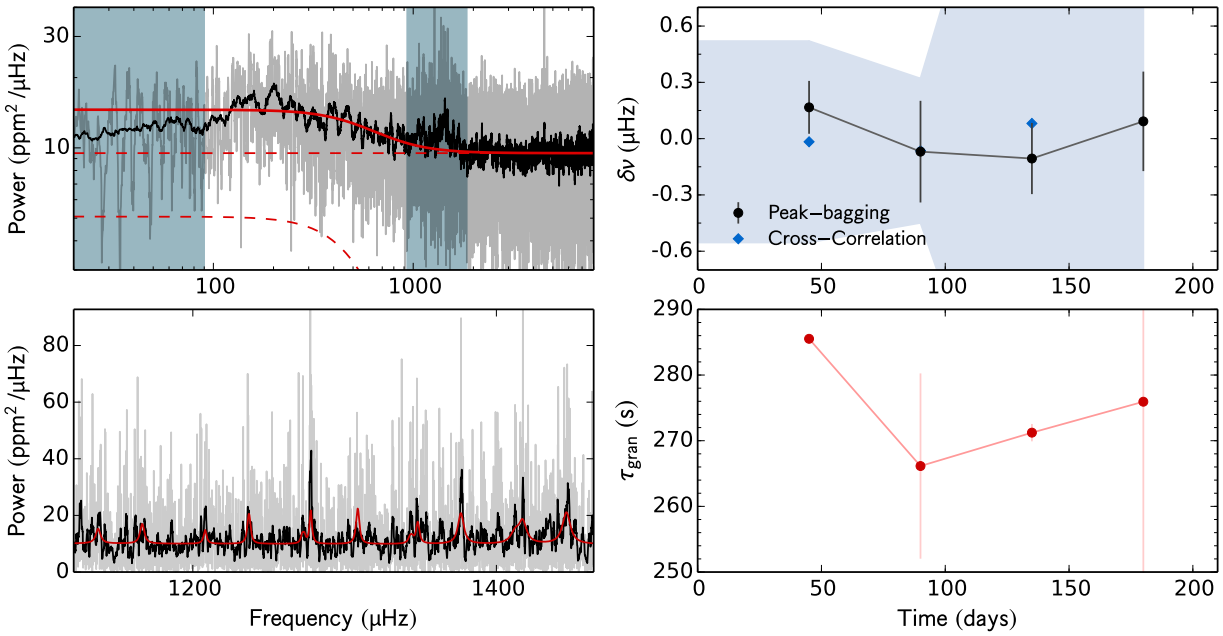

Fig. A.70 – Same as in Fig. A.1, but for KIC 10586004.

time (days)	d_c %	τ_{gran} (s)	Peak-bagging $\delta\nu_{l=0}$ (μHz)	$\delta\nu_{l=1}$ (μHz)	$\delta\nu_{l=2}$ (μHz)	$\delta\nu$ (μHz)	Cross-correlation $\delta\nu$ (μHz)
45	0.98	285.5 ± 0.0	0.13 ± 0.16	0.25 ± 0.27	-0.07 ± 0.77	0.17 ± 0.17	-0.02 ± 0.54
90	0.97	266.1 ± 14.1	0.02 ± 0.33	-0.25 ± 0.48	0.10 ± 0.90	-0.07 ± -0.07	-0.06 ± 0.38
135	0.96	271.2 ± 1.3	-0.10 ± 0.25	-0.11 ± 0.29	-0.13 ± 0.53	-0.11 ± -0.11	0.08 ± 2.22
180	0.48	275.9 ± 29.9	-0.10 ± 0.33	0.46 ± 0.45	-0.07 ± 0.83	0.09 ± 0.09	–

Table A.70 – Same as in Table A.1, but for KIC 10586004.

KIC 10644253

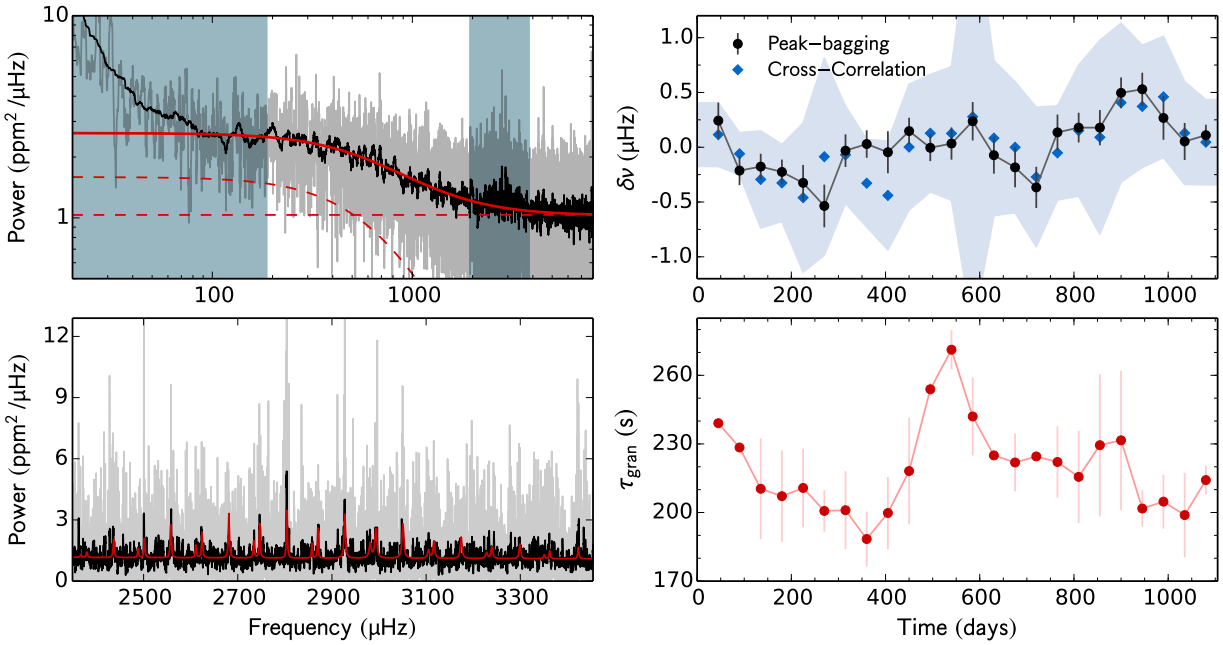

Fig. A.71 – Same as in Fig. A.1, but for KIC 10644253.

time (days)	d_c %	τ_{gran} (s)	Peak-bagging $\delta\nu_{l=0}$ (μHz)	$\delta\nu_{l=1}$ (μHz)	$\delta\nu_{l=2}$ (μHz)	$\delta\nu$ (μHz)	Cross-correlation $\delta\nu$ (μHz)
45	0.98	239.1 ± 0.2	0.36 ± 0.25	0.15 ± 0.22	-0.08 ± 0.34	0.24 ± 0.24	0.11 ± 0.29
90	0.97	228.4 ± 0.5	-0.31 ± 0.18	-0.10 ± 0.20	-0.25 ± 0.36	-0.21 ± -0.21	-0.06 ± 0.19
135	0.96	210.4 ± 22.0	-0.50 ± 0.19	0.00 ± 0.15	0.24 ± 0.28	-0.18 ± -0.18	-0.29 ± 0.44
180	0.97	207.1 ± 20.1	-0.58 ± 0.20	-0.06 ± 0.14	0.26 ± 0.26	-0.23 ± -0.23	-0.33 ± 0.35
225	0.96	210.7 ± 17.2	-0.23 ± 0.30	-0.36 ± 0.20	0.01 ± 0.51	-0.33 ± -0.33	-0.46 ± 0.68
270	0.80	200.7 ± 9.1	0.39 ± 0.32	-1.08 ± 0.25	0.47 ± 0.37	-0.54 ± -0.54	-0.09 ± 0.90
315	0.78	201.0 ± 17.0	-0.44 ± 0.25	0.18 ± 0.18	0.18 ± 0.27	-0.03 ± -0.03	-0.07 ± 0.44
360	0.89	188.4 ± 12.0	-0.49 ± 0.25	0.21 ± 0.15	-0.13 ± 0.37	0.03 ± 0.03	-0.33 ± 0.40
405	0.93	199.8 ± 15.8	0.00 ± 0.35	-0.07 ± 0.23	-0.73 ± 0.45	-0.05 ± -0.05	-0.44 ± 0.50
450	0.97	218.1 ± 23.3	-0.18 ± 0.20	0.33 ± 0.15	-0.98 ± 0.20	0.15 ± 0.15	0.00 ± 0.57
495	0.97	253.9 ± 2.8	-0.23 ± 0.17	0.24 ± 0.17	-0.16 ± 0.37	-0.00 ± -0.00	0.13 ± 0.53
540	0.98	271.2 ± 8.5	-0.26 ± 0.21	0.33 ± 0.21	0.12 ± 0.31	0.03 ± 0.03	0.13 ± 0.61
585	0.94	242.0 ± 17.1	-0.16 ± 0.29	0.47 ± 0.22	0.15 ± 0.33	0.24 ± 0.24	0.28 ± 1.93
630	0.92	225.0 ± 1.9	-0.26 ± 0.40	-0.03 ± 0.19	0.17 ± 0.31	-0.07 ± -0.07	0.08 ± 0.71
675	0.90	221.9 ± 12.7	0.03 ± 0.37	-0.25 ± 0.21	-0.41 ± 0.33	-0.18 ± -0.18	-0.00 ± 0.60
720	0.90	224.5 ± 0.9	-0.37 ± 0.34	-0.36 ± 0.22	-0.33 ± 0.46	-0.37 ± -0.37	-0.27 ± 0.64
765	0.95	222.1 ± 15.6	0.10 ± 0.33	0.15 ± 0.19	0.70 ± 0.31	0.14 ± 0.14	-0.05 ± 0.43
810	0.89	215.6 ± 20.2	0.08 ± 0.24	0.23 ± 0.17	0.43 ± 0.38	0.18 ± 0.18	0.15 ± 0.60
855	0.89	229.4 ± 31.1	0.33 ± 0.24	0.06 ± 0.21	0.32 ± 0.32	0.18 ± 0.18	0.09 ± 0.88
900	0.95	231.6 ± 30.5	0.55 ± 0.24	0.47 ± 0.17	0.27 ± 0.30	0.50 ± 0.50	0.41 ± 0.72
945	0.90	201.7 ± 7.9	0.62 ± 0.24	0.47 ± 0.19	0.23 ± 0.30	0.53 ± 0.53	0.37 ± 0.56
990	0.89	204.8 ± 11.8	0.24 ± 0.24	0.32 ± 0.35	0.22 ± 0.51	0.27 ± 0.27	0.46 ± 0.55
1035	0.85	198.9 ± 18.5	-0.03 ± 0.24	0.14 ± 0.24	0.11 ± 0.42	0.05 ± 0.05	0.13 ± 0.47
1080	0.85	214.2 ± 6.3	0.09 ± 0.12	0.14 ± 0.16	0.02 ± 0.28	0.11 ± 0.11	0.05 ± 0.39

Table A.71 – Same as in Table A.1, but for KIC 10644253.

KIC 10666592

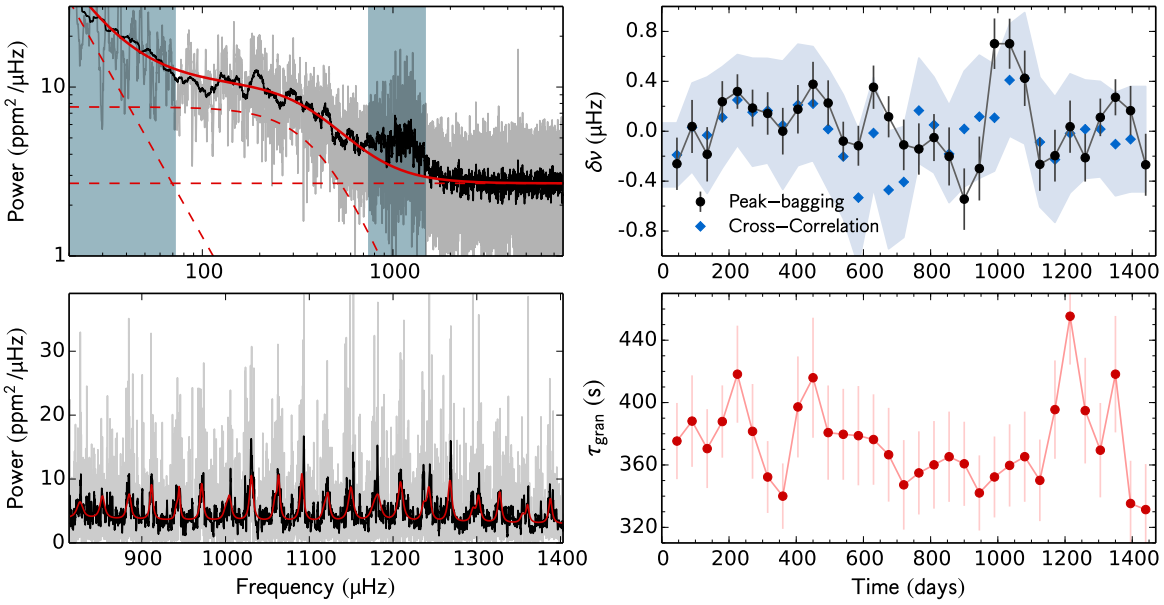

Fig. A.72 – Same as in Fig. A.1, but for KIC 10666592.

time (days)	d_c %	τ_{gran} (s)	Peak-bagging $\delta\nu_{l=0}$ (μHz)	$\delta\nu_{l=1}$ (μHz)	$\delta\nu_{l=2}$ (μHz)	$\delta\nu$ (μHz)	Cross-correlation $\delta\nu$ (μHz)
45	0.91	375.3 ± 24.4	-0.46 ± 0.33	-0.13 ± 0.27	-0.35 ± 0.50	-0.26 ± -0.26	-0.19 ± 0.26
90	0.91	388.1 ± 29.3	0.03 ± 0.37	0.04 ± 0.26	-0.20 ± 0.47	0.04 ± 0.04	0.03 ± 0.36
135	0.93	370.5 ± 25.3	0.47 ± 0.39	-0.48 ± 0.26	-0.18 ± 0.40	-0.19 ± -0.19	-0.03 ± 0.47
180	0.93	387.8 ± 23.2	0.62 ± 0.24	-0.09 ± 0.23	-0.17 ± 0.40	0.24 ± 0.24	0.11 ± 0.41
225	0.93	418.2 ± 31.1	0.57 ± 0.20	0.10 ± 0.19	-0.36 ± 0.42	0.32 ± 0.32	0.25 ± 0.36
270	0.91	381.5 ± 30.4	0.40 ± 0.23	0.04 ± 0.19	-1.23 ± 0.37	0.19 ± 0.19	0.15 ± 0.43
315	0.92	352.3 ± 23.0	-0.08 ± 0.26	0.30 ± 0.22	-0.63 ± 0.45	0.14 ± 0.14	0.16 ± 0.42
360	0.96	340.0 ± 21.0	-0.01 ± 0.28	0.01 ± 0.25	-0.61 ± 0.58	0.00 ± 0.00	0.05 ± 0.51
405	0.97	397.2 ± 32.4	0.55 ± 0.25	-0.43 ± 0.31	-0.02 ± 0.68	0.18 ± 0.18	0.21 ± 0.49
450	0.96	415.9 ± 38.5	0.64 ± 0.25	0.08 ± 0.26	0.29 ± 0.57	0.38 ± 0.38	0.22 ± 0.46
495	0.97	380.7 ± 30.2	0.13 ± 0.29	0.29 ± 0.23	-0.78 ± 0.62	0.23 ± 0.23	0.02 ± 0.49
540	0.97	379.7 ± 29.2	-0.12 ± 0.22	-0.03 ± 0.23	-0.22 ± 0.59	-0.08 ± -0.08	-0.20 ± 0.50
585	0.80	378.8 ± 31.8	-0.06 ± 0.21	-0.19 ± 0.24	-0.49 ± 0.42	-0.12 ± -0.12	-0.53 ± 0.55
630	0.78	376.3 ± 29.0	0.75 ± 0.27	0.07 ± 0.23	0.60 ± 0.44	0.35 ± 0.35	-0.01 ± 0.45
675	0.90	366.6 ± 30.1	0.27 ± 0.26	0.01 ± 0.21	-0.08 ± 0.47	0.12 ± 0.12	-0.47 ± 0.47
720	0.91	347.2 ± 28.7	-0.14 ± 0.29	-0.08 ± 0.29	0.09 ± 0.54	-0.11 ± -0.11	-0.41 ± 0.44
765	0.97	354.9 ± 26.7	-0.43 ± 0.32	0.05 ± 0.27	0.57 ± 0.53	-0.14 ± -0.14	0.17 ± 0.42
810	0.97	360.1 ± 28.1	-0.27 ± 0.33	0.06 ± 0.23	0.03 ± 0.48	-0.05 ± -0.05	0.05 ± 0.38
855	0.97	365.3 ± 28.9	-0.18 ± 0.45	-0.21 ± 0.27	-0.02 ± 0.47	-0.20 ± -0.20	-0.18 ± 0.39
900	0.97	360.7 ± 27.0	-0.17 ± 0.36	-0.86 ± 0.33	-0.32 ± 0.62	-0.54 ± -0.54	0.02 ± 0.46
945	0.94	342.0 ± 24.1	-0.15 ± 0.40	-0.41 ± 0.34	-0.14 ± 0.69	-0.30 ± -0.30	0.12 ± 0.49
990	0.91	352.3 ± 26.0	1.47 ± 0.32	0.19 ± 0.26	0.18 ± 0.50	0.70 ± 0.70	0.11 ± 0.43
1035	0.88	359.7 ± 26.4	1.26 ± 0.31	0.29 ± 0.26	1.19 ± 0.50	0.70 ± 0.70	0.41 ± 0.45
1080	0.92	365.3 ± 28.9	0.23 ± 0.36	0.55 ± 0.28	0.90 ± 0.49	0.42 ± 0.42	0.42 ± 0.53
1125	0.95	350.1 ± 26.2	-1.37 ± 0.34	0.42 ± 0.27	-0.19 ± 0.54	-0.27 ± -0.27	-0.09 ± 0.52
1170	0.90	395.5 ± 31.5	-1.64 ± 0.36	0.55 ± 0.26	0.20 ± 0.59	-0.20 ± -0.20	-0.23 ± 0.50
1215	0.89	455.4 ± 31.0	-0.41 ± 0.39	0.22 ± 0.25	0.26 ± 0.52	0.04 ± 0.04	-0.02 ± 0.48
1260	0.89	394.8 ± 33.9	-0.25 ± 0.32	-0.19 ± 0.24	0.45 ± 0.52	-0.21 ± -0.21	0.02 ± 0.39
1305	0.91	369.5 ± 30.3	0.26 ± 0.23	0.00 ± 0.20	0.17 ± 0.43	0.11 ± 0.11	0.02 ± 0.38
1350	0.85	418.2 ± 37.3	0.34 ± 0.21	0.21 ± 0.20	-0.27 ± 0.34	0.27 ± 0.27	-0.10 ± 0.41
1395	0.83	335.3 ± 27.4	-0.57 ± 0.38	0.43 ± 0.23	0.36 ± 0.33	0.16 ± 0.16	-0.06 ± 0.42
1440	0.75	331.4 ± 29.2	-0.84 ± 0.55	-0.13 ± 0.28	1.24 ± 0.45	-0.27 ± -0.27	–

Table A.72 – Same as in Table A.1, but for KIC 10666592.

KIC 10730618

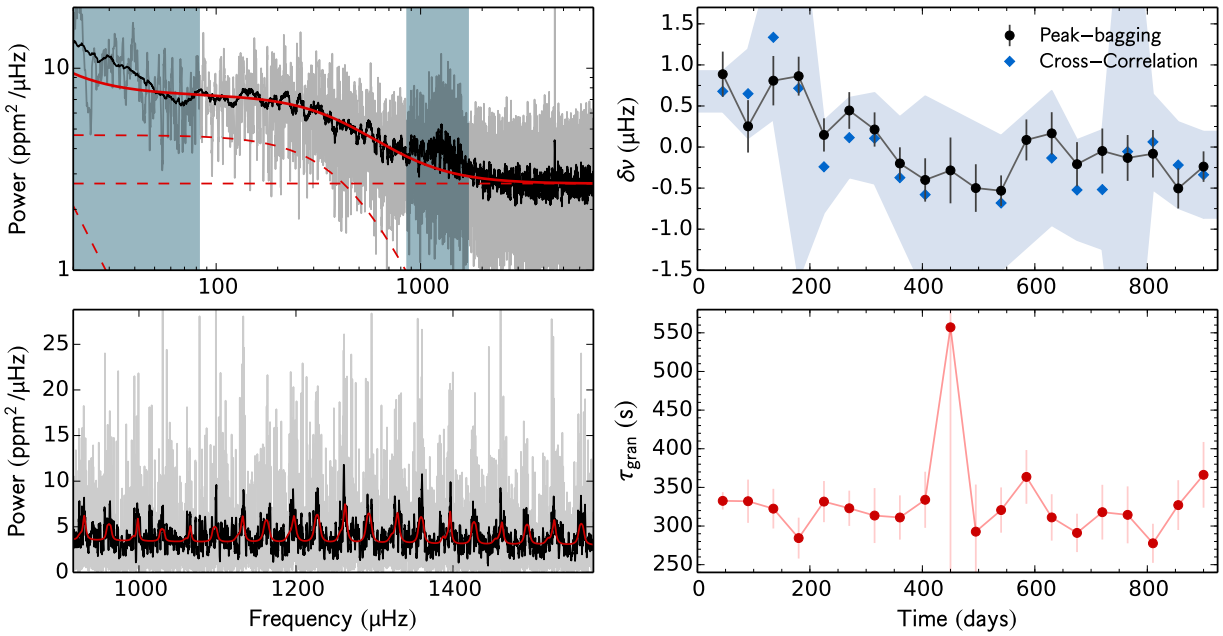

Fig. A.73 – Same as in Fig. A.1, but for KIC 10730618.

time (days)	d_c %	τ_{gran} (s)	Peak-bagging $\delta\nu_{l=0}$ (μHz)	$\delta\nu_{l=1}$ (μHz)	$\delta\nu_{l=2}$ (μHz)	$\delta\nu$ (μHz)	Cross-correlation $\delta\nu$ (μHz)
45	0.91	332.6 ± 11.3	1.09 ± 0.40	0.70 ± 0.38	0.56 ± 0.60	0.89 ± 0.89	0.68 ± 0.25
90	0.91	332.1 ± 28.0	0.83 ± 0.47	-0.23 ± 0.43	0.32 ± 0.54	0.25 ± 0.25	0.65 ± 0.54
135	0.93	322.5 ± 25.7	0.94 ± 0.45	0.70 ± 0.41	-0.00 ± 0.56	0.81 ± 0.81	1.34 ± 1.00
180	0.93	284.4 ± 26.5	1.23 ± 0.32	0.42 ± 0.35	-0.54 ± 0.50	0.86 ± 0.86	0.72 ± 2.32
225	0.93	331.6 ± 26.6	0.57 ± 0.30	-0.21 ± 0.27	-0.20 ± 0.45	0.15 ± 0.15	-0.24 ± 0.56
270	0.91	323.0 ± 22.8	0.39 ± 0.31	0.50 ± 0.32	0.37 ± 0.52	0.45 ± 0.45	0.11 ± 0.49
315	0.92	313.5 ± 35.6	0.23 ± 0.30	0.20 ± 0.29	0.53 ± 0.38	0.21 ± 0.21	0.11 ± 0.55
360	0.96	311.1 ± 28.6	-0.22 ± 0.30	-0.19 ± 0.26	-0.65 ± 0.46	-0.20 ± -0.20	-0.37 ± 0.74
405	0.63	334.0 ± 36.3	-0.66 ± 0.41	-0.22 ± 0.34	-0.84 ± 0.45	-0.40 ± -0.40	-0.58 ± 1.20
450	0.14	557.1 ± 569.8	-0.39 ± 0.52	-0.12 ± 0.63	0.60 ± 0.51	-0.28 ± -0.28	–
495	0.33	292.7 ± 61.0	-0.76 ± 0.41	-0.23 ± 0.41	-0.37 ± 0.46	-0.50 ± -0.50	–
540	0.49	320.7 ± 29.3	-0.72 ± 0.24	-0.26 ± 0.29	-0.55 ± 0.37	-0.53 ± -0.53	-0.68 ± 0.82
585	0.48	363.6 ± 34.8	-0.19 ± 0.32	0.49 ± 0.39	-0.09 ± 0.49	0.09 ± 0.09	–
630	0.79	311.1 ± 30.0	-0.19 ± 0.39	0.44 ± 0.34	-0.24 ± 0.40	0.17 ± 0.17	-0.13 ± 0.82
675	0.90	291.1 ± 24.8	0.15 ± 0.47	-0.38 ± 0.33	-0.76 ± 0.44	-0.21 ± -0.21	-0.52 ± 0.61
720	0.91	317.9 ± 35.4	0.19 ± 0.45	-0.18 ± 0.34	-0.42 ± 0.55	-0.05 ± -0.05	-0.52 ± 0.73
765	0.97	314.5 ± 36.8	0.03 ± 0.40	-0.29 ± 0.39	0.08 ± 0.64	-0.13 ± -0.13	-0.06 ± 3.78
810	0.97	277.7 ± 25.3	-0.09 ± 0.41	-0.07 ± 0.41	0.50 ± 0.53	-0.08 ± -0.08	0.06 ± 0.58
855	0.97	327.1 ± 32.2	-0.58 ± 0.31	-0.38 ± 0.39	0.55 ± 0.57	-0.50 ± -0.50	-0.22 ± 0.52
900	0.97	366.3 ± 42.5	-0.43 ± 0.29	-0.10 ± 0.24	-0.18 ± 0.43	-0.24 ± -0.24	-0.34 ± 0.52

Table A.73 – Same as in Table A.1, but for KIC 10730618.

KIC 10963065

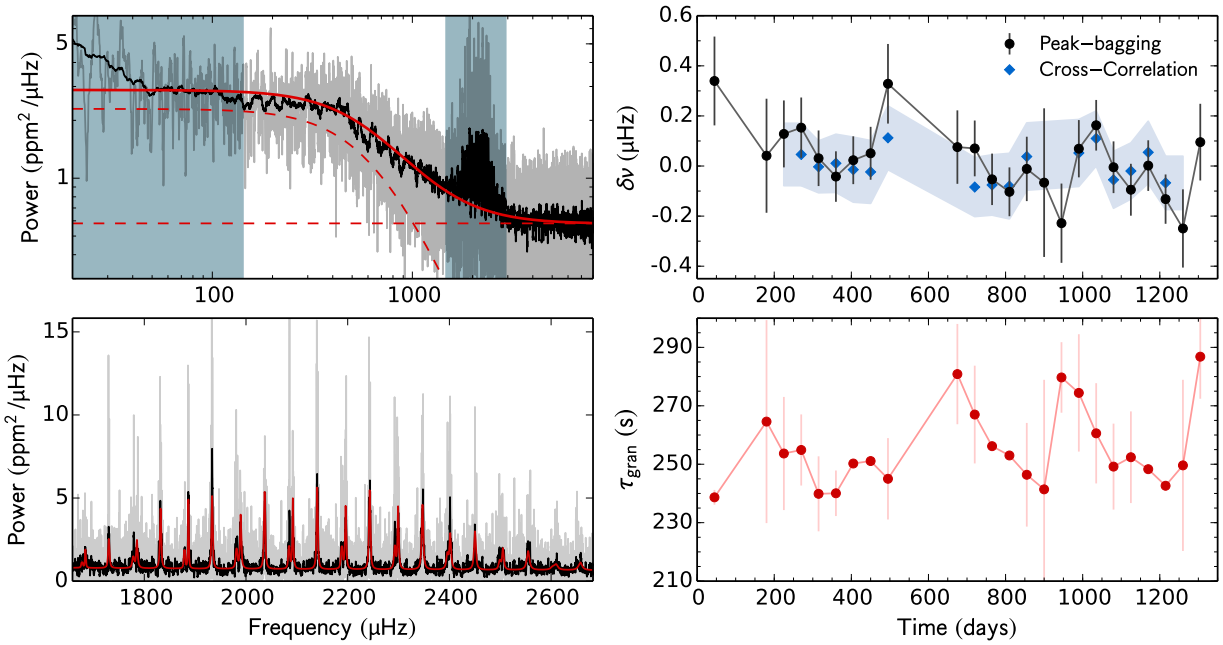

Fig. A.74 – Same as in Fig. A.1, but for KIC 10963065.

time (days)	d_c %	τ_{gran} (s)	Peak-bagging $\delta\nu_{l=0}$ (μHz)	$\delta\nu_{l=1}$ (μHz)	$\delta\nu_{l=2}$ (μHz)	$\delta\nu$ (μHz)	Cross-correlation $\delta\nu$ (μHz)
45	0.29	238.7 ± 2.5	0.60 ± 0.25	0.09 ± 0.25	-0.36 ± 0.40	0.34 ± 0.34	–
180	0.14	264.6 ± 34.7	-0.28 ± 0.34	0.30 ± 0.31	-0.08 ± 0.39	0.04 ± 0.04	–
225	0.63	253.7 ± 19.4	0.15 ± 0.19	0.11 ± 0.19	0.11 ± 0.30	0.13 ± 0.13	–
270	0.96	254.9 ± 12.2	0.32 ± 0.17	-0.01 ± 0.17	0.17 ± 0.28	0.15 ± 0.15	0.05 ± 0.12
315	0.97	239.9 ± 12.8	0.28 ± 0.16	-0.18 ± 0.15	0.15 ± 0.22	0.03 ± 0.03	-0.00 ± 0.10
360	0.97	240.1 ± 7.8	0.03 ± 0.14	-0.11 ± 0.14	0.22 ± 0.21	-0.04 ± -0.04	0.01 ± 0.12
405	0.97	250.2 ± 0.2	0.03 ± 0.13	0.01 ± 0.14	-0.06 ± 0.19	0.02 ± 0.02	-0.01 ± 0.13
450	0.90	251.1 ± 1.3	-0.00 ± 0.15	0.10 ± 0.15	0.11 ± 0.22	0.05 ± 0.05	-0.02 ± 0.13
495	0.41	245.0 ± 13.9	0.47 ± 0.22	0.18 ± 0.23	0.80 ± 0.34	0.33 ± 0.33	0.11 ± 0.13
675	0.48	280.9 ± 17.2	0.31 ± 0.20	-0.19 ± 0.22	-0.05 ± 0.31	0.08 ± 0.08	–
720	0.97	267.0 ± 16.7	0.28 ± 0.16	-0.15 ± 0.16	-0.08 ± 0.22	0.07 ± 0.07	-0.08 ± 0.12
765	0.97	256.2 ± 0.4	-0.03 ± 0.15	-0.08 ± 0.14	-0.22 ± 0.18	-0.05 ± -0.05	-0.08 ± 0.12
810	0.94	253.0 ± nan	-0.19 ± 0.15	-0.04 ± 0.13	-0.22 ± 0.18	-0.10 ± -0.10	-0.08 ± 0.13
855	0.60	246.4 ± 17.7	-0.12 ± 0.18	0.10 ± 0.19	-0.17 ± 0.30	-0.01 ± -0.01	0.04 ± 0.13
900	0.13	241.4 ± 37.5	-0.26 ± 0.41	0.14 ± 0.43	0.34 ± 0.47	-0.07 ± -0.07	–
945	0.42	279.7 ± 12.1	-0.29 ± 0.21	-0.15 ± 0.24	0.15 ± 0.25	-0.23 ± -0.23	–
990	0.91	274.4 ± 20.1	0.02 ± 0.15	0.13 ± 0.17	0.33 ± 0.22	0.07 ± 0.07	0.05 ± 0.13
1035	0.89	260.6 ± 17.2	0.13 ± 0.13	0.21 ± 0.16	-0.26 ± 0.24	0.16 ± 0.16	0.11 ± 0.11
1080	0.89	249.2 ± 14.7	-0.09 ± 0.14	0.10 ± 0.16	-0.83 ± 0.19	-0.00 ± -0.00	-0.06 ± 0.11
1125	0.96	252.4 ± 15.7	-0.19 ± 0.14	0.01 ± 0.15	-0.76 ± 0.21	-0.09 ± -0.09	-0.02 ± 0.11
1170	0.89	248.3 ± 0.0	-0.05 ± 0.15	0.05 ± 0.14	-0.06 ± 0.21	0.00 ± 0.00	0.05 ± 0.12
1215	0.69	242.6 ± 1.7	-0.06 ± 0.13	-0.22 ± 0.15	0.42 ± 0.21	-0.13 ± -0.13	-0.07 ± 0.11
1260	0.27	249.6 ± 29.3	-0.11 ± 0.20	-0.46 ± 0.25	0.13 ± 0.40	-0.25 ± -0.25	–
1305	0.24	286.8 ± 14.4	0.33 ± 0.21	-0.16 ± 0.22	-0.35 ± 0.32	0.10 ± 0.10	–

Table A.74 – Same as in Table A.1, but for KIC 10963065.

KIC 11081729

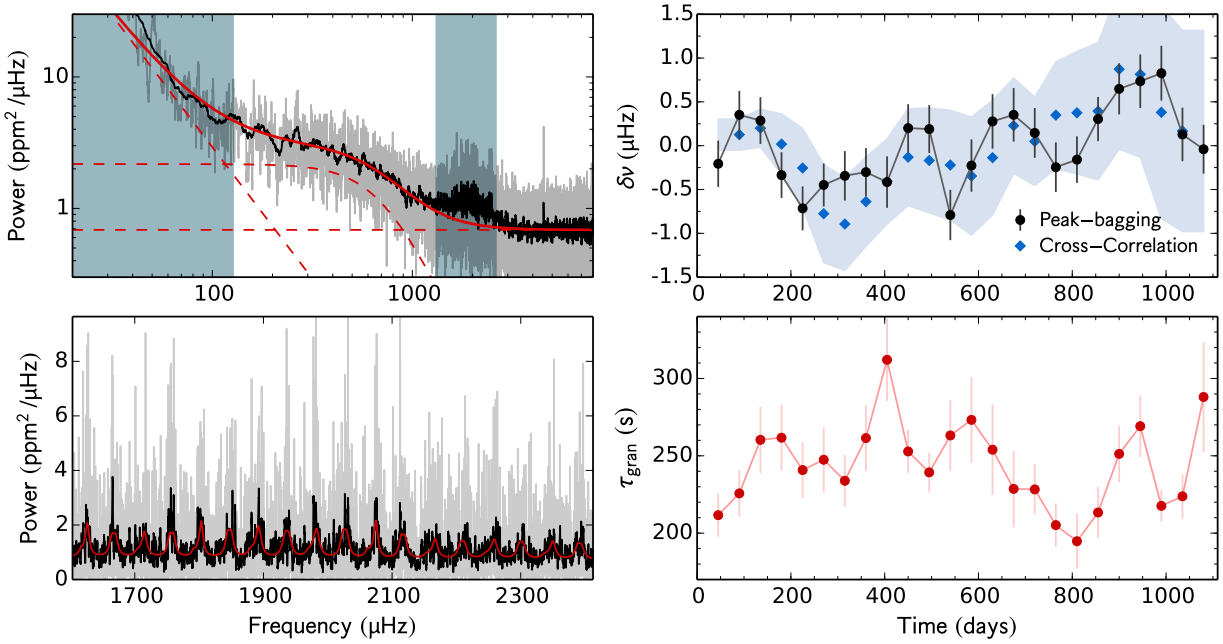

Fig. A.75 – Same as in Fig. A.1, but for KIC 11081729. Due to the extremely large error bars, the results from the cross-correlation method, that are shown here, were obtained from 180-d sub-series.

time (days)	d_c %	τ_{gran} (s)	Peak-bagging $\delta\nu_{l=0}$ (μHz)	$\delta\nu_{l=1}$ (μHz)	$\delta\nu_{l=2}$ (μHz)	$\delta\nu$ (μHz)	Cross-correlation $\delta\nu$ (μHz)
45	0.98	211.6 ± 13.9	-0.66 ± 0.36	0.33 ± 0.39	-0.04 ± 0.55	-0.21 ± -0.21	–
90	0.97	225.7 ± 15.1	-0.05 ± 0.37	0.83 ± 0.40	-0.04 ± 0.62	0.35 ± 0.35	0.13 ± 0.18
135	0.96	260.3 ± 21.4	-0.04 ± 0.36	0.68 ± 0.40	-0.04 ± 0.62	0.29 ± 0.29	0.20 ± 0.22
180	0.97	261.7 ± 21.3	-0.63 ± 0.33	0.18 ± 0.43	0.08 ± 0.59	-0.34 ± -0.34	0.02 ± 0.34
225	0.96	240.8 ± 18.1	-1.12 ± 0.32	-0.08 ± 0.40	-0.45 ± 0.61	-0.71 ± -0.71	-0.25 ± 0.45
270	0.81	247.5 ± 20.8	-0.90 ± 0.34	0.05 ± 0.36	-0.62 ± 0.55	-0.45 ± -0.45	-0.78 ± 0.56
315	0.78	233.8 ± 16.6	-0.15 ± 0.41	-0.53 ± 0.39	-0.01 ± 0.56	-0.34 ± -0.34	-0.89 ± 0.53
360	0.89	261.5 ± 21.3	-0.10 ± 0.43	-0.43 ± 0.35	0.57 ± 0.57	-0.30 ± -0.30	-0.64 ± 0.51
405	0.93	312.1 ± 26.7	-0.53 ± 0.41	-0.30 ± 0.42	0.09 ± 0.59	-0.42 ± -0.42	-0.41 ± 0.48
450	0.97	252.8 ± 14.1	0.49 ± 0.36	-0.22 ± 0.43	-0.53 ± 0.59	0.20 ± 0.20	-0.13 ± 0.55
495	0.97	239.3 ± 12.8	0.30 ± 0.36	0.04 ± 0.42	-0.04 ± 0.63	0.19 ± 0.19	-0.17 ± 0.60
540	0.98	263.2 ± 22.9	-0.66 ± 0.38	-0.97 ± 0.44	0.15 ± 0.64	-0.79 ± -0.79	-0.22 ± 0.62
585	0.94	273.2 ± 27.7	-0.23 ± 0.41	-0.23 ± 0.43	0.15 ± 0.59	-0.23 ± -0.23	-0.35 ± 0.67
630	0.92	253.9 ± 29.2	0.07 ± 0.46	0.46 ± 0.42	0.05 ± 0.60	0.28 ± 0.28	-0.14 ± 0.65
675	0.90	228.6 ± 24.7	0.39 ± 0.46	0.32 ± 0.41	-0.02 ± 0.56	0.35 ± 0.35	0.23 ± 0.54
720	0.91	228.3 ± 16.5	0.17 ± 0.44	0.13 ± 0.38	-0.22 ± 0.58	0.15 ± 0.15	0.05 ± 0.50
765	0.95	205.2 ± 14.0	0.25 ± 0.41	-0.68 ± 0.39	0.11 ± 0.54	-0.25 ± -0.25	0.35 ± 0.61
810	0.90	194.8 ± 17.7	0.63 ± 0.34	-1.30 ± 0.42	0.51 ± 0.47	-0.16 ± -0.16	0.38 ± 0.70
855	0.89	213.3 ± 16.6	0.82 ± 0.30	-1.00 ± 0.47	0.06 ± 0.59	0.30 ± 0.30	0.39 ± 0.78
900	0.95	251.2 ± 18.3	0.98 ± 0.36	0.00 ± 0.50	0.18 ± 0.57	0.65 ± 0.65	0.87 ± 0.91
945	0.90	269.2 ± 19.9	0.82 ± 0.38	0.58 ± 0.52	0.17 ± 0.54	0.73 ± 0.73	0.81 ± 0.94
990	0.89	217.6 ± 10.1	0.47 ± 0.42	1.27 ± 0.47	-0.13 ± 0.62	0.83 ± 0.83	0.38 ± 1.21
1035	0.85	223.8 ± 14.5	-0.24 ± 0.42	0.53 ± 0.44	0.50 ± 0.61	0.13 ± 0.13	0.17 ± 1.15
1080	0.85	288.0 ± 35.6	-0.32 ± 0.37	0.31 ± 0.42	-0.07 ± 0.57	-0.04 ± -0.04	–

Table A.75 – Same as in Table A.1, but for KIC 11081729. Due to the extremely large error bars, the results from the cross-correlation method, that are shown here, were obtained from 180-d sub-series.

KIC 11253226

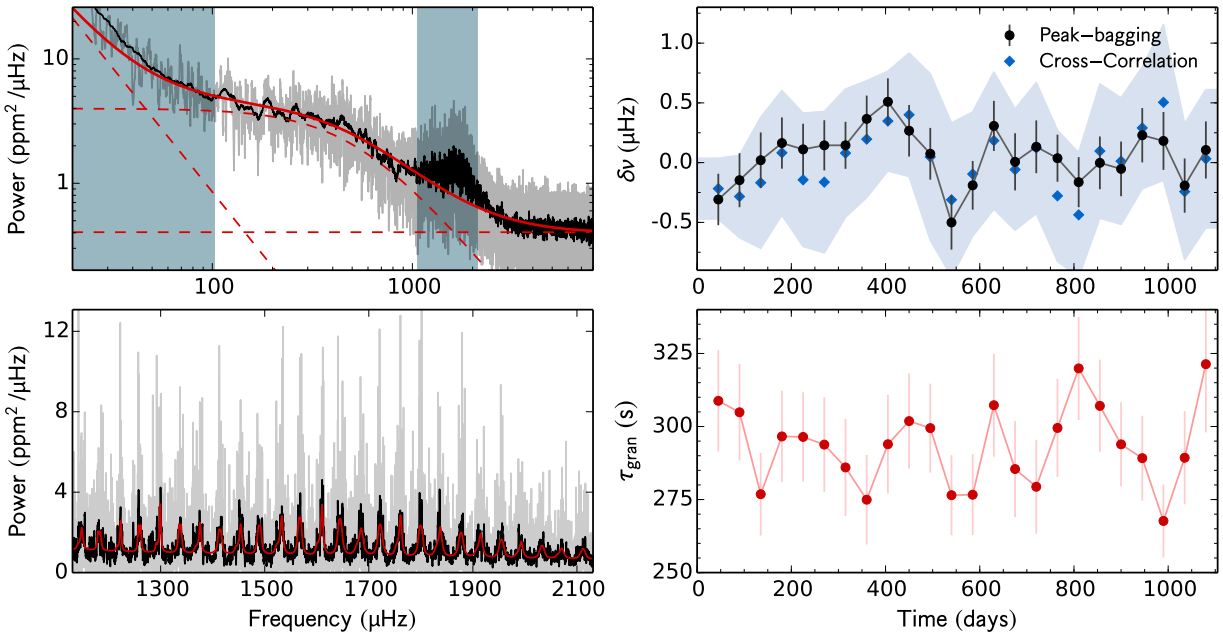

Fig. A.76 – Same as in Fig. A.1, but for KIC 11253226.

time (days)	d_c %	τ_{gran} (s)	Peak-bagging $\delta\nu_{l=0}$ (μHz)	$\delta\nu_{l=1}$ (μHz)	$\delta\nu_{l=2}$ (μHz)	$\delta\nu$ (μHz)	Cross-correlation $\delta\nu$ (μHz)
45	0.98	308.8 ± 17.4	0.06 ± 0.31	-0.65 ± 0.30	0.78 ± 0.40	-0.31 ± -0.31	-0.22 ± 0.25
90	0.97	304.9 ± 16.6	0.53 ± 0.32	-0.86 ± 0.32	-0.02 ± 0.49	-0.15 ± -0.15	-0.28 ± 0.34
135	0.96	276.8 ± 14.1	-0.12 ± 0.33	0.15 ± 0.32	-0.42 ± 0.54	0.02 ± 0.02	-0.17 ± 0.55
180	0.97	296.6 ± 15.6	-0.34 ± 0.30	0.68 ± 0.30	0.81 ± 0.37	0.16 ± 0.16	0.08 ± 0.52
225	0.96	296.4 ± 15.3	0.01 ± 0.29	0.23 ± 0.32	0.79 ± 0.39	0.11 ± 0.11	-0.14 ± 0.56
270	0.80	293.8 ± 16.2	0.43 ± 0.27	-0.27 ± 0.33	-0.04 ± 0.50	0.14 ± 0.14	-0.16 ± 0.59
315	0.78	286.0 ± 16.6	0.64 ± 0.26	-0.49 ± 0.30	0.15 ± 0.50	0.14 ± 0.14	0.08 ± 0.54
360	0.89	275.0 ± 15.3	0.51 ± 0.27	0.20 ± 0.29	0.16 ± 0.45	0.37 ± 0.37	0.20 ± 0.49
405	0.93	293.9 ± 16.9	0.36 ± 0.26	0.70 ± 0.30	0.36 ± 0.40	0.51 ± 0.51	0.35 ± 0.42
450	0.97	301.9 ± 16.3	0.02 ± 0.29	0.57 ± 0.32	0.47 ± 0.43	0.27 ± 0.27	0.40 ± 0.52
495	0.97	299.5 ± 15.2	0.07 ± 0.29	0.08 ± 0.33	0.19 ± 0.47	0.07 ± 0.07	0.05 ± 0.70
540	0.98	276.5 ± 13.7	-0.65 ± 0.32	-0.34 ± 0.33	0.54 ± 0.45	-0.50 ± -0.50	-0.31 ± 0.64
585	0.94	276.7 ± 13.8	-0.37 ± 0.28	0.00 ± 0.29	0.83 ± 0.46	-0.19 ± -0.19	-0.10 ± 0.52
630	0.92	307.3 ± 17.6	0.26 ± 0.29	0.36 ± 0.31	-0.51 ± 0.54	0.31 ± 0.31	0.18 ± 0.57
675	0.90	285.4 ± 16.5	-0.09 ± 0.37	0.08 ± 0.31	-0.45 ± 0.55	0.01 ± 0.01	-0.06 ± 0.51
720	0.90	279.4 ± 16.1	0.23 ± 0.31	0.04 ± 0.31	0.14 ± 0.46	0.13 ± 0.13	0.12 ± 0.55
765	0.95	299.5 ± 16.8	-0.00 ± 0.28	0.07 ± 0.27	-0.64 ± 0.44	0.04 ± 0.04	-0.28 ± 0.55
810	0.89	319.9 ± 17.6	-0.07 ± 0.30	-0.25 ± 0.29	-0.58 ± 0.52	-0.16 ± -0.16	-0.44 ± 0.52
855	0.89	307.1 ± 15.8	-0.05 ± 0.31	0.05 ± 0.31	-0.15 ± 0.49	-0.00 ± -0.00	0.10 ± 0.56
900	0.95	293.9 ± 14.4	-0.01 ± 0.32	-0.09 ± 0.33	-0.64 ± 0.47	-0.05 ± -0.05	0.01 ± 0.53
945	0.90	289.2 ± 14.5	0.30 ± 0.32	0.16 ± 0.33	-0.17 ± 0.52	0.23 ± 0.23	0.29 ± 0.51
990	0.89	267.7 ± 12.5	-0.32 ± 0.35	0.66 ± 0.34	0.00 ± 0.52	0.18 ± 0.18	0.50 ± 0.65
1035	0.85	289.3 ± 15.9	-0.31 ± 0.34	-0.10 ± 0.30	-0.20 ± 0.52	-0.19 ± -0.19	-0.24 ± 0.57
1080	0.85	321.3 ± 23.4	0.70 ± 0.34	-0.51 ± 0.34	-0.22 ± 0.52	0.11 ± 0.11	0.03 ± 0.58

Table A.76 – Same as in Table A.1, but for KIC 11253226.

KIC 11295426

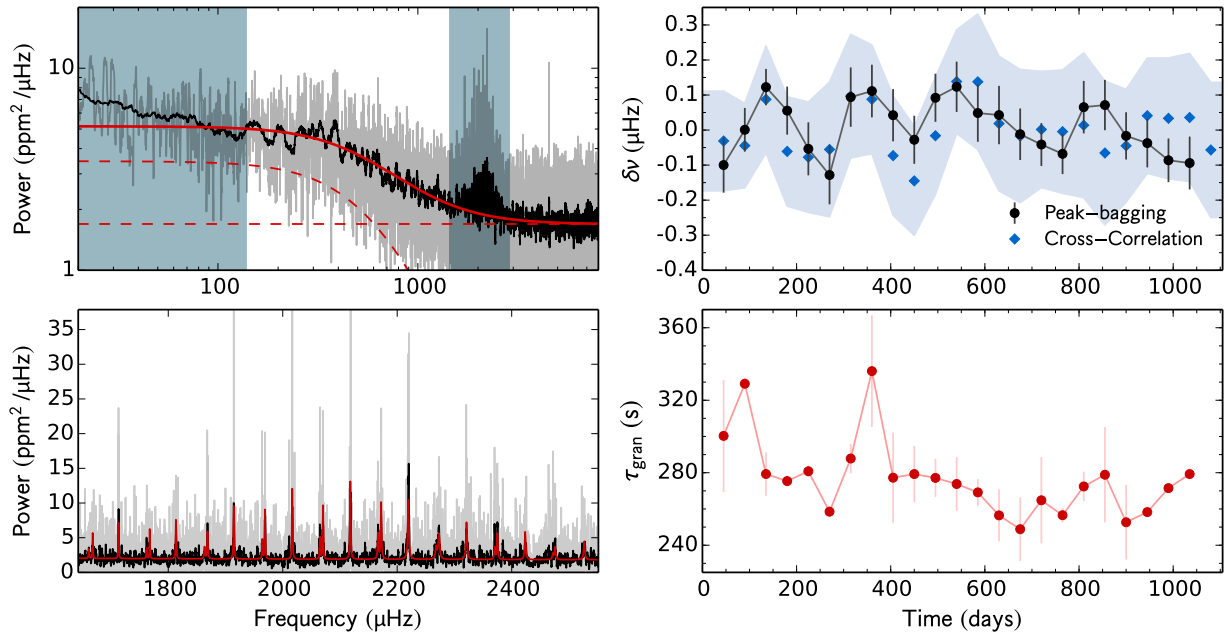

Fig. A.77 – Same as in Fig. A.1, but for KIC 11295426.

time (days)	d_c %	τ_{gran} (s)	Peak-bagging $\delta\nu_{l=0}$ (μHz)	$\delta\nu_{l=1}$ (μHz)	$\delta\nu_{l=2}$ (μHz)	$\delta\nu$ (μHz)	Cross-correlation $\delta\nu$ (μHz)
45	0.98	300.3 ± 31.0	-0.09 ± 0.12	-0.11 ± 0.10	-0.01 ± 0.17	-0.10 ± -0.10	-0.03 ± 0.14
90	0.97	329.1 ± 3.1	0.08 ± 0.10	-0.06 ± 0.08	-0.12 ± 0.14	0.00 ± 0.00	-0.04 ± 0.12
135	0.96	279.3 ± 12.0	0.18 ± 0.07	0.03 ± 0.08	-0.10 ± 0.12	0.12 ± 0.12	0.09 ± 0.15
180	0.97	275.4 ± 2.9	0.18 ± 0.10	-0.08 ± 0.10	-0.14 ± 0.15	0.06 ± 0.06	-0.06 ± 0.16
225	0.96	280.8 ± 3.1	0.11 ± 0.12	-0.15 ± 0.10	-0.26 ± 0.17	-0.05 ± -0.05	-0.08 ± 0.16
270	0.80	258.5 ± 3.1	-0.03 ± 0.14	-0.18 ± 0.10	-0.01 ± 0.18	-0.13 ± -0.13	-0.06 ± 0.19
315	0.78	287.8 ± 8.1	0.15 ± 0.14	0.06 ± 0.11	0.10 ± 0.16	0.09 ± 0.09	0.10 ± 0.18
360	0.89	336.1 ± 30.8	0.13 ± 0.13	0.10 ± 0.09	-0.00 ± 0.12	0.11 ± 0.11	0.09 ± 0.16
405	0.93	277.3 ± 25.0	0.11 ± 0.10	-0.05 ± 0.12	-0.19 ± 0.14	0.04 ± 0.04	-0.07 ± 0.17
450	0.97	279.3 ± 15.5	0.04 ± 0.09	-0.12 ± 0.10	-0.15 ± 0.12	-0.03 ± -0.03	-0.15 ± 0.16
495	0.97	277.1 ± 10.5	0.12 ± 0.10	0.07 ± 0.10	0.02 ± 0.15	0.09 ± 0.09	-0.02 ± 0.17
540	0.98	273.8 ± 14.8	0.10 ± 0.11	0.14 ± 0.10	0.10 ± 0.17	0.12 ± 0.12	0.14 ± 0.15
585	0.94	269.2 ± 7.5	-0.01 ± 0.12	0.10 ± 0.12	0.36 ± 0.21	0.05 ± 0.05	0.14 ± 0.19
630	0.92	256.5 ± 14.3	0.05 ± 0.13	0.04 ± 0.11	-0.30 ± 0.18	0.04 ± 0.04	0.02 ± 0.19
675	0.90	248.9 ± 17.6	0.03 ± 0.10	-0.06 ± 0.11	-0.29 ± 0.16	-0.01 ± -0.01	-0.02 ± 0.19
720	0.90	264.8 ± 23.8	-0.02 ± 0.08	-0.08 ± 0.10	0.02 ± 0.21	-0.04 ± -0.04	0.00 ± 0.17
765	0.95	256.6 ± 4.0	-0.07 ± 0.07	-0.05 ± 0.10	-0.20 ± 0.16	-0.07 ± -0.07	-0.00 ± 0.18
810	0.90	272.4 ± 8.2	0.07 ± 0.09	0.06 ± 0.13	-0.25 ± 0.13	0.07 ± 0.07	0.01 ± 0.21
855	0.89	278.9 ± 26.3	0.18 ± 0.09	-0.10 ± 0.12	0.24 ± 0.16	0.07 ± 0.07	-0.07 ± 0.21
900	0.95	252.7 ± 20.6	0.04 ± 0.09	-0.08 ± 0.10	0.16 ± 0.17	-0.02 ± -0.02	-0.04 ± 0.16
945	0.90	258.3 ± 2.4	-0.08 ± 0.10	0.01 ± 0.10	0.06 ± 0.17	-0.04 ± -0.04	0.04 ± 0.16
990	0.89	271.5 ± 0.6	-0.15 ± 0.08	-0.02 ± 0.09	0.03 ± 0.17	-0.09 ± -0.09	0.03 ± 0.17
1035	0.85	279.3 ± 0.7	-0.19 ± 0.11	-0.01 ± 0.10	-0.11 ± 0.15	-0.09 ± -0.09	0.04 ± 0.18
1080	–	–	–	–	–	–	-0.06 ± 0.19

Table A.77 – Same as in Table A.1, but for KIC 11295426.

KIC 11401755

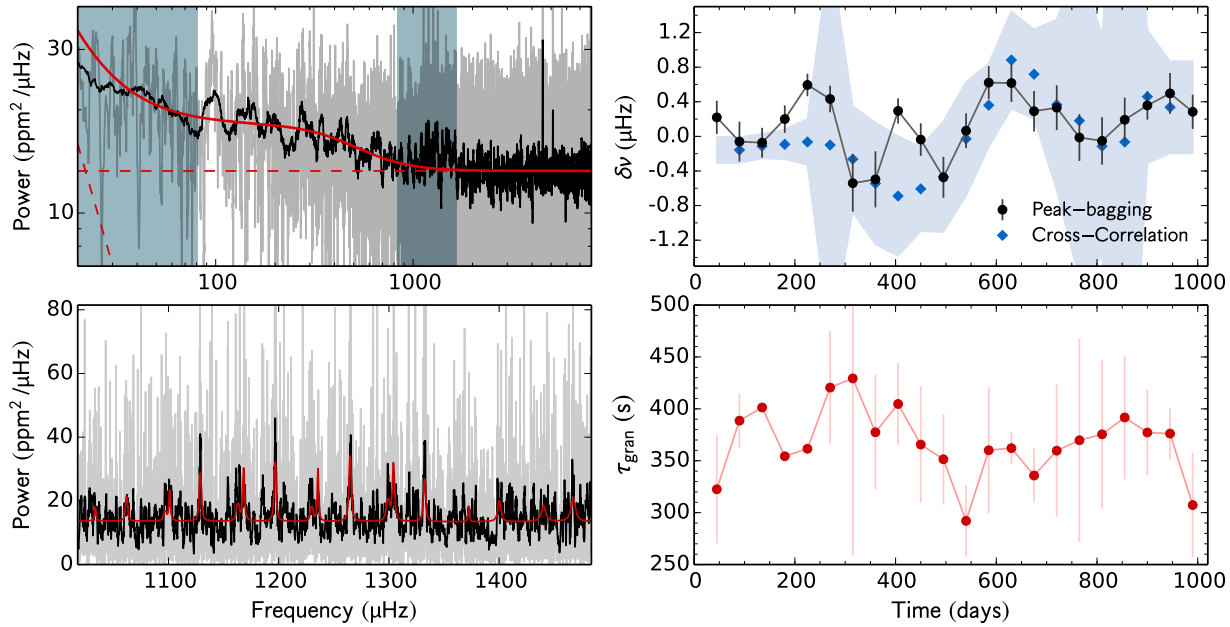

Fig. A.78 – Same as in Fig. A.1, but for KIC 11401755. Due to the extremely large error bars, the results from the cross-correlation method, that are shown here, were obtained from 180-d sub-series.

time (days)	d_c %	τ_{gran} (s)	Peak-bagging $\delta\nu_{l=0}$ (μHz)	$\delta\nu_{l=1}$ (μHz)	$\delta\nu_{l=2}$ (μHz)	$\delta\nu$ (μHz)	Cross-correlation $\delta\nu$ (μHz)
45	0.98	322.5 ± 52.3	0.58 ± 0.39	0.11 ± 0.22	-0.31 ± 0.67	0.22 ± 0.22	–
90	0.97	388.6 ± 26.5	-1.78 ± 0.59	0.24 ± 0.25	0.09 ± 0.93	-0.06 ± -0.06	-0.16 ± 0.15
135	0.96	401.3 ± 0.2	0.10 ± 0.28	-0.18 ± 0.22	-0.25 ± 0.86	-0.07 ± -0.07	-0.11 ± 0.14
180	0.78	354.3 ± 2.2	0.63 ± 0.26	-0.07 ± 0.20	-1.22 ± 0.61	0.20 ± 0.20	-0.09 ± 0.17
225	0.72	361.5 ± 0.2	0.57 ± 0.17	0.62 ± 0.20	-0.16 ± 0.67	0.59 ± 0.59	-0.06 ± 0.27
270	0.92	420.5 ± 54.5	0.39 ± 0.19	0.50 ± 0.25	0.33 ± 0.58	0.43 ± 0.43	-0.10 ± 2.25
315	0.98	429.3 ± 171.1	-0.81 ± 0.67	-0.45 ± 0.38	0.04 ± 0.85	-0.54 ± -0.54	-0.26 ± 0.61
360	0.97	377.4 ± 55.3	-0.60 ± 0.65	-0.46 ± 0.37	-0.32 ± 0.83	-0.50 ± -0.50	-0.54 ± 0.70
405	0.97	404.7 ± 39.4	0.46 ± 0.19	0.06 ± 0.23	0.82 ± 0.70	0.29 ± 0.29	-0.69 ± 0.69
450	0.97	365.6 ± 56.1	0.17 ± 0.24	-0.34 ± 0.30	0.82 ± 0.72	-0.04 ± -0.04	-0.61 ± 0.49
495	0.94	351.4 ± 43.6	-0.05 ± 0.37	-0.78 ± 0.31	-0.51 ± 0.82	-0.47 ± -0.47	-0.47 ± 0.64
540	0.91	292.1 ± 34.4	0.67 ± 0.29	-0.48 ± 0.28	-1.33 ± 1.24	0.07 ± 0.07	-0.03 ± 0.66
585	0.88	360.1 ± 60.6	0.75 ± 0.24	0.40 ± 0.31	1.05 ± 1.35	0.62 ± 0.62	0.36 ± 0.48
630	0.92	362.1 ± 15.4	0.58 ± 0.36	0.64 ± 0.27	-1.12 ± 0.59	0.62 ± 0.62	0.88 ± 0.56
675	0.97	335.8 ± 26.0	-0.02 ± 0.40	0.46 ± 0.29	-0.82 ± 0.72	0.29 ± 0.29	0.72 ± 0.52
720	0.90	359.7 ± 64.0	0.25 ± 0.36	0.42 ± 0.37	-0.22 ± 1.05	0.33 ± 0.33	0.37 ± 0.99
765	0.89	369.7 ± 97.9	0.09 ± 0.47	-0.06 ± 0.33	-0.36 ± 1.11	-0.01 ± -0.01	0.18 ± 1.84
810	0.95	375.5 ± 71.6	0.09 ± 0.39	-0.20 ± 0.39	0.29 ± 1.06	-0.05 ± -0.05	-0.11 ± 1.28
855	0.89	391.7 ± 59.4	0.13 ± 0.42	0.23 ± 0.32	0.61 ± 1.04	0.19 ± 0.19	-0.07 ± 4.50
900	0.82	377.2 ± 40.9	0.13 ± 0.21	0.69 ± 0.26	-0.46 ± 1.14	0.36 ± 0.36	0.46 ± 0.77
945	0.85	376.2 ± 24.7	0.44 ± 0.36	0.54 ± 0.31	0.63 ± 0.88	0.50 ± 0.50	0.34 ± 0.53
990	0.92	307.3 ± 50.2	0.67 ± 0.35	0.09 ± 0.24	1.47 ± 0.61	0.28 ± 0.28	–

Table A.78 – Same as in Table A.1, but for KIC 11401755. Due to the extremely large error bars, the results from the cross-correlation method, that are shown here, were obtained from 180-d sub-series.

KIC 11772920

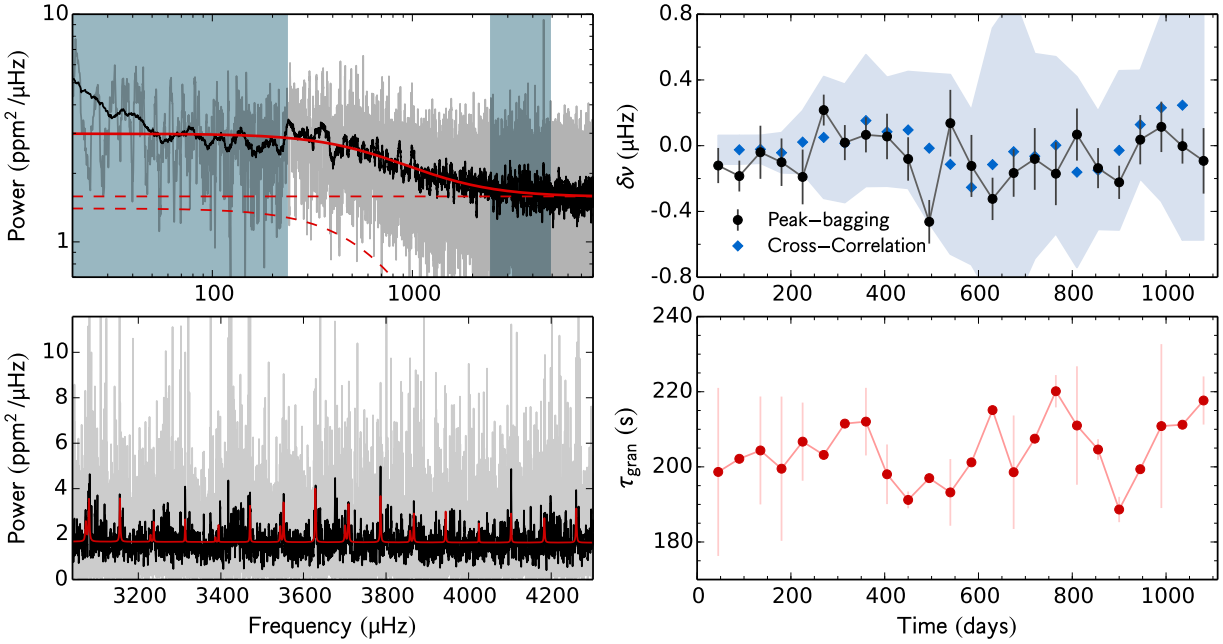

Fig. A.79 – Same as in Fig. A.1, but for KIC 11772920. Due to the extremely large error bars, the results from the cross-correlation method, that are shown here, were obtained from 180-d sub-series.

time (days)	d_c %	τ_{gran} (s)	Peak-bagging $\delta\nu_{l=0}$ (μHz)	$\delta\nu_{l=1}$ (μHz)	$\delta\nu_{l=2}$ (μHz)	$\delta\nu$ (μHz)	Cross-correlation $\delta\nu$ (μHz)
45	0.97	198.7 ± 22.4	-0.15 ± 0.13	-0.06 ± 0.18	-0.49 ± 0.36	-0.12 ± -0.12	–
90	0.97	202.1 ± 0.6	-0.17 ± 0.13	-0.20 ± 0.13	-0.44 ± 0.59	-0.18 ± -0.18	-0.03 ± 0.09
135	0.96	204.4 ± 14.4	0.03 ± 0.23	-0.10 ± 0.22	0.33 ± 0.56	-0.04 ± -0.04	-0.02 ± 0.08
180	0.97	199.5 ± 19.2	-0.10 ± 0.19	-0.10 ± 0.22	0.40 ± 0.46	-0.10 ± -0.10	-0.04 ± 0.12
225	0.96	206.7 ± 10.4	-0.35 ± 0.22	0.06 ± 0.26	0.14 ± 0.49	-0.19 ± -0.19	0.02 ± 0.19
270	0.81	203.2 ± 0.7	-0.03 ± 0.12	0.61 ± 0.15	-0.21 ± 0.32	0.22 ± 0.22	0.05 ± 0.37
315	0.78	211.5 ± 0.7	-0.03 ± 0.13	0.13 ± 0.19	0.11 ± 0.39	0.02 ± 0.02	0.01 ± 0.36
360	0.89	212.0 ± 9.0	0.03 ± 0.14	0.10 ± 0.16	0.25 ± 0.35	0.07 ± 0.07	0.15 ± 0.40
405	0.93	198.0 ± 7.9	-0.04 ± 0.21	0.13 ± 0.18	0.51 ± 0.43	0.06 ± 0.06	0.08 ± 0.33
450	0.97	191.2 ± 2.2	0.14 ± 0.20	-0.26 ± 0.18	0.29 ± 0.52	-0.08 ± -0.08	0.10 ± 0.36
495	0.97	197.0 ± 0.7	-0.76 ± 0.25	-0.34 ± 0.16	0.04 ± 0.49	-0.46 ± -0.46	-0.02 ± 0.46
540	0.98	193.2 ± 8.9	-0.13 ± 0.49	0.19 ± 0.22	0.18 ± 0.61	0.14 ± 0.14	-0.11 ± 0.55
585	0.94	201.2 ± 1.1	-0.53 ± 0.30	0.15 ± 0.24	-0.45 ± 0.53	-0.12 ± -0.12	-0.25 ± 0.47
630	0.92	215.1 ± 0.6	-0.55 ± 0.19	-0.12 ± 0.18	0.39 ± 0.45	-0.32 ± -0.32	-0.12 ± 0.83
675	0.90	198.6 ± 15.1	-0.31 ± 0.23	-0.07 ± 0.19	-0.01 ± 0.48	-0.17 ± -0.17	-0.04 ± 0.94
720	0.90	207.5 ± 0.0	-0.18 ± 0.24	0.06 ± 0.29	-0.52 ± 0.59	-0.08 ± -0.08	-0.06 ± 0.62
765	0.95	220.1 ± 4.3	-0.23 ± 0.23	-0.02 ± 0.35	-0.64 ± 0.59	-0.17 ± -0.17	0.00 ± 0.54
810	0.90	211.0 ± 15.8	0.06 ± 0.21	0.08 ± 0.24	0.06 ± 0.45	0.07 ± 0.07	-0.16 ± 0.58
855	0.89	204.6 ± 2.7	-0.03 ± 0.15	-0.32 ± 0.20	0.33 ± 0.57	-0.14 ± -0.14	-0.15 ± 0.36
900	0.95	188.6 ± 3.4	-0.22 ± 0.14	-0.23 ± 0.15	-0.90 ± 0.43	-0.22 ± -0.22	-0.03 ± 0.48
945	0.90	199.4 ± 1.1	-0.24 ± 0.29	0.14 ± 0.17	-0.41 ± 0.40	0.04 ± 0.04	0.13 ± 0.33
990	0.89	210.9 ± 21.8	0.13 ± 0.30	0.11 ± 0.18	-0.06 ± 0.33	0.11 ± 0.11	0.23 ± 0.57
1035	0.85	211.2 ± 0.7	0.03 ± 0.16	-0.03 ± 0.15	0.10 ± 0.26	-0.00 ± -0.00	0.25 ± 0.82
1080	0.85	217.7 ± 6.4	0.04 ± 0.29	-0.21 ± 0.27	0.26 ± 0.55	-0.09 ± -0.09	–

Table A.79 – Same as in Table A.1, but for KIC 11772920. Due to the extremely large error bars, the results from the cross-correlation method, that are shown here, were obtained from 180-d sub-series.

KIC 11807274

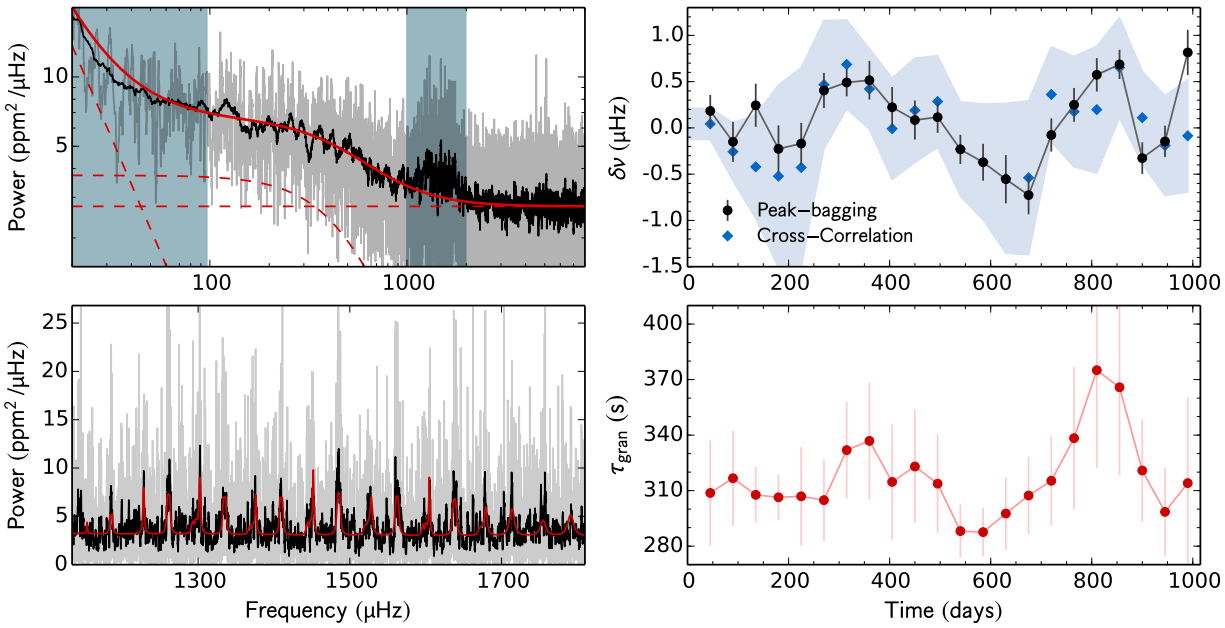

Fig. A.80 – Same as in Fig. A.1, but for KIC 11807274, with the exception of the final average frequency shifts from the peak-bagging analysis that, in this case, result from combining the $l = 1$ and $l = 2$ modes.

time (days)	d_c %	τ_{gran} (s)	Peak-bagging $\delta\nu_{l=0}$ (μHz)	$\delta\nu_{l=1}$ (μHz)	$\delta\nu_{l=2}$ (μHz)	$\delta\nu$ (μHz)	Cross-correlation $\delta\nu$ (μHz)
45	0.98	308.7 ± 28.4	0.55 ± 0.25	0.11 ± 0.24	0.54 ± 0.53	0.18 ± 0.18	0.04 ± 0.17
90	0.97	316.7 ± 25.8	-0.42 ± 0.33	-0.31 ± 0.29	0.45 ± 0.56	-0.15 ± -0.15	-0.26 ± 0.31
135	0.96	307.7 ± 15.0	-0.22 ± 0.36	0.14 ± 0.31	0.63 ± 0.58	0.24 ± 0.24	-0.42 ± 0.56
180	0.78	306.4 ± 12.4	-0.05 ± 0.38	-0.28 ± 0.34	-0.09 ± 0.57	-0.23 ± -0.23	-0.52 ± 0.99
225	0.72	306.9 ± 26.6	0.36 ± 0.37	-0.22 ± 0.28	0.03 ± 0.55	-0.17 ± -0.17	-0.43 ± 1.08
270	0.92	304.8 ± 22.1	-0.08 ± 0.25	0.48 ± 0.30	0.15 ± 0.53	0.40 ± 0.40	0.47 ± 0.69
315	0.98	331.9 ± 26.2	-0.24 ± 0.19	0.65 ± 0.24	-0.51 ± 0.61	0.49 ± 0.49	0.69 ± 0.48
360	0.97	336.9 ± 31.6	0.26 ± 0.27	0.29 ± 0.34	1.06 ± 0.52	0.52 ± 0.52	0.42 ± 0.43
405	0.97	314.7 ± 31.2	-0.29 ± 0.30	-0.01 ± 0.32	0.83 ± 0.52	0.22 ± 0.22	-0.01 ± 0.55
450	0.97	323.0 ± 30.6	0.28 ± 0.34	-0.06 ± 0.27	0.63 ± 0.52	0.08 ± 0.08	0.19 ± 0.56
495	0.94	313.8 ± 26.6	0.43 ± 0.24	0.09 ± 0.24	0.29 ± 0.59	0.12 ± 0.12	0.29 ± 0.49
540	0.91	288.1 ± 14.4	0.44 ± 0.21	-0.05 ± 0.24	-1.03 ± 0.51	-0.23 ± -0.23	-0.23 ± 0.51
585	0.88	287.6 ± 13.2	0.52 ± 0.28	-0.35 ± 0.28	-0.43 ± 0.54	-0.37 ± -0.37	-0.37 ± 0.63
630	0.92	297.6 ± 19.6	0.06 ± 0.37	-0.67 ± 0.37	-0.21 ± 0.64	-0.55 ± -0.55	-0.54 ± 0.81
675	0.97	307.3 ± 20.9	0.15 ± 0.26	-0.72 ± 0.36	-0.76 ± 0.68	-0.73 ± -0.73	-0.54 ± 0.83
720	0.90	315.3 ± 24.0	-0.29 ± 0.23	0.07 ± 0.28	-0.64 ± 0.55	-0.08 ± -0.08	0.36 ± 0.51
765	0.89	338.3 ± 38.6	-0.66 ± 0.26	0.35 ± 0.25	-0.07 ± 0.45	0.25 ± 0.25	0.18 ± 0.60
810	0.95	375.1 ± 52.8	0.27 ± 0.23	0.44 ± 0.29	0.92 ± 0.48	0.57 ± 0.57	0.20 ± 0.69
855	0.89	365.8 ± 47.5	0.26 ± 0.18	0.46 ± 0.32	1.28 ± 0.52	0.69 ± 0.69	0.65 ± 0.54
900	0.82	320.9 ± 27.7	0.29 ± 0.21	-0.32 ± 0.30	-0.34 ± 0.46	-0.33 ± -0.33	0.11 ± 0.50
945	0.84	298.5 ± 23.7	0.02 ± 0.24	-0.15 ± 0.24	-0.15 ± 0.64	-0.15 ± -0.15	-0.19 ± 0.54
990	0.92	314.1 ± 46.4	-0.48 ± 0.37	1.08 ± 0.33	-0.51 ± 0.73	0.82 ± 0.82	-0.09 ± 0.61

Table A.80 – Same as in Table A.1, but for KIC 11807274, with the exception of the final average frequency shifts from the peak-bagging analysis that, in this case, result from combining the $l = 1$ and $l = 2$ modes.

KIC 11904151

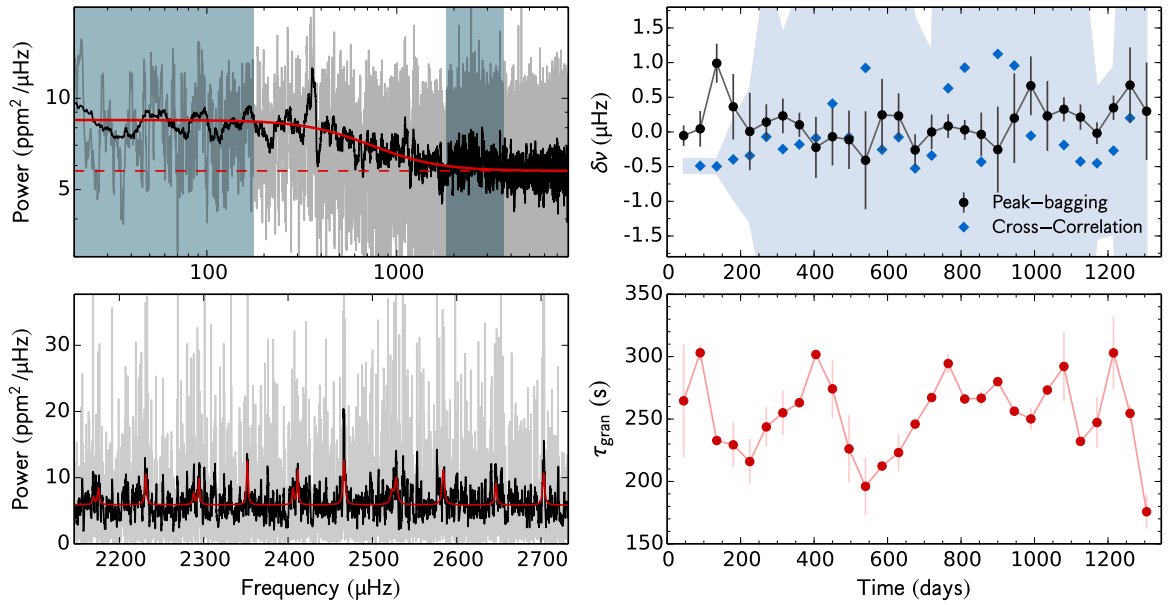

Fig. A.81 – Same as in Fig. A.1, but for KIC 11904151. Due to the extremely large error bars, the results from the cross-correlation method, that are shown here, were obtained from 180-d sub-series.

time (days)	d_c %	τ_{gran} (s)	Peak-bagging $\delta\nu_{l=0}$ (μHz)	$\delta\nu_{l=1}$ (μHz)	$\delta\nu_{l=2}$ (μHz)	$\delta\nu$ (μHz)	Cross-correlation $\delta\nu$ (μHz)
45	0.65	264.6 ± 45.4	-0.37 ± 0.84	-0.01 ± 0.13	-0.26 ± 0.59	-0.02 ± -0.02	–
90	0.79	303.1 ± 6.1	-0.28 ± 0.74	0.16 ± 0.26	-0.05 ± 1.06	0.11 ± 0.11	-0.49 ± 0.10
135	0.85	232.8 ± 0.0	0.60 ± 0.55	1.17 ± 0.33	0.18 ± 0.92	1.03 ± 1.03	-0.50 ± 0.10
180	0.39	229.3 ± 17.8	0.77 ± 0.70	0.08 ± 0.62	0.81 ± 0.97	0.38 ± 0.38	-0.40 ± 0.57
225	0.30	215.9 ± 18.2	-0.48 ± 0.92	0.26 ± 0.77	-0.62 ± 1.17	-0.04 ± -0.04	-0.34 ± 0.96
270	0.77	243.7 ± 15.8	-0.59 ± 0.68	0.32 ± 0.20	0.42 ± 1.00	0.25 ± 0.25	-0.07 ± 2.43
315	0.96	255.0 ± 17.9	-0.01 ± 0.28	0.54 ± 0.33	0.70 ± 0.87	0.22 ± 0.22	-0.25 ± 1.67
360	0.96	263.1 ± 3.5	0.05 ± 0.16	0.13 ± 0.42	0.03 ± 0.78	0.06 ± 0.06	-0.18 ± 2.25
405	0.97	301.7 ± 2.0	-0.09 ± 0.77	-0.12 ± 0.48	-0.31 ± 1.00	-0.11 ± -0.11	-0.09 ± 2.63
450	0.97	274.2 ± 23.3	-0.09 ± 0.78	0.10 ± 0.42	-0.49 ± 1.04	0.06 ± 0.06	0.41 ± 4.81
495	0.74	226.1 ± 27.1	0.09 ± 0.72	-0.17 ± 0.50	-0.14 ± 0.83	-0.09 ± -0.09	-0.08 ± 3.63
540	0.26	196.1 ± 23.1	-0.40 ± 0.91	-0.63 ± 1.02	0.02 ± 1.14	-0.50 ± -0.50	0.92 ± 10.23
585	0.24	212.3 ± 0.2	0.55 ± 0.73	0.11 ± 0.56	-0.43 ± 1.23	0.27 ± 0.27	-0.25 ± 3.07
630	0.72	223.1 ± 15.2	0.25 ± 0.30	0.35 ± 0.32	-0.74 ± 1.22	0.29 ± 0.29	-0.07 ± 3.02
675	0.97	246.0 ± 1.4	-0.60 ± 0.29	0.14 ± 0.25	-0.48 ± 1.06	-0.18 ± -0.18	-0.53 ± 2.16
720	0.98	267.2 ± 1.5	-0.18 ± 0.43	0.12 ± 0.20	0.21 ± 0.70	0.07 ± 0.07	-0.34 ± 1.49
765	0.97	294.5 ± 7.5	0.10 ± 0.27	0.06 ± 0.17	0.31 ± 0.76	0.07 ± 0.07	0.63 ± 11.85
810	0.97	266.1 ± 0.2	-0.24 ± 0.22	0.25 ± 0.16	-0.65 ± 0.68	0.07 ± 0.07	0.93 ± 12.02
855	0.93	266.7 ± 6.0	-0.04 ± 0.46	-0.01 ± 0.39	0.60 ± 1.02	-0.02 ± -0.02	-0.43 ± 6.43
900	0.44	279.9 ± 0.3	0.13 ± 0.92	-0.20 ± 0.72	-0.17 ± 1.21	-0.08 ± -0.08	1.12 ± 5.56
945	0.08	256.3 ± nan	0.19 ± 0.88	0.35 ± 0.75	0.31 ± 1.14	0.29 ± 0.29	0.96 ± 3.80
990	0.57	250.1 ± 8.7	0.48 ± 0.41	0.72 ± 0.46	0.17 ± 0.77	0.59 ± 0.59	-0.05 ± 3.19
1035	0.96	273.3 ± 1.4	0.36 ± 0.62	0.26 ± 0.58	0.25 ± 0.93	0.31 ± 0.31	0.23 ± 3.20
1080	0.89	292.1 ± 27.5	0.01 ± 0.48	0.39 ± 0.18	-0.07 ± 0.88	0.34 ± 0.34	-0.19 ± 2.84
1125	0.91	232.1 ± 1.5	-0.17 ± 0.31	0.35 ± 0.23	-0.24 ± 0.78	0.17 ± 0.17	-0.43 ± 3.27
1170	0.92	247.2 ± 20.2	-0.17 ± 0.22	0.14 ± 0.22	-0.98 ± 0.38	-0.01 ± -0.01	-0.45 ± 1.09
1215	0.89	303.0 ± 29.1	-0.04 ± 0.24	0.79 ± 0.27	-1.07 ± 0.41	0.34 ± 0.34	-0.27 ± 1.21
1260	0.57	254.6 ± 7.0	0.60 ± 0.87	0.56 ± 0.76	-0.10 ± 1.19	0.58 ± 0.58	0.20 ± 5.75
1305	0.12	175.7 ± 13.5	0.31 ± 0.93	0.06 ± 0.99	-0.58 ± 1.17	0.20 ± 0.20	–
1350	0.29	231.0 ± 0.3	0.37 ± 0.76	0.07 ± 0.41	0.51 ± 0.99	0.13 ± 0.13	–

Table A.81 – Same as in Table A.1, but for KIC 11904151. Due to the extremely large error bars, the results from the cross-correlation method, that are shown here, were obtained from 180-d sub-series.

KIC 12009504

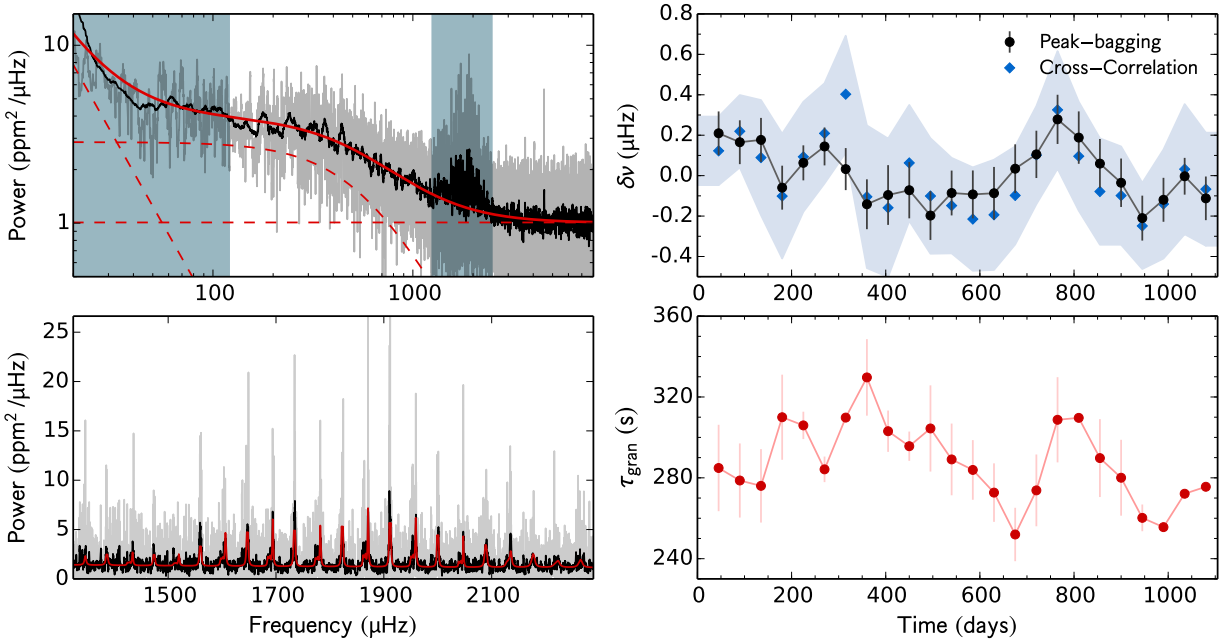

Fig. A.82 – Same as in Fig. A.1, but for KIC 12009504.

time (days)	d_c %	τ_{gran} (s)	Peak-bagging $\delta\nu_{l=0}$ (μHz)	$\delta\nu_{l=1}$ (μHz)	$\delta\nu_{l=2}$ (μHz)	$\delta\nu$ (μHz)	Cross-correlation $\delta\nu$ (μHz)
45	0.98	284.9 ± 21.4	0.24 ± 0.13	0.20 ± 0.17	-0.39 ± 0.29	0.21 ± 0.21	0.12 ± 0.17
90	0.97	278.7 ± 18.3	0.19 ± 0.13	0.22 ± 0.18	-0.27 ± 0.28	0.17 ± 0.17	0.22 ± 0.18
135	0.96	276.0 ± 18.2	0.09 ± 0.17	0.23 ± 0.15	-0.22 ± 0.29	0.18 ± 0.18	0.09 ± 0.28
180	0.97	310.0 ± 21.1	-0.26 ± 0.15	0.08 ± 0.16	-0.36 ± 0.37	-0.06 ± -0.06	-0.10 ± 0.31
225	0.96	305.9 ± 6.8	-0.05 ± 0.13	0.26 ± 0.13	0.27 ± 0.18	0.06 ± 0.06	0.09 ± 0.27
270	0.81	284.2 ± 6.3	-0.00 ± 0.13	0.49 ± 0.14	0.10 ± 0.26	0.14 ± 0.14	0.21 ± 0.25
315	0.78	309.8 ± 2.3	-0.16 ± 0.14	0.43 ± 0.19	0.26 ± 0.37	0.03 ± 0.03	0.40 ± 0.29
360	0.89	329.7 ± 18.9	-0.34 ± 0.18	-0.05 ± 0.19	-0.35 ± 0.33	-0.14 ± -0.14	-0.10 ± 0.35
405	0.93	303.1 ± 10.2	-0.24 ± 0.22	0.07 ± 0.20	-0.14 ± 0.51	-0.10 ± -0.10	-0.16 ± 0.34
450	0.97	295.7 ± 7.2	-0.13 ± 0.21	-0.07 ± 0.18	0.19 ± 0.39	-0.07 ± -0.07	0.06 ± 0.29
495	0.97	304.4 ± 21.3	-0.28 ± 0.19	-0.30 ± 0.18	-0.23 ± 0.35	-0.20 ± -0.20	-0.10 ± 0.29
540	0.98	289.1 ± 17.7	0.14 ± 0.19	-0.28 ± 0.16	0.45 ± 0.23	-0.09 ± -0.09	-0.15 ± 0.24
585	0.94	283.9 ± 14.8	0.02 ± 0.17	-0.17 ± 0.18	0.07 ± 0.30	-0.09 ± -0.09	-0.21 ± 0.26
630	0.92	272.7 ± 14.5	-0.05 ± 0.19	-0.07 ± 0.19	0.37 ± 0.33	-0.09 ± -0.09	-0.19 ± 0.27
675	0.90	252.0 ± 13.2	0.13 ± 0.17	-0.18 ± 0.18	0.45 ± 0.30	0.03 ± 0.03	-0.10 ± 0.24
720	0.90	273.8 ± 17.8	0.13 ± 0.17	-0.10 ± 0.18	0.45 ± 0.32	0.11 ± 0.11	0.10 ± 0.24
765	0.95	308.7 ± 21.1	0.25 ± 0.20	0.24 ± 0.18	0.42 ± 0.35	0.28 ± 0.28	0.33 ± 0.29
810	0.90	309.7 ± 0.8	0.34 ± 0.21	0.22 ± 0.19	0.59 ± 0.36	0.19 ± 0.19	0.10 ± 0.27
855	0.89	289.8 ± 19.3	0.24 ± 0.18	0.05 ± 0.18	0.46 ± 0.40	0.06 ± 0.06	-0.08 ± 0.26
900	0.95	280.0 ± 18.8	0.11 ± 0.16	-0.19 ± 0.19	-0.13 ± 0.33	-0.04 ± -0.04	-0.10 ± 0.24
945	0.90	260.2 ± 6.6	-0.10 ± 0.15	-0.34 ± 0.18	-0.38 ± 0.29	-0.21 ± -0.21	-0.25 ± 0.21
990	0.89	255.6 ± 0.6	0.07 ± 0.16	-0.25 ± 0.16	-0.14 ± 0.32	-0.12 ± -0.12	-0.14 ± 0.27
1035	0.85	272.1 ± 0.5	-0.00 ± 0.14	0.17 ± 0.19	0.25 ± 0.30	-0.00 ± -0.00	0.03 ± 0.32
1080	0.85	275.6 ± nan	-0.05 ± 0.15	-0.07 ± 0.18	-0.05 ± 0.37	-0.11 ± -0.11	-0.07 ± 0.28

Table A.82 – Same as in Table A.1, but for KIC 12009504.

KIC 12069127

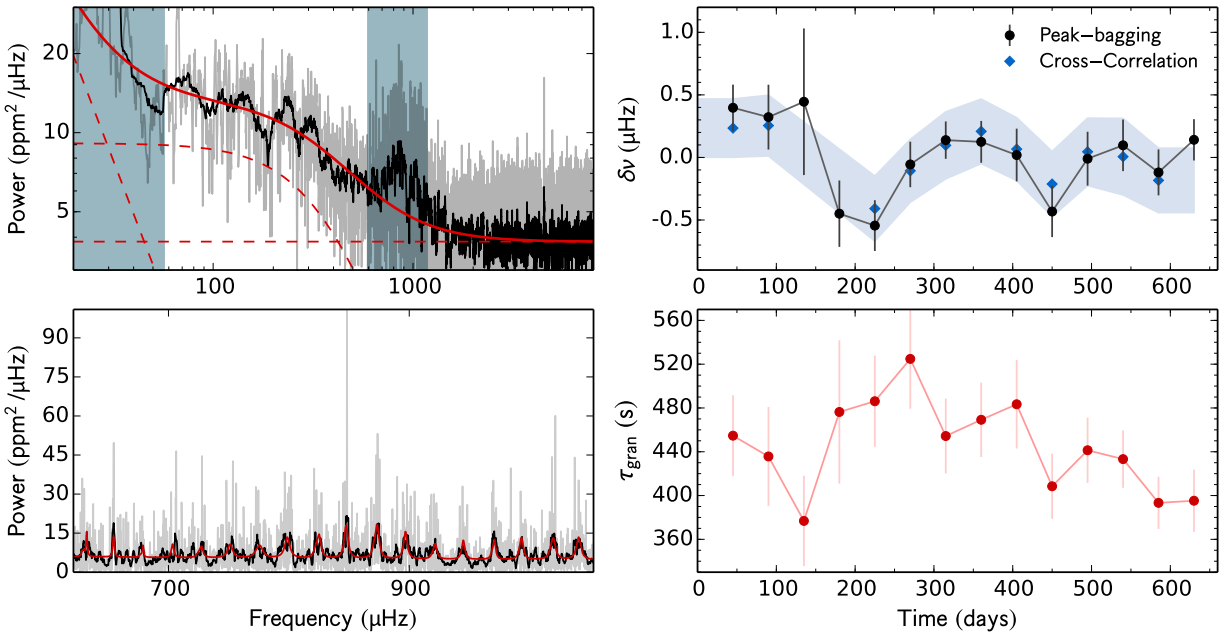

Fig. A.83 – Same as in Fig. A.1, but for KIC 12069127.

time (days)	d_c %	τ_{gran} (s)	Peak-bagging $\delta\nu_{l=0}$ (μHz)	$\delta\nu_{l=1}$ (μHz)	$\delta\nu_{l=2}$ (μHz)	$\delta\nu$ (μHz)	Cross-correlation $\delta\nu$ (μHz)
45	0.98	454.7 ± 36.9	0.62 ± 0.28	0.22 ± 0.25	0.36 ± 0.48	0.40 ± 0.40	0.23 ± 0.23
90	0.54	435.7 ± 45.2	-0.20 ± 0.40	0.72 ± 0.34	0.70 ± 0.59	0.32 ± 0.32	0.25 ± 0.24
135	0.05	376.8 ± 41.3	0.50 ± 0.82	0.39 ± 0.84	-0.75 ± 0.79	0.45 ± 0.45	–
180	0.42	476.4 ± 65.5	-0.15 ± 0.48	-0.58 ± 0.32	0.14 ± 0.59	-0.45 ± -0.45	–
225	0.90	486.1 ± 41.6	-0.68 ± 0.37	-0.48 ± 0.24	0.23 ± 0.54	-0.54 ± -0.54	-0.41 ± 0.26
270	0.80	524.8 ± 45.5	0.15 ± 0.29	-0.18 ± 0.23	-0.25 ± 0.44	-0.06 ± -0.06	-0.11 ± 0.25
315	0.78	454.4 ± 34.2	0.12 ± 0.24	0.15 ± 0.19	-0.64 ± 0.34	0.14 ± 0.14	0.10 ± 0.27
360	0.89	469.2 ± 34.0	-0.08 ± 0.29	0.23 ± 0.20	-0.20 ± 0.51	0.12 ± 0.12	0.21 ± 0.26
405	0.93	483.4 ± 40.5	-0.19 ± 0.43	0.09 ± 0.24	1.16 ± 0.55	0.02 ± 0.02	0.07 ± 0.25
450	0.97	408.5 ± 29.8	-0.37 ± 0.30	-0.48 ± 0.28	1.19 ± 0.53	-0.43 ± -0.43	-0.21 ± 0.26
495	0.97	441.4 ± 29.8	0.09 ± 0.35	-0.08 ± 0.28	0.29 ± 0.59	-0.01 ± -0.01	0.04 ± 0.27
540	0.98	433.3 ± 26.2	0.23 ± 0.35	0.03 ± 0.26	-0.83 ± 0.54	0.10 ± 0.10	0.01 ± 0.31
585	0.94	393.3 ± 23.8	0.13 ± 0.28	-0.31 ± 0.24	-0.80 ± 0.44	-0.12 ± -0.12	-0.18 ± 0.26
630	0.73	395.3 ± 28.4	0.54 ± 0.24	-0.21 ± 0.23	-0.90 ± 0.43	0.14 ± 0.14	–

Table A.83 – Same as in Table A.1, but for KIC 12069127.

KIC 12069424

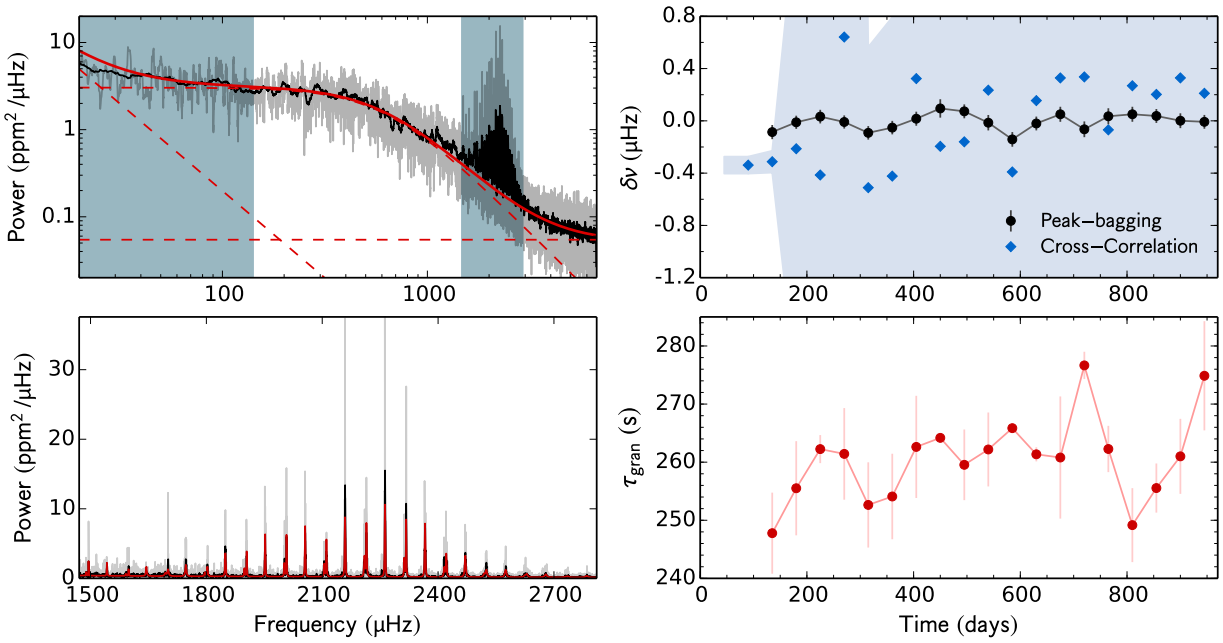

Fig. A.84 – Same as in Fig. A.1, but for KIC 12069424. Due to the extremely large error bars, the results from the cross-correlation method, that are shown here, were obtained from 180-d sub-series.

time (days)	d_c %	τ_{gran} (s)	Peak-bagging $\delta\nu_{l=0}$ (μHz)	$\delta\nu_{l=1}$ (μHz)	$\delta\nu_{l=2}$ (μHz)	$\delta\nu$ (μHz)	Cross-correlation $\delta\nu$ (μHz)
90	–	–	–	–	–	–	-0.34 ± 0.06
135	–	–	–	–	–	–	-0.31 ± 0.08
180	0.97	219.5 ± 0.0	-0.02 ± 0.08	-0.15 ± 0.08	-0.00 ± 0.11	-0.09 ± -0.09	-0.21 ± 1.81
225	0.97	445.7 ± 0.0	-0.03 ± 0.07	0.01 ± 0.07	0.18 ± 0.11	-0.01 ± -0.01	-0.41 ± 1.58
270	0.96	247.8 ± 5.7	0.01 ± 0.07	0.06 ± 0.08	0.02 ± 0.10	0.03 ± 0.03	0.64 ± 12.46
315	0.78	255.5 ± 6.3	-0.06 ± 0.07	0.06 ± 0.08	-0.04 ± 0.09	-0.01 ± -0.01	-0.51 ± 1.08
360	0.72	262.3 ± 6.8	-0.17 ± 0.07	-0.01 ± 0.07	-0.02 ± 0.09	-0.09 ± -0.09	-0.42 ± 1.22
405	0.92	261.4 ± 6.3	-0.09 ± 0.07	-0.02 ± 0.07	-0.19 ± 0.09	-0.05 ± -0.05	0.32 ± 6.86
450	0.98	252.6 ± 5.9	-0.02 ± 0.07	0.06 ± 0.08	-0.34 ± 0.11	0.02 ± 0.02	-0.19 ± 1.62
495	0.97	254.1 ± 6.5	0.08 ± 0.09	0.11 ± 0.11	0.00 ± 0.14	0.09 ± 0.09	-0.16 ± 1.88
540	0.96	262.6 ± 8.1	0.08 ± 0.07	0.06 ± 0.08	0.12 ± 0.11	0.07 ± 0.07	0.23 ± 2.33
585	0.96	264.2 ± 0.5	-0.05 ± 0.08	0.02 ± 0.08	-0.00 ± 0.12	-0.01 ± -0.01	-0.39 ± 1.84
630	0.94	259.5 ± 5.5	-0.20 ± 0.08	-0.08 ± 0.08	0.04 ± 0.11	-0.14 ± -0.14	0.15 ± 2.62
675	0.91	262.2 ± 6.0	-0.04 ± 0.07	0.00 ± 0.08	0.04 ± 0.10	-0.02 ± -0.02	0.33 ± 3.50
720	0.88	265.9 ± 6.1	0.12 ± 0.08	-0.03 ± 0.09	-0.07 ± 0.13	0.05 ± 0.05	0.34 ± 2.92
765	0.90	261.4 ± 7.5	0.04 ± 0.09	-0.16 ± 0.08	-0.11 ± 0.12	-0.06 ± -0.06	-0.07 ± 1.64
810	0.93	260.8 ± 1.4	0.04 ± 0.09	0.03 ± 0.08	-0.01 ± 0.11	0.03 ± 0.03	0.27 ± 2.39
855	0.86	276.7 ± 1.6	0.05 ± 0.08	0.05 ± 0.08	0.08 ± 0.11	0.05 ± 0.05	0.20 ± 2.73
900	0.87	262.3 ± 4.7	0.03 ± 0.08	0.04 ± 0.07	0.17 ± 0.10	0.04 ± 0.04	0.33 ± 2.32
945	0.93	249.2 ± 7.7	-0.00 ± 0.08	0.00 ± 0.08	0.09 ± 0.09	0.00 ± 0.00	0.21 ± 1.98
990	0.88	255.5 ± 7.2	0.04 ± 0.07	-0.06 ± 0.08	-0.01 ± 0.08	-0.01 ± -0.01	–

Table A.84 – Same as in Table A.1, but for KIC 12069424. Due to the extremely large error bars, the results from the cross-correlation method, that are shown here, were obtained from 180-d sub-series.

KIC 12069449

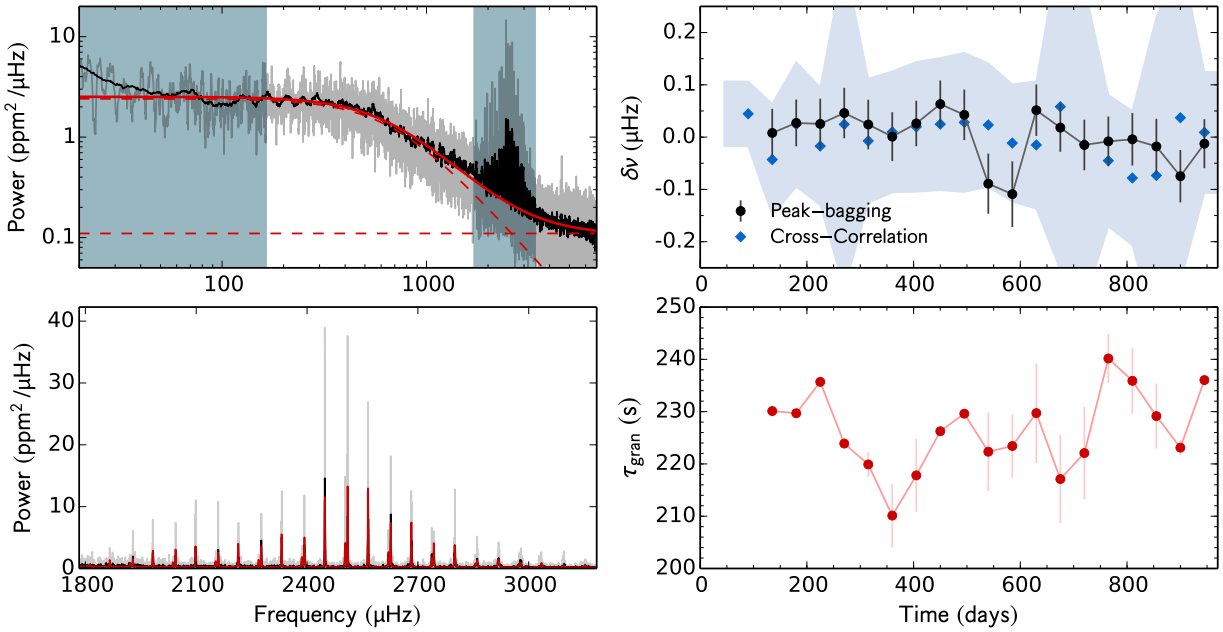

Fig. A.85 – Same as in Fig. A.1, but for KIC 12069449. Due to the extremely large error bars, the results from the cross-correlation method, that are shown here, were obtained from 180-d sub-series.

time (days)	d_c %	τ_{gran} (s)	Peak-bagging $\delta\nu_{l=0}$ (μHz)	$\delta\nu_{l=1}$ (μHz)	$\delta\nu_{l=2}$ (μHz)	$\delta\nu$ (μHz)	Cross-correlation $\delta\nu$ (μHz)
90	–	–	–	–	–	–	0.04 ± 0.06
135	–	–	–	–	–	–	-0.04 ± 0.11
180	0.97	416.4 ± 16.6	0.10 ± 0.06	-0.11 ± 0.07	-0.04 ± 0.10	0.01 ± 0.01	0.02 ± 0.12
225	0.96	388.3 ± 7.6	0.10 ± 0.06	-0.06 ± 0.07	-0.17 ± 0.10	0.03 ± 0.03	-0.02 ± 0.11
270	0.96	230.1 ± 8.2	0.02 ± 0.07	0.03 ± 0.07	-0.16 ± 0.09	0.03 ± 0.03	0.02 ± 0.31
315	0.77	229.7 ± 0.6	0.08 ± 0.07	0.01 ± 0.07	-0.08 ± 0.08	0.05 ± 0.05	-0.01 ± 0.12
360	0.72	235.7 ± 0.3	-0.00 ± 0.06	0.05 ± 0.07	-0.01 ± 0.08	0.02 ± 0.02	0.01 ± 0.12
405	0.92	223.9 ± 0.4	-0.00 ± 0.06	0.01 ± 0.07	0.06 ± 0.08	0.00 ± 0.00	0.02 ± 0.12
450	0.98	219.9 ± 5.2	0.09 ± 0.06	-0.05 ± 0.06	0.05 ± 0.08	0.03 ± 0.03	0.02 ± 0.13
495	0.97	210.1 ± 5.9	0.12 ± 0.06	-0.00 ± 0.07	0.04 ± 0.09	0.06 ± 0.06	0.03 ± 0.13
540	0.97	217.8 ± 6.4	0.03 ± 0.07	0.05 ± 0.06	-0.07 ± 0.10	0.04 ± 0.04	0.02 ± 0.12
585	0.96	226.3 ± 7.3	-0.07 ± 0.09	-0.11 ± 0.08	0.10 ± 0.11	-0.09 ± -0.09	-0.01 ± 0.11
630	0.94	229.6 ± 7.8	-0.02 ± 0.09	-0.19 ± 0.09	0.21 ± 0.10	-0.11 ± -0.11	-0.01 ± 0.12
675	0.90	222.3 ± 8.3	0.08 ± 0.06	0.01 ± 0.08	0.12 ± 0.08	0.05 ± 0.05	0.06 ± 0.31
720	0.86	223.4 ± 6.8	-0.00 ± 0.06	0.05 ± 0.07	0.06 ± 0.08	0.02 ± 0.02	-0.01 ± 0.30
765	0.90	229.7 ± 0.5	-0.11 ± 0.07	0.10 ± 0.07	0.03 ± 0.08	-0.02 ± -0.02	-0.05 ± 0.13
810	0.94	217.1 ± 9.1	-0.04 ± 0.07	0.02 ± 0.07	0.04 ± 0.10	-0.01 ± -0.01	-0.08 ± 0.13
855	0.87	222.1 ± 9.0	-0.01 ± 0.07	-0.00 ± 0.07	-0.18 ± 0.10	-0.00 ± -0.00	-0.07 ± 0.30
900	0.88	240.2 ± 0.6	-0.09 ± 0.07	0.08 ± 0.08	-0.07 ± 0.10	-0.02 ± -0.02	0.04 ± 0.31
945	0.94	235.9 ± 7.9	-0.14 ± 0.07	0.00 ± 0.07	0.19 ± 0.09	-0.07 ± -0.07	0.01 ± 0.12
990	0.88	229.1 ± 0.4	-0.07 ± 0.07	0.03 ± 0.06	0.07 ± 0.08	-0.01 ± -0.01	–

Table A.85 – Same as in Table A.1, but for KIC 12069449. Due to the extremely large error bars, the results from the cross-correlation method, that are shown here, were obtained from 180-d sub-series.

KIC 12258514

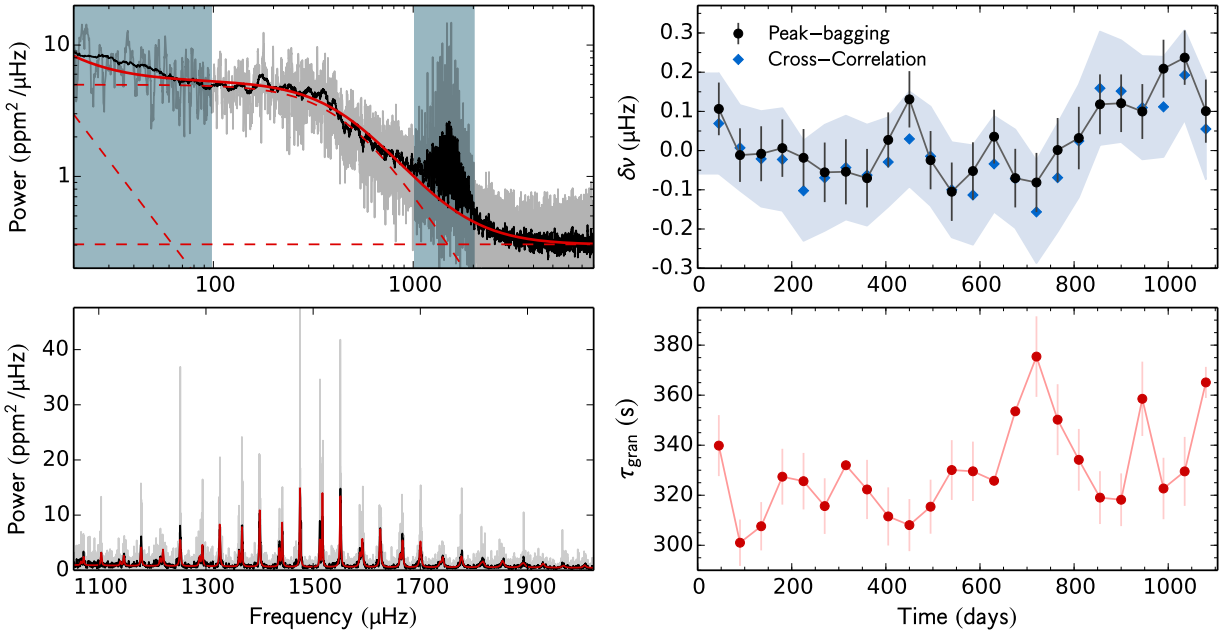

Fig. A.86 – Same as in Fig. A.1, but for KIC 12258514.

time (days)	d_c %	τ_{gran} (s)	Peak-bagging $\delta\nu_{l=0}$ (μHz)	$\delta\nu_{l=1}$ (μHz)	$\delta\nu_{l=2}$ (μHz)	$\delta\nu$ (μHz)	Cross-correlation $\delta\nu$ (μHz)
45	0.98	339.8 ± 12.2	0.10 ± 0.10	0.11 ± 0.09	-0.18 ± 0.13	0.11 ± 0.11	0.07 ± 0.13
90	0.97	301.0 ± 9.3	-0.12 ± 0.10	0.07 ± 0.09	-0.09 ± 0.15	-0.01 ± -0.01	0.01 ± 0.11
135	0.96	307.6 ± 9.7	-0.10 ± 0.11	0.04 ± 0.09	-0.06 ± 0.13	-0.01 ± -0.01	-0.02 ± 0.12
180	0.97	327.4 ± 11.2	0.05 ± 0.12	-0.02 ± 0.09	0.04 ± 0.12	0.01 ± 0.01	-0.02 ± 0.13
225	0.96	325.6 ± 11.3	0.01 ± 0.11	-0.04 ± 0.10	0.18 ± 0.12	-0.02 ± -0.02	-0.10 ± 0.13
270	0.80	315.7 ± 11.1	-0.03 ± 0.11	-0.08 ± 0.10	0.23 ± 0.11	-0.06 ± -0.06	-0.07 ± 0.14
315	0.78	332.0 ± 1.4	-0.07 ± 0.13	-0.04 ± 0.11	-0.20 ± 0.13	-0.05 ± -0.05	-0.04 ± 0.13
360	0.89	322.3 ± 11.8	0.02 ± 0.11	-0.15 ± 0.10	-0.21 ± 0.12	-0.07 ± -0.07	-0.06 ± 0.13
405	0.93	311.5 ± 11.6	0.15 ± 0.10	-0.09 ± 0.10	-0.05 ± 0.13	0.03 ± 0.03	-0.03 ± 0.11
450	0.97	308.1 ± 10.4	0.20 ± 0.10	0.06 ± 0.10	-0.15 ± 0.13	0.13 ± 0.13	0.03 ± 0.12
495	0.97	315.4 ± 10.8	-0.02 ± 0.11	-0.03 ± 0.10	0.09 ± 0.14	-0.02 ± -0.02	-0.01 ± 0.13
540	0.98	330.1 ± 12.0	-0.17 ± 0.11	-0.05 ± 0.10	0.24 ± 0.16	-0.10 ± -0.10	-0.10 ± 0.12
585	0.94	329.6 ± 11.9	-0.00 ± 0.10	-0.10 ± 0.11	-0.20 ± 0.14	-0.05 ± -0.05	-0.11 ± 0.13
630	0.92	325.8 ± 0.1	0.11 ± 0.10	-0.05 ± 0.10	-0.12 ± 0.12	0.04 ± 0.04	-0.03 ± 0.12
675	0.90	353.5 ± 1.9	-0.07 ± 0.11	-0.07 ± 0.10	0.02 ± 0.13	-0.07 ± -0.07	-0.07 ± 0.13
720	0.90	375.4 ± 16.1	-0.08 ± 0.11	-0.08 ± 0.10	0.05 ± 0.13	-0.08 ± -0.08	-0.16 ± 0.13
765	0.95	350.2 ± 14.2	0.05 ± 0.13	-0.03 ± 0.11	0.12 ± 0.14	0.00 ± 0.00	-0.07 ± 0.14
810	0.89	334.2 ± 12.3	0.07 ± 0.13	0.01 ± 0.10	0.11 ± 0.15	0.03 ± 0.03	0.02 ± 0.14
855	0.89	319.0 ± 10.6	0.09 ± 0.12	0.14 ± 0.10	0.23 ± 0.17	0.12 ± 0.12	0.16 ± 0.14
900	0.95	318.2 ± 10.5	0.03 ± 0.11	0.20 ± 0.10	0.25 ± 0.16	0.12 ± 0.12	0.15 ± 0.13
945	0.90	358.5 ± 14.9	-0.01 ± 0.10	0.22 ± 0.10	0.17 ± 0.14	0.10 ± 0.10	0.11 ± 0.13
990	0.89	322.7 ± 12.3	0.21 ± 0.11	0.21 ± 0.10	-0.06 ± 0.16	0.21 ± 0.21	0.11 ± 0.13
1035	0.85	329.5 ± 13.8	0.28 ± 0.09	0.19 ± 0.10	0.11 ± 0.13	0.24 ± 0.24	0.19 ± 0.11
1080	0.85	365.1 ± 6.2	0.03 ± 0.12	0.16 ± 0.11	0.10 ± 0.14	0.10 ± 0.10	0.06 ± 0.13

Table A.86 – Same as in Table A.1, but for KIC 12258514.

KIC 12317678

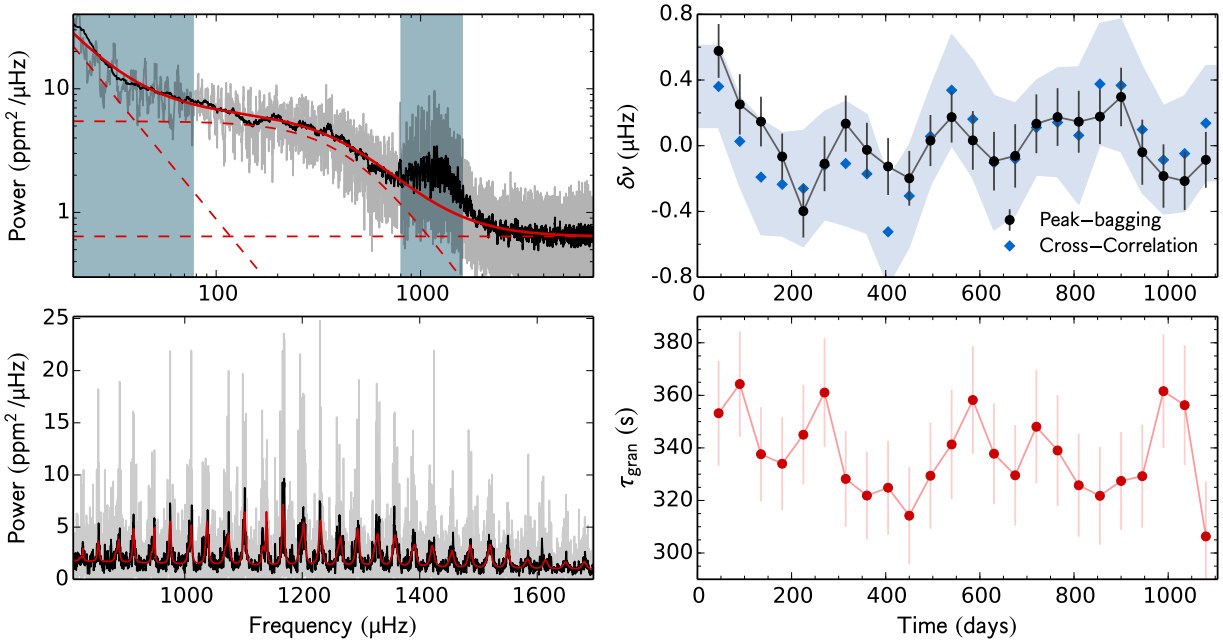

Fig. A.87 – Same as in Fig. A.1, but for KIC 12317678.

time (days)	d_c %	τ_{gran} (s)	Peak-bagging $\delta\nu_{l=0}$ (μHz)	$\delta\nu_{l=1}$ (μHz)	$\delta\nu_{l=2}$ (μHz)	$\delta\nu$ (μHz)	Cross-correlation $\delta\nu$ (μHz)
45	0.98	353.2 ± 20.0	0.62 ± 0.26	0.55 ± 0.21	0.45 ± 0.36	0.58 ± 0.58	0.36 ± 0.25
90	0.97	364.3 ± 20.1	0.56 ± 0.32	0.10 ± 0.22	0.59 ± 0.37	0.25 ± 0.25	0.03 ± 0.27
135	0.96	337.6 ± 17.9	0.39 ± 0.24	-0.02 ± 0.20	-0.35 ± 0.42	0.15 ± 0.15	-0.19 ± 0.35
180	0.97	334.0 ± 17.7	-0.03 ± 0.21	-0.10 ± 0.19	-0.44 ± 0.38	-0.07 ± -0.07	-0.24 ± 0.31
225	0.96	345.0 ± 19.0	-0.42 ± 0.24	-0.38 ± 0.22	0.57 ± 0.40	-0.40 ± -0.40	-0.26 ± 0.35
270	0.81	361.1 ± 20.7	-0.16 ± 0.26	-0.08 ± 0.22	0.16 ± 0.39	-0.11 ± -0.11	-0.12 ± 0.33
315	0.78	328.2 ± 18.2	0.33 ± 0.24	-0.05 ± 0.24	0.12 ± 0.42	0.13 ± 0.13	-0.11 ± 0.38
360	0.89	321.9 ± 16.6	0.40 ± 0.23	-0.49 ± 0.24	-0.02 ± 0.40	-0.03 ± -0.03	-0.17 ± 0.36
405	0.93	324.8 ± 17.9	0.21 ± 0.26	-0.39 ± 0.23	-0.13 ± 0.37	-0.13 ± -0.13	-0.52 ± 0.32
450	0.97	314.2 ± 18.4	-0.65 ± 0.28	0.05 ± 0.21	0.24 ± 0.35	-0.20 ± -0.20	-0.31 ± 0.31
495	0.97	329.4 ± 20.2	-0.19 ± 0.23	0.20 ± 0.21	0.08 ± 0.39	0.03 ± 0.03	0.06 ± 0.30
540	0.98	341.3 ± 20.8	0.09 ± 0.22	0.25 ± 0.21	0.21 ± 0.37	0.17 ± 0.17	0.34 ± 0.34
585	0.94	358.2 ± 20.5	-0.30 ± 0.27	0.29 ± 0.24	0.25 ± 0.48	0.03 ± 0.03	0.16 ± 0.36
630	0.92	337.8 ± 19.2	-0.27 ± 0.26	0.07 ± 0.25	-0.74 ± 0.45	-0.09 ± -0.09	-0.10 ± 0.41
675	0.90	329.6 ± 19.1	-0.21 ± 0.29	0.05 ± 0.26	-1.37 ± 0.40	-0.06 ± -0.06	-0.08 ± 0.34
720	0.90	348.1 ± 21.6	0.20 ± 0.25	0.06 ± 0.25	-1.42 ± 0.43	0.13 ± 0.13	0.11 ± 0.29
765	0.95	339.0 ± 21.1	0.31 ± 0.26	0.06 ± 0.24	-0.25 ± 0.45	0.17 ± 0.17	0.14 ± 0.33
810	0.90	325.8 ± 19.6	0.38 ± 0.28	-0.04 ± 0.25	-0.35 ± 0.49	0.15 ± 0.15	0.06 ± 0.42
855	0.89	321.8 ± 18.6	0.22 ± 0.24	0.14 ± 0.23	-0.28 ± 0.58	0.18 ± 0.18	0.38 ± 0.37
900	0.95	327.4 ± 18.6	0.75 ± 0.27	-0.07 ± 0.24	0.31 ± 0.49	0.30 ± 0.30	0.37 ± 0.40
945	0.90	329.2 ± 19.6	-0.14 ± 0.32	0.02 ± 0.26	1.66 ± 0.57	-0.04 ± -0.04	0.10 ± 0.38
990	0.89	361.6 ± 21.6	-0.65 ± 0.30	0.15 ± 0.25	0.38 ± 0.47	-0.18 ± -0.18	-0.09 ± 0.33
1035	0.85	356.3 ± 22.8	-0.41 ± 0.28	-0.09 ± 0.23	-0.18 ± 0.45	-0.22 ± -0.22	-0.05 ± 0.35
1080	0.85	306.3 ± 20.9	-0.29 ± 0.28	0.03 ± 0.21	0.39 ± 0.44	-0.09 ± -0.09	0.14 ± 0.35

Table A.87 – Same as in Table A.1, but for KIC 12317678.

B. First-author publications

Spot cycle reconstruction: an empirical tool - Application to the sunspot cycle
The increasing interest in understanding stellar magnetic activity cycles is a strong motivation for the development of parameterized starspot models which can be constrained observationally. In this work we develop an empirical tool for the stochastic reconstruction of sunspot cycles, using the average solar properties as a reference. The synthetic sunspot cycle is compared with the sunspot data extracted from the National Geophysical Data Center, in particular using the Kolmogorov-Smirnov test. This tool yields synthetic spot group records, including date, area, latitude, longitude, rotation rate of the solar surface at the group's latitude, and an identification number. Comparison of the stochastic reconstructions with the daily sunspot records confirms that our empirical model is able to successfully reproduce the main properties of the solar sunspot cycle. As a by-product of this work, we show that the Gnevyshev-Waldmeier rule, which describes the spots' area-lifetime relation, is not adequate for small groups and we propose an effective correction to that relation which leads to a closer agreement between the synthetic sunspot cycle and the observations.

On the contribution of sunspots to the observed frequency shifts of solar acoustic modes
Activity-related variations in the solar oscillation properties have been known for 30 years. However, the relative importance of the different contributions to the observed variations is not yet fully understood. Our goal is to estimate the relative contribution from sunspots to the observed activity-related variations in the frequencies of the acoustic modes. We use a variational principle to relate the phase differences induced by sunspots on the acoustic waves to the corresponding changes in the frequencies of the global acoustic oscillations. From the sunspot properties (area and latitude as a function of time), we are able to estimate the spot-induced frequency shifts. These are then combined with a smooth frequency shift component, associated with long-term solar-cycle variations, and the results compared with the frequency shifts derived from the Global Oscillation Network Group data. The result of this comparison is consistent with a sunspot contribution to the observed frequency shifts of roughly 30 per cent, with the remaining 70 per cent resulting mostly from a global, non-stochastic variation, possibly related to the changes in the overall magnetic field. Moreover, analysis of the residuals obtained after the subtraction of the model frequency shifts from the observations indicates the presence of a 1.5-yr periodicity in the data in phase with the quasi-biennial variations reported in the literature.

A thorough analysis of the short- and mid-term activity-related variations in the solar acoustic frequencies
The frequencies of the solar acoustic oscillations vary over the activity cycle. The variations in other activity proxies are found to be well correlated with the variations in the acoustic frequencies. However, each proxy has a slightly different time behaviour. Our goal is to characterize the differences between the time behaviour of the frequency shifts and of two other activity proxies, namely the area covered by sunspots and the 10.7-cm flux. We define a new observable that is particularly sensitive to the short-term frequency variations. We then compare the observable when computed from model frequency shifts and from observed frequency shifts obtained with the Global Oscillation Network Group (GONG) for cycle 23. Our analysis shows that on the shortest time-scales, the variations in the frequency shifts seen in the GONG observations are strongly correlated with the variations in the area covered by sunspots. However, a significant loss of correlation is still found. We verify that the times when the frequency shifts and the sunspot area do not vary in a similar way tend to coincide with the times of the maxima of the quasi-biennial variations seen in the solar seismic data. A similar analysis of the relation between the 10.7-cm flux and the frequency shifts reveals that the short-time variations in the frequency shifts follow even more closely those of the 10.7-cm flux than those of the sunspot area. However, a loss of correlation between frequency shifts and 10.7-cm flux variations is still found around the same times.

Starspot signature on the light curve Learning about the latitudinal distribution of spots
Quasi-periodic modulations of the stellar light curve may result from dark spots crossing the visible stellar disc. Owing to differential rotation, spots at different latitudes generally have different rotation periods. Hence, by studying spot-induced modulations, it is possible to learn about stellar surface (differential) rotation and magnetic activity. Recently, a method based on the Lomb-Scargle periodogram of light curves has been proposed to identify the sign of the differential rotation at the stellar surface. Our goal is to understand how the modulation of the stellar light curve due to the presence of spots and the corresponding periodogram are affected by both the stellar and spot properties. We generate synthetic light curves of stars with different properties (inclination angle, limb darkening, and rotation rate) and spot configurations (number of spots, latitude, intensity contrast, and size). By analysing their Lomb-Scargle periodograms, we compute the ratio between the heights of the second and first harmonics of the rotation period (peak-height ratio). We find that the peak-height ratios are essentially a function of a single parameter, the fraction of time the spot is visible, which is related to the sinusoidality of the spot modulation. We identify the conditions under which the periodogram analysis can actually provide an estimate of the spot latitudes and/or the stellar inclination angle. We also identify possible sources of error in the identification of the sign of the differential rotation.

A&A 580, A62 (2015)
DOI: 10.1051/0004-6361/201425299

Astronomy & Astrophysics

Spot cycle reconstruction: an empirical tool⋆

Application to the sunspot cycle

A. R. G. Santos[1,2,3,4], M. S. Cunha[1,2,3], P. P. Avelino[1,2,3], and T. L. Campante[4]

[1] Instituto de Astrofísica e Ciências do Espaço, Universidade do Porto, CAUP, Rua das Estrelas, 4150-762 Porto, Portugal
e-mail: asantos@astro.up.pt
[2] Centro de Astrofísica da Universidade do Porto, Rua das Estrelas, 4150-762 Porto, Portugal
[3] Departamento de Física e Astronomia, Faculdade de Ciências, Universidade do Porto, Rua do Campo Alegre 687, 4169-007 Porto, Portugal
[4] School of Physics and Astronomy, University of Birmingham, Edgbaston, Birmingham B15 2TT, UK

Received 7 November 2014 / Accepted 4 June 2015

ABSTRACT

Context. The increasing interest in understanding stellar magnetic activity cycles is a strong motivation for the development of parameterized starspot models which can be constrained observationally.
Aims. In this work we develop an empirical tool for the stochastic reconstruction of sunspot cycles, using the average solar properties as a reference.
Methods. The synthetic sunspot cycle is compared with the sunspot data extracted from the National Geophysical Data Center, in particular using the Kolmogorov-Smirnov test. This tool yields synthetic spot group records, including date, area, latitude, longitude, rotation rate of the solar surface at the group's latitude, and an identification number.
Results. Comparison of the stochastic reconstructions with the daily sunspot records confirms that our empirical model is able to successfully reproduce the main properties of the solar sunspot cycle. As a by-product of this work, we show that the Gnevyshev-Waldmeier rule, which describes the spots' area-lifetime relation, is not adequate for small groups and we propose an effective correction to that relation which leads to a closer agreement between the synthetic sunspot cycle and the observations.

Key words. Sun: activity – Sun: oscillations – stars: activity – stars: oscillations – sunspots – starspots

1. Introduction

In the Sun, the level of magnetic activity varies over time showing a periodic behaviour known as the solar cycle. The most direct evidence for this is the 11-yr variation in the number of sunspots observed at the solar photosphere. As the cycle proceeds, the sunspot formation zone gradually migrates towards the equator until the next minimum is reached and a new cycle begins. At that point, the polarity of the magnetic field reverses and returns to the original state at the end of the second 11-yr cycle, thus completing a 22-yr Hale cycle (the sunspot polarity law – Hale et al. 1919; Hale & Nicholson 1925).

Evidence for the presence of activity cycles in other solar-like stars, including exoplanet hosts, has also been accumulating over the past years. Starspots cannot be observed directly at the surface of distant stars, but can be detected indirectly through the effects they induce, such as the strong emission at the centre of the Ca H and K lines. By monitoring this emission, it is possible to infer the rotation period of the star and the period of its magnetic cycle (e.g. Wilson 1978; Duncan et al. 1991; Gray & Baliunas 1995; Saar & Brandenburg 1999; Cincunegui et al. 2007; Hall et al. 2007; Metcalfe et al. 2010, 2013). Moreover, since spots are darker than the average stellar surface they can also be detected through the inspection of the photometric light curves of stars observed by CoRoT (Baglin et al. 2006) and *Kepler* (Borucki et al. 2010; Koch et al. 2010) space missions. In an active star with starspots crossing the visible disk, the light curve shows a quasi-periodic modulation which results from the combination of the effects of stellar rotation and magnetic activity (e.g. Mosser et al. 2009; Mathur et al. 2010; García et al. 2010; Ballot et al. 2011; Campante et al. 2011). That modulation is more significant in periods of maximum activity, making the light curves a possible starspot proxy. In addition, through the wavelet analysis of the light curves it might be possible to obtain information about the time evolution of the starspots at the stellar surface and, in turn, derive the period of the activity cycle and the rotation period of the star (e.g. Campante 2012; Mathur et al. 2014; García et al. 2014; Bravo et al. 2014). Finally, stellar activity cycles may also be detected through their impact on stellar oscillations because the magnetic activity affects the wave propagation, inducing changes to the oscillation frequencies, amplitudes, and line widths, which are thus found to vary in phase with other sun-/starspot proxies (e.g. Woodard & Noyes 1985; Libbrecht & Woodard 1990; Chaplin et al. 2004; Metcalfe et al. 2007; García et al. 2010; Tripathy et al. 2011).

Starspots simulations can be used to study how the activity-induced variability in the light curve and in the oscillation properties depends on the characteristics of the activity cycle. These simulations are important in other astrophysical contexts, such as in the quest for exoplanets, where they can be used to design new strategies to reduce the signatures induced by stellar activity on the radial velocity and transit observations (e.g. Pont et al. 2008; Czesla et al. 2009; Figueira et al. 2010; Dumusque et al. 2011; Oshagh et al. 2013, 2014). With the above in mind, in this work we develop a parameterized model aimed at reproducing the main properties of the sunspot cycle that can also be applied

⋆ Appendix A is available in electronic form at http://www.aanda.org

to reproducing the activity cycles of other stars. In order to build our empirical model, we use as inputs a number of properties of the observed sunspot cycle. These properties are summarized in Sect. 2 and their implementation in our model is discussed in Sect. 3. The results obtained with this tool and their comparison with the solar data extracted from the National Geophysical Data Center (NOAA/NGDC) are presented in Sect. 4. Finally, in Sect. 5 we draw our main conclusions.

2. Properties of the solar cycle

In order to reproduce the sunspot cycle, a number of important observational constraints must be considered. In what follows we review key observational properties of the sunspot cycle that will be used in our model, namely: the number of sunspot groups and its dependence on the phase of the cycle; the sunspots' areas and their relation with the sunspots' lifetimes; the formation latitude of the sunspots and the width of the formation region; the differential rotation of the solar surface.

The number of sunspots and sunspot groups varies over the solar cycle. Its evolution is asymmetric: the rising phase of the cycle is faster than the declining towards the next minimum. Different authors have used different functions to describe the asymmetric shape of the sunspot cycle (e.g. Setwart & Panofsky 1938; Elling & Schwentek 1992; Sabarinath & Anilkumar 2008; Volobuev 2009; Du 2011). In particular, Hathaway et al. (1994) found that the observed number of sunspots is nicely fitted by the following function of time,

$$N_S(t) = \frac{a_1(t-t_0)^3}{\exp((t-t_0)^2/b_1^2) - c_1}, \quad (1)$$

where t_0 is the starting time (about four months prior to the minimum for an average cycle (Hathaway 2010)), a_1 is the amplitude, b_1 is related to the size of the cycle, and c_1 is related to the asymmetry of the cycle.

The asymmetric shape of the solar cycle is also evident in the temporal variation of the sunspot areas. Bogdan et al. (1988) were the first to notice that the accumulated umbral areas distribution (derived from daily records by counting each spot as many times as the number of days it remains visible) can be described by a log-normal distribution. Since the ratio between the umbral area and the total area of the spot does not depend significantly on the spot size (e.g. Brandt et al. 1990; Solanki 2003; Vaquero et al. 2005; Kiess et al. 2014), the accumulated spot areas also follow a log-normal distribution. This finding was confirmed by later studies (e.g. Baumann & Solanki 2005; Hathaway & Choudhary 2008; Kiess et al. 2014). Moreover, Baumann & Solanki (2005) have shown that the log-normal distribution also nicely fits the observed distributions for the instantaneous area and for the maximum area of sunspots. However, according to Jiang et al. (2011), the area distribution for groups smaller than 60 MSH (millionth of the solar hemisphere) is better described by a power law.

During its life, a given sunspot group grows until it reaches a maximum area and then decays. The growth (Ψ) and decay (Γ) rates, i.e. the time derivative of the group's area during each of these phases, are found to be dependent on the group areas, the activity cycle, the phase of the cycle, and the latitude (e.g. Moreno-Insertis & Vázquez 1988; Howard 1992; Petrovay & van Driel-Gesztelyi 1997; Hathaway & Choudhary 2008; Javaraiah 2012). Small groups grow faster than they decay, while the growth rates of large groups are smaller than their decay rates (Howard 1992). Hathaway & Choudhary (2008) found a linear relation between the decay rates and the group area, but the erosion model proposed earlier by Petrovay & van Driel-Gesztelyi (1997) indicates a non-linear relation of the type $\Gamma \propto A^{0.5}$, where A is the group area at a given time. More recently, Javaraiah (2012) suggested that the relation between the decay rates and areas could be better described by a power law of the form $\Gamma = \exp(\gamma_1)A^{\gamma_2}$. The constant γ_2 was found to vary from ~0.45 to ~0.70, when considering individual cycles and different phases of each cycle (with A expressed in MSH). When assuming the sunspot data from 1874–2011, Javaraiah (2012) found that $\gamma_1 \sim 0.26$ and $\gamma_2 \sim 0.613$. On the other hand, the same study did not produce conclusive results regarding the relation between the group's growth rate and its area.

The areas of sunspots and sunspot groups are also related to their lifetimes, which can range from hours to months, depending on their size. This dependency is described by the Gnevyshev-Waldmeier (GW) rule (Gnevyshev 1938; Waldmeier 1955), according to which,

$$A_m = D_{GW}T. \quad (2)$$

Here, A_m is the sunspot or sunspot group maximum area (in MSH), T is the corresponding lifetime, and D_{GW} is a constant of proportionality (around 10 MSH day^{-1}). The determination of a precise value for D_{GW} is hampered by the difficulty in measuring the spots' lifetimes due to the nightfall, the solar rotation (lack of observations of the invisible side of the Sun), and limb darkening (e.g. Henwood et al. 2009; Blanter et al. 2006; Solanki 2003). In spite of these difficulties, some studies have been carried out, indicating that D_{GW} might be larger than first estimated. Petrovay & van Driel-Gesztelyi (1997) found that D_{GW} is 10.89 ± 0.18 MSH day^{-1} for individual sunspots. More recently, Henwood et al. (2009) studied long-lived sunspot groups and estimated that $D_{GW} = 11.73 \pm 0.26$ MSH day^{-1}.

As was first reported by Carrington (1863), the sunspot formation latitude also varies periodically with time. At the beginning of a new cycle the first spots appear at latitudes of about ±40°. The succeeding spots form at progressively lower latitudes, being rarely observed within ±5°. At the solar minimum the last spots of the cycle emerge at low latitudes, while spots of the new cycle start to form at high latitudes. This behaviour is known as the Spörer law and it may be seen in the butterfly diagram (or Maunder diagram; Maunder 1904). Despite the presence of short plateaus at intermediate latitudes (~10° – around maximum; Chang 2012), Hathaway (2011) found that the drift of the sunspot zones follows an exponential function, where the average latitude, L_S, is given by

$$L_S(t) = L_0 \exp\left(-\frac{t-t_0}{7.5}\right), \quad (3)$$

where L_0 is the mean latitude at the time t_0, and t is expressed in years. By considering the intermediate phases of the cycle where there is no overlap between consecutive cycles, Jiang et al. (2011) verified that the evolution of the average latitude can also be described by a second-order polynomial.

Chang (2012) found that the spatial distribution of the sunspot groups at each time t is bimodal and that it can be described by a double Gaussian; instead, Ivanov et al. (2011) showed that one single Gaussian describes the data reasonably well. Moreover, the width of the sunspot formation zone, σ_L, also varies over the solar cycle (Gleissberg 1958). According to Miletskii & Ivanov (2009), Ivanov et al. (2011), and Ivanov & Miletskii (2011), this width is a linear function of the activity

level. However, according to Jiang et al. (2011), it can be described in relation to the average sunspot group latitude by a second-order polynomial of the form

$$\frac{\sigma_L}{L_S} = a_\sigma + b_\sigma \frac{t - t_{min}}{P_c} + c_\sigma \left(\frac{t - t_{min}}{P_c} \right)^2, \quad (4)$$

where a_σ, b_σ, and c_σ are the coefficients of the polynomial, t_{min} corresponds to the minimum, and P_c is the period of the cycle.

We note that sunspots are depressed (Wilson depression), thus they move according to the subphotospheric layers, i.e. slightly faster than the solar surface (e.g. Zappalà & Zuccarello 1991; Zuccarello 1993; Abuzeid & Marik 1997; Schou et al. 1998; Kitchatinov 2011). Since the spots' depths decrease as they evolve, younger spots also move faster than the older ones.

Finally, we note that the properties described above vary from cycle to cycle and some are found to be correlated (e.g. Solanki et al. 2002, 2008; Hathaway 2010; Jiang et al. 2011).

3. Empirical solar cycle model

The primary goal of this work is to produce a tool capable of reproducing an activity cycle that retains the main observational properties of the solar cycle. To that end, we develop an empirical model to generate sunspot groups as a function of time and gradually adapt the model assumptions and inputs until our goal is reached. To decide whether or not a given assumption/input is a better representation of the observational data than the previous ones we use the Kolmogorov-Smirnov test, which is described in Sect. 4.2.

3.1. Number of sunspot groups

In our model, each sunspot group is generated independently from the others. This could not be assumed if we were considering individual spots, since the formation of spots within the same group is not independent.

At each time step (fixed on one day to be comparable to the daily records of the sunspot data), N groups are formed. The number of generated groups is randomly determined using a Poisson distribution with a mean value N_m that depends on time. In the current version of the model, N_m is taken to be one sixth of N_s, where the function of time N_s is derived from a fit of Eq. (1) to the number of observed sunspot groups for solar cycle 23 (Fig. 1). With this choice for N_m, we find that the function N_s derived from the fit to the synthetic data is always in reasonable agreement with that derived from the solar data.

Other ways to determine N_s from the solar data were explored. The functions used by Du (2011) and Sabarinath & Anilkumar (2008; the latter takes into account the double peak feature of the solar cycle) led to results that are comparable to those obtained with Eq. (1).

3.2. Sunspot formation zone

In our model, the latitude of each spot, L, is determined randomly through a single-Gaussian distribution, with a mean latitude L_S and dispersion σ_L, both dependent on time. For L_S, we use Hathaway's exponential function given by Eq. (3) fitted to the northern hemisphere solar data for cycle 23 (Fig. 2), with t_0 fixed at the value found in Sect. 3.1. We opted to use solar data from a single hemisphere because in our model we do not account for the north-south asymmetry. For σ_L, we assume a second-order polynomial (Fig. 3), as suggested by Jiang et al. (2011). Other functions were considered to describe the latitudinal distribution of the sunspot groups (both for L_S and σ_L). However, those led to a lower level of agreement between the synthetic and the observational data.

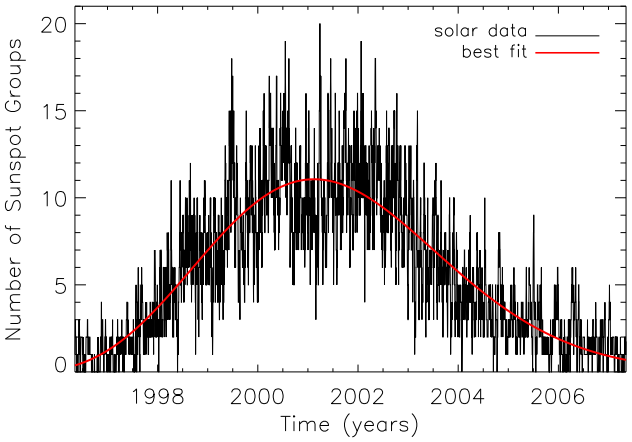

Fig. 1. Variation of the number of sunspot groups over the solar cycle 23 (black). The red smooth line corresponds to the fit obtained using the function defined by Hathaway et al. (1994). The observational data were extracted from NOAA.

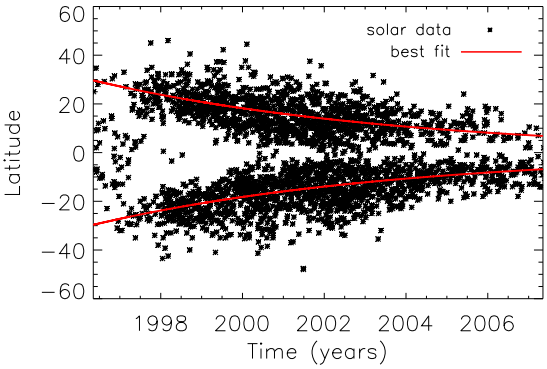

Fig. 2. Comparison between the latitudinal distribution of sunspots and the exponential fit of Hathaway (2011). The observational data was extracted from NOAA.

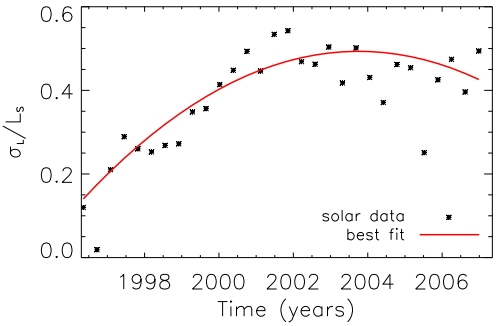

Fig. 3. Ratio between the standard deviation of the latitudinal distribution and the corresponding mean latitude (observational data from NOAA). The red solid line corresponds to the best fit.

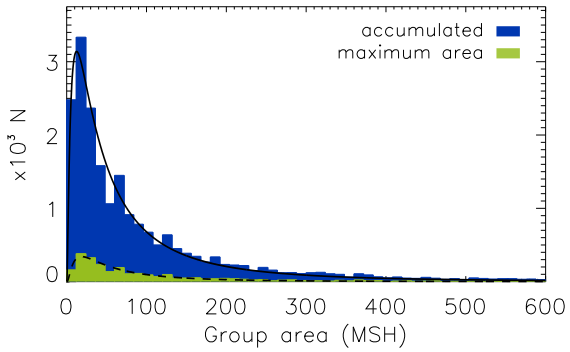

Fig. 4. Accumulated (blue) and maximum (green) area distributions for the solar data from NOAA. The black lines are the respective log-normal fits.

3.3. Sunspot group areas and lifetimes

Having defined the procedure to generate the number of sunspot groups and their position in latitude at each time step, we need to associate a maximum area (A_m) to each of them. Although the mean group area varies over the solar cycle (e.g. Jiang et al. 2011), we fix the area distribution. In accordance with the discussion in Sect. 2, in our model the sunspot group maximum areas are drawn from a log-normal distribution whose parameters are obtained from a log-normal fit to the sunspot groups observations for cycle 23, considering each group only once and its maximum area (Fig. 4).

With the sunspot maximum area in hand, we can in principle determine the group's lifetime through the GW rule. However, we have found that when the GW rule is taken for all ranges of areas, the accumulated area distribution obtained with the empirical tool is not in agreement with the observed distribution: the number of small groups in the synthetic distribution is lower than that found in the Sun and the peaks of the two distributions do not coincide. The upper panel of Fig. 5 illustrates this disagreement.

The GW rule is based on the observation of long-lived spot groups (e.g. groups that live longer than ~20 days; Henwood et al. 2009). Hence, it is possible that this rule may not be adequate for the smallest groups. In fact, by tracking the small groups in the solar data for cycle 23 and comparing the time they remain visible with the lifetime predicted by the GW rule, it is possible to verify that the GW rule generally underestimates the lifetimes of the small groups. Moreover, there is a significant dispersion around the area-lifetime relation, which for the smallest groups is strongly asymmetric (since lifetimes cannot be negative). With this in mind, we have checked whether increasing the lifetimes for the small groups would improve the agreement between the observed and synthetic accumulated area distributions and found that substituting the GW linear relation by an exponential relation at the lower areas end, our model produces an accumulated area distribution that is in better agreement with the observed one (lower panel of Fig. 5). The modification of the GW rule for groups with areas smaller than 85 MSH used in our model is

$$T = 5\exp(6.2591 \times 10^{-3} A_m). \quad (5)$$

Figure 6 shows the current area-lifetime relation used in our empirical model (red line).

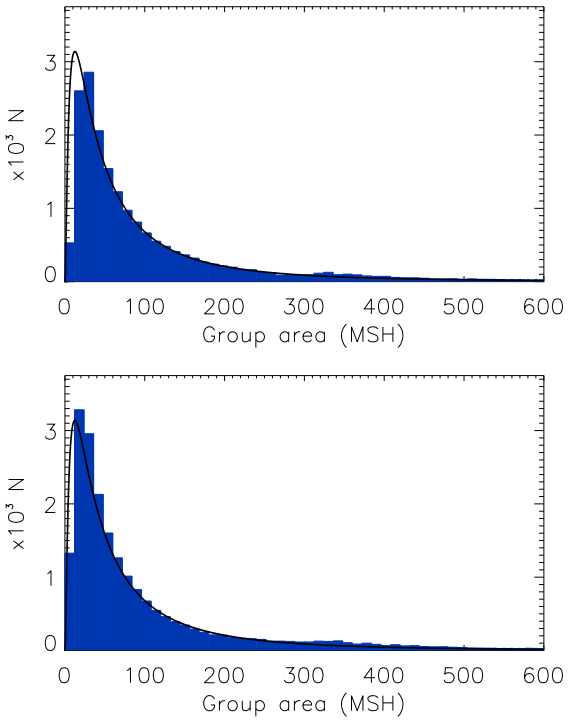

Fig. 5. Accumulated area distribution for synthetic sunspot groups when assuming the GW rule for all areas (*upper panel*) and when using the modified area-lifetime relation (*lower panel*). The black, solid line is the log-normal fit to the observational data[1].

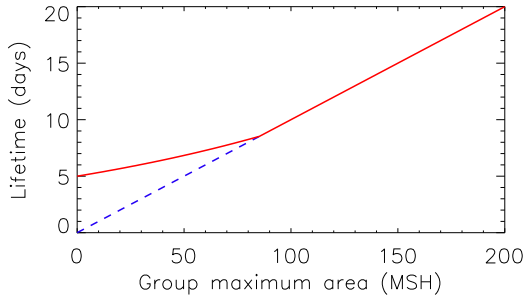

Fig. 6. The red line shows the area-lifetime relation assumed in the current model while the blue dashed line shows the lifetime predicted for small groups by the GW rule.

Taking the group's maximum area and lifetime, we determine the group's area at a posterior time (while $A > 0$) by applying a decay rate of the form $\Gamma = \exp(\gamma_1)A^{\gamma_2}$. We then assume that the period during which the group grows corresponds to the difference between its lifetime and the decay time. In the absence of a well-established relation between the group's growth rate and its area, we opted for a power law to describe that relation, i.e. $\Psi = \exp(\psi_1)A^{\psi_2}$. We started by considering the values found by Javaraiah (2012) for γ_1 and γ_2, making $\gamma_1 = \psi_1 = 0.26$ and $\gamma_2 = \psi_2 = 0.613$. These parameters were progressively changed until a reasonable agreement between the observations and the synthetic data was reached. The current version of the model

[1] The bin for the smallest groups is incomplete, as the sunspot records are limited to areas larger than 10 MSH.

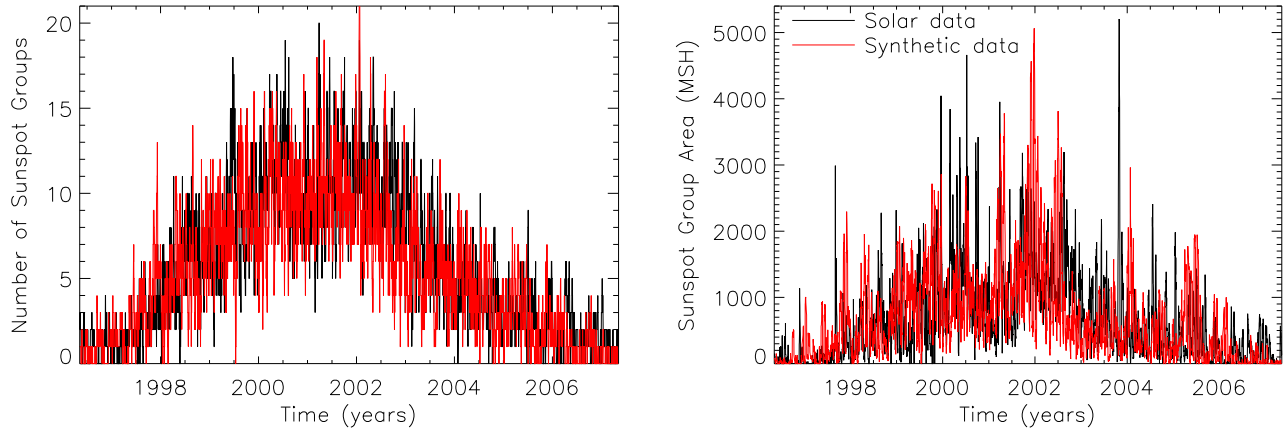

Fig. 7. Comparison between real solar data for cycle 23 (black) and synthetic data (red). Shown are the number of sunspot groups (*left panel*) and the total group area (*right panel*).

considers $\Psi = \exp(0.17)\, A^{0.46}$ and $\Gamma = \exp(0.17)\, A^{0.47}$, which is consistent with the fact that large groups have higher decay rates than growth rates. For small groups the growth and decay rates given by the expressions above are essentially the same. However, since the growth time is taken as the difference between the lifetime and the decay time, in practice the smallest groups do not show a growth phase in the daily records, which might be interpreted as a fast growth, where they reach the maximum area in a time shorter than the interval between consecutive records (one day). We also tested the linear relation found by Hathaway & Choudhary (2008), but we found that decay rates are too high when compared with the lifetime of the group. Assuming the linear relation for the growth and decay rates, the time interval from the first appearance (with $A \sim 0$) to the last appearance (with $A \sim 0$) is much shorter than the lifetime from the modified GW rule.

3.4. Sunspot visibility

To reproduce the daily sunspot records of the Sun, we take into account the solar rotation and the fact that spots are observed only when they are on the Sun's visible side. The group's longitude is determined randomly from a uniform distribution between 0 and 2π. If this quantity is smaller than π, we consider that the sunspot group is on the visible side, otherwise we consider that it cannot be observed. Taking into account that the rotation velocity of the subphotospheric layers is not very different from that of the solar surface, we assume the following parameterization of the groups' rotation velocity, ω, as a function of their latitude, L (Snodgrass 1983; Snodgrass & Ulrich 1990)

$$\omega(L) = 14.71 - 2.33 \sin^2 L - 1.78 \sin^4 L. \quad (6)$$

Spot groups that emerge on the visible side of the Sun can move towards the invisible side and then eventually become visible again depending on their lifetimes and on the solar angular velocity at the latitude they emerge. Moreover, groups that emerge on the invisible side of the Sun can become visible. Both these facts are taken into account in our model and only groups with an area greater than ~10 MSH are considered visible (in analogy to the sunspot data).

A schematic summary of our empirical model is shown in Appendix A.

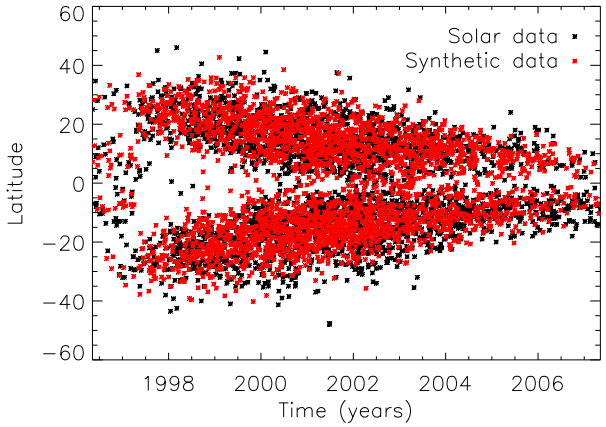

Fig. 8. Same as in Fig. 7, but for the real and synthetic latitudinal distribution of sunspot groups.

4. Results

4.1. Synthetic data

The synthetic data produced with our empirical model provide information about each generated group. In analogy to what is done in the NOAA databases, the code yields the sunspot group records, which include date, latitude, group area, lifetime, position in longitude, rotation rate of the solar surface at the group's latitude, and an identification number. These records are then used to compare our results with observed data.

A comparison between the number of sunspot groups observed over cycle 23 (in black) and those obtained in one realization of our model (in red) is shown in the left panel of Fig. 7. The similarity in the shape and spread of the two curves is quite evident. The same similarity is found when comparing the total group areas, i.e. the total area covered by sunspot groups in each day, (Fig. 7, right panel) and the group latitudes (Fig. 8) for the real and synthetic data.

4.2. Comparison test

In order to test and improve our model we have quantified how closely related the observed and synthetic data sets are

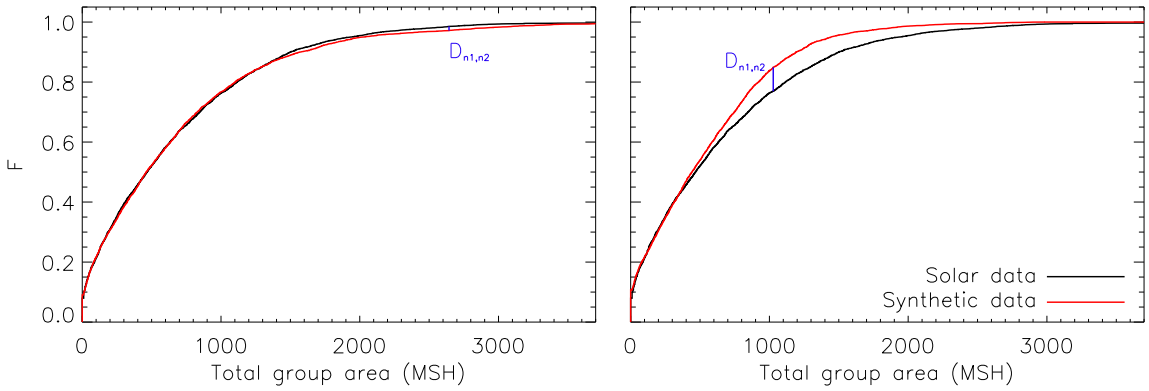

Fig. 9. Cumulative distribution functions of the synthetic (red) and real data (black) for the total group areas of a reconstruction obtained from the current version of the model (*left panel*; $D_{n_1,n_2} \sim 0.0141$) and a reconstruction obtained when assuming the GW rule for the area-lifetime relation (*right panel*; $D_{n_1,n_2} \sim 0.0798$).

by applying the Kolmogorov-Smirnov test (Kolmogorov 1933; Smirnov 1939). This test compares the cumulative distribution functions of two samples, using the maximum deviation between them,

$$D_{n_1,n_2} = \max_x |F_{1,n_1}(x) - F_{2,n_2}(x)|, \quad (7)$$

where n_1 and n_2 are the number of elements of sample 1 and sample 2, respectively, and F_1 and F_2 are the corresponding cumulative distribution functions.

The null hypothesis – i.e. that both samples result from the same distribution – is rejected at significance level α if

$$D_{n_1,n_2} > c(\alpha)\sqrt{\frac{n_1+n_2}{n_1 n_2}}, \quad (8)$$

where $c(\alpha)$ is a constant that depends of the significance level to be considered.

More than to reject the null hypothesis at a given level α, in our case this test was used to identify the aspects of the model which needed to be improved. The synthetic sunspot cycles obtained from early versions of the model resulted in large values of D_{n_1,n_2}, indicating that they did not provide a good description of the observed properties of the sunspot cycle. By comparing the observed and synthetic cumulative distribution functions for the total area covered by sunspot groups and for the groups' latitudinal distribution, we could decide where and how to improve our model. An example of this is provided in Fig. 9, where we compare the cumulative distribution functions for the total group areas of the synthetic and real data. In this case, F corresponds to the fraction of days with total area below a given value, and $n_1 = n_2 = 4017$ is the total number of days considered in the real and synthetic data. The left panel corresponds to a sunspot cycle reconstruction obtained with the current version of the model that considers an exponential function (Eq. (5)) to correct the GW rule for groups smaller than 85 MSH, while the right panel shows the results for a reconstruction obtained when adopting the GW rule for all group areas. Small groups from the former reconstruction live longer than groups with similar areas from the latter. This leads to an increase in the daily number of sunspot groups and, consequently, to a larger total area covered by the groups in the reconstruction obtained with the model that incorporates the corrected area-lifetime relation than with the other. The result is a shift of the cumulative distribution function towards larger areas and a better agreement with the observations.

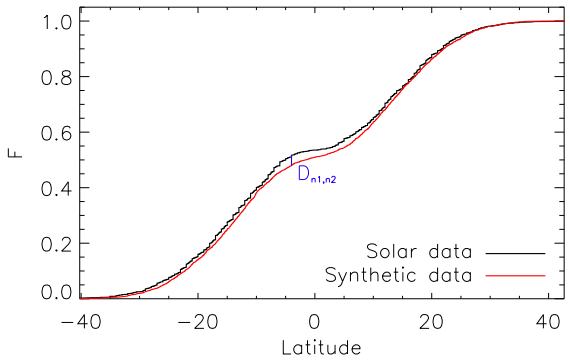

Fig. 10. Cumulative distribution functions of the synthetic (from the current model; red) and real data (black) for the spot latitudes. The maximum difference is $D_{n_1,n_2} \sim 0.0377$ (blue).

Figure 10 compares the cumulative functions for the real and synthetic latitudes resulting from the same reconstruction, obtained with the current version of the empirical model. Here, the cumulative distribution functions, F, represent the fraction of groups that become visible (first appearance) at a latitude lower than a given value, and $n_1 = 2801$ and $n_2 = 2919$ correspond to the total number of different observed groups in the real and synthetic data, respectively. Despite the small value of the statistics D_{n_1,n_2}, the difference between the two distributions is significant and its interpretation is relatively straightforward: the cumulative distribution function for the solar data indicates that the southern hemisphere retains almost 55% of the visible sunspot groups, while for the synthetic data the groups are more evenly distributed by the two hemispheres. This discrepancy results from the hemispheric asymmetry that is known to be present in the data, but that is not accounted for in our model. To verify this, we compared the cumulative distribution functions for the absolute values of the latitude (Fig. 11), finding a lower value of the statistics D_{n_1,n_2}.

The results from the KS-test for the synthetic sunspot cycle discussed above are summarized in Table 1. At the significance level $\alpha = 0.1$ the null hypothesis for the total group area and absolute group latitudes is not rejected. Although the non-rejection of the null hypothesis does not allow us to conclude about its veracity, it certainly reinforces the expectation born from the direct inspection of Figs. 7 and 8 that the synthetic

Table 1. Results from the KS-test for the synthetic sunspot cycle discussed in the text.

	n_1	n_2	D_{n_1,n_2}	$\mathcal{D}(\alpha = 0.1)$
Total group area: Fig. 9, left	4017	4017	0.0141	0.0272
Latitudes – Fig. 10	2801	2919	0.0377	0.0323
Absolute latitudes – Fig. 11			0.0283	

Notes. The n_1 and n_2 are the sample sizes for the real and synthetic data, respectively. $\mathcal{D} = c(0.1)\sqrt{(n_1 + n_2)/(n_1 n_2)}$ is the right-hand side of Eq. (8) for a significance $\alpha = 0.1$.

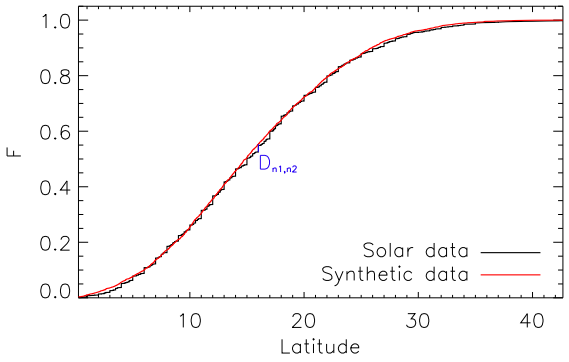

Fig. 11. Cumulative distribution functions of the synthetic (from the current model; red) and real data (black) for the absolute values of the group latitudes. The maximum deviation is $D_{n_1,n_2} \sim 0.0283$.

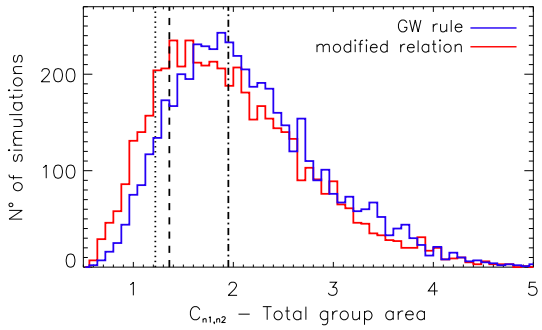

Fig. 12. Distribution of $C_{n_1,n_2} = D_{n_1,n_2}/\sqrt{(n_1 + n_2)/(n_1 n_2)}$ for the total area covered by sunspot groups, when assuming the GW rule for all areas (blue histogram) and when using the modified area-lifetime relation (red histogram). The vertical lines indicate the levels of significance $\alpha = 0.1$ (dotted), $\alpha = 0.05$ (dashed) and $\alpha = 0.001$ (dash-dotted).

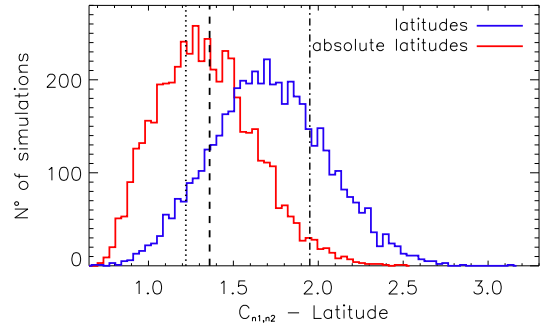

Fig. 13. Distribution of $C_{n_1,n_2} = D_{n_1,n_2}/\sqrt{(n_1 + n_2)/(n_1 n_2)}$ for the latitudinal distribution: from the group latitudes (blue) and absolute latitudes (red). The vertical lines indicate the levels of significance $\alpha = 0.1$ (dotted), $\alpha = 0.05$ (dashed) and $\alpha = 0.001$ (dash-dotted).

cycles obtained from our model retain the main observed properties of the sunspot cycle.

As the results from our empirical model are stochastic, we can perform Monte Carlo simulations to obtain the distributions for the statistics D_{n_1,n_2}. While n_2 is constant for the total area covered by sunspot groups, for the latitudinal distribution n_2 varies from reconstruction to reconstruction and according to the case considered (both, southern or northern hemispheres). Thus, rather than considering the distributions for D_{n_1,n_2}, we consider those for the n_2-independent quantity $C_{n_1,n_2} = D_{n_1,n_2}/\sqrt{(n_1 + n_2)/(n_1 n_2)}$. Figures 12 and 13 summarize the results obtained from 5000 cycle reconstructions. The distribution of C_{n_1,n_2} obtained from the analysis of the total group area when the GW rule is assumed for all ranges of area (Fig. 12, blue histogram) is shifted towards larger values of C_{n_1,n_2} than that obtained from reconstructions that apply the correction to the area-lifetime relation for small groups (Fig. 12, red histogram). This confirms that the modified area-lifetime relation used in our model produces results that are statistically in better agreement with the solar data. Concerning the sunspot groups' latitudes (Fig. 13), the comparison of the distributions for C_{n_1,n_2} clearly confirms our earlier findings. The consequence of the non-inclusion of the hemisphere asymmetry in our model is that our synthetic cycles compare significantly better when considering the absolute values of the latitude.

The properties of the sunspot emergence are cycle-dependent, stronger cycles usually having higher latitudes and wider sunspot formation zones than weaker cycles (e.g. Solanki et al. 2008; Jiang et al. 2011). With this in mind we have applied our model to a second cycle, namely cycle 22, which is stronger and more asymmetric than cycle 23. In agreement with the works mentioned above, we found that the average latitude and the width of the sunspot formation zone obtained in our reconstructions for cycle 22 are larger than those obtained for cycle 23. Although the results from the KS-test for the latitudes were found to be worse for cycle 22 owing to the hemispheric asymmetry, we found that with regard to the total area covered by spots and to the absolute latitudes the synthetic data for this cycle is also in qualitative agreement with the real sunspot data.

5. Conclusions

In this work, we have presented an empirical tool for the stochastic reconstruction of sunspot cycles. With the parameters adopted in the version presented here, our tool produces synthetic daily sunspot records which retain the main properties of the real solar data.

A crucial assumption of our model is that different sunspot groups are generated independently. Despite evidence that

sunspots tend to form within active longitudes (e.g. Bumba & Howard 1965; Bogart 1982; Jiang et al. 2011), pointing to possible correlations between their emergence, we found that the properties of the sunspot cycle are reasonably well reproduced under this model assumption. If a significant dependence between the generation existed we would expect that to have been reflected, for example, in a lack of agreement between the dispersion of the number of synthetic and observed sunspot groups as a function of time. In fact, we have checked that this problem would occur if individual spots were (incorrectly) considered as independent events.

An important by-product of our work was the verification that the GW rule is only appropriate for the largest sunspot groups. For the smallest sunspot groups, this rule seems to underestimate the groups' lifetime. We have proposed a modified area-lifetime relation for small groups which leads to a closer agreement of the synthetic sunspot cycle with observations.

The quantity, quality, and diversity of solar data, can only be adequately reproduced by a relatively complex model that includes a number of empirical parameters and functions describing the average observed properties of the sunspot number, area, latitude and rotation. In contrast, for other stars the observational constraints are much more limited. Thus, the application of our tool to the study of activity cycles on other stars will require the identification of the model parameters that have a significant impact on the activity-related stellar observables, including the frequency shifts (work in progress). Another potential application of this kind of tool is related to the search for exoplanets, where new strategies for reducing activity signatures in the radial velocity and transit observations can be designed.

Acknowledgements. A.R.G.S. acknowledges the support from FCT (Portugal) through the grant reference SFRH/BD/88032/2012. M.S.C. and P.P.A. are supported by FCT through the Investigador FCT contracts of reference IF/00894/2012 and IF/00863/2012 and POPH/FSE (EC) by FEDER funding through the program COMPETE. Funds for this work were provided also by the EC, under FP7, through the projects FP7-SPACE-2012-31284 and PIRSES-GA-2010-269194. T.L.C. acknowledges the support of the UK Science and Technology Facilities Council (STFC).

References

Abuzeid, B., & Marik, M. 1997, Sol. Phys., 173, 25
Baglin, A., Michel, E., Auvergne, M., & Team, C. 2006, in Proc. of SOHO 18/GONG 2006/HELAS I, Beyond the spherical Sun, ESA SP, 624, 34
Ballot, J., Gizon, L., Samadi, R., et al. 2011, A&A, 530, A97
Baumann, I., & Solanki, S. K. 2005, A&A, 443, 1061
Blanter, E. M., Le Mouël, J.-L., Perrier, F., & Shnirman, M. G. 2006, Sol. Phys., 237, 329
Bogart, R. S. 1982, Sol. Phys., 76, 155
Bogdan, T. J., Gilman, P. A., Lerche, I., & Howard, R. 1988, ApJ, 327, 451
Borucki, W. J., Koch, D., Basri, G., et al. 2010, Science, 327, 977
Brandt, P. N., Schmidt, W., & Steinegger, M. 1990, Sol. Phys., 129, 191
Bravo, J. P., Roque, S., Estrela, R., Leão, I. C., & De Medeiros, J. R. 2014, A&A, 568, A34
Bumba, V., & Howard, R. 1965, ApJ, 141, 1502
Campante, T. L. 2012, Ph.D. Thesis, Universidade do Porto
Campante, T. L., Handberg, R., Mathur, S., et al. 2011, A&A, 534, A6
Carrington, R. G. 1863, MNRAS, 23, 203
Chang, H.-Y. 2012, New Astron., 17, 247
Chaplin, W. J., Elsworth, Y., Isaak, G. R., Miller, B. A., & New, R. 2004, MNRAS, 352, 1102
Cincunegui, C., Díaz, R. F., & Mauas, P. J. D. 2007, A&A, 469, 309
Czesla, S., Huber, K. F., Wolter, U., Schröter, S., & Schmitt, J. H. M. M. 2009, A&A, 505, 1277
Du, Z. 2011, Sol. Phys., 273, 231
Dumusque, X., Santos, N. C., Udry, S., Lovis, C., & Bonfils, X. 2011, A&A, 527, A82
Duncan, D. K., Vaughan, A. H., Wilson, O. C., et al. 1991, ApJS, 76, 383
Elling, W., & Schwentek, H. 1992, Sol. Phys., 137, 155
Figueira, P., Marmier, M., Bonfils, X., et al. 2010, A&A, 513, L8
García, R. A., Mathur, S., Salabert, D., et al. 2010, Science, 329, 1032
García, R. A., Ceillier, T., Salabert, D., et al. 2014, A&A, 572, A34
Gleissberg, W. 1958, Z. Astrophys., 46, 219
Gnevyshev, M. N. 1938, zv. Gl. Astron. Obs. Pulkove, 16, 36
Gray, D. F., & Baliunas, S. L. 1995, ApJ, 441, 436
Hale, G. E., & Nicholson, S. B. 1925, ApJ, 62, 270
Hale, G. E., Ellermen, F., Nicholson, S. B., & Joy, A. H. 1919, ApJ, 49, 153
Hall, J. C., Lockwood, G. W., & Skiff, B. A. 2007, ApJ, 133, 862
Hathaway, D. H. 2010, Liv. Rev. Sol. Phys., 7, 1
Hathaway, D. H. 2011, Sol. Phys., 273, 221
Hathaway, D. H., & Choudhary, D. P. 2008, Sol. Phys., 250, 269
Hathaway, D. H., Wilson, R. M., & Reichmann, E. J. 1994, Sol. Phys., 151, 177
Henwood, R., Chapman, S. C., & Willis, D. M. 2009, Sol. Phys., 262, 299
Howard, R. F. 1992, Sol. Phys., 137, 51
Ivanov, V. G., & Miletskii, E. V. 2011, Sol. Phys., 268, 231
Ivanov, V. G., Miletskii, E. V., & Nogovitsyn, Y. A. 2011, Astron. Rep., 55, 911
Javaraiah, J. 2012, Astrophys. Space Sci., 338, 217
Jiang, J., Cameron, R. H., Schmitt, D., & Schüssler, M. 2011, A&A, 528, A82
Kiess, C., Rezaei, R., & Schmidt, W. 2014, A&A, 565, A52
Kitchatinov, L. L. 2011, in Astron. Soc. India Conf. Ser., 2, 71
Koch, D. G., Borucki, W., Basri, G., et al. 2010, ApJ, 713, L79
Kolmogorov, A. N. 1933, Giornale dell'Instituto Italiano degli Attuari, 4, 89
Libbrecht, K. G., & Woodard, M. F. 1990, Nature, 345, 779
Mathur, S., García, R. A., Catala, C., et al. 2010, A&A, 518, A53
Mathur, S., García, R. A., Ballot, J., et al. 2014, A&A, 562, A124
Maunder, E. W. 1904, MNRAS, 64, 747
Metcalfe, T. S., Dziembowski, W. A., Judde, P. G., & Snow, M. 2007, MNRAS, 379
Metcalfe, T. S., Basu, S., Henry, T. J., et al. 2010, ApJ, 723, L213
Metcalfe, T. S., Buccino, A. P., Brown, B. P., et al. 2013, ApJ, 763, L26
Miletskii, E. V., & Ivanov, V. G. 2009, Astron. Rep., 53, 857
Moreno-Insertis, F., & Vázquez, M. 1988, A&A, 205, 289
Mosser, B., Baudin, F., Lanza, A. F., et al. 2009, A&A, 506, 245
Oshagh, M., Santos, N. C., Boisse, I., et al. 2013, A&A, 556, A19
Oshagh, M., Santos, N. C., Ehrenreich, D., et al. 2014, A&A, 568, A99
Petrovay, K., & van Driel-Gesztelyi, L. 1997, Sol. Phys., 166, 249
Pont, F., Knutson, H., Gilliland, R. L., Moutou, C., & Charbonneau, D. 2008, MNRAS, 385, 109
Saar, S. H., & Brandenburg, A. 1999, ApJ, 524, 295
Sabarinath, A., & Anilkumar, A. K. 2008, Sol. Phys., 250, 183
Schou, J., Antia, H. M., Basu, S., et al. 1998, ApJ, 505, 390
Setwart, J. Q., & Panofsky, A. A. 1938, ApJ, 88, 385
Smirnov, N. V. 1939, Bulletin Moscow University, 2, 3
Snodgrass, H. B. 1983, ApJ, 270, 288
Snodgrass, H. B., & Ulrich, R. K. 1990, ApJ, 351, 309
Solanki, S. K. 2003, A&ARv, 11, 153
Solanki, S. K., Krivova, N. A., Schüssler, M., & Fligge, M. 2002, A&A, 396, 1029
Solanki, S. K., Wenzler, T., & Schmitt, D. 2008, A&A, 483, 623
Tripathy, S. C., Jain, K., Salabert, D., et al. 2011, J. Phys.: Conf. Ser. 271, 012055:1
Vaquero, M. J., Gordillo, A., Gallego, M. C., Sánchez-Bajo, F., & García, J. A. 2005, Observatory, 125, 152
Volobuev, D. M. 2009, Sol. Phys., 258, 319
Waldmeier, M. 1955, Ergebnisse und Probleme der Sonnenforschung (Leipzig: Geest & Portig)
Wilson, O. C. 1978, ApJ, 226, 379
Woodard, M. F., & Noyes, R. W. 1985, Nature, 318, 449
Zappalà, R. A., & Zuccarello, F. 1991, A&A, 242, 480
Zuccarello, F. 1993, A&A, 272, 587

Appendix A: Schematic overview of the empirical model for the solar cycle

Figure A.1 provides a schematic summary of the procedure underlying our empirical tool. The green box illustrates the detailed treatment of the evolution of a sunspot group. All the parameters included in the model have been found to be important in order to obtain results that are in reasonable agreement with the observations. In the following scheme, U, Pois, $\mathcal{N}$, and $\ln\mathcal{N}$ are, respectively, the uniform, Poisson, Gaussian, and log-normal distributions. The location in longitude of each sunspot group is represented by O.

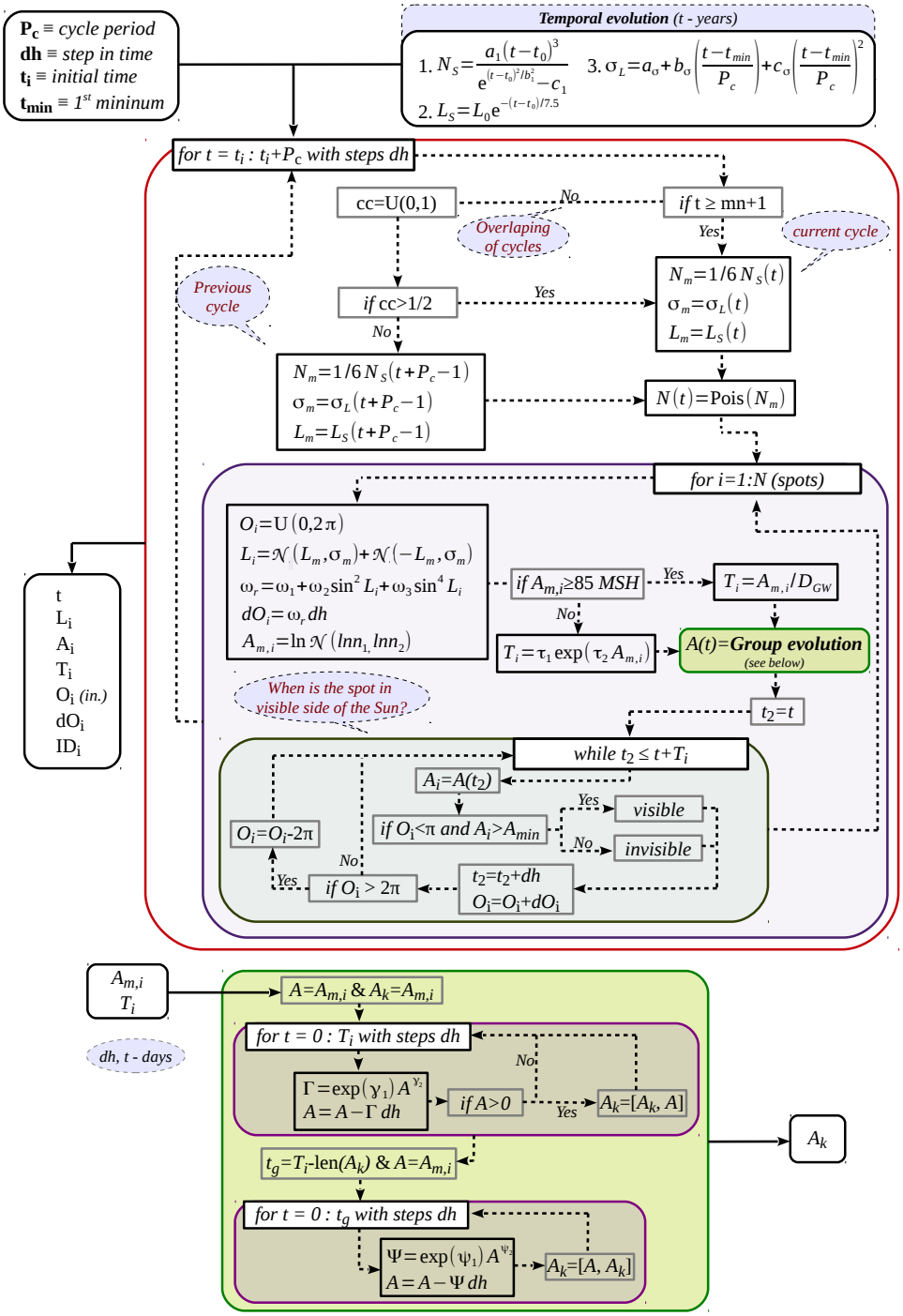

Fig. A.1. Summary of the empirical cycle model. The green box shows how the evolution of a spot group is determined in our model.

Monthly Notices
of the
ROYAL ASTRONOMICAL SOCIETY

MNRAS **461,** 224–229 (2016)
Advance Access publication 2016 June 8

doi:10.1093/mnras/stw1348

On the contribution of sunspots to the observed frequency shifts of solar acoustic modes

A. R. G. Santos,[1,2,3★] M. S. Cunha,[1,2★] P. P. Avelino,[1,2] W. J. Chaplin[3,4] and T. L. Campante[3,4]

[1]*Instituto de Astrofísica e Ciências do Espaço, Universidade do Porto, CAUP, Rua das Estrelas, PT4150-762 Porto, Portugal*
[2]*Departamento de Física e Astronomia, Faculdade de Ciências, Universidade do Porto, Rua do Campo Alegre 687, PT4169-007 Porto, Portugal*
[3]*School of Physics and Astronomy, University of Birmingham, Edgbaston, Birmingham B15 2TT, UK*
[4]*Stellar Astrophysics Centre (SAC), Department of Physics and Astronomy, Aarhus University, Ny Munkegade 120, DK-8000 Aarhus C, Denmark*

Accepted 2016 May 27. Received 2016 May 25; in original form 2016 April 20

ABSTRACT

Activity-related variations in the solar oscillation properties have been known for 30 years. However, the relative importance of the different contributions to the observed variations is not yet fully understood. Our goal is to estimate the relative contribution from sunspots to the observed activity-related variations in the frequencies of the acoustic modes. We use a variational principle to relate the phase differences induced by sunspots on the acoustic waves to the corresponding changes in the frequencies of the global acoustic oscillations. From the sunspot properties (area and latitude as a function of time), we are able to estimate the spot-induced frequency shifts. These are then combined with a smooth frequency shift component, associated with long-term solar-cycle variations, and the results compared with the frequency shifts derived from the Global Oscillation Network Group data. The result of this comparison is consistent with a sunspot contribution to the observed frequency shifts of roughly 30 per cent, with the remaining 70 per cent resulting mostly from a global, non-stochastic variation, possibly related to the changes in the overall magnetic field. Moreover, analysis of the residuals obtained after the subtraction of the model frequency shifts from the observations indicates the presence of a 1.5-yr periodicity in the data in phase with the quasi-biennial variations reported in the literature.

Key words: Sun: activity – Sun: oscillations – sunspots.

1 INTRODUCTION

As a result of the solar cycle, the properties of the acoustic oscillations are observed to vary in a periodic way: as the activity level increases, the mode frequencies and the damping rates increase, while the amplitudes decrease (e.g. Woodard & Noyes 1985; Elsworth et al. 1990; Libbrecht & Woodard 1990; Chaplin et al. 1998; Dziembowski & Goode 2005; Metcalfe et al. 2007; Salabert et al. 2011; Tripathy et al. 2011; Salabert, García & Turck-Chièze 2015). These activity-related variations are expected to be common in solar-like pulsators. In fact, the signature of magnetic cycles in the seismic data was detected in three solar-type stars: HD 49933 observed by the *CoRoT* space telescope (García et al. 2010a, 2010b; Régulo, García & Ballot 2016), and the *Kepler* targets KIC 10644253 (Salabert et al. 2016) and KIC 3733735 (Régulo et al. 2016).

★E-mail: asantos@astro.up.pt (ARGS); mcunha@astro.up.pt (MSC)

The activity-related variations in acoustic frequencies can result from different contributions, whose impact is still not well understood. Magnetic cycles lead to periodic changes in the global magnetic field, as well as in the total area covered by active regions, where sunspots emerge. The impact of the global magnetic field and its associated structural and thermal variations on the oscillations was addressed, e.g., by Dziembowski & Goode (2005). However, localized regions of strong magnetic field can also contribute with direct (Lorentz force) and indirect effects (thermal and structural changes).

The frequency shifts are found to be more strongly correlated with the activity proxies that are sensitive to the weak component of the magnetic field (e.g. Chaplin et al. 2007; Tripathy et al. 2007; Jain, Tripathy & Hill 2009). However, Tripathy et al. (2007) and Jain et al. (2009) argued that the strong magnetic field component also affects significantly the acoustic frequencies. This is corroborated by the frequency shifts' sensitivity to the latitudinal distribution of active regions (e.g. Hindman et al. 2000; Howe, Komm & Hill 2002; Chaplin et al. 2004).

The main goal of this work is to estimate the contribution of sunspots to the observed variations in the acoustic frequencies. In order to do so, we follow the approach of Cunha & Gough (2000) to construct a model for the frequency shifts induced by spots (Section 2). Given the sunspot properties at each epoch, the model allows for the estimation of the spot-induced frequency shifts over the solar cycle. The results obtained with real sunspot data and the corresponding comparison with the observational data are presented in Section 3. In Section 4, we apply our model to synthetic data and we discuss the results. Section 5 summarizes our main conclusions.

2 MODEL FOR THE SPOT-INDUCED FREQUENCY SHIFTS

The presence of sunspots on the solar photosphere can affect the propagation of acoustic waves, hence modifying the frequencies of global modes of oscillation. One way to quantify the sunspots' impact on the frequencies of global acoustic modes is by considering how the normal-mode solutions are locally perturbed by the presence of a sunspot. That perturbation can be expressed as a phase difference ($\Delta\delta$) between the solutions that would be obtained in the presence and in the absence of a spot. To fully incorporate the spot's effect, including both the direct and indirect effects, the phase must be computed at a fiducial depth, R^*, that is below the region of influence of the sunspot (while still sufficiently close to the surface, for the local plane-parallel approximation to be valid). We note that ($\Delta\delta$) represents a local shift in the phase of the normal modes and should not be confused with the phase shift determined in a local helioseismic analysis (for details see Cunha, Brüggen & Gough 1998; Cunha & Gough 2000).

Previous studies carried out in the context of strongly magnetic pulsating stars (e.g. Cunha & Gough 2000) show that the phase difference $\Delta\delta$ depends on the magnetic field strength and inclination, as well as on the mode frequency, which affects the phase with which the wave enters the region of influence of the sunspot. However, the dependence on the mode degree is very weak, as the velocity fields of the modes of low and intermediate degree, and similar frequency, have a similar depth dependence in the very superficial layers, propagating almost vertically there, and thus interacting in a similar manner with the magnetic field.

The dependence of $\Delta\delta$ on the properties of the magnetic field implies that this phase difference varies with the position within the spot. Nevertheless, the associated impact on the frequencies of the global oscillations is only an integrated one, which can be obtained by applying a variational principle. Based on the latter, Cunha & Gough (2000) [see also Cunha et al. (1998) and Cunha (1999) for an application to sunspots] derived the following relation for the fractional spot-induced frequency shifts, in spherical coordinates (r,θ,ϕ),

$$\frac{\delta\omega}{\omega} \simeq -\frac{\overline{\Delta\delta}}{\omega^2 \int_{r_1^l}^{R^*} c^{-2}\kappa^{-1}\mathrm{d}r}, \tag{1}$$

where ω is the angular frequency of the mode ($\omega = 2\pi\nu$), c is the sound speed, κ is the radial component of the acoustic wavenumber, r_1^l is the lower turning point of the mode, and $\overline{\Delta\delta}$ is the integral phase difference,

$$\overline{\Delta\delta} = \frac{\int_0^{2\pi}\int_0^{\pi}\Delta\delta (Y_l^m)^2 \sin\theta \mathrm{d}\theta\mathrm{d}\phi}{\int_0^{2\pi}\int_0^{\pi}(Y_l^m)^2 \sin\theta \mathrm{d}\theta\mathrm{d}\phi}. \tag{2}$$

In the above, $(Y_l^m)^2 = Y_l^m Y_l^{m*} = (P_l^m)^2$ and P_l^m are Legendre polynomials normalized such that the denominator is unity. The indices l and m indicate the mode angular degree and azimuthal order, respectively. At any given time, $\Delta\delta$ in equation (2) is non-zero only where spots are located.

According to equations (1) and (2), the computation of the spot-induced frequency shifts from first principles would require the knowledge of the function $\Delta\delta$ within each individual sunspot. Modelling each individual sunspot over a solar cycle is clearly an impossible task, but an estimate of the spot-induced frequency shifts may still be made by considering a characteristic phase difference, $\Delta\delta_{\rm ch}$, equal for all spots. This is accomplished by substituting $\Delta\delta$ in equation (2) by a function that is zero outside the sunspots and equal to a constant value $\Delta\delta_{\rm ch}$ inside the sunspots. In practice, this corresponds to assuming that the sunspot area and position on the solar surface are the only properties that distinguish the impact of different sunspots on the frequencies.

Two different approaches may be followed to estimate $\Delta\delta_{\rm ch}$. The first is to consider a model for the stratification and magnetic field of a characteristic sunspot and solve the pulsation equations adequate for a plasma permeated by a strong magnetic field. This was performed in part in an earlier work (Santos, Cunha & Lima 2012), where the authors considered an incomplete case in which only the indirect effect of the magnetic field on the oscillations (via the magnetically induced changes in the stratification) was taken into account. They concluded that this indirect effect is small compared to the total spot's effect, in agreement with earlier findings by Cally, Crouch & Braun (2003) and Gordovskyy & Jain (2007). While this approach may have the advantage of determining the phase difference from first principles, including the presumably dominant direct effect of the magnetic field is a rather complex task. Moreover, the results will necessarily depend on our ability to correctly model a typical sunspot.

A second approach, which we will adopt in the current work, consists in taking $\Delta\delta_{\rm ch}$ as a parameter to be constrained by direct comparison of the frequency shifts derived from equations (1) and (2) and the observations. A potential difficulty in this case comes from the fact that the observed frequency shifts are not produced exclusively by the sunspots. Nevertheless, for observations with sufficient time resolution, the short-term, stochastic-like frequency variations associated with the effect of the sunspots may be distinguished from the longer term variations. This will be illustrated in Section 3 where the relative importance of the two contributions will be established.

To proceed, we substitute the phase difference in equations (1) and (2) by the characteristic parameter $\Delta\delta_{\rm ch}$. This parameter will be considered frequency-dependent, but, for the reasons explained previously, we shall neglect its dependence on mode degree. Taking the central colatitude (θ_i) and longitude (ϕ_i) of a given spot i, and having in mind that the spherical harmonic functions do not vary significantly within the spot, we approximate, for each spot, $\left(Y_l^m\right)_i = Y_l^m(\theta_i, \phi_i)$. Under these assumptions, equation (1) becomes

$$\frac{\delta\omega}{\omega} \simeq -\frac{\Delta\delta_{\rm ch}}{I_l}\sum_{i=1}^{N}\left[\left(P_l^m(\cos\theta_i)\right)^2 \int_{\phi_{\min_i}}^{\phi_{\max_i}}\int_{\theta_{\min_i}}^{\theta_{\max_i}} \sin\theta \mathrm{d}\theta\mathrm{d}\phi\right], \tag{3}$$

where $I_l = \omega^2 \int_{r_1^l}^{R^*} c^{-2}\kappa^{-1}\mathrm{d}r$ is related to the inertia of the mode and $\phi_{\min_i}, \phi_{\max_i}, \theta_{\min_i}, \theta_{\max_i}$ define the limits of the spot.

Considering the temporal variation of the sunspot properties, equation (3) can be rewritten as

$$\frac{\delta\omega}{\omega}(t) \simeq -\frac{\Delta\delta_{\rm ch}}{I_l R^2}\sum_{i=1}^{N(t)}\left[\left(P_l^m(\cos\theta_i)\right)^2 A_i\right], \quad (4)$$

where R is the solar radius and A_i the area of a given spot i. In addition to the temporal variation, the fractional frequency shifts given by equation (4) depend on mode frequency, due to the frequency dependence of $\Delta\delta_{\rm ch}$, and on mode degree, due to the degree dependence of the Legendre polynomial and the degree dependence of the mode inertia (reflected in the integral I_l).

3 RESULTS

In order to study the contribution of the sunspots to the observed activity-related frequency shifts, we have used the sunspot daily records from the National Geophysical Data Center, part of the National Oceanic and Atmospheric Administration (NGDC/NOAA; www.ngdc.noaa.gov). This data base includes daily information about each observed sunspot group, such as latitude and area. With the sunspot group area and latitude in hand, equation (4) allows for the estimation of the spot-induced frequency shifts for different radial orders, angular degrees, and azimuthal orders, for any given characteristic phase difference.

In this work, the model frequency shifts will be compared with the observational data from Global Oscillation Network Group (GONG) presented in Tripathy et al. (2011). In the latter, the acoustic frequencies were obtained with a cadence of 36 d and an overlap of 18 d. Tripathy et al. (2011) used in their calculations the modes of degree between $l = 0$ and 100 with frequencies ranging from 2000 to 3300 μHz that are present in all the sub-data sets. For each multiplet, the authors first derived a central frequency. The central frequency shifts, defined by comparison with a reference value, were then combined, weighted by the corresponding mode inertias, to establish a mean frequency shift for the observed frequency range.

Within the frequency range considered by Tripathy et al. (2011), the observed frequency shifts are almost a linear function of the frequency (e.g. Libbrecht & Woodard 1990; Chaplin et al. 2001; Basu 2002). Therefore, the mean frequency shifts derived by the authors provide a good estimate of the frequency shifts of modes with frequencies close to the middle of the observed interval. With this in mind, in the computation of the model frequency shifts, we will consider the frequency closest to the centre of the frequency range used by Tripathy et al. (2011) (frequencies from Rabello-Soares & Appourchaux 1999). This implies that the phase difference $\Delta\delta_{\rm ch}$ that will be inferred from comparison of our model with the observations must be interpreted as the characteristic phase difference at that frequency.

The NGDC/NOAA data include only the sunspots emerging on the visible side of the Sun. Since all sunspots on the solar surface, and not only the visible ones, contribute to the frequency shifts, we must make an assumption about the contribution of the invisible spots. As there is no reason to expect systematic differences between the two sides, it is reasonable to assume that on average the contributions are equal. Therefore, the fractional frequency shifts will be computed from equation (4) by taking twice the value obtained when only the visible spots are considered. The impact of doing so will be discussed at length in Section 4, where we will repeat our analysis using synthetic solar-cycle data. The spot-induced frequency shifts, $\delta\nu_{lm} = \delta\omega_{lm}/2\pi$, are computed for $l = 0$–100 and the corresponding azimuthal orders. In this calculation, we have taken R^* to correspond to a radius of 10 Mm below the photosphere. The model frequency shift associated with a given angular degree, $\delta\nu_l$, is then calculated following the same procedure used by Tripathy et al. (2007, 2011). In particular, we fit the $\delta\nu_{lm}$ to a polynomial expansion of the form

$$\delta\nu_{lm} = \delta\nu_l + \sum_{j=1}^{j_{\rm max}} a_j(l) P_j(m/l), \quad (5)$$

where $j_{\rm max}$ is $2l$ for $l \leq 4$ and 9 for $l > 4$, a_j are the splitting coefficients, and P_j is the Legendre polynomial of order j.

The model mean frequency shifts $\delta\nu(t)$ are then defined as

$$\delta\nu(t) = \sum_l Q_l \delta\nu_l(t) \Big/ \sum_l Q_l \equiv \delta\nu_{\rm spots}, \quad (6)$$

where Q_l is the inertia ratio ($E_l/E_0(\nu_l)$; Christensen-Dalsgaard & Berthomieu 1991). $\delta\nu_{\rm spots}$ is thus the model equivalent to the observable constructed by Tripathy et al. (2011) based on the GONG data, but including only the spot-induced part of the frequency shifts. For a known sunspot distribution, it depends on the single parameter $\Delta\delta_{\rm ch}$.

It is well known that the observed frequency shifts do not result only from the effect of the sunspots (e.g. Chaplin et al. 2007; Tripathy et al. 2007; Jain et al. 2009). Other effects, such as the variation of the global magnetic field and structural and thermal changes, act on much longer time-scales. As a consequence, in order to reproduce the observations, it is necessary to add to our model an additional component of the frequency shifts, varying on longer time-scales. That will be done later in this section. Nevertheless, it is instructive to consider, for a moment, the hypothetical case in which spots are the sole responsible source of the observed frequency shifts. In this case, the characteristic phase difference may be determined by fitting the model for the spot-induced frequency shifts to the observational data ($\delta\nu_{\rm obs}$). To that end, we obtain the 36-d averages (with an overlap of 18 d) of the daily spot-induced frequency shifts. Then, using the consecutive independent data points,[1] the best fit is obtained through a χ^2 minimization between the observational values and the model values, $\delta\nu_{\rm spots}$. We find that $\Delta\delta_{\rm ch} \sim -1.51$ and the corresponding model-data comparison is shown in Fig. 1.

As seen from Fig. 1, the amplitude of the frequency shifts' variations is about three times larger in the model than in the observed data. This is a consequence of having taken the spots to be the sole responsible for the observed frequency shifts, which, as mentioned earlier, is well known not to be the case. In other words, while sunspots contribute both to the long- and short-term variations in the oscillation frequencies, if they were the single cause for the frequency shifts, the observations would show a much more significant short-term variance. We can thus ask the question of how significant would a long-term-varying component originating from sources other than the sunspots have to be, in order to adequately fit the observations. To address this question, we add the long-term-varying component ($\delta\nu_{\rm global}$) to the frequency shifts, which may be associated with the effect of the overall solar magnetic field and to global structural and thermal changes. Different approaches may be used to define the smooth component. Given that the long-term

[1] Since the observations have a cadence of 36 d with an overlap of 18 d, consecutive data points are not independent. In the χ^2 minimization, we have thus used only every second data point and the corresponding results from the model.

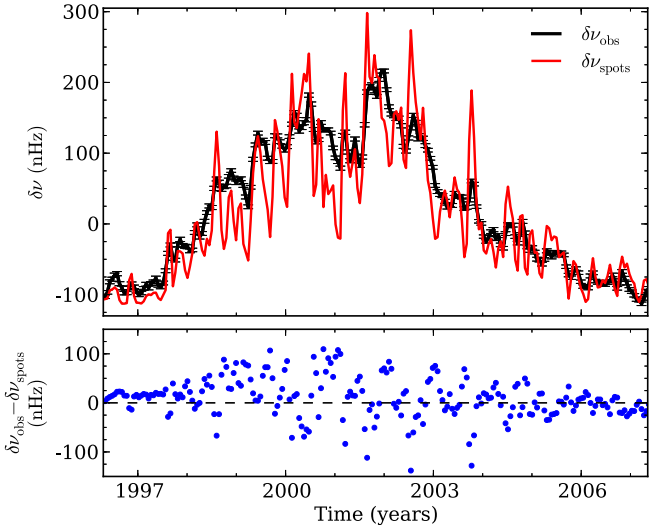

Figure 1. Top panel: observed (black; Tripathy et al. 2011) and model spot-induced frequency shifts (red) for the hypothetical case in which spots are taken to be the only contribution for the observed frequency shifts (see the text for details). The amplitude of the variations in $\delta\nu$ is much larger in our results than in the observational data, indicating that the spots are not the only contribution to the frequency shifts. Bottom panel: residuals between the observed and model spot-induced frequency shifts.

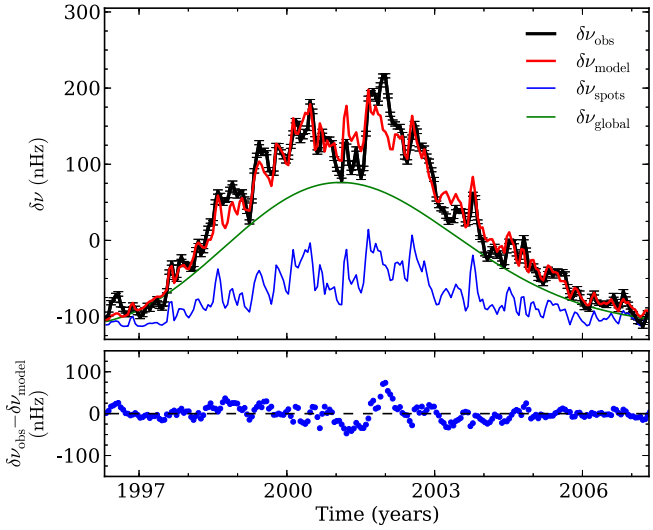

Figure 2. Top panel: observed (black; Tripathy et al. 2011) and model frequency shifts (red). The total model frequency shifts correspond to the combination of a global (green) and a spot-induced (blue) components. Bottom panel: residuals between the observed and model frequency shifts.

frequency shifts variations are well correlated with the long-term variations in the sunspot number (e.g. Chaplin et al. 2007; Tripathy et al. 2007; Jain et al. 2009, 2012), one option is to use the function that was proposed by Hathaway, Wilson & Reichmann (1994) to fit the sunspot number. Accordingly, we fit the observed frequency shifts with the function

$$f(t) = \frac{A(t-t_0)^3}{\exp((t-t_0)^2/B^2) - C}, \tag{7}$$

where A is the amplitude, t_0 is the starting time, B is related to the size of the rising phase, and C is the asymmetry parameter. The values of the parameters found from the fit are $A \sim 6.76$, $B \sim 4.71$, $C \sim -0.46$, and $t_0 \sim 1995.06$.

The model frequency shifts are then given by

$$\delta\nu_{\rm model} = \delta\nu_{\rm global} + \delta\nu_{\rm spots}, \tag{8}$$

where $\delta\nu_{\rm global} = wf(t)$ and w is the weight of the smooth component, to be defined by fitting the data. Thus, our model contains two parameters, w and $\Delta\delta_{\rm ch}$.

From a χ^2 minimization between $\delta\nu_{\rm model}$ and the observations, we find $w \sim 0.71$ and $\Delta\delta_{\rm ch} \sim -0.44$. The latter can be used to estimate the travel-time perturbation induced by a sunspot (relative to the quiet sun). An explicit relation between the double-skip travel-time perturbation, τ_2 (e.g. Zhao & Kosovichev 2006), and the phase shift of normal modes has been derived by Cunha et al. (1998, equation 8). Using the value of $\Delta\delta_{\rm ch}$ and the frequency of the centre of the observed interval in this equation, we estimate the one-half of the double-skip travel-time perturbation to be $\tau_2/2 \sim -0.37$ min.

Fig. 2 shows the comparison between the observed frequency shifts and the results for $\delta\nu_{\rm model}$ with the parameters derived above. The resulting frequency shifts are in reasonable agreement with the observational data indicating that our simple, two-parameter model captures the main features contained in the observed frequency shifts. The weight of the smooth component, w, gives an estimate of the contribution resulting from the changes in the global magnetic field and associated structural and thermal variations, which is ∼70 per cent. The remaining ∼30 per cent correspond then to the spot-induced contribution.

4 DISCUSSION

Different approaches may be considered to model the smooth component introduced in Section 3. While we have opted to use the function defined by Hathaway et al. (1994), we have also assessed the robustness of our results to changes in the modelling of the smooth component. We considered an alternative approach in which the function *f(t)* is defined by a smoothed version of the observed frequency shifts obtained through the application of a 360-d filter. Moreover, we have also considered an alternative approach to the model-data comparison, by which we have first subtracted a smooth component to both the observed and the spot-induced frequency shifts (obtained through the application of a 360-d filter to each set) and, then, fitted the residuals. In both cases, the global and spot-induced fractional contributions were found to be similar to the values estimated in the original analysis, with the parameter w agreeing to better than 10 per cent with the value estimated in Section 3.

While the results from our two-parameter model reproduce reasonably well the observed frequency shifts, we see from the lower panel of Fig. 2 that some differences still exist between the two. Part of these residuals may be connected to the fact that only the visible sunspot groups are recorded in the NGDC/NOAA daily records. The observed frequency shifts are affected by the spots appearing throughout the whole solar surface. Thus, using the visible groups in the computation of the spot-induced frequency shifts from equation (4) and considering that the total spot-induced component is twice the value may introduce statistical differences between the model predictions and the observations. Since there are no data for the sunspots emerging on the invisible side of the Sun, the only way to check the impact of this limitation is to recur to simulations, which we will do by performing the same analysis as in Section 3 but using synthetic sunspot records obtained with the empirical tool developed by Santos et al. (2015). With this tool, we simulate the number of sunspot groups, the total area covered by them, and their

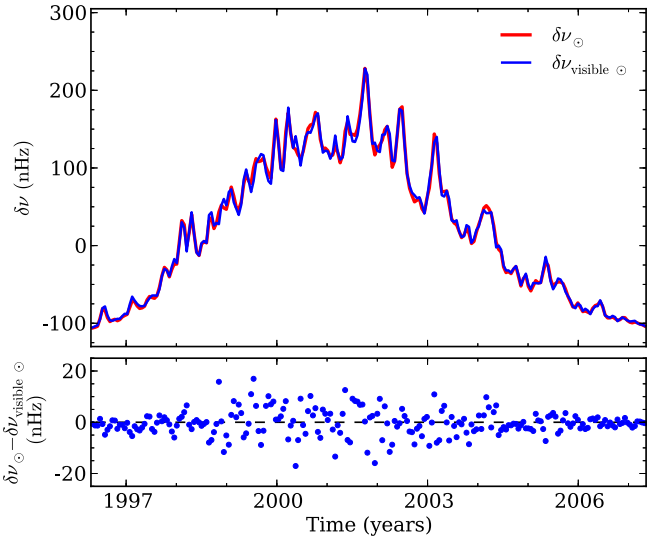

Figure 3. Top panel: frequency shifts derived from synthetic sunspot data – when considering all synthetic sunspot groups at the solar surface (red) and when considering only the visible groups (blue). Bottom panel: residuals between the frequency shifts shown in the top panel.

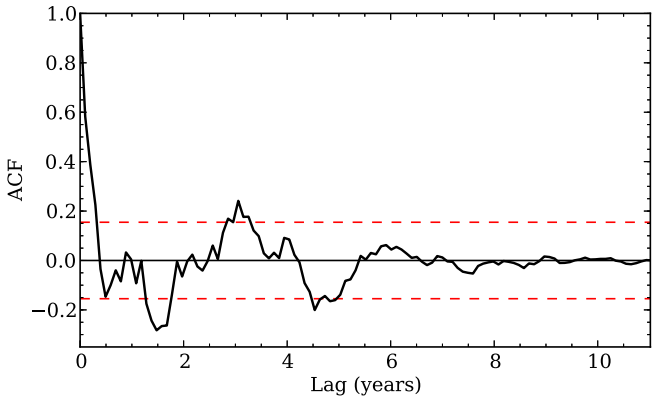

Figure 4. Autocorrelation function of the residuals in Fig. 2. The red dashed lines indicate the 95 per cent significance level.

latitudinal distribution along one complete solar cycle. The output from this tool is analogous to that of the real daily records.

Following the methodology described in Section 3, we obtain the daily frequency shifts induced by all the groups on the solar surface (case 1) and by the visible groups alone assuming that they are a reasonable representation of both (visible and invisible) sides of the Sun (case 2). The first of these cases is used to simulate a model frequency shift cycle, i.e. a model equivalent of the observations considered in the previous section, while the second is used to estimate the error made when taking only the visible sunspot groups for the frequency shift calculations, with a factor of 2 to account for the invisible side. Since we want our model-simulated cycle to be as similar to the real data as possible, in the first case the parameter $\Delta\delta_{\text{ch}}$ needed to compute $\delta\nu_{\text{spots}}$ is determined in such a way that the sum of the variations of the frequency shifts obtained from synthetic data coincides with the value found using the observed frequency shifts, i.e. $\sum_k |\Delta\delta\nu|_{\text{obs},k} = \sum_k |\Delta\delta\nu|_{\text{synt-spots},k}$, where $\Delta\delta\nu = \delta\nu_{k+1} - \delta\nu_k$ and different indices k correspond to the different data points. To the synthetic $\delta\nu_{\text{spots}}$, we add the smooth component found in Section 3, with a weight w, to obtain the model frequency shifts for case 1 (hereafter $\delta\nu_{\odot}$). The weight w is determined through a χ^2 minimization with the observed data. The frequency shifts $\delta\nu_{\odot}$ are now taken as the reference with which we compare the results obtained from the visible spots alone. We then proceed exactly as in Section 3, but substituting the observed frequency shifts by the reference-model frequency shifts, and the frequency shifts based on sunspot data from NGDC/NOAA by the frequency shifts obtained from simulated data for the visible side alone, hereafter $\delta\nu_{\text{visible}\odot}$. Fig. 3 shows the comparison between $\delta\nu_{\odot}$ and $\delta\nu_{\text{visible}\odot}$ for a given simulation of the sunspot cycle.

The differences between the model frequency shifts derived when considering all synthetic sunspot groups at the surface and when considering just the visible groups (in Fig. 3) are significantly smaller and more evenly distributed than the ones found in Section 3. We, therefore, conclude that the main differences seen in Fig. 2 are not explained by the fact that the sunspot data used for the computation of the model frequency shifts in Section 3 only contain information on the groups emerging on the visible side of the Sun.

Since the simulations of the sunspot cycles are stochastic, we repeated the procedure described above for a large number of synthetic data sets. We found that the spot-induced contributions to the frequency shifts obtained when considering all synthetic sunspot groups and the visible groups alone differ, on average, by less than 3 per cent. The difference is small due to the 36-d averaging of the frequency shifts. This average dilutes the daily differences that may exist between the area and position of the spots in each side of the Sun. This reassures us that the estimated value for the spot-induced frequency shifts' contribution found in Section 3 is robust, even if computed from data for the visible sunspots only.

A closer inspection of the residuals shows that these seem to be in phase with the quasi-biennial variations found in the frequency shifts by Fletcher et al. (2010) and Broomhall et al. (2012), having a significant periodicity of ∼1.5 yr (Fig. 4). A more detailed analysis indicates that the 1.5-yr periodicity is intrinsic to the observed frequency shifts.

This may point to a global contribution with structure in an intermediate time-scale, as opposed to one that varies only on the time-scale of the solar cycle, as considered in Section 3. In addition, the characteristic phase difference may vary during the solar cycle, e.g. as a result of changes in the typical structure and magnetic field within the sunspots. This could also contribute to the differences seen in Fig. 2.

5 CONCLUSIONS

Our results indicate that there are two main contributions to the total activity-related frequency shifts. A spot-induced contribution of about 30 per cent, that is responsible for the stochastic behaviour of the frequency shifts as well as for part of their long-term variations, and a global contribution of about ∼70 per cent, varying on the time-scale of the solar cycle, that is possibly related to the changes in the overall magnetic field. This is consistent with the results obtained by Jain et al. (2009) when studying the correlations between the frequency shifts and different activity indices. Furthermore, the characteristic phase shift derived from the fit of our two-parameter model to the data translates into a travel-time perturbation that is consistent with those inferred from time–distance helioseismology (Duvall 1995; Duvall et al. 1996; Zhao & Kosovichev 2006).

We have checked that our results are robust against changes in the form adopted for the global component. Moreover, based on synthetic data, we have demonstrated that they would not change in

any significant way, if all the sunspots emerging on the surface of the Sun could be considered, rather than just the visible ones.

Although our model frequency shifts agree reasonably well with the observed frequency shifts, we find evidence for variations in the data at time-scales not accounted for in our model. These could either be associated with intermediate-term variations in the spot-induced phase shifts or with intermediate-term variations in the non-spot contributions. Despite these differences, we note that the contributions of 70 and 30 per cent derived from our model are robust, as they depend essentially on the relative amplitudes of the stochastic and smooth components seen in the observations. In fact, we also verified by testing models with an additional intermediate-term component, that small corrections to the model associated with activity on intermediate time-scales will not change the estimated fractional contribution of the spot-induced and global components in any significant way.

With the increasing number of solar-like stars with detected activity-related variations in the frequencies of the acoustic modes (García et al. 2010a; Régulo et al. 2016; Salabert et al. 2016), the understanding of the different contributions to those variations becomes even more important. If the contribution from starspots to the frequency shifts in solar-like pulsators is comparable to that found in this work for the case of the Sun, the amplitude of those shifts can be used to estimate the surface coverage of starspots.

ACKNOWLEDGEMENTS

This work was supported by Fundação para a Ciência e a Tecnologia (FCT) through the research grant UID/FIS/04434/2013. ARGS acknowledges the support from FCT through the Fellowship SFRH/BD/88032/2012 and from the University of Birmingham. MSC and PPA acknowledge support from FCT through the Investigador FCT Contracts No. IF/00894/2012 and IF/00863/2012 and POPH/FSE (EC) by FEDER funding through the programme Programa Operacional de Factores de Competitividade (COMPETE). TLC and WJC acknowledge the support of the UK Science and Technology Facilities Council (STFC). The research leading to these results has received funding from EC, under FP7, through the grant agreement FP7-SPACE-2012-312844 and PIRSES-GA-2010-269194. ARGS, MSC, and PPA are grateful for the support from the High Altitude Observatory (NCAR/UCAR), where part of the current work was developed.

REFERENCES

Basu S., 2002, in Wilson A., ed., ESA SP-508: From Solar Min to Max: Half a Solar Cycle with SOHO. ESA, Noordwijk, p. 7
Broomhall A.-M., Chaplin W. J., Elsworth Y., Simoniello R., 2012, MNRAS, 420, 1405
Cally P. S., Crouch A. D., Braun D. C., 2003, MNRAS, 346, 381
Chaplin W. J., Elsworth Y., Isaak G. R., Lines R., McLeod C. P., Miller B. A., New R., 1998, MNRAS, 300, 1077
Chaplin W. J., Appourchaux T., Elsworth Y., Isaak G. R., New R., 2001, MNRAS, 324, 910
Chaplin W. J., Elsworth Y., Isaak G. R., Miller B. A., New R., 2004, MNRAS, 352, 1102
Chaplin W. J., Elsworth Y., Miller B. A., Verner G. A., New R., 2007, ApJ, 659, 1749
Christensen-Dalsgaard J., Berthomieu G., 1991, in Cox A. N., Livingston W. C., Mathews M., eds, Solar Interior and Atmosphere. University of Arizona Press, Tucson, AZ, p. 401
Cunha M. S., 1999, PhD thesis, Cambridge University, UK
Cunha M. S., Gough D., 2000, MNRAS, 319, 1020
Cunha M. S., Brüggen M., Gough D. O., 1998, in Korzennik S. G., Wilson A., eds, Structure and Dynamics of the Interior of the Sun and Sun-like Stars. ESA, Noordwijk, p. 905
Duvall T. L., Jr, 1995, Ulrich R. K., Rhodes E. J., Jr, Dappen W., eds, ASP Conf. Ser. Vol. 76, GONG '94: Helio- and Astero-Seismology from the Earth and Space. Astron. Soc. Pac., San Francisco, p. 465
Duvall T. L., Jr, D'Silva S., Jefferies S. M., Harvey J. W., Schou J., 1996, Nature, 379, 235
Dziembowski W. A., Goode P. R., 2005, ApJ, 625, 548
Elsworth Y., Howe R., Isaak G. R., McLeod C. P., New R., 1990, Nature, 345, 322
Fletcher S. T., Broomhall A.-M., Salabert D., Basu S., Chaplin W. J., Elsworth Y., Garcia R. A., New R., 2010, ApJ, 718, L19
García R. A., Mathur S., Salabert D., Ballot J., Regulo C., Metcalfe T. S., Baglin A., 2010a, Science, 329, 1032
García R. A., Ballot J., Mathur S., Salabert D., Regulo C., 2010b, preprint (arXiv:1012.0494)
Gordovskyy M., Jain R., 2007, ApJ, 661, 586
Hathaway D. H., Wilson R. M., Reichmann E. J., 1994, Sol. Phys., 151, 177
Hindman B., Haber D., Toomre J., Bogart R., 2000, Sol. Phys., 192, 363
Howe R., Komm R. W., Hill F., 2002, ApJ, 580, 1172
Jain K., Tripathy S. C., Hill F., 2009, ApJ, 695, 1567
Jain R., Tripathy S. C., Watson F. T., Fletcher L., Jain K., Hill F., 2012, A&A, 545, A73
Libbrecht K. G., Woodard M. F., 1990, Nature, 345, 779
Metcalfe T. S., Dziembowski W. A., Judge P. G., Snow M., 2007, MNRAS, 379, L16
Rabello-Soares M. C., Appourchaux T., 1999, A&A, 345, 1027
Régulo C., García R. A., Ballot J., 2016, A&A, 589, A103
Salabert D., García R. A., Pallé P. L., Jiménez A., 2011, J. Phys.: Conf. Ser., 271, 012030
Salabert D., García R. A., Turck-Chièze S., 2015, A&A, 578, A137
Salabert D. et al., 2016, A&A, 589, A118
Santos A. R. G., Cunha M. S., Lima J. J. G., 2012, Astron. Nachr., 333, 1032
Santos A. R. G., Cunha M. S., Avelino P. P., Campante T. L., 2015, A&A, 580, A62
Tripathy S. C., Hill F., Jain K., Leibacher J. W., 2007, Sol. Phys., 243, 105
Tripathy S. C., Jain K., Salabert D., García R. A., Hill F., Leibacher J. W., 2011, J. Phys.: Conf. Ser., 271, 012055
Woodard M. F., Noyes R. W., 1985, Nature, 318, 449
Zhao J., Kosovichev A. G., 2006, ApJ, 643, 1317

This paper has been typeset from a TEX/LATEX file prepared by the author.

Monthly Notices
of the
ROYAL ASTRONOMICAL SOCIETY

MNRAS **464,** 4408–4414 (2017)
Advance Access publication 2016 October 23

doi:10.1093/mnras/stw2716

A thorough analysis of the short- and mid-term activity-related variations in the solar acoustic frequencies

A. R. G. Santos,[1,2,3★] M. S. Cunha,[1,2] P. P. Avelino,[1,2] W. J. Chaplin[3,4] and T. L. Campante[3,4]

[1]*Instituto de Astrofísica e Ciências do Espaço, Universidade do Porto, CAUP, Rua das Estrelas, PT-4150-762 Porto, Portugal*
[2]*Departamento de Física e Astronomia, Faculdade de Ciências, Universidade do Porto, Rua do Campo Alegre 687, PT-4169-007 Porto, Portugal*
[3]*School of Physics and Astronomy, University of Birmingham, Edgbaston, Birmingham B15 2TT, UK*
[4]*Stellar Astrophysics Centre, Department of Physics and Astronomy, Aarhus University, Ny Munkegade 120, DK-8000 Aarhus C, Denmark*

Accepted 2016 October 19. Received 2016 September 27; in original form 2016 June 20

ABSTRACT

The frequencies of the solar acoustic oscillations vary over the activity cycle. The variations in other activity proxies are found to be well correlated with the variations in the acoustic frequencies. However, each proxy has a slightly different time behaviour. Our goal is to characterize the differences between the time behaviour of the frequency shifts and of two other activity proxies, namely the area covered by sunspots and the 10.7-cm flux. We define a new observable that is particularly sensitive to the short-term frequency variations. We then compare the observable when computed from model frequency shifts and from observed frequency shifts obtained with the Global Oscillation Network Group (GONG) for cycle 23. Our analysis shows that on the shortest time-scales, the variations in the frequency shifts seen in the GONG observations are strongly correlated with the variations in the area covered by sunspots. However, a significant loss of correlation is still found. We verify that the times when the frequency shifts and the sunspot area do not vary in a similar way tend to coincide with the times of the maxima of the quasi-biennial variations seen in the solar seismic data. A similar analysis of the relation between the 10.7-cm flux and the frequency shifts reveals that the short-time variations in the frequency shifts follow even more closely those of the 10.7-cm flux than those of the sunspot area. However, a loss of correlation between frequency shifts and 10.7-cm flux variations is still found around the same times.

Key words: Sun: activity – Sun: oscillations – sunspots.

1 INTRODUCTION

The frequencies of the solar acoustic modes vary periodically and in phase with the magnetic activity over the so-called 11-yr solar cycle (e.g. Woodard & Noyes 1985; Elsworth et al. 1990; Libbrecht & Woodard 1990; Chaplin et al. 1998; Dziembowski & Goode 2005; Salabert et al. 2011; Tripathy et al. 2011; Howe et al. 2015; Salabert, García & Turck-Chièze 2015). Activity-related frequency shifts were also detected in three solar-like stars (García et al. 2010; Régulo, García & Ballot 2016; Salabert et al. 2016) and are expected to be common in solar-type pulsators.

It has been argued that the frequency shifts result from variations of both the weak and strong components of the solar magnetic field (Tripathy et al. 2007; Jain, Tripathy & Hill 2009; Broomhall & Nakariakov 2015; Santos et al. 2016). This is corroborated by their strong correlation with the 10.7-cm flux (Chaplin et al. 2007; Tripathy et al. 2007; Jain et al. 2009; Broomhall et al. 2012; Simoniello et al. 2012), which is mostly sensitive to the weak component, but also affected by the strong component of the magnetic field (e.g. Covington 1969; Tapping 1987; Tapping & Detracey 1990), as well as by their sensitivity to the latitudinal distribution of active regions (e.g. Hindman et al. 2000; Howe, Komm & Hill 2002; Chaplin et al. 2004; Broomhall et al. 2012) and their strong correlation with the sunspot areas (Jain et al. 2012; Broomhall & Nakariakov 2015). Still, different studies have shown a decrease in the correlation between the activity proxies and the frequency shifts around the maximum of the solar cycle (e.g. Jain et al. 2009; Simoniello et al. 2012; Broomhall & Nakariakov 2015).

In addition to the 11- yr variation, the solar acoustic frequencies also show a quasi-biennial variation (Fletcher et al. 2010; Broomhall et al. 2012; Simoniello et al. 2012, 2013; Broomhall & Nakariakov 2015), which is strongly correlated with the mid-term periodicities found in other activity proxies (Broomhall et al. 2012; Broomhall &

★ E-mail: asantos@astro.up.pt

Nakariakov 2015). The signature of this quasi-biennial variation in the frequencies is seen over all phases of solar activity. However, its amplitude is highest around the solar maximum, suggesting that it is modulated by the 11- yr cycle. These mid-term frequency shifts show a weaker dependence on the frequency than the longer term (11- yr) frequency shifts (Fletcher et al. 2010; Broomhall et al. 2012; Simoniello et al. 2013), which has been interpreted as an indication that they originate from changes in layers that are located deeper than those inducing the 11- yr signal.

One of the difficulties in interpreting the correlations found between variations in the different activity proxies and variations in the oscillation frequencies comes from the fact that the latter result from the combination of different physical phenomena. In fact, the oscillation frequencies are not only sensitive to the direct effect of the magnetic field, which might be significant in active regions, but also to variations in the solar structure and dynamics that are induced both by the weak and the strong magnetic field components. Luckily, these phenomena do not all have the same characteristic time-scale, and thus, by considering the behaviour of the frequency shifts on short-, mid-, and long-terms one may hope to move forward in the interpretation of the observed correlations.

In this work, we propose a new observable to investigate the short- and mid-term variations of the frequency shifts. We argue that this observable, based on a weighted sum of frequency-shift variations, is insensitive to the long-term cycle variations, allowing us to amplify the signature of the short-term variations contained in the data.

2 OBSERVED AND MODEL FREQUENCY SHIFTS

In order to study the short-term variations of the solar acoustic frequencies, one must consider observed frequency shifts obtained from relatively short time series, such as those derived by Tripathy et al. (2011) using data from the Global Oscillation Network Group (GONG). In that work, the authors computed oscillation frequencies and the corresponding frequency shifts with a cadence of 36 d and an overlap of 18 d. These observations, thus, provide two data sets that we will analyse separately, each composed of a sequence of consecutive, independent, frequency shifts obtained from 36-d time series: Sample 1 and Sample 2 – starting, respectively, on the first and second data point of the original data set from Tripathy et al. (2011).

For the model frequency shifts, we use a parametrized model proposed by Santos et al. (2016, hereafter Paper I). Accordingly, the model frequency shifts are described by the sum of two components

$$\delta\nu_{\rm model} = \delta\nu_{\rm spots} + \delta\nu_{\rm global}, \quad (1)$$

where the first term on the right-hand side of equation (1) represents the frequency shifts induced by sunspots (essentially proportional to the variation of the total area covered by sunspots) and the second represents a smooth 11-yr variation induced by other phenomena, such as the variation of the global magnetic field and structural and thermal changes acting on a solar-cycle time-scale. The spot-induced component, $\delta\nu_{\rm spots}$, is derived from the daily sunspot records of the National Geophysical Data Center, part of the National Oceanic and Atmospheric Administration (NGDC/NOAA; www.ngdc.noaa.gov), while the long-term smooth component is obtained by fitting the observed frequency shifts with the function proposed by Hathaway, Wilson & Reichmann (1994) to describe the sunspot number over the solar cycle. By comparing the total model frequency shifts with the frequency shifts observed over the solar cycle 23 (from Tripathy et al. 2011), Santos et al. (Paper I) found that the shortest term variations seen in the GONG observational data are well described by the spot-induced frequency shifts, which they estimate to account for about 30 per cent of the long-term variations observed throughout the solar cycle. The comparison between the model predictions and the GONG data for the two observational sets of independent frequency shifts is shown in Fig. 1.[1]

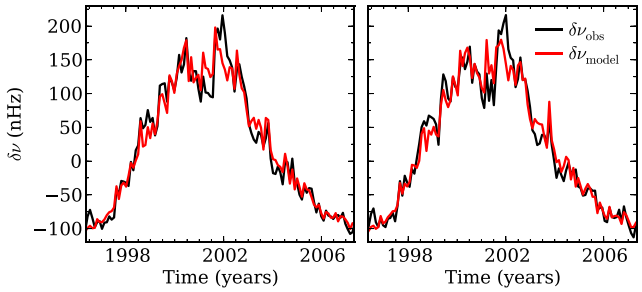

Figure 1. Comparison between the observed (black) and model (red) frequency shifts over the solar cycle 23 obtained using Samples 1 and 2 (left- and right-hand panel, respectively – see text for details).

A quasi-biennial variation with an 11-yr amplitude modulation was also identified by the authors in the residuals of the model-data comparison. This component, as well as the 11-yr variation, has been identified previously in data obtained from different space- and ground-based instruments and discussed in a number of works (cf. Section 1), while the shortest term component (varying on a time-scale of days) was first discussed in Paper I.

3 DESCRIPTION OF THE METHOD

The variations in the solar acoustic frequencies are known to be correlated with the variations in the solar activity indicators, in particular with the area covered by sunspots. The latter varies on a time-scale of days and induces frequency variations on a similar time-scale. Unfortunately, it is not possible to derive accurate frequency shifts from time series as short as a few days. Nevertheless, such short time-scale variations are expected to be the main source of the 36-d frequency variations seen in the GONG data. To test this possibility and investigate more closely the short-term frequency shifts, we define a new observable

$$W_{\rm D} = \sum_k \Delta\delta\nu_k \times S_k, \quad (2)$$

as the weighted sum of the frequency-shift differences. Here $\Delta\delta\nu_k$ is the difference between the frequency shifts measured in two consecutive data bins (associated with times k and $k-1$, i.e. $\Delta\delta\nu_k = \delta\nu_k - \delta\nu_{k-1}$), thus corresponding to the bin-to-bin frequency variation. Also, S is a weight to be determined according to the variation of the area covered by sunspots. At a given time k, if the total area covered by spots increases with respect to its value at the time $k-1$, the weight, S_k, will be 1, otherwise $S_k = -1$. If the short-term frequency-shift differences are indeed strongly correlated with the variations in the area covered by spots, as predicted by the model for the spot-induced frequency shifts, they will be summed positively when performing this weighted sum. Thus,

[1] A similar comparison was shown in Paper I, but for the two data sets combined.

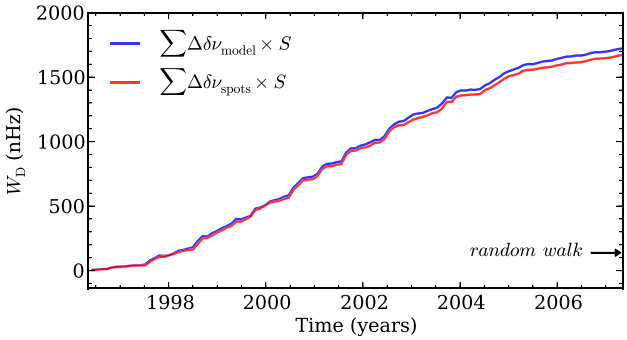

Figure 2. Weighted sum of the variations in the model (blue) and spot-induced (red) frequency shifts (derived from the observational sunspot data), where the weight S, in equation (2), is determined by the variation in the area covered by sunspots. The black arrow marks the expected standard deviation for a random walk.

the new variable W_D is expected to be most sensitive to the short-term variation component of the frequency shifts, with the smooth, long-term component, being essentially cancelled due to the varying positive and negative weights. To show that this is indeed the case, we compute W_D using the spot-induced frequency shifts alone ($\delta\nu_{spots}$), derived from the observational sunspot data, and using the total model frequency shifts ($\delta\nu_{model}$, which includes the spot contribution and the long-term smooth component; cf. equation 1), where the weight S is determined from the observed sunspot areas (NGDC/NOAA). The comparison between the two cases is shown in Fig. 2, where the maximum difference between the two curves is one order of magnitude smaller than what would be found if the large-scale variations were summed positively, thus confirming that the smooth, long-term component almost cancels out when computing W_D for the 36- d cadence. The arrow marks the expected standard deviation at the end of the solar cycle for the case in which the frequency-shift variations are described by a random walk, thus providing an indication of the interval where the maximum value of the curves would be expected to lie, if the frequency-shift differences were completely uncorrelated with the variations in the area covered by sunspots. The fact that the maxima of the two curves is so much greater than that value is a consequence of the almost perfect correlation between the spot-induced frequency-shift differences predicted by the model and the corresponding variations in the area covered by spots.

We now compute W_D for the Samples 1 and 2 of the observed frequency shifts obtained from GONG data and compare the results with the hypothetical case of complete correlation, defined as the case in which the variations in the area covered by sunspots and in the frequency shifts always have the same sign [meaning that an increase (decrease) in one always correspond to an increase (decrease) in the other]. In that case, the weighted sum defined by equation (2) reduces to the sum of the absolute (modulus) values of the frequency-shift differences (M_D)

$$M_D = \sum_k |\Delta\delta\nu_k|. \quad (3)$$

The quantities W_D (black solid line) and M_D (black dashed line) obtained from Samples 1 and 2 (left- and right-hand panels, respectively) are shown in Fig. 3. The comparison between the maximum of the black solid line and the expected standard deviation for a random walk allows us to conclude that a significant correlation exists between the sunspot-area variations and the frequency-shift differences. In fact, in both cases, the black continuous curve reaches a maximum value that is 7σ above that of a random walk, meaning that if the short-term variations in the frequency shifts and in the areas were uncorrelated, the probability of obtaining the deviation reached by the black solid lines would be less than 10^{-11}. For comparison, we show in the same plot the results for the model spot-induced frequency shifts derived from the observational sunspot data. The red solid and dashed lines correspond to the quantities W_D and M_D, respectively, obtained from Samples 1 and 2 (left- and right-hand panels, respectively). In this case, the correlation is perfect and, unlike in the case of the observed frequency shifts, the solid and dashed curves overlap.

We also verified to what extent the results for W_D are affected by the error associated with the observed frequency shifts. By taking the observational data points and assuming that the corresponding errors are Gaussian, we obtain random samples for the frequency shifts. We then estimate the standard deviation from W_D, which is represented by the grey area in Fig. 3. For some data points, the observational errors are of the same order as the frequency-shift differences. However, those data points do not contribute significantly to W_D. Clearly, the uncertainty in the black curve (grey region) associated with the observational errors in the frequency shifts does not explain the loss of correlation found.

We thus conclude that a strong, but not complete correlation exists between the short-term variations in the frequency shifts and in the spots' areas. The origin of the observed loss of correlation

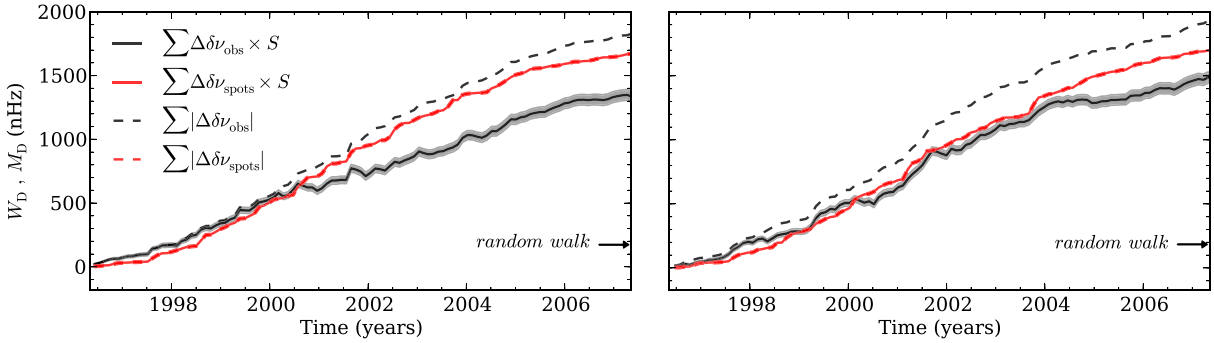

Figure 3. Left- and right-hand panels correspond to the results obtained for Samples 1 and 2, respectively. Weighted sum W_D of the variation in the observed (black solid line) and spot-induced (red solid line) frequency shifts (derived from the observational sunspot data), where the weight, S, is determined by the variation in the total observed area covered by sunspots. The grey region represents the 1σ confidence interval from the black continuous curve resulting from the errors in the observed frequency shifts. The dashed lines represent the sum, M_D, of the absolute (modulus) values of the frequency-shift differences. The arrow marks the expected standard deviation for a random walk.

can be twofold: it may result from our inability to compute the true correlation between these two variations, or it may correspond to a genuine loss of correlation introduced either by changes in the effect that sunspots have on the frequencies or by the effect of other physical phenomena (besides spots), which may influence the solar frequency shifts on short time-scales. In the next section, we will discuss a potential source for that loss of correlation, associated with the lack of information about the sunspots on the invisible side of the Sun.

4 IMPACT OF IGNORING THE SOLAR INVISIBLE SIDE ON THE COMPUTATION OF W_D

Even if a complete correlation existed between the variations in the frequency shifts and in the total area covered by spots, we would still expect to see a significant loss of correlation when comparing the quantities W_D and M_D derived from the observations. The reason is that the sunspot areas we consider for the computation of W_D, obtained from the NGDC/NOAA data bases, concern only the visible sunspot groups, while the acoustic frequencies are affected by sunspot groups emerging over the whole solar surface. In this section, we estimate the effect of having ignored the invisible sunspot groups in the computation of W_D of the previous section. To that end, we use synthetic sunspot data obtained with an empirical tool developed by Santos et al. (2015). This tool generates synthetic sunspot daily records analogous to the real sunspot data from NGDC/NOAA, starting from simulations of sunspot groups on both the visible and invisible sides of the Sun.

Using the model presented in Paper I, we compute the spot-induced frequency shifts for the synthetic sunspot data, $\delta\nu_{\rm synthetic}$, taking into account all the spots, including those appearing on the visible and invisible sides of the Sun. Since the model for the frequency shifts is parametrized, it needs to be calibrated by comparison with the observed data. In this case, we are interested in analysing the short-term variations in the frequency shifts. We thus have calibrated the frequency shifts such as to make their absolute sum equal to the absolute sum of the observed counterparts, i.e. $\sum_k|\Delta\delta\nu_{\rm obs}|_k = \sum_k|\Delta\delta\nu_{\rm synthetic}|_k$. We then compute W_D for the synthetic data, by combining the variations in the frequency shifts obtained from all the synthetic sunspot groups with the weights S_k computed only from the visible synthetic sunspot areas. Since the sunspot cycle simulations are stochastic, we repeated this exercise 1000 times, computing the values of W_D and M_D for all simulations.

The quantities M_D and W_D derived from the synthetic data are shown in the top panel of Fig. 4 for one particular simulation. The difference between these quantities gives an estimate of the loss of correlation that can be explained by our not accounting for the sunspot groups on the invisible side of the Sun when computing the weights S_k. The bottom panel of Fig. 4 shows the distribution of that difference at the end of the solar cycle. Taking the average of the distribution as an indicator and comparing it with the difference between M_D and W_D computed in Section 3 for the observations, we conclude that only about 30 per cent of the loss of correlation found in the analysis of the real data may be explained by this non-physical effect. Therefore, a significant part of the loss of correlation detected in Section 3 is expected to have its origin in physical effects other than sunspots that affect the short-term frequency shifts and that are not, themselves, fully correlated with the total area covered by sunspots.

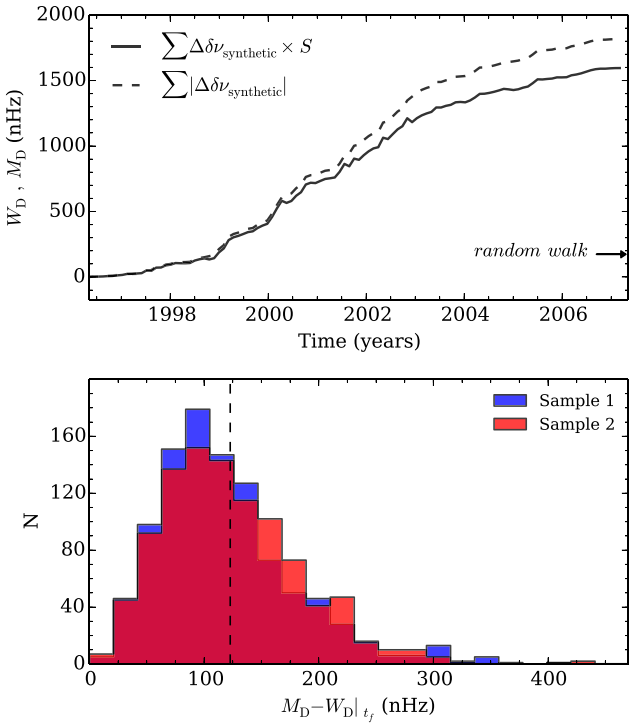

Figure 4. Top panel: comparison between the quantities M_D (dashed line) and W_D (solid line) for a particular synthetic cycle. The arrow marks the expected standard deviation for a random walk. Bottom panel: distribution of the difference between the quantities M_D and W_D at the end of the synthetic solar cycle (at t_f). The dashed line marks the averaged difference found for both samples of independent frequency shifts.

5 EPOCHS OF DISTINCT BEHAVIOUR BETWEEN THE FREQUENCY SHIFTS AND THE SUNSPOT AREAS

While the frequency-shift differences are found to be strongly correlated with the variations in the area covered by sunspots, there are particular epochs when the frequency shifts and the sunspot areas vary in the opposite way, leading to the loss of correlation found in Section 3. In this section, we identify those epochs.

The top panels of Fig. 5 show the difference between M_D (black dashed line in Fig. 3) and W_D (black solid line in Fig. 3) for the observed frequency shifts. The results for the two samples differ slightly. For Sample 1 (left-hand panel), the differences have a larger amplitude around the solar maximum, while for Sample 2 they are more evenly spread. We recall that the two samples provide 36- d averages of the frequency shifts that are shifted by 18 d. The differences seen in the results for the two samples highlight that a significant loss of correlation takes place on shorter time scales than 18 d. In the discussion that follows we will, therefore, consider only aspects that are identified in both samples.

The bottom panels of Fig. 5 show the derivative of the difference between M_D and W_D with respect to the time. This quantity is zero when the variations in the frequency shifts have the same sign as those in the sunspot areas, differing from zero when the two variations have an opposite sign. The most significant correlation losses occur around the same times for the two samples of independent frequency shifts. The peaks are quasi-periodic, coinciding with the maxima of the quasi-biennial periodicity observed in the solar acoustic frequencies. This is illustrated by the grey bars in

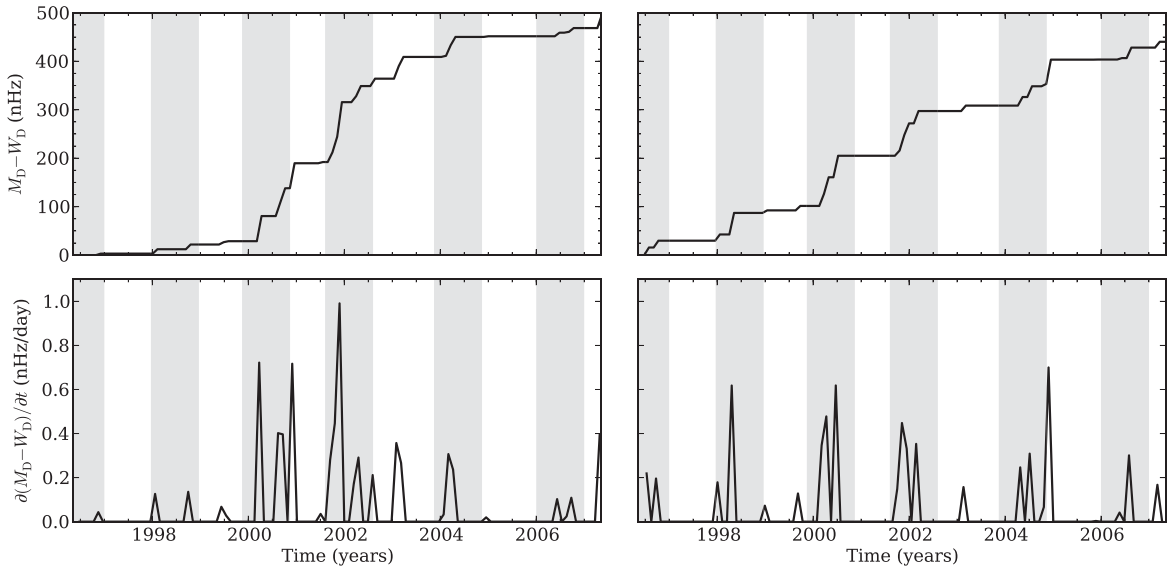

Figure 5. The left-hand panel concerns Sample 1, while the right-hand panel corresponds to Sample 2 (see text for details). Top panels: difference between the absolute sum, M_D, and the weighted sum, W_D, of the observed frequency-shift variations, i.e. between the black-dashed and solid lines in Fig. 3. Bottom panels: time derivative of the difference shown in the top panels. The grey bars, with a width of one year, are centred around the approximate location of the maxima of the quasi-biennial signal detected by Broomhall et al. (2012).

Fig. 5, which have a width of 1 yr and are centred at the locations of maxima of the quasi-biennial signal found by Broomhall et al. (2012).

6 DISCUSSION

Our results show that there is a strong correlation between the short-term variations in the frequency shifts and in the area covered by sunspots. However, the loss of correlation between the two is still significant and cannot be fully explained by the combined effect of the sunspot groups on the invisible side of the Sun and of the observational error in the observed frequency-shift differences. Moreover, the detailed analysis of the difference between the quantities W_D and M_D shows that opposite variations in the frequency shifts and in the sunspot area are more significant around the times of maxima of the quasi-biennial signal. This clear signature of the quasi-biennial variations in the quantity W_D highlights the fact that the short time-scale variations are modulated on a quasi-biennial time-scale.

The above findings could point to a quasi-biennial change in the effect of the sunspots. However, we find this possibility difficult to understand on physical grounds because it would require that an increase in the sunspot area leads to a decrease in the frequency shifts at the maximum of the quasi-biennial variations. According to the model for the spot-induced frequency shifts (Paper I), this would imply that the phase shift induced by a sunspot on the acoustic wave travelling through it changed sign from the minimum to the maximum of the quasi-biennial variation. Another, perhaps more likely possibility is that other active-related features, such as plage, not accounted for in the computation of W_D, could contribute to the short-term variations in the frequency shifts. However, given the asymmetry found between the behaviour of the correlations at the maximum and minimum of the quasi-biennial variations, their effect would have to dominate the short-term frequency-shift variations during the former, but be unimportant, compared to the effect of sunspots, during the latter. This possibility will be further investigated by inspecting the behaviour of 10.7-cm flux, discussed in the next subsection.

6.1 Short-term variations in the 10.7-cm flux

The acoustic frequency shifts are found to be better correlated with the 10.7-cm flux than with other activity proxies (e.g. Chaplin et al. 2007; Tripathy et al. 2007; Jain et al. 2009). Besides the contribution from sunspots, the 10.7-cm flux is also affected by radio plages and the quiet-Sun background in the upper chromosphere and lower corona (e.g. Covington 1969; Tapping 1987; Tapping & Detracey 1990). Given its sensitivity to both sunspots and plages, the 10.7-cm flux may provide a more complete picture of the short-term variations in the solar activity than the sunspot areas alone. To test this possibility, we repeated our analysis using the variations in the 10.7-cm flux (from NGDC/NOAA) instead of the sunspot area variations as the weight in equation (2). The results, shown in Fig. 6, confirm that the loss of correlation is less pronounced in this case than when the sunspot area variations are used (around 40 per cent smaller than that found in Figs 3 and 5). Despite this, we still find that, in general, the loss of correlation is more significant around the maxima of the quasi-biennial variations.

The comparison between the results found for the area covered by sunspots and for the 10.7-cm flux confirms that the latter contains contributions from additional activity-related features (besides sunspots) that vary on short time-scales and that these features have a significant impact on the short-term variations of the frequency shifts. Moreover, we may conclude from the results for the 10.7 cm that spots and plages alone do not fully explain the short-term variations in the observed frequency shifts.

7 CONCLUSIONS

In this work we investigated the correlation between the variation in the solar frequency shifts and in the area covered by sunspots. In particular, we proposed a new observable, consisting in the sum

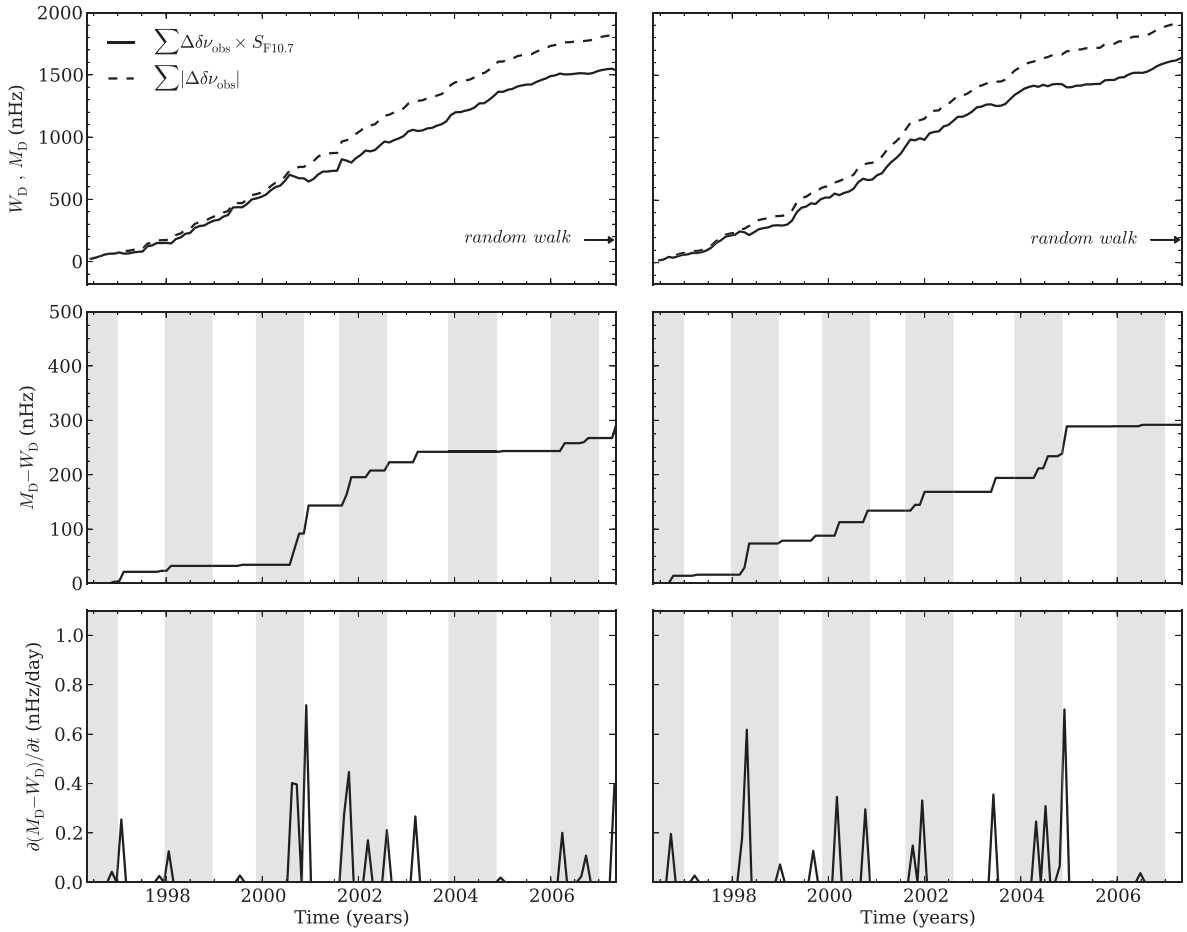

Figure 6. The left-hand panel concerns Sample 1, while the right-hand panel corresponds to Sample 2. Top panels: weighted sum of the variations in the observed frequency shifts (black solid line), where the weight S, in equation (2), is determined by the variation in the 10.7-cm flux. The dashed line represents the sum of the absolute (modulus) values of the frequency-shift differences, $M_{\rm D}$. Middle panels: difference between the dashed and solid lines in the top panels. Bottom panels: derivative of the difference shown in the middle panels. The grey bars, with a width of one year, are centred around the approximate location of the maxima of the quasi-biennial signal detected by Broomhall et al. (2012).

of the frequency shifts weighted by the variation of the sunspot area, which isolates and amplifies the signal from the short-term variations in the frequency shifts. Using this new observable, we found a strong correlation between the short-term variations in the area covered by sunspots and in the frequency shifts. Nevertheless, a significant loss of correlation is still observed, generally coinciding with the times of maxima of the quasi-biennial variations seen in the solar acoustic frequencies. The loss of correlation on short time-scales suggests that other physical phenomena, besides sunspots, acting on time-scales shorter than 36 d contribute to the frequency shifts and that their relative importance changes in phase with the quasi-biennial signal.

We also considered the case in which the variation of the 10.7-cm flux, rather than the visible sunspot area, is used as a weight in the computation of the new observable. The short-term variation in the frequency shifts was found to vary even more closely in line with the 10.7-cm flux than with the sunspot areas, confirming that the 10.7-cm flux contains information about additional activity-related features which contribute to the frequency shifts. Nevertheless, a significant loss of correlation, whose physical origin remains to be fully understood, is again observed around the times of maxima of the quasi-biennial signal.

ACKNOWLEDGEMENTS

This work was supported by Fundação para a Ciência e a Tecnologia (FCT) through the research grant UID/FIS/04434/2013. ARGS acknowledges the support from FCT through the Fellowship SFRH/BD/88032/2012 and from the University of Birmingham. MSC and PPA acknowledge support from FCT through the Investigador FCT Contract numbers IF/00894/2012 and IF/00863/2012 and POPH/FSE (EC) by FEDER funding through the programme Programa Operacional de Factores de Competitividade (COMPETE). TLC and WJC acknowledge the support of the UK Science and Technology Facilities Council (STFC). The research leading to these results has received funding from EC, under FP7, through the grant agreement FP7-SPACE-2012-312844 and PIRSES-GA-2010-269194. ARGS, MSC, and PPA are grateful for the support from the High Altitude Observatory (NCAR/UCAR), where part of the current work was developed.

REFERENCES

Broomhall A.-M., Nakariakov V. M., 2015, Sol. Phys., 290, 3095
Broomhall A.-M., Chaplin W. J., Elsworth Y., Simoniello R., 2012, MNRAS, 420, 1405

Chaplin W. J., Elsworth Y., Isaak G. R., Lines R., McLeod C. P., Miller B. A., New R., 1998, MNRAS, 300, 1077
Chaplin W. J., Elsworth Y., Isaak G. R., Miller B. A., New R., 2004, MNRAS, 352, 1102
Chaplin W. J., Elsworth Y., Miller B. A., Verner G. A., New R., 2007, ApJ, 659, 1749
Covington A. E., 1969, J. R. Astron. Soc. Can., 63, 125
Dziembowski W. A., Goode P. R., 2005, ApJ, 625, 548
Elsworth Y., Howe R., Isaak G. R., McLeod C. P., New R., 1990, Nature, 345, 322
Fletcher S. T., Broomhall A.-M., Salabert D., Basu S., Chaplin W. J., Elsworth Y., Garcia R. A., New R., 2010, ApJ, 718, L19
García R. A., Mathur S., Salabert D., Ballot J., Regulo C., Metcalfe T. S., Baglin A., 2010, Science, 329, 1032
Hathaway D. H., Wilson R. M., Reichmann E. J., 1994, Sol. Phys., 151, 177
Hindman B., Haber D., Toomre J., Bogart R., 2000, Sol. Phys., 192, 363
Howe R., Komm R. W., Hill F., 2002, ApJ, 580, 1172
Howe R., Davies G. R., Chaplin W. J., Elsworth Y. P., Hale S. J., 2015, MNRAS, 454, 4120
Jain K., Tripathy S. C., Hill F., 2009, ApJ, 695, 1567
Jain R., Tripathy S. C., Watson F. T., Fletcher L., Jain K., Hill F., 2012, A&A, 545, A73
Libbrecht K. G., Woodard M. F., 1990, Nature, 345, 779
Régulo C., García R. A., Ballot J., 2016, A&A, 589, A103
Salabert D., García R. A., Pallé P. L., Jiménez A., 2011, J. Phys.: Conf. Ser., 271, 012030
Salabert D., García R. A., Turck-Chièze S., 2015, A&A, 578, A137
Salabert D. et al., 2016, A&A, 589, A118
Santos A. R. G., Cunha M. S., Avelino P. P., Campante T. L., 2015, A&A, 580, A62
Santos A. R. G., Cunha M. S., Avelino P. P., Chaplin W. J., Campante T. L., 2016, MNRAS, 461, 224 (Paper I)
Simoniello R., Finsterle W., Salabert D., García R. A., Turck-Chièze S., Jiménez A., Roth M., 2012, A&A, 539, A135
Simoniello R., Jain K., Tripathy S. C., Turck-Chièze S., Baldner C., Finsterle W., Hill F., Roth M., 2013, ApJ, 765, 100
Tapping K. F., 1987, J. Geophys. Res., 92, 829
Tapping K. F., Detracey B., 1990, Sol. Phys., 127, 321
Tripathy S. C., Hill F., Jain K., Leibacher J. W., 2007, Sol. Phys., 243, 105
Tripathy S. C., Jain K., Salabert D., García R. A., Hill F., Leibacher J. W., 2011, J. Phys.: Conf. Ser., 271, 012055
Woodard M. F., Noyes R. W., 1985, Nature, 318, 449

This paper has been typeset from a TEX/LATEX file prepared by the author.

A&A 599, A1 (2017)
DOI: 10.1051/0004-6361/201629923

Astronomy & Astrophysics

Starspot signature on the light curve

Learning about the latitudinal distribution of spots

A. R. G. Santos[1,2,3], M. S. Cunha[1,2], P. P. Avelino[1,2], R. A. García[4], and S. Mathur[5]

[1] Instituto de Astrofísica e Ciências do Espaço, Universidade do Porto, CAUP, Rua das Estrelas, 4150-762 Porto, Portugal
e-mail: asantos@astro.up.pt
[2] Departamento de Física e Astronomia, Faculdade de Ciências, Universidade do Porto, Rua do Campo Alegre 687, 4169-007 Porto, Portugal
[3] School of Physics and Astronomy, University of Birmingham, Edgbaston, Birmingham B15 2TT, UK
[4] Laboratoire AIM, CEA/DRF-CNRS-Université Paris 7 Diderot; IRFU/SAp, Centre de Saclay, 91191 Gif-sur-Yvette Cedex, France
[5] Center for Extrasolar Planetary Systems, Space Science Institute, 4750 Walnut street, Suite 205, Boulder, CO 80301, USA

Received 17 October 2016 / Accepted 22 November 2016

ABSTRACT

Context. Quasi-periodic modulations of the stellar light curve may result from dark spots crossing the visible stellar disc. Owing to differential rotation, spots at different latitudes generally have different rotation periods. Hence, by studying spot-induced modulations, it is possible to learn about stellar surface (differential) rotation and magnetic activity. Recently, a method based on the Lomb-Scargle periodogram of light curves has been proposed to identify the sign of the differential rotation at the stellar surface.
Aims. Our goal is to understand how the modulation of the stellar light curve due to the presence of spots and the corresponding periodogram are affected by both the stellar and spot properties.
Methods. We generate synthetic light curves of stars with different properties (inclination angle, limb darkening, and rotation rate) and spot configurations (number of spots, latitude, intensity contrast, and size). By analysing their Lomb-Scargle periodograms, we compute the ratio between the heights of the second and first harmonics of the rotation period (peak-height ratio).
Results. We find that the peak-height ratios are essentially a function of a single parameter, the fraction of time the spot is visible, which is related to the sinusoidality of the spot modulation. We identify the conditions under which the periodogram analysis can actually provide an estimate of the spot latitudes and/or the stellar inclination angle. We also identify possible sources of error in the identification of the sign of the differential rotation.

Key words. stars: solar-type – stars: rotation – stars: activity – starspots – techniques: photometric

1. Introduction

Stellar rotation, in particular differential rotation, is a key ingredient of the dynamo mechanism, which is responsible for the generation of the magnetic field in the Sun and solar-like stars. As a manifestation of the magnetic activity, dark spots emerge at the stellar surface. Spots are regions of strong magnetic field that suppresses the convection, resulting in less efficient heat transport. Therefore, spots are cooler and, consequently, darker than the surroundings, having an impact on the stellar brightness. As the spots cross the stellar visible disc, they modulate the light curve. Such modulation provides information about the stellar rotation and magnetic activity (e.g. Mosser et al. 2009; Mathur et al. 2010; García et al. 2010, 2014; Ballot et al. 2011; Mathur et al. 2014).

High-precision photometric time series obtained with space telescopes allowed the detection of rotational periods for a large number of stars (e.g. Reinhold et al. 2013; Nielsen et al. 2013; McQuillan et al. 2013a,b, 2014; García et al. 2014) through methods based on the Lomb-Scargle periodogram, the autocorrelation function, and/or the wavelet transform. Moreover, the high quality of these time series provides a good opportunity to measure differential rotation since the spot-induced modulations of the light curves enclose specific signatures of spots at different latitudes. The amplitude of the differential rotation can be recovered through spot modelling (e.g. Mosser et al. 2009; Huber et al. 2010; Lanza et al. 2011, 2014). By fitting a given model to the observed light curve, a number of stellar and spot parameters can be constrained, including the spots' rotation rates. Differential rotation has also been measured through the periodogram analysis (e.g. Reinhold & Reiners 2013; Reinhold et al. 2013; Reinhold & Gizon 2015; Nagel et al. 2016; Distefano et al. 2016). In the periodogram, broad or multiple peaks associated with the stellar rotation are usually interpreted as evidence of the differential rotation. The analysis of individual subseries of the full light curve, whose modulation might be dominated by a given spot at a given latitude, allows the identification of temporal variations in the recovered rotation period, which can also be an indication of differential rotation.

Recently, based on the periodogram analysis, Reinhold & Arlt (2015) proposed a new method to detect the sign of differential rotation, i.e. whether the equatorial regions rotate faster (+, solar differential rotation) or slower (−, antisolar differential rotation) than the poles. When they apply the method to a particular set of synthetic light curves with solar differential rotation, a low false-positive rate (11.3–20%) was recovered. The method was also applied to a sample of 50 stars observed by

Kepler. Solar differential rotation was reported for 21–34 stars, while 5−10 stars were found to be consistent with anti-solar differential rotation (for details, see Reinhold & Arlt 2015).

In this work, we investigate the spot's signature on the light curve and, consequently, on the periodogram. In particular, we are interested in understanding the conditions that lead to the successful or unsuccessful detection of the sign of differential rotation.

2. Determining the sign of the surface differential rotation

The Lomb-Scargle periodogram (LSP) can be used to determine the stellar surface rotation. Secondary peaks close to the main rotation period are interpreted as evidence for differential rotation, being associated with spots/active regions at different latitudes, thus rotating at different rates.

Reinhold & Arlt (2015) proposed a new and simple method for determining the sign of differential rotation, which consists in comparing the ratios between the height of the second and first harmonics (hereafter peak-height ratios) associated with different rotation periods. For a given rotation period P_j (first harmonic), the peak-height ratios are computed as

$$r_j = \frac{h(P'_j)}{h(P_j)}, \tag{1}$$

where P'_j is the second harmonic of the rotation period, and $h(P_j)$ and $h(P'_j)$ are the heights of the first and second harmonics, respectively (hereafter, h_j and h'_j).

The authors argue that spots at lower latitudes lead to less sine-shaped light curves than spots at higher latitudes, resulting in extra power on the second harmonic and, thus, larger peak-height ratios. While they based their argument on results for synthetic light curves with specific configurations, the authors do not provide any further explanation. In Sect. 4.1. we address in detail the latitudinal dependence of the peak-height ratios.

Following their argument that spots at lower latitudes lead to larger peak-height ratios than spots at higher latitudes, when comparing the peak-height ratios of two periods associated with the surface rotation, P_j and P_{j+1}, the method allows for the determination of a relative latitude ("high" or "low") and, thus, the sign of differential rotation. Reinhold & Arlt (2015) define the observed relative differential rotation as

$$\alpha_{\rm obs} = \frac{P_{\rm high} - P_{\rm low}}{P_{\rm high}}. \tag{2}$$

Here $\alpha_{\rm obs} > 0$ corresponds to solar differential rotation (the equator rotates faster than the poles) and $\alpha_{\rm obs} < 0$ corresponds to antisolar differential rotation (the poles rotate faster than the equator).

3. Synthetic light curves

In order to study the modulation of the stellar light curves due to the presence of spots, we developed a tool to simulate the light curves of spotted stars based on the models of Lanza et al. (1993) and Eker (1994).

Each spot is assumed to be circular and is decomposed in a number of area elements. The total decrease in flux due to spots corresponds to the sum of the contributions from each element k

$$\frac{\Delta F}{F} = \sum_k \left(\frac{\Delta F}{F}\right)_k. \tag{3}$$

The decrease in flux associated with an element k is given by

$$\left(\frac{\Delta F}{F}\right)_k = (1 - C_{\rm S})\frac{S_k}{\pi R_*^2}\mu_k \frac{I(\mu_k)}{I(1)}, \tag{4}$$

where S_k is the element area, R_* is the stellar radius, $I(\mu_k)/I(1)$ is the relative photospheric intensity given by the limb-darkening law, and $\mu_k = \cos\psi_k$, where ψ_k is the angle between the line of sight and the normal to the surface element given by

$$\mu_k = \cos\psi_k = \cos i \cos\theta_k + \sin i \sin\theta_k \cos\phi_k. \tag{5}$$

Here, i is the stellar inclination angle, i.e. the angle between the stellar rotation axis and the line of sight, and θ_k and ϕ_k are the colatitude and longitude of the element. The element k is visible whenever $0 \leq \mu_k \leq 1$. $C_{\rm S}$ is the spot-to-photosphere intensity ratio, i.e. $C_{\rm S} = I_{\rm S}/I_{\rm P}$, which, for simplicity, we shall assume to be a constant.

4. Results

4.1. One-spot simulations

The modulation on the light curve induced by spots crossing the visible disc of the star depends on a number of stellar and spot parameters, e.g. the stellar inclination angle, rotation rate, limb-darkening law, spot size, latitude, and contrast.

We start by investigating to what extent the peak-height ratios, $r = h'/h$, are a measure of the sinusoidality of the spot modulation on the light curve. To do so, we start by considering the simplest case of one-spot simulations. We obtain the synthetic light curves for stars with different inclination angles, i, and a single spot at different latitudes, L. For this set of simulations we assume a circular spot of constant radius $R_{\rm S} \sim 5.7°$ ($A = 5000\,\mu$Hem; about the area covered by sunspots at solar maximum), infinite lifetime, and an intensity contrast of $C_{\rm S} = 0.67$ (e.g. Sofia et al. 1982; Lanza et al. 2003; Walkowicz et al. 2013). Also, we consider a quadratic limb-darkening law

$$\frac{I(\mu)}{I(1)} = 1 - a(1-\mu) + b(1-\mu)^2, \tag{6}$$

where we have assumed $a = 0.5287$ and $b = 0.2175$, which are adequate for solar-like stars observed by *Kepler* (Claret 2000; Reinhold & Reiners 2013). The differential rotation is assumed to be solar and is given by

$$\Omega(L) = \Omega_{\rm eq}(1 - \alpha \sin^2 L - \beta \sin^4 L), \tag{7}$$

where $\Omega_{\rm eq}$ is the angular velocity at the equator, and α and β are the parameters that determine the latitudinal dependency of the rotation rate. For this set of synthetic data, we have considered $\Omega_{\rm eq} = 0.2567\,{\rm rad\,d^{-1}}$, $\alpha = 0.1584$, and $\beta = 0.1210$ (Snodgrass 1983; Snodgrass & Ulrich 1990). The initial longitude of the spot for each simulation in this section is determined randomly.

We compute the Lomb-Scargle periodogram for each synthetic light curve and the corresponding ratios between the second and first harmonics. We find that the peak-height ratios are essentially a function of a single parameter: the visibility time of the spot. Figure 1 shows how the peak-height ratios change as a function of the ratio between the visibility time and the rotation period. Spots that are visible for most of the rotation period lead to more sine-shaped signals than spots that are visible for a smaller fraction of time. The spot is considered visible whenever there is a decrease in flux. Using this definition for the visibility

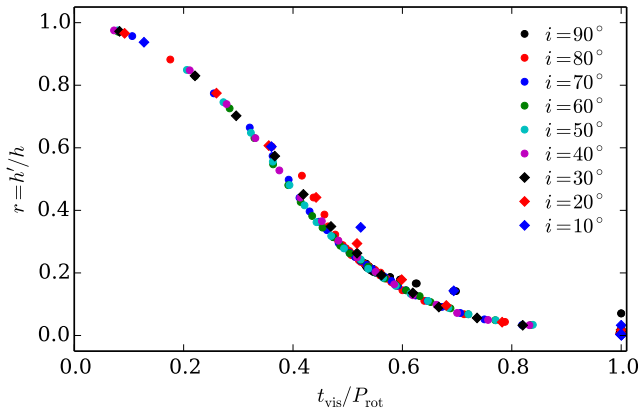

Fig. 1. Peak-height ratios associated with spots at different latitudes (ranging from 0° to ±85°) as a function of the spot visibility time. Different colours indicate different stellar inclination angles, i.

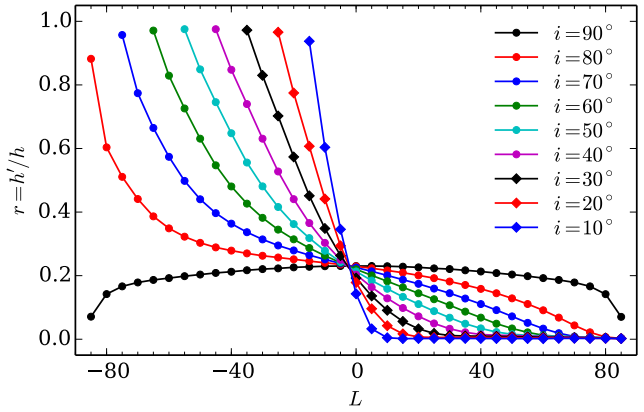

Fig. 2. Peak-height ratios as a function of the spot latitude, L, for different inclination angles, i.

time of the spot ($t_{\rm vis}$), we might be overestimating the true visibility time, especially for low inclination angles. Nevertheless, we can clearly conclude that the longer the spots are visible, the smaller the peak-height ratios are.

Figure 2 shows the peak-height ratios as a function of the spot latitude. The spot latitude and the stellar inclination angle are the most determinant parameters for the spot visibility. As different combinations of i and L result in the same spot visibility time, there is a degeneracy between latitude and inclination. Nevertheless, the peak-height ratios provide constraints on the possible solutions (i, L) that can lead to the spot signature on the observed light curve. If the stellar inclination is known, the spot latitude can be estimated.

The method proposed by Reinhold & Arlt (2015) for the determination of the sign of the surface differential rotation relies on the correct identification of a relative latitude (low/high) for at least two rotation periods (first harmonics) in the LSP. Implicit to their method is the assumption that spots at lower absolute latitudes are associated with higher peak-height ratios, $r = h'/h$, than are spots at higher absolute latitudes. Except for inclination angles very close to $i = 90°$, this is only true for spots on the same hemisphere as the observer (which we will call the northern hemisphere). Spots emerging at higher latitudes on the southern hemisphere are visible for a smaller fraction of time, thus, inducing a less sinusoidal signature and leading to higher peak-height ratios than spots at lower latitudes on the northern or southern hemispheres. Hence, for values of the inclination angle not too close to $i = 90°$, the method will suggest the wrong sign for the differential rotation when comparing the peak-height ratios of periods associated with spots on the southern hemisphere. The wrong sign will also be recovered when one of the spots is at L_1 on the northern hemisphere, the second is at L_2 on the southern, and $|L_2| > |L_1|$.

For an inclination angle of $i = 90°$, the behaviour of the peak-height ratios is hemispheric symmetric and nearly independent on the latitude of the spot (except for $|L|$ very close to 90°). Therefore, for this inclination, the association of the detected rotation periods with different latitudes is difficult. Also, for small inclination angles, the ratios become saturated at high latitudes on the northern hemisphere as spots at that location are always visible.

Although our results show that the peak-height ratios are essentially a function of the visibility time of the spot, which is determined mainly by the stellar inclination angle and the spot latitude, the modulation in the light curves induced by spots also depends on other parameters. In what follows, we investigate the impact on the peak-height ratios of other spot and stellar properties, such as the spot area and relative intensity, rotation rate, and limb-darkening law.

The top panel of Fig. 3 shows the peak-height ratios as a function of latitude (left panel) and visibility time (right panel) for different inclination angles and spot sizes. The impact of the spot size on the recovered ratios is more significant for spots at higher latitudes on the southern hemisphere and lower inclinations. For a given latitude and inclination, a larger spot will be visible for a longer time than a smaller spot, thus larger spots lead to smaller ratios than smaller spots.

As the spot-to-photosphere intensity contrast does not affect the visibility time of the spot, it also does not have a significant impact on the peak-height ratios. This is shown in the second row of Fig. 3. As mentioned before, for these synthetic light curves the initial phase of the spot is determined randomly, taking into consideration that the light curve is discrete, this introduces a small effect on the estimated spot visibility time. The small differences seen in the right panel of the second row in Fig. 3 show that the phase of a given spot alone has little impact on the visibility time of the spot.

In order to investigate the impact of the rotation rate on the peak-height ratios, we have considered different rotation profiles in the synthetic data, including solar ($\alpha > 0$) and anti-solar ($\alpha < 0$) differential rotation. In this set of simulations, we consider the simplified version of Eq. (7) that is commonly used,

$$\Omega(L) = \Omega_{\rm eq}(1 - \alpha \sin^2 L). \tag{8}$$

The third row of Fig. 3 summarizes the results from this study, where $\Omega_{\rm eq,\odot} = 0.2567\,{\rm rad\,d^{-1}}$ and $\alpha_\odot = 0.1584$ denote the solar values considered above. Since the rotation rate does not change the fraction of time the spot is visible, it does not significantly affect the peak-height ratios. However, small discrepancies are still visible, which result first from the random initial spot phases, and second from the fact that while the characteristic time-scale of the light curves changes when considering different rotation rates, the length and cadence of the light curves are unchanged.

The bottom panel of Fig. 3 shows the results obtained from synthetic data considering different limb-darkening laws: the quadric limb-darkening law (Eq. (6)), the linear limb-darkening law

$$\frac{I(\mu)}{I(1)} = 1 - u(1 - \mu), \tag{9}$$

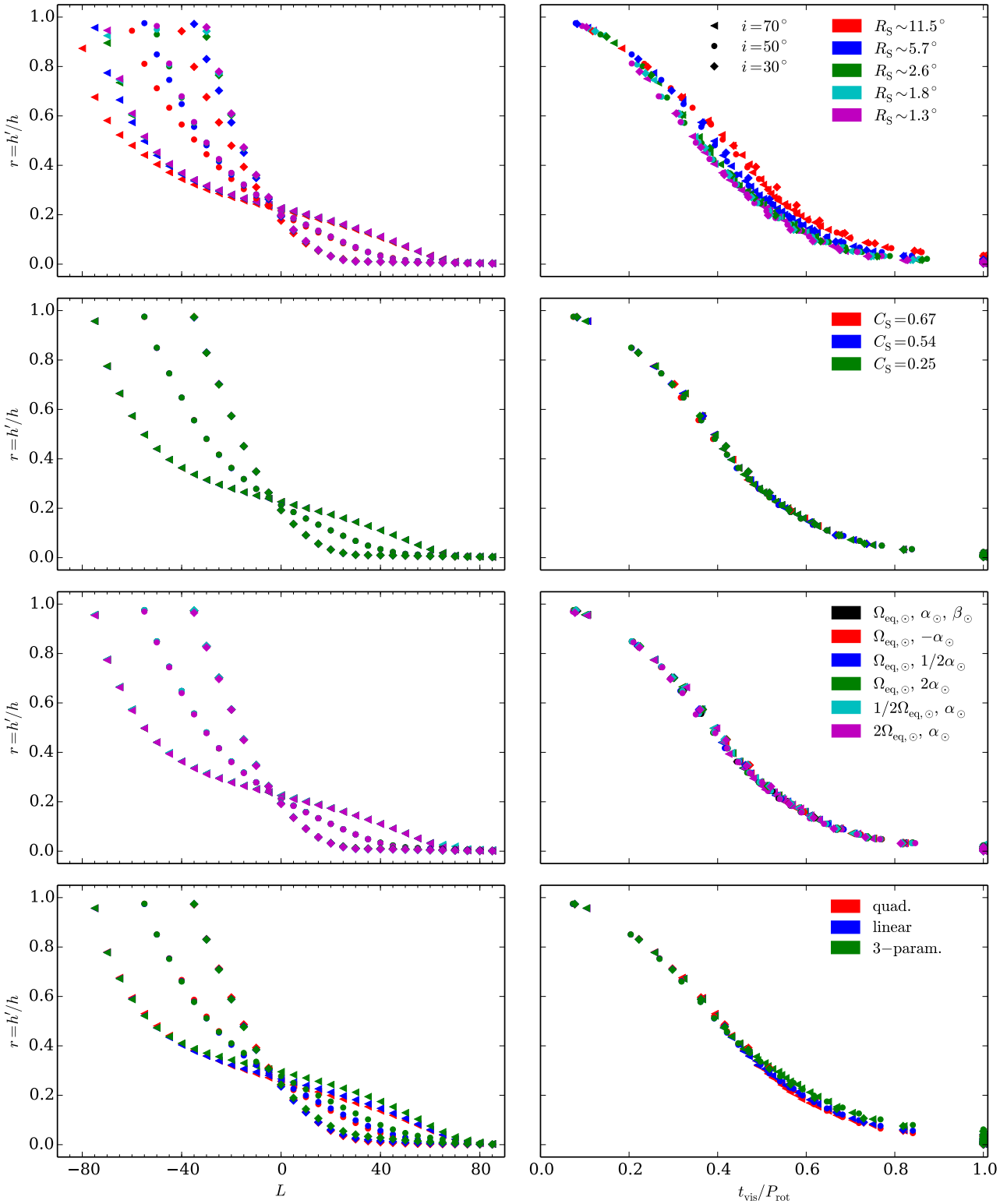

Fig. 3. Peak-height ratios as a function of the spot latitude (*left*) and visibility time (*right*) for the inclination angles i = 30°, 50°, and 70° and for different spot areas (*top panel*), different spot-to-photosphere intensity ratios (*second row*), various differential rotation parameters (*third row*), and different limb-darkening laws (*bottom panel*). For these simulations, the default values of the spot radius and intensity contrast are $R_{\rm S} \sim 5.7°$ and $C_{\rm S} = 0.67$. We use the solar rotation ($\Omega_{\rm eq,\odot}$, $\alpha_\odot$, and $\beta_\odot$) as the default rotation profile. Finally, the default limb-darkening law is the quadratic one with parameters $a = 0.5287$ and $b = 0.2175$. [$R_{\rm S} \sim 11.5° \Leftrightarrow A_{\rm S} = 20\,000\,\mu$Hem, $R_{\rm S} \sim 5.7° \Leftrightarrow A_{\rm S} = 5000\,\mu$Hem, $R_{\rm S} \sim 2.6° \Leftrightarrow A_{\rm S} = 1000\,\mu$Hem, $R_{\rm S} \sim 1.8° \Leftrightarrow A_{\rm S} = 500\,\mu$Hem, $R_{\rm S} \sim 1.3° \Leftrightarrow A_{\rm S} = 250\,\mu$Hem]

and the three-parameter non-linear limb-darkening law

$$\frac{I(\mu)}{I(1)} = 1 - c_2\,(1-\mu) - c_3\left(1-\mu^{3/2}\right) - c_4\left(1-\mu^2\right), \qquad (10)$$

where u, c_2, c_3, and c_4 are the limb-darkening coefficients, which we take from the study by Sing (2010) for *Kepler* data. Since the effective temperature ($T_{\rm eff}$), the surface gravity ($\log g$), and metallicity ([M/H]) are, in principle, known parameters, Fig. 3 shows the results for $T_{\rm eff}$ = 5750 K, $\log g$ = 4.50 and [M/H] = 0.00. As the limb-darkening changes the shape of the spot modulation, it also affects the sinusoidality of the modulation seen through the peak-height ratios (bottom panel of Fig. 3). Also, for different inclinations, spots with the same $t_{\rm vis}/P_{\rm rot}$ have different trajectories over the visible disc, corresponding to different limb-darkening and projected spot areas. In turn, the sinusoidality of the spot signature changes. This effect is small and can be seen through the differences between different inclinations (for example, second row of Fig. 3).

4.2. Two-spot simulations

In this section, we analyse synthetic light curves obtained considering two spots on the stellar surface, in a broad range of latitudes, and we explore possible sources for contamination of the peak-height ratios.

For the first set of synthetic light curves, the rotation rate is defined by Eq. (8) with parameters $\Omega_{\rm eq,\odot}$ and $\alpha_\odot$, and the spot radius is fixed at 5.7°. The length of the synthetic light curves is four years, consistent with the typical length of the *Kepler* light curves. The two spots have the same longitude at the beginning of the simulation.

The analysis performed in Sect. 4.1 will only be valid in cases for which at least two rotation periods are clearly detected in the Lomb-Scargle periodogram. As peaks in the LSP can interfere with each other, we impose a detectability limit for the period separation. Because of the non-infinite light curve, we fit a sinc function in frequency (being symmetric in frequency, not in period) to the main peak, P_1, and define the detectability limit to be equal to 1.5 times the width of the sinc function at half maximum. Figure 4 shows the LSP for three different cases: (i) a case where there are two spots at different latitudes, but only one rotation period can be recovered (top panel), (ii) a case where two rotation periods might be recovered but they do not fulfil the chosen criteria on the minimum distance between two peaks (middle panel); and (iii) a case where two rotation periods are clearly detected being separated by more than the imposed limit (bottom panel). Also, we discard peaks that may be significantly affected by the side lobes related to the first period.

4.2.1. Spots' latitude effect

The first source for false-positives/negatives for the sign of differential rotation was already identified from the one-spot simulations. The method summarized in Sect. 2 is only fully valid for light curves whose spot modulation is induced by spots on the northern hemisphere. The method will also return the correct sign when the two spots are on opposite hemispheres, but only if the spot on the southern hemisphere is at a lower absolute latitude than the spot on the northern hemisphere. This is shown in Fig. 5, confirming that if the two surface rotation periods are successfully detected and distinguishable, the conclusions for one-spot simulations will be valid for two-spot simulations. Here, the sign of the surface differential rotation is determined by $\alpha_{\rm obs}$ (Eq. (2)).

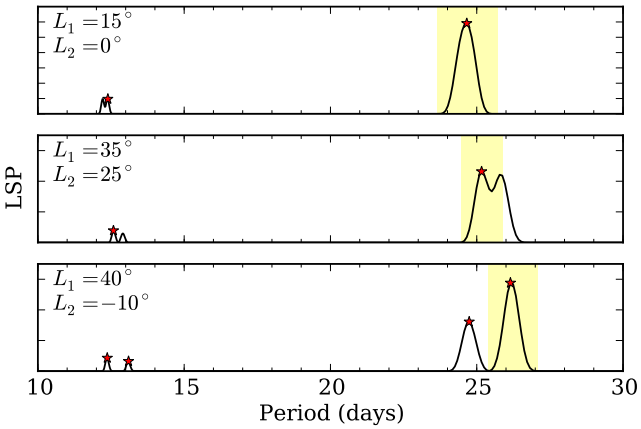

Fig. 4. Lomb-Scargle periogram for three synthetic light curves from simulations with two spots at different latitudes, L_1 and L_2. *Top panel*: only one rotation period is detected. *Middle panel*: two peaks associated with the surface rotation are seen but the second is not within the detectable period range. *Bottom panel*: the rotation periods associated with each spot latitude are successfully detected. The spot latitudes are indicated in the left top left corner of each panel. The red symbols mark the first and second harmonics if detected. The yellow regions mark the detectability limit we impose (see text for details).

Figure 6 shows the errors on the recovered peak-height ratios and inferred latitudes as a function of L_2 for two particular cases with i = 70°. The left and right panels correspond to L_1 = 40° and L_1 = −10°, respectively. The errors on the ratios are determined in relation to the reference values shown in Fig. 2. Taking the reference latitude-ratio relation and the peak-height ratios recovered from the two-spot simulations, the observed spot latitudes L can be inferred and then compared with the input latitudes. The yellow areas mark the latitude intervals where only one rotation period is successfully detected. For the cases shown, the error on the spot latitude is at most ∼15°. If the stellar inclination angle is known, this indicates that the observed peak-height ratios, together with the results from one-spot simulations (the latitude-ratio relation for the corresponding i), can be used to estimate the latitudinal distribution of spots.

4.2.2. Spot area effect

Figure 7 shows the errors on the peak-height ratios and latitudes as a function of the spot area ratio, A_2/A_1. For this set of simulations, the spot latitudes ($L_1 = 40°$ and $L_2 = 20°$), stellar inclination angle ($i = 70°$), and the surface rotation ($\Omega_{\rm eq} = \Omega_{\rm eq,\odot}$, $\alpha = \alpha_\odot$) are fixed. The spots at $L_1 = 40°$ have a constant radius of $R_1 = 5.7°$, while the radius of the spots at $L_2 = 20°$ varies between 1.8° and 11.5°. The results show that the errors in the inferred peak-height ratios and latitudes are not significantly affected by variations in the relative area of the spots. In this case, a solar differential rotation ($\alpha_{\rm obs} > 0$) is correctly recovered for all the synthetic light curves.

4.2.3. Spots phase effect

The phase of the spots also has an impact on the peak-height ratios. In particular, when spots have similar rotation rates and are in anti-phase, the LSP shows an excess of power on the second harmonic. In some cases the second harmonic can even be the main peak in the LSP, being wrongly identified

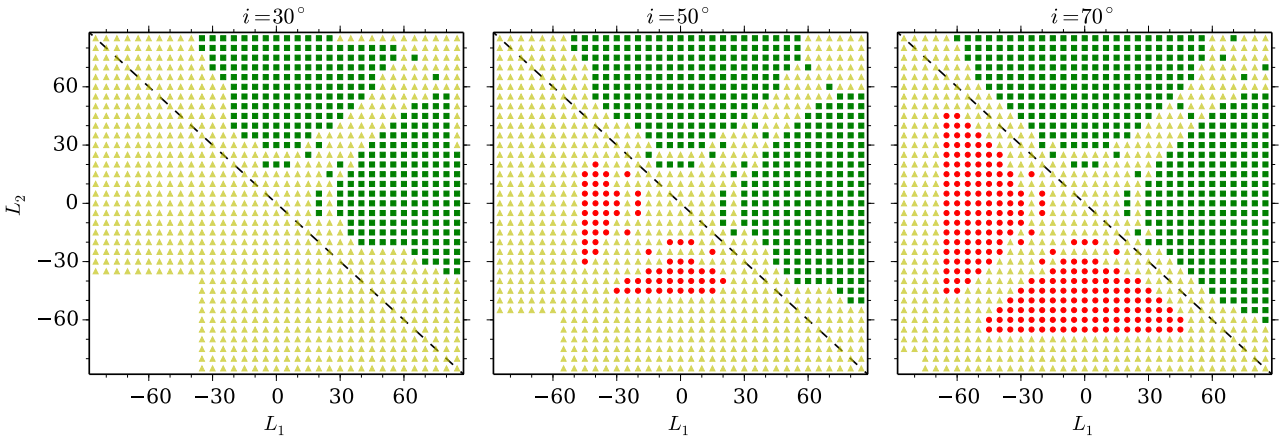

Fig. 5. Sign of the surface differential rotation, α_{obs}, for two-spot simulations with stellar inclination angles of i = 30° (*left*), i = 50° (*middle*), and i = 70° (*right*). The spot latitudes (L_1 and L_2) range from −85° to 85° with steps of 5°. The yellow triangles represent the cases where only one rotation period is detected according to the criteria (see text). The red dots represent the cases where the wrong sign of differential rotation ($\alpha_{obs} < 0$) is found, while the green squares mark the cases where the correct sign ($\alpha_{obs} > 0$) is recovered. The dashed line divides the regions where the correct (above) or wrong (below) sign of α_{obs} is expected from the results of Sect. 4.1 (see text for details).

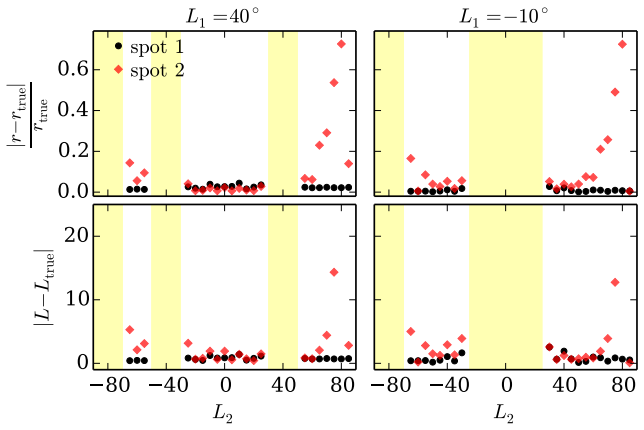

Fig. 6. Error on the peak-height ratios (*top*) and latitudes (*bottom*) as a function of the latitude of the second spot. Black and red symbols concern spots 1 and 2, respectively. The *left panels* correspond to $L_1 = 40°$, while the *right panels* show the results for $L_1 = -10°$. The yellow areas mark the latitude intervals where only one rotation period was detected. Here we disregarded the cases in which the peak-height ratios were outside the one-spot peak-height ratio range given in Fig. 2.

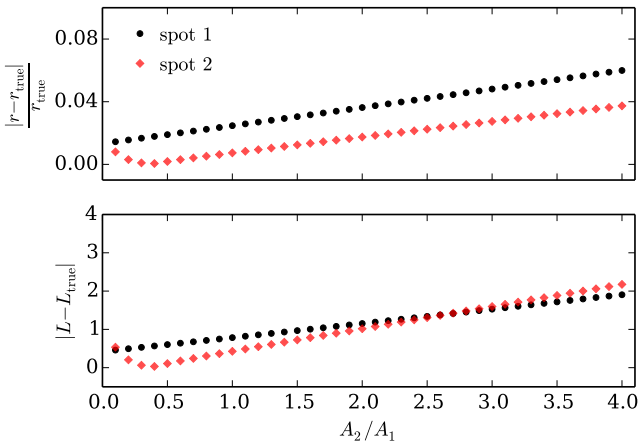

Fig. 7. Error on the peak-height ratios (*top*) and latitudes (*bottom*) as a function of the ratio between the areas of spot 2 (red) and spot 1 (black). For all the cases, $\alpha_{obs} > 0$.

as the rotation period of the star (e.g. McQuillan et al. 2013a; Reinhold & Reiners 2013). In these cases, the resulting peak-height ratios should not be used to infer the spot latitude or the sign of differential rotation. Two examples are shown in Fig. 8, where we consider a stellar inclination angle of 70° and the spot latitudes L_1 = 40° and L_2 = ±40°. When L_2 = −40° the two spots have the same size (corresponding to $R_S \sim 5.7°$); instead, when L_2 = 40° the second spot is half the size of the first spot[1]. For comparison, the black line corresponds to the reference LSP for one spot at 40°, with a radius of 5.7°. In both cases (top panel, red; middle panel, blue), the observer could be wrongly led to assume that the peak in the LSP is being produced by a single spot, but the peak-height ratios in both cases would be very different from the case of a single spot (in black). This is also evident from the bottom panel, which compares the recovered ratios with the reference ratios from Fig. 2 for the inclination of 70°. If we still considered the higher period as the first harmonic, the peak-height-ratio that would be inferred in the first case (red) would be outside the expected range for a single spot for the chosen inclination, while in the second case (blue) a very low latitude would be inferred if the single spot scenario were to be wrongly assumed. The longitude of the second spot (in both examples) is $\phi_2 = \phi_1 + \pi$.

Figure 9 shows the error on the estimated peak-height ratios and inferred latitudes as a function of the phase difference between the two spots rotating with equal velocities (for the same latitudes of Fig. 8, L_1 = 40° and L_2 = ±40°). Clearly, for certain phase differences the inferred latitudes and peak-height ratios would be far from the true values. The results in both Figs. 8 and 9 thus confirm that caution is needed when using the analysis of light curves showing evidence of spots rotating in anti-phase.

[1] If the spots have the same size and latitude, the modulations produced by each spot will have equal amplitude. In this case, the signature of the two spots rotating in anti-phase would be equivalent to the modulation of one spot rotating two times faster than the rotation period. This means that one would retrieve half of the rotation period.

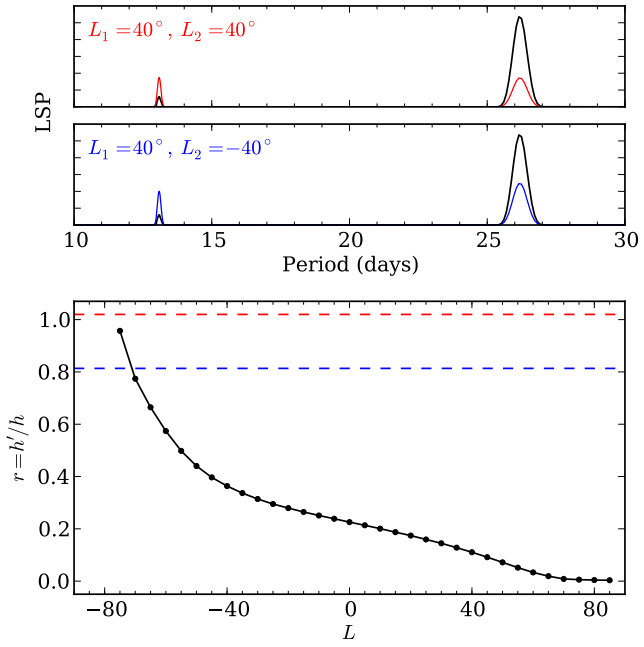

Fig. 8. *Top and middle panels*: Lomb-Scargle periodogram of two synthetic light curves whose modulation is produced by two spots rotating with equal velocity and in anti-phase. In the first example (red) both spots are on the northern hemisphere, while in the second panel (blue) the spots are on opposite hemispheres. The black line corresponds to the reference case of one spot at $L_1 = 40^\circ$. *Bottom*: comparison between the peak-height ratios recovered from the top and middle panels (red and blue, respectively) and the reference ratios for $i = 70^\circ$ (black).

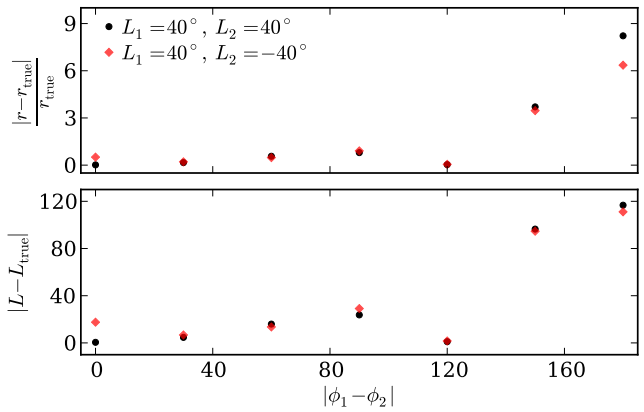

Fig. 9. Error on the peak-height ratios (*top*) and latitudes (*bottom*) as a function of the phase difference between two spots rotating with equal velocity, both on the northern hemisphere (black) and on opposite hemispheres (red). The reference case corresponds to one spot at $L = 40^\circ$ (see Fig. 8).

5. Conclusions

The main goal of this work was to understand under what conditions the spot modulation on the light curve and its signature on the periodogram can provide insights into the latitudinal distribution of starspots and, consequently, into stellar surface differential rotation. In particular, we studied the dependence of the peak-height ratios, computed from the periodogram, on the spot and stellar parameters.

We found that the peak-height ratios depend essentially on the fraction of time the spot is visible. Spots that are visible for a longer time compared to $P_{\rm rot}$ produce smaller ratios than spots that are visible for a shorter time. In turn, the spot visibility time depends more significantly on the stellar inclination angle and spot latitude.

Our results from one-spot and two-spot simulations show that the method proposed by Reinhold & Arlt (2015) provides the wrong sign of surface differential rotation when the following conditions are met:

- $i \neq 90^\circ$ and the peak-height ratios are associated with spots on the opposite hemisphere of the observer;
- $i \neq 90^\circ$, one of the spots (spot 1) is on the opposite hemisphere while the second spot (spot 2) is on the same hemisphere of the observer and $|L_1| > |L_2|$;
- the peak-height ratios are related to spots rotating with similar velocities and nearly in anti-phase.

Moreover, for low inclinations, the peak-height ratios become saturated as a result of spots being always visible for a wide range of latitudes. Also, for $i = 90^\circ$ the peak-height ratios are almost constant. In these cases, attributing a latitude to each rotation period and determining the sign of differential rotation will be difficult.

Despite the degeneracy between stellar inclination angle and spot latitude, we find that the peak-height ratios provide a simple and fast way to constrain these parameters. This is a clear advantage of this method in comparison with other time consuming methods (e.g. Mosser et al. 2009; Huber et al. 2010; Walkowicz et al. 2013; Lanza et al. 2014) where the inclination, spot latitude, area, and intensity contrast may be strongly degenerated. Moreover, if the inclination angle is known, the peak-height ratios can constrain the latitudinal distribution of spots.

The spot signature on the light curves depends on a number of stellar and spot properties, such as the stellar surface rotation, limb-darkening law, spot size, and intensity contrast. We have investigated how the peak-height ratios depend on those parameters. We found that the effect of the spot size and limb-darkening on the peak-height ratios is small but not negligible.

We have also shown that when two rotation periods are successfully recovered, the conclusions taken from the one-spot simulations are also valid for two-spot simulations. Moreover, although the relative size of the spots (for two-spot simulations) affects the ratios, the effect is in general not strong enough to lead to an incorrect inference of the sign of differential rotation.

We have not considered spot evolution, which is beyond the scope of this study. However, we note that the multiple peaks in the periodogram can also result from spot evolution (e.g. Lanza et al. 2014; Aigrain et al. 2015; Reinhold & Gizon 2015; Nagel et al. 2016). For stars showing evidence of long-lived spot/active regions that induce stable signals, the LSP and the peak-height ratios will be less affected by the spot evolution. The analysis of different subseries of the full light curve may also help in discriminating between periodic (or quasi-periodic) signals related to the stellar rotation and those resulting from other sources.

Finally, we note that there is an observational bias, which contributes to the small number of false-positives reported in Reinhold & Arlt (2015): the modulation induced by spots on the same hemisphere as the observer will be preferentially observed in comparison with spots on the opposite hemisphere, in particular for small inclination angles.

Acknowledgements. This work was supported by Fundação para a Ciência e a Tecnologia (FCT) through national funds (UID/FIS/04434/2013) and by FEDER

through COMPETE2020 (POCI-01-0145-FEDER-007672). A.R.G.S. acknowledges the support by the fellowship SFRH/BD/88032/2012 funded by FCT (Portugal) and POPH/FSE (EC), and from the University of Birmingham. M.S.C. and P.P.A. acknowledge support from FCT through the Investigador FCT Contracts Nos. IF/00894/2012 and IF/00863/2012. R.A.G. acknowledges the support of the GOLF and PLATO grants. S.M. would like to acknowledge support from NASA grants NNX12AE17G and NNX15AF13G and NSF grant AST-1411685. The research leading to these results has received funding from EC, under FP7, through the grant agreement FP7-SPACE-2012-312844 (SPACEINN) and PIRSES-GA-2010-269194 (ASK). A.R.G.S., M.S.C., and P.P.A. are grateful for the support from the High Altitude Observatory (NCAR/UCAR), where part of the current work was developed.

References

Aigrain, S., Llama, J., Ceillier, T., et al. 2015, MNRAS, 450, 3211
Ballot, J., Gizon, L., Samadi, R., et al. 2011, A&A, 530, A97
Claret, A. 2000, A&A, 363, 1081
Distefano, E., Lanzafame, A. C., Lanza, A. F., Messina, S., & Spada, F. 2016, A&A, 591, A43
Eker, Z. 1994, ApJ, 420, 373
García, R. A., Ballot, J., Mathur, S., Salabert, D., & Regulo, C. 2010, ArXiv e-prints [arXiv:1012.0494]
García, R. A., Ceillier, T., Salabert, D., et al. 2014, A&A, 572, A34
Huber, K. F., Czesla, S., Wolter, U., & Schmitt, J. H. M. M. 2010, A&A, 514, A39
Lanza, A. F., Rodono, M., & Zappala, R. A. 1993, A&A, 269, 351
Lanza, A. F., Rodonò, M., Pagano, I., Barge, P., & Llebaria, A. 2003, A&A, 403, 1135
Lanza, A. F., Bonomo, A. S., Pagano, I., et al. 2011, A&A, 525, A14
Lanza, A. F., Das Chagas, M. L., & De Medeiros, J. R. 2014, A&A, 564, A50
Mathur, S., García, R. A., Catala, C., et al. 2010, A&A, 518, A53
Mathur, S., García, R. A., Ballot, J., et al. 2014, A&A, 562, A124
McQuillan, A., Aigrain, S., & Mazeh, T. 2013a, MNRAS, 432, 1203
McQuillan, A., Mazeh, T., & Aigrain, S. 2013b, ApJ, 775, L11
McQuillan, A., Mazeh, T., & Aigrain, S. 2014, ApJS, 211, 24
Mosser, B., Baudin, F., Lanza, A. F., et al. 2009, A&A, 506, 245
Nagel, E., Czesla, S., & Schmitt, J. H. M. M. 2016, A&A, 590, A47
Nielsen, M. B., Gizon, L., Schunker, H., & Karoff, C. 2013, A&A, 557, L10
Reinhold, T., & Arlt, R. 2015, A&A, 576, A15
Reinhold, T., & Gizon, L. 2015, A&A, 583, A65
Reinhold, T., & Reiners, A. 2013, A&A, 557, A11
Reinhold, T., Reiners, A., & Basri, G. 2013, A&A, 560, A4
Sing, D. K. 2010, A&A, 510, A21
Snodgrass, H. B. 1983, ApJ, 270, 288
Snodgrass, H. B., & Ulrich, R. K. 1990, ApJ, 351, 309
Sofia, S., Schatten, K., & Oster, L. 1982, Sol. Phys., 80, 87
Walkowicz, L. M., Basri, G., & Valenti, J. A. 2013, ApJS, 205, 17